NIST Special Publication 949

Ninth International Conference on Computer Technology in Welding

T. Siewert
C. Pollock
Editors

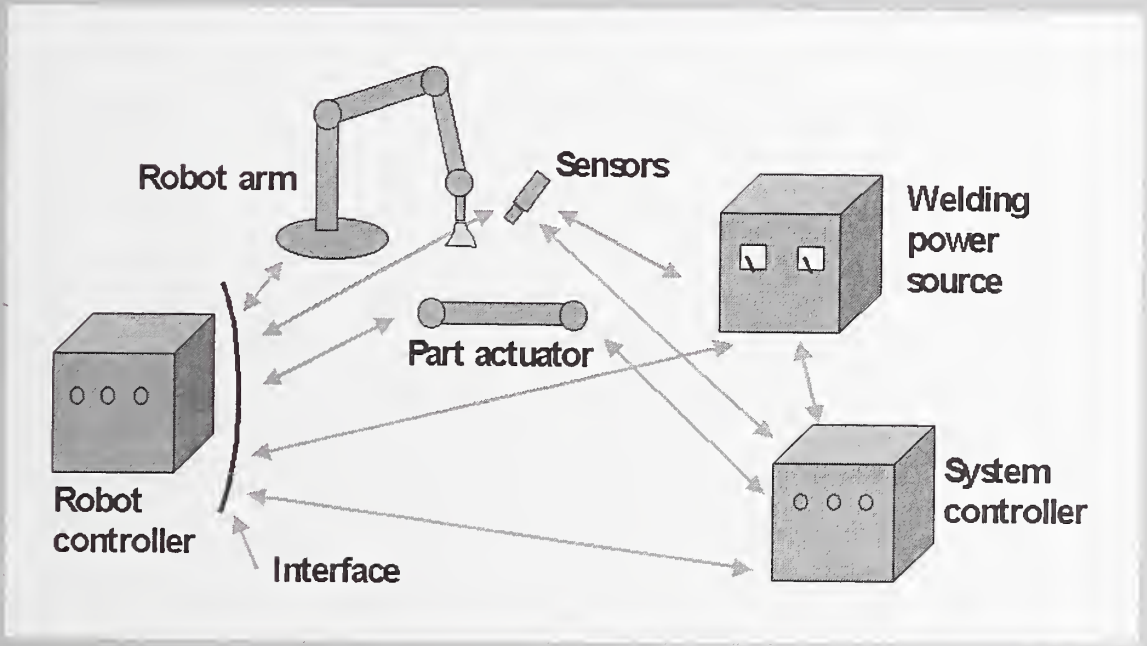

National Institute of Standards and Technology • Technology Administration • U.S. Department of Commerce

The National Institute of Standards and Technology was established in 1988 by Congress to "assist industry in the development of technology . . . needed to improve product quality, to modernize manufacturing processes, to ensure product reliability . . . and to facilitate rapid commercialization . . . of products based on new scientific discoveries."

NIST, originally founded as the National Bureau of Standards in 1901, works to strengthen U.S. industry's competitiveness; advance science and engineering; and improve public health, safety, and the environment. One of the agency's basic functions is to develop, maintain, and retain custody of the national standards of measurement, and provide the means and methods for comparing standards used in science, engineering, manufacturing, commerce, industry, and education with the standards adopted or recognized by the Federal Government.

As an agency of the U.S. Commerce Department's Technology Administration, NIST conducts basic and applied research in the physical sciences and engineering, and develops measurement techniques, test methods, standards, and related services. The Institute does generic and precompetitive work on new and advanced technologies. NIST's research facilities are located at Gaithersburg, MD 20899, and at Boulder, CO 80303. Major technical operating units and their principal activities are listed below. For more information contact the Publications and Program Inquiries Desk, 301-975-3058.

Office of the Director
- National Quality Program
- International and Academic Affairs

Technology Services
- Standards Services
- Technology Partnerships
- Measurement Services
- Information Services

Advanced Technology Program
- Economic Assessment
- Information Technology and Applications
- Chemistry and Life Sciences
- Materials and Manufacturing Technology
- Electronics and Photonics Technology

Manufacturing Extension Partnership Program
- Regional Programs
- National Programs
- Program Development

Electronics and Electrical Engineering Laboratory
- Microelectronics
- Law Enforcement Standards
- Electricity
- Semiconductor Electronics
- Radio-Frequency Technology[1]
- Electromagnetic Technology[1]
- Optoelectronics[1]

Materials Science and Engineering Laboratory
- Intelligent Processing of Materials
- Ceramics
- Materials Reliability[1]
- Polymers
- Metallurgy
- NIST Center for Neutron Research

Chemical Science and Technology Laboratory
- Biotechnology
- Physical and Chemical Properties[2]
- Analytical Chemistry
- Process Measurements
- Surface and Microanalysis Science

Physics Laboratory
- Electron and Optical Physics
- Atomic Physics
- Optical Technology
- Ionizing Radiation
- Time and Frequency[1]
- Quantum Physics[1]

Manufacturing Engineering Laboratory
- Precision Engineering
- Automated Production Technology
- Intelligent Systems
- Fabrication Technology
- Manufacturing Systems Integration

Building and Fire Research Laboratory
- Applied Economics
- Structures
- Building Materials
- Building Environment
- Fire Safety Engineering
- Fire Science

Information Technology Laboratory
- Mathematical and Computational Sciences[2]
- Advanced Network Technologies
- Computer Security
- Information Access and User Interfaces
- High Performance Systems and Services
- Distributed Computing and Information Services
- Software Diagnostics and Conformance Testing
- Statistical Engineering

[1] At Boulder, CO 80303.
[2] Some elements at Boulder, CO.

NIST Special Publication 949

Ninth International Conference on Computer Technology in Welding

T. Siewert
Mateirlas Reliability Division
Materrials Science and Engineering Laboratory
National Institute of Standards and Technology
Boulder, CO 80303-3328

C. Pollock
American Welding Society
Miami, FL 33126

Sponsored by
American Welding Society
The Welding Institute
National Institute of Standards and Technology

May 2000

U.S. Department of Commerce
William M. Daley, Secretary

Technology Administration
Dr. Cheryl L. Shavers, Under Secretary of Commerce for Technology

National Institute of Standards and Technology
Raymond G. Kammer, Director

National Institute of Standards and Technology Special Publication 949
Natl. Inst. Stand. Technol. Spec. Publ. 949, 523 pages (May 2000)
CODEN: NSPUE2

U.S. GOVERNMENT PRINTING OFFICE
WASHINGTON: 2000

For sale by the Superintendent of Documents
U.S. Government Printing Office
Washington, DC 20402-9325

CONTENTS

Preface

This is the proceedings of the ninth conference in this series. It was held September 28 to 30, 1999 in Detroit, Michigan, under the sponsorship of the American Welding Society, NIST, and The Welding Institute. There were 57 papers grouped into sessions on resistance weld simulation, simulation of gas metal arc welding, modeling of weld shape and distortion, modeling of solidification, general modeling, welding documentation, sensing and control of arc quality, droplet control and process automation, automation communication and interfaces, and documentation and database applications. The large number of papers required the papers to be divided into two parallel tracks: a modeling track, and a sensing and control track. In addition, there were tutorials on weld cell communication issues and on web page design. This proceedings includes the 39 printed manuscripts that were submitted (including the viewgraphs from the two tutorials. Additional copies are available from NTIS (National Technical Information Service) or GPO as NIST Special Publication 949.

The first U.S. workshop on computerization of welding data was held in 1986, under the sponsorship of the American Welding Institute (AWI) and the then National Bureau of Standards (now, National Institute of Standards and Technology—NIST). The workshop produced a list of national needs in welding data, a list designed to guide database developers. The proceedings of that first workshop are available from NTIS as NIST Special Publication 742.

There had been sufficient advances in database activity by 1988 to justify a second meeting, this time as a joint workshop–conference under the sponsorship of AWI, NIST, and the American Welding Society (AWS). The scope was expanded to include a conference on the latest developments and a preconference tutorial to provide novices with a background in common computer applications. The conference was attended by 61 managers, welding engineers, and computer professionals. The proceedings of the workshop and conference are available from NTIS as NIST Special Publication 781.

By 1990, the welding database activity had grown large enough to justify another conference on this topic, again sponsored by AWI, AWS, and NIST. It consisted of a series of tutorials, a keynote presentation, and technical sessions on the topics: off-line planning, real-time welding information, data systems and standards, and industrial applications. The conference included demonstrations of welding software, and was followed by a meeting of the AWS Committee on Computerization of Welding Data.

The fourth conference, held during November 1992 in Orlando, Florida, was truly an international conference; speakers representing 10 countries presented papers on the topics of standards, applications, quality and NDE, sensing, control, and databases. Once again, a preconference tutorial was organized and taught by AWI personnel covering PC networks, expert systems, neural networks, Windows and the Excel Spreadsheet, and databases. The conference also included a keynote presentation, tabletop exhibits, and hands-on demonstrations of welding software. The AWS Committee on Computerization of Welding Data met following the Conference. These proceedings are available from AWS (Code: CP-1192).

The fifth conference, held August 1994 in Golden, Colorado, continued the trend of growth in size and scope. It consisted of 31 papers (by 69 authors) on the topics of quality control, off-line planning and simulation, commercial software systems, control and automation, welding optimization, data acquisition and sensors, application case studies, welder and procedure qualification systems, weld prediction and control, and large-scale systems. This year the preconference tutorials were on the topics of computing platforms, sensing and data acquisition, and line planning for welding automation. These tutorials were taught by experts from AMET, NIST, CSM, Ford Research Laboratory, and ABB Robotics. The conference was cosponsored by AWS, the Colorado School of Mines, NIST, and AWI. The conference proceedings are available from AWS (code: CP-794).

The sixth conference was held June 9-12, 1996, in the 'Heart of Europe,' where Belgium, Germany, and the Netherlands converge in the Limberg region. The Technical Program was aimed to embrace all known facets of computing practice as applied to welded fabrication and manufacturing. Expert advice was provided in process selection, consumable selection, and welding procedure generation and interpretation of standards. Proceedings are available through Woodhead Publishing Ltd. (see below).

The seventh conference was held July 8-12, 1997, in San Francisco, California, and was presented in conjunction with the American Welding Society, The Welding Institute and the National Institute of Standards and Technology. Attendees were able to observe how computers can be used for more than just databases. In addition to tutorials, the following were covered: case studies, controls and controllers, sensing, process automation, modeling heat and fluid flow, modeling thermomechanical effects, and modeling residual stress or mechanical effects. Also covered were the Internet and networked systems in the welding industry. Additional copies of the proceedings are available from NTIS as NIST Special Publication 923.

The eighth conference was held June 22 to 24, 1998 in Liverpool, U.K., and was sponsored by The Welding Institute. The significant advances in technologies such as expert systems, neural networks, and the internet, were highlighted in tutorial sessions. The 35 papers were grouped into sessions on: sensors/vision, modeling and control, modeling of process and joint properties, modeling and simulation, education and training, and quality control and quality assurance.

To order the NIST Special Publications, contact:

Superintendent of Documents
Government Printing Office
Washington, DC 20402
(202) 512-1800
http://www.access.gpo.gov/

or

National Technical Information Service
Springfield, VA 22161
(703) 487-4650
http://www.ntis.gov/

To order the 1992 and 1994 proceedings, contact:

Order Department
American Welding Society
550 N.W. LeJeune Road
Miami, Florida 33126
(800) 334-9353 (or (305) 443-9353, Ext. 280)

To order the 1996 or 1998 proceedings, contact:

Woodhead Publishing Ltd.
Abington Hall, Abington
Cambridge CB1 6AH
England
+44(0)1223 891358

Acknowledgment: The editors wish to express their appreciation to those who helped run the conference and to prepare these proceedings: Gladys Santana, Marilyn Levine, and Martica Ventura, American Welding Society, and Vonnie Ciaranello, National Institute of Standards and Technology.

Session A1: Resistance Welding Simulation

REAL TIME VISUALIZATION OF WELDING STATE IN SPOT WELDING

K. Matsuyama*

ABSTRACT

A high-speed numerical simulation algorithm was developed to establish a phenomenon-based quality monitoring/state sensing system for resistance spot welds. The system can show temperature distribution patterns in weld part and in electrode tips besides the information on the weld size. In the system, contact diameters at electrode-plate interfaces and at faying surfaces are estimated with dynamic resistance values between electrode tips to calculate the current distribution in workpieces. Then, the temperature distribution is computed by a new scheme with finite differential method (FDM). The calculations are repeated at every short welding period during each welding to simulate the nugget formation process on computer memories. Then the computation speed has been remarkably improved by using a pre-calculated chart for estimation of the current distribution in workpieces, and by improving the CPU speed with a new personal computer, so that a real time quality monitoring system has been realized even by using a numerical simulation algorithm. In the present report, the procedure how to improve the calculation speed without reducing the accuracy.

INTRODUCTION

Recently, many reports regarding neural networks have been presented to estimate and evaluate the weld quality without non-destructive tests (Ref.1-4). The author has also investigated the neural network leaning system, and reported it two years ago (Ref. 5). The Neuro-Fuzzy technique is remarkably effective to shorten the treatment time, so that the system can easily apply to real time quality monitoring and control systems because the equations used for estimation are quite simple after learning, and there is no difficulty to learn the relation with experimental data.

The learning results, however, only apply to estimation only for direct measured results. This means that the procedure only apply to the estimation of weld size and/or weld strength if the teaching was achieved for the parameters.

On the contrary, the phenomenon-based simulation with mathematical model can give results of not only weld sizes but also temperature distributions and its heat cycle although longer treatment time is required than that with the Neuro-Fuzzy system. If the treatment speed could be improved, these temperature information is useful and helpful to control the welding process, estimate cooling rate of the spot welds, optimize weld condition in real time and so on.

The original three-dimensional model, however, needs 30 to 60 min for the treatment with an old type of personal computer implemented Intel i80386/80387 which is a latest one at that time. The system can be applied not only for zinc-coated steel sheets (Ref.6-7) but also aluminum alloy ones (Ref. 8). So, the author has closely considered the governing factors and processes of the

* MIT, Mechanical Engineering Dept., 77 Massachusetts Ave., Room 35-237, Cambridge. MA 021 39, USA

welding phenomena in resistance spot welding. Then, the procedure has been improved and optimized for realizing a real time working system as a virtual welding machine with the numerical simulator concept.

Then, a new real time working system was realized to estimate nugget formation process with a latest type of personal computer implemented a Pentium CPU, where the two monitoring parameters of welding current and welding voltage are measured as the input data. An application as an adaptive control system of welding condition has been reported at the last AWS conference to suppress expulsion occurrence and reduce welding power input (Ref.9). In the present paper, the principle of the high-speed calculation system, its algorithm and the adaptability have been described with some experimental data.

KEYWORDS

Resistance spot welding, Quality monitoring, Numerical simulation, Real time monitoring, Phenomenon model, Heat conduction equation.

PRINCEPLE OF THE ORIGINAL MONITORING SYSTEM WITH A THREE-DIMENTIONAL MODEL AND ITS PROBLEM

Original phenomenon-based quality monitoring and state sensing system (Ref.7) had been developed as a three-dimensional model based on a fully simulation procedure reported at the 7th international conference on computer technology in welding (Ref.10). In the phenomenon-based system, the contact diameters at plate-electrode interfaces and at faying surface were estimated with the dynamic resistance curve deduced by the calculation with dynamic voltage between tips and welding

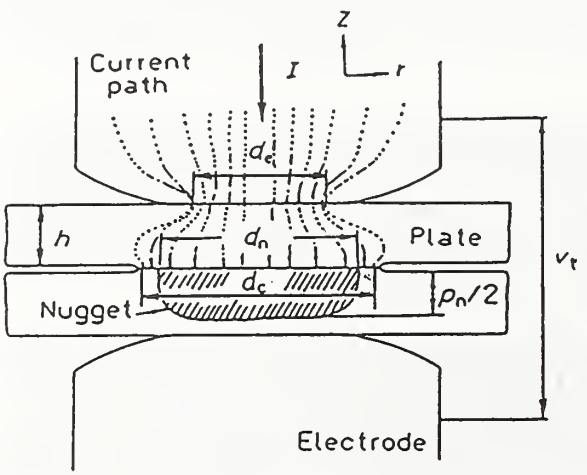

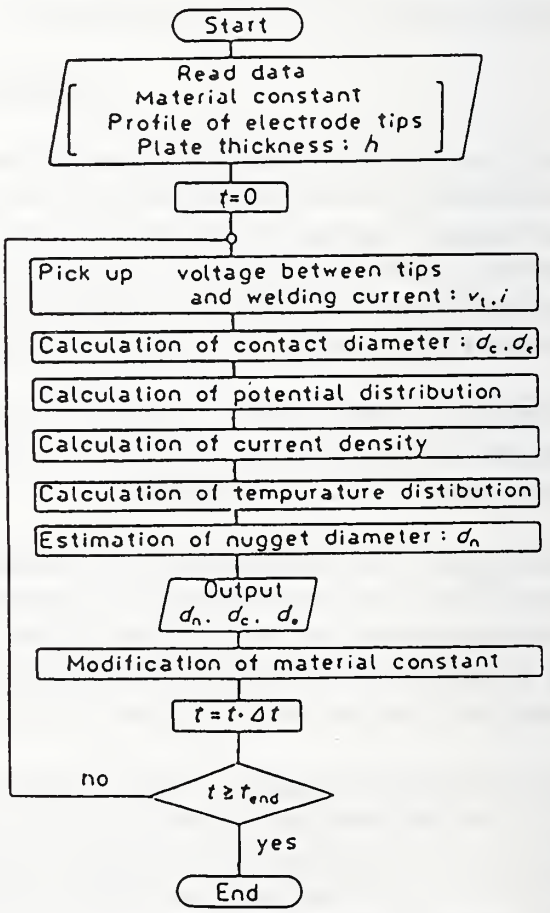

(a) Definition of the weld part (b) A flow chart to simulate the welding process

Fig. 1 A quality monitoring system with three-dimensional numerical simulator

current wave forms which are measured through A/D converter mounted into a personal computer. The calculations of the current distribution and temperature rise in the workpieces and electrode tips have been achieved with the same algorithm used in the fully numerical simulation procedure for the nugget formation process by using a flow stress model described in the above document (Ref. 10). The flowchart and some definition of the parameters used are shown in Fig. 1.

Welding voltage and welding current are measured as the input data to get the dynamic resistance curve. Then, contact diameters are estimated in an idea of that the contact diameter de can be decided with the dynamic resistance value and resistivity of weld part yielded by temperature distribution in the weld part under an assumption that the difference between "dc" and "de" is constant (Ref.11). After that, potential distribution within the workpiece and the electrode tips is calculated by a finite differential method based on the Laplace equation described in Eqs. (1) and (2) to get the current distribution. Then, temperature rise within the workpiece and the electrode tips is computed by another finite differential method deduced from the thermal conductance equation shown in Eq, (3) by the Crank-Nicolson method.

$$\nabla (\kappa \nabla V) = 0 \tag{1}$$

κ : Electric conductivity (S/cm)
V : Electric potential (V)

$$\delta = |\kappa \, \mathrm{grad}\ V| \tag{2}$$

δ : Current density (A/cm^2)

$$C \sigma \frac{\partial T}{\partial t} = \nabla(K \nabla T) + \rho \delta^2 \tag{3}$$

K : Thermal conductivity (J/s·cm·K)
C : Specific heat (J/g·K) δ : Current density(A/cm^2)
T : Temperature (°C) σ : Density (g/cm^3)
ρ : Electric resistivity ($\mu\Omega$·cm) t : Time (s)

The nugget formation process is estimated by repeating the above procedure in each short welding period Δt. Typical monitoring results with the above three-dimensional model are shown in Fig.2. In the present cases, the time period Δt was setup in quarter cycle of power line frequency.

Fig.2 (a) shows relationships between the estimated and experimental results where zinc coated steel sheets were used for the test piece. The monitoring system works well not only for new electrode tips but also for used tip condition after 2000 welds. The system with the fully three-dimensional model is applicable to the case of that there is shunting current flowing into the pre-spot welds as shown in Fig. 2 (b). The monitoring results and the measured ones have a good agreement with each other within a small error less than $0.5\sqrt{t}$ (t: plate thickness in mm unit).

The system, however, has a demerit that needs long duration to get monitoring results. For example, if an old personal computer machine implemented the Intel i80386/i80387 CPUs that run in 33MHz of front bus speed was used for the calculation, 30 to 60 min of calculation time was

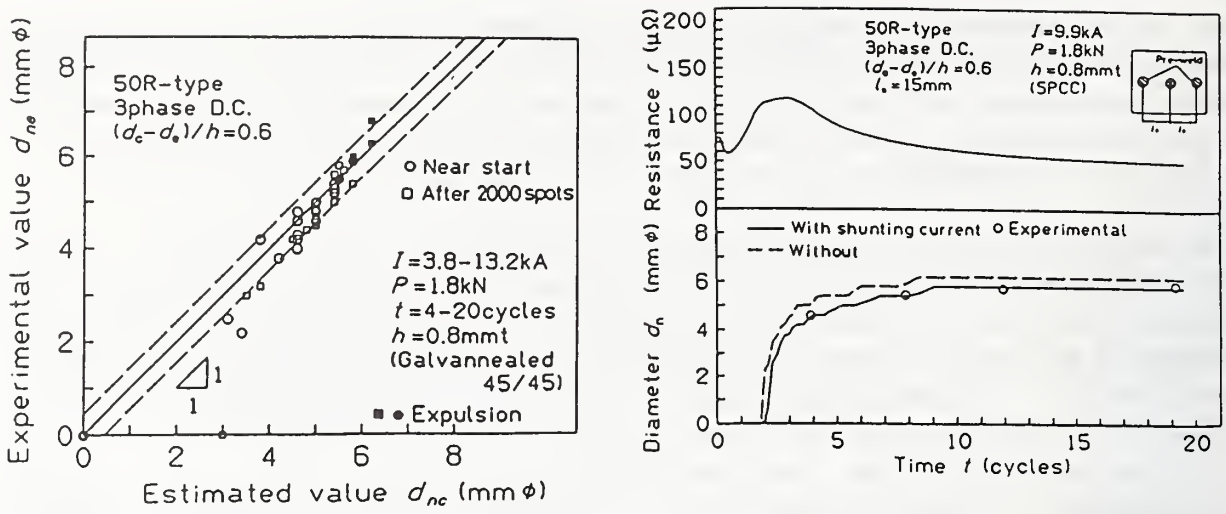

(a) (b)

Fig. 2 Adaptability of a phenomenon-based quality monitoring system with numerical simulator

needed to get the monitoring results. Even if a latest CUP one would be hired for the calculation, the time is remarkably improved but the value is longer than 30 s. This means that specification of the original system is not sufficient to use for the real time monitoring system. It is only effective for researches to understand what phenomena occurs during welding. So, the author has tried to make a new high-speed version with the same concept of using numerical simulator in order to get temperature information beside the nugget size one.

EXAMINATION OF THE PROCEDURE TO REALIZE A HIGH SPEED VERSION

In the above three-dimensional model, much time has been spent for the estimation of contact diameters and current distribution, and the calculation of the temperature rise in electrode. So, these routines were examined to shorten the treatment time.

Routine for the current distribution in workpiece

The current distribution pattern along radial direction can be calculated with the three-dimensional model as shown in Fig.3 (a). The calculation was carried out where the contact diameter "de" at electrode-plate interface and "dc" at faying surface are equal, and plate thickness "h" is 0.8mm. The solid line indicates the distribution pattern across the faying surface or electrode-plate interface. The broken line shows the calculated result across mid plane in each stacked plate. The ordinate indicates a non-dimensional current density divided by a value defined in the figure. The abscissa corresponds to the radius from the center axis of electrode tips.

Both lines almost coincide with each other because the plate thickness of workpiece in resistance spot welding is relatively thin if the value would be compared with the contact diameters dc or de. Such a feature can be also recognized in another setting conditions. This suggests that the current density along the plate thickness direction could be supposed not to change in workpieces along thickness direction. It also means that the deviation can be supposed to be negligible for the estimation of contact diameters and the calculation of temperature rise, if adequate correction factor could be given for estimation of the current density in the weld part.

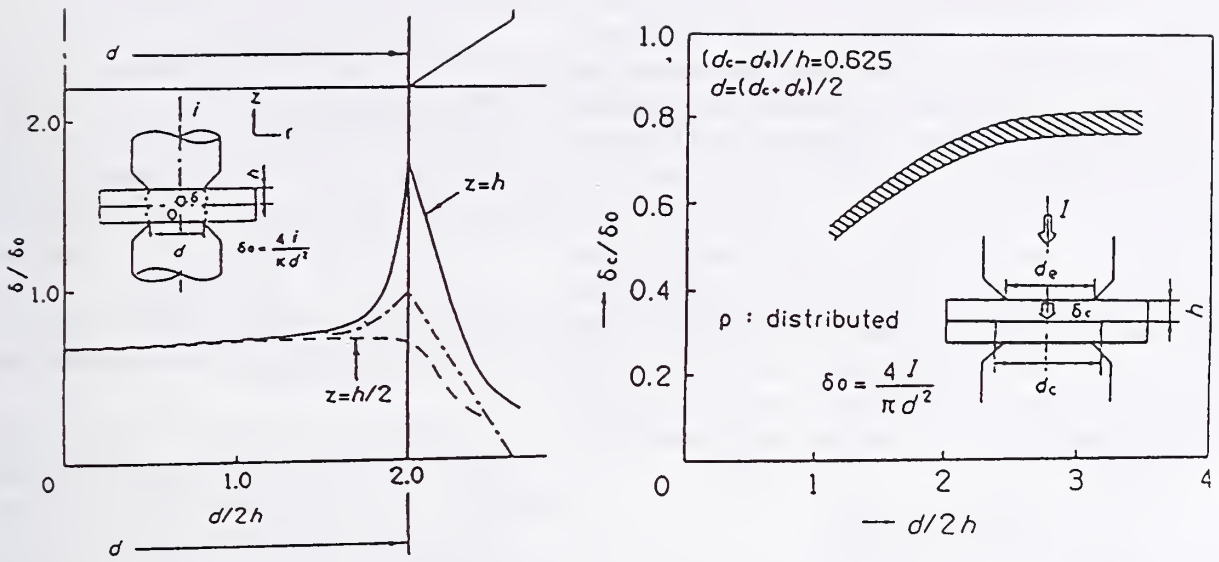

Fig. 3 Estimation of current density with a pre-calculated chart to improve the simulation speed

The examined results for evaluation of the correction factors are shown in Fig. 3 (b). The calculations were carried out in various contact diameter and various temperature distribution conditions in order to find the fringing effect and some influences of resistivity distribution in the weld part. Moreover, in the calculation it was defined that the dc is larger then the de, and the difference is constant that is 0.625 times of plate thickness. The ratio is normal in the contact condition for resistance spot welding bare steel sheets. Those calculated results are plotted as hatched zone in the figure. The ordinate also indicates the non-dimensional current density at the center of weld, and the abscissa displays a non-dimensional contact diameter d/2h. The value "d" was defined with an equation; d = (dc+de)/2.

There is a good correlation between the mean contact diameter d and the non-dimensional current density δ/δ_0. This suggests that the current density in welding zone can be simply estimated with the midpoint of the hatched zone as a function of the mean contact diameter, so that it could be realized to reduce the treatment time remarkably. This means that the procedure with the finite differential method for computation of the potential distribution within workpiece and electrode tips can be omitted from the flowchart shown in Fig. 1.

Routine for the temperature rise in electrode tip

The outer size of electrode tip is larger than the weld size. For example, in case of making a nugget of 5 mmϕ for 0.8mm thickness steel sheets, big outer diameter electrode tips of 16 mmϕ to 19 mmϕ are usually used, and the cooling end length is longer than 10 mm. The latter value of length is more than 5 to 10 times of the plate thickness for the automotive body. Then, it seems to be effective to reduce the calculation time if the mesh number in electrode tips could be decreased because the calculation time increases to be proportional to three powers of mesh numbers.

So, an equivalently one-dimensional model shown in Fig. 4 (a) was employed to reduce the calculation time remarkably. In order to guarantee the calculated accuracy, the thermal conductivity of electrode material has been modified to get same temperature distribution in spite of the deference of electrode profiles for calculation as an actual shape.

The examined results regarding the cooling end position and modification of the coefficient against the actual thermal conductivity were shown in Fig. 4 (b) and Fig. 4 (c). The consideration was done by the comparison between the calculated results with the three-dimensional model and with the one-dimensional

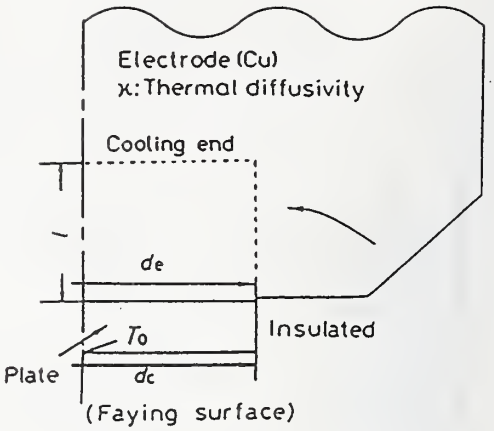

(a)

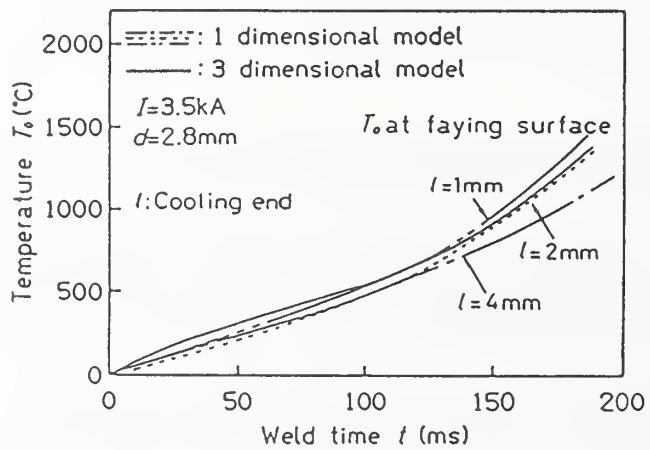

(b)

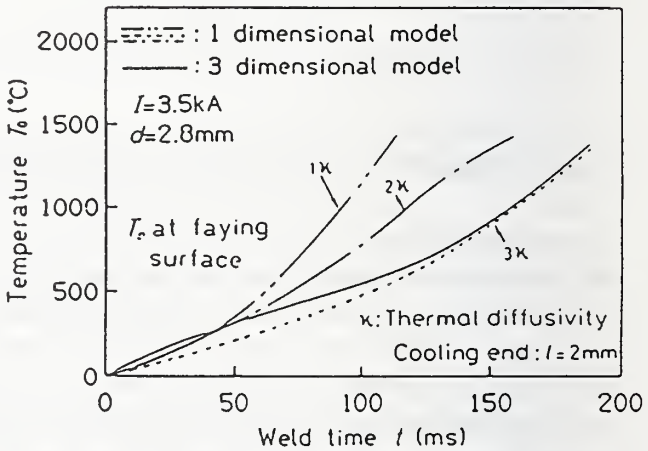

(c)

Fig. 4 Reducing the calculation zone in electrode tips to improve the simulation speed

model. In the present study, suitable values for the one-dimensional model were determined with the calculated temperature results at faying surface. Each solid line in the Fig.4 (b) and Fig.4 (c) indicates the calculated results with the three-dimensional model, and dotted lines, one dotted chain lines and two dotted chain lines are also indicate the calculated results with the new one-dimensional model.

The figures suggest that a high speed version for thin steel sheet can be realized with an equivalently one-dimensional model to estimate the temperature distribution if about 2 mm and three times were chosen as the cooling end length and modified coefficient for the actual thermal conductivity. Such results were similarly recognized in the calculation for another plate thickness cases.

HIGH-SPEED SIMULATION ALGORITHM WITH ONE-DIMENTIONAL MODEL

A new procedure for the high-speed version

It is important to determine what scheme is used for the calculation of temperature rise with the

finite differential method, and how to estimate correct current distribution by the correction because the resistivity remarkably changes as a function of the weld part temperature.

So, the author has developed a new one-dimensional procedure under some considerations where the contact diameter is remarkably larger than the plate thickness, and potential value at electrode-plate interface is almost constant in spite of the surface position, and changes only depending on the welding state. While, the previous idea, that the contact diameter should increase in accordance with softening the weld region, has been kept for an important concept to get highly accurate results.

A mesh system shown in Fig. 5 was used for the calculation of current distribution and temperature rise in workpieces and electrode tips.

The current density is estimated in some assumptions that the value can be calculated with sum of the resistance in each set of the elements along the plate thickness direction, and that the potential at the electrode-plate interface is constant.

The temperature rise at each time step is calculated with a tridiagonal matrix method for the each set of elements located along the plate thickness direction to reduce the computing time. Then, a few elements were arranged in electrode tip to consider the effect of electrode materials and cooling end in electrode. The effect of heat loss toward radial direction has been adjusted by using another calculation along radius direction with the same tridiagonal matrix method.

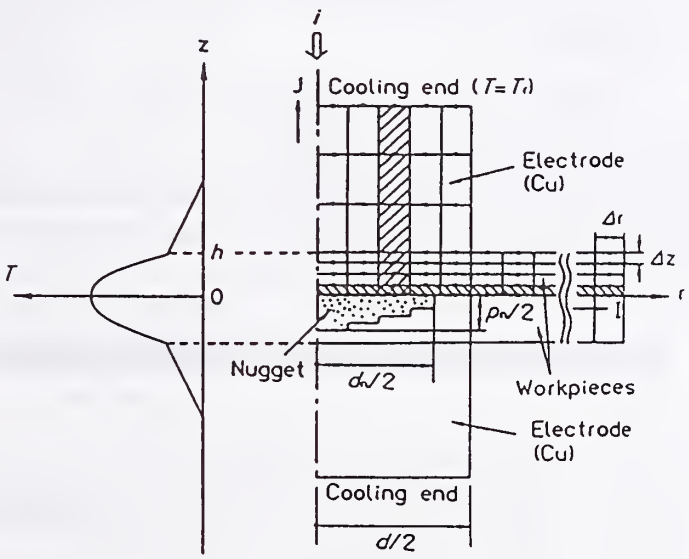

Fig. 5 Mesh system in the high-speed version

The effect of fringing current in the workpiece has been considered by using a modified current distribution pattern as shown with the one-dotted chain line indicated in Fig.3 (a).

Simulation algorithm for the high-speed version

A flowchart for the simulation with new procedures is almost same as that shown in Fig. 1(b). Only details of each routine are modified according to the description in the previous section.

In the new procedure, contact diameters are also estimated with temperature information for previous time step, so that the current distribution is determined from the resistance value of each set of elements located along the z-axis of plate thickness direction. The temperature rise is computed with two step calculation procedure. First, temperature distribution along the z-axis is calculated. Then, the calculated results are adjusted with another calculation along the radial axis.

After both the temperature calculations and a treatment for latent heat, the temperature distribution within workpiece and electrode tips is determined to estimate the nugget size. Thus, the calculations are repeated after modification of the material properties for the workpieces in each time step of the calculation.

Examination of the applicability

A computed result with the new algorithm is shown in Fig. 6. Broken line indicates the result with the high-seed version of one dimensional model. The solid line in the figure indicates a calculated result with the previous three-dimensional model described in the other report (Ref. 6, 7).

Both lines well coincide with each other. This means that the high-speed version can be applicable for estimation of the nugget growth pattern in resistance spot welding.

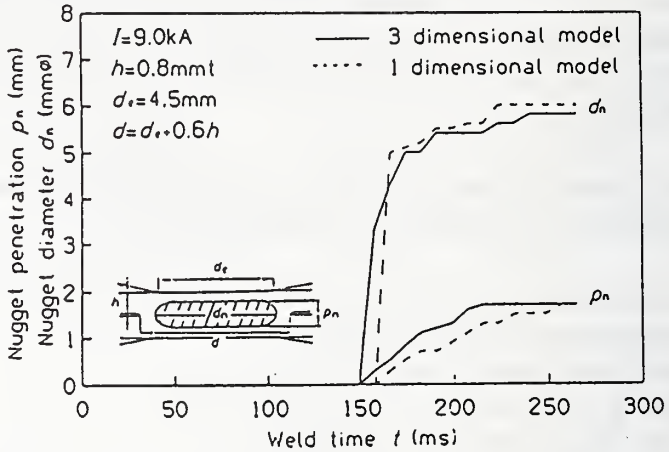

Fig. 6 Comparison of simulated results with the three-dimensional and high speed versions

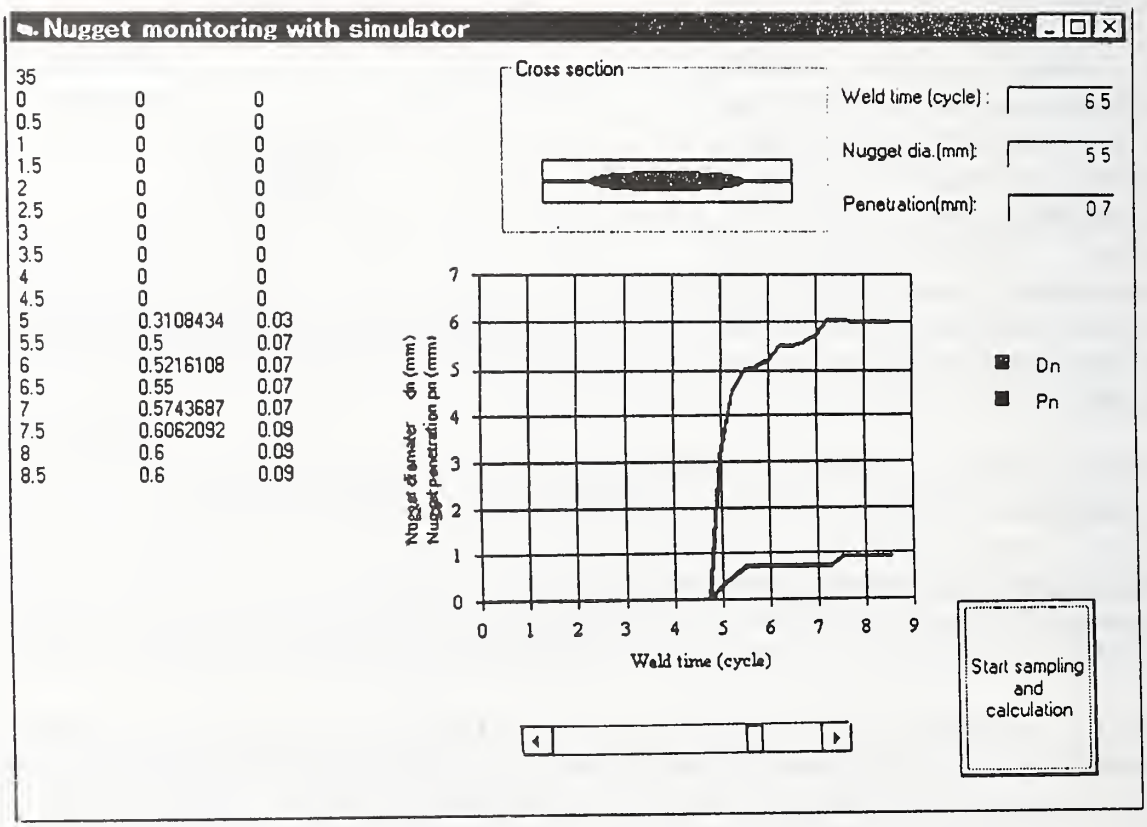

Fig. 7 User interface screen for real time quality monitoring with the high-speed version

In addition, the simulation program has been made as a dynamic link library that can bc linked to any programs run on the Window 95/98. An interface sample with Microsoft visual Basic is shown in the Fig. 7. The program can show input data to the simulation program which was converted from measuring data of welding current and welding voltage during welding, simulated results of nugget formation process, and nugget shape at each time step which can be controlled with a scroll bar appeared on the display. The engine part for simulation as the dynamic link library can be run in almost twice of the actual nugget formation speed. For example, welding of 150 ms can be simulated only in 60 ms with a personal computer mounted Pentium II of 233MHz where the front bus speed is 66 MHz. Of course, the DLL program can give the calculated results of temperature distribution not only in workpieces but also in electrode tips.

ADAPTABILITY OF THE HIGH SPEED VERION

Measuring system of monitoring parameters

A voltage between tips and a welding current are measured for the monitoring parameters. An example of the system is schematically shown in Fig. 8. The welding current was picked up with a non-inductive shunt in the present study. But the value can be also got by a welding current meter with a toroidal coil, which is usually used for the resistance welding current meter. In the present study, the voltage between tips was picked up from both electrode tips although it can be measured at the electrode tip holders. And then, these monitoring parameters were recorded on computer memories through an A/D converter of 12bit type. The sampling rate of A/D converter was setup in 500 Samples/s in the present case to yield the input data for the simulator.

Examination of the adaptability

The adaptability of new algorithm was examined for zinc coated steel sheets with a H.F.D.C. spot welding machine. Dome type specified in JIS (Tip end shape is 6mmϕ, 50mmR) was selected for electrode tips because the shape has been ordinarily used in all Japanese automotive companies. The voltage drop in the electrode tips was corrected as a tip resistance value. The value can be previously measured without workpieces. In the present case, the value was almost 15 μΩ as the

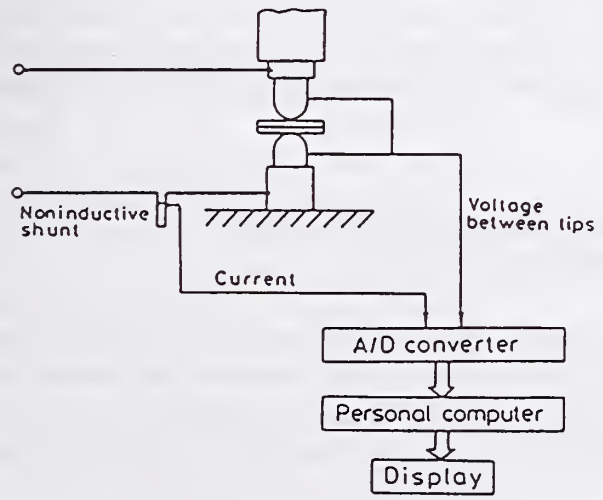

Fig. 8 Sensing system used for the measurement of the welding current and voltage between tips

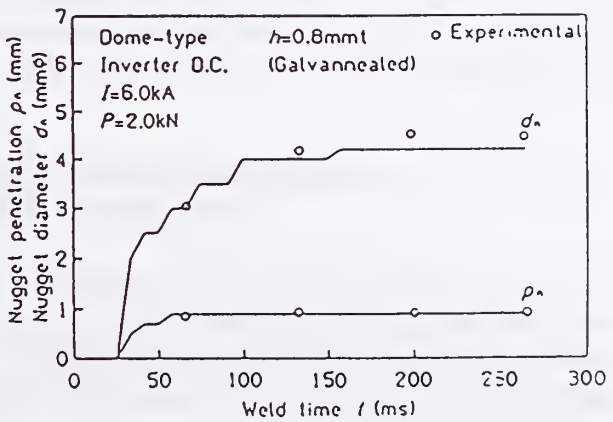

Fig. 9 Adaptability of the high-speed version for nugget size monitoring

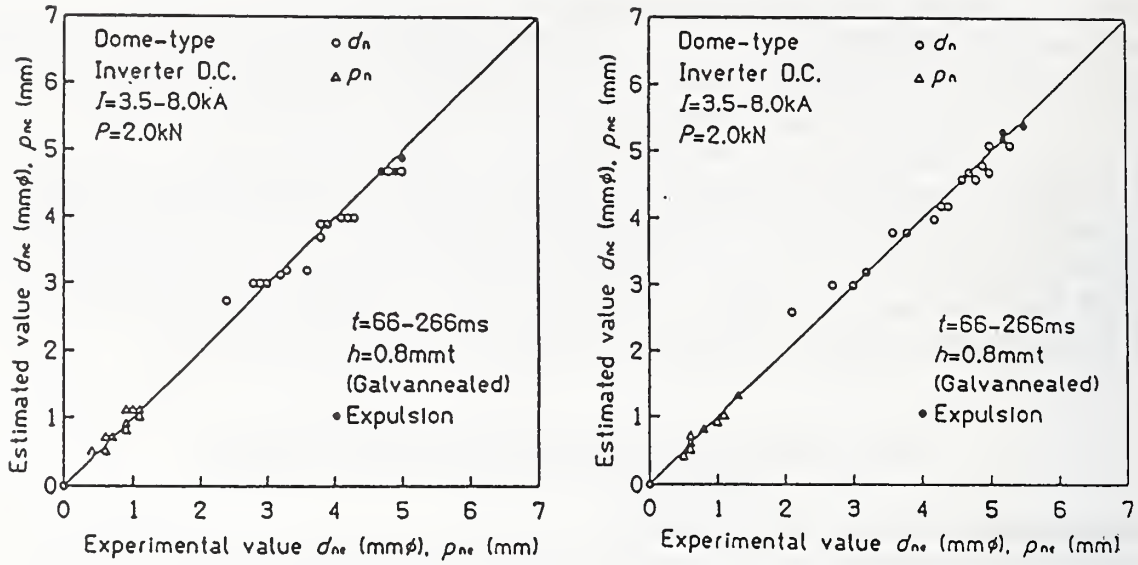

(a) by the high-speed version (b) by the three-dimensional model

Fig. 10 Accuracy of the estimated results by the high-speed version

total correction value of both electrode tips. In addition, 0.25 mm for dr and 0.1 mm for dz were chosen as the mesh sizes in the calculation.

The examined results with the high-speed version are shown in Fig. 9 and Fig.10 (a). Solid lines in the Fig. 9 show the calculated results with the high-speed version. Upper one indicates the nugget diameter, and lower one is penetration depth, respectively. The "o" marks show the measured results from the etched cross section of weld parts, "o" and "Δ" marks in the Fig.10 show the measured results of nugget diameters and penetration depth, respectively. Furthermore, each close mark means that expulsion occurs in the welding condition. Good prediction has been realized with the new algorithm.

Estimated results with the previous three-dimensional model are also shown in Fig.10 (b) with the same input data as used in the high-speed version. Both results show that the accuracy of simulated results with the high-speed version is not inferior than that with the three-dimensional full model. This means that the new high-speed version is applicable for estimation of nugget formation process in the resistance spot welding.

COMPARISON BETWEEN THE NEW SYSTEM AND THE NEURAL NETWORK SYSTEM

The neural network system can be applicable to estimate the weld diameter if the relationships have been taught by an adequate learning system. The neural net works, however, can answer the results only regarding the learning parameters. If the weld diameters are chosen for the output parameter, the system can only estimated the weld diameter, and cannot answer anything about the temperature distribution.

On the contrary, the new monitoring system with a numerical simulator based on the welding

On the contrary, the new monitoring system with a numerical simulator based on the welding phenomena can estimated the temperature and current distributions besides the weld diameters even though the optimization of the system was achieved only by using the weld diameters as the output parameter. This feature caused by that the new system involves a heat conduction equation as the estimation engine. Therefore, the system has a week point that requires higher CUP power than that for the neural network system. The problem, however, has been resolved by using high-speed algorithm described here.

The features are shown in Table 1 comparing the results for neural networks. Most important point is that the new system can give users temperature values in workpieces and electrode tips during welding in real time. Such a property must not realized by using neural networks

Table 1 Comparison between the new system and the neural network system

Items	by simulation technique	by neural network technique
Engine	Numerical simulator	Non-linear equations
Merits	Wide adaptability All phenomena can be estimated	Easily high speed treatment Relatively high accurate estimation
Demerit	High CPU power required Optimization required	Narrow adaptability Teaching process required

Where the new system based on the numerical simulator is installed as the monitoring system, not only the temperature distribution during welding, but also the cooling temperature patterns in the weld part can be estimated only by sensing the welding current and welding voltage wave forms.

A typical result estimated a cooling process is shown in Fig. 11. The marks "o" and "Δ" indicate the estimated temperature values at the center part of a nugget and in the HAZ zone at faying surface of weld part, respectively when two stack plates of 0.8 mm steel sheets were used as the workpieces.

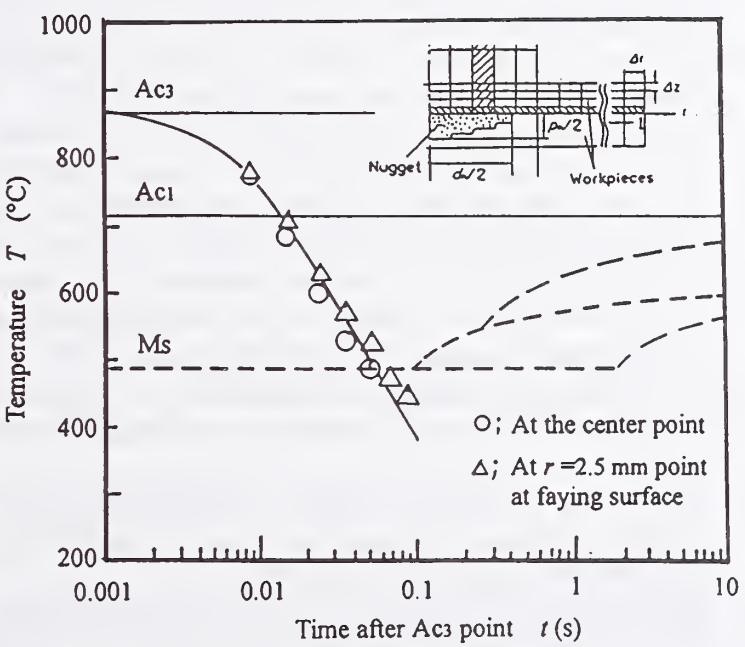

Fig. 11 An example applying to estimation of cooling process by the new monitoring system assisted by a numerical simulator

The data are plotted on a CCT diagram (Ref. 12) after Ac3 point in cooling duration. Both marks are located near one curve, and the estimated results agreed with another research results (Ref.12). This suggests that the system is also applicable to estimate the welding state after current flowing

SUMMARY AND CONCLUSIONS

The treatment time to obtain the simulated results has been remarkably reduced by using the new high-speed version without decreasing the simulated accuracy to realize the real-time quality monitoring with a phenomenon-based system.

The new system can show the temperature distribution in weld part besides the weld nugget size in real time. And it is applicable to estimate the welding state not only in two stack cases, that are usually setup in laboratory, but also in three or four stack cases, which are usually used in automotive works. Furthermore, the system can be also applied to the resistance spot welding aluminum alloy sheets in addition to the steel ones with and without coated zinc on the surface although the details have omitted here because of the limitation of pages described.

REFERENCES

1. M. Jou, R.W.Messle, Jr., C.J.Li; A Fuzzy Logic Control System for Resistance Spot Welding Based on a Neural Network Model, Proc, of Sheet Metal Welding Conference (1994)
2. D.Spinella; Using Fuzzy Logic to Determine Operating Parameters for Resistance Spot Welding Aluminum, Proc. of Sheet Metal Welding Conference (1994)
3. J.D.Brown, C.P.Jobling, N.T.Williams; Optimisation of Signal Inputs to a Neural Network for Modeling Spot Welding of Zinc Coated Steels, IIW, Doc. No.III- 1117-98(1998)
4. G.Monari, O.Dieraert, H.Oberel, G.Dreyfus; Prediction of Spot Welding Diameter using Neural Networks, IIW, Doc. No.III-1108-98(1998)
5. K.Matsuyama; Nugget size sensing of spot weld based on neural network learning. Proc. of Seventh International Conference on Computer Technology in Welding, (1997), pp486-495
6. K. Matsuyama, H. Sato, Y. Nishiu, K. Nishiguchi; Computer-Aided Monitoring System of Nugget formation Process, Proc. of 5WS of JIW in Makuhari, pp577-582(1990)
7. K. MATSUYAM et al.; Model reference type monitoring system to estimate nugget and contact diameters in resistance spot welding (in Japanese), Technical Commission on Joining and Material Processing for Light Structures of JWS, MP-5-88 (1988)
8. K. Matsuyama; Numerical Simulation of Nugget Formation Process in Spot Welding Aluminum Alloys and its Application to the Quality Monitoring, I.I.W., Doc, No. III-1060-96 (1996)
9. M. Ryudou, Y. Gotoh, K. Fujii, K. Matsuyama; Development of Inprocess Control System for Resistance Spot Welding, Proc. of AWS Conference on Resistance Welding; Theory and Applications held in Chicago (1997- 10)
10. K, Matsuyama; Modeling of Nugget Formation Process in Resistance Spot Welding, Proc. of Seventh International Conference on Computer Technology in Welding, (1997), pp435-446
11. NAKANE et al.; A Study on Determination of Suitable Welding Conditions in Spot Welding (in Japanese), J. of the Japan Welding Society, Vol.42(1973), No.3, p50
12. M.V. Li et al.; Analysis of Microstructure Evolution snd Residual Stress Development in Resistance Spot Welds of High Strength Steels, Proc. of SMWC VIII in Detroit, (1998-10)

FINITE ELEMENT MODELING OF RESISTANCE SPOT AND PROJECTION WELDING PROCESSES

W. Zhang and L. Kristensen

ABSTRACT

Based on long time engineering expertise on resistance welding and close collaboration with industry, a unique finite element program, SORPAS, is developed for simulation of resistance projection and spot welding processes. In order to make the program directly applicable by engineers to simulate industrial problems, all the important parameters involved in resistance welding have been considered and implemented into the program. With the specially designed Windows 95/98/NT graphic user interface, engineers (even without prior knowledge of the finite element method) are able to quickly learn and easily operate the program for implementing the practical parameters, running simulations, displaying the simulated results and analyzing the dynamic welding processes. With the four-fold coupling of the electrical, thermal, metallurgical and mechanical models as well as the user-friendly facility for flexible geometric design of workpieces and electrodes, the program can be readily applied for product development or rapid prototyping and process analysis in industry applying resistance welding. After simulation, the dynamic process parameters are graphically displayed. The distributions of temperature, current, stress, strain and strain rate in the materials are displayed in color, which can be animated like a slow-motion video. In the past two years, the program has been extensively verified and applied by engineers in industry and students at universities.

KEYWORDS: Resistance welding, FEM modeling, rapid prototyping, process analysis

INTRODUCTION

Resistance welding including spot welding of metal sheets and projection welding of more complex components is widely applied for joining similar as well as dissimilar metals in various industries, e.g. automotive, aeronautic, electronic and metal working industries. The process is, however, very difficult to understand and complicated to manage in production, which involves interactions of electrical, thermal, metallurgical and mechanical phenomena. In order to design new products, to select appropriate welding machines or to optimize process settings in industry, a large number of running-in experiments have to be carried out with a method of trial and error. This increases the product costs and results in substantial delay in the onset of production. Another important aspect is the difficulties in identification of the causes for arbitrary

Department of Manufacturing Engineering
Technical University of Denmark, Building 425
DK-2800 Lyngby, DENMARK

fluctuations in product quality due to the very fast process time (0.02-0.5 seconds) resulting in problems monitoring the welding process parameters. There have been keen interests expressed by engineers in various industries to obtain advanced development tools that are able to extend the working capacity and skills of engineers thereby to reduce the development costs and time for product design or rapid prototyping and optimization of production lines.

Among resistance welding processes spot welding and projection welding are the most common ones as illustrated in Fig. 1. Current, force and time are the basic process parameters. Plastic deformation of metals is often involved, especially in projection welding due to collapse of the projection part.

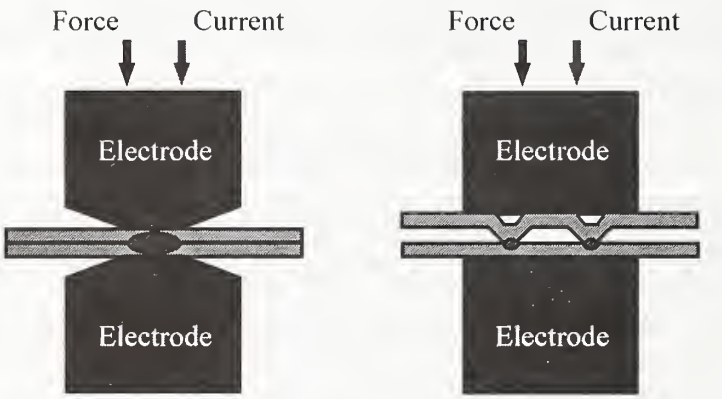

(a) Spot welding (b) Projection welding

Fig. 1: Variants of the resistance welding processes.

In order to facilitate industrial applications of resistance welding, numerical modeling of resistance welding processes applying the finite element method (FEM) has been carried out at the Technical University of Denmark in the past five years. Considering the physical process of resistance welding, the numerical modeling tasks have been divided into four models, namely *an electrical model*, *a thermal model*, *a metallurgical model* and *a mechanical model.* The electrical, thermal and metallurgical models are simultaneously coupled considering the dynamics of the process parameters and the influence of temperature on the properties of materials. The mechanical model is coupled stepwise with the other models for development of the stress distribution and the deformation of the workpieces and the electrodes.

Considering engineers as direct end users, an integrated software system, named SORPAS, has been developed for Windows 95/98/NT. An engineering language familiar to engineers is used in the graphic user interface. The simulation can be easily operated and the progress is dynamically indicated and easily controlled. A post-processor is developed for display of process parameters and animated distributions of electric current, temperature, stress and strain in both workpieces and electrodes. Large plastic deformation is modeled in the program that can thereby be applied for spot welding as well as projection welding. Due to the fact that the program is developed in close contact with industry, practical aspects of the processes have been thoroughly considered in the program. The software system has been applied in several European companies for evaluation

of the geometry and material combination of the product, the main process parameters and also for determination of the required type and capacity of welding machines. Examples are presented for demonstration of the applications of the program.

PARAMETERS IN RESISTANCE WELDING

In order to obtain industrial relevant numerical results, it is very important to understand the process of resistance welding completely and systematically. The practical process of resistance welding involves not only the workpieces and the electrodes, but also the machine characteristics and the dynamic features of the process. In order to make realistic and applicable simulations of the resistance welding process all important parameters should be considered.

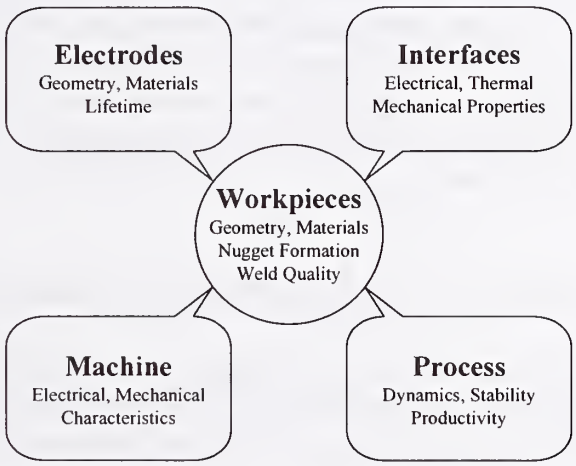

Fig. 2: System of parameters in resistance welding.

Fig. 2 illustrates the system of parameters in resistance welding, which is classified into five groups, namely the workpieces, the electrodes, the contact interfaces, the machine characteristics and the process features.

The *workpieces* are the products to be manufactured applying resistance welding. Parameters related to the workpieces include the geometry and the material properties, the weld nugget formation and the resulting weld quality. The *electrodes* are applied to conduct the welding current to the workpieces to be welded. Parameters related to the electrodes include the geometry and the material properties, the cooling passage and the lifetime. The electrodes influence the heat development and eventually the nugget formation in the workpieces. The lifetime of electrodes has a vital importance in production especially in automatic production lines. Another important group of parameters is the contact *interfaces* between the workpieces and between the workpieces and the electrodes. Parameters related to the interfaces are the electrical contact resistivity, the thermal contact conductivity and the friction if relative movement (sliding) occurs at the interface. All these parameters are dynamic and dependent on many other factors. These make the contact properties very difficult to handle both in practice and in theoretical modeling. However, they have great influence on the weld nugget formation and the resulting weld quality.

Without careful consideration and reliable modeling of the contact properties, it will be difficult to obtain accurate numerical results.

Besides the parameters directly in connection with the workpieces, parameters related to the welding machine and the process are also important. The welding machine decides how the energy is delivered to the electrodes and the workpieces. For example, alternating current (AC) welding machines will have different dynamics in energy delivery comparing to condensator discharge (CD) welding machines. Furthermore, each individual welding machine will have its own electrical and mechanical characteristics including its dynamic response to a rapid current variance and a sudden mechanical movement. The dynamic characteristics of the process parameters such as the welding current and the welding force are very important, too. Stability of the process indicates how sensitive the weld quality is to the variation in the process parameters since the process parameters may be disturbed by many factors in industrial production. Productivity is another factor. A low welding current and a long welding time may result in a similar welding result as a high current and a short time. For stability reason the former case may be preferred but for productivity reason the latter case is preferable. The changing properties of the electrodes along with the number of welds have also great influence to the dynamic behaviors of the welding machines and processes.

PROCESS STAGES OF RESISTANCE WELDING

In order to carry out the numerical modeling, the physical processes of resistance welding should be first understood. Considering the process parameters and the behaviors of materials, the process of resistance welding is divided into three stages, which are squeezing stage, welding stage and holding stage.

In the *squeezing stage*, the metals to be welded are brought into contact by applying a welding force to the joint. The contacting workpieces may be plastically deformed especially in projection welding, but the welding current is not applied in this stage. In the *welding stage*, the welding current is applied to the joint and heat is generated at the interfaces and in the workpieces and electrodes while the weld force is still applied. Due to increase of temperature, the material properties are changed and deformation of the contacting materials is accelerated. If the welding time is long enough, melting occurs in the workpieces while deformation of materials continues. In the *holding stage*, the current is switched off thus heat generation is stopped, but the welding force is still applied to maintain the weld. As temperature decreases due to heat transfer, the melted metal returns to solid state. Welding force will be released when there is no risk of damaging the welds.

FINITE ELEMENT MODELING OF RESISTANCE WELDING

According to the basic parameters and the physical processes occurring in resistance welding, resistance welding is simulated with four numerical models: an electrical model, a thermal model, a metallurgical model and a mechanical model. The *electrical model* calculates the distributions of the voltage and the current as well as the heat generation in materials and electrodes. The *thermal*

model calculates the heat transfer and the temperature distribution. The *metallurgical model* calculates the phase transformation and the material properties dependent on temperature. The *mechanical model* calculates the deformation and geometry of materials, the stress distribution and the contact properties at interfaces.

These models are strongly interrelated to each other and they are all influenced by the dynamic behaviors of the materials, the interfaces, the machines and the processes. In order to make an efficient simulation, a simultaneous coupling is made for electrical, thermal and metallurgical models, whereas the mechanical model is coupled stepwise with the others, see Fig. 3. In this way, convergence of the models can be easily achieved while the accuracy of solutions is maintained.

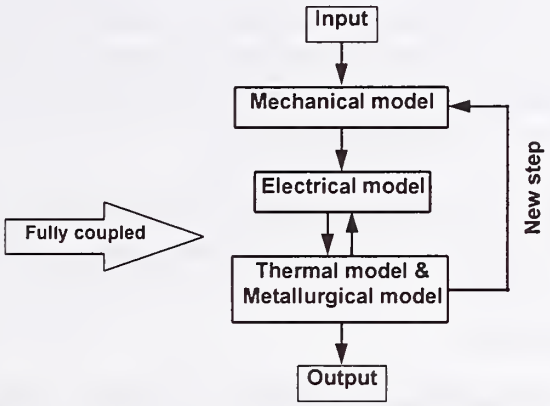

Fig. 3: Algorithm for dynamic coupling of the numerical models in FEM modeling of resistance welding.

IMPLEMENTATION OF PRACTICAL PARAMETERS

In order to simulate a resistance welding process, the geometry and material properties of the workpieces and the electrodes have to be specified. The material properties are temperature dependent, which include the electric resistivity, thermal conductivity, heat capacity and flow stress etc.. To obtain industrial relevant results some other practical parameters have also to be considered.

Dynamics of Process Parameters

Dynamics of the process parameters such as the welding current and the welding force during welding is very important in resistance welding especially in projection welding due to a very short welding time. In order to simulate an actual process, the slope-up of the welding current (how it rises from zero to a specified level) and the follow-up of the electrode (how it reacts to a sudden collapse of workpiece due to softening of materials) are determined as functions of the welding time.

Types of Resistance Welding Machines

The type of the welding machine is normally defined by the type of its power source. There are basically three types of welding machines, *i.e.* the direct current (DC) welding machines, the alternating current (AC) welding machines and the condensator discharge (CD) welding machines. The mid-frequency (or inverter) welding machines may be treated as a DC machine. The impulsed welding machines can also be derived as variations of the DC machines.

In simulations, the input of electrical power may be defined either by a dynamic curve of the welding voltage or by current. The welding current in a DC machine is directly defined as a function of the welding time taking into account the slope-up and slope-down of the welding current while switching on and off. The welding current in an AC machine is defined by a sine function combined with a profile curve for the slope-up and slope-down of the current as well as the efficiency by phase shifting. The welding current in a CD machine is simulated with a slope-up curve and a discharge curve of the welding voltage.

By consideration of the actual process and machine characteristics in the simulations in a way similar to the practice, the program is made very easy for engineers to understand and to operate.

Contact Properties at Interfaces

The contact properties are as mentioned earlier very important although difficult to handle in resistance welding processes. The most important ones are the electric contact resistivity, the thermal contact conductivity and the friction conditions at the interface. For instance, in simulations, the contact resistivity $\rho_{contact}$ at the interfaces is modelled according to the real area of contact between surface asperities and the influence of surface contaminant films:

$$\rho_{contact} = 3\left(\frac{\sigma_{s\_soft}}{\sigma_{cn}}\right)\left(\frac{\rho_1 + \rho_2}{2} + \rho_{contaminant}\right)$$

where σ_{s_soft} is the flow stress of the softer metal which is a function of the temperature, strain and strain rate, σ_{cn} is the normal contact pressure at the interface, ρ is the resistivity and the subscripts 1 and 2 indicate the two metals in contact. An extra term is introduced in the equation to include the influence of surface contaminant films, which is determined as a function of temperature.

APPLICATIONS OF SORPAS

Based on the numerical models and in-depth engineering expertise, an integrated software system, SORPAS, has been developed for finite element modeling of resistance welding, which include a graphic user interface for data input and automatic mesh generation, simulation operations and graphical display of simulation results. The user interface has been made in an

engineering language familiar to engineers. The parameters required for simulation are similar to the parameters needed for a numerical controlled welding machine.

The program is released to several European manufacturing companies for applications in product design and process analysis. It is proved by a number of industrial applications that the program can be applied for the following analyses:

- Evaluation of the weld nugget formation and location influenced by the geometry and material combination of the weld products.
- Evaluation of the electrode design influenced by the geometry and material properties of the electrodes in connection with the weld quality, e.g. the heat balance etc.
- Evaluation of the welding results responding to the adjustment of basic process parameters in order for improving the product quality.
- Comparison of the welding results of the same weld combination obtained with different machines in order to select the optimal machine type and capacity.
- Evaluation of the lifetime of electrodes by estimation of the heat transfer and temperature development as well as the stress distribution in the electrodes

Two examples, one for spot welding and one for projection welding, are given below to show the general applications of the program.

Fig. 4 shows an example of spot welding a 1 mm stainless steel sheet to a 2 mm mild steel sheet, where the numerical result (on the right side) is compared with the experimental observation (on the left side). It is shown that the formation of the weld nugget in the stainless steel and the mild steel obtained by numerical simulation is similar to the one obtained by experiment. It is also found that an indentation of the electrodes into the workpieces occurred both in the experiment and in the simulation.

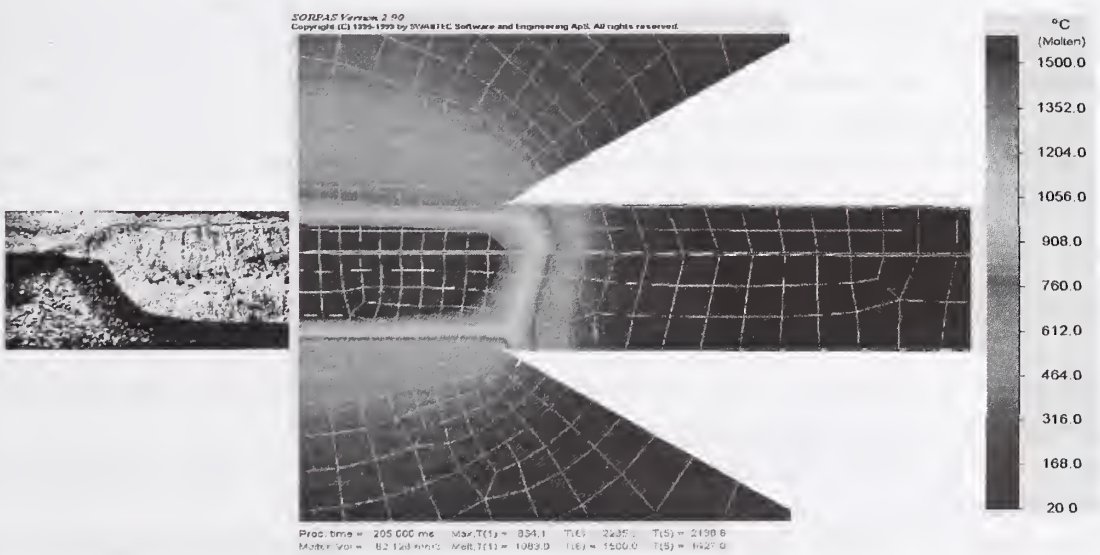

Fig. 4: Comparison of numerical and experimental results for spot welding of stainless steel (upper part) to mild steel (lower part).

Fig. 5 shows a comparison of the simulation results with the micrographs of projection welding stainless steel to stainless steel. It is seen that the deformation of the material and the development of the contact area in projection welding is simulated similarly as seen in the micrographs. This example demonstrates that the program is able to simulate large deformation whereby also applicable for modeling the process of projection welding.

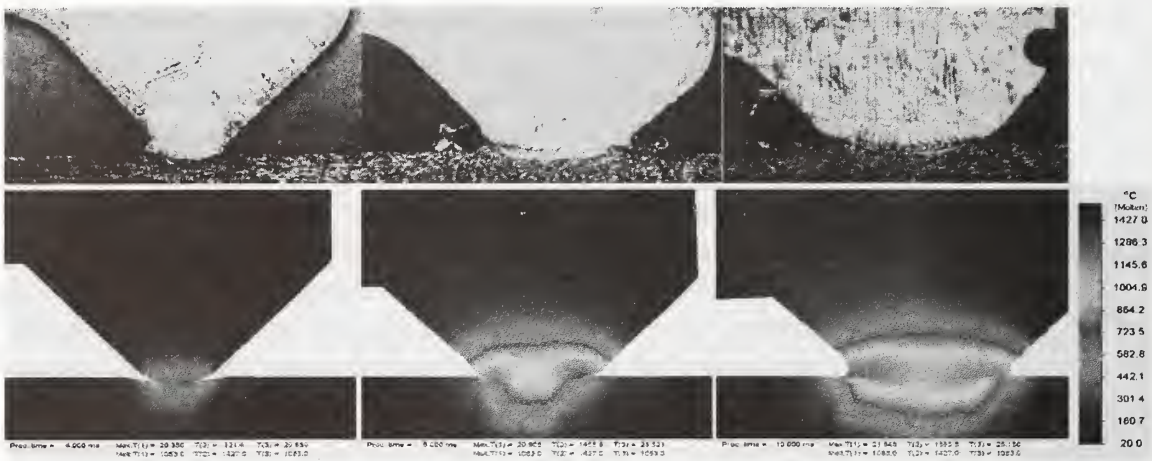

Fig. 5: Comparison of the simulation results with the micrographs of projection welding stainless steel to stainless steel.

CONCLUSIONS

A unique finite element program, SORPAS, has been developed for simulation of resistance projection and spot welding processes. Results of simulation showed that the program is able to successfully demonstrate the influence of the main process parameters as well as the geometry and the material properties of workpieces and electrodes considering also the practical aspects such as the dynamics of the process and the welding machine characteristics. The program is thus applicable for quantitative analysis and understanding of resistance welding processes as a development tool for welding engineers to more efficiently design new products and to optimize process settings applying resistance welding.

REFERENCES

1. Roberts, D. K.; Roberts, J. E.; and Wells, A. A. 1958. Fundamental Resistance Welding Investigations. *British Welding Journal* (3): 117 to 126.
2. Archer, G. R. 1960. Calculations for Temperature Response in Spot Welding. *Welding Journal* (8): 327-s to 330-s.
3. Greenwood, J. A. 1961. Temperatures in Spot Welding. *British Welding Journal* (3): 316 to 322.

4. Rice, W.; and Funk, E. J. 1967. An Analytical Investigation of the Temperature Distributions during Resistance Welding. *Welding Journal* (4): 175-s to 186-s.
5. Cho, H. S.; and Cho, Y. J. 1989. A Study of the Thermal Behaviour in Resistance Spot Welds. *Welding Journal* (6): 236-s to 244-s.
6. Nied, H. A. 1984. The Finite Element Modelling of the Resistance Spot Welding Process. *Welding Journal* (4): 123-s to 132-s.
7. Tsai, C. L.; Jammal, O. A.; Papritan, J. C.; and Dickinson, D. W. 1992. Modelling of Resistance Spot Weld Nugget Growth. *Welding Journal* (2): 47-s to 54-s.
8. Browne, D. J.; Chandler, H. W.; Evans, J. T. and Wen, J. 1995. Computer Simulation of Resistance Spot Welding in Aluminium: Part I. *Welding Journal* (10): 339-s to 344-s.
9. Browne, D. J.; Chandler, H. W.; Evans, J. T.; James, P. S.; Wen, J.; and Newton, C. J. 1995. Computer Simulation of Resistance Spot Welding in Aluminium: Part II. *Welding Journal* (12): 417-s to 422-s.
10. Zhang, W. and Kristensen, T. F. 1997. Finite Element Modeling of Resistance Welding Processes, *Proc. 8th Int. Conf. on Joining of Materials - JOM-8*, Helsingør, Denmark, 226 to 233.
11. Zhang, W.; Jensen H. H. and Bay N. 1997. Finite Element Modeling of Spot Welding Similar and Dissimilar Metals, *Proc. 7th International Conference on Computer Technology in Welding*, San Francisco, USA, 364 to 373.
12. Zhang, W.; and Bay N. 1998. Finite Element Modeling Aided Process Design in Resistance Welding, *Proc. 8th Int. Conf. on Computer Technology in Welding*, Liverpool, UK, S36.1 to 11.
13. Zhang, W. 1998. A Finite Element Program for Simulation of Resistance Welding Processes, *Int. Conf. on Education, Training, Certification and Accreditation in Welding*, Helsingør, Denmark.
14. Zhang, W. 1999. Finite Element Simulation of Resistance Welding, *Porc. 9th Int. Conf. on Joining of Materials - JOM-9*, Helsingør, Denmark, 54 to 59.
15. Kristensen, L.; Zhang, W. and Bay, N. 1999. Influence of Geometric Parameters on Weld Quality in Resistance Projection Welding. *Proc. 9th Int. Conf. on Joining of Materials - JOM-9*, Helsingør, Denmark, 112 to 117.

FINITE ELEMENT MODELING OF RESISTANCE UPSET WELDING

B. Palotas – D. Malgin

ABSTRACT

The resistant upset welding is a widely applied procedure in the technical practice. The quality of products welded by this procedure depends on the welding parameters, because the resistance upset welding is a fully mechanized procedure. In order to increase the reliability of welding parameters the Computer Aided Process Planning can be used, especially in the case of fully mechanized procedures, so thus in the case of upset resistance welding as well. The paper shows the resistance upset welding procedure with main welding parameters and a possibility of the process parameters planning aided by computer. There are many literature which give formulas for calculation of welding parameters of upset welding, but these formulas are generally based on empirical investigations. The paper tries to give the method of parameters calculation on the physical bases. After the application of analytical solutions for temperature distribution, the finite element modeling of plastic deformation is shown. The results of paper can be applied in the technical practice.

INTRODUCTION

The quality of welded structures is depended on the quality of welds. The quality of welds might be increased by application of fully mechanized welding procedures, because the human factors can be minimized.

The resistance upset welding is a fully mechanized welding procedure, so it is widely applied procedure of mass production in the technical practice. The wrong welding parameter setting might produce many welding defects during mass production, so the correct welding parameter setting is especially important in the case of fully mechanized welding procedures.

The human factors should be also taken into consideration in the welding parameter planning.

The Computer Aided Welding Parameter Planning can close out the human factors in the welding parameter calculation, so it is an important way of process planning.

The possibility of Computer Aided Process Planning is a reality of our days, but reliable mathematical models are required.

The resistance upset welding is based on plastic deformation of elements, so the plastic deformation theories can be used for its modeling.

The resistance heating of elements can be written by analytical equations, but the modeling of plastic deformation is very difficult by the analytical methods.

The finite element modeling of plastic deformation gives applicable results for technical practice.

The paper will show the resistance upset welding procedure, gives the welding parameters and calculation methods of them.

The block - diagram of welding parameters calculation of resistance upset welding concluded by paper might give a base of Computer Aided Process Planning of this procedure.

The mathematical modeling of resistance upset welding might give a base of modeling of other resistance welding procedures or other pressure welding procedures.

RESISTANCE UPSET WELDING

The resistance upset welding is a pressure welding procedure, which uses the resistance heating for decreasing the flow strength of materials (k_f , MPa). The welded joint is a result of high plastic deformation and the materials do not melt during welding. It means that, the procedure shall be applied below 250 mm^2 cross section of elements. The limitation of cross section is due to the contamination and oxides of the welded surfaces, which are can not be pressed out from joint surface to flash if the cross section is more than 250 mm^2. The procedure is generally used for welding of steel, aluminum, cooper, nickel and their alloys with circular, pipes, triangle, square, H sections, rectangular etc. shape (Ref. 1.).

The sketch of procedure can be seen in the Figure 1. (Ref. 2.). The figure shows the main welding parameters of procedure, as well.

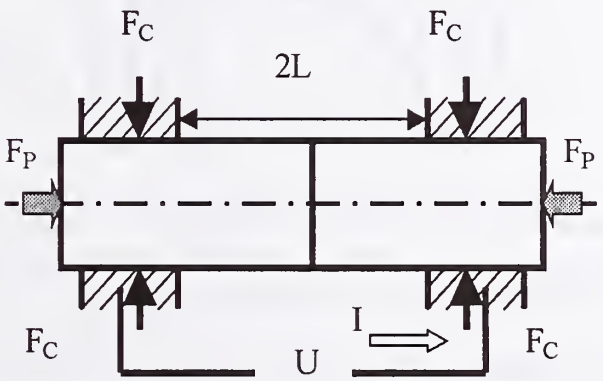

Figure 1.Sketch of resistance upset welding (F_P : Pressure Force, F_C: Clamping Force, 2L: Initial extension of elements, I: Welding current, U: Voltage of transformer)

The sequence of operations applied during resistance upset welding can be seen in the Figure 2. (Ref. 2.) ("work order diagram"). After the clamping of elements with welding force (F_C) an upset force (F_P) is applied and switched on the welding current (I), after welding time (t_W) will be cut off the current and will be released the pressure force (F_P'). After unclamp the weldment the welded joint will be ready. Generally the upset force is equal to pressure force ($F_P = F_P$'), but some equipment can increase the pressure force. The increasing of pressure force is useful for mechanical properties of joints. The equipment generally controlled by measuring of deformation, after obtaining the required deformation the welding current will be switched off. In the case of upset welding the required deformation is high, which can be expressed by "surface factor" (Ref. 3.):

$$k_{surf} = CS_{fin} / CS_{beg} \qquad (1)$$

Where:

k_{surf} is the surface factor,
CS_{fin} is the cross section after welding, mm^2,

CS_{big} is the cross section before welding, mm^2.

The required deformation is high, $k_{surf} \geq 4$ given by Ref. 3.

The high deformation given by (1) shows that, the most important parameter of upset welding is the pressure force.

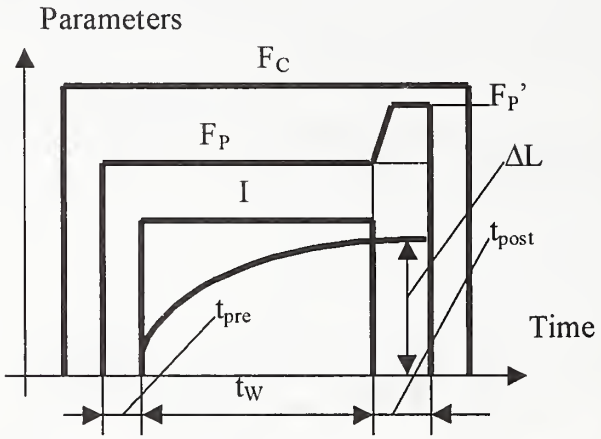

Figure 3. Work Order Diagram of Resistance Upset Welding (F_C: clamping force, F_P: pressure force (upset force), F_P': pressure force, I: welding current, ΔL: changing of length of elements , t_{pre}: pre-pressure time, t_w: welding time, t_{post}: post-pressure time)

We try to give a solution for calculation of welding parameters of resistance upset welding in the followings.

CALCULATION OF WELDING PARAMETERS

The main parameters of upset welding are the welding current, the welding time and the pressure force. The other parameters are not effected the weld quality directly (F_C, t_{pre}, t_{post}). The ΔL parameter will be calculated by finite element modeling.

The Welding Current and Welding Time

On the base of Rosenthal's or Rikalyn's theory of heat conductivity written for welding conditions, we can calculate the temperature distribution as it follows (Ref. 3.) :
We take into consideration the heating of an infinite rod with constant, uniform current. We suppose that, the temperature is constant in a plane and the resistant heating occurred in the connected surfaces of elements in momentary. After heating of elements, the rods conduct the heat by heat conduction.
We suppose that, the thermo-physical properties are depended on temperature linearly.

$$\frac{\rho}{c\gamma} = \frac{\rho_0}{(c\gamma)_0}(1 + \beta T) \qquad (2)$$

Where:

ρ_0 and $(c\gamma)_0$ are the electrical resistance and specific heat at T = 0 °C,

β is the temperature coefficient of $(\rho/c\gamma)$.

The temperature of rod can be written as follows:

$$T(x, t) = T_1(t) + T_2(x, t) \tag{3}$$

Where:

T_1 (t) is the temperature of infinite rod, heated by current, and its resistance depends on only its material and temperature linearly,

T_2 (x, t) is the temperature of infinite rod heated by momentary local heat source.

The uniform heating is as follows:

$$T_1(t) = \frac{1}{\beta}(\exp \beta w_0 t - 1) \tag{4}$$

Where:

$$w_0 = \frac{\rho_0}{(c\gamma)_0} J^2 \tag{5}$$

w_0 is the initial rate of heating, °C/s

J is the current density, A/cm^2.

The T_2 (x, t) temperature can be calculated by following equation:

$$T_2(x,t) = \frac{Q_2}{c'\gamma\sqrt{4\pi a^* t}} \exp\left(\beta w_0 t - \frac{x^2}{4a^* t}\right) \tag{6}$$

Here:

$$Q_2 = \frac{k\sqrt{\lambda^* c^* \gamma}}{\beta J/(c)_0} \tag{7}$$

Q_2 is the summa heat in the specific cross section arised during welding,

c*, λ*, a* are the average values of specific heat, heat conductivity and temperature conductivity during welding,

k is an efficiency factor takes into consideration the material, pressure and efficiency of heating. It is 2.6 ... 3.0 for carbon steel, 0.07 ... 0.08 for stainless steel, 0.34 ... 0.36 for aluminum and 0.14 ... 0.15 for cooper. If the pressure is higher, then the smaller values of k should be used.

The temperature distribution is given in Figure 3. calculated by above written equations. The temperature is calculated for short extension of elements, but in the case of long extension the temperature distribution is different from one given in Figure3.
If the extension of elements were too long, then possible buckling would occur. In order to avoid the buckling, the 2L = 2d where d is the diameter of elements or typical dimension of elements.
In the case of resistance upset welding the maximum temperature of elements is (T_{max} = (0.8 ... 0.9) $T_{melting}$) in the plane of connection.
From temperature we can calculate the welding current, welding time and we can use it in the plastic deformation modeling.

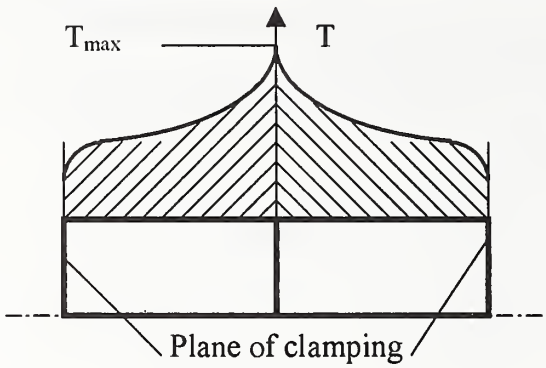

Figure 3. Temperature distribution at the resistance upset welding

The welding current and welding time can be calculated by iteration from T_{max} , using the equations (2) ... (7).
The beginning welding current density (J_0) and beginning welding time (t_{w0}) used in the iteration can be calculated from Table 1. (Ref. 3.).

A, mm^2	J_0, A/mm^2	t_{w0}, s
25	200	0.6
50	160	0.8
100	140	1.0
250	90	1.5

Table 1. Beginning welding current density and welding time

The required welding current density and welding time have to give the specified T_{max}, using iteration by computer this parameters can be calculated easy.

The Pressure Force

Finite Element Method (FEM) can model the pressure force (FP) required for plastic deformation.
We show the FEM modeling for unalloyed carbon steel (type is C15 by Hungarian Standard).
Geometrical data of model is shown in the Figure 4.

We used the MARC/AutoForge 2.2.0 software for FEM modeling, the materials were given as elasto-plastic materials.
The initial condition of modeling is given in the Figure 5.
The force distribution can be seen in the Figure 6.
The results of modeling gave that, the required Pressure Force is 55kN for $k_{surf} = 2.15$ when the diameter of deformed element is 22mm. The applied pressure rate was 12m/s. The $\Delta L = 5.5$ mm at both side.

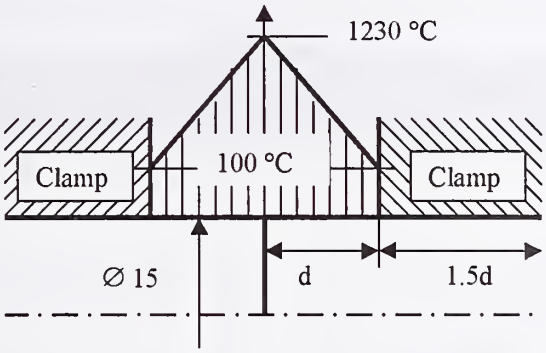

Figure 4. Initial geometrical data of FEM modeling

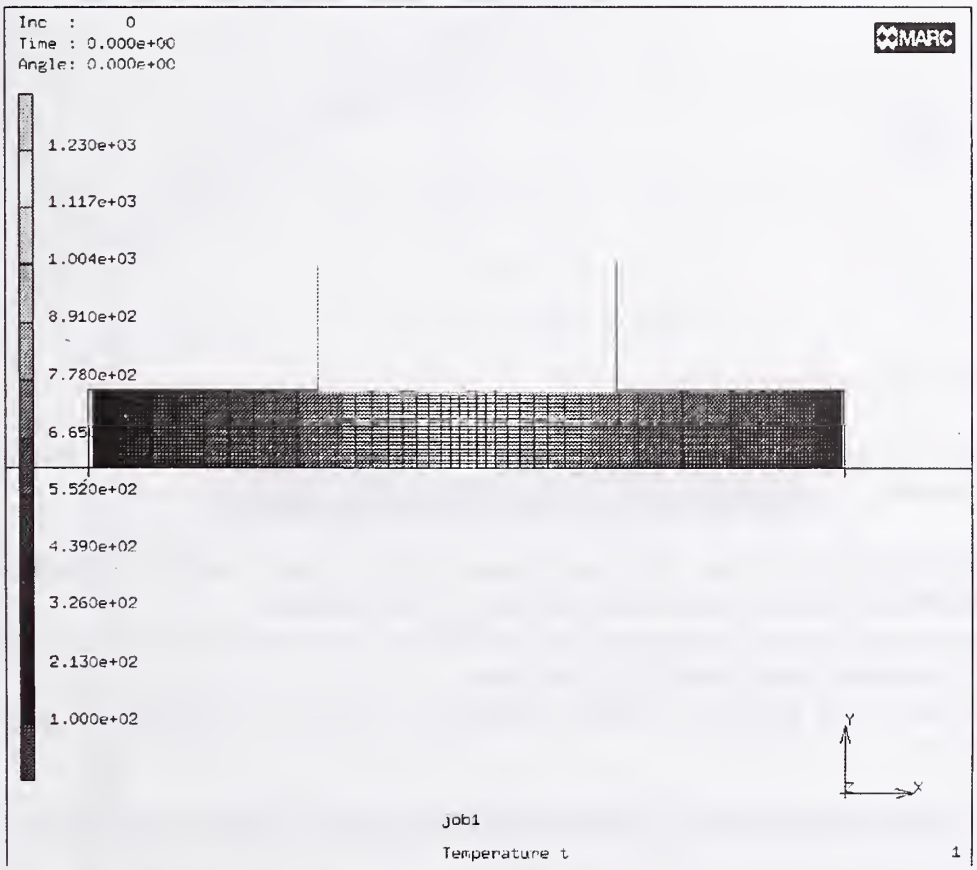

Figure 5. Initial temperature condition of FEM model

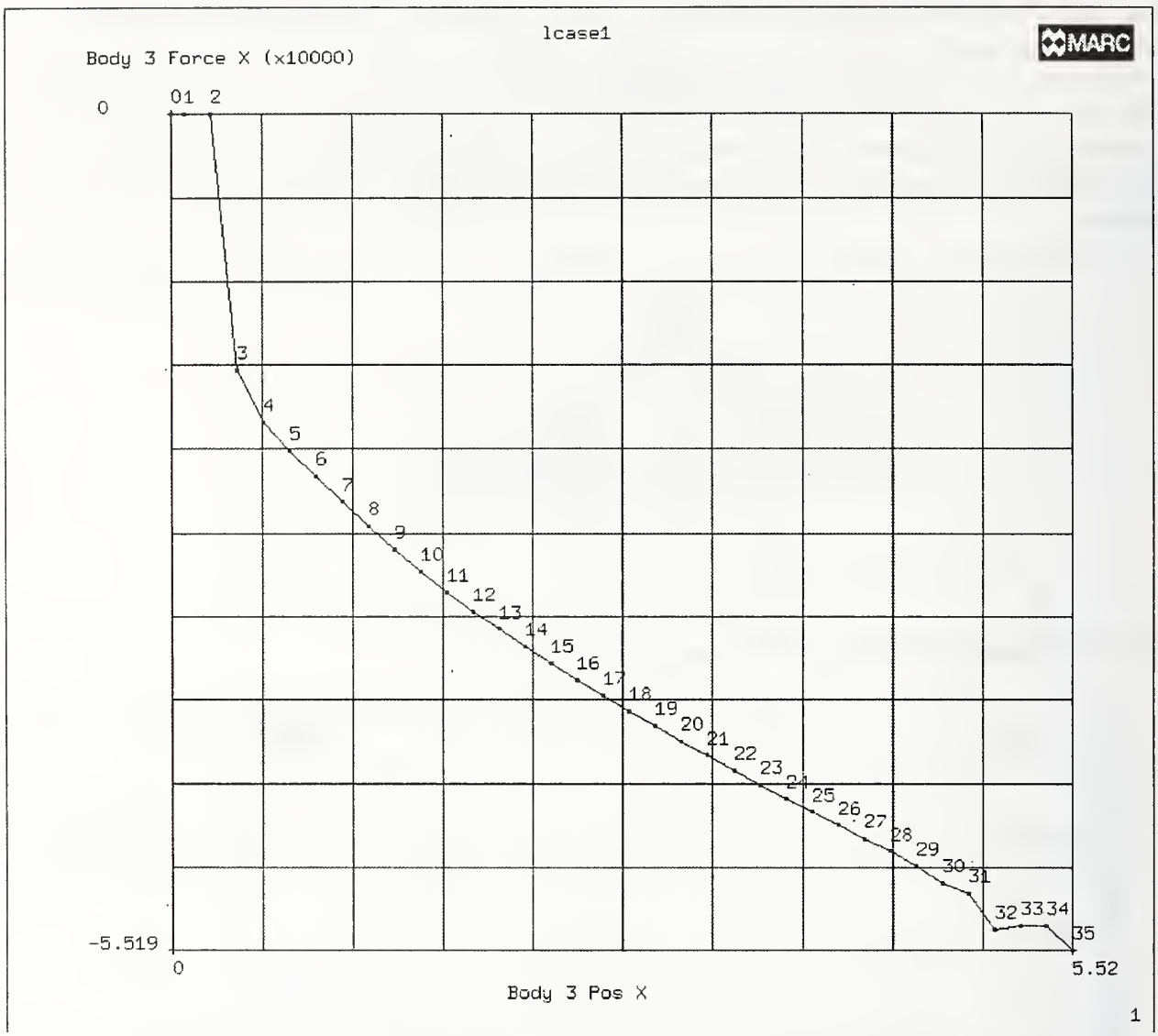

Figure 6. Force distribution in the case of $k_{surf} = 2.15$

The strain distribution is given in the Figure 7., and the Figure 8. shows the temperature distribution at the moment of $k_{surf} = 2.15$.

The results of FEM modeling show that, the Finite Element Method can be used for calculation of pressure force and length changing required by resistance upset welding.
Principle, the resistance heating can be also modeled by FEM and we would like to carry out the complex modeling of resistance upset welding in the future.
Our results proved that, the pressure welding procedures could be modeled as plastic deformation procedures.

COMPUTER AIDED PROCESS PLANING OF RESISTANCE UPSET WELDING

On the base of above written, we have prepared the flowchart of CAPP of Resistance Upset Welding. The flowchart is given in the Figure 9.

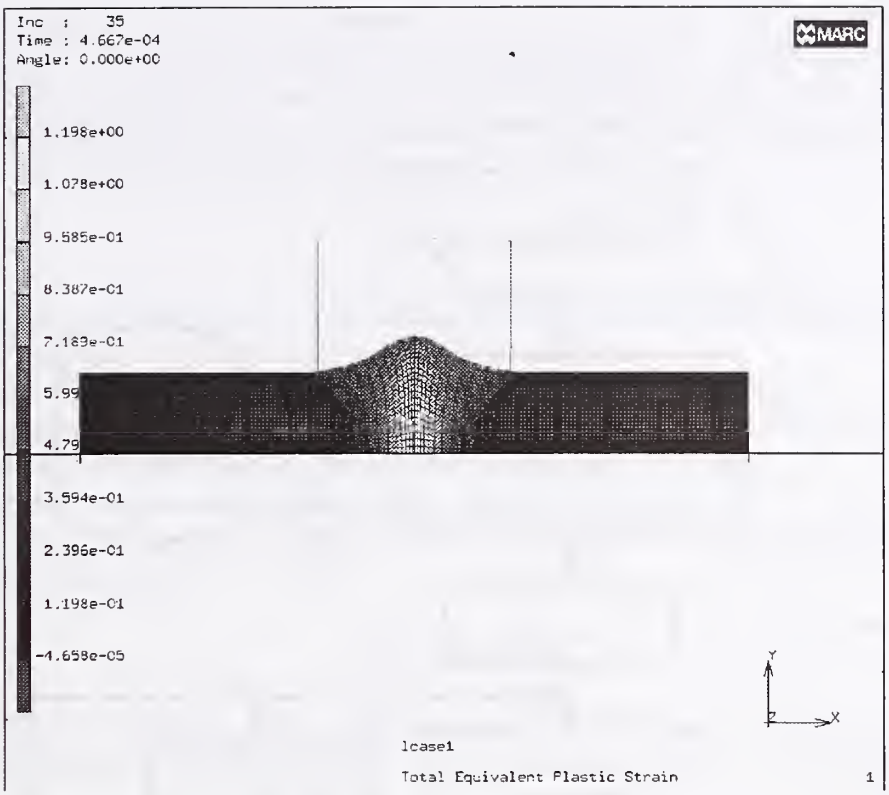

Figure 7. The strain distribution in the case of $k_{surf} = 2.15$

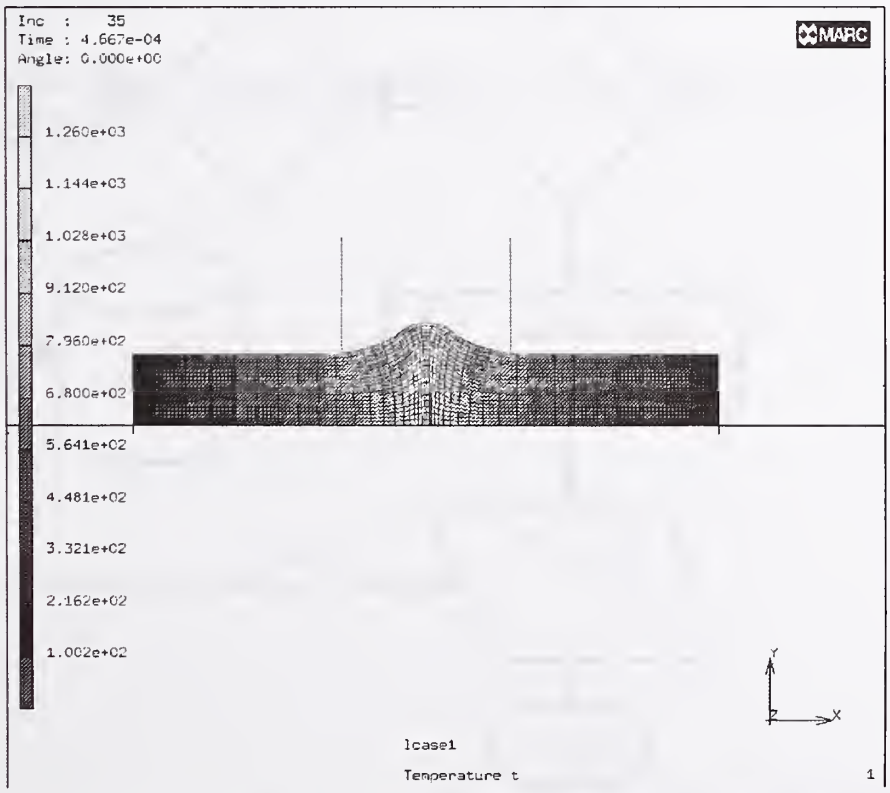

Figure 8. The temperature distribution in the case of $k_{surf} = 2.15$

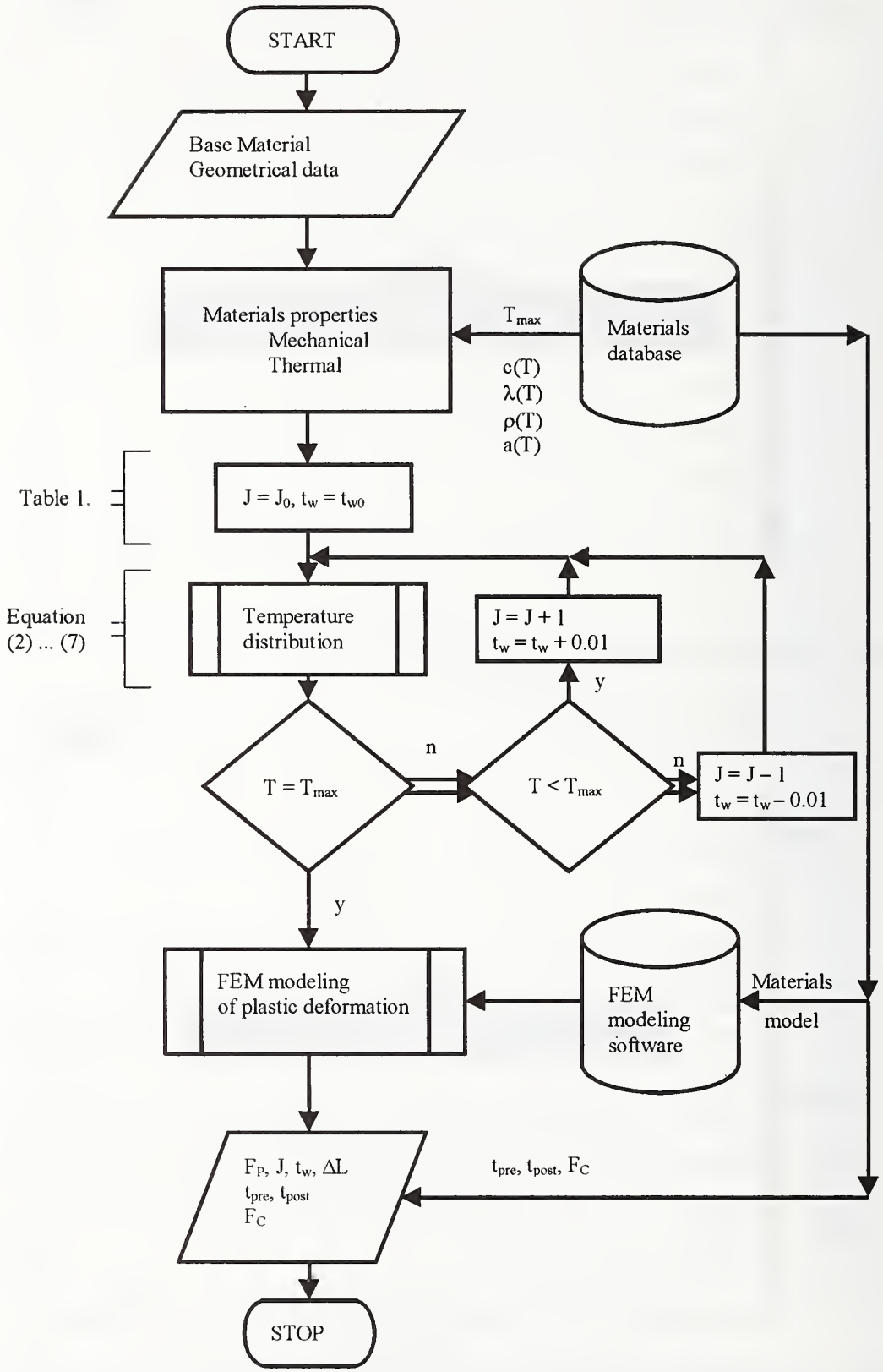

Figure 9. Flowchart of Resistance Upset Welding CAPP

The parameter calculation starts with input of geometrical data and base materials specification. Materials database gives the required data of materials, the calculation of temperature distribution gives the welding current density and welding time, by iteration. The FEM modeling of plastic deformation gives the required pressure force and length changing of elements. The output of calculation gives the welding parameters.

CONCLUSION

The Resistance Upset Welding is a fully mechanized procedure and the calculation of welding parameters by computer is possible and reasonable in our time.
Analytical and Finite Element Method can calculate the welding parameters.
We suggest using an analytical model for calculation of heating parameters and FEM model for required pressure force calculation in the case of resistance upset welding.
The FEM modeling can be used for all pressure welding procedure.
We would like to calculate all welding parameters of Resistance Upset Welding on the base of FEM modeling in the future.

REFERENCES

1. O'Brien, R. L. Editor, 1991. Welding Handbook, Volume 2. Welding Processes: 955 Miami: American Welding Society

2. Buránszky, J. I. Editor, 1985. Welding Handbook: 969 Budapest: Műszaki Könyvkiadó (In Hungarian)

3. Orlov, B.D. 1980. Resistance Welding: 410 Budapest: Műszaki Könyvkiadó (In Hungarian)

Session A2: Simulation of GMAW and RW

MAGSIM AND SPOTSIM - SIMULATION OF GMA- AND SPOT WELDING FOR TRAINING AND INDUSTRIAL APPLICATION

Authors: Prof. Dr.-Ing. U. Dilthey, Dr.-Ing. A. Brandenburg,
Dipl.-Ing. H.-C. Bohlmann, Dipl.-Inf. R. Sattler
ISF-Welding Institute, Aachen University, Germany,
Prof. Dr.-Ing. habil. W. Sudnik, Dr.-Ing. W. Erofeew, Dipl.-Ing. R. Kudinow,
ComHighTech Institute, Tula University, Russia

Abstract: Simulation systems allow a close inspection of the relation between welding parameters and the resulting weld seam. So such systems are very useful in education of weld staff as well as production and planning. In training the influence of variations of parameters can be investigated without the need for real welding experiments. In the design phase requirements of the welding process can be taken into account without several iteration cycles. By estimating a good parameter set for the given welding task the set up phase for a new production cycle can be reduced.
Simulation systems were developed for GMA welding as well as spot welding. MAGSIM calculates the weld shape and the temperature cycle of a unpulsed and pulsed GMA welding process for a butt weld as well as fillet welds. A graphical display of the cross section of the weld shape and a three dimensional visualisation allow a close inspection of the weld result. The seam is classified according to the European Standard EN25817. The simulation system takes 50 different parameters including parameters into account.
The SPOTSIM software is a program simulating the process of resistance spot welding (RSW) which includes a material data bank relating to the thermo-physical and thermo-mechanical qualities of the steels as well as a data bank concerning the welding-machines and electrodes. The mathematical model of the process is a system of differential equations of the electronic potential, the thermal energy and the equation of the plastic deformation of the metal depending on the power of the electrodes and the temporal alteration of the welding current. By this simulation it is possible to calculate the measurements of the weld nugget, of the electrode indentation and the sheet separation.

1.0 INTRODUCTION

The determination of optimal welding parameters is still a difficult task for both spot welding and GMA welding. Based on experimental data and a statistical analysis the result of the welding process can be estimated quite good. This approach works only in determined valid boundaries and doesn't consider important details like contact-tube distance, length of hose assembly, characteristic of power source, dimensions of the gap, and so on. Another cause for the non-exact reproducibility of such predictions are the

neglected influences of the chosen measuring methods, e.g. the location of voltage measuring points.

A simulation of the weld formation under consideration of all influences would considerably diminish the efforts for the determination of suitable process parameters. Non-experts would also be able to produce solutions for specific welding tasks by means of a computer dialogue. By variations of welding parameters the relations between welding parameters and the result can be investigated. In addition based on simulation systems the knowledge of the physical and chemical processes in the welding process can be extended and verified.

To achieve a detailed description of the weld formation which is also in accordance to the process mechanisms, extensive mathematical models are necessary, which, however, can only be solved by numerical methods.

2.0 MAGSIM

The computer program MAGSIM was published already 1993 as a simulation system for GMA welding processes. It was designed for running on standard personal computers using the MSDOS operating system. The main goal for MAGSIM is the fast simulation of the weld shape and the classification of the result according to the European standard EN 25817. For the simulation of GMA welding processes a mathematical model [1,2] and a simulation software [3,4] were developed. It simulates the physical processes of the electric welding circuit and the arc as well as the formation of the temperature field and the bead surface numerically. The particular algorithms are based upon physical laws, numerical mathematics and verification adjustment. They allow the analysis of real welding processes regarding up to 50 parameter values, the optimisation of welding parameters for given tasks and the diagnosis of butt joint welding processes [5,6]. The model is self-consistent so that no additional assumptions (e.g. the efficiency of the arc) are necessary. Aside of the estimation of the weld shape it can be used for the optimisation of the welding parameter.

The program MAGSIM2 extends the simulation capabilities of MAGSIM to pulse arc processes, fillet welds, additional mixed gases with O_2 components and high-alloy steels. It allows the calculation of the arc efficiency and the part of drop heat regarding of all pulse parameters including current leading and trailing edge. The mathematical

model takes the influence of the weld surface to the temperature field into account. The simulation results of the model were verified by comparison with a lot of real welding experiments covering GMA pulsed and non-pulsed welding of fillet and butt joints. The simulation results have an exactness of better than 85 % within a wide range of parameter modifications.

The next step is the transfer of MAGSIM2 to the graphically orientated operation system Windows 3.1 and Windows95. For a better visualisation of the simulation results a new 3D display of the simulation results is developed. The advanced complex model algorithms allow a fast and precise calculation of efficiency, heat input and geometrical parameters of the weld shape, the selection of the best weld position as well as the statistical prediction of quality. This features makes MAGSIM2 useful for trainees, students, engineers and scientists in training and research.

In Fig. 1 a screenshot of a 3D-visualisation of the simulation result for a fillet weld is shown.

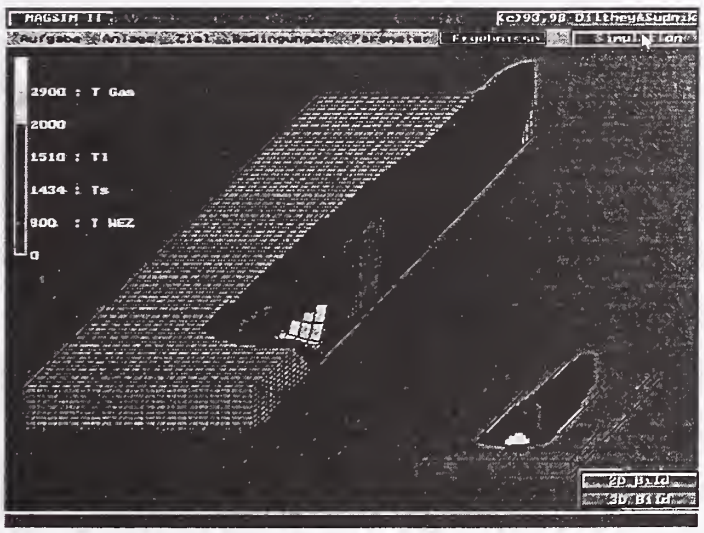

Figure 1: Screenshot of the 3D-visualisation of the simulation result.

2.1 Simulation of the GMA welding process: The formation of the weld shape is mainly influenced by three combined processes:

- Heat generation within the arc area with melting electrode,
- Heat expansion within the welded work pieces,
- Deformation of the weld pool surface.

Each of the above mentioned single processes is analysed sufficient and completely described mathematically. However the construction of complete physical-mathematical

models describing the welding processes and their numerical realisation is very complex already for plain joint geometry like butt joints. It is about the necessity of solving the very non-linear coupled three-dimensional temperature problem at the uncovered surface.

Essers and Walter [7] have shown by experiment that the enthalpy of the separated metallic drops sets the common area of the seam cross-section, while their dynamic effect to the metallic molten bath effects the depth of the melting zone. Tsao and Wu [8] have examined the two-dimensional process of spot welding regarding a volume source and the flow of the molten metal. Kumar and Bhaduri [9] have developed a three-dimensional model of the transient temperature field regarding the kinetic energy and enthalpy of the drops coming from the electrode. The enthalpy of the drops is regarded as a volume source.

[10] describes the development of a three-dimensional mathematical model for the formation of the melting pool surface in fillet welds including the numerical solution of the two differential equations describing the heat transfer and the static balance of the three forces arc pressure, gravity and surface tension. The heat flow depends on the configuration of the melting pool and vice versa, so the solution of this coupled problem had to be iterative. The change of the co-ordinates of the uncovered surface caused by the iterations was regarded by supplement or removal of the control volume within the simulation zone. For the solution of this task Sudnik proposes deformed adaptive numerical networks [11].

The numerical simulation of the two-dimensional temperature field and the analytic description of the seam cross-section profile for GMA welding of fillet welds regarding deformations as undercuts and excessive distorted weld shapes was published in [12]. The analytic solution of the non-stationary three-dimensional temperature distribution for a sheet with normal source distribution and the following transformation for the T joint is described in [13]. The arc heat source is described using an elliptical Gaussian distribution. The adjustment of the calculation results for correspondence of melting zone and HAZ with the welding experiments was done by adaptation of the concentration coefficients.

For the easy selection and optimisation of adequate welding procedures a computer program for the simulation of temperature distribution and weld seam formation for given tasks of GMA welding with various welding positions is introduced [14].

2.2 Physical-mathematical model of the process for fillet welds: The wide propagation of the welding of fillet welds (T and overlap joint) required the expansion of the base model and the simulation software. The model description and there simulation are made more difficult for the welding of fillet welds by serious interrelationships:

- The UI diagram of the arc required for the model differs near the inner edge of the groove from that used for the butt joint model,
- the efficiency of the arc is actually higher for the fillet weld model, because the surfaces of the groove sides are heated more by the radiation of the arc stream,
- the share of the molten base metal within the seam is more than 50 %. This fact requires a more precise description of the superficial heat source of the arc with melting electrode,
- a widespread hypothesis about the normal circular power density distribution of the arc has to be extended to a hypothesis of a normal elliptical distribution,
- the existence of a gap - even a gap width of zero - effects a dissymmetry of the temperature field relative to the heat source axis and excludes the calculation of only one symmetric half of the welding zone,
- the melting pool when welding T and overlap joints in horizontal position is not symmetric to the gravity vector. Therefore its components have been taken into consideration for the differential equation describing the melting pool surface,
- The modelling of the pulsed spray arc with frequencies above 100 Hz requires a more accurate description of the electrode drop force.

The general physical-mathematical model can be divided into four partial models:

- work piece
- heat source for pulsed and non-pulsed welding
- temperature field within the work pieces to be welded
- deformation of the weld pool surface

The partial model of the work piece describes parameters of the base material like the enthalphy etc. Experiences with the numerical modelling of arc welding processes have shown that for the correct consideration of the phase transition heat at melting and crystallisation it is better to the use the equation for the energy transmission instead of the temperature.

Three heat sources for the welding process have to be distinguished: the power of the

anode which includes the heating of the wire, the cathode zone and the arc stream. The energy of the arc stream is only partially used for the process depending of the depth of the crater. For the pulsed arc process the power of the arc results from the calculation of the integrate average value of the instantaneous arc power over one period t_{per}. The partial model of the pulsed arc allows the calculation of the arc efficiency and the part of drop heat in consideration of all parameters of the pulsed power source including the leading and trailing pulse edges [15].

The equation of the stationary thermal conduction of the temperature model is described for movements along the x-axis of the medium in Cartesian co-ordinates. The z-axis is identical with the axis of the wire electrode and the y-axis is perpendicular to the xy-plane. The boundary conditions at the outer surface of the joint describe the thermal heat flows of the hot spot q_k and the arc stream $q_{\Delta Qc}$ as well as the thermal radiation flowing off, the heat convection and the vaporisation. The heat flow of the hot spot is described by an elliptical probability curve. The boundary condition for the second surface is given by the loss of energy by radiation and vaporisation.

The melting pool surface is changed in shape by the electromagnetic and gas kinetic arc influence of the falling drops and the gravity which is balanced by the forces of the surface tension. The surface shape is calculated by the equation for the balance of the above mentioned forces [1]. The front part of the melting pool is identical with the base material. For the rear part of the melting pool the boundary conditions reflect the parallelism of the crystallisation surface of the x-axis. When turning the work pieces with their co-ordinate system by the angle Θ the term of the hydrostatic pressure changes to a sum of the components $\rho g Z_l \cos\Theta + \rho g Y \sin\Theta$, in which Y is a co-ordinate of a spot at the melting pool surface.

2.3 Realisation: The numerical approximation of the three-dimensional model is done by the finite difference method applied to a regular net with the dimensions 80 x 80 x 100 mm with the mesh width $\Delta x = \Delta y = \Delta z = 0.2$ mm. The widths were adapted additionally for the minimisation of inaccuracies of the stepped approximation. The heat transfer is calculated neglecting the molecular heat transfer along the axis ox. The algorithm of the numerical solution is based upon the use of efficient methods for solving of three-dimensional problems - the local one-dimensional pattern.

After finding the surface $Z_l(x,y)$ the simulation area for the partial model of the temperature field is specified more exact and then the calculation procedure is repeated.

For a precise determination of the weld shape 2-3 repetitions are necessary.

Knowing the surface of the molten metal, the co-ordinates of the seam surface can be used as a first approximation for the boundary surface of the simulation zone for the partial model of the temperature field. The selection of the start approximation of the surface mostly allows a solution for the melt surface of the model in one cycle of temperature field calculation.

2.4 Verification of the Simulation Results: The important verification of the simulation software was done by the comparison of the calculation results with the polished sections of welding experiments. The extensive verification experiments needed for the extended welding tasks of MAGSIM2 were done at the Welding Institute (ISF) Aachen using the steel St37-2 for butt welds and fillet welds with different parameters and seam types. A good correspondence of the simulation results compared to the experimental outcome is obtained for the melting pool parameters and the HAZ area for a T joint, Fig. 2, 3.

Figure 2: Comparison of welding experiment and its simulation for pulsed MAG welding, butt weld (thickness 2 mm), D_w = 1.2 mm, Z_K = 15 mm, I_G = 40 A, U_P = 35,5 V, CORGON 18
a) v_w = 7,1 m/min, f_P = 175 Hz, v_w = 1.31 m/min,
b) v_w = 4.4 m/min, f_P = 100 Hz, v_w = 0.91 m/min

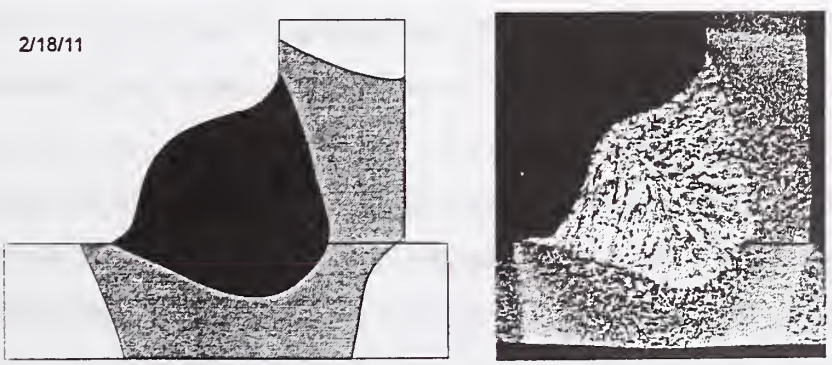

Figure 3: Comparison of welding experiment and its simulation for steel St37-2, fillet weld (thickness 2 + 2 mm), D_w = 1.2 mm, Z_K = 11 mm, torch angle 45°, inclination neutral, v_w = 0,7 m/min, v_w= 4 m/min (I = 185 A), U = 19 V, CORGON 18

3.0 SPOTSIM

According to the DVS-leaflet 2916 the criterions of quality of resistance spot welding are the diameter of the weld nugget, the zone of the heat-influence, the electrode indentation as well as the joint-gap between the sheets. These depend on the welding parameters of the process, which are adjustable on the welding-machine, and the shape of the electrodes. The experimental estimation of quality can be carried out with the help of the computer model of the process. Already in 1949 Gelmann [16] formulated the first model of the process of resistance spot welding as a system of differential equations of the electric potential and the heat conductivity. The two-dimensional distribution of temperature concerning steel was determined numerically by Greenwood [17]. Ruge and Hildebrandt [18] determined it for aluminium. Tschakalew [19] developed an axis-symmetrical model based on the numerical solution of the differential equation of the heat conductivity. By means of the method of finite elements Nixed [20] took into consideration the deformation of the welded workpieces. Wei and Ho [21] applied the instationary model of the heat conductivity on the studies of the measurements of the weld nuggets with different currents, different types of electrodes and varying thickness of sheets. Sudnik and Erofeew [22] developed the coupled numerical model of the process based on the system of differential equations of the mechanical balance of the electrode force and the plastic deformation of the workpiece. In the edge conditions of the equation of the electric potential the ohmic and the inductive resistances of the welding machine were taken into consideration. During the development of the model [22] Erofeew and Kudinow [23] additionally considered the formation conditions of the gap and the probability of spatter. The programs for resistance spot welding were developed by means of the commercially accessible soft-ware ANSYS [24] and SYSWELD [25].

In the present model the welding current adjustment by phase shift by means of the input of the retardation angle of the control and the ignition of the thyristors. To simulate real conditions data banks for resistance welding machines and electrode types exist. In order to test the model a series of verification welds of steel sheets with a thickness up to 1,2 mm has been executed. As a result the software SPOTSIM was developed for the IBM PC under MS DOS.

3.1 The mathematical model: The basis of the model is a system of differential equations in a cylindric coordinate system of the electric potential and the thermal energy and the integral equation of the plastic deformation of the welding zone. Alternating current welding machines roughly grade the effective value of the current by the open-circuit voltage U_{LL} of the welding transformer and shift it infinitely variable by the regulation of the phase displacement α of the thyristors. In the edge conditions of the differential equation of the potential the momentary voltage between the electrodes of the machine u_{EE} is taken account of. For the determination of this parameter the welding current and the resistance R_{EE} between the electrodes is calculated from the solution of the differential equation of the potential [22].

$$u_{EE} = \frac{\sqrt{2}U_{LL}R_{EE}}{\sqrt{(\omega L)^2 + (R_M + R_{EE})^2}} \cdot \left[\sin\omega t - \sin(\alpha - \varphi)\exp(-t_1 \frac{R_M + R_{EE}}{L})\right], \qquad (1)$$

when ω equals the circular frequency of the sinus current, L equals the inductivity of the welding current circuit, R_M equals the inner resistance of the machine, φ equals the efficiency factor of the welding current circuit, $\varphi = \arctan(\omega L/(R_M+R_{EE}))$, t equals the time, α equals the displacement of the phase angle and t_1 equals the time since the starting of the thyristor.

The solution of the differential equation of the potential takes into consideration the influence of the temperature on the resistances of the material and the electrode tip and calculates the specific density of the generation of heat. The temperature distribution is determined by the solution of the non-linear equation of the energy with observance of the thermal conductivity and the phase transitions [22,23].

The electrode geometry for the calculation of the plastic deformation is described by the tip radius R_1 according to ISO 5821. Concerning resistance spot welding the density of the generation of heat and the speed of temperature rise depends on the contact between the sheets. This contact zone increases significantly during the welding process due to the strength reduction of the metal. In the molten area the strength of the metal equals zero and the inner pressure equals the deformation resistance on the periphery of the softened zone. In the model it is assumed that the contact pressure between the sheets derives from the deformation resistance $\sigma(T)$ on the edge of the softened area. By this device it is possible to determine the momentary value of the tip radius r_K by the

temperature distribution T(r) and the electrode force F_{el} by means of the iterative solution of the integral equation [22,23].

$$2\pi \int_0^{r_K} \sigma\left(T_{r=r_K}\right) r dr = F_{El}, \tag{2}$$

The depth e of the electrode indentation derives from the momentary value of the tip radius between the working pieces and the electrode radius R_1

$$e = R_1 - \sqrt{R_1^2 - r_K^2} \approx \frac{r_K^2}{2R_1}, \tag{3}$$

The thermal expansion and the plastic deformation lead to the formation of the gap width x between the working pieces:

$$x = \frac{e_1 + e_2}{2} + \int_0^{e_1+e_2} \alpha_T T dz, \tag{4}$$

when e_1 and e_2 as depths of the upper and lower electrode indentation, α_T as coefficient of the thermal expansion.

3.2 Numerical Approximation: The solution of the differential equations is produced by means of the finite-differences-method. The instationary process of resistance spot welding with alternating current welding machines is calculated with a width Δ t = 0.5 ms in consideration of current variations. With every pace the equations of the electrical potential, the energies and the plastic deformations are solved. The edge condition U_{LL} of the equation of the current-depending electrical potential and the current derive from this equation; thus the solution is calculated iteratively. Thereby the distribution of density of the generation of heat is determined. The distribution of temperature derives from the solution of the instationary equations of the energy. Afterwards the integral equation is solved and the tip radiuses of the current moment are determined. These values are used to solve the equations of the next pace.

3.3 Calculation algorithm: After all parameters are chosen from the data banks, the starting conditions are calculated (Tab. 1). The main cycle of the calculation includes a solution of the two differential equations and a solution of one integral equation for every pace in time.

The edge conditions of the potential equations consider the variations of the sinus voltage between the electrodes. The iterative solution of the potential equation is executed in consideration of the non-linearity of the specific resistance. Concerning the

solution of the energy equation for the very small time pace the non-linearity of the temperature-depending heat conductivity can be neglected. The calculation of the plastic deformation with a variable tip radius r_K is continued until the correspondence of the calculated and the adjusted electrode force is reached. The calculation process is repeated for the next time pace.

Selection of sheet thickness and alloying. Selection from the data banks of: thermo-physical properties of the material, mechanical properties of the material, parameters of the machine, parameters of the electrodes, parameters of the process: no load voltage U_{LL}, welding time t_S, electrode force F_{el}, phase shift of the thyristors α	
starting conditions: t=0, H=H_0, r_K=$r_{K,0}$, R_{EE}=$R_{EE,0}$, i=i_0	
repeat	t=t + dt
	calculation of the tip resistance $\rho_K(T)$. calculation of the edge conditions of the potential differential equation and momentary value of electrode voltage $u_{EE}=f(U_{LL}, t, R_{EE}, Z_m, i, \alpha)$.
	N=0, $u_n(\rho_K,r_K) = u_n(\rho_K,r_K)$
	repeat: n=n+1 solution of the differential equation of the potential $u(\rho_K, r_K)$, calculation of the welding current and of the electric resistance between the electrodes R_{EE}.
	Until $\lvert u_n - u_{n-1}\rvert < \varepsilon_u$
	solution of the differential equation of energy, determination of temperature and measurements of the weld nugget
	repeat: $r_K = r_K + dr$ solution of the integral equation of the plastical deformation in the contact area with the radius r_K and determination of the electrode force F_{Mod}, of the gap-width between the workpieces and of the electrode indentation
	Until $\lvert F_{Mod} - F_{el}\rvert < \varepsilon_r$
Until t<t_S	
record of results of the simulation	

Table 1: Scheme of the algorithm

3.4 The data banks: The data bank concerning material contains information about enthalpy, heat conductivity, density, specific resistance and deformation resistance of steels. The properties of the steels can be entered at 6 degrees which are freely to choose for the temperatures from 20 to approximately 2000°C. The data concerning the alternating current machines contain power, short circuit current, power factor, scope of adjustment of the electrode force as well as the primary no load voltage of the trans-

formators. Information about the standardised electrodes are the measurements of the tip radiuses and the material. These data can easily be completed and edited by the user.

3.5 Possibilities of the model: The model calculates the momentary value of the welding current, the weld nugget diameter, the resistance (Fig. 4), the temperature (Fig. 5), the sheet gap and the tip diameter between the work pieces depending on the chosen steels, the sheet thickness, the electrode geometry and material geometry as well as the welding parameters. Furthermore the model is able to determine a welding lobe of parameters after determination of the range and limits. That way the user has the possibility to choose appropriate welding parameters depending on the input of the problem.

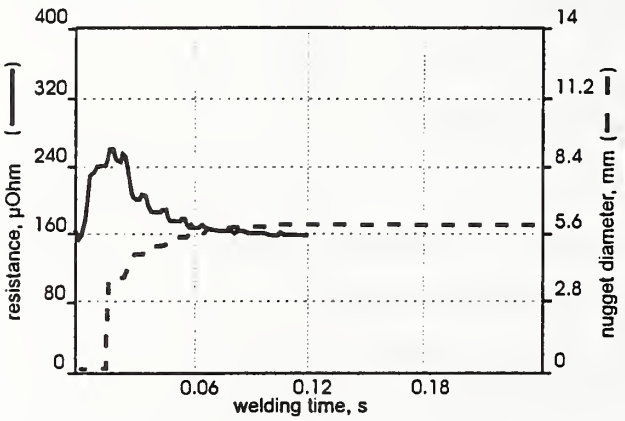

Figure 4: Resistance and nugget diameter,

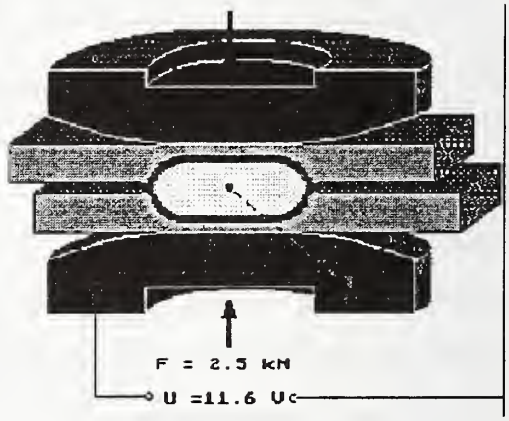

Figure 5: Simulation of thermal field of a spot weld Simulation

3.6 Parameter study and verification: For the validation of the correctness of the calculations a series of experiments is executed. The material chosen for the experiments was St12 with a sheet thickness of 1,2 mm. The experiments were carried out on a alternating current machine of the type Schlatter Selekta P3 with the electrodes G 16X20 (CuCrZr). The welding current was altered between 5 and 10 kA. Electrode forces from 1,5 to 4 kN and welding times from 6 to 18 periods were chosen as further welding parameters. Comparisons between the cross-section of the welded joints and the calculated geometries are exposed in Fig. 6.

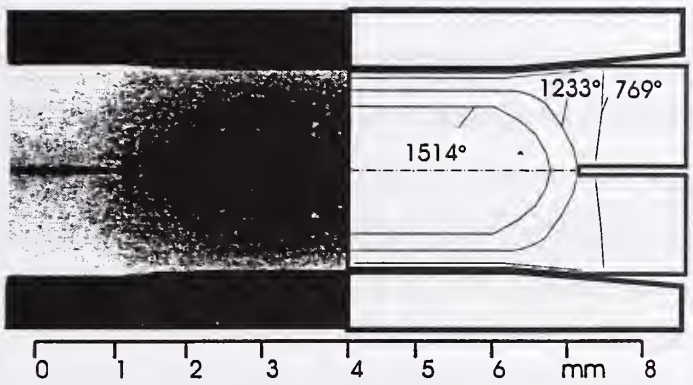

Figure 6: Comparison of welding nugget in cross-section and simulation, St12, 1,2 mm, F_{el}=4 kN, U_{LL}=14 V, t_S=18 Per, ϕ=108°

4.0 HARD- AND SOFTWARE DEMANDS

To run the programs the following hard- and software is required: at least IBM PC 386 with a mathematical coprocessor or higher, operating system MS-DOS and a VGA-graphical interface. The programs, which are programmed with Borland Pascal 7.0 in an object-orientated way, is mouse and menu controlled. This way simulation systems allow the direct evaluation of the simulation results and a better understanding by visualisation. The time required for the calculation of one simulation on a PC Pentium with a clock-frequency of 200 MHz is about 10 seconds.

5.0 SUMMARY

With the support of the data banks SPOTSIM proves to be a device which eases considerably the engineer practice of production planning in the field of resistance spot welding. By the calculated results the expenses and costs concerning operations scheduling and production can be reduced drastically in comparison to the usual proceedings. The verification has shown that the model simulates sufficiently accurate the welding current, the voltage, the measurements of the weld nugget and the welding zone, the deformation of the working piece surface and the variation of the gap width between the working pieces.

Especially in the field of education and teaching the effects of resistance welding, as there are the formation of the weld nugget during the process of welding, the influence of the welding parameters and of the measurements and types of the electrodes on the

geometry of the weld nugget, which can otherwise only difficulty or even not be shown, can with the support of SPOTSIM be demonstrated in a clear and vivid manner.

Therefore the simulation systems are not only recommended for the use in the engineering practice, but also for the education for a better understanding of the quantitative and qualitative proceedings of the process of GMA and resistance spot welding and its optimisation.

Acknowledgement: The investigations and results reported in this paper were promoted partly by the German society „Deutsche Forschungsgemeinschaft DFG". The authors wish to record their thanks for this funding.

6.0 LITERATURE

[1] Sudnik W. A. 1991 Untersuchung von Schmelzschweißtechnologien anhand physikalisch-mathematischer Modelle. Schweißen und Schneiden 43 (10). S. 588 - 590.

[2] Dilthey U., Habedank G., Reichel T., Sudnik W. A. and Iwanow A. W. 1993 Numerical Simulation of the metal-arc active gas welding process. 45 (3). E50 - E53.

[3] Dilthey U., Reichel T., Sudnik W. A., Iwanow A. W., Mokrow O. A. and Habedank G. 1993 MAGSIM - Anforderungsgerechtes MAG-Schweißen von Dünnblechteilen mit Unterstützung durch die Computersimulation. DVS Berichte 156, DVS Verlag, Düsseldorf, S. 87-91.

[4] Habedank G., Dilthey U. and Sudnik W 1996 MAGSIM and SPOTSIM - PC aided simulation of GMA and spot welding processes for educational purposes and production scheduling. 6th International Conference on Computer Technology in Welding, Lanaken, Belgium, 9 - 12 June 1996. Abington Publishing, UK.

[5] Dilthey U., Habedank G., Reichel T., Sudnik W. A. and Mokrow O. A. 1994 Analytical system for metal arc active gas welding of thin walled steel sheet in conformance with requirement. Welding and Cutting 46 (2). p. E24 / E25.

[6] Dilthey U., Habedank G., Reichel T., Sudnik W. A. and Mokrow O. A. 1996 Numerical process diagnosis for weld seam formation in active-gas metal-arc welding of light gauge steel sheet. Welding and Cutting. 48 (12). P. E234 - E 236.

[7] Essers W.G. and Walter R. 1981 Heat transfer and penetration mechanisms with GMA and Plasma-GMA welding. Welding Journal. 60 (2) Pp. 37s - 42s.

[8] Tsao K. S. and Wu C. S.1988 Fluid flow and heat transfer in GMA weld pools. Welding Journal 67(3), pp. 70s-75s.

[9] Kumar S. and Bhaduri S.C. 1994 Three-dimensional finite element modelling og gas metal arc welding. Metall. Mater. Trans. B, Vol. 25B, pp. 435-441.

[10] Ohji T., Nishiguchi K. 1983 Mathematical modelling of a molten pool in arc welding of thin plate. Technology Reports of Osaka University, Vol 33 No 1688 pp. 65-43.

[11] Sudnik W. A. 1985 Digitale und experimentelle Temperaturverteilung in der Schweißzone bei Einwirkung des defokussierten Energiestromes. DVS Berichte 99, DVS Verlag, Düsseldorf, S. 58-61.

[12] Hyeong-Soon Moon and Suck-Joo. 1997 Prediction of weld defect in horizontal fillet welding using numerical analysis and current measurement. ASM Int. Eur. Conf. Weld. And Join. Sci. And Technol., Madrid, 10-12 March, 1997: Book Proc. Brussels, p 463 - 471.

[13] Jeong S. K. and Cho H. S. 1997 An analytical solution to predict the transient temperature distribution in fillet arc welds. Welding Journal. 76(6) Pp. 223s-232s.

[14] Weiß D; Schmidt J; Franz U; Cronacher F; Quaissa B. Simulation von Temperaturverteilung und Nahtausbildung beim Schweißen von Blechen in unterschiedlicher Position. DVS-Berichte, 156 (1993) S. 140-143.

[15] Dilthey U., Sudnik W., Iwanow A., Roosen S. and Habedank G. A study on mathematical modelling of effective heat input in pulsed GMA welding of steels with experimental verification (under preparation).

[16] Gelmann A. S. Elektrisches Widerstandspreßschweißen. Moskau: Maschgiz, 1949. 499 s.(in Russisch)

[17] Greenwood J. A. Temperatures in Spot Welding // British Welding Journal, 1961. Vol. 8. P. 316-322.

[18] Ruge J. und Hildebrand P. Einfluß von Temperaturverteilung und Werkstoff-eigenschaf-ten auf das Haften der Elektroden beim WPS von Aluminium und Aluminiumlegierungen. Schweißen und Schneiden. 16(1964), H. 4, S.115/124.

[19] Chakalev À. À. Et al. Evaluation of the thermal state of the metal in spot welding with the help of the computer. Welding Production. 20 (1973), H. 10. S. 9/12.

[20] Nied H. A. The Finite Element Modelling of the Resistance Spot Welding Process // Welding Journal, 1984. Vol. 63. P. 123-132.

[21] Wei P.S., Ho C.Y. Axisymmetric Nugget Growth During Resistance Spot Welding // Modern Machinebuilding, 1990. Vol. 10. P. 10-17.

[22] Sudnik W. A., Erofeew W. A. Berechnungen der Schweißprozesses mit Computern. Tula: Technische Universität, 1986. 100 S. (in Russisch).

[23] Erofeew W. A., Kudinow R. A. Computermodell des WPSs für die Qualitäts-analyse von Verbindungen. In: CAD und Expertensysteme in der Schweißtechnik. Tula: Technische Universität, 1995. S. 84/92 (in Russisch).

[24] Greitmann M.J., Kessler A. Qualitätssicherung durch Prozeßanalyse bei Wider-standpunktschweißen von Aluminium. Schweißen und Schneiden. 48(1996), H.1. S. 11/17

[25] N. N. Resistance welding. SYSWELD + Application. Fa Framasoft + CSI.

WELDSIM - AN ADVANCED SIMULATION MODEL FOR ALUMINIUM WELDING

O. R. Myhr [(*)], H. G. Fjær [(**)], S. Klokkehaug [(**)], E. J. Holm [(**)], Ø. Grong [(***)] and A. O. Kluken [(*)]

ABSTRACT

This article illustrates the applications of an advanced simulation model, *WELDSIM*, for prediction of microstructure evolution, residual stresses and distortions during welding of age hardening aluminium alloys. The model consists of three components, i.e. a numerical heat flow model, a microstructure model, and a mechanical model that are sequentially coupled. A comparison with experiments shows that the model predicts adequately the temperature and local strength distribution as well as the thermally induced deformations. In the present paper the versatility of *WELDSIM* is illustrated in different numerical examples pertaining to welding of critical components for automotive applications.

INTRODUCTION

High volume production of aluminium based components for the automotive industry represents a growing market for aluminium consumption. This market is a challenge to serve due to its extreme focus on quality, consistency and productivity. In large–scale production of automotive parts it is essential that the different components fit together during assembly. This means that the dimensional tolerances have to be very tight. Since thermally induced deformations are unavoidable in fusion welding, these will usually represent the most difficult problem to overcome in joining of automotive parts in aluminium. Other typical problems associated with welding are cracking, porosity, lack of fusion and degradation of the base material due to softening of the HAZ.

Simulations represent a means of controlling the welding process since the method offers the possibility to test out how different designs, geometries and welding parameters affect the resulting properties. The development of useful and reliable software for weld simulations requires insight into different scientific disciplines like physical metallurgy, continuum mechanics as well as numerical methods and finite element analyses. During the last few years significant progress has been made in the understanding of physical processes that take place during welding of aluminium alloys. A synthesis of that knowledge has, in turn, been consolidated into a process model, *WELDSIM*, which provides a mathematical description of

(*) Hydro Raufoss Automotive Technical Centre, N-2831, Raufoss, Norway
(**) Institute for Energy Technology, N-2007 Kjeller, Norway
(***) Norwegian University of Science and Technology, N-7491 Trondheim, Norway

the relation between the main welding variables and the subsequent weld properties, based on sound physical principles. The present paper illustrates different applications of this computer program and shows some examples where the model has been applied to provide practical guidelines for welding of specific components for automotive applications.

GENERAL OUTLINE OF MODEL

The different input and output of *WELDSIM* are shown in Fig. 1. Alloy composition and temper condition must be specified as well as the geometry of the welded component. The fixture design is represented in the model by appropriate mechanical boundary conditions. The welding parameters are accounted for by specifying the net heat input, the spatial heat distribution, and the time dependent position of the heat source for the different weld segments.

The main outputs from *WELDSIM* are illustrated by means of symbols in the figure, and include the evolution of temperature, microstructure and strength, as well as thermally induced deformations and stress fields.

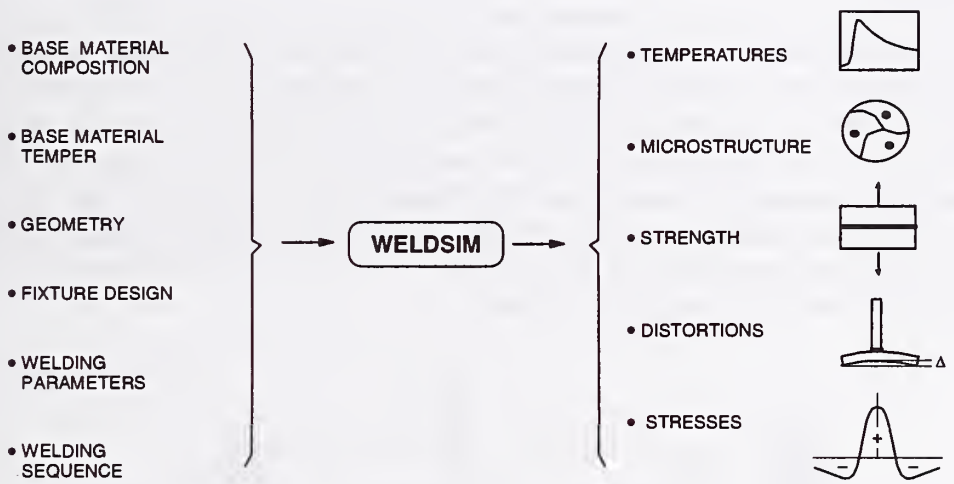

Fig. 1. Schematic diagram showing the main input and output of *WELDSIM*.

COMPONENTS OF WELDSIM

The process model consists of three components, i.e. a numerical heat flow model, a microstructure model, and a mechanical model that are sequentially coupled. The coupling between the different models is shown in Fig. 2. According to the assumptions, the imposed temperature field influences both the microstructure evolution and the stress-deformation fields. At the same time there is a link between the microstructure model and the mechanical

model taking into account the important effect of heat affected zone (HAZ) softening on the strain relaxation during cooling. In the following, a brief outline of the different components of WELDSIM is provided. Further details are give in Refs.[1-3].

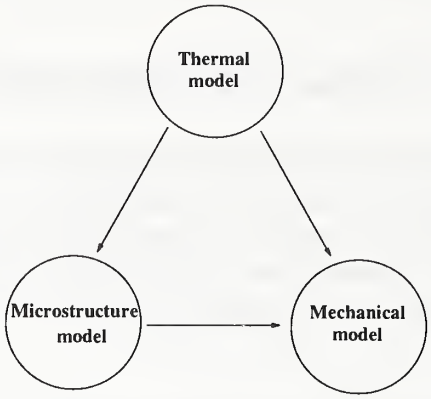

Fig. 2. Schematic diagram illustrating the coupling between the different submodels in *WELDSIM*.

Thermal model

The thermal model solves the three dimensional, time dependent heat conduction equation by a finite element technique. The heat released by the welding arc is represented by an ellipsoid volume distributed source, where the heat distribution is calibrated against measurements of the weld pool geometry. In order to account for the metal deposition from the filler wire, elements that are part of the weld reinforcement are activated when they are approached by the heat source. An example of output from the thermal model is given in Fig. 3(a), which compares calculated and measured thermal cycles during robotic GMA welding of a T-joint. The element mesh and dimensions are shown in Figs. 3(b) and (c). This component will be used in different case studies throughout the paper.

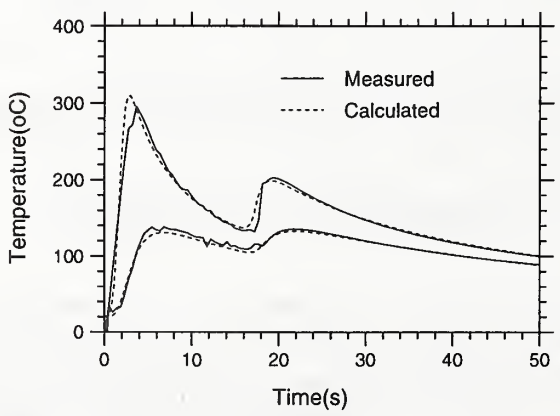

(a)

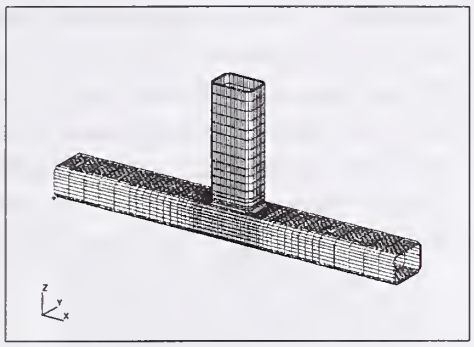

(b)

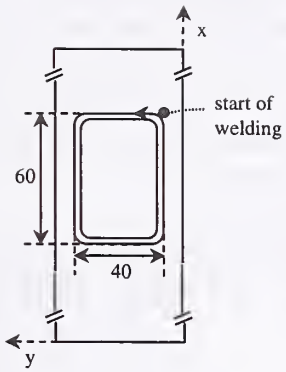

(c)

Fig. 3. (a) Comparison between measured and predicted thermal cycles, (b) Details of the T-joint geometry and the element mesh, (c) A top view of the component showing the starting position of the weld and the dimensions of the cross section of the tube. The wall thickness is 3mm.

Microstructure model

The HAZ microstructure evolution is calculated from thermodynamic and kinetic theory, using the models described in Refs. [1-4]. The microstructure state at a specific material point is represented by the volume fraction of hardening precipitates relative to the unaffected base material, i.e. the f/f_0 -ratio. Figs. 4(a) and (b) show the softening of the HAZ represented by the parameter f/f_0, immediately after welding for two different temper conditions, i.e. peak aged (T6) and naturally aged (T4), respectively. It is evident that the T4 temper condition yields a much wider soft zone than the former. This is because the size of the hardening precipitates is smaller which, in turn, reduces their thermal stability.

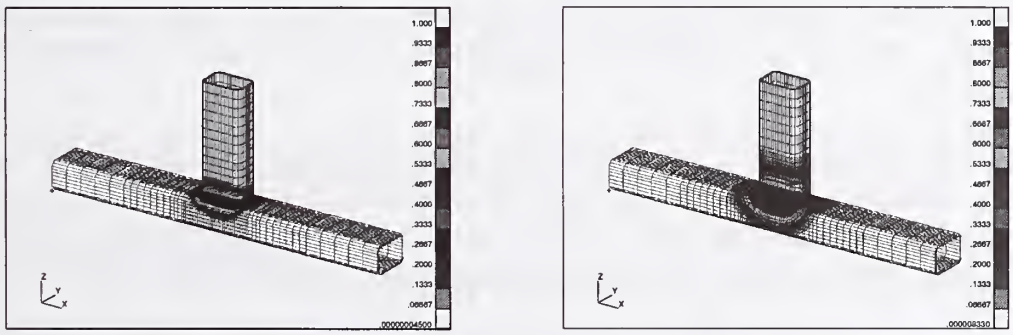

Fig. 4. Examples of outputs from the microstructure model showing details of the HAZ softening during welding of 6082; (a) Peak aged (T6) temper condition; (b) Naturally aged (T4) temper condition.

In *WELDSIM* the parameter f/f_0 represents the instantaneous state of the microstructure at each material point of the solution domain and is transmitted to the mechanical model as illustrated in Fig. 2. This parameter is conveniently transformed to an equivalent base material strength, e.g. the local hardness or yield strength, which are easier to measure in a weldment than the internal microstructure parameter f/f_0. Fig. 5 shows a comparison between measured and predicted hardness values in different surface positions across the weld HAZ of the horizontal member (i.e. the chord) of the T-joint. It is obvious that the observed asymmetry in the hardness distribution, resulting from a corresponding asymmetry in the thermal field, is adequately predicted by WELDSIM.

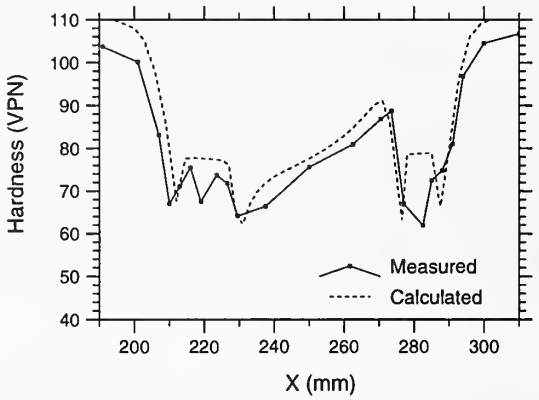

Fig. 5. Comparison between measured and predicted hardness profiles in different positions across the upper horizontal surface of the chord after prolonged room temperature ageing. (Alloy: 6082-T6).

Mechanical model

In the mechanical model, isotropic elastic-viscoplastic material behaviour is assumed. In the applied constitutive equations for viscoplastic flow, the flow stress is expressed as a function of the temperature, the microstructure parameter f/f_0, a hardening parameter, and the viscoplastic strain rate. The material dependent constants entering the constitutive equations are determined on the basis of experiments carried out in a weld thermal simulator. Here the samples were tensile tested at different temperatures and strain rates for different starting microstructures.

The governing equations are solved by a finite element method. The elements in the weld regions are activated when the temperature has dropped below the coherency temperature after passage of the weld heat source. At the interface between the welded parts, no gap is allowed to form, but tangential slip is permitted prior to local solidification.

PREDICTIONS OF DISTORTIONS

Fig. 6 shows a schematic representation of the sequence of deformations taking place during welding of a T-joint. The vertical displacement is, at first, in the upward direction as shown in Fig. 6(a). This is due to thermal expansion of the heated material adjacent to the weld. The

direction is, however, reversed during cooling as the material contracts. Eventually, the deformation becomes as shown in Fig. 6(b). By means of *WELDSIM* the evolution of this vertical distortion with time can be calculated with a high degree of accuracy, as illustrated by the plots in Fig. 7. This means that the mechanical model is sufficiently relevant and comprehensive to be used in numerical case studies to simulate how changes in the welding conditions affect the evolution of the distortions.

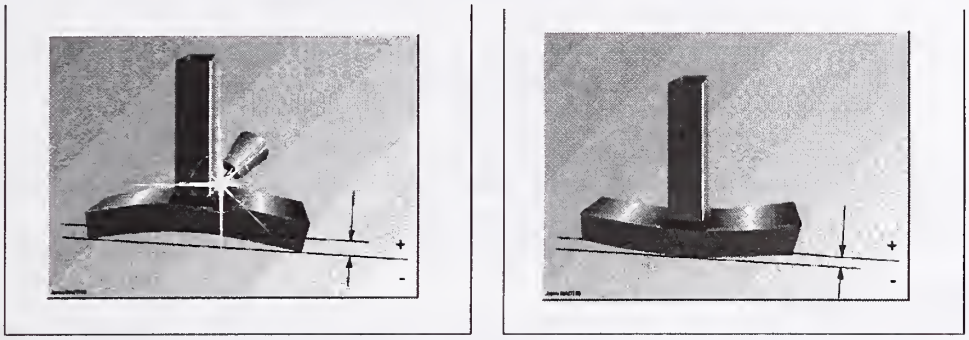

Fig. 6. Schematic diagrams illustrating the evolution of thermally induced distortions during welding of a T-joint. (a) Before completion of the weld, and (b) After completion of the weld.

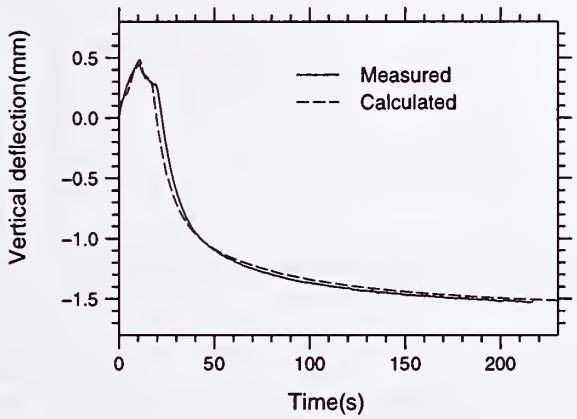

Fig. 7. Comparison between measured and predicted vertical deflections at the centre of the side wall of the horizontal tube (i.e. the chord). Alloy: 6082-T4.

Effect of weld travel speed

Fig. 8 illustrates how the weld travel speed affects the vertical deflection at the centre of the horizontal tube when all other parameters are fixed in the simulations. In general, an increase in the travel speed will tend to narrow the width of the soft zone where the plastic strains build up. Since these plastic strains are the cause of the deformations, one would expect that the increase in the travel speed should result in smaller deflections. This is also in accordance with the *WELDSIM* predictions as shown in Fig. 8.

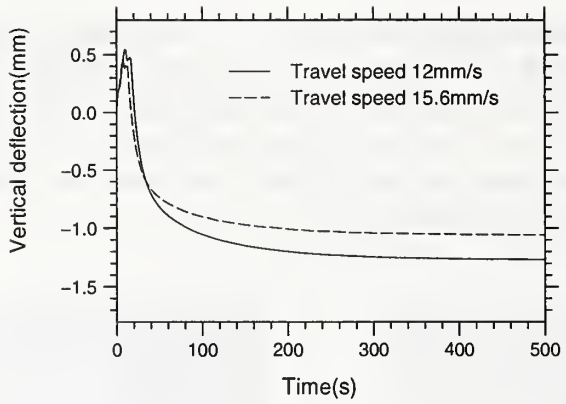

Fig. 8. Calculated vertical deflection at the centre of the side wall of the horizontal tube (i.e. the chord) for two different weld travel speeds.

Effect of wall thickness

The wall thickness of the tubes used in the T-joint has a significant effect on the distortions. This is seen from Fig. 9. It follows that the end deflection of the horizontal tube is reduced when the wall thickness increases. This is due to a corresponding increase in the stiffness resulting from the larger wall thickness.

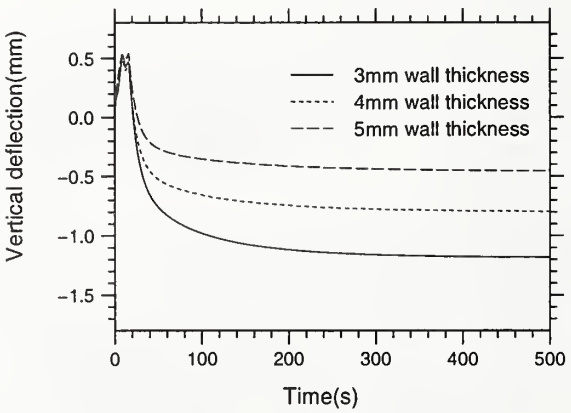

Fig. 9. Calculated vertical deflection at the centre of the side wall of the horizontal tube (i.e. the chord) for three different tube wall thicknesses.

Effect of welding sequence

WELDSIM has also been used to simulate how different welding sequences affect the course of the deformations. The different welding conditions examined are summarised in Fig. 10. The possibility of splitting up the weld length into smaller parts that are welded successively is investigated. Also a consideration of changing the start and stop positions is included. The results of the simulations are presented in Table 1. Generally speaking, smaller distortions are expected when the weld length is split up into smaller parts. Moreover, it seems to be an advantage to start at the centre of the short side of the tube compared with the centre of the long side. This follows from a comparison of Sequence 3 and 2 in Fig. 10 and Table 1, respectively.

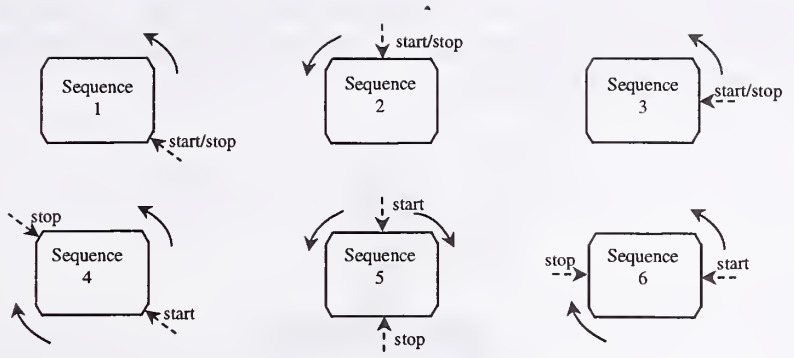

Fig. 10. Schematic representation of the different welding sequences applied in the simulations.

Table 1. Calculated vertical end deflections for the different welding sequences shown in Fig. 10.

Sequence #	End deflection [mm]
1	1.27
2	1.33
3	1.09
4	1.02
5	1.26
6	0.88

Effect of welding fixture

The effect of three different welding fixtures on the resulting deflections were simulated by manipulating the mechanical boundary conditions (BC). Fig. 11 illustrates the different boundary conditions applied, while Table 2 shows the results from the simulations with respect to the final vertical deflection. Note that BC 1 is the standard set-up used in the simulations if nothing else is stated. In the BC 1 set-up, the horizontal tube (i.e. the chord) is fixed vertically to the base at both ends throughout the whole simulation, while horizontal displacement at one of the ends is allowed, as shown in Fig. 11. Considering BC 2, no vertical displacements are allowed for at the bottom of the chord during welding. However, when the welding stops, this restriction is immediately relaxed and the further deformations take place with boundary conditions identical to BC 1. In practice, this corresponds to a situation where the components are heavily clamped during the welding operation and then suddenly released allowing the component to deform freely during the cooling stage. As shown in Table 2, this represents the worst case with respect to the end deformations because the rigid clamping during the welding stage introduces severe plastic yielding in a large domain of the HAZ. The resulting driving force for deformation will then act over a correspondingly large part of the HAZ.

The BC 3 case is initially identical to BC 2, but here the constraints are maintained until the whole component has cooled down. This corresponds to a situation where the component is kept heavily clamped in the fixture for a long time after welding is completed. This results in the smallest end distortion among the three cases investigated, since the deformations taking place during the cooling will be suppressed .

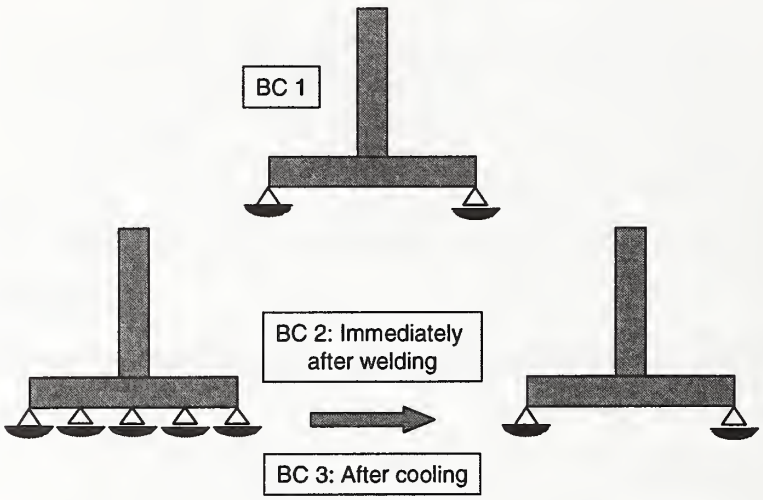

Fig. 11. Schematic illustration of different mechanical boundary conditions (BC) applied in the simulations.

Table 2. Calculated vertical end deflections for different mechanical boundary conditions.

Boundary condition (BC)	End deflection [mm]
BC 1	1.30
BC 2	1.56
BC 3	1.06

Effect of base material

Different alloys respond differently to the imposed temperature field from the heating source during heating and cooling. *WELDSIM* accounts for the microstructure reactions within the material during welding, and can therefore be used to investigate their resulting effects on deformations. Fig. 12 shows the vertical deflection during welding and cooling for the alloys 6082, 7108 and 6063, all assumed to be in the initial peak aged (T6) condition. It is evident that the end-deformation is smaller for the latter alloy compared with the former two. This can be attributed to the lower yield stress of the material in the fully reverted (soft) condition. The significance of HAZ softening will be further discussed in the following section.

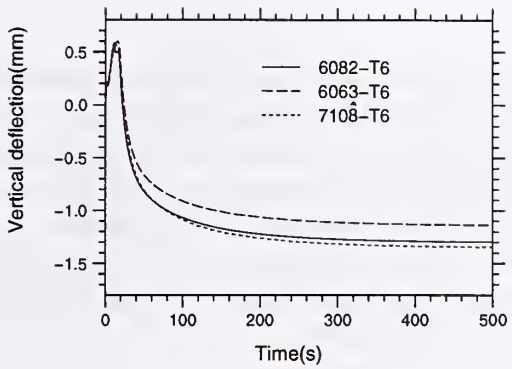

Fig. 12. Calculated vertical deflection at the centre of the side wall of the horizontal tube (i.e. the chord) for three different base materials.

SIGNIFICANCE OF THE HAZ SOFTENING

In simulations dealing with welding of age hardening aluminium alloys, it is essential to include the softening of the HAZ which takes place during welding due to the reversion of hardening precipitates. As an illustration of principles, we shall consider the same problem as in Ref. [5], where thermal strains in a fully constrained bar induce uniaxial stresses and plastic flow. Fig. 13 shows schematically how a material point within the HAZ responds to a thermal cycle reaching a peak temperature of approximately 400°C when the effect of reversion is either included (Case A) or ignored (Case B). Also shown in the figure are curves representing the yield stress as a function of temperature for two extreme situations where the relative volume fraction of hardening particles is kept at its maximum and minimum level during the heating and cooling cycle, corresponding to f/f_0=1 and 0, respectively. A more realistic stress-temperature curve for a typical evolution of f/f_0 is also indicated in the figure. Initially, the compressive stress increases during heating due to thermo-elastic behavior. After the yield limit is reached, the compressive stress decreases more rapidly with temperature in Case A than in Case B due to the reversion.

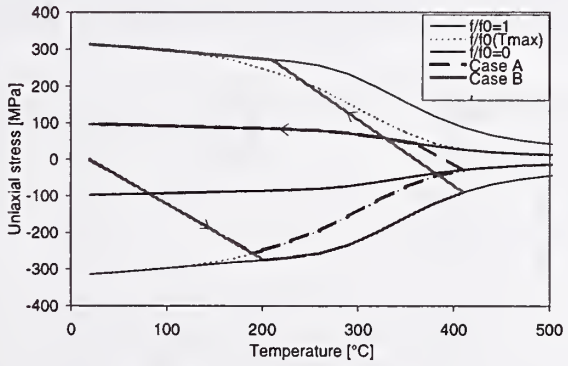

Fig.13. Schematic diagram showing the stress evolution in a material point within the HAZ undergoing a thermal cycle under uniaxial constraint. Softening due to reversion of hardening precipitates is accounted for in Case A, but not in Case B.

The most striking difference occurs between Case A and B is during the cooling stage, where the stresses go from compression to tension. In Case A the residual stresses will soon follow the tensile flow stress curve for the fully reverted material (f/f_0=0), and accordingly a low residual stress of approximately 100 MPa is obtained. In Case B the situation will be different, since no softening due to reversion is assumed. This results in a longer thermo-elastic transition from compression to tension. Eventually, the flow stress curve for the unaffected base material (f/f_0=1) is reached, and a residual stress of about 300 MPa is obtained. The latter value represents a tremendous overestimation.

In *WELDSIM* the important effect of the HAZ softening due to reversion of hardening precipitates is fully accounted for. Fig. 14 shows that the calculated residual stresses are qualitatively very different when reversion is either included or ignored, corresponding to case A and B, respectively. Also the calculated distortions will be significantly overestimated if reversion of the hardening precipitates is ignored in the simulation. This is shown in Fig. 15.

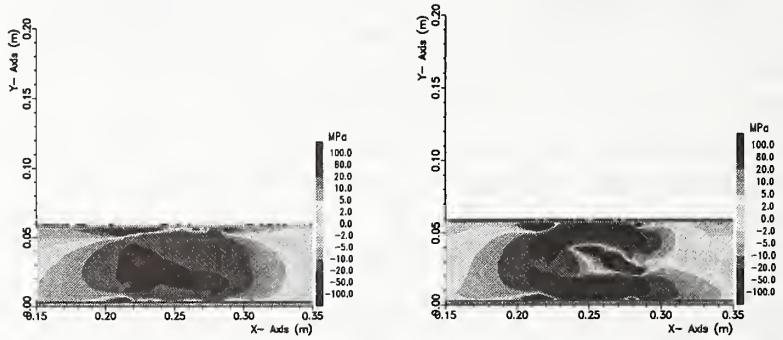

(a) (b)

Fig. 14. Calculated longitudinal components of the residual stresses near the upper surface of the chord; (a) Inclusion of reversion of hardening particles (i.e. Case A); (b) No consideration of reversion of hardening particles (i.e. Case B). Alloy 6082-T6

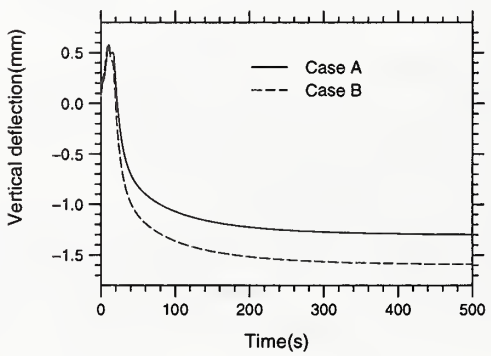

Fig. 15. Calculated vertical deflection at the centre of the side wall of the horizontal tube (i.e. the chord). Case A: Inclusion of reversion of hardening particles. Case B: No consideration of reversion of hardening particles. Alloy 6082-T6

SUMMARY

In this article the applications of a newly developed process model (*WELDSIM*) for welding of age-hardening aluminium alloys is illustrated. It is shown that the model predicts adequately the temperature and the local strength distribution as well as the thermally induced deformations. The model has been applied in different case studies pertaining to welding of hollow extruded profiles for automotive applications. It has been demonstrated that the model is capable of accounting for a wide range of different welding conditions, including variations in the weld travel speed, the tube wall thickness, the base material composition as well as the welding sequence and the fixture design. Moreover, the local softening of the heat affected zone is shown to have a significant effect on the simulated stress distribution and deformations. Hence due consideration must be given to the HAZ microstructure evolution in the weld simulations. It is believed that the present model is sufficiently comprehensive and flexible to be applied as a tool in manufacturing and design of welded components in aluminium where the mechanical integrity is of particular concern.

ACKNOWLEDGEMENTS

The authors wish to acknowledge the financial support of Hydro Raufoss Automotive Structures and The Research Council of Norway. Moreover, thanks are due to Dr. J. Strid at Hydro Raufoss Automotive Technical Centre for his contributions to this article.

REFERENCES

1. O. R. Myhr, Ø.Grong, S.Klokkehaug, H.G.Fjær and A.O.Kluken. 1997. *Science and Technology of Welding and Joining*, Vol. 2, No. 6, 245-254.
2. O. R. Myhr, S. Klokkehaug, Ø. Grong, H. G. Fjær and A. O. Kluken. 1998. *Welding Journal*, Vol. 77, No. 7, 286-292.
3. O. R. Myhr, S.Klokkehaug, H.G.Fjær, Ø.Grong and A.O.Kluken. 1998: Proceedings of the 5th International Conference on Trends in Welding Research, Georgia, USA.
4. Ø. Grong: Metallurgical modelling of welding, Second Edition 1997, London (UK), The Institute of Materials.
5. H. Murakawa, Y. Luo and Y. Ueda. 1998: in Mathematical modelling of weld phenomena, Ed. H. Cerjak, Vol 4, 597-619.

DYNAMIC MODELING OF ELECTRODE MELTING RATE IN THE GMAW PROCESS

Z. Bingul*, G. E. Cook*, and A. M. Strauss*

ABSTRACT

A model has been developed correlating the anode temperature profile with the dynamic melting rate in gas metal arc welding. Components of this model are identified, as the electrode melting rate, temperature-dependent resistivity of the electrode and arc voltage. The differential equations describing the dynamic behavior of the electrode extension were derived from mass continuity and energy relations. The temperature of the electrode extension was determined by conductive heat transfer and joule heating. One-dimensional solutions of temperature and heat content were used to obtain the dynamic melting rate equation. The purpose of the present paper is to provide quantitative analyses, concentrating on the thermal behavior and the electrical characteristics of the arc welding system, to aid in a fundamental understanding of the process, and to develop a dynamic model that may be used in adaptive control. The model is tested by comparing simulations to experimental results.

INTRODUCTION

The variables of the welding process can be separated into two categories [1]: direct weld parameters (DWP) and indirect weld parameters (IWP) as shown Figure 1. The disturbance parameters can be varied on line during welding to affect change in the DWP so they must be controlled by the other indirect welding parameters. Since a nonlinear relationship exits between the highly coupled direct and indirect weld parameters, the coefficients of the differential equations that relate the direct and indirect weld parameters vary as a function of operating conditions.

Arc stability is essential for good quality welds. Ensuring maximum arc stability is a function of many factors: selecting satisfactory welding parameters, maintaining the same parameters in production, monitoring internal and external changes in the process, correcting them, maintaining uniform metal transfer, chemical composition of the material being melted, and dynamic characteristics of the power source and process variables. Abnormal changes in the process variables can result in an unstable arc (spatter and fume). To reduce the spatter and fume, feedback control systems with the added capability of self-adjustment are necessary to maintain a stable arc over the operating range of the process.

Electrode melting rate is one of the most important parameters in the gas metal arc welding (GMAW) process because arc stability depends on how closely the electrode feed rate and the electrode melting rate are balanced to maintain a constant arc length. For constant potential GMAW, arc length regulation is an inherent part of the "self-regulation" characteristic [19] inherent with this mode of operation. While instabilities may occur with this mode [3-5], it is an easy matter to choose stable zones of operation. For constant current and pulsed current GMAW

*Welding Automation Laboratory, Vanderbilt University, Nashville, TN

however, arc-length regulation must be provided by sensing and controlling the voltage [6]. Design and testing of the arc-length regulation system requires an accurate dynamic melting rate model.

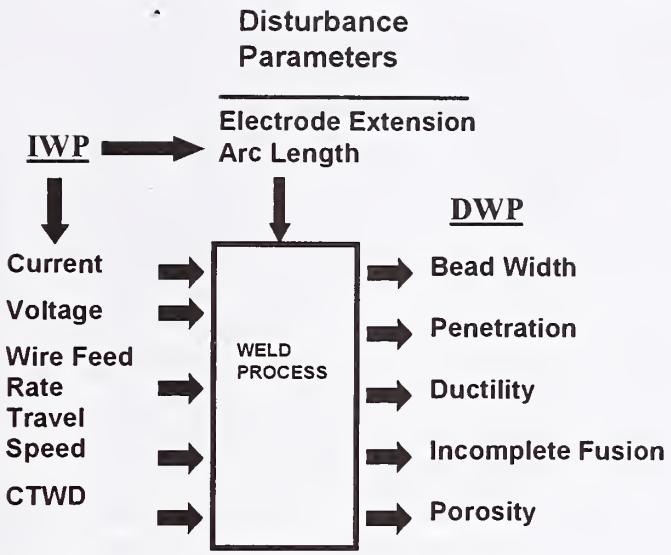

Figure 1. Input and output variables of welding process

Lesnewich [7] conducted extensive experimentation with GMA welding of mild steel and empirically derived his well-known equation expressing the steady-state relationship between current, electrode diameter, and melting rate. Halmoy [8] used an energy balance to derive a result of the same form as Lesnewich, and he calculated the "effective anode heating voltage" and the temperature of the discharged droplets. Other authors [9-15] have contributed to our general knowledge and use of the melting rate relationships for both constant potential and pulsed current GMAW. While there has been limited work describing dynamic melting rate relationships [16-18], most of the efforts have been based, at least in part, on steady-state conditions. Unfortunately, in most cases these conditions become unacceptable for practical control purposes.

A good understanding of arc physics is the most important step to develop the dynamic melting rate model based on relationships between the energy, mass transfer and heat transfer. The electrical energy supplies the arc energy, which generates the heat at the anode and cathode regions and within the plasma column. Mathematical modeling of the welding system is complicated because of the complex distribution of temperature throughout the system. A distributed-parameter model governed by partial differential equations or nonlinear differential equations with appropriate boundary conditions is required for a precise analysis of the system.

MATHEMATICAL MODEL

The mathematical model developed here of the GMAW process consists of three components, the melting rate model, the electrode resistivity model, and the arc voltage model. A schematic diagram of the model is shown in Figure 2.

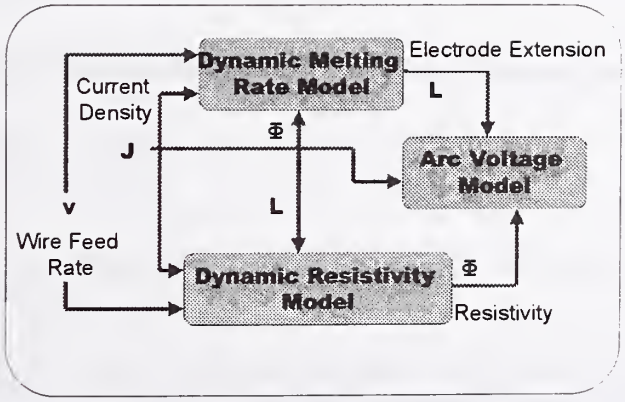

Figure 2. Schematic diagram of the GMAW model

Melting Rate Model

Developing an explicit melting rate model which explains the relationship in arc current and electrode extension for a

given wire size and wire composition is important to global control of the process variables. The melting rate is determined by the balance between energy and mass entering and leaving the electrode. The arc can be considered to be a moving energy (heat) source in the z direction. Therefore, energy conservation and mass conservation theories can be applied by specifying the boundary conditions and initial conditions. The difficulties arising in the modeling of the electrode are mainly due to the complex nature of the boundary conditions. However, treating the electrode and the arc column as separate blocks helps to eliminate these boundary conditions [2]. This is illustrated in Figure 3. The assumptions made for the model are that the heat dissipation losses due to convection, vaporization and radiation, and the influence of metal droplets are negligible. These assumptions don't affect the model accuracy's because many authors [8-10] have shown that the convective heat produced by the electric current is the major part of the energy transferred to the anode from the welding arc. Based on the above assumptions, the conservation equations are expressed in terms of the z-axis as follows:

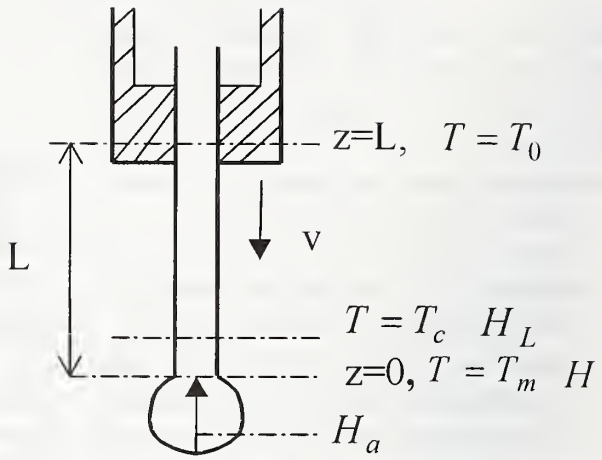

Figure 3. Temperature and energy along electrode extension.

Mass continuity:

$$\frac{\partial \rho}{\partial t} + v\frac{\partial \rho}{\partial z} = 0 \tag{1}$$

Conservation of Energy:

$$\frac{\partial}{\partial z}\left(\lambda(\mathrm{T})\frac{\partial \mathrm{T}}{\partial z}\right) + J^2\Phi(\mathrm{T}) = C_p(\mathrm{T})\rho(\mathrm{T})\left(\frac{\partial \mathrm{T}}{\partial t} + v\frac{\partial \mathrm{T}}{\partial z}\right) \tag{2}$$

The energy equation contains a Joule heating term. The boundary conditions are:

$$\begin{aligned} T &= T_0 \qquad z = L \\ T &= T_m \qquad z = 0 \\ \frac{\partial T}{\partial r} &= 0 \end{aligned} \tag{3}$$

Combining the mass continuity equation and the energy equation, the *damped nonlinear heat equation* can be obtained as follows.

$$\frac{\partial}{\partial z}\left(\lambda(T)\frac{\partial T}{\partial z}\right)+J^2\Phi(T)=0 \tag{4}$$

Heat transfer and temperature distributions during welding are complex and a solution to the equations is dependent on the thermal conductivity, specific heat and density of the mass as a function of temperature. To find analytical solutions to the equations, it is therefore helpful to eliminate the relationship between temperature and the above variables by means of defining a new variable, which serves as a bridge between them. The heating effect, called the heat content is defined as:

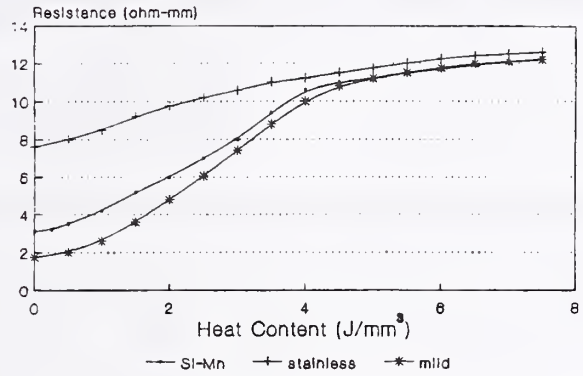

Figure 4. Resistivity vs. heat content for typical wires.

$$H=\frac{\lambda(T)}{v}\frac{\partial T}{\partial z} \tag{5}$$

Replacing the parenthesis expression with $H\ v$ in Equation 4 yields an equivalent first order nonlinear differential equation given by:

$$\frac{\partial H}{\partial z}=-\frac{J^2\Phi(T)}{v} \tag{6}$$

The resistivity versus heat content is shown for three representative electrode wire materials in Figure 4. The curves may be approximated with two straight lines about the knee of the curve. The resistivity can be written in terms of heat content as,

$$\Phi(H)=\begin{Bmatrix} a_1H+b_1 & H\le H_c \\ a_2H+b_2 & H>H_c \end{Bmatrix} \tag{7}$$

where H_c $(4\ J/mm^3)$ is heat content at the Curie temperature. From Equation 6, the heat content as a function of time can be written as:

$$\frac{\partial H}{\partial t}=-J^2\Phi(T) \tag{8}$$

The desired relationship between heat content, time and current density can be obtained by rearranging and integrating Equation 8 over time.

$$\int_0^{H_L}\frac{\partial H}{\Phi(H)}=\int_{t-\frac{z}{v}}^{t}J^2\,\partial t \tag{9}$$

where H_L is the Joule heating energy per unit volume of wire. The left side of Equation 9 is called the *action integral* [16]. It is dominant in the dynamic behavior of the process. Equation 9 shows that the heat content based on temperature and temperature history is related to the current density and current density history. Substitution of Equation 7 into Equation 9 gives:

$$\int_0^{H_L} \frac{\partial H}{a_2 H + b_2} = W \qquad H > H_c \tag{10}$$

This equation can be solved for the Joule heating energy:

$$H_L = \begin{cases} \dfrac{b_1}{a_1}\left(e^{a_1 W} - 1\right) & H \le H_c \\ \dfrac{b_2}{a_2}\left(k e^{a_2 W} - 1\right) & H > H_c \end{cases} \tag{11}$$

The total heat content along the electrode extension is composed of the following elements:

$$H(z,t) = H_a(0,t) + H_L(z,t) \tag{12}$$

where H_a is called the anode heat content and is derived using Equation 5. This equation is still valid at the electrode tip, but the melting rate instead of wire feed rate must be used in the equation. Therefore, Equation 5 can be written as:

$$\frac{\partial T}{\partial z} = \frac{v_m H}{\lambda(T)} \tag{13}$$

By using the chain rule, the temperature as a function time and z can be expressed in the following form:

$$\frac{\partial T(z,t)}{\partial z} = \frac{\partial T}{\partial H}\frac{\partial H}{\partial z} + \frac{\partial T}{\partial t}\frac{\partial t}{\partial z} \tag{14}$$

The melting wire is assumed to have constant melting temperature at the anode tip so that $\partial T/\partial t$ is considered to be zero. After substituting Equations 6 and 13 into Equation 14, the heat content at the anode tip becomes:

$$H = -\frac{\Phi(T)\lambda(T)J^2}{{v_m}^2}\frac{\partial T}{\partial H} \tag{15}$$

In order to formulate the anode heat content in terms of current density and melting rate, the above equation associated with the boundary conditions is rearranged and integrated over H and T.

$$-\int_{H_L}^{H} H\,\partial H = \frac{J^2}{v_m^2}\int_{T_c}^{T_m}\lambda(T)\Phi(T)\partial T \tag{16}$$

The solution to Equation 16 under these conditions is given by:

$$-H_a = \frac{J}{v_m}\sqrt{\int_{T_c}^{T_m}\frac{\lambda(T)\Phi(T)}{0.5+\delta(T)}\partial T} = \frac{J\phi(T)}{v_m} \tag{17}$$

where $0 \le \delta(T) \le 1$ is the relative proportion of solid in the two-phase zone and $\phi(T)$ is called the *work function*. The physical meaning of the negative sign is that the droplet has to supply thermal energy to decrease the temperature difference. After substituting for H_a and H_L from Equations 11 and 17, the final form of the heat content is:

$$H = \begin{cases} \dfrac{J\phi(T)}{v_m} + \dfrac{b_1}{a_1}(e^{a_1 W} - 1) & H \le H_c \\ \dfrac{J\phi(T)}{v_m} + \dfrac{b_2}{a_2}(ke^{a_2 W} - 1) & H > H_c \end{cases} \tag{18}$$

The results of wire melting experiments show that the heat content can be described by the exponential.

$$H = H_0(1 - e^{-ct}) \tag{19}$$

Differentiating this equation gives the dynamic nature of the heat content as represented in the following equation.

$$\frac{\partial H}{\partial t} = c(H_0 - H) \tag{20}$$

The solution of Equation 20 gives the dynamic melting rate.

$$v_m = \begin{cases} \dfrac{c\phi(T)J + \phi(T)\dfrac{\partial J}{\partial t} + J\dfrac{\partial \phi(T)}{\partial t}}{-b_1 e^{a_1 W}\left(\dfrac{c}{a_1} + \dfrac{\partial W}{\partial t}\right) + c\left(\dfrac{b_1}{a_1} + H_0\right)} & H \le H_c \\ \dfrac{c\phi(T)J + \phi(T)\dfrac{\partial J}{\partial t} + J\dfrac{\partial \phi(T)}{\partial t}}{-b_2 k e^{a_2 W}\left(\dfrac{c}{a_2} + \dfrac{\partial W}{\partial t}\right) + c\left(\dfrac{b_2}{a_2} + H_0\right)} & H > H_c \end{cases} \tag{21}$$

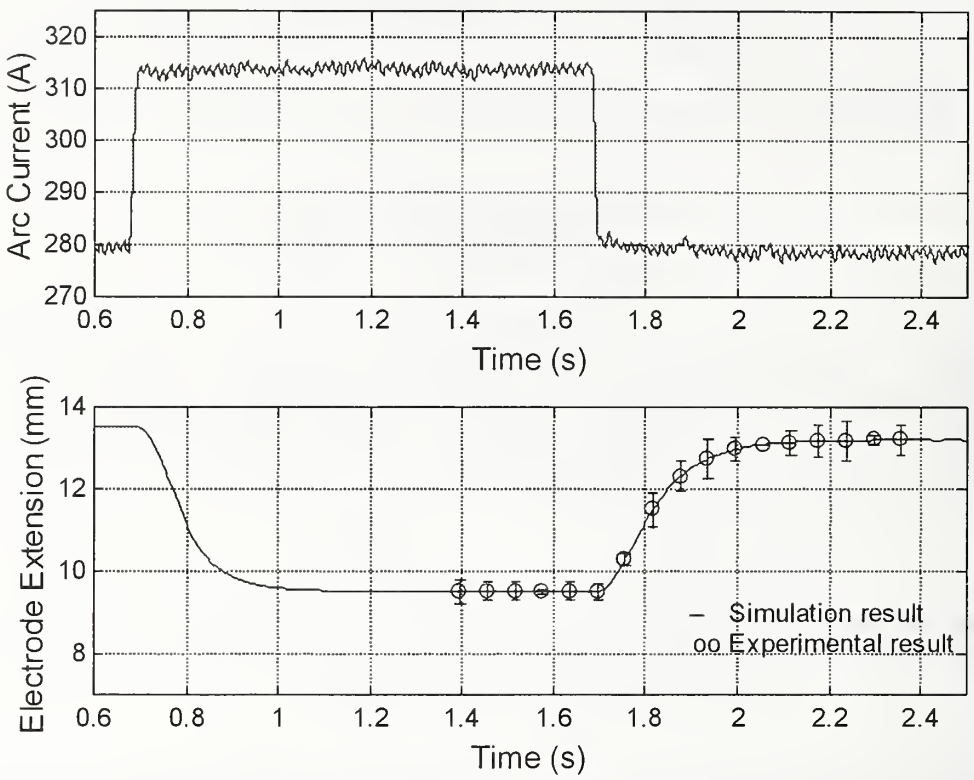

Figure 5. Simulation and experimental results for 30A increase in arc current.

Shepard's burn-off rate model [16] is also derived from this equation under appropriate simplifying assumptions. He assumed that the work function is constant and the heat content for the wire is above H_c ($4\ J/mm^3$). It is concluded from his assumptions that the power is dissipated in a constant potential drop in the arc. By using his assumptions, the equation reduces to:

$$v_m = \frac{k_1 J}{1 - k_2 W} \qquad H > H_c \tag{22}$$

Under steady state conditions, this equation reduces to Lesnewich's equation [7].

$$v_m = k_1 J + k_2 L J^2 \tag{23}$$

Electrode Voltage Model

The current changes in the GMAW process cause significant temperature changes along the electrode extension. These changes lead to a temperature-dependent resistance which produces the electrode voltage drop. The basic equation for the resistance is given by:

$$R_L = \frac{\Phi(T)}{A} L \tag{24}$$

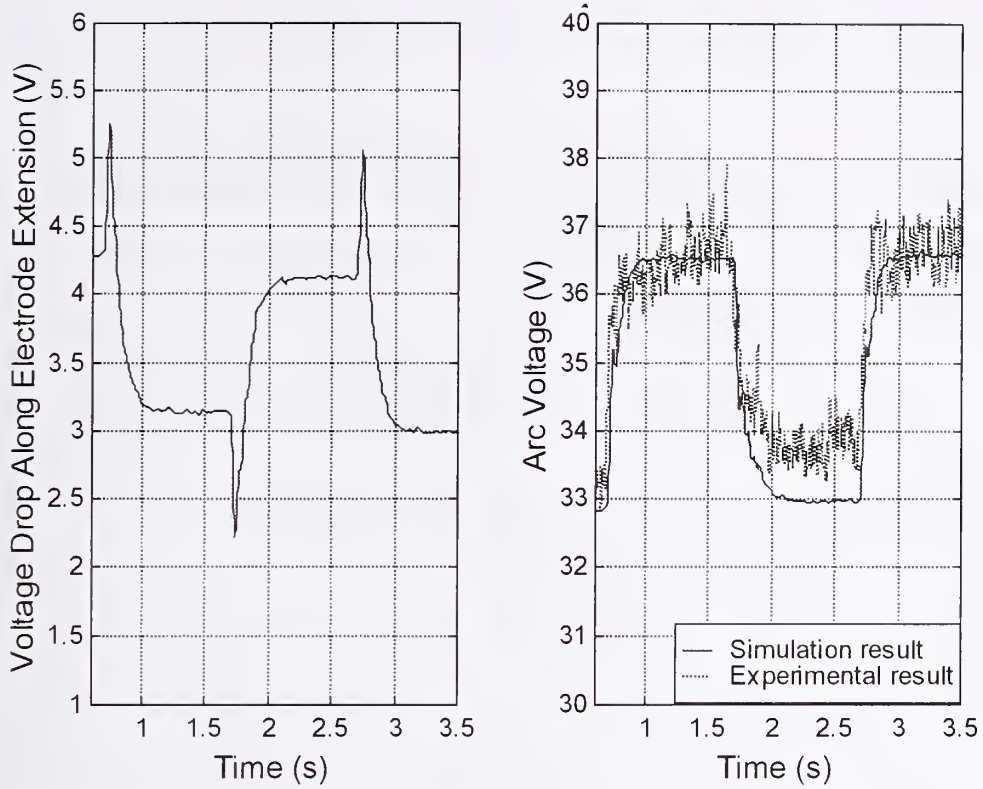

Figure 6. Electrode voltage drop and comparison of simulation and experimental results for total voltage.

The voltage drop is the product of the welding current and resistance of the electrode extension.

$$V_L = I R_L \tag{25}$$

Arc Voltage Model

There have been a number of models for the arc voltage model in the gas tungsten arc welding (GTAW) and the GMAW processes. These models show that as the welding current is increased, the relationship between the voltage and current is approximately linear. The arc voltage drop can be modeled as

$$V_{arc} = V_0 + R_a I + E_a l \tag{26}$$

where R_a defines the current dependency of the arc voltage and E_a defines the length dependency of the arc. The total voltage can be obtained by adding the electrode voltage drop and arc voltage drop.

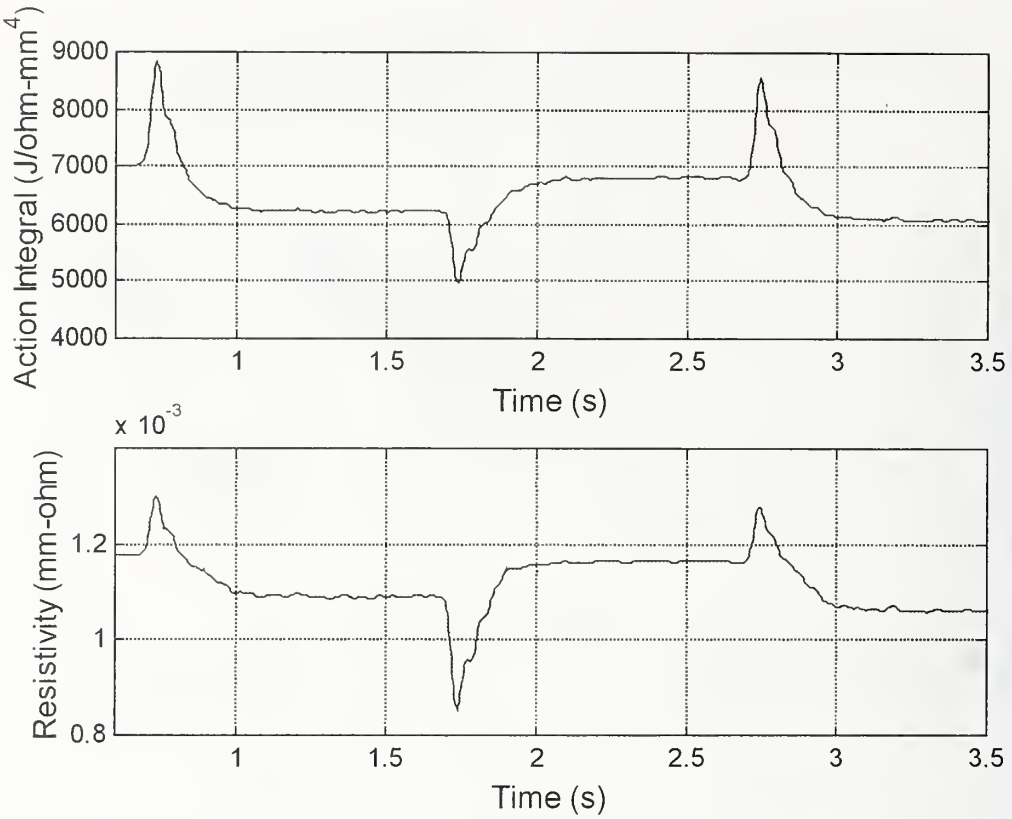

Figure 7. Dynamic action integral and resistivity.

EXPERIMENTAL PROCEDURES

Welding experiments were structured to examine the dynamic nature of the electrode extension and arc length from both electrical signal measurements and a high-speed video system (2000 frames/s). A 1.2mm (0.045") diameter ER705-2 steel wire and Argon+5%CO^2 shielding gas were used. The contact-tip-to-work distance (CTWD) was 20mm (3/4") and the travel speed was set at 6 mm/s. The current and voltage signals were collected at 5000Hz. Using a constant current power source with electrode positive, both square wave and sinusoidal perturbations, of variable amplitude (20 A, 30 A and 40 A peak-to peak), were superimposed on the current to allow measurement of changes in the electrode extension, arc length, and total voltage. The square wave perturbations provided a direct measure of the time response of the electrode melting.

RESULTS AND DISCUSSION

The model was tested by introducing 30A step changes to the arc current, as the wire feed rate was constant at 140 mm/s. Comparison of the experimental and simulation results is shown in Figure 5. The electrode extension settles from an initial value of 13.5mm to 9.5mm in 0.4s. Similarly, the arc voltage changes from 33.5 V to 36.5 V. The effect of electrode voltage drop changes on the dynamic behavior of the process can be seen in Figure 6. As shown, the voltage suddenly decreases to about 2.3 V and increases to about 4.1 V during the current transition. This

shows that the electrode voltage drop is a significant factor in the dynamic response of the process. Figure 7 shows the dynamic behavior of the action integral and resistivity. From the figure, it can be seen that the resistivity of the wire can not be assumed to be constant during the current transition.

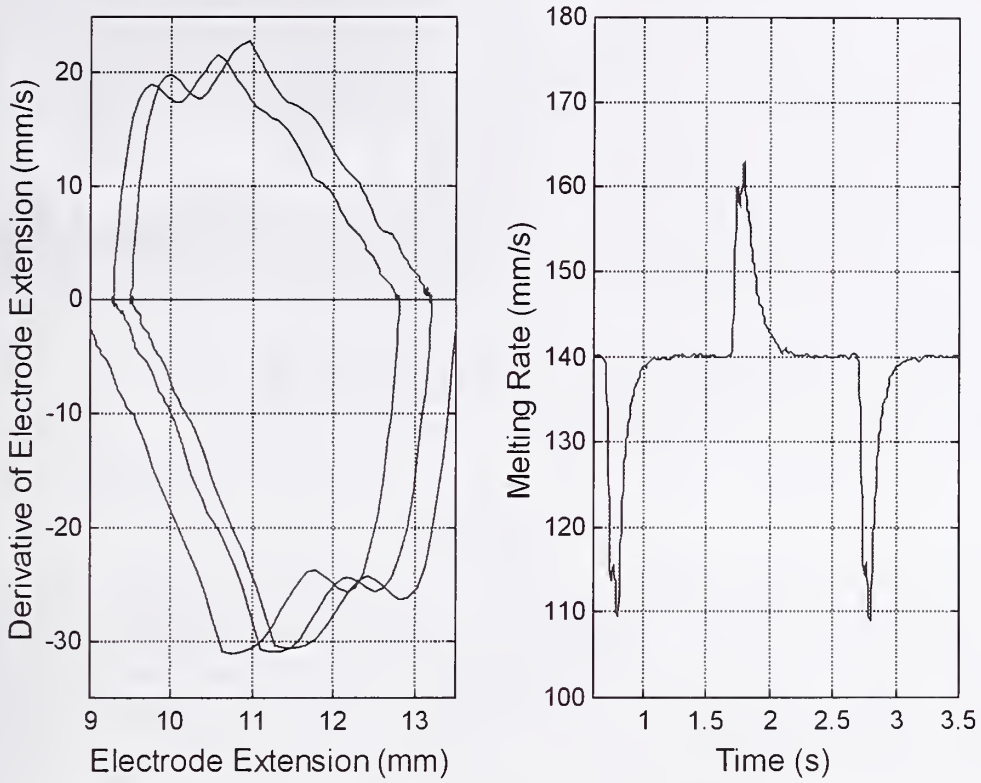

Figure 8. Phase plain analysis and dynamic melting rate.

In order to examine motion trajectories corresponding to various initial conditions and information concerning the system stability, a phase plane analysis was made. As seen in Figure 8, the initial point (13.5mm) for the electrode extension is moved to another point (9.5mm) in the phase plane. Oscillatory behavior of the curve results from the dynamic resistance changes in the electrode extension.

Figure 9 illustrates the relationship between droplet frequency and arc current. The

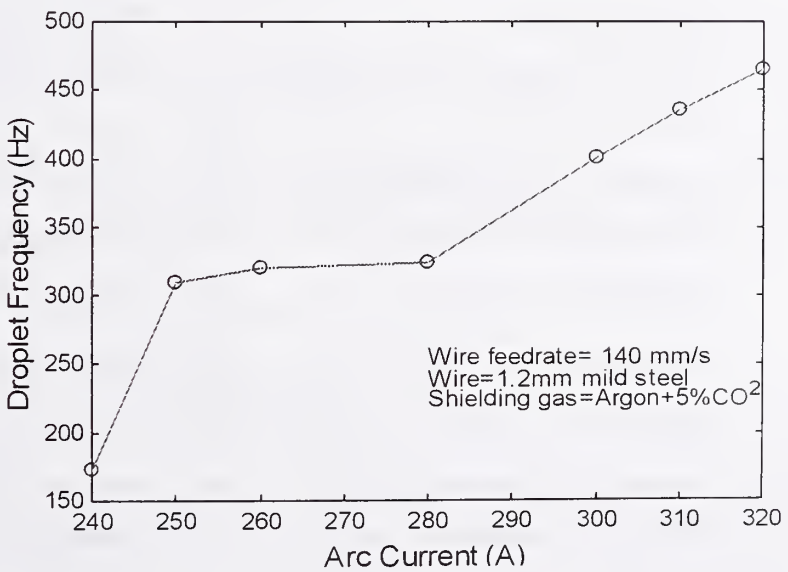

Figure 9. Relationship between droplet frequency and arc current.

droplet frequency increases markedly at the transition from globular to drop spray transfer, and at the transition from drop spray transfer to streaming spray transfer.

An interesting aspect of the high-speed video system used in capturing the experimental electrode extension dynamics is its ability to capture the power source and droplet dynamics as well. Power spectrum analysis of a single pixel corresponding to the high-speed video is illustrated in Figure 10. As seen, the frequency components are at 120Hz, 240Hz and 320Hz. These results match results of the same analysis for the arc current. The high-speed video system has been shown to be capable of capturing the dynamics of the power supply and the process itself, and it can also be used to detect the droplet transfer frequency.

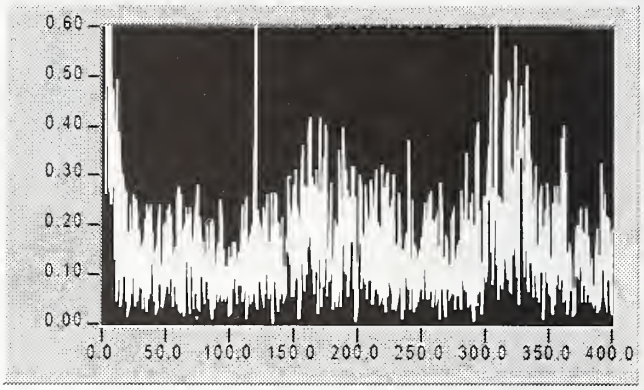

Figure 10. Power spectral density of the pixel of high-speed films

CONCLUSIONS

A dynamic model of the GMAW process has been developed and tested by comparing simulations to experimental results. The model is applicable to both constant potential and constant current modes (including pulse current) of the GMAW process. The dynamic model developed in this work is essential to development of a truly adaptive arc length regulation with the pulsed current GMAW process.

NOMENCLATURE

ρ	Density (g/mm^3)	T_m	Melting temperature (K)
λ	Thermal conductivity ($W/(mm\,K)$)	T_0	Initial temperature (K)
ϕ	Work function (V)	W	Action integral ($J/(\Omega\, mm^4)$)
Φ	Resistivity of wire ($\Omega\, mm$)	V_L	Voltage drop along electrode extension (V)
J	Current density (A/mm^2)	V_{arc}	Arc voltage drop (V)
v	Wire feed rate (mm/s)	k_{12}	Coefficients of Lesnewich's equation
v_m	Melting rate (mm/s)	a_{12} b_{12}	Coefficients of the resistivity
C_p	Specific heat capacity ($J/(g\,K)$)	H_a	Anode heating content (J/mm^3)
H	Heat content (J/mm^3)	H_L	Joule heating content (J/mm^3)
H_0	Melting heat content (J/mm^3)	T	Temperature (K)

REFERENCES

1. Cook, G. E., Andersen K. and Barrett R.J. 1992. Keynote Address: Feedback and Adaptive Control in Welding. *International Trends in Welding Science and Technology*, ASM International, 891-s to 903-s.
2. P. Zhu and J.J. Lowke; 1993. Theoretical study of the melting of the cathode tip of a free burning arc in argon for various conical angles. *J. Phys.* D: *Appl Phys,* (26): 1073-1079.
3. Halmoy, E., Pulsating Welding Arc, *SINTEF Report STF16-A79021*, Trondheim, Netherlands.
4. Bingul, Z.1996. Stability Considerations for the Gas Metal Arc Welding Process, M.S. Thesis, Vanderbilt University.
5. Bingul, Z., Cook, G. E., Barnett, R. J., Strauss, A. M., and Wells, B. S., 1998. An Investigation of Constant Potential GMAW Instability Behavior, 5th International Conference on Trends in Welding Research.
6. Cook, G. E., 1998. Decoupling of Weld Variables for Improved Automatic Control, 5th International Conference on Trends in Welding Research.
7. Lesnewich, A., 1958. Control of Melting Rate and Metal Transfer in Gas-Shielded Metal-Arc Welding; Part 1 – Control of Electrode Melting Rate, *Welding Journal*, 37 (8): 343-s to353-s.
8. Halmoy, E., 1979. Wire melting rate, droplet temperature, and effective anode melting potential, Proc. Int. Conf. On Arc Physics and Weld Pool Behavior, The Welding Institute, Cambridge, UK.
9. Wilson, J. L. and Claussen, G. E., 1956. The Effect of I^2R Heating on Electrode Melting Rate, *Welding Journal*, 35(1): 1-s to 8-s.
10. Waszink, J. H. and van den Heuvel, G. J. P. M., 1982. Heat Generation and Heat Flow in the Filler Metal in GMA Welding, *Welding Journal*, 61(8): 269-s to 282-s.
11. Quintino, L. and Allum, C. J., 1984. Pulsed GMAW Interactions Between Process Parameters, Part 1," *Welding and Metal Fabrication*, March.
12. Amin, M., 1983. Pulse current parameters for arc stability and controlled metal transfer in arc welding, *Metal Construction*, May.
13. Amin, M., 1986. Microcomputer control of synergic pulsed MIG welding," *Metal Construction*, April.
14. Smati, Z., 1986. Automatic pulsed MIG welding, *Metal Construction*, January.
15. Richardson, M. I., Bucknall, P. W., and Stares, I., 1994. The Influence of Power Source Dynamics on Wire Melting Rate in Pulsed GMAW Welding, *Welding Journal*, 73(2): 32-s to 37-s.
16. Shepard, M. E., 1991. Modeling of Self-Regulation in Gas-Metal Arc Welding, Ph.D. Dissertation.
17. Quinn, T. P. and Madigan, R. B., 1993. Dynamic Model of Electrode Extension for Gas Metal Arc Welding, *International Trends in Welding Science and Technology*, ASM International,1003-1008, 1993.
18. Mao, W. and Ushio, M., 1997. Measurement and theoretical investigation of arc sensor sensitivity in dynamic state during gas metal arc welding," *Science and Technology of Welding and Joining*, 2(5): 191-198.
19. Shepard, M. E. and Cook, G. E., 1993. A Frequency-Domain Model of Self-Regulation in Gas-Metal Arc Welding, *International Trends in Welding Science and Technology*, Eds: S. A. David and J. M. Vitek, ASM International, 899-903.

EMPIRICAL MODELS FOR GMAW FILLET WELD PROFILES

D. Barborak[†], R. Richardson[†], D. Farson[†], and H. Ludewig[‡]

ABSTRACT

Response Surface Methodology (RSM) with regression modeling was utilized to develop process models for use in a closed-loop multivariate weld geometry control system. A D-Optimal experimental design of 140 single-pass GMAW fillet welds was conducted with twelve process variables. This Resolution V experimental matrix allowed all main and two-factor effects to be determined without confounding. The ranges for these factors were centered around an optimal welding procedure developed from screening experiments in order to develop a locally accurate model. The response variables measured were various aspects of the welds' profile including leg lengths, convexity/concavity, theoretical throat and weld toe angles. Analysis of Variance (ANOVA) and correlation was used to identify important process inputs and linear least-sqaures regression was used to fit input/output relationships. A second-order quadratic equation was developed for each geometric weld feature. These equations were then embedded into software that allowed visualization of the process behavior through Dynamic Response Surface (DRS) plots. These dynamic response surface plots were used to study the effects of commonly encountered disturbing inputs such as variations in root gap or CTWD.

KEYWORDS

GMAW, Fillet Weld, Weld Geometry, Weld Profile, Modeling, Design-of-Experiments, Least Squares Regression, Response Surface Methodology

INTRODUCTION

The basic objectives of applying closed-loop control in automated GMAW applications is to ensure that the desired weld properties are achieved i.e. desired weld geometry, microstructure, mechanical properties and minimal discontinuities. For most automated applications, open-loop control alone is not sufficient to overcome variations in these properties due to a variety of disturbances. Closed-loop control is desired to overcome these deficiencies. From the standpoint of feedback control, the GMA welding process present three principle challenges:

1. In most cases, the relationships between the process inputs and outputs are non-linear.
2. The process inputs and outputs are generally highly related.
3. Not all of the disturbing inputs nor their effects on process outputs are known.

A relatively straightforward approach to closed-loop control system design for welding is to manipulate one process input (such as travel speed or wire feed speed) to control the value of one weld property. In this single-variable control, the other weld properties may fluctuate. This technique is not suitable for weld geometry control because of the highly coupled nature of the

[†] The Ohio State University
[‡] Caterpillar Inc.

welding process inputs that affect weld geometry. Therefore a multivariate control system is required for weld geometry control. The challenge of a multivariable closed-loop control system design is to use a process model to design a control law which maintains the response of the process to within pre-specified tolerance limits despite the effects of uncertainty in the system.

GMAW Models

Theoretical process models for the Gas Tungsten Arc Welding (GTAW) Process has been the focus of the majority of research in physical studies and model development for arc welding. The principle reason is the lessor number of process inputs and cleaner experimental environment for GTAW as compared to the consumable electrode processes such as GMAW. With the GTAW process, plasma arc physics and weld pool dynamics can be studied with the heat source separated from metal transfer. Also, the experimental conditions are cleaner than with consumable electrode processes where experimental measurements must deal with smoke, spatter, and increased sensory noise due to the mass transfer of metal across the arc.

Only recently have the principals of analytical models from GTAW been extended to the consumable electrode processes such as GMAW. The advances include the modeling of heat-flow, microstructural evolution, thermal and residual stresses, and distortion based on the welding parameters. However, accurate theoretical models for weld geometry, profile, or shape do not exist due to the complicated nature of weld pool phenomena such as fluid flow and effects of electro-hydrodynamics for consumable arc welding processes.

Even with accurate theoretical models, a distinguishing characteristic of process models used for control purposes is they must be computable in real-time. Thus, most of the numerical models such as finite element or finite difference methods cannot be applied. Another important aspect of models utilized for control is they generally need to provide both static and dynamic process information.

There has been research focused on developing empirical models for weld geometry. These models derive the relationships between process inputs and outputs with model coefficients chosen to minimize the error between the model prediction and experimental data. The majority of this research has focused on the development of static linear regression models. These models are typically developed using statistical experimental design techniques[1] to predict weld geometry during steady state conditions. Examples of this research include modeling bead-on-plate weld geometry[2,3], and modeling the geometry of consumable electrode processes other than GMAW[4,5,6,7]. A few specific studies on modeling fillet weld geometry have been conducted[8,9].

The development of a robust multivariate control system for weld geometry requires an accurate model with both statics and dynamics. Preliminary work on dynamic models has been conducted using system identification techniques[10] that can predict weld geometry changes during transient conditions. These studies measured the response of the weld pool and final weld shape in real-time to step changes inputs and sinusoidal inputs to the welding parameters[11,12].

RESULTS AND DISCUSSION

In this work, experiments were conducted in three phases with an initial screening experiment, main experimental run, then augmented experimental runs. The data analysis consisted of several techniques including Analysis of Variance, Regression Modeling, and Response Surface Methodology.

Experimental Setup

Tests were conducted with a 6-axis articulated arm welding robot interfaced with a 600 amp power supply. A non-restrained welding fixture was utilized to hold the T-joint in a flat 1F or downhand position during welding. Tests were conducted with a standard 0.052 inch(1.32mm) diameter ER70-S3 wire with 90%Argon-10%CO_2 shielding gas. The material was standard ASTM A36 steel in various thickness' with the T-joint configured from 24 x 12 inch(61 x 15cm) plates.

A data acquisition system was utilized to verify voltage, current, and wire feed speed during welding. All welds were scanned with a laser-based machine vision metrology sensor to digitize the solidified weld profile. Once the weld surface was digitized, a machine vision algorithm then calculated various geometric features of the weld face along its length. These features and their description are as follows:

- Leg Lengths - the distance from the joint root to the weld toe.
- Theoretical Throat - the distance from the beginning of the joint root perpendicular to the hypotenuse of the largest right triangle that can be inscribed within the cross section of the fillet weld.
- Convexity/Concavity - the maximum distance from the face of the weld perpendicular to a line joining the weld toes.
- Toe Angles - the angle formed at the junction of the weld face and the base metal.

Because these variables are being used in the development of a weld geometry control system, the individual leg lengths and toe angels were combined to form a "additive leg length", "differential leg length", "additive toe angle" and "differential toe angle". These variables provide a better picture of the symmetry and magnitude of each weld feature to model for the control system. Geometry weld features such as penetration profile and sidewall fusion were ignored because they could not be directly measured in real-time for use in control. A summary of the response variable nomenclature for the experiments is shown in Table 1.

Table 1 Response Variables.

Description	Notation	Units
Additive Leg Length	ALL	mm
Differential Leg Length	DLL	mm
Additive Toe Angle	ATA	degrees
Differential Toe Angle	DTA	degrees
Theoretical Throat	TT	mm
Convexity/Concavity	CVCC	mm

Experimental Design

The Design of Experiments (DOE) approach was chosen because the data involved has experimental error and contains process noise. Therefore, statistical analysis is the only objective approach to the analysis. To use Response Surface Methodology, all factors had to be varied with at least three levels in order to allow non-linearity's in the model. Also, to know the main effects and two-factor interactions without aliasing and confounding, the experimental design had to be of resolution V. This allowed construction of a full quadratic model for each response variable. An initial screening experiment was performed to find a baseline welding procedure that produced acceptable welds with the desired geometric shape. Based on the results of the screening experiment thirteen factors were chosen. In order to reduce the number of experimental runs to be conducted, Voltage and Wire Feed Speed were treated as covariates i.e. they were varied together linearly, and were combined to form what was called the Power Setting Pair (PSP). Also, the three weaving parameters were combined to form a block in the experimental design.

For the experiment, the twelve factors were to be varied in a combination of three levels each in order to form a full quadratic model. This required that at least 91 (1+2*12+12(12-1)/2 = 91) distinct tests or runs be conducted. Various experimental designs are compared in Table 2. While it is recommended that a standard design such as the Central Composite (CCD) or Box-Behhnken (BBD) be used, this is not usually practical for welding applications because of the large number of experiments required. An alternative is to use a saturated or nearly saturated design that requires near the minimal amount of runs as calculated above. These design types include the small-composite (SCD), Koshal designs, hybrid designs, or optimal designs. The D-optimal design criteria[13,14,15] was used here because it produces the absolute minimum number of experiments required to estimate the second order model with a resolution of V. By adding nine center points, the initial experimental design totaled 100 tests.

Table 2 Experimental Designs and Their Required Number of Tests.

Design	Notation	# Tests
Full Factorial Design	3^{12}	531,441
Res.V Central Composite Design	2^{12}+2*12+5	4125
Res.IV Central Composite Design	2^{12-1}+2*12+5	2077
Box-Behnken Design	2^3*12+5	101
D-optimal Design	D^{12}	91

After analysis of the data from the original experimental design, it was decided to augment the experimental matrix by adding an additional 41 tests. This augmentation accounted for slower travel speeds down to 7 inches/minute, while the original experimental matrix went no slower than 10 inches/minute. The GMAW variables with their corresponding ranges and levels utilized for the experiment are shown in Table 3

Table 3 DOE Variables, Range and Levels.

Variable	Notation	Range	Units	Factor Levels
Voltage	PSP	31.5 to 34.5	volts	3
Wire Feed Speed	PSP	375 to 425	inches/minute	3
Travel Speed	TS	7 to 12	inches/minute	5
Torch Offset	TO	-1.3 to 1.3	mm	3
Root Gap	GAP	0 to 1.25	mm	2
Plate Thickness	PT	6 to 24	mm	4
CTWD	CTWD	25 to 30	mm	2
Travel Angle	TA	-15 to -5	degrees	3
Work Angle	WA	-5 to 5	degrees	3
Part Angle	PA	6 to 10	degrees	3
Weave Amplitude	WVA	0 to 8	mm	3
Weave Frequency	WVF	0 to 1	Hz.	3
Weave Dwell	WVD	0 to 0.2	seconds	3

Factor Significance

In order to determine which variables significantly affected the various weld geometry, features two techniques namely ANOVA and Correlation analysis were utilized. The confidence interval was chosen to be 95% (α=0.05) to provide a 95% or more certainty that a variable significantly affects a response. Analysis of Variance or ANOVA techniques help to determine the effects of a parameter on a response by partitioning the total variance into its component parts. Variance analysis permits the differentiation between significant and insignificant parameters where comparison of means plays a key role. The correlation coefficient is a measure of the degree of linear relationship between two variables or a factor and response.

A summary of the response variables, and the significant factors is shown in Table 4. The main significance level was 95%, with factors showing at least 90% significant in parenthesis. Some of the cause-and-effect relations are intuitive such as the effect of Power Setting Pair (PSP), and Travel Speed (TS) on Additive Leg Length (ALL). Other relations such as the absence of Torch Offset (TO) affect on Differential Leg Length (DLL), and Differential Toe Angle (DTA). Experience would say that any offset of the torch from the weld centerline should affect weld symmetry, which would show up in these responses.

Table 4 Significant Factors.

Response Variable	Significant Factor, α=0.05(α=0.1)
ALL	PSP, TS, GAP, PT, (WEAVE)
DLL	TS, GAP, PT, WA, (PA)
ATA	TS, GAP, PT, PA, (TA)
DTA	GAP, (TS), (PT), (PA)
TT	PSP, TS, PA, (TO)
CVCC	TS, GAP, PT, TA, PA, (WEAVE)

Regression Modeling

In order to further study the relationships between factors and response variables, linear-regression was used to develop several models for each response variable. Various forms of polynomial approximator structures were constructed including linear without the affine term, linear with affine, linear with affine and cross terms, linear with affine and square terms, and finally a full quadratic approximator. Each of these are summarized as follows:

- Linear without affine

$$y = \theta_1 pt + \theta_2 gap + \theta_3 ts + \theta_4 psp + \theta_5 pa + \theta_6 ctwd + \theta_7 wva + \theta_8 wvd + \theta_9 wvf + \theta_{10} ta + \theta_{11} to + \theta_{12} wa$$

- Linear with affine

$$y = \theta_1 pt + \theta_2 gap + \theta_3 ts + \theta_4 psp + \theta_5 pa + \theta_6 ctwd + \theta_7 wva + \theta_8 wvd + \theta_9 wvf + \theta_{10} ta + \theta_{11} to + \theta_{12} wa + \theta_{13}$$

- Linear with affine and square terms

$$y = \theta_1 pt + \theta_2 gap + \theta_3 ts + \theta_4 psp + \theta_5 pa + \theta_6 ctwd + \theta_7 wva + \theta_8 wvd + \theta_9 wvf + \theta_{10} ta + \theta_{11} to + \theta_{12} wa + \theta_{13} pt^2 + \theta_{14} gap^2 + \theta_{15} ts^2 + \theta_{16} wfs^2 + \theta_{17} volt^2 + \theta_{18} ctwd^2 + \theta_{19} wva^2 + \theta_{20} wfs^2 + \theta_{21} wvd^2 + \theta_{22} ta^2 + \theta_{23} to^2 + \theta_{24} ta^2 + \theta_{25} to^2 + \theta_{26} wa^2 + \theta_{27}$$

- Linear with affine and cross terms

$$y = \theta_1 pt + \theta_2 gap + \theta_3 ts + \theta_4 psp + \theta_5 pa + \theta_6 ctwd + \theta_7 wva + \theta_8 wvd + \theta_9 wvf + \theta_{10} ta + \theta_{11} to + \theta_{12} wa + \theta_{13} pt*gap + \theta_{14} pt*ts + \theta_{15} pt*wfs + \theta_{16} pt*volt + \theta_{17} pt*pa + \theta_{18} pt*wva + \theta_{19} pt*wvd + \theta_{20} pt*wvf + \theta_{21} pt*ta + \theta_{22} pt*to + \theta_{23} pt*wa + \theta_{24} gap*ts + \ldots etc\ldots + \theta_{90}$$

- Full Quadratic

$$y = \theta_1 pt + \theta_2 gap + \theta_3 ts + \theta_4 psp + \theta_5 pa + \theta_6 ctwd + \theta_7 wva + \theta_8 wvd + \theta_9 wvf + \theta_{10} ta + \theta_{11} to + \theta_{12} wa + \theta_{13} pt^2 + \theta_{14} gap^2 + \theta_{15} ts^2 + \theta_{16} wfs^2 + \theta_{17} volt^2 + \theta_{18} ctwd^2 + \theta_{19} wva^2 + \theta_{20} wfs^2 + \theta_{21} wvd^2 + \theta_{22} ta^2 + \theta_{23} to^2 + \theta_{24} ta^2 + \theta_{25} to^2 + \theta_{26} wa^2 + \theta_{27} pt*gap + \theta_{28} pt*ts + \theta_{29} pt*wfs + \theta_{30} pt*volt + \theta_{31} pt*pa + \theta_{32} pt*wva + \theta_{33} pt*wvd + \theta_{34} pt*wvf + \theta_{35} pt*ta + \theta_{36} pt*to + \theta_{37} pt*wa + \theta_{38} gap*ts + \ldots etc\ldots + \theta_{116}$$

Analysis of the residuals and mean-square-error (MSE) for the training data, shown in Table 5, indicates that model accuracy increases with the number of terms in the model. The full quadratic model was the most accurate, having the lowest MSE of all models for each response variable. There is a large discrepancy between the "Linear with Square Terms" and "Linear with Cross Terms" models with the cross terms adding the most accuracy. This indicates that two-factor interactions have more influence on the response variables than the square terms indicating curvature in the hyperplane does not account for as much error as does interactions between input variables. Also, it was interesting to note that the affine term has no effect on linear model accuracy. This must be attributed to the fact that the linear model alone has twelve degrees of freedom that account for the variation in response variables, and that by adding one more degree of freedom i.e. the affine term has no affect.

Table 5 Mean-Square Error for Training Data using Polynomial Approximators

Approximator	ALL	DLL	ATA	DTA	TT
Linear without Affine	2.32	0.22	14.23	7.07	0.30
Linear with Affine	2.32	0.22	14.23	7.07	0.30
Linear with Square Terms	2.18	0.19	11.05	6.30	0.28
Linear with Cross Terms	1.07	0.09	5.89	3.20	0.12
Full Quadratic	0.94	0.09	5.18	2.84	0.11

Dynamic Response Surface Software

Response Surface Methodology (RSM) is a collection of statistical and mathematical techniques useful for studying process behavior. RSM shows graphically, the relationship between the process inputs and process outputs. Because of its graphical nature, only three dimensions or less can be visualized at one time i.e. the effect of two input variables and their interaction on a single response variable or process output. Higher order relations (i.e. greater than three degrees of freedom) are simplified to 3 dimensions for visualization. First order models are used for linear approximations while higher order models such as a full quadratic can show curvature. While such models are reasonably accurate for a small experimental region such as the 141 run DOE, they can be quite inaccurate over larger experimental regions such as in broader screening experiments.

In order to aid in the visualization of the complex relationships between variables such as in welding, Dynamic Response Surface (DRS) software was developed using Matlab™. The DRS software contained a graphical user interface that allowed the user to generate the 3-D response surface of any two process inputs and process response variables (Figure 1). Then the user can manipulate the other process inputs to see their effect on the chosen relationship. The full quadratic models developed in the previous section were incorporated in the DRS software. Figure 1 shows the relationship between Additive Leg Length (ALL), Power Pair (PP), and Travel Speed (TS). The response surface basically indicates that the higher the wire feed speed or slower the travel speed, the larger the leg lengths become, as would be expected from experience.

The graphical user interface of the DRS software (Figure 1) shows all of the process input variables on the left, the response surface plot in the middle, and the modeled process response variables on the right. The user can choose any variables to plot by choosing its corresponding check box. The controls allow the user to manipulate the other variables in the model to see the effect on the chosen response surface. Another software feature is the optimized search were the software will search within the model region for the optimized welding procedure based on the constraints chosen by the user. The search method utilized is steepest descent gradient.

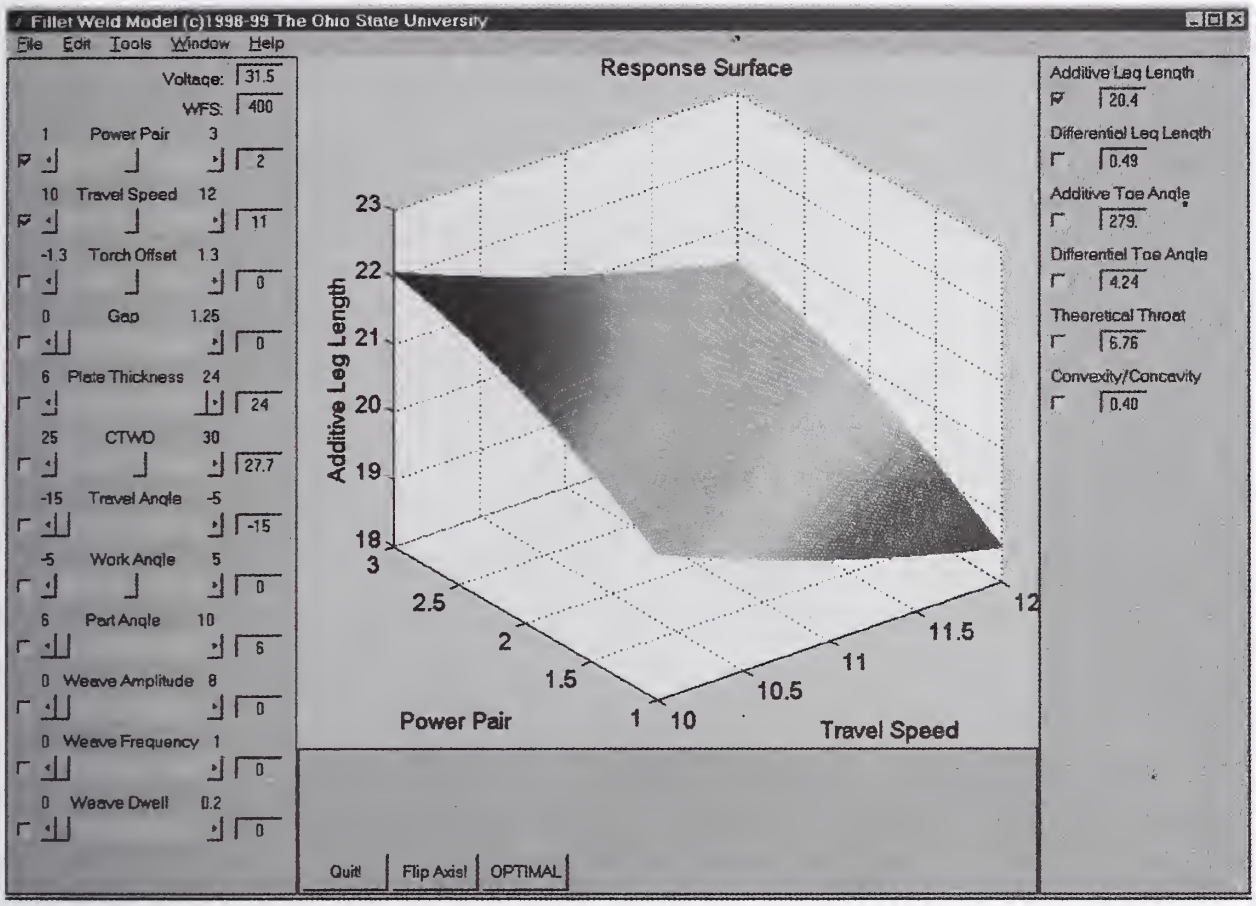

Figure 1 DRS response surface for Additive Toe Angle as a function of Power Pair and Travel Speed.

The some of the response surfaces such as Figure 1 appear very linear, other response surfaces such as shown in Figure 2 are highly non linear. In Figure 2, the Differential Leg Length (DLL) is plotted as a function of Torch Offset (TO) and Work Angle (WA). This response surface basically indicates that the further the Torch Offset or Work Angle are from the center position in the joint, the more asymmetric the weld becomes as their leg lengths differ. In fact, for all combinations of Torch Offset and Work Angle with all other parameters held fixed at their current values, one leg is always larger than the other. This was a trend present within most of the experimental region. It should be noted that the range for Torch Offset and Work Angle during these experiments were fixed relatively small, and that extreme values of either would certainly skew the weld symmetry in the corresponding opposite direction. The fact that this trend was present throughout most of the experimental region leads the belief that other phenomena is affecting the weld symmetry.

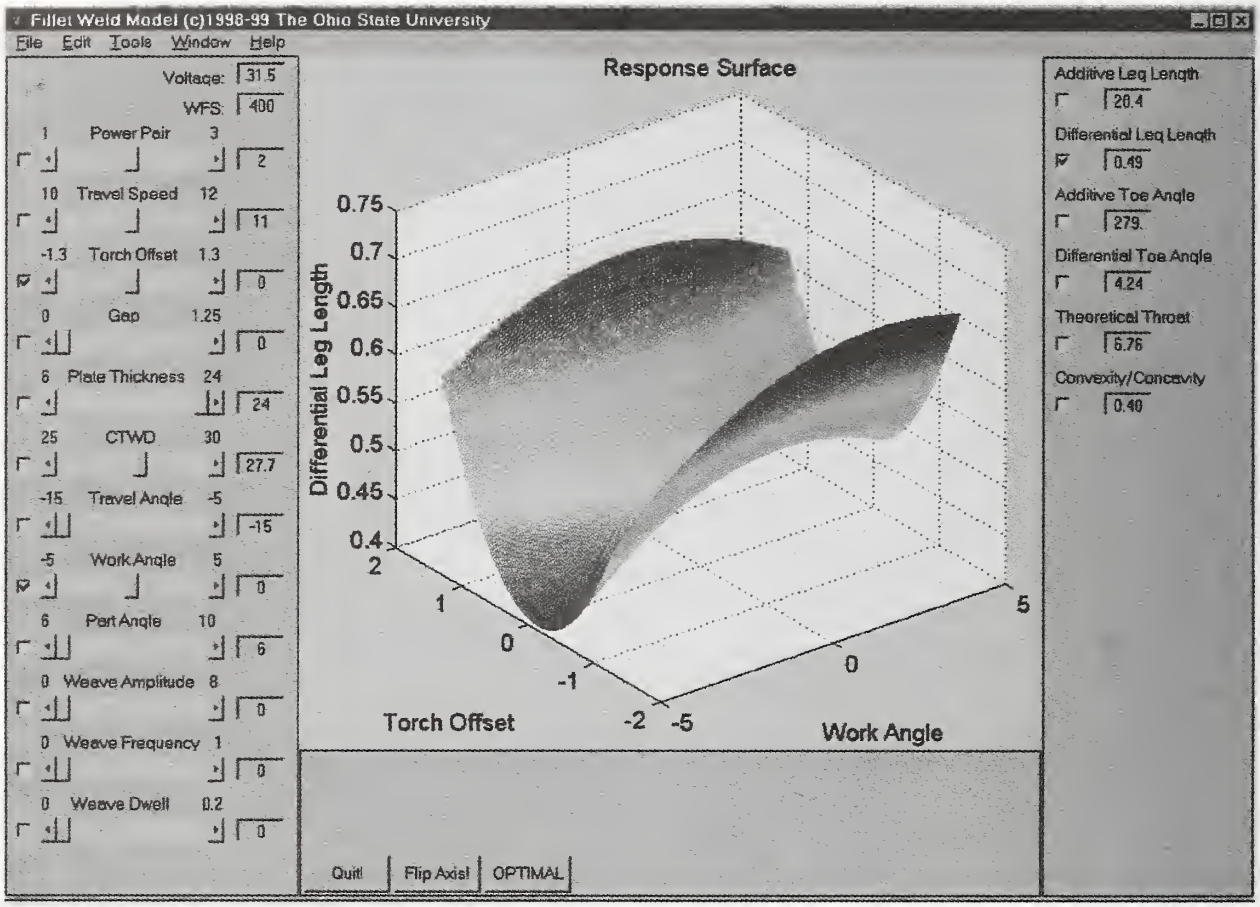

Figure 2 DRS response surface for Differential Leg Length as a function of Torch Offset and Work Angle.

CONCLUSIONS

This paper discusses development of static empirical models for fillet weld profiles to be used in a weld geometry controller. During the development of the models, Design of Experiments (DOE) techniques were utilized to produce statistically accurate results. Analysis of Variance (ANOVA) techniques were then employed to identify important variables to be used in the control system. Regression modeling techniques were used to develop second order process models to used in both control simulations and control algorithm development. Finally, Response Surface Methodology (RSM) was utilized to further study variable relationships and interactions and to aid in the development of a fuzzy control system.

REFERENCES

[1] Montgomery, D.C. 1997. "Design and Analysis of Experiments", ISBN #0471157465, John Wiley & Sons Inc.

[2] Kim, I.S., Siores, E., and Basu, A. 1993. "Relationships Between Process Parameters and Weld Bead Geometry for GMAW Process", Proc. 41st. WTIA/AINDT Fabocn/Fabfair Conf. Wollongong Astralia.

[3] Kumar, R.S., and Parmar, R.S. 1986. "Weld Bead Geometry Prediction for Pulse MIG Welding", Proc. Int. Conf. on Advances in Welding Science and Technology, ASM International.

[4] McConnell, I.A., and McPherson, N.A. 1997. "The Application of Statistical Process Design to a FCAW Process", Welding Journal, 76(10)412s-416s.

[5] Raveendra, J., and Parmar, R.S. 1987. Mathematical Models to Predict Weld Bead Geometry for Flux Cored Arc Welding", Metal Construction, 19(1)31R-35R.

[6] McGlone, J.C., 1982. "Weld Bead Geometry Prediction - A Review", Metal Construction, 14(7)378-384.

[7] Salter, G.R., and Doherty, J. 1981. "Procedure Selection for Arc Welding", Metal Construction, 13(9)544-550.

[8] Moon, H-S., and Na, S-J. 1996. "A Neuro-Fuzzy Approach to Select Welding Conditions for Welding Quality Improvement in Horizontal Fillet Welding", Journal of Manufacturing Systems, 15(6)392-403.

[9] Barton, D.J. 1997. "The Effect of GMA Process Variables on Weld Quality", Proc. SAE Conf. on Earthmoving Industry, paper #981522, Society of Automotive Engineers.

[10] Ljung, L. 1999. "System Identification - Theory for the User", ISBN# 0136566952, Prentice-Hall Inc.

[11] Hale, M.B. and Hardt, D.E. 1990. "Multivariable Geometry Control of Welding - Part I: Process Modeling", Proc. Symp. On Manufacturing Process Modeling and Control, ASME.

[12] Hellinga, M.C., Huissoon, J.P., and Kerr, H.W. 1996. "Identifying Weld Pool Dynamics for GMAW", Proc. 6th Int. Conf. on Computer Technology in Welding. TWI.

[13] Atkinson, A.C. and Donev, A.N. 1992. "Optimum Experimental Designs", Oxford Science Publications.

[14] Nguyen, N-K. and Miller, A.J. 1992. "A Review of Some Exchange Algorithms for Constructing Discrete D-Optimal Designs", Computational Statistics and Data Analysis 14(1992)489-498.

[15] Mitchell, T.J. 1974. "An Algorithm for the Construction of D-Optimal Experimental Design", Technometrics 16(2)203-219.

APPENDIX

ALL = 35.4 + 2.85*psp - 2.65*ts + 3.96*to - 0.52*gap - 0.417*pt - 0.122*ctwd - 0.058*ta +
0.567*wa + 0.83*pa - 1.15*wva + 25.3*wvf - 2.9*wvd - 0.267*psp*psp + 0.133*ts*ts + 0.432*to*to +
0.0113*pt*pt + 0.0017*ta*ta - 0.0070*wa*wa - 0.120*pa*pa + 0.0172*wva*wva - 11.8*wvf*wvf +
0.0109*psp*ts + 0.039*psp*to - 0.097*psp*gap - 0.0112*psp*pt - 0.0268*psp*ctwd - 0.0315*psp*ta -
0.0166*psp*wa - 0.0665*psp*pa + 0.0909*psp*wva - 0.766*psp*wvf - 0.37*psp*wvd - 0.0646*ts*to -
0.013*ts*gap - 0.0079*ts*pt - 0.0288*ts*ctwd + 0.0196*ts*ta - 0.0105*ts*wa + 0.0289*ts*pa +
0.0272*ts*wva - 0.403*ts*wvf - 0.83*ts*wvd - 0.552*to*gap - 0.0067*to*pt - 0.0655*to*ctwd +
0.0007*to*ta + 0.122*to*wa - 0.139*to*pa - 0.0331*to*wva + 0.001*to*wvf - 0.61*to*wvd -
0.0685*gap*pt + 0.001*gap*ctwd - 0.0110*gap*ta - 0.0467*gap*wa + 0.266*gap*pa - 0.169*gap*wva +
0.647*gap*wvf + 3.54*gap*wvd + 0.0071*pt*ctwd + 0.00169*pt*ta + 0.00322*pt*wa + 0.0056*pt*pa -
0.00588*pt*wva - 0.0444*pt*wvf - 0.248*pt*wvd - 0.0094*ctwd*ta - 0.0176*ctwd*wa + 0.0331*ctwd*pa
- 0.0015*ctwd*wva - 0.152*ctwd*wvf - 0.326*ctwd*wvd - 0.00385*ta*wa + 0.0230*ta*pa -
0.0122*ta*wva - 0.015*ta*wvf + 0.394*ta*wvd - 0.0081*wa*pa - 0.0011*wa*wva - 0.036*wa*wvf +
0.055*wa*wvd - 0.0088*pa*wva - 0.335*pa*wvf + 1.47*pa*wvd + 0.739*wva*wvf + 1.65*wva*wvd -
3.29*wvf*wvd

DLL = 1.29 + 0.23*psp - 0.115*ts - 0.318*to - 0.29*gap + 0.137*pt + 0.092*ctwd - 0.102*ta +
0.057*wa - 0.818*pa - 0.520*wva + 7.36*wvf - 5.57*wvd + 0.034*psp*psp + 0.0064*ts*ts +
0.0952*to*to - 0.00178*pt*pt - 0.00399*ta*ta - 0.00239*wa*wa + 0.0435*pa*pa + 0.0131*wva*wva -
5.17*wvf*wvf + 0.0139*psp*ts + 0.0445*psp*to + 0.0623*psp*gap + 0.00556*psp*pt - 0.0224*psp*ctwd
- 0.0008*psp*ta - 0.0110*psp*wa + 0.0063*psp*pa + 0.0005*psp*wva - 0.074*psp*wvf + 0.006*psp*wvd
+ 0.0822*ts*to + 0.0692*ts*gap - 0.00357*ts*pt + 0.0069*ts*ctwd + 0.00966*ts*ta - 0.00426*ts*wa -
0.0217*ts*pa + 0.0012*ts*wva - 0.029*ts*wvf - 0.220*ts*wvd + 0.181*to*gap + 0.00716*to*pt -
0.0112*to*ctwd + 0.0157*to*ta - 0.00434*to*wa - 0.0489*to*pa - 0.0081*to*wva + 0.048*to*wvf +
0.410*to*wvd - 0.0059*gap*pt - 0.0243*gap*ctwd - 0.0064*gap*ta + 0.0202*gap*wa + 0.0001*gap*pa +
0.0129*gap*wva - 0.258*gap*wvf + 1.20*gap*wvd - 0.00376*pt*ctwd - 0.00101*pt*ta - 0.00105*pt*wa +
0.00523*pt*pa - 0.00315*pt*wva - 0.0015*pt*wvf - 0.071*pt*wvd - 0.00034*ctwd*ta + 0.00347*ctwd*wa
- 0.0014*ctwd*pa - 0.00089*ctwd*wva - 0.0835*ctwd*wvf + 0.304*ctwd*wvd + 0.00245*ta*wa -
0.0101*ta*pa - 0.00598*ta*wva + 0.0535*ta*wvf + 0.113*ta*wvd - 0.00268*wa*pa + 0.00250*wa*wva -
0.0248*wa*wvf + 0.056*wa*wvd + 0.0060*pa*wva + 0.171*pa*wvf - 0.052*pa*wvd + 0.384*wva*wvf +
0.011*wva*wvd + 1.06*wvf*wvd

ATA = 342 - 8.9*psp - 9.53*ts - 2.42*to - 4.1*gap - 2.30*pt - 0.11*ctwd - 1.98*ta - 0.32*wa +
4.51*pa + 0.40*wva - 15.1*wvf - 71.0*wvd + 0.76*psp*psp + 0.304*ts*ts - 0.554*to*to +
0.0233*pt*pt - 0.0673*ta*ta + 0.0319*wa*wa - 0.325*pa*pa - 0.0146*wva*wva + 11.4*wvf*wvf +
0.286*psp*ts - 0.184*psp*to + 0.161*psp*gap - 0.0058*psp*pt - 0.027*psp*ctwd - 0.137*psp*ta -
0.108*psp*wa + 0.122*psp*pa + 0.119*psp*wva - 0.47*psp*wvf + 3.22*psp*wvd - 0.208*ts*to -
0.818*ts*gap - 0.0010*ts*pt - 0.007*ts*ctwd - 0.0444*ts*ta - 0.0408*ts*wa + 0.096*ts*pa +
0.078*ts*wva + 0.96*ts*wvf + 3.87*ts*wvd + 0.723*to*gap - 0.0173*to*pt + 0.151*to*ctwd +
0.0504*to*ta - 0.0840*to*wa + 0.134*to*pa - 0.020*to*wva + 0.80*to*wvf + 0.67*to*wvd +
0.103*gap*pt + 0.372*gap*ctwd - 0.086*gap*ta + 0.051*gap*wa - 0.227*gap*pa - 0.014*gap*wva -
1.39*gap*wvf - 0.19*gap*wvd + 0.0339*pt*ctwd - 0.0015*pt*ta - 0.0090*pt*wa + 0.0460*pt*pa +
0.0194*pt*wva - 0.122*pt*wvf + 1.01*pt*wvd + 0.0340*ctwd*ta + 0.0215*ctwd*wa + 0.014*ctwd*pa -
0.0148*ctwd*wva - 0.294*ctwd*wvf - 0.24*ctwd*wvd + 0.0066*ta*wa + 0.0438*ta*pa + 0.0237*ta*wva -
0.248*ta*wvf + 0.19*ta*wvd + 0.0293*wa*pa + 0.0465*wa*wva + 0.118*wa*wvf - 1.11*wa*wvd -
0.007*pa*wva + 0.371*pa*wvf + 1.76*pa*wvd - 1.03*wva*wvf - 0.31*wva*wvd - 14.2*wvf*wvd

DTA = 27.4 + 6.04*psp - 3.33*ts + 2.80*to - 9.33*gap + 0.367*pt - 0.12*ctwd - 0.27*ta + 1.22*wa -
3.11*pa - 1.07*wva + 22.3*wvf - 73.1*wvd - 1.05*psp*psp + 0.074*ts*ts + 0.416*to*to +
0.0091*pt*pt - 0.0181*ta*ta - 0.0344*wa*wa + 0.160*pa*pa + 0.0479*wva*wva - 19.6*wvf*wvf +
0.143*psp*ts + 0.375*psp*to + 0.686*psp*gap + 0.0385*psp*pt - 0.172*psp*ctwd - 0.0385*psp*ta -
0.0767*psp*wa + 0.038*psp*pa + 0.049*psp*wva - 0.52*psp*wvf - 1.40*psp*wvd + 0.400*ts*to +
0.479*ts*gap - 0.0351*ts*pt + 0.107*ts*ctwd + 0.0329*ts*ta - 0.0331*ts*wa - 0.146*ts*pa +
0.0272*ts*wva - 0.085*ts*wvf + 0.97*ts*wvd + 0.903*to*gap + 0.0325*to*pt - 0.180*to*ctwd +
0.0746*to*ta - 0.0663*to*wa - 0.346*to*pa - 0.0456*to*wva + 0.424*to*wvf + 1.73*to*wvd -
0.055*gap*pt - 0.025*gap*ctwd - 0.069*gap*ta + 0.102*gap*wa + 0.383*gap*pa - 0.041*gap*wva -
1.24*gap*wvf + 12.4*gap*wvd - 0.0205*pt*ctwd - 0.00500*pt*ta - 0.00217*pt*wa + 0.0269*pt*pa -
0.0233*pt*wva - 0.006*pt*wvf - 0.500*pt*wvd + 0.0033*ctwd*ta - 0.0032*ctwd*wa - 0.0102*ctwd*pa -
0.0470*ctwd*wva - 0.218*ctwd*wvf + 2.50*ctwd*wvd + 0.0164*ta*wa - 0.0500*ta*pa - 0.0403*ta*wva +
0.200*ta*wvf + 0.428*ta*wvd - 0.0311*wa*pa + 0.0206*wa*wva - 0.208*wa*wvf - 0.301*wa*wvd +
0.0143*pa*wva + 0.876*pa*wvf + 0.02*pa*wvd + 1.84*wva*wvf - 0.51*wva*wvd + 8.6*wvf*wvd

TT = 8.25 + 1.59*psp - 0.375*ts + 1.52*to - 0.21*gap - 0.005*pt - 0.064*ctwd + 0.045*ta +
0.244*wa + 0.060*pa - 0.431*wva + 9.67*wvf + 1.8*wvd - 0.187*psp*psp + 0.0260*ts*ts + 0.162*to*to
+ 0.00299*pt*pt + 0.00291*ta*ta - 0.00323*wa*wa - 0.0302*pa*pa + 0.00716*wva*wva - 4.83*wvf*wvf -
0.0036*psp*ts + 0.0283*psp*to - 0.0501*psp*gap - 0.00305*psp*pt - 0.0074*psp*ctwd - 0.0019*psp*ta
+ 0.0009*psp*wa - 0.0310*psp*pa + 0.0238*psp*wva - 0.229*psp*wvf - 0.297*psp*wvd - 0.0087*ts*to +
0.0306*ts*gap - 0.00232*ts*pt - 0.0089*ts*ctwd + 0.00842*ts*ta - 0.00246*ts*wa + 0.0074*ts*pa +
0.0070*ts*wva - 0.173*ts*wvf - 0.595*ts*wvd - 0.237*to*gap - 0.00268*to*pt - 0.0300*to*ctwd +
0.0005*to*ta + 0.0452*to*wa - 0.0556*to*pa - 0.0102*to*wva - 0.055*to*wvf - 0.250*to*wvd -
0.0309*gap*pt - 0.0118*gap*ctwd - 0.0054*gap*ta - 0.0226*gap*wa + 0.120*gap*pa - 0.0652*gap*wva +
0.349*gap*wvf + 1.12*gap*wvd + 0.00027*pt*ctwd + 0.00105*pt*ta + 0.00193*pt*wa - 0.00184*pt*pa -
0.00238*pt*wva - 0.0184*pt*wvf - 0.130*pt*wvd - 0.00462*ctwd*ta - 0.00866*ctwd*wa +
0.0139*ctwd*pa - 0.00068*ctwd*wva - 0.0335*ctwd*wvf - 0.073*ctwd*wvd - 0.00185*ta*wa +
0.00678*ta*pa - 0.00653*ta*wva + 0.0127*ta*wvf + 0.110*ta*wvd - 0.00303*wa*pa - 0.00363*wa*wva -
0.0146*wa*wvf + 0.067*wa*wvd - 0.0036*pa*wva - 0.146*pa*wvf + 0.524*pa*wvd + 0.319*wva*wvf +
0.581*wva*wvd - 0.12*wvf*wvd

CVCC = 1.86 - 0.112*psp - 0.347*ts + 0.234*to + 0.193*gap - 0.122*pt + 0.0105*ctwd - 0.0592*ta +
0.0155*wa + 0.284*pa - 0.046*wva + 1.52*wvf - 1.98*wvd + 0.0102*psp*psp + 0.0159*ts*ts +
0.0281*to*to + 0.00159*pt*pt - 0.00203*ta*ta + 0.00019*wa*wa - 0.0218*pa*pa + 0.00066*wva*wva -
0.585*wvf*wvf + 0.0078*psp*ts - 0.0127*psp*to - 0.0122*psp*gap - 0.00157*psp*pt -
0.00420*psp*ctwd - 0.00838*psp*ta - 0.00617*psp*wa + 0.0028*psp*pa + 0.0107*psp*wva -
0.0527*psp*wvf + 0.106*psp*wvd - 0.0157*ts*to - 0.0206*ts*gap - 0.00051*ts*pt -
0.00293*ts*ctwd + 0.00063*ts*ta - 0.00139*ts*wa + 0.00540*ts*pa + 0.00144*ts*wva + 0.0031*ts*wvf
+ 0.092*ts*wvd - 0.0147*to*gap + 0.00024*to*pt + 0.00043*to*ctwd - 0.00007*to*ta + 0.00776*to*wa
- 0.0077*to*pa - 0.00376*to*wva + 0.0279*to*wvf - 0.025*to*wvd - 0.00280*gap*pt + 0.0051*gap*ctwd
+ 0.00145*gap*ta - 0.00144*gap*wa - 0.0008*gap*pa - 0.0118*gap*wva - 0.017*gap*wvf +
0.254*gap*wvd + 0.00215*pt*ctwd + 0.000301*pt*ta + 0.000031*pt*wa + 0.00227*pt*pa +
0.00021*pt*wva - 0.00397*pt*wvf + 0.0088*pt*wvd - 0.00015*ctwd*ta - 0.00010*ctwd*wa +
0.00071*ctwd*pa - 0.00024*ctwd*wva - 0.0277*ctwd*wvf - 0.070*ctwd*wvd - 0.000268*ta*wa +
0.00240*ta*pa + 0.00018*ta*wva - 0.0094*ta*wvf + 0.0436*ta*wvd - 0.00075*wa*pa +
0.00156*wa*wva + 0.0032*wa*wvf - 0.0175*wa*wvd - 0.00077*pa*wva - 0.0033*pa*wvf + 0.196*pa*wvd +
0.0140*wva*wvf + 0.122*wva*wvd - 0.63*wvf*wvd

Session A3: Weld Shape and Distortion Modeling

NUMERICAL AND EXPERIMENTAL STUDY ON THE TRANSPORT PHENOMENA IN THE PLASMA ARC WELDING

H. G. Fan, R. Kovacevic, B. Zheng, H. J. Wang

ABSTRACT

A mathematical model is developed to describe the heat transfer and fluid flow in stationary keyhole plasma arc welding. Using the Volume of Fluid (VOF) method, the processes of heating, melting, collapsing and subsequent solidifying in the molten pool are dynamically studied. The predicted results have been compared with the experimental weld and keyhole shape. Theoretical predictions and experimental results are in close agreement, suggesting the theoretical treatment of the model is good.

Keywords: Plasma welding, Numerical simulation, Keyhole mode.

INTRODUCTION

In plasma arc welding, a constricting plasma arc is used as the concentrated energy source to melt the workpiece. Due to its high energy density, and its high velocity plasma jet, the plasma arc welding process can produce deeper weld penetrations, faster travel speeds, and reduced thermal distortions when compared with gas tungsten arc welding [1]. Plasma arc welding fusion can be categorized as either melt-in or keyhole mode. The keyhole mode is the primary attribute of plasma arc welding that makes it so attractive. In the keyhole-welding mode, as shown in Figure 1, the plasma jet completely penetrates the weld pool, forming a symmetric, funnel-shaped cavity called a keyhole, and a similarly shaped liquid-solid metal phase boundary. Some mathematical models on the prediction of weld and keyhole shapes have been developed for electron beam and laser beam welding. But the mechanism of keyhole formation in these processes is different from that in the plasma arc welding process. In plasma arc welding the keyhole is produced and maintained mainly by the pressure of the arc plasma, rather than by the recoil pressure of the evaporating metal as in electron beam and laser welding. Up to the present, the most comprehensive models of plasma arc welding are Rubinsky's two-dimensional (2D) and three-dimensional (3D) finite element simulation[2,3]. The 2D quasi-stationary model neglects surface tension effects and simplifies the pool geometry by assuming flat upper and lower free surfaces and a keyhole of constant radius. The developed 3D steady model is used to predict the weld pool shape based on heat transfer and fluid flow, while the keyhole shape is assumed according to experimental results. Currently, theoretical study on the transient development of the keyhole shape in plasma arc welding has not been found in the open literature.

In this paper, a two-dimensional, transient model is developed to describe the heat transfer and fluid flow in keyhole plasma arc welding. In the model, the weld pool surface is depressed by the arc pressure, and the fluid flow in the molten pool is induced by surface tension gradient, electromagnetic force, and buoyancy force. The VOF (Volume of Fluid), modified to include heat transfer and the electromagnetic force, was used to track the transient deformed shape of the

Department of Mechanical Engineering, southern Methodist University, PO Box 750337, Dallas, TX, 75275

weld pool surface. The processes of heating, melting, collapsing and subsequent solidifying are simulated in the keyhole plasma arc welding. Experiments have been done with AISI 304 stainless steel. The resultant weld and keyhole shapes have been compared with the predicted ones, which are in good agreement. This study may enhance our understanding of the heat transfer related phenomena during plasma arc welding.

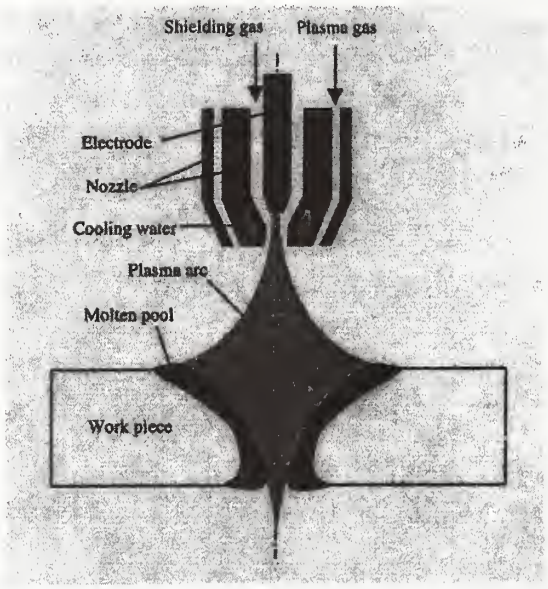

Figure 1. Schematic of plasma arc and weld pool.

MATHEMATICAL FORMULATION

Governing Equations

In order to simplify the mathematical model, the following assumptions have been made:

(1) the welding process is restricted to the stationary plasma arc welding, and the system is assumed to be axisymmetric;

(2) laminar flow is assumed;

(3) the thermophysical properties, listed in Table 1, are assumed to be constant;

(4) the fluid in the pool is driven by a combination of buoyancy, electromagnetic, and surface tension forces; however, plasma jet shear is neglected;

Table 1. Physical Properties of the Workpiece

Symbol	Value	Symbol	Value
β	10^{-4} K^{-1}	ρ	7200 kg/m^3
γ	1.2 N/m	μ_0	1.26×10^{-6} H/m
μ	0.006 kg/m.s	σ	7.7×10^{5}mho/m
$d\gamma/dT$	10^{-4} N/m.K	ε	0.9
C_P	753 J/kg.K	ΔH	2.47×10^{5} J/kg
T_l	1723 K	T_s	1523 K
k	20 W/m.K	K_{max}	10^{4} s^{-1}

Based on the above assumptions, the governing differential equations used to describe heat and fluid flow in the weld pool can be expressed as follows:

Equation of mass continuity:

$$\frac{1}{r}\frac{\partial(ru)}{\partial r}+\frac{\partial w}{\partial z}=0 \tag{1}$$

Conservation of radial momentum:

$$\begin{aligned}&\frac{\partial}{\partial t}(\rho u)+\frac{1}{r}\frac{\partial}{\partial r}(\rho ruu-\mu r\frac{\partial u}{\partial r})+\frac{\partial}{\partial z}(\rho uw-\mu\frac{\partial u}{\partial z})=\\&-\frac{\partial P}{\partial r}+\frac{1}{r}\frac{\partial}{\partial r}(\mu r\frac{\partial u}{\partial r})-2\mu\frac{u}{r^2}+\frac{\partial}{\partial z}(\mu\frac{\partial w}{\partial r})-j_z B_\theta-Ku\end{aligned} \tag{2}$$

Conservation of axial momentum:

$$\begin{aligned}&\frac{\partial}{\partial t}(\rho w)+\frac{1}{r}\frac{\partial}{\partial r}\left(\rho ruw-\mu r\frac{\partial w}{\partial r}\right)+\frac{\partial}{\partial z}\left(\rho ww-\mu\frac{\partial w}{\partial z}\right)=\\&-\frac{\partial P}{\partial z}+\frac{1}{r}\frac{\partial}{\partial r}(\mu r\frac{\partial u}{\partial z})+\frac{\partial}{\partial z}(\mu\frac{\partial w}{\partial z})-Kw+j_r B_\theta+\rho g\beta(T-T_r)\end{aligned} \tag{3}$$

The temperature-dependent drag term which represents fluid flow in the mushy zone is incorporated into the momentum equation *via* $-Ku$ and $-Kw$ where

$$K=\begin{cases}0 & T>T_l\\ K_{max}(T_l-T)/(T_l-T_s) & T_s\le T\le T_l\\ \infty & T<T_s\end{cases} \tag{4}$$

Conservation of energy:

$$\frac{\partial}{\partial t}(\rho h)+\frac{1}{r}\frac{\partial}{\partial r}\left(\rho ruh - r\frac{k}{C_p}\frac{\partial h}{\partial r}\right)+\frac{\partial}{\partial z}\left(\rho wh - \frac{k}{C_p}\frac{\partial h}{\partial z}\right)=\frac{j_r^2+j_z^2}{\sigma}-\Delta H\frac{\partial f_L}{\partial t} \qquad (5)$$

In the energy equation, Ohmic heating is considered. Latent heat of fusion is included by employing the liquid fraction, f_L, which is defined as follow:

$$f_L=\begin{cases}1 & T>T_l\\ (T-T_s)/(T_l-T_s) & T_s\le T\le T_l\\ 0 & T<T_s\end{cases} \qquad (6)$$

where T_l and T_s are the liquidus and solidus temperature, respectively.

Conservation of electrical charge:

In order to obtain the electromagnetic force terms in Equations (2) and (3), electric potential ϕ is calculated by solving the equation for current continuity,

$$\frac{1}{r}\frac{\partial}{\partial r}(\sigma r\frac{\partial \phi}{\partial r})+\frac{\partial}{\partial z}(\sigma\frac{\partial \phi}{\partial z})=0 \qquad (7)$$

and current density is calculated from Ohm's law,

$$j_r=-\sigma\frac{\partial \phi}{\partial r} \quad j_z=-\sigma\frac{\partial \phi}{\partial z} \qquad (8)$$

while the self-induced azimuthal magnetic field $B\theta$ is derived from Ampere's law.

$$B_\theta=\frac{\mu_0}{r}\int_o^r j_z r dr \qquad (9)$$

Tracking of Free Surfaces

The moving free surface is tracked using a volume of fluid function, F, which represents the volume of fluid in the computational cell. The function F takes the value of 1 for the cell filled with the fluid, and becomes 0 for the empty cell. If the cell is located on the free surface, the function F has a value between 0 and 1. The function F is governed by the equation [4]

$$\frac{\partial F}{\partial t}+\frac{1}{r}\frac{\partial}{\partial r}(ruF)+\frac{\partial}{\partial z}(wF)=0 \qquad (10)$$

Boundary Conditions

Boundary conditions for momentum

The boundary conditions needed to specify the fluid flow problem are:

(1) symmetry about the centerline

(2) no slip at the solid boundaries

(3) at the free surface, the plasma arc pressure P_{arc} can be approximated by

$$P_{arc} = P_{\max} \exp(-\frac{3r^2}{r_p^2}) \tag{11}$$

where P_{max} is calculated by $\frac{1}{2}\rho_{arc} v_{arc}^2$, using values of ρ_{arc} and v_{arc} determined earlier[5]. The Marangoni force due to the variation of the surface tension coefficient with temperature is described by

$$\tau_s = \mu \frac{\partial V_s}{\partial n} = \frac{d\gamma}{dT}\frac{\partial T}{\partial s} \tag{12}$$

The plasma arc pressure P_{arc} and the Marangoni force τ_s are included by adding source terms to the momentum equation. The method used is detailed in Ref. 6, which is called Continuum Surface Force (CSF) model.

Boundary conditions for thermal energy

The boundary conditions pertaining to the heat-transfer problem are

(1) symmetry about the axial centerline

(2) at the free surface of the molten pool, the heat flux from the welding arc is assumed to obey a Gaussian-type distribution of the form

$$-k\frac{\partial T}{\partial n} = \frac{\eta UI}{2\pi r_q^2}\exp(-\frac{r^2}{2r_q^2}) - h_c(T - T_r) \tag{13}$$

where h_c is a combined heat transfer coefficient for the radiate and convective boundary expressed in the following equation[7]

$$h_c = 24.1\times10^{-4}\varepsilon T^{1.61} \tag{14}$$

The heat flux from the arc plasma (Equation 13) is considered to be a source term of energy conservation equation in the cells along the weld pool surface. Arc efficiency η is set as 0.55 according to the earlier experiment[12].

(3) the boundary conditions for the surfaces without heat input are expressed as

$$-k\frac{\partial T}{\partial n} = h_c(T - T_r) \tag{15}$$

Electric potential boundary conditions

The boundary conditions concerning electrical potential in the area of the molten pool are:

(1) symmetry about the centerline

(2) an isopotential line (ϕ =0) is selected at the right wall because the right wall is far from the weld pool. $\partial\phi / \partial z = 0$ is set at the bottom wall.

(3) at the free surface, the assumed Gaussian-type current flux is described by

$$-\sigma\frac{\partial\phi}{\partial n} = \frac{I}{2\pi r_c^2}\exp(-\frac{r^2}{2r_c^2}) \tag{16}$$

EXPERIMENTAL PROCEDURE

A power supply designed for PAW and GTAW was used to make stationary spot welds on a 3.0 mm thick 304 stainless steel plate. The welding was performed under direct current, electrode negative condition. Pure argon was used as the shielding gas and the plasma gas. Other experimental conditions are given in Table 2.

Table 2. PAW Experiment Conditions

Welding current	100 A	Arc voltage	31 V
Shield flow rate	19 l/min	Plasma flow rate	2.5 l/min
Orifice diameter	3.2 mm	Torch standoff distance	5 mm

RESULTS AND DISCUSSION

The development of keyhole in plasma arc welding is presented in Figure 2. The surface profile of the weld pool is determined by the arc pressure, gravitational force and surface tension acting on the weld pool. In the partially penetrated weld pool, the molten metal is pushed out by arc pressure; thus, the pool surface is depressed in the center and humped at the pool boundary. A hole with V-shape cross section is formed before full penetration because of the high-velocity, concentrated plasma arc. Since the plasma arc in the cone hole heats the base metal, the liquid-solid boundary has shown a similar V-shape. Around 2.62s, the molten pool is fully penetrated. The molten metal is held by surface tension. In the newly developed bottom surface, surface tension also tends to form a shape that minimizes the surface energy. As shown in Figure 2, a keyhole with X-shape cross section is developed at t = 2.69 s.

The keyhole is collapsed after the arc is extinguished. At t=2.71s in Figure 2b, the fluid is accelerated into the hole, causing the hole to fill soon. At t = 2.72s, the inward flows impinge in the center; thus, the top part fluid moves upward and the bottom part moves downward. At t = 2.73s, the top part of the pool which overpasses the equilibrium begins to move downward. The downward flow is dominant in the weld pool at t = 2.74s. Meanwhile, influenced by surface tension, the flow direction of the bottom part begins to change. It is obvious that the upward flow from the bottom will affect the flow in the top. Then, the upward flow is dominant at t = 2.76s. At t = 2.77s and 2.79s, it is seen that the flow directions in the weld pool change again. The weld pool oscillation will continue until equilibrium is achieved or the weld pool is solidified.

The temperature distribution is shown in Figure 2a. The keyhole is developed so fast that the highest temperature appears near the top surface, although the heat flux from arc plasma is higher in the center of the weld pool. This is because the high temperature molten metal is always pushed toward the top surface by plasma arc; furthermore, the central pool always approaches first and is cooled by the low temperature base metal. After the collapse of the molten pool, the high temperature molten metal from the top moves to the center which result in a higher temperature distribution at the center. In the process of solidification, the higher temperature fluid remains near to the top and the bottom surface. Finally, the solidification is completed near the bottom surface, because heat loss is mainly from the surrounding base metal.

The experimental results have been shown in Figure 3. The reasonable agreement between the predicted and experimentally observed fusion zone shape and size is obtained. Figure 3b shows the weld shape after burn through. This helps to understand the keyhole shape under the influence of the plasma arc. The cross section of the burn through weld is nearly X-shape, which agrees well with the predicted results.

a)

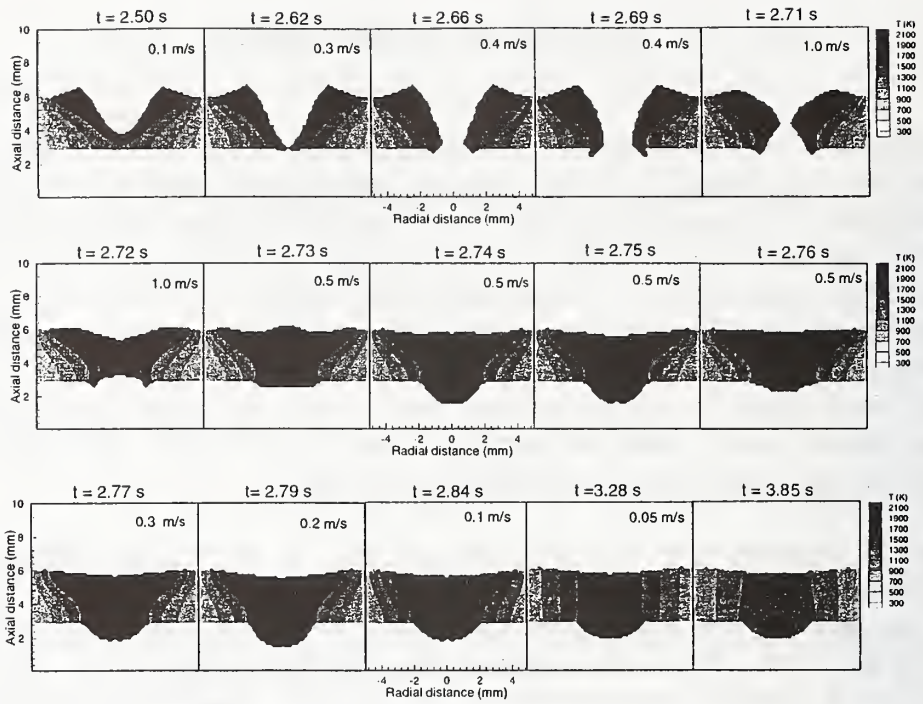

b)

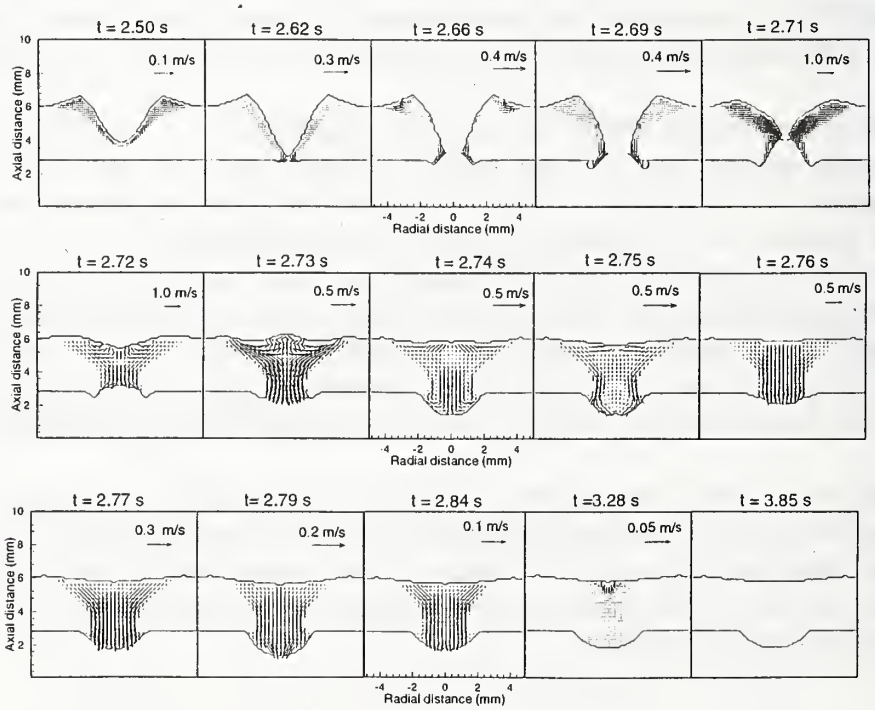

Figure 2. Simulation results:
(a) Temperature distribution in the molten pool:
(b) Velocity distribution in the molten pool.

(a)

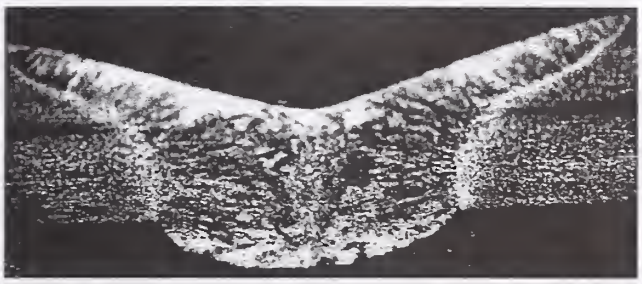

(b)

Figure 3. (a) Resultant weld shape
(b) Keyhole shape after burn through

CONCLUSION

A two-dimensional heat and fluid flow model has been developed to analyze keyhole formation and collapse in stationary plasma arc. The keyhole with a X-shape cross-section has been predicted and observed.

The weld pool oscillation could be triggered after the collapse of the molten pool. In the fully penetrated weld, the addition of a free bottom surface results in a more significant weld pool oscillation, and the bottom and the top surface oscillation have close connections. The weld pool oscillation will continue until the equilibrium or solidification has been achieved.

The calculated temperature distribution during keyhole formation reveals that the highest temperature appears near the top of the molten pool. After the keyhole collapse, the fluid temperature around the periphery is lower than the temperature at the center. Heat lose is mainly from the base metal, thus, solidification is initiated at the solid-liquid interface and advance toward the center. In the process of solidification, the higher temperature remains near to the bottom.

REFERENCE

1. Fuerschloach, P.W.; and Knorousky, G.A. 1991. *Welding Journal* 70(10): 287 to 297s.
2. Hsu J.F.; and Rubinsky, B. 1998 *Int. J. Heat Mass Transfer* 31(7): 1409 to 1421.
3. Keanini, R.G.; and Rubinsky, B. 1993. Three-dimensional simulation of the plasma arc welding process. *Int. J. Heat Mass Transfer* 36(13): 3283 to 3298.
4. Nichols, B.D.; Hirt C.W.; and Hotchkiss R.S. 1980. SOLA-VOF: A solution algorithm for transient fluid flow with multiple free boundaries. *Report LA-8355. Los Alamos Scientific Laboratory*.
5. Metcalfe J.C.; and Quigeley, M.B.C. 1975. Heat tranfer in plasma arc welding. *Welding Journal* 54(3): 93 to 103.
6. Kothe, D.B.; Mjolsness R.C.; and Torrey M.D. 1991. RIPPLE: A computer program for incompressible flows with free surfaces. *Report LA-12007-MS. Los Alamos Scientific Laboratory.*
7. Goldak, J.; Bibby, M.; Moore, J.; and Patel, B. 1986. *Metallurgical Transaction B* 17B: 587 to 600.
8. Evans, D.W., Huang D., McClure J.C.; and Nunes A.C. 1998. *Welding Journal* 77(2): 53 to 58.

PREVENTION OF OUT-OF-PLANE DEFORMATION GENERATED BY FILLET WELDING

Y. C. Kim*, K. H. Chang and K. Horikawa***

ABSTRACT

The validity of the preset distortion method was confirmed. The prevention accuracy of out-of-plane deformation by the preset distortion was determined by the prediction accuracy of welding deformation. Angular distortion could be prevented by heating two points on the flange under the welding heat source or one point on the flange under the web in order to reduce the temperature gradient for the thickness direction of the flange. Residual stress σ_x was a little larger with heating from the opposite side comparing to without heating. Considering the manufacture site, the prevention of angular distortion was investigated for the one point heating from the opposite side. If the heating temperature became higher, the heating width may be narrow. However, the maximum heating temperature from the opposite side should be 650-700℃. Angular distortion could prevent by controlling the heating width from the opposite side for any flange thickness.

KEY WORDS: (Fillet Welding)(Welding Distortion)(Distortion Prevention)(Preset Distortion) (Angular Distortion Prevention)(Residual Stress)(FEM Modelling)

INTRODUCTION

Fillet welding was performed in constructing the steel structures such as ships, the deck plate of bridges which were assembled by plates and stiffeners. Welding deformation is necessarily generated by fillet welding. As out-of-plane deformation in welding deformation lowers the constructing accuracy and the appearance of the steel structures, it is generally reformed.

The reformation often causes the obstruction in manufacture, that is the increment of the manufacturing time and the standstill of the manufacturing systems. The reformation influences the strength of the structures directly or indirectly (Ref. 1). So, it is required that the system, which controls and prevents welding deformation before welding, is constructed (Ref. 2, 3). Concerning to this, the authors found the characteristics and the production mechanism of out-of-plane deformation generated by butt welding with the initial deflection and by fillet welding (Ref. 4, 5). The effects of the welding conditions on out-of-plane deformation and residual stress were elucidated. At the same time, the generality of the production mechanisms for out-of-plane deformation was investigated together with the validity (Ref. 4-6).

In this paper, the validity of the preset distortion, which has been well known as a prevention method of out-of-plane deformation, is investigated. The conditions, which should be satisfied to prevent welding out-of-plane deformation by preset distortion method, are found. On the other hand, the prevention method of angular distortion is proposed and the validity is shown.

---

* Joining & Welding Research Institute, Osaka University, Japan

** Graduate student, Osaka University, Japan

FEM modelling

Figure 1 shows the model, the coordinate systems and the model sizes. The dotted line in the figure expresses the position of the neutral axis for the cross section of the object.

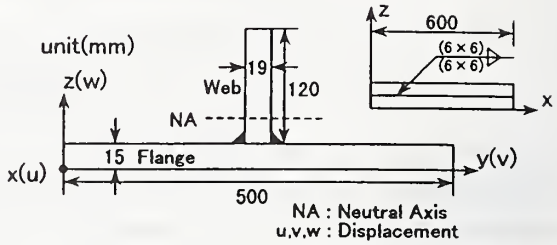

Fig.1 Coordinate systems and model sizes (Standard model).

Three models are provided here.

Standard model: There is not any initial deformation.

Model A: The initial state is regarded as the state that is given the preset distortion of welding out-of-plane deformation (longitudinal bending deformation and angular distortion).

Model B: The initial state is regarded as the state, which the preset distortion is given only to angular distortion.

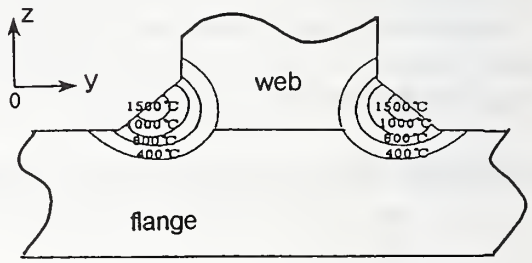

Fig.2 Isothermal contours (Standard model).

One pass fillet welding is performed simultaneously on the left and right sides with the welding speed (v=6(mm/s) and the welding heat input (Q=1200(J/mm). Material is mild steel. The temperature dependency of the physical constants and the mechanical properties of the mild steel are considered in the thermal elastic-plastic analysis by FEM (it was analysed by applying the Von Mises' criterion) (Ref. 7). As the boundary conditions, only the rigid displacements of the object are restricted.

Temperature distribution

Temperature history was obtained by three-dimensional non-steady heat conduction analysis. Figure 2 shows the isothermal contours in the thickness direction when the maximum temperature at the end cools down to 1500℃ after welding.

Longitudinal bending deformation

Figure 3 shows longitudinal bending deformation generated at the top of the web of each model. As mentioned in the paper describing the production mechanism (Ref. 5), longitudinal bending deformation is generated in the convex shape because the neutral axis of the standard model exists above the welding heat source (Fig.3 (a)).

In Model A which preset distortion of welding out-of-plane deformation are given as initial deformation, no longitudinal bending deformation is generated (Fig.3(b)). In Model B which no longitudinal bending deformation is treated and the preset distortion is given to only angular distortion, longitudinal bending deformation is generated in the convex shape (Fig.3(c)).

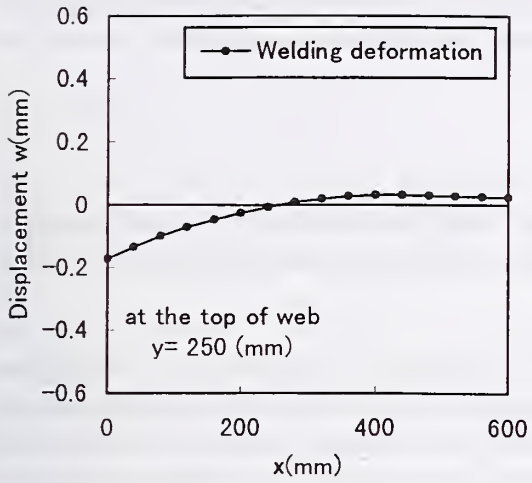

(a) Standard model.

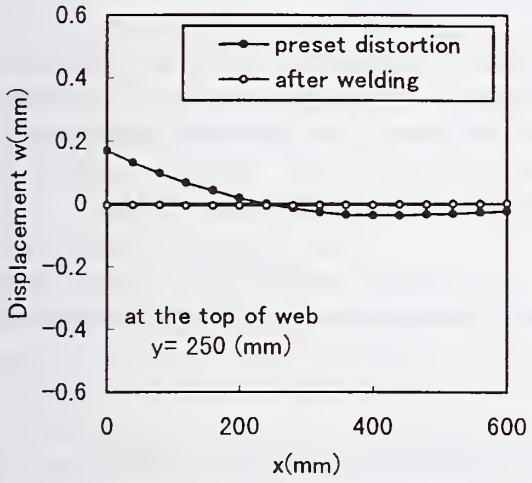

(b) Model A.

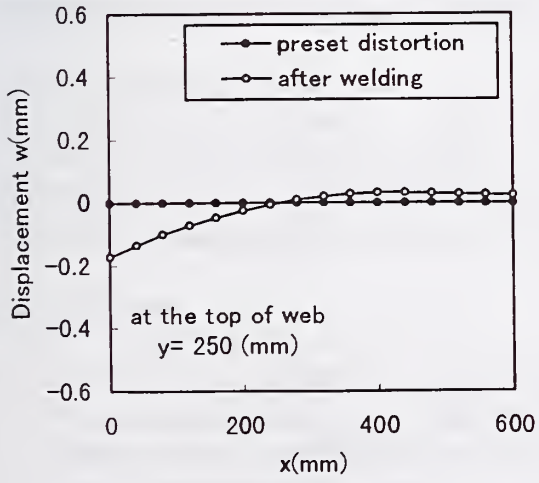

(c) Model B.

Fig.3 Longitudinal bending deformation.

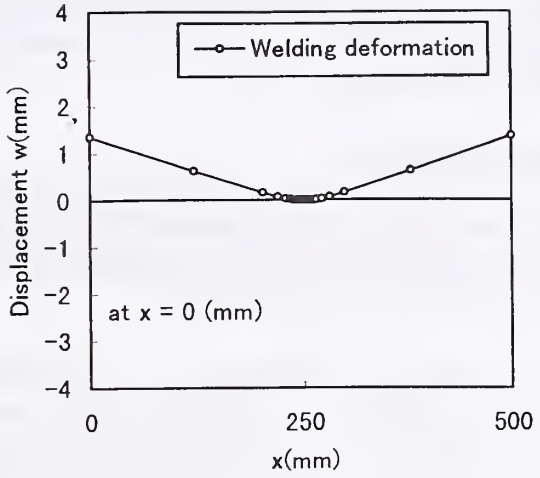

(a) Standard model.

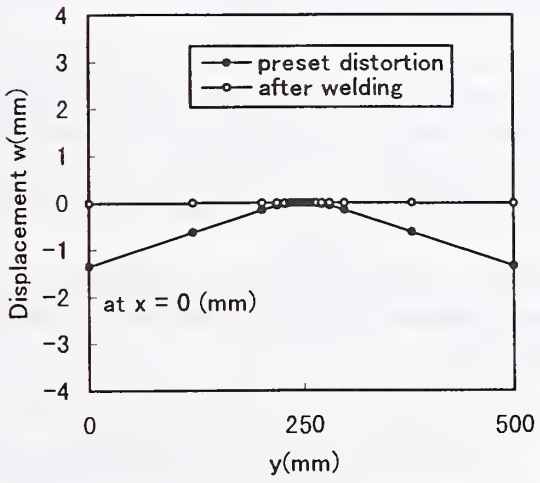

(b) Model A.

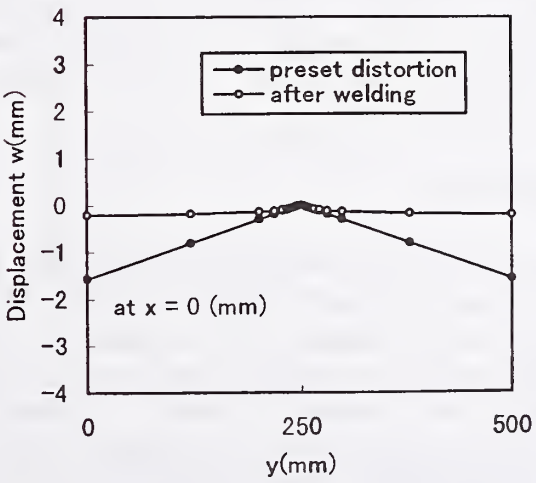

(c) Model B.

Fig.4 Angular distortion.

Therefore, it is found that longitudinal bending deformation can be prevented only when the same magnitude of the deformation with longitudinal bending deformation generated by welding is given as the preset distortion.

Angular distortion

There was no difference in the shape and the magnitude of angular distortion at the starting edge, the center part and the finishing edge (Ref. 6). Figure 4 shows angular distortion generated at the starting edge of welding (x=0(mm)).

As mentioned in the paper describing the production mechanism (Ref. 5), angular distortion of the standard model is generated in V-shape because the welding heat source exists above the neutral axis (z=7.5(mm)) for the flange (Fig.4 (a)). On the other hand, angular distortion in Model A, which welding out-of-plane deformation are given as preset distortion, is perfectly prevented (Fig.4 (b)). However, angular distortion in Model B, which the preset distortion is given to only angular distortion, is not perfectly prevented but is largely controlled.

In the preset distortion method, it is found that out-of-plane deformation generated by welding can be perfectly prevented only when welding out-of-plane deformation (longitudinal bending deformation and angular distortion) is given as the preset distortion. This means that the accuracy of the prevention of welding out-of-plane deformation by the preset distortion method is determined by the prediction accuracy of out-of-plane deformation generated by welding.

By the way, longitudinal bending deformation is not largely generated but angular distortion is largely generated in fillet welding. Hereinafter, the prevention of angular distortion is investigated.

INVESTIGATION OF THE PREVENTION OF ANGULAR DISTORTION

When the temperature gradient for the thickness direction of the flange became small, angular distortion became small (Ref. 6). Here, the method to prevent angular distortion by reducing the temperature gradient for the thickness direction of the flange is proposed and the validity is investigated.

FEM model

Two types of the model (Fig.5) are provided based on the standard model (Fig.1). That is, **Type-w** (Fig.5(a)): two points on the opposite side of the flange under the welding heat source of fillet welding are heated in order to reduce the temperature gradient for the thickness direction of the flange directly. **Type-s** (Fig.5(b)): one point on the opposite side of the flange under the web is heated considering the manufacturing site.

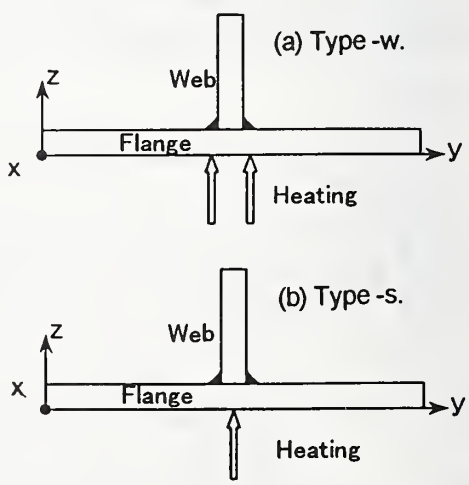

Fig.5 Heating point on the flange surface.

Heating from the opposite side of the flange is performed with the same time and speed as welding.

Temperature

Temperature history of welding was obtained by three-dimensional non-steady heat conduction analysis. Figure 6 shows the isothermal contours for the thickness direction in Type-w and Type-s when the maximum temperature at the end cools down to 1500℃ after welding.

These isothermal contours consequently correspond to the heating temperature where angular distortion can prevent. The maximum temperature from the opposite side is 550℃ in Type-w and is 700℃ in Type-s, respectively.

It can be known that the temperature gradient for the thickness direction of the flange becomes small directly in Type-w.

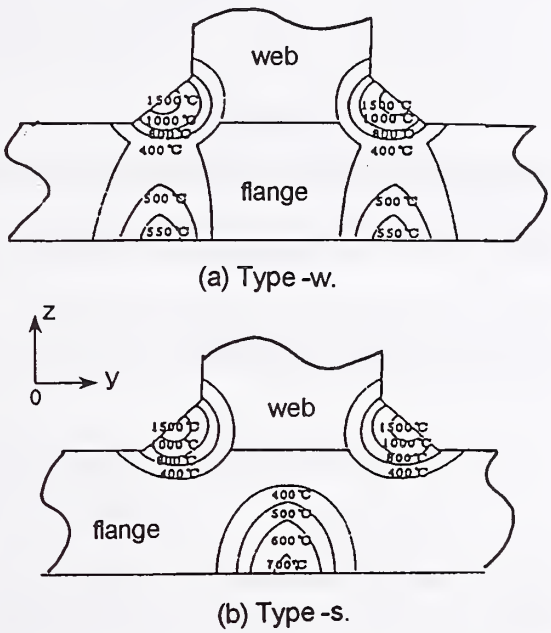

Fig.6 Isothermal contours with heating at the opposite side of the welding surface.

Angular distortion

Figure 7 shows angular distortion generated at the central position (x=300(mm)).

Angular distortion can be prevented both in Type-w and Type-s. It is found that reducing the temperature gradient for the thickness direction of the flange with heating from the opposite side of the flange can prevent angular distortion. So, the validity is confirmed. In the same way, the applicability of the prevention of angular distortion is variously investigated (Ref. 8).

Considering the manufacturing site, Type-s is more useful than Type-w. The heating temperature and the heating width from the opposite side to be necessary for the change of the flange thickness are investigated by using Type-s.

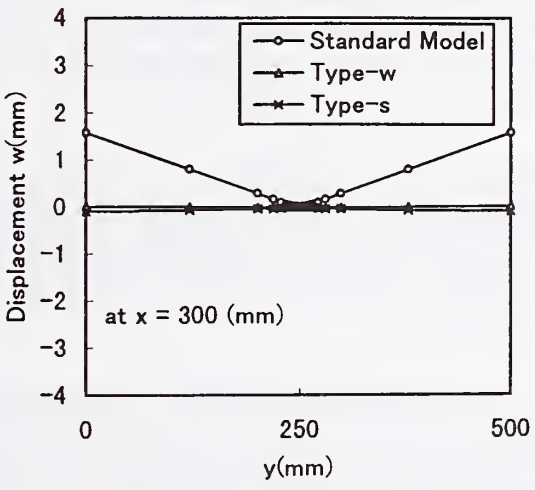

Fig.7 Angular distortion with heating at the opposite side of the welding surface.

Residual stress

It was found that heating from the opposite side can prevent angular distortion. Therefore, it is necessary to know the influence of heating from the opposite side on residual stress.

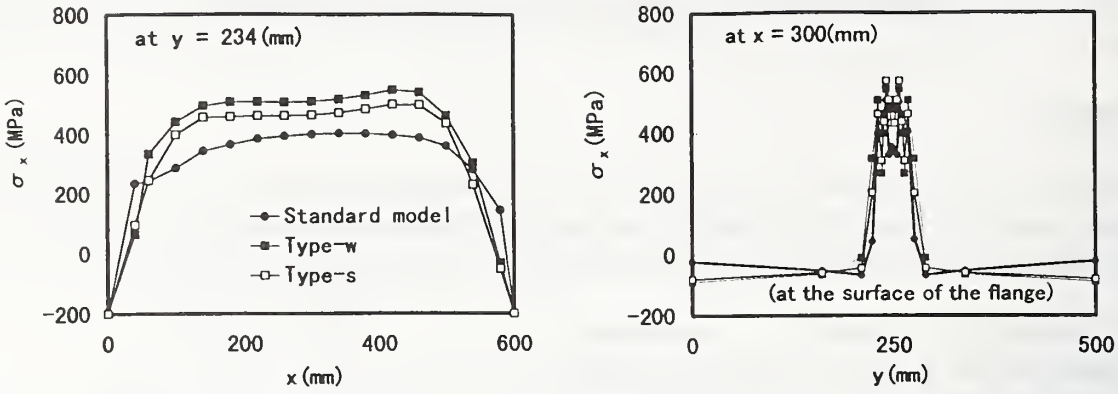

(a) σ_x along the weld line. (b) σ_x of perpendicular to the weld line.

Fig.8 Distributions of residual stress with heating at the opposite side of the welding surface.

Figure 8 shows the distribution of the residual stress components along the weld line, σ_x.

The absolute value of σ_x seems to be a little larger with heating from the opposite side comparing to without heating. However, the difference between Type-w and Type-s is small.

PREVENTION OF ANGULAR DISTORTION BY REDUCTION OF TEMPERATURE GRADIENT

Here, the heating temperature and the heating width from the opposite side to be necessary for the change of the flange thickness are investigated.

Heating temperature

The flange thickness (15(mm)) and the total heat input from the opposite side are fixed, angular distortion is obtained for each case in which the heating width, B_H, is changed respectively 7, 9 and 13(mm). Figure 9 shows the relation between the heating temperature, T_H and the heating width, B_H by which angular distortion could be prevented (see Fig.7).

If the heating temperature, T_H is higher, the heating width, B_H may be narrow. So, this is advantageous to the prevention of angular distortion. However, it is hopeful from the view points of the materials science that the maximum temperature by the heating is under 700℃, because the mechanical properties has the possibility of change if the heating temperature becomes over 700℃ (Ref. 1).

It is proposed that the maximum heating temperature, T_H from the opposite side should be 650-700℃.

Flange thickness and heating width

Heating width necessary for the prevention of angular distortion was obtained for each case in which the flange thickness, t, is changed respectively 10, 15, 20, 25, 30, 35, 100(mm) and the

maximum heating temperature 700℃ is fixed. It is found that controlling the heating width for change of the flange thickness can prevent angular distortion.

Figure 10 shows the heating width for the prevention of angular distortion. According to the results, there are two lines. The reason is considered below.

When the flange thickness is extremely thin, no temperature gradient occurs for the thickness direction of the flange. As the flange thickness becomes thicker, the temperature gradient occurs for the thickness direction (see Fig.2). In order to reduce the temperature gradient, it is necessary to make the heating width suddenly wider. When the flange thickness becomes more thicker and it is a certain thickness, the isothermal contours for the thickness direction of the flange become same including the temperature history while the temperature of the weld metal cools down from 500 to 400℃. Angular distortion was generated while the temperature of the weld metal cools down from 500 to 400℃ (Ref. 5). Therefore, the heating width from the opposite side may be made to be a little wider in order to reduce the temperature gradient for the thickness direction of the flange.

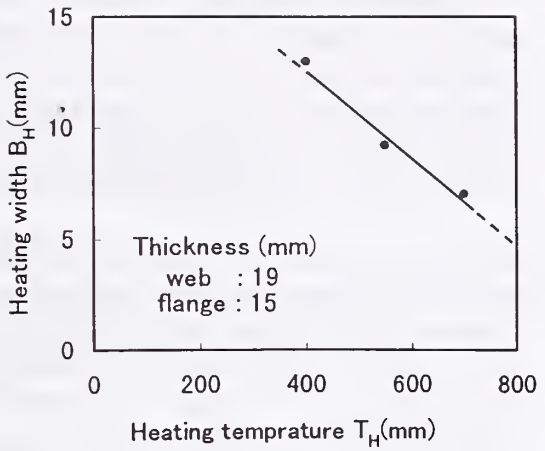

Fig.9 Relation between heating temperature at the opposite side of the welding surface and heating width.

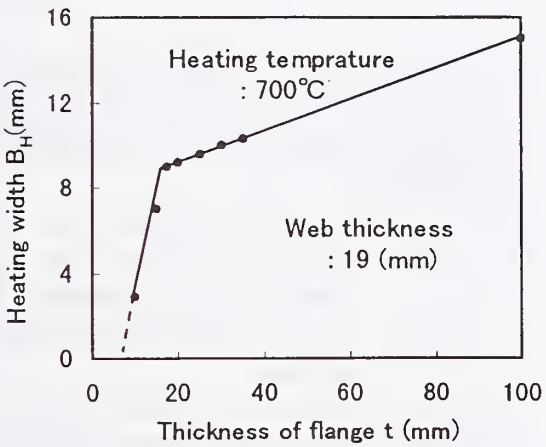

Fig.10 Relation between flange thickness and heating width at the opposite side of the welding surface.

CONCLUSION

The validity of the preset distortion method, which has been well known as a prevention method of welding out-of-plane deformation, was investigated. The conditions, which should be satisfied to prevent welding out-of-plane deformation by the preset distortion method, were elucidated. The prevention method of angular distortion was proposed and its applicability was investigated.

The results can be summarised as follows:

1. The validity of the preset distortion method was confirmed. As the conditions of the prevention of out-of-plane deformation (longitudinal bending deformation and angular distortion), it was found that welding deformation could be prevented only when the same magnitude of the deformation with out-of-plane deformation generated by welding was given as the preset distortion. This means that the prevention accuracy of welding out-of-plane deformation by the preset distortion was determined by the prediction accuracy of out-of-plane deformation generated by welding.

2. It was found that angular distortion could be prevented by heating two points on the flange under the welding heat source or one point on the flange under the web in order to reduce the temperature gradient for the thickness direction of the flange.
3. Residual stress σ_x was a little larger with heating from the opposite side comparing to without heating. However, the difference between residual stress σ_x generated by the two points heating and by one point heating was not so large.

Considering the manufacture site, the applicability of the prevention of angular distortion was investigated for the one point heating from the opposite side as mentioned above.

4. If the heating temperature from the opposite side became higher, the heating width may be narrow. However, the maximum heating temperature from the opposite side should be 650-700℃ from the view points of the materials science.
5. Angular distortion could prevent by controlling the heating width from the opposite side for any flange thickness.

REFERENCES

1. For example, Satoh, K. et al. 1979. Welding Engineering, Rikougaku-sha (in Japanese).
2. For example, Kamichika, R. 1996. Welding Technique (5-7), J of JWES (in Japanese).
3. For example, Kim, Y.C. 1996. Prediction of Welding Deformation. J. of JWS (7): 563-567 (in Japanese)
4. Kim, Y.C.; Park, J.U.; Horikawa, K. 1998. Effects of Welding Conditions on Welding Deformation and Residual Stress. Steel Construction Engineering (17): 85-91 (in Japanese).
5. Kim, Y.C.; Chang, K.H.; Horikawa, K. 1999. Production Mechanism for Out-of-Plane Deformation in Fillet Welding and Its Investigation of Generality. Quarterly J. of JWS (2): 294-300 (in Japanese).
6. Kim, Y.C.; Chang, K.H.; Horikawa, K. 1999. Effects of Welding Conditions on Out-of-Plane Deformation and Residual Stress in Fillet Welding. Steel Construction Engineering (21): 77-82 (in Japanese).
7. Kim, Y.C.; Chang, K.H. 1998. Prediction of Welding Out-of-Plane Deformation by 3D-FEM Analysis and Its Accuracy. The 76th JSME Fall Annual Meeting: 295-296 (in Japanese).
8. Toda, Y; Toyoda, M; Takeno, S. 1997. Control of Welding Distortion in Fillet Welds of Aluminium Alloy. Welding Structural Symposium: 304-307 (in Japanese).

THERMO-MECHANICAL COMPUTER MODELING OF RESIDUAL STRESS AND DISTORTION DURING WELDING PROCESS

Y. J. Chao and X. Qi

Department of Mechanical Engineering, University of South Carolina
Tel: (803)777-5869; Fax: (803)777-0106; Chao@sc.edu

ABASTRACT

A three-dimensional finite element simulation of welding process is presented. A de-coupled heat transfer and thermo-mechanical analysis is adopted for the determination of residual stress and distortion. Special features for the welding process are developed in the modeling to reduce the computational cost and time of the analysis. A butt-welded aluminum plate was analyzed and the results are compared with experimental data. The good comparison for both the residual stress distribution and the distortion verifies the modeling procedures. It is further shown that the full three-dimensional model can reveal more realistic results, which cannot be obtained by the simplified two-dimensional simulation. In addition, the efficiency of the code in computational time is demonstrated.

INTODUCTION

Welding is a popular joining method used in many industries, e.g. from offshore drilling platform to electronic packaging. By going through heating, melting and solidification processes, two workpieces are joined together using torch, laser, electron beam or other heat sources. The highly localized, transient heat input and extremely non-uniform temperature fields in both heating and cooling processes cause non-uniform thermal expansion and contraction, and thus plastic deformation in the weld and its neighborhood. Consequently, residual stress, strain and distortion of the welded structure are developed. The residual stress in the weld region affects the service life of the structure, e.g. stress corrosion cracking of the weld, and the distortion directly influence the fabrication of the structure. Thus, control of residual stress and distortion from the welding process is extremely important in the manufacturing and construction industry. Besides the determination of the residual stress and distortion of the welded structure, modeling effort for the welding process can also be used to incorporate the welding procedures and pattern into the design evaluation, optimization and manufacturing of the structures.

Due to its complexity, analytical solutions to the welding process can rarely address the practical manufacturing processes. Numerical solutions, on the other hand, can provide more detailed results and address more realistic problems. Hibbitt and Marcal (Ref. 1) marks the first step in applying a two-dimensional finite element analysis (FEA) to predict residual stress in a weldment. Most modeling efforts in the 70's and 80's are for two-dimensional or simple three-dimensional geometries due to the limitations from the computer, i.e. time and

cost. With the rapid advancement in computing speed from modern computers, numerical modeling of practical welding processes now becomes feasible. Recently, three-dimensional modeling using commercial finite element codes are reported by Tekriwal and Mazumder (Ref. 2), Michaleris and DeBiccari (Ref. 3), and Dong, et al (Ref. 4) among others. Brown and Song (Refs. 5,6) used three-dimensional models to demonstrate the inadequacy of using two-dimensional models for the determination of distortions due to welding process. In particular they demonstrated that the fixture used for the welding process in general cannot be modeled as a two-dimensional case and thus a two-dimensional model could give erroneous distortion results. Dike, et al (Ref. 7) pointed out the two-dimensional models cannot account for restraint and solidification effects and significantly underpredicts the distortion of multi-pass welds.

Note that in using the commercial finite element codes, many user subroutines must be added to handle the special features of the welding process, e.g. melting and annealing, which are usually not accounted for in the general-purpose finite element codes. In this paper we first demonstrate a numerical modeling procedure which includes advanced features to improve the computational efficiency. The modeling procedure was then developed into a FEA code for the welding process simulation. The developed FEA program is three-dimensional and runs on PC platform. A flow chart of a complete modeling of the welding process involving a heat transfer analysis and a subsequent thermo-mechanical analysis is shown in fig.1. A moving heat source is modeled first to generate the temperature fields at various time steps during the welding process and then the temperature history is used for the calculation of the thermal stresses and displacement fields during and after the welding process. Unique features of the welding process are built into the code and appropriate convergence can be controlled by the user with flexibility. The computer code is developed in order to study the welding process and for practical engineering applications.

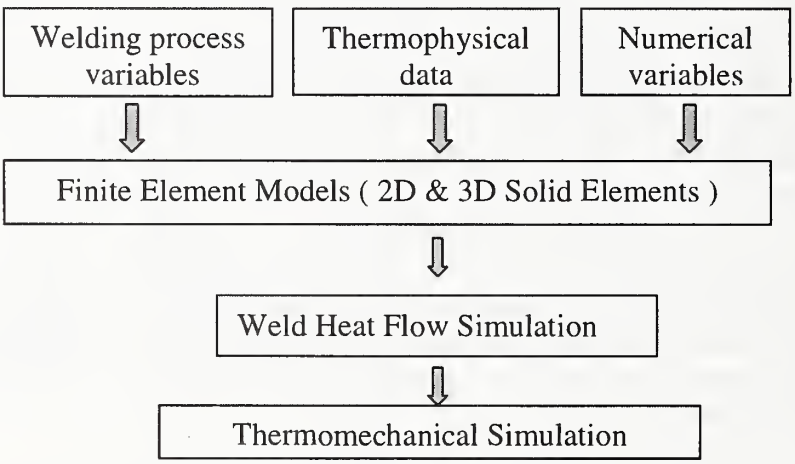

Figure 1 Flow chart of the welding process modeling

In the following sections we first outline the basic principles of the finite element analysis, then discuss special features of the code, present the results from the modeling of a gas metal arc welding (GMAW) of a rectangular Aluminum plate, and finally compare the analytical

results to experimental data. Further results are presented to show that why a three-dimensional modeling is needed for the simulation of practical welding problems. A discussion is then given to conclude the paper.

FINITE ELEMENT FORMULATION

It has been shown by Argyris, et al (Ref. 8) and Papazoglou and Masubuchi (Ref. 9) that the difference between a coupled and de-coupled analysis for residual stress and distortion in a welding process is very small. Therefore, we have adopted a de-coupled finite element analysis; i.e. a thermo-mechanical stress analysis following an independent heat transfer analysis.

The finite element formulation and solver follow the standard procedures and can be found in many textbooks (Ref. 10, Ref. 11). In the heat transfer analysis, the differential equations governing the transient heat conduction problems can be obtained by using the first and second law of thermodynamics. A moving heat source is formulated into the code to simulate the movement of the torch. The temperature history at each finite element node is determined and stored for the subsequent thermo-mechanical stress analysis. The basic mechanics formulation starts from the constitutive equation, in incremental (differential) form for the thermal elastic-plastic material, i.e. $d\varepsilon^{total} = d\varepsilon^{elastic} + d\varepsilon^{plastic} + d\varepsilon^{thermal} + d\varepsilon^{creep}$. The creep strain is for modeling the post-weld heat treatment used to reduce or alter the distortion and the residual stress pattern of the welded structure. The finite element formulation uses a rate independent plasticity model with kinematic hardening to model the reverse plasticity and Bauschinger effect. Either power law or linear relation for the uniaxial stress-strain curve beyond the yielding can be used for the non-linear material behavior. Von Mises yield criterion with an associated flow rule is used to determine the onset of yielding and the amount of incremental plastic strain.

SPECIAL FEATURES TO IMPROVE THE COMPUTATION SPEED AND ACCURACY

One of the drawbacks of using the commercial finite element codes for modeling welding process is the slow speed and the lack of unique features of the welding process in the codes. In order to improve the computation speed, several strategies are introduced in our welding process simulation and built into the code. These include

1. A moving heat source to simulate the movement of the torch

2. Flexibility in convergence tolerance

3. Using an appropriate cut-off temperature

4. Appropriate weight factor for elastic to plastic transition

5. Dummy elements used for multi-pass welding

6. Flexibility in finite element meshes

7. Using adjustable time and temperature increments in the iteration

The details of these computational strategies are discussed elsewhere and are not reported here due to the length limit of the current paper.

MODELING OF ALUMINUM PLATES JOINED BY GMAW

This section reports results from modeling a butt joint by gas metal arc welding (GMAW). The numerical results from our analysis are compared with the experimental data by Canas et. al. (Ref. 12). In addition, results that can only be obtained from a three-dimensional analysis and cannot generally be obtained by the simplified two-dimensional analysis are reported.

Figure 2 shows the geometry and welding configuration of the problem under consideration. A half model was used in the simulation due to symmetry. The FEM model consists of 4040 nodes and 2700 (8 nodes) solid elements in the heat transfer analysis, and 2040 nodes and 1350 solid elements in the thermo-mechanical analysis. Figure 3 shows the FEA mesh for the thermo-mechanical analysis. The material is the aluminum alloy *Al*5083-O with the thermo-mechanical properties shown in fig. 4 (Ref. 12). A cut-off temperature 550^0C was used in the computation. The electricity provided to the GMAW process is 23.4 Volt and 170 Amp. A Gaussian distribution with an effective arc radius of 7 mm and efficiency of 64% is used to simulate the heat flux applied to the workpiece. The heat is applied in the Z=0 plane and moves along the +X-direction with a speed of 11 mm/sec, as shown in figure 2. The total welding time lasts 23 seconds.

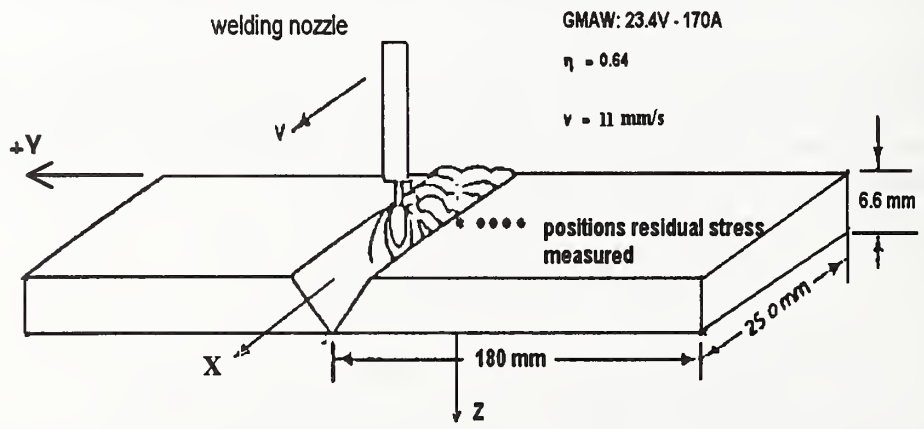

Figure 2 Configuration of the model

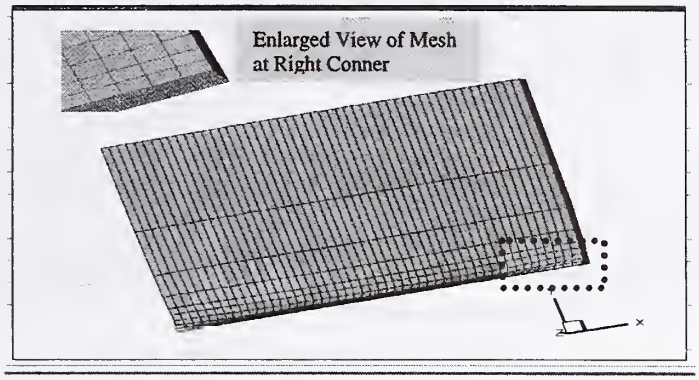

Figure 3 FEA mesh in the thermo-mechanical model

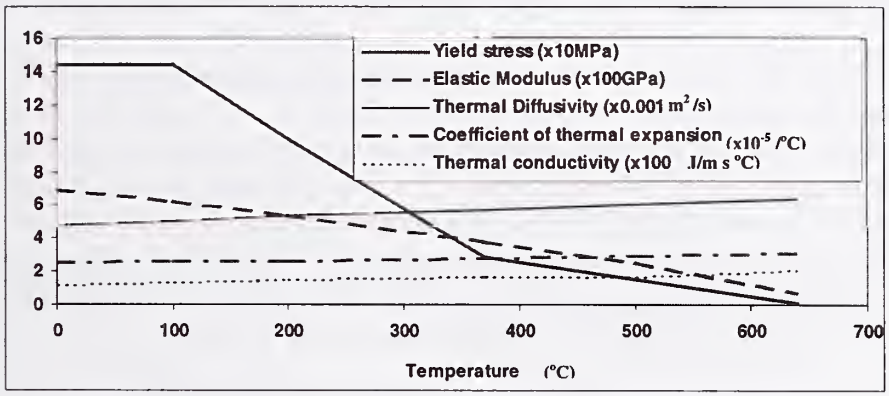

Figure 4 Thermo-mechanical properties of the aluminum alloy *Al*5083-O (640^0C is the melting temperature)

RESULTS FROM THE THERMO-MECHANICAL ANALYSIS AND COMPARISON TO THE EXPERIMENTAL DATA

Residual Stresses

Residual stresses σ_{xx}, σ_{yy}, σ_{xy} at the centroids of the elements along a section in the middle of the plate (X, Y, Z) = (122.5, Y, 1) mm are shown in Fig.5 along with the experimental data. It is shown in Fig. 5 that the analytical results compare well with the test data.

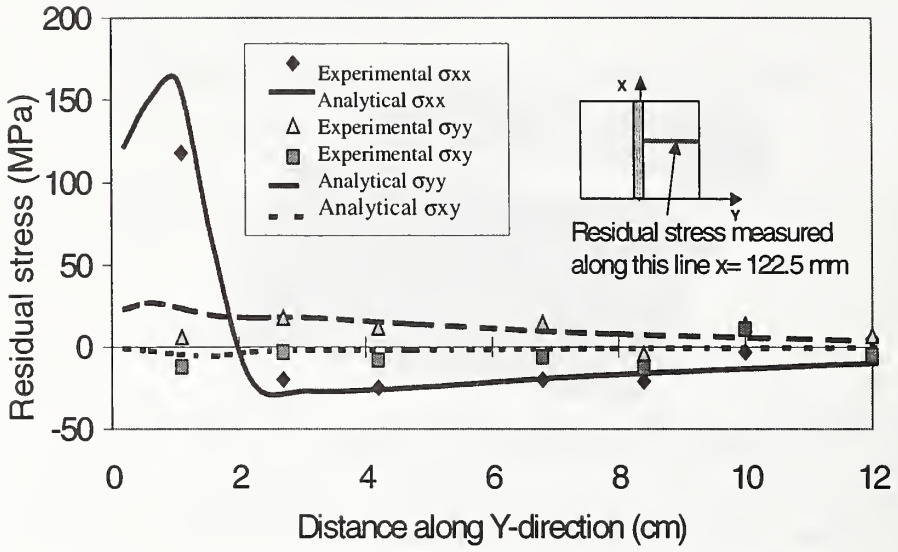

Figure 5. Residual stress : comparison of numerical and experimental data

Residual stresses from the centroids of the elements along the weld line, i.e. (X, Y, Z)=(X, 2, 1) mm, which is near the center of the weld are shown in figure 6. It is seen that in the area of x = 40 ~200 mm uniform values of the three components of residual stresses are obtained. However, near the edges of the plate, i.e. X = 0~40 mm and X = 200~250 mm, the residual stresses are not the same as those in the central area. In fact, the maximum residual stress occurs near the free edge, i.e. see σ_{yy} near X =0 and 250 mm in figure 6. It should be mentioned that a two-dimensional modeling could at most obtain the steady-state results in the central portion of the welded plate shown in figure 5. The 2D models cannot obtain the variation of the residual stress near the edges.

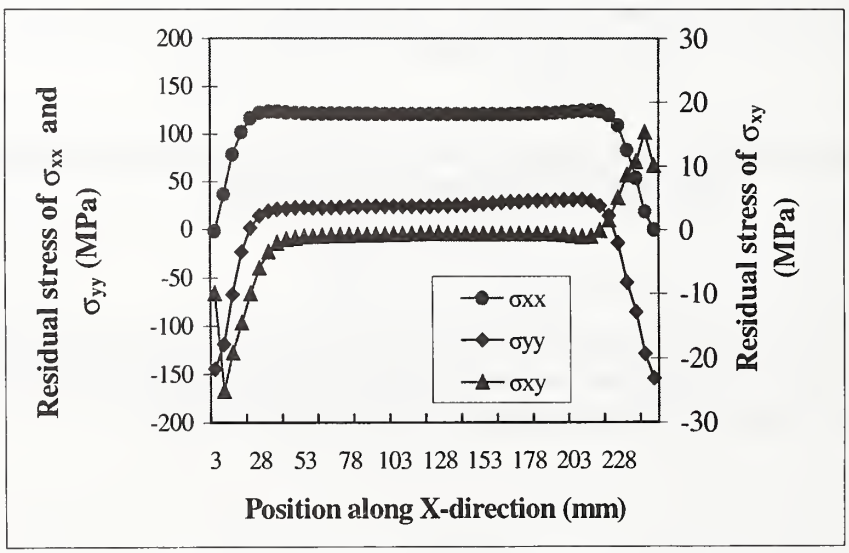

Figure 6 Residual stress along the weld line (x, 2, 1)

Figure 7 shows the residual stress distributions along the Y-direction in three sections; one at X=7.5 mm near the starting edge, one in the central part X= 122.5 mm and one at X= 242.5 mm near the finishing edge. Again, significant difference in the residual stress distribution in the three sections is present.

The maximum tensile residual stress appears to be parallel to the weld and near the weld as can be seen from Figures 5 and 7. This σ_{xx} has a maximum value of 161 MPa, which is slightly higher than the yield stress of the material at room temperature σ_{ys} = 145.1 MPa.

Distortion

Due to the highly localized, transient heating and hence non-uniform heat distribution in the workpiece, the plate exhibits complicated distortion during the welding. Fig.8 shows the distorted plate during and after welding. One half of the plate is modeled and shown in Fig.8. Recall that the torch moves at 11 mm/second; thus, the torch is at X= 55 mm as t = 5 seconds for figure 10(a), X= 165 mm as t = 15 seconds for figure 10(b). And, figure 10 (c) demonstrates the deformed workpiece right after the welding was completed (i.e. t=23 seconds), while Fig.10 (d) is after the workpiece completely cooled down to room

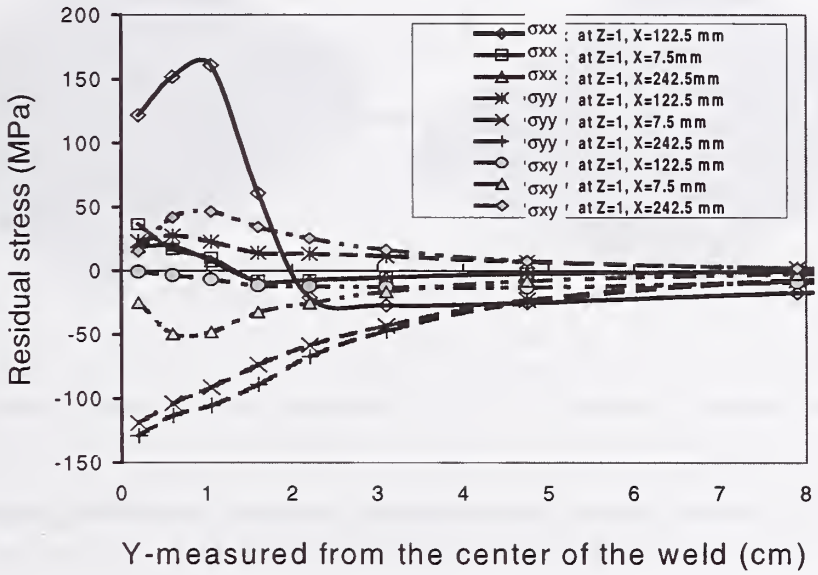

Figure 7 Residual stresses at three different sections along the Y-direction

temperature. Note that the distortion is magnified by 100 times in figure 8. The final deformed shape of the originally flat plate is a warped surface resembling a double-curvatured plate. The maximum residual distortion (or warpage) in the out of plane or Z-direction is about 2.2 mm in this case.

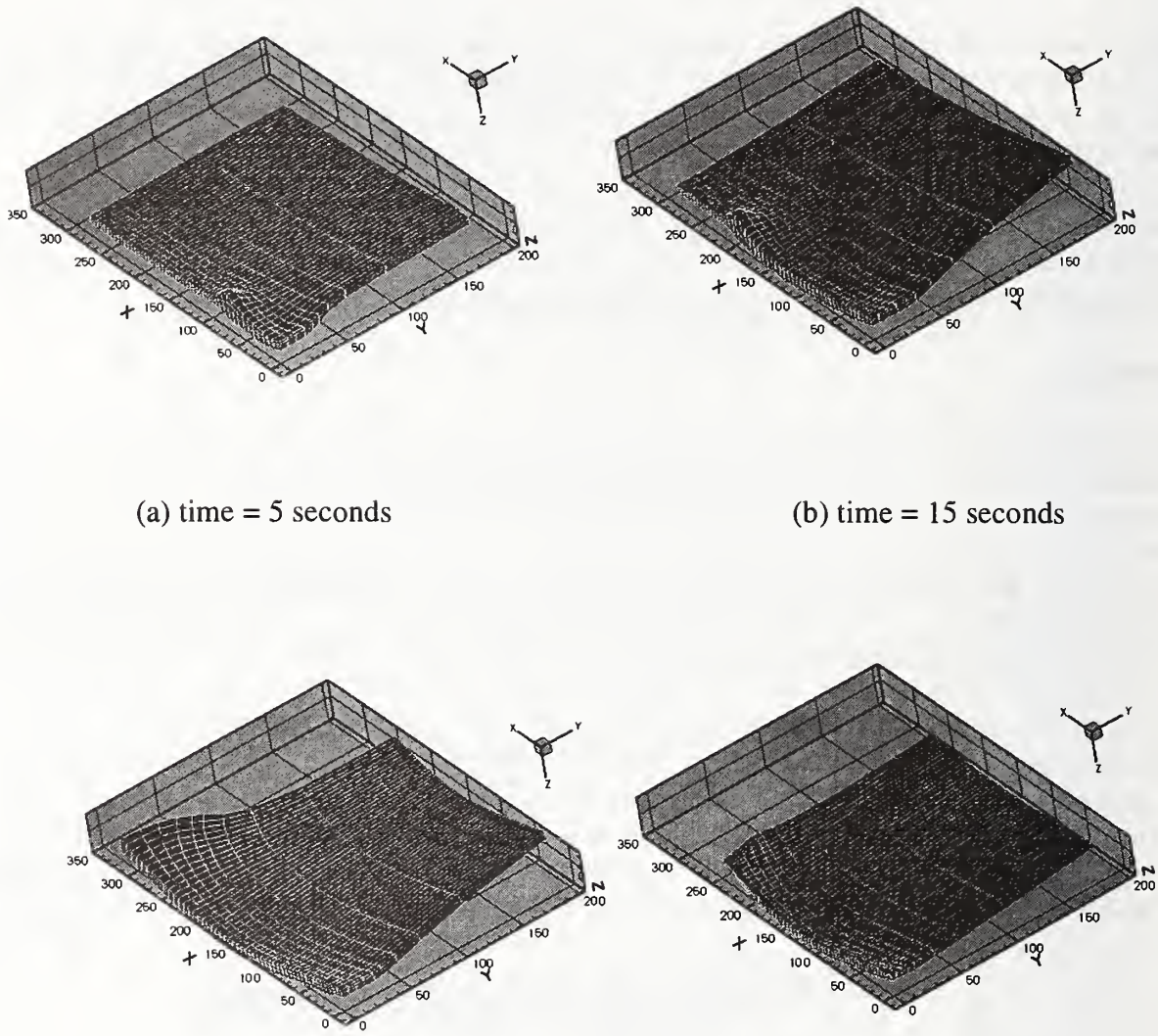

(a) time = 5 seconds

(b) time = 15 seconds

(c) time = 23 seconds

(d) time = after cooling to room temperature

Figure 8 Distorted shape of the plate during and after the welding process
(Magnification of distortion: x 100)

The distribution of the longitudinal strains in the welding direction, ε_{XX} , along the line in the center of the plate (X, Y,Z) = (125, Y, 0 mm) is shown in Fig. 9. Fig. 9 indicates that the longitudinal strain, which is transverse to the weld line is non-uniform with the maximum compressive strain at the weld-line. The resulted shrinkage along the weld-line (X, 0, 0) for the plate is about 0.18 mm, while there is almost no shrinkage at the edges (X, 180, 0 mm). Note that modeling using a plane strain assumption has been used by many researchers to study the steady-state welding process, which may seem to be valid in the central part of the plate, e.g. a cross section of the plate. The results in Fig. 9 cannot be obtained by a plane strain model and indicate that the plane strain model is not realistic.

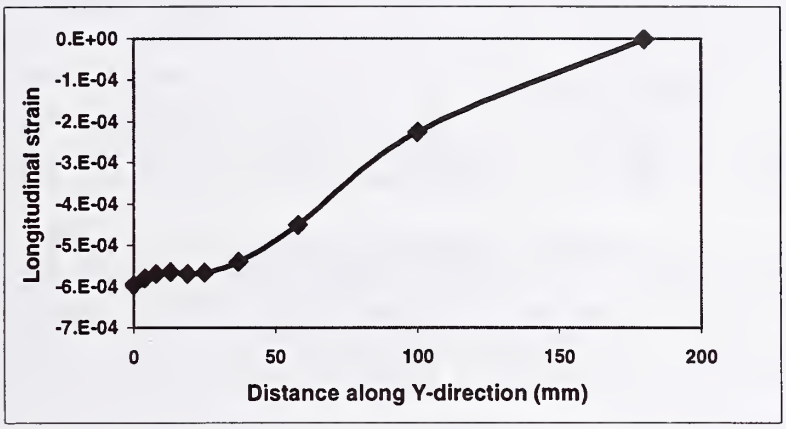

Figure 9 The longitudinal strains ε_{XX} along the line in the center of the plate, (125, Y, 0) mm

The computed shrinkage in the transverse direction, the longitudinal direction, as well as the angular distortion β are also compared with available empirical predictions from open literature. The comparison is very good and is reported elsewhere (Ref. 13).

COMPUTATION SPEED

In order to study the computational speed for various features discussed previously, several cases were carried out. Table 1 shows the total time required to complete the analyses for the six cases. The FEM code was compiled and linked using VISUAL FORTRAN on the MS developer studio. Cases 1-5 were carried out on a PC platform with Pentium II 266MHz, 128M RAM. Case 6 was on a Pentium III 450 MHz and 256M RAM. Case 1 includes all the special features for the code as discussed previously. The other cases have the same features in Case 1 except that (1) in Case 2 the tolerance limit for the residual force is 1/5 of that used in Case 1, (2) in Case 3 the melting point of the material (640°C) was used as the cut-off temperature instead of 550°C used in case 1, (3) in Case 4 the FEA mesh in the heat transfer analysis was again used in the thermo-mechanical analysis, (4) in Case 5 a smaller time increment and a larger temperature increment were used in the thermo-mechanical analysis, and (5) in case 6 same input files as case 1 were used but with a better computer. Note that all five cases yield similar results for the residual stress and distortion and the difference is of little physical significance.

The data shown in table 1 indicates that the special features in the code can indeed increase the computational speed for the analysis. It is noted although adopting a cut-off temperature of 550°C only improve the speed slightly as shown by Case 3 in Table 1, it is because the workpiece is made of Aluminum alloy. For steel, however, the saving in computation could be significant since the cut-off temperature can be substantially less than the melting temperature, In Case 4, approximately one-half of the number of nodes used for the heat transfer analysis (4040 nodes) was used in the thermo-mecahnical stress analysis (2040 nodes) and the time-saving is significant.

Table 1 Comparison of computational time for various cases

Case number	1 (the basic case)	2	3	4	5	6
Time (hours)	18	36	20	45	24	9
% of the basic case	***100***	200	111	250	133	50

Many welding processes require more complex modeling effort such the latent heat effect, complex heat source models, local coordinate transformation, phase transformation, micro-structure evolution, reduced integration (for mesh locking), large deformation (for buckling analysis), dummy element (for multi-pass welding), and fixture relief after welding. These features are either implemented into our code already or in the process of inclusion to study more complicated welding processes.

CONCLUSIONS

A three-dimensional finite element simulation of GMAW process is presented. The analysis adopts a de-coupled heat transfer and thermo-mechanical analysis for the determination of residual stress and distortion. Special features for the welding process are developed in the finite element model to reduce the computational time of the analysis. A butt-welded aluminum plate was analyzed and the numerical results compared well with the available experimental data. It is further demonstrated that the full three-dimensional model can reveal more realistic results, which generally cannot be obtained by the simplified two-dimensional simulation.

Three-dimensional modeling of welding process is time consuming, however, essential for practical problems. The butt-welded plate analyzed in the paper took about 9 hours to complete both the heat transfer and thermo-mechanical analyses on a Pentium 450 MHz PC with 256 MB RAM. This computation speed for such a three-dimensional problem is very efficient compared to any of the published results the authors are aware of. This high efficiency is achieved primarily by incorporating the special computational techniques into the code. With efficient computational code such as the current one available, modeling of welding process can then be applied to more practical problems to address the fabrication process of welded structures.

ACKNOWLEDEMENT

This work is a part of the research program in *structural joints*, sponsored by the NSF Cooperative Agreement No. EPS-9630167 at the University of South Carolina. The support from NSF is greatly appreciated.

REFERENCES

1. Hibbitt, H.D.; and Marcal, P.V. 1973. A Numerical Thermo-Mechanical Model of the Welding and Subsequent Loading of a Fabricated Structure. *Computers and Structures* 3(5): 1145 to1174.

2. Tekriwal, P.; and Mazumder, J. 1991. Transient and Residual Thermal Strain-Stress Analysis of GMAW. *ASME Journal of Engineering Materials and Technology* 113(7): 336 to 343.
3. Michaleris, P.; and DeBiccari, A. 1997. Prediction of Welding Distortion. *Welding Journal* 76(4): 172s to181s.
4. Dong, Y.; Hong, J.K.; Tsai, C.L.; and Dong, P. 1997. Finite element Modeling of Residual Stresses in Austenitic Stainless Steel Pipe Girth Welds. *Welding Journal* 76(10): 442s to 449s.
5. Brown, S. and Song, H. 1992. Finite Element Simulation of Welding Large Structures. *ASME Journal of Engineering for Industry* 114: 441 to 451.
6. Brown, S. and Song, H. 1992. Implications of Three Dimensional Numerical Simulations of Welding of Large Structures, Welding Research Supplement, Welding Journal 71(2): 55 to 62.
7. Dike, J.; Cadden, C.; Corderman, R.; Schultz, C. and McAninch, M. 1995. Finite Element Modeling of Multipass GMA Welds in Steel Plates. Proceedings of the 4th International Conference of Trends in Welding Research, Gatlinburg, TN, June 4-8.
8. Arrgyris, J.H.; Szimmat, J. and William, K.J. 1982. Computational aspects of welding stress analysis. Computer Methods in Applied Mechanical Engineering, 33: 635 to 666.
9. Papazoglou, V.J. and Masubuchi, K. 1982. Numerical Analysis of Thermal Stresses during Welding Including Phase Transformation Effects. *ASME Journal of Pressure Vessel Technology*, 104: 198 to 203.
10. Karlsson, L, 1986. Thermal Stresses in Welding. Chapter 5, Thermal Stresses I, Volume I of Thermal Stress, editor R.B. Hetnarski, Elsevier Science Publishers.
11. Chao, Y. J.; Qi, X. 1999. Three-Dimensional Modeling of Gas Metal Arc Welding Process. Transaction of NAMRC XXVII, North American Manufacturing Research Institution:MR99-164.
12. Canas, J.; Picon, R.; Paris, F.; Blazquez, A. and Marin, J.C. 1996. A Simplified Numerical Analysis of Residual Stresses in Aluminum Welded Plates. *Computers & Structures* 58(1): 59 to 69.
13. Chao, Y.J. and Qi, X., "Thermo-mechanical Modeling of Residual Stress and Distortion during Welding Process," *Fracture, Fatigue and Weld Residual Stresses*, ASME 1999 PVP-Vol ???.

FINITE ELEMENT MODELING OF ANGULAR DISTORTION IN STIFFENED THIN-SECTION PANELS

W. Cheng, J. R. Dydo, Z. Feng, Y. Chen, J. S. Crompton*

ABSTRACT

Welding-induced angular distortion is a common form of distortion developed during construction of ship hulls. Excessive angular distortions often result from fillet welding of stiffened thin-section panels, causing quality and performance concerns. In this study, a finite element modeling approach called the "Moving Heat Source Model" is presented to predict the angular distortion of fillet welding of T-sections. In this work, both in-plane shrinkage and angular distortion predictions are used together with experimental measurements to investigate the validity and accuracy of the Moving Source Model.

INTRODUCTION

Welding processes have frequently been observed to cause macro-variations in weld joint shapes. This phenomenon is commonly referred to as welding distortion (Ref. 1). In complex welded structures, distortion problems present a challenge to welding engineers. The more complex the structure, the more difficult the distortion is to control. Thin-section panel structures are often used in the construction of ship hulls, superstructures, bulkheads, and decking structures (Ref. 2, 3). Angular distortion is one of the primary distortion types manifested in these structures. Distortion correction techniques such as flame straightening are very labor-intensive and costly. A better alternative is to reduce distortion during fabrication. Several distortion-mitigation methods, including preheating, pre-stressing and selecting proper welding sequence, can be used to achieve in-process distortion control. However, these distortion control procedures are more art then science and methods to predict the resulting shape after completion of these techniques are lacking. Finite element modeling is likely to result in the best predictions for distortion currently available. Therefore, development of accurate finite element methods is a necessity.

Although empirical formulae are available for distortion prediction (Ref. 1, 4-8), there are several disadvantages associated with their use. Empirical methods can only be applied to specific geometry and fixturing conditions. In other words, these methods are not predictive if used on arbitrary shapes. Finite element modeling is increasingly used to determine welding distortion. However, limited information is currently available having a correlation of computed and measured welding distortion. In this paper, a three-dimensional finite element (FE) model is developed to predict angular distortion. The computed temperature and distortion profiles are compared with measured values. The finite element technique described in this paper consists of a full-scale detailed model development, which consumes huge computing resources and time. The efforts to reduce computational time are also discussed.

***Edison Welding Institute, Columbus, OH 43221**

PREDICTION OF WELDING DISTORTION USING THE "MOVING SOURCE MODEL"

The moving source model is formulated and verified for two different configurations. The first verification is for in-plane shrinkage of a butt joint. The finite element results are compared with the published experimental data (Ref. 9) to verify the validity of the model. After this verification, the finite element model is used to predict the angular distortion in a stiffened thin panel typical of a ship hull. The predicted results are also compared with the experimental measurements.

Finite Element Model

Typically, a GMAW or FCAW process is used to produce dual fillet welds on T-sections of thickness commonly used in shipyard for thin-section panel fabrications. A three-dimensional finite element model is described that simulates the transient, nonlinear thermomechanical deformation process associated with welding. The motion of welding arc and the associated filler metal deposition processes are simulated in the model. Thermo-elasto-plastic analyses are performed using the commercial code ABAQUS enhanced with USER subroutines. The thermal and elastic-plastic analyses are decoupled and solved independently.

The temperature fields during welding are computed based on the welding process conditions. The welding heat input is applied using the "double ellipsoid" heat source model (Ref. 10), where the heat generated by welding is simulated with a power density moving along with the torch. The double ellipsoid model is implemented via a user subroutine DFLUX in ABAQUS. The method described in (Ref. 10) is used directly. The total heat input Q is evaluated from the following expression:

$$Q = \eta \, VI \qquad (1)$$

where η is the process efficiency, V is the voltage, and I is the current. The process efficiency is determined by a trial and error approach such that the computed fusion zone matches the actual one. A process efficiency of 90% is found to give the best correlation of computed and observed fusion zones in both in-plane shrinkage and angular distortion studies. Temperature-dependent material properties including thermal conductivity, specific heat are used. Convection boundary conditions are used for all free surfaces in the thermal analysis.

In the mechanical analysis, the calculated transient temperature fields are used as the thermal loading for the thermomechanical deformation computations performed using ABAQUS enhanced with user defined subroutines. The user subroutines are used to deal with the materials behavior at elevated temperatures and simulate the filler metal addition process (Ref. 11).

The FE mesh of the Butt Joint is illustrated in Figure 1a. The model consists of 15880 elements and 19603 nodes. The joint has a dimension of 24 inch X 24 inch and plate thickness is 2-3/4 inch. It is a multipass weld, using 4 passes, as shown in Figure 1b. The FE mesh used for the Tee Joint is shown in Figure 2, which contains 21600 elements and 26487 nodes. The joint is symmetric, therefore, a half model with symmetry boundary conditions is used in the FE model. Heat conduction 8-node linear brick elements (ABAQUS DC3D8) are used in the thermal

analyses and reduced integration 8-node linear brick elements (ABAQUS C3D8R) in the mechanical analyses for both joints.

Experimental Procedure

The in-plane shrinkage resulted from multipass GMA welding were reported in the literature by J. Dike, et al (Ref. 9). The double-fillet Tee Joint was welded with FCAW. The experimental set-up is illustrated in Figure 3. The bottom plate measures 20 inch x 20 inch and the height of the stiffener is 8 inches. During welding the two torches traveled simultaneously on both sides of the stiffener to maintain symmetry about the stiffener. The FCAW process used 24 V, 245 A, and 14 in/min travel speed. The fillet size is nominal 1/4 inch. To obtain the thermal response during welding, the thermocouples are placed beneath the weld bead and on the surface of the plate. The plate and stiffener are tack welded together before welding. As shown in Figure 3, two brackets mounted on the stiffener are used to support the joint and prevent any rigid body motion. Figure 3 also indicates the LVDT's used to record the real-time displacement of the plate are positioned beneath the plate. In addition to the thermocouple and LVDT data, the temperature and displacement fields were measured using both thermal and stereoscopic imaging systems.

RESULTS AND DISCUSSIONS

For the in-plane shrinkage study, the comparison of cumulative average in-plane shrinkage for 4 passes using FE analysis and experiment is shown in Figure 4. The FE analysis gives a reasonably accurate prediction of shrinkage resulted from the first pass but also accurately predicts significant additional shrinkage subsequently.

The fillet weld results are given in Figures 5 through 12. The temperature history, weld bead shape, transient and final out-of-plane displacements are predicted for the fillet welds with different welding parameters. The FE predictions are shown in good agreement with the experimental measurement results. The predicted and observed bead shapes are demonstrated in Figure 5. The calculated transient temperature fields are verified with both thermocouple and thermal imaging results. The thermocouple data was compared directly to the nodal temperatures as predicted by the finite element analysis, as illustrated in Figure 6. In addition thermographic plots were obtained of the underside of the test plate for comparison as well, see Figures 7 through 9. The predicted final out-of-plane displacement fields during welding are compared with stereographic mapping results, Figures 10 and 11. The calculated out-of-plane (angular) displacement history is compared with measurement using LVDTs, as shown in Figure 12.

Both FE modeling and experiment measurements show that the primary distortion mode is angular distortion for the cases studied. The FE model is capable of accurately simulating the angular distortion of the welds. Parametric studies using the FE model reveals that, in order to adequately simulate the angular distortion, it is critical to properly simulate the accumulated structural rigidity changes along the weld line caused by the continuous deposition of the fillet metal during welding. Other factors significantly influencing the magnitude of distortion include weld bead shape and the heat input levels.

ACKNOWLEDGEMENT

The authors wish to thank the US Navy and the Manufacturing Technology Program (MANTECH) for their sponsorship of this research.

REFERENCES

1. Masubuchi, K. 1980. Analysis of Welded Structures: 235-240, Pergamon Press.
2. Michaleris, P.; and DeBiccari, A. 1996. A Predictive Technique for Buckling Analysis of Thin Section Panels Due to Welding. Journal of Ship Production 12(4): 269-275.
3. Conrardy, C.; and Dull, R. 1997, Control of Distortion in Thin Ship Panels. Journal of Ship Production 13(2): 83-92.
4. Watanabe, M.; and Satoh, K. 1961. Effect of Welding Conditions on the Shrinkage Distortion in Welded Structures. Welding Journal 40(8): 377s to 384s.
5. Spraragen, W.; and Cordov, M. 1944. Shrinkage Distortion in Welding. Welding Journal 23(11): 545s to 559s.
6. Spraragen, W.; and Ettinger, W. 1950. Shrinkage Distortion in Welding. Welding Journal 29(6): 292s to 294s.
7. Goglio, L.; and Gola, M. 1993. Shrinkage in Butt Welded Joints: Measurement and Prediction. Welding International 7(10): 776-787.
8. Kumose, T.; Yoshida, T.; Abbe, T.; and Onoue, H. 1954. Prediction of Angular Distortion Caused by One-Pass Fillet Welding. Welding Journal 33(10): 945s to 956s.
9. Dike, J.; Cadden, C.; Corderman, R.; Schultz, C.; and McAninch, M. 1995. Finite Element Modeling of Multipass GMA Welds in Steel Plates. Proc. 4th International Conference on Trends in Welding Research: 1-9.
10. Goldak, J.; Chakravarti, A.; and Bibby, M. 1984. A New Finite element Model for Welding Heat Sources. Metallurgical Transactions B 15(6): 299-305.
11. Feng, Z.; Wang, X. L.; Spooner, S.; Goodwin, G. M.; Maziasz, P. J.; Hubbard, C. R.; and Zacharia, T. 1996. A Finite Element Model for Residual Stress in Repair Welds. Residual Stress in Design, Fabrication, Assessment and Repair, ASME PVP Volume 327: 119-125.

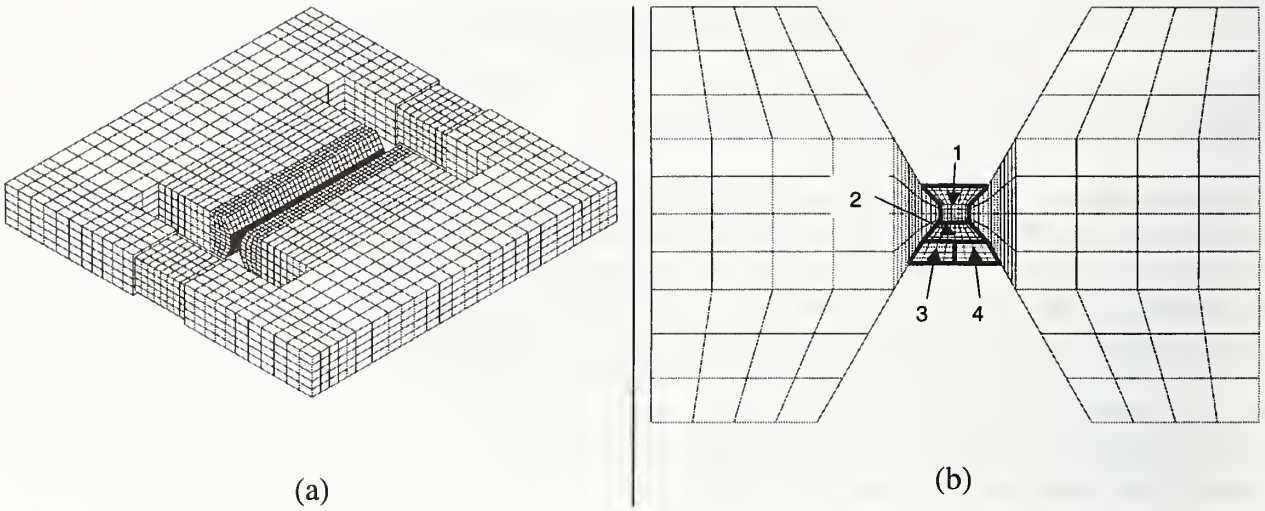

Figure 1 (a) FE mesh of the Butt Joint (b) Cross section of the Butt Joint

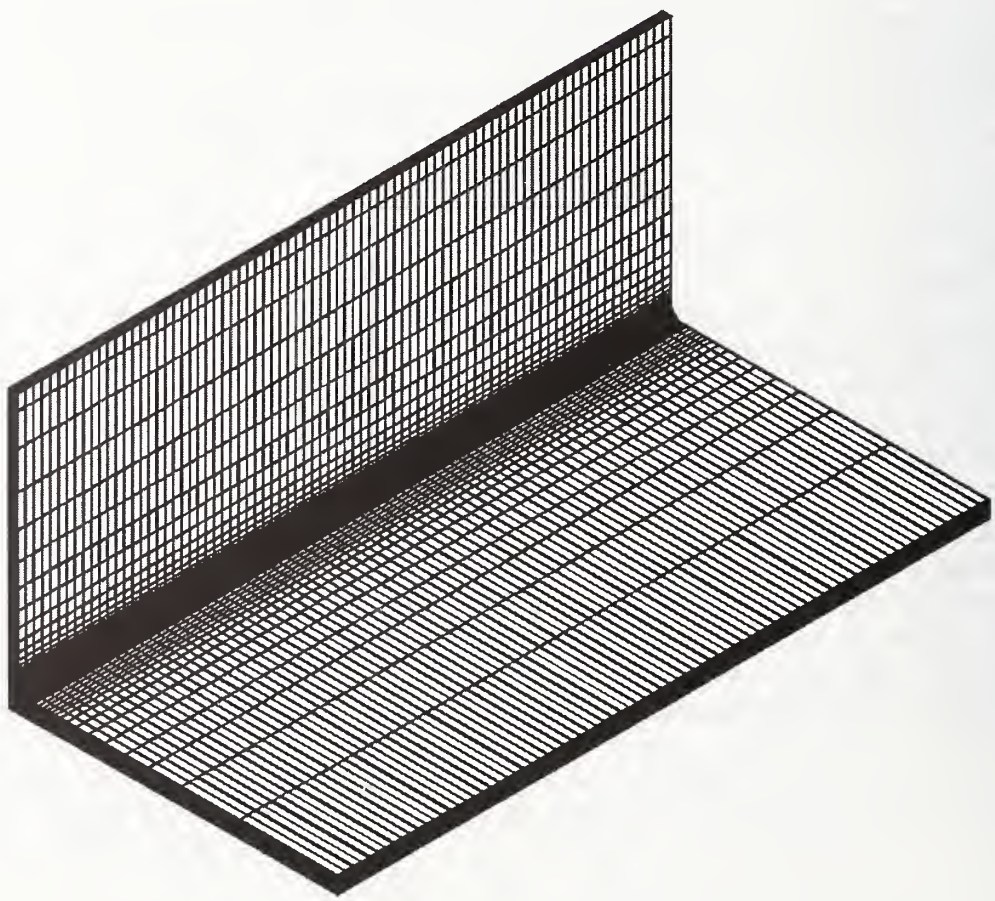

Figure 2 FE mesh of the Tee Joint

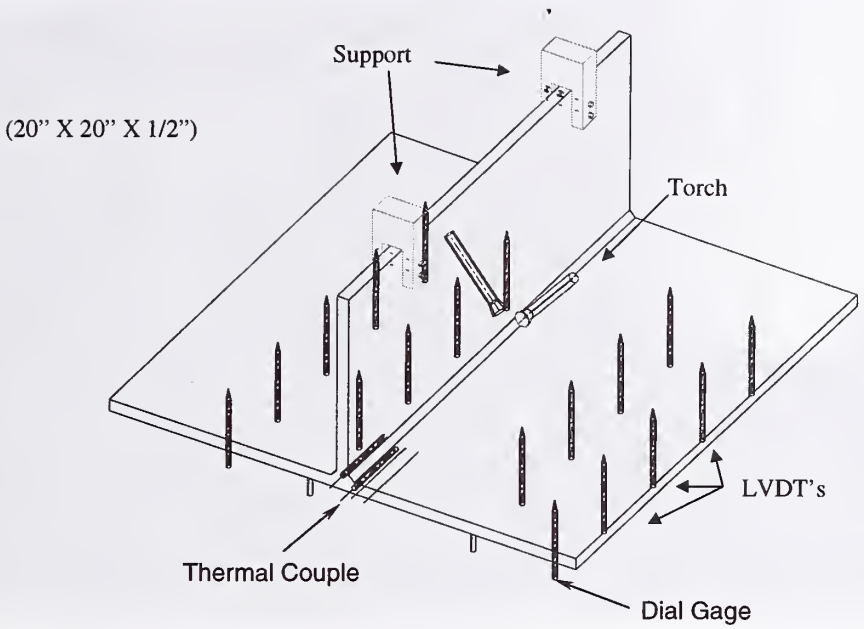

Figure 3 Experimental set-up of welding of stiffened panels (Tee Joints). Plate size (20x 20 in.), stiffener Height (8 in.), thickness (1/2 in.)

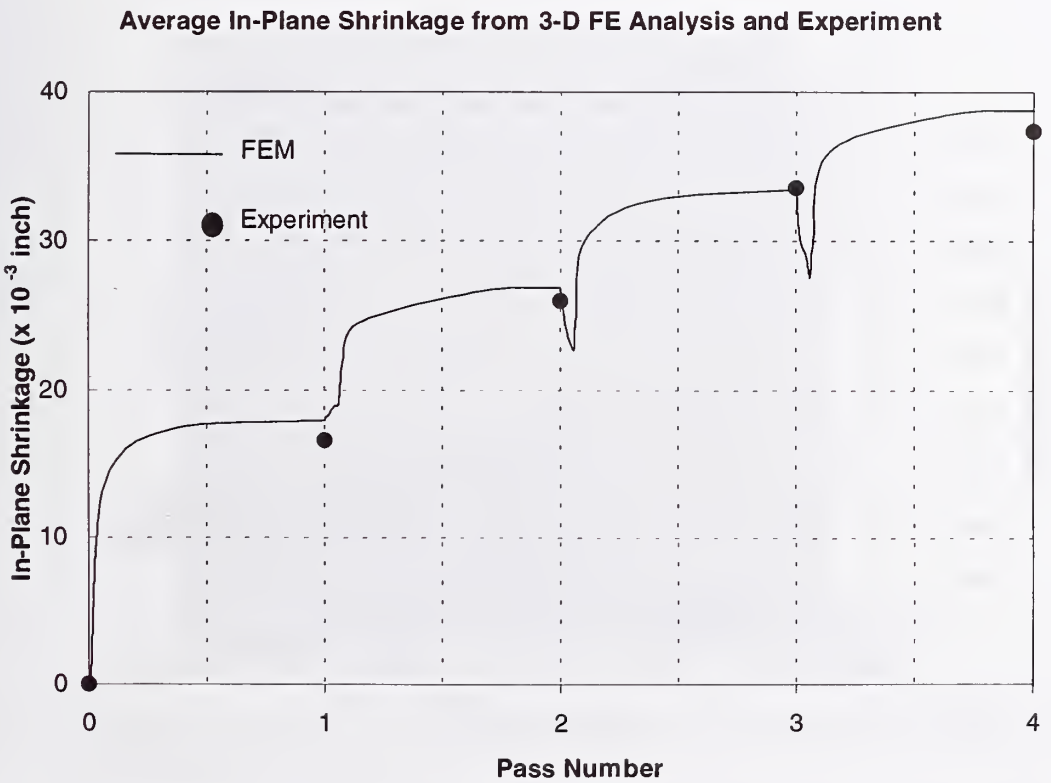

Figure 4 Comparison of cumulative average in-plane shrinkage for 4 passes from FE analysis and Experiment (Ref. 9)

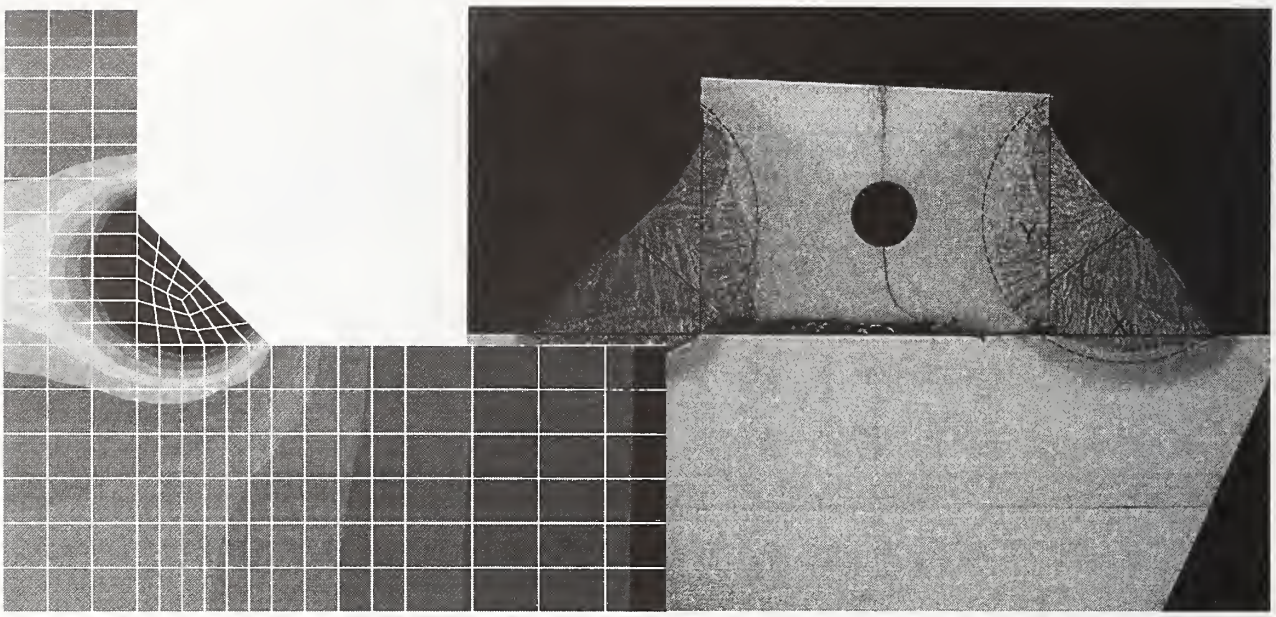

FEM Experimental

Figure 5 Predicted and observed bead shapes

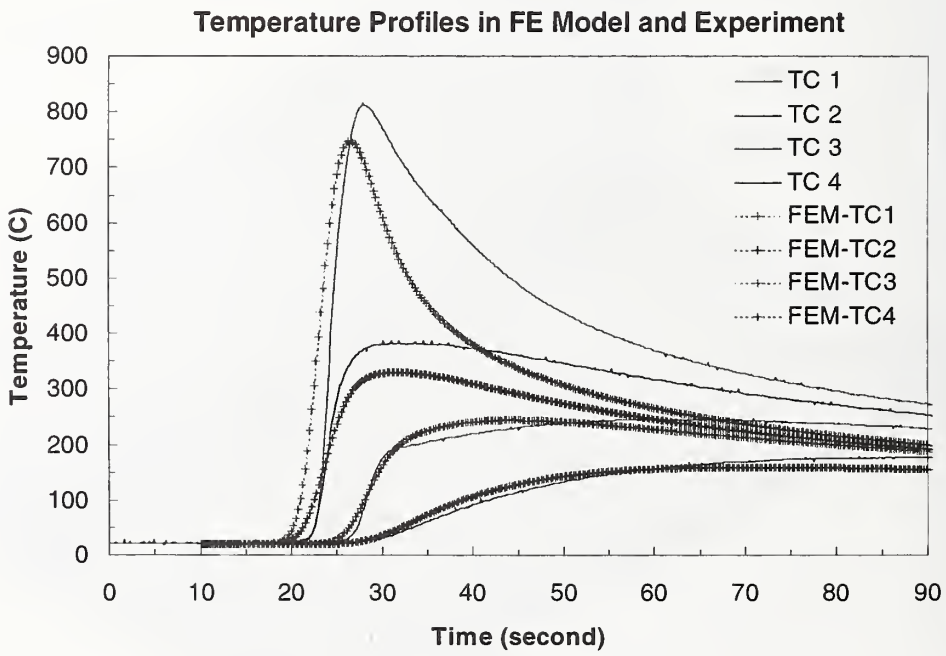

Figure 6 Predicted and measured temperature history

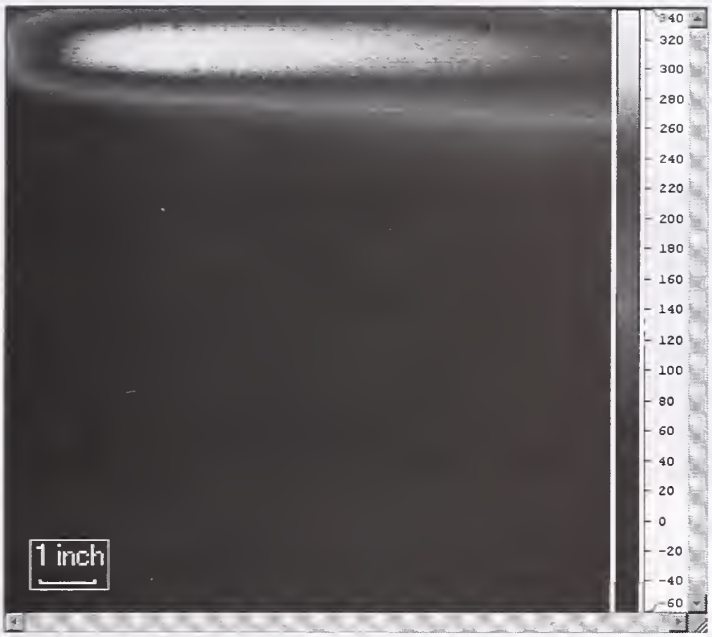

Figure 7 Thermographic Plot Depicting the Temperature Distribution on the Bottom of the Plate with Torch Near Mid-Length of Travel

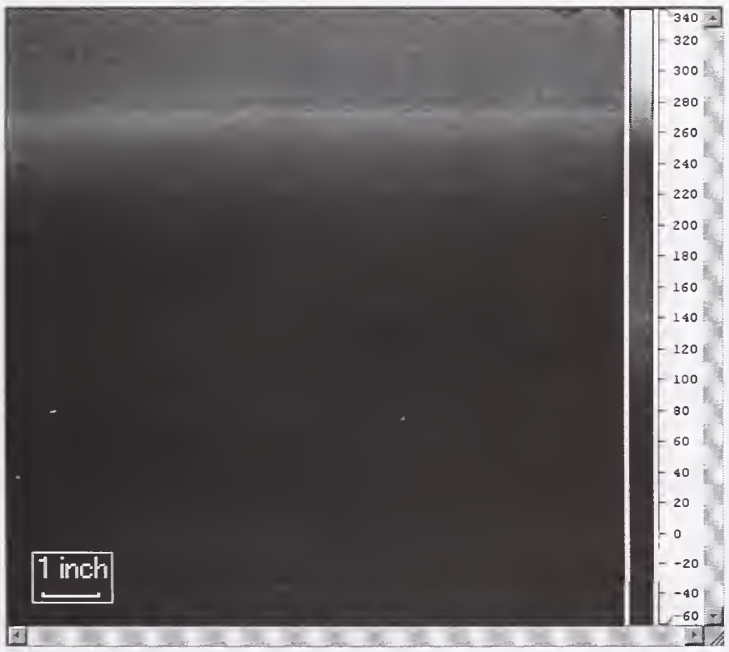

Figure 8 Thermographic Plot Depicting the Temperature Distribution on the Bottom of the Plate with Torch Near End of Welding

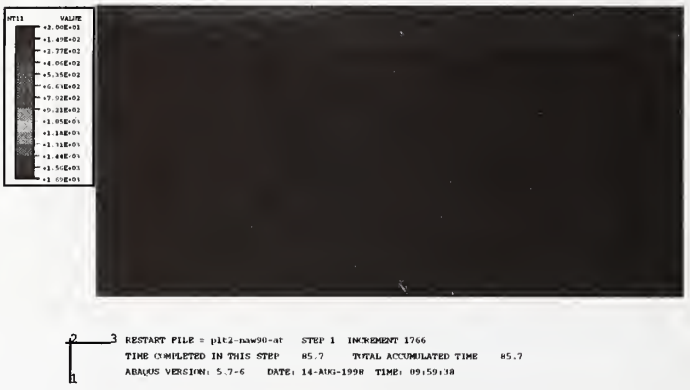

Figure 9 Predicted temperature field on the bottom of plate at near end of welding

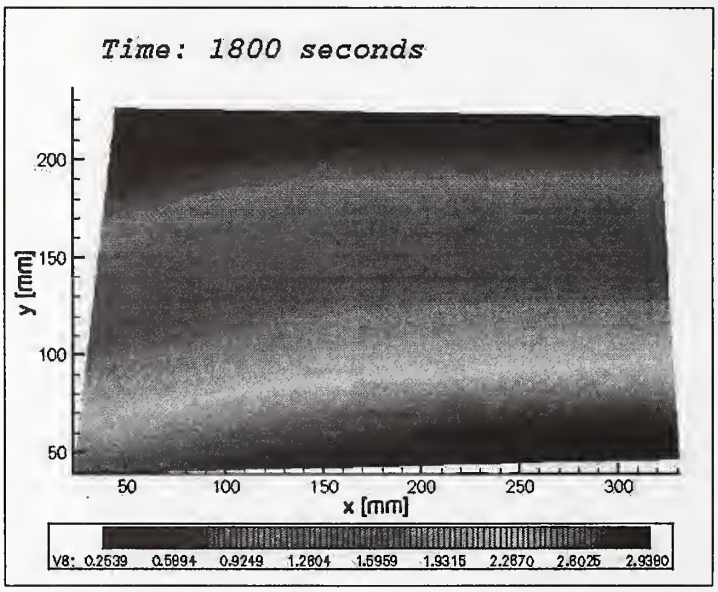

Figure 10 Measured Out-of-Plane Displacement After Cooling

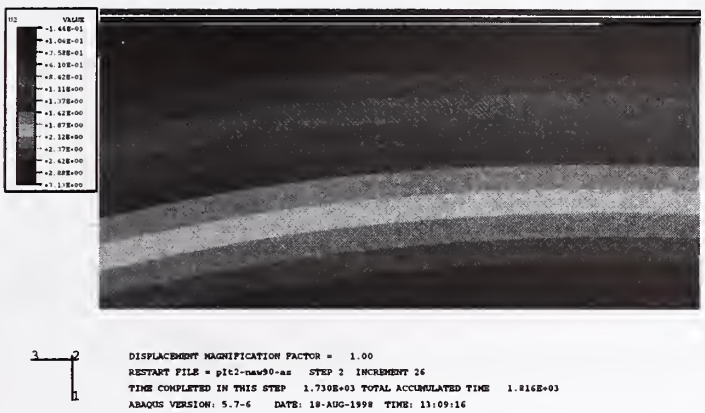

Figure 11 Finite Element Predicted Out-of-Plane Displacement After Cooling

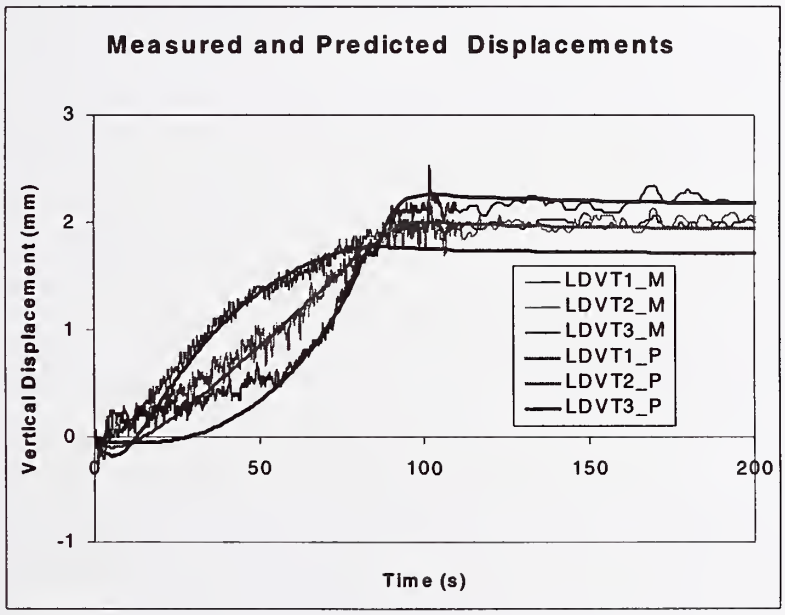

Figure 12 LVDT Measured Displacements Compared to Finite Element Predictions

Session A4: Solidification/Weld Composition Modeling

THE USE OF COMPUTERIZED THERMODYNAMIC DATABASES FOR SOLIDIFICATION MODELING OF FUSION WELDS IN MULTI-COMPONENT ALLOYS

J.N. DuPont [1], B.D. Newbury [1], C.V. Robino [2], and G.A. Knorovsky [2]

ABSTRACT

Most engineering alloys contain numerous alloying elements and their solidification behavior can not typically be modeled with existing binary and ternary phase diagrams. There has recently been considerable progress in the development of thermodynamic software programs for calculating solidification parameters and phase diagrams of multi-component systems. These routines can potentially provide useful input data that are needed in multi-component solidification models. However, these thermodynamic routines require validation before they can be confidently applied to simulations of alloys over a wide range of composition. In this article, a preliminary assessment of the accuracy of the Thermo-Calc NiFe Superalloy database is presented. The database validation is conducted by comparing calculated phase diagram quantities to experimental measurements available in the literature. Comparisons are provided in terms of calculated and measured liquidus and solidus temperatures and slopes, equilibrium distribution coefficients, and multi-component phase diagrams. Reasonable agreement is observed among the comparisons made to date. Examples are provided which illustrate how the database can be used to approximate the solidification sequence and final segregation patterns in multi-component alloys. An additional example of the coupling of calculated phase diagrams to solute redistribution computations in a commercial eight component Ni base superalloy is also presented.

1. Lehigh University, Bethlehem, PA
2. Sandia National Laboratories, Albuquerque, NM

INTRODUCTION

The microstructure of fusion welds in engineering alloys is dependent on the redistribution of solute (microsegregation) during solidification as well as the form of the phase diagram. Previous studies conducted to fundamentally quantify the relation between alloy composition, microsegregation, and weld microstructure often utilized binary alloy systems (Refs. 1,2). This approach is convenient because the alloy parameters required for microsegregation calculations (e.g., liquidus temperature, distribution coefficient, eutectic temperature and composition) can be determined directly from the binary phase diagram. However, many alloys of engineering significance contain numerous solute additions, and can undergo one or more eutectic-type reactions over a broad temperature and composition range. In this case, microsegregation calculations require the knowledge of multi-component phase diagrams and the distribution coefficients for all solutes which significantly affect development of the final microstructure. In addition, when a eutectic-type reaction occurs over an appreciable temperature and composition range, it then becomes necessary to know *two* distribution coefficients for *each* important solute; one which describes solute partitioning between the liquid and primary solid phase, and a second which describes partitioning between the liquid and secondary solid phase within the eutectic constituent. The lack of such information restricts solute redistribution modeling of multi-component alloys.

In recent years there has been considerable progress in the development of thermodynamic software programs for calculating solidification parameters and phase diagrams of multi-component systems (Ref. 3). This progress is likely to lead to more frequent use of solute redistribution models and their application to alloy systems containing many elements. In view of this fact, it is useful to consider how such thermodynamic databases can be integrated into modeling efforts directed at understanding weldability phenomenon. In this article, preliminary results of an assessment of the accuracy of the Thermo-Calc thermodynamic routine for modeling solidification of nickel base superalloys will be presented. An example on the integration of thermodynamic calculations and solute redistribution models for the purpose of modeling microstructural evolution in alloy IN 718 will also be provided.

APPROACH

Some of the nickel base alloys of primary interest in this work are summarized in Table 1 along with their chemical composition. The table also includes references to previous work which investigated the solidification behavior of these alloys through differential thermal analysis (DTA) and microstructural characterization techniques. DTA has been used to determine the liquidus and solidus temperatures as well as the temperatures of eutectic-like reactions which occur near the end of solidification. Phase identification of secondary constituents has been conducted using electron microscopy. The combination of DTA data with microscopy results has been used to experimentally determine the solidification reaction sequences and the details of the procedures can be found within the references cited. In the current study the Thermo-Calc routine was used in conjunction with the NiFe Superalloy database (Ref. 4) to estimate various phase diagram quantities and solidification reaction sequences for comparison to the experimental data. This database has been shown to provide accurate descriptions of solid-solid

phase equilibria in multi-component Ni base alloys (Ref. 4), but an assessment for modeling solidification reactions has not yet been reported.

Table 1. Concentration of major elements of some of the alloys under investigation. All values in weight percent.

Alloy	Composition					Ref.
	Fe	Ni	Cr	Mo	Other	
C-22	3.17	Bal	21.22	13.43	3.29 W	5
C-276	5.44	Bal	15.83	15.56	3.93W	5
IN 718	18.2	Bal	18.2	3.1	5.2 Nb-0.04C	6
IN 625	2.4	Bal	22.7	9.6	Range of Nb,Si, and C	7
Experimental	11-45	Bal	19.0	--	Range of Nb,Si, and C	8

RESULTS AND DISCUSSION

Reaction Temperatures and Phase Diagrams

Liquidus and solidus slopes are important for solidification modeling as they can be used to provide values for the equilibrium distribution coefficients. Experimental measurement of these quantities can be accomplished by measuring the liquidus and solidus temperatures with DTA on homogeneous, single phase alloys with systematic variations in composition (Refs. 7,9). Although this approach is effective, it is also quite time consuming. Direct calculation of liquidus and solidus temperatures through thermodynamic databases would thus provide a useful technique for minimizing the extent of experimental measurements. Figure 1 compares the measured and calculated liquidus and solidus temperatures for the alloys listed in Table 1 in addition to data on other alloys reported in the literature, and the agreement is reasonable. These

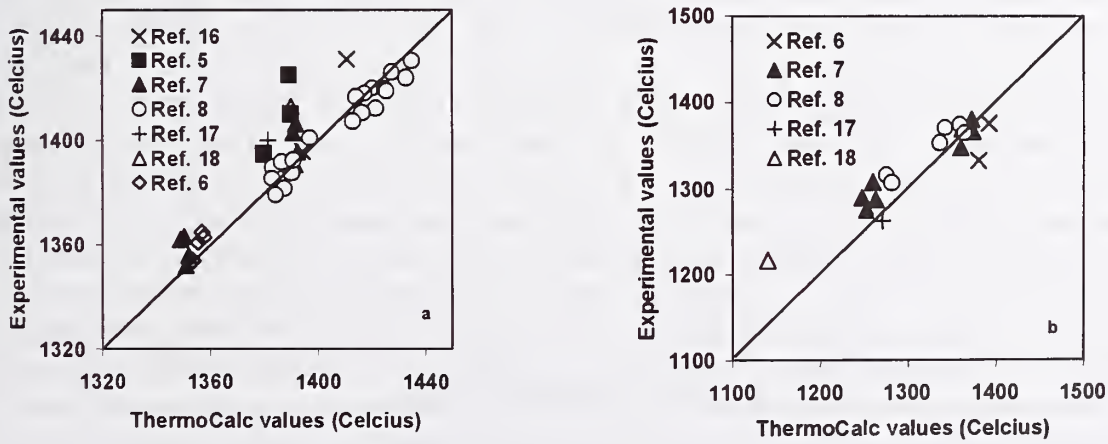

Figure 1. Comparison of calculated and measured liquidus (a) and solidus (b) temperatures.

calculations can easily be extended to determine the liquidus and solidus temperatures over a range of composition for a particular alloying element, and an example is shown in Figure 2 for a five component alloy (Ni-11Fe-19Cr-0.02C-XNb). The liquidus and solidus slopes with respect to Nb in this system have been measured to be –8.3 and –17.9°C/wt% Nb, respectively. The calculated slopes are in reasonable agreement with these values (–11 and –24°C/wt%). The equilibrium distribution coefficient for Nb, which is given by the ratio of liquidus to solidus slope, has also been measured for this system and is 0.46. This is in excellent agreement with the value of 0.46 obtained from the slopes given in Figure 2.

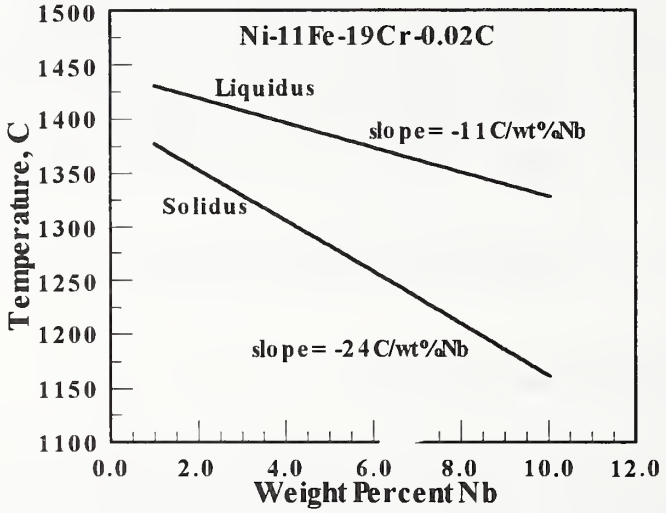

Figure 2. Calculated variation in liquidus and solidus temperature as a function of Nb content for Ni-11Fe-19Cr-0.02C-XNb alloys.

Phase diagrams are needed in order to follow the progression of reactions over the entire solidification range. Various experimental measurements of multi-component equilibria have been reported, and these are usually portrayed by using simplified binary or ternary-like diagrams. These experimentally derived diagrams are useful for database validation. Knorovsky *et al.* presented a binary-like phase diagram for IN 718. This alloy exhibits a three step solidification reaction according 1: L -> γ, 2: L -> (γ + NbC), 3: L -> (γ + Laves). The L -> (γ + NbC) reaction occurs over a relatively wide temperature range and forms a small amount of the γ/NbC eutectic-type constituent. The L -> (γ + Laves) reaction occurs over a small temperature interval and the γ/Laves accounts for most of the eutectic-type constituent in the as-solidified microstructure. Neglecting the small amount of γ/NbC that forms, Knorovsky *et al.* developed a binary-like eutectic phase diagram at solidification temperatures that includes the primary L -> γ and eutectic-type L -> (γ + Laves) reactions. Key temperature/composition points on the diagram were determined by a combination of DTA and electron microscopy. Their diagram is compared to a calculated diagram for IN 718 in Figure 3. The calculated liquidus line and L -> (γ + Laves) reaction composition are in reasonable agreement with experimental values. The calculated solidus line is 75-100 °C below the experimental line, and the calculated eutectic temperature is approximately 50 °C below the measured value. The difference in solidus values could, in part, be attributed to the sample used in the DTA measurements. These samples

contained a combination of NbC and austenite. The presence of NbC depletes the austenite of Nb and C relative to the bulk composition of the alloy. Since the solidus slopes for Nb and C are negative (Refs. 7,9), this reduction in Nb and C would increase the effective solidus temperature of the austenite. Additional comparisons are, however, needed to confirm this effect.

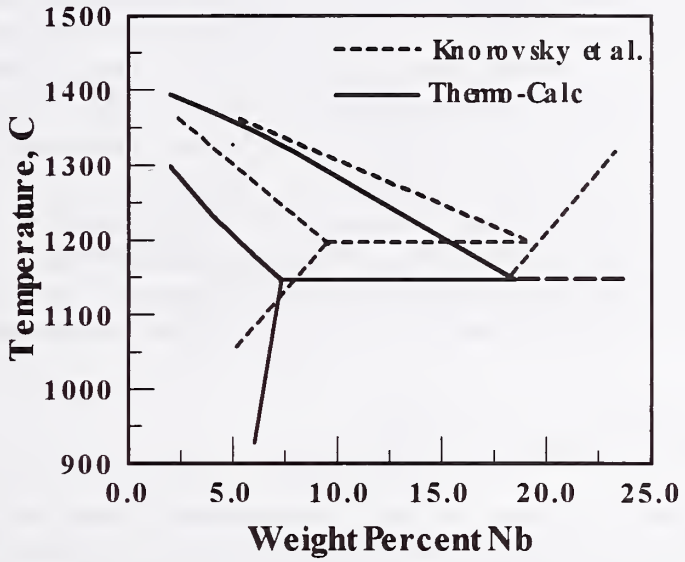

Figure 3. Comparison of measured and calculated binary-like phase diagram for IN 718.

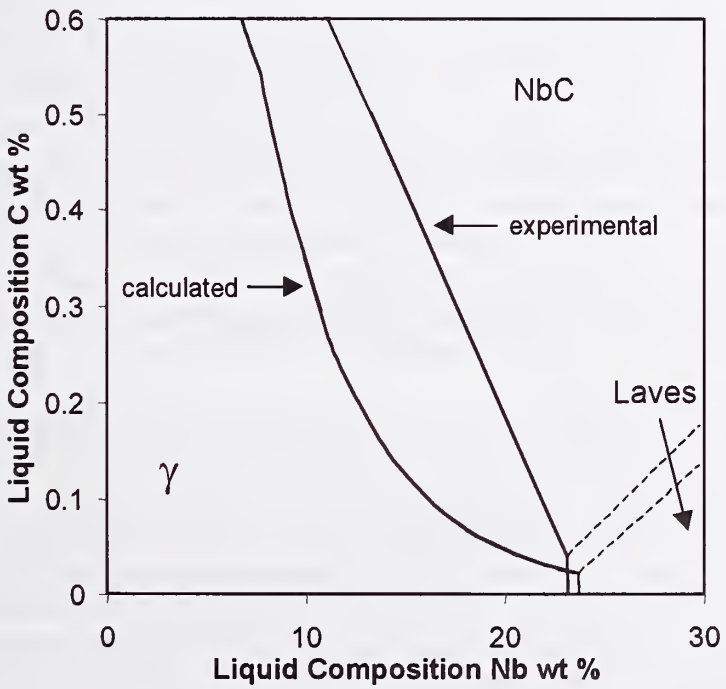

Figure 4. Comparison of measured and calculated ternary-like liquidus projection for Fe-Ni-Cr-Nb-Si-C alloys.

The small amount of γ/NbC which forms in the IN 718 investigated by Knorovsky *et al.* can be attributed to it's low carbon content (~ 0.04 wt%). However, it has been shown (Refs. 7,9) that the amount of γ/NbC constituent that forms in Nb bearing superalloys will increase significantly with relatively minor increases in carbon content. In this case, binary-like diagrams that account for only one eutectic-type reaction must be replaced by ternary-like liquidus surfaces. A γ-Nb-C liquidus surface has recently been reported for Fe-Ni-Cr-Nb-Si-C alloys and is reproduced in Figure 4 along with a calculated version for the same alloy system. The general shape of this diagram is very similar to that reported for the simple Ni-Nb-C ternary system (Ref. 10), except that the Ni_3Nb phase is replaced by the Laves phase (because of the presence of Fe and Cr). Ternary solute redistribution models (Refs. 11,12) require *a priori* knowledge of the slope of the two fold saturation line and the liquid composition at which the L -> (γ + NbC) reaction is replaced by the L -> (γ + Laves) reaction. Reference to Figure 4 indicates these values are in reasonable agreement, indicating that the calculated liquidus surface should provide sufficiently accurate input values for solidification models. This will be assessed in more detail under the section on "Coupling of Solidification Models and Calculated Phase Diagrams".

Reaction Sequences and Elemental Partitioning

The sequence of solidification reactions and final microsegregation patterns depend on both the shape of the phase diagram and the solute redistribution behavior. For example, a binary alloy that is below the maximum solid solubility and solidifying under equilibrium conditions exhibits only a primary solidification reaction, since the liquid is consumed before the eutectic composition is reached. Immediately after solidification the alloy is single phase with uniform composition. However, under "Scheil-type" conditions (Ref. 13), where the diffusivity of solute in the solid is negligible, the liquid will become progressively enriched in solute until the eutectic composition is reached, thus initiating a eutectic reaction as solidification terminates isothermally (for a simple binary system). In this case, the as-solidified microstructure contains cored primary dendrites and interdendritic eutectic. In many alloys of engineering importance, however, some solid state redistribution is possible. Thus, in the general case, the reaction sequence and distribution of alloying elements cannot be accurately estimated until both the kinetic and thermodynamic considerations are understood. For these situations, calculated phase diagrams must be integrated with more complex solute redistribution models. An example of this integration for multi-component alloys exhibiting both Scheil-type and more complex solidification behavior are given below.

Considering Scheil-type solidification first, it has been shown that microstructural evolution during solidification in many nickel based alloys is controlled by subtitutional alloying elements which exhibit negligible diffusion in the primary austenite constituent (Ref. 5). For these alloys, a simple Scheil simulation can be easily coupled to phase equilibria calculations to approximate the sequence of solidification reactions and final segregation patterns. Computationally, this coupling is accomplished sequentially by using the Scheil equation and re-setting the nominal alloy composition to that of the liquid composition from the previous temperature step. This ensures the liquid composition will always reach a local minimum on the liquidus surface, as expected from the Scheil equation. The corresponding fraction liquid is determined by the product of the fraction liquid from the previous and current temperature steps. Under the assumptions of negligible diffusivity, this approach can be used to compute the fractions and

compositions of solid and liquid during solidification without the need for any kinetic data. The Thermo-Calc application contains a module for making these calculations.

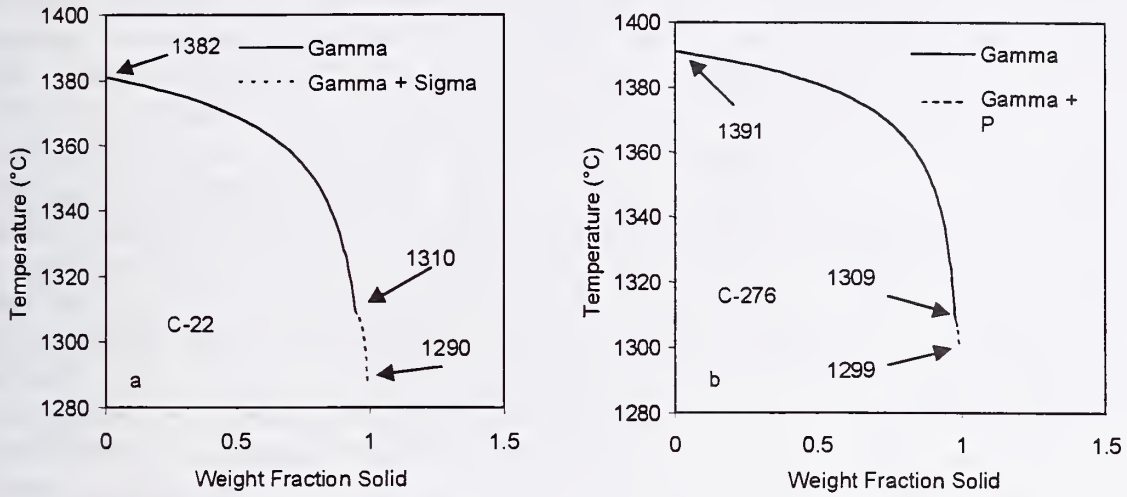

Figure 5. Scheil simulations for alloys C-22 and C-276.

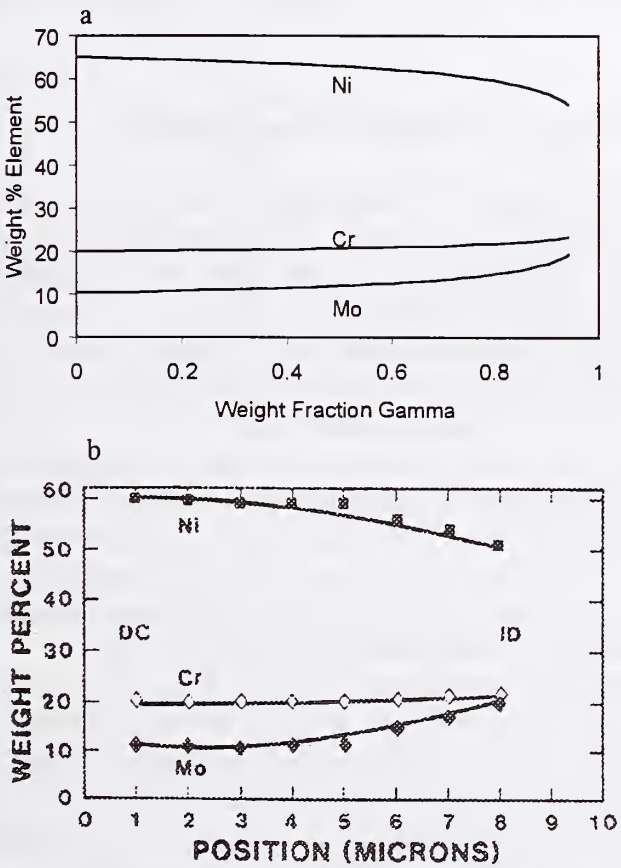

Figure 6. Comparison of calculated (a) and measured (b) segregation patterns for Ni, Cr, and Mo in alloy C-22.

Microstructural evolution of fusion welds in Hastelloy alloys C-22 and C-276 has been shown to be governed primarily by partitioning of Mo and Cr (Ref. 5). These subtitutional elements exhibit negligible solid state diffusion during the time frames associated with the cooling rates of conventional arc welds (Ref. 5,8). The final segregation pattern of Mo is of particular interest since welds in these alloys are known to be susceptible to localized corrosion attack at the Mo-depleted dendrite cores (Ref.14). Figure 5 shows a Scheil simulation for these alloys. For Hastelloy C-22, the simulations predict a two step solidification reaction consisting of L -> γ followed by L -> ($\gamma + \sigma$) which initiates at 1310 °C. For the C-276 alloy, a reaction sequence of L -> γ followed by L -> (γ + P) initiating at 1309 °C is predicted. These solidification sequences are in agreement to those experimentally observed by Cieslak *et al.*, with the exception that the final reactions occur at 1285 °C in each alloy. Figure 6a shows the calculated concentrations of Ni, Cr, and Mo in austenite as a function of fraction solid in Hastelloy C-22. Since solid state diffusion is assumed to be negligible, these results are analogous to the final distribution of solute that should exist across the dendritic substructure, where the fraction solid (fraction gamma in the figure) is equal to zero at the dendrite core and equal to one at the center of two neighboring dendrites. Figure 6b shows the experimentally measured segregation patterns of Ni, Cr, and Mo across the dendritic substructure in Hastelloy C-22 (Ref. 5). The segregation profiles in Figures 6a and 6b are comparable in terms of both segregation direction and magnitudes (assuming constant density across the range of compositions estimated). Similar results were obtained for the C-276 alloy.

Coupling of Solidification Models and Calculated Phase Diagrams

As indicated above, conditions exist where the solidification behavior can not be estimated with a simple Scheil-type analysis because one or more of the important solutes do not obey the assumption of negligible solid state diffusion. In these cases, the solidification path must be calculated with a more complex solute redistribution model and combined with the pertinent liquidus surface to understand the solidification behavior. The binary-like diagram presented for alloy IN 718 in Figure 3 is useful for alloy compositions (heats) with low carbon contents that form negligible quantities of γ/NbC. In higher carbon alloys, the L -> (γ + NbC) reaction will occur over an appreciably larger temperature range, and γ/NbC will account for a large fraction of the total eutectic-type constituent present in the final microstructure. The binary-like diagram can not account for this additional reaction, and higher order diagrams are needed to represent the multiple eutectic reactions. In this final section, an example is presented where a calculated ternary-like liquidus projection is combined with a solute redistribution model to understand the influence of composition on the solidification behavior of alloy IN 718.

Table 2 lists the chemical composition of five heats of IN 718 that contain variations in the Nb and C concentrations. Figure 7 shows typical DTA cooling curves for Heats 1 and 5, where the three step L -> γ, L -> (γ + NbC), L -> (γ + Laves) reaction sequence is displayed for each alloy. However, note that a seemingly small change in carbon content from 0.04 to 0.09 wt% increases the L -> (γ + NbC) start temperature by an average of 36 °C. These experimentally determined reaction start temperatures are summarized in Table 2. In agreement with previous results (Ref. 6), the L -> (γ + Laves) reaction occurs near 1200 °C over a relatively small temperature interval. Figure 8 shows a calculated ternary-like liquidus projection for IN 718. This diagram was computed by determining the position of the lines of two-fold saturation which separate the γ,

NbC, and Laves primary phase fields. Although the diagram is displayed in ternary-like fashion, it accounts for the presence of eight elements (Ni-Fe-Cr-Mo-Al-Ti-Nb-C) by approximating "γ" as an elemental constituent. The liquid composition at which the L -> (γ + NbC) reaction is replaced by L -> (γ + Laves) is calculated at 19.1 wt% Nb and 0.03 wt% C. These values are in excellent agreement with those previously reported as 19.1 wt% Nb (Ref. 6) and 0.04 wt% C (Ref. 8). Superimposed on the diagram are the primary solidification paths, which were computed with the solute redistribution model described in Ref. 11. This model assumes negligible diffusion of Nb in austenite (which has been experimentally validated – Ref. 8), but permits C to diffuse infinitely fast. Based on previous results (Ref. 15), this latter assumption is expected to be valid. The intersection of the primary solidification path with the line of two fold saturation separating the γ and NbC phase fields provides a predicted value for the start temperature of the L -> (γ + NbC) reaction. These predicted values are summarized in Table 2, and good agreement is observed between the calculated and measured reaction temperatures. This provides a positive, preliminary indication on the usefulness of calculated phase diagrams for solidification modeling in this alloy system. Work is in progress to assess the validity of this approach over a wider range of alloy compositions.

Table 2. Summary of alloy compositions and measured and calculated L -> (γ + NbC) reaction start temperatures. Compositions in weight percent, temperatures in °C.

Element	Heat 1	Heat 2	Heat 3	Heat 4	Heat 5
Ni	Bal.	Bal.	Bal.	Bal.	Bal.
Al	0.46	0.41	0.28	0.46	0.42
Cr	17.65	17.15	17.68	17.32	17.19
Fe	19.36	20.56	19.47	19.49	19.19
Mo	2.90	2.92	2.87	2.88	2.86
Nb	5.17	5.02	2.97	6.38	5.07
Ti	0.90	0.87	0.84	0.88	0.90
C	0.04	0.02	0.05	0.06	0.09
Measured L -> (γ + NbC) Temperature (°C)	1260 +/- 12	Not Detected	1290 +/- 9	1283 +/- 9	1296 +/- 9
Calculated L -> (γ + NbC) Temperature (°C)	1260	1237	1297	1264	1294

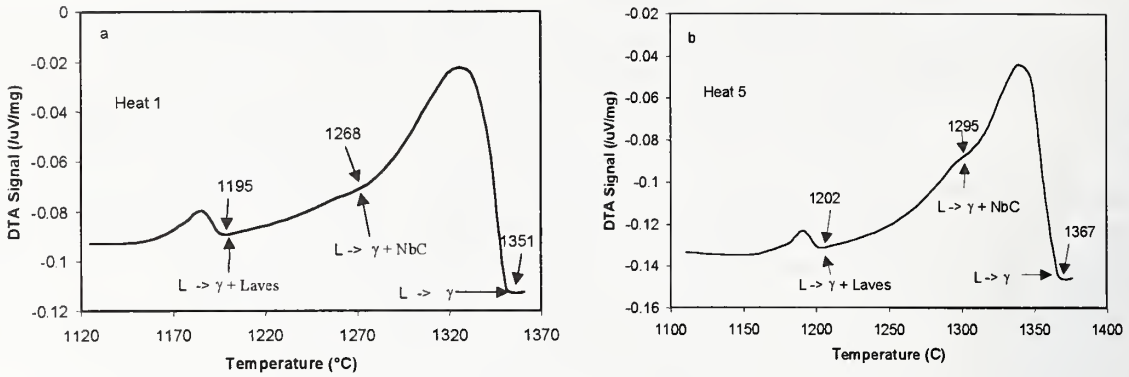

Figure 7. DTA cooling curves for Heat 1 (a) and Heat 5 (b).

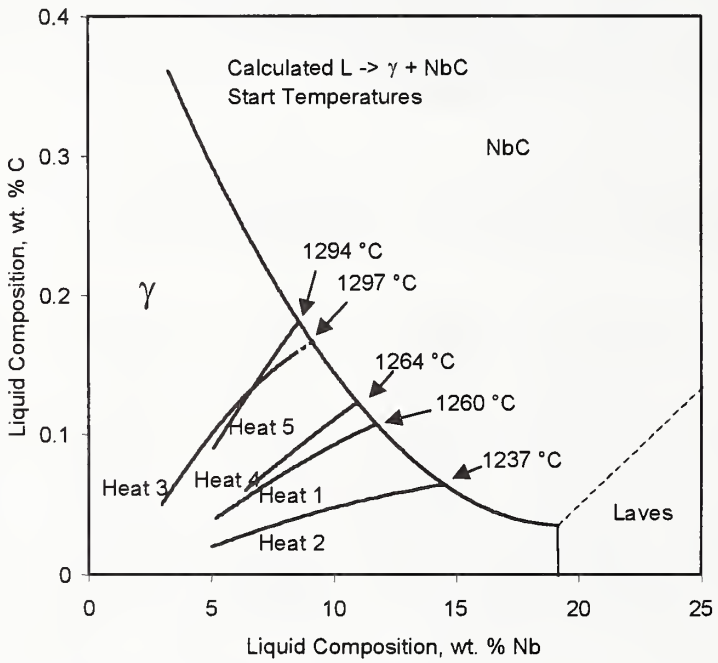

Figure 8. Calculated ternary-like liquidus projection and solidification paths for five different heats of alloy IN 718.

SUMMARY

A preliminary assessment on the applicability of the Thermo-Calc NiFe Superalloy database to solidification problems in complex multi-component alloys has been conducted. To this point, the validation has been conducted by comparing calculated phase diagram quantities to experimental measurements available in the literature. The comparisons indicate the database provides useful estimates of phase equilibrium information that is needed as inputs for solidification models. Work is in progress to extend the validation study to a wider range of alloy compositions and to couple the calculated thermodynamic information to more realistic solute redistribution models.

ACKNOWLEDGEMENTS

This work was performed at Lehigh University under contract to Sandia National Laboratories. Sandia is a multiprogram laboratory operated by Sandia Corporation, a Lockheed Martin Company, for the United States Department of Energy under Contract No. DE-AC04-95AL85000.

REFERENCES

1. T.W. Clyne and G.J. Davies, *Proceedings Solidification and Casting of Metals*, July 18-21, 1977, TMS, 275-278.
2. J.A. Brooks, *Proceedings of Weldability of Materials*, October 8-12, 1990, ASM, 41-48.
3. B. Sundman, B. Jansson, and J.O. Anderson, *CALPHAD*, 1985, **9**, 153-190.
4. N. Saunders, *Superalloys 1996*, R.D. Kissinger *et al.* (eds.), TMS, Warrendale, PA, p. 101.
5. M.J. Cieslak, T.J. Headley, and A.D. Romig, Metallurgical and Materials Transactions, Vol. 17A, 1986, p. 2035.
6. G.A. Knorovsky, M.J. Cieslak, T.J. Headley, A.D. Romig, Jr., and W.F. Hammetter, *Metall. Trans.* A, 1989, Vol. 20A, pp. 2149-2158.
7. M.J. Cieslak, T.J. Headley, T. Kollie, and A.D. Romig, Jr., *Metall. Trans.* A, 1988, Vol. 19A, pp. 2319-2331.
8. J.N. DuPont, C.V. Robino, A.R. Marder, M.R. Notis, and J. R. Michael, *Metallurgical and Material Transactions A,* 1998, Vol. 29A, pp. 2785-2796.
9. J.N. DuPont, C.V. Robino, and A.R. Marder, *Science and Technology of Welding and Joining,* Vol 4, No. 1, pp. 1-14, 1999.
10. H.H. Stadelmaier and M.L. Fiedler, *Z. Metallkd.*, 1975, vol. 66 (4), pp. 224-225.
11. J.N. DuPont, C.V. Robino, and A.R. Marder, *Acta Materialia,* 1998, vol. 46 (13), pp. 4781-4790.
12. R. Mehrabian and M.C. Flemings, *Metallurgical Transactions A*, 1970, Vol. 1, pp. 455-464.
13. E. Scheil, Z. Metallk, 1942, Vol. 34, p. 70.
14. C.D. Lundin, W. Liu, G. Zhou, and C.Y. Qiao, (1998), *Unmixed Zones in Arc Welds: Significance on Corrosion Resistance of High Molybdenum Stainless Steels*, Welding Research Council, Bulletin No. 428, January, WRC, New York, NY.
15. T.W. Clyne and W. Kurz, *Metall. Trans. A*, 1981, Vol. 12A, pp. 965-971.
16. T. J. Lienert, *Conference Proceedings Weldability of Materials.* Edited by R.A. Patterson and K.W. Mahin. October 8-12, 1990, ASM 1990, pp. 159-165.
17. M.J. Cieslak, T.J. Headley, G.A. Knorovsky, A.D. Romig, Jr., and T. Kollie, *Metallurgical Transactions A*, Vol. 21A, February 1990, pp. 479-488.
18. C.V. Robino, J.R. Michael, and M.J. Cieslak, *Science and Technology of Welding and Joining*, Vol. 2, No. 5, pp. 220-230.

Modeling of Multipass Weldments

E. A. Metzbower
US Naval Research Laboratory
Code 6320
Washington DC 20375-5320

Abstract

Computer programs have been developed that present a realistic cross section of a gas metal arc weld. Experimental data derived from bead-on-plate welds at different heat inputs are used to calculate the width, penetration, and weld bead re-enforcement. Typical computer calculated cross sections are shown for a single V weld configuration. A methodology to determine the temperature at any point in the weld after each subsequent pass is developed.

Introduction

This is a preliminary report on a program that has been initiated to model the microstructural development in multipass welds. The impetus for this work lies in a similar effort on laser beam welding. In that effort the hardness, properties, and microstructure of the fusion and heat-affected zones were modeled and calculated with surprisingly good results. By knowing the composition of the steel, the thermal profile resulting from laser beam welding, and the grain size of the base plate, the volume fraction of the microstructures and consequently the hardness and properties of the fusion and heat-affected zones were determined.

Reed and Bhadeshia (1) reported on a computer program that they developed to estimate the cooling conditions that exist in various regions of a multipass weld. Their effort was directed towards the shielded metal arc welding of 21/4Cr1Mo multipass welds which are used to join 1/2CrMoV steam pipes in modern steam-generating power plants. This report utilizes their concepts for gas metal arc welding of naval structures.

Bead-on-Plate Welds

Data on bead-on-plate welds was provided by the David Taylor Naval Research and Development Center (DNSRDC) (2) and is given in Table 1. The data is for five different heat inputs, ranging from 1.6 to 4.9 kJ/mm (40 to 120 kJ/in). This data was used to calculated the weld width, height, depth of penetration, and weld bead area as a function of the heat input. Figure 1 shows the correlation between the weld width and the heat input, E (=Volts * Amps/Welding Speed). Figure 2 shows a similar plot for depth of penetration as a function of E. Expressions were also obtained for weld bead area and weld bead height as a function of E.

Table 1. Experimental Bead-on-Plate Data

Heat Input	Current	Voltage	Welding Speed	Width	Depth	Height	Total Area
KJ/mm	Amps	Volts	mm/s	mm	mm	mm	mm^2
1.6	250	24.8	3.89	14.0	4.4	3.2	55.0
2.8	310	32.0	3.60	19.0	6.3	3.3	72.7
3.1	300	28.5	2.75	19.0	5.9	3.8	87.8
3.9	413	32.0	3.39	23.0	8.0	4.0	115.9
4.9	490	35.0	3.51	25.0	10.0	3.8	138.8

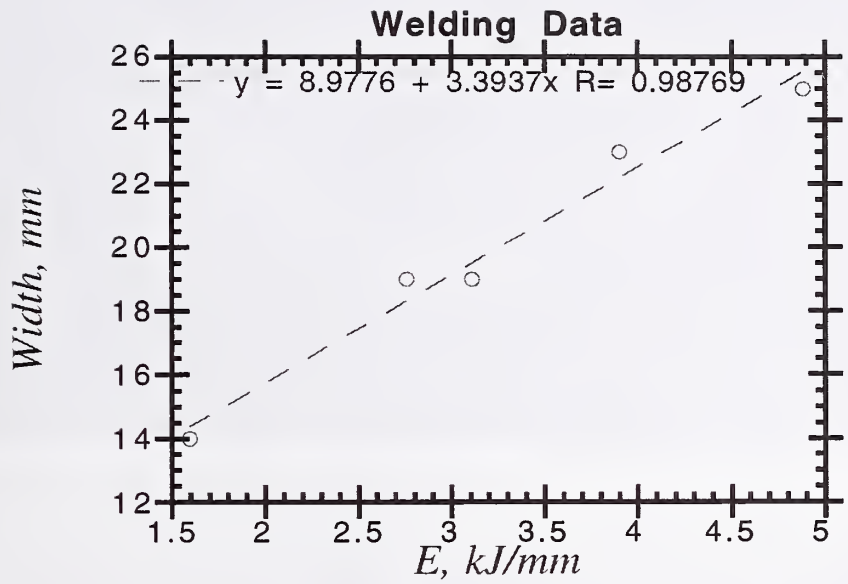

Figure 1 Bead-on-plate width as a function of heat input.

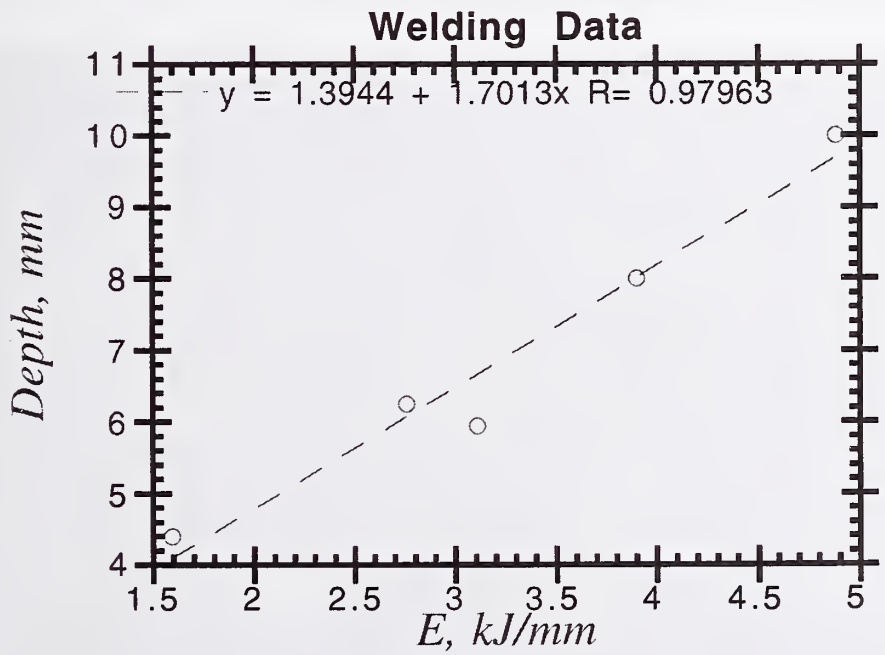

Figure 2 Depth of penetration as a function of heat input.

The bead-on-plate weld consist of a reinforcement above the top of the plate. This reinforcement can be characterized as a spherical cap. Knowing the width of the bead-on-

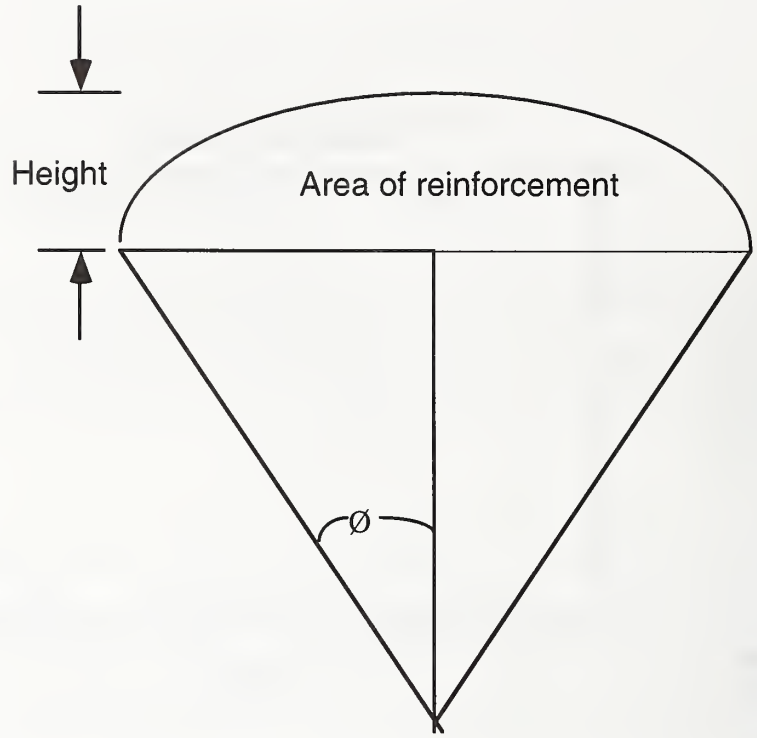

Figure 3. The drawing depicts the geometry of the cross section of the bead-on-plate weld.

plate weld and the area of the fusion zone, the half angle of the spherical cap can be calculated. This geometrical arrangement is shown in Fig. 3.

Rosenthal's (3,4) equations for heat flow around a finite heat source moving at constant speed across the surface of a plate have been modified by several authors (5,6). One such modification by Ashby and Easterling (5) modifies the time by including the additional time require for the source to transverse a given point and modifies the height by replacing the real source by an apparent source above the plate. These modifications result in the following equations for heat flow

$$T - To = \frac{q/v}{2\pi\lambda\left[t(t+t_o)\right]^{\frac{1}{2}}} \exp\left\{-\frac{1}{4a}\left(\frac{(z+z_o)^2}{t} + \frac{y^2}{(t+t_o)}\right)\right\}$$

$$z_o^2 = \left[\frac{r_b}{e}\left(\frac{\pi a r_b}{v}\right)^{\frac{1}{2}}\right]$$

$$t_o = \frac{r_b^2}{4a}$$

Where T is the temperature, t is the time, λ is the thermal conductivity, a is thermal diffusivity, q is the watts (current * amps), v is the welding speed, and r_b is the radius of the source.

By solving these equations with the appropriate thermodynamic values, a bead-on-plate profile can be constructed at any heat input. Figure 4 depicts a bead-on-plate weld calculated at 1.6 kJ/mm. The various degrees of shading represent the temperatures that are

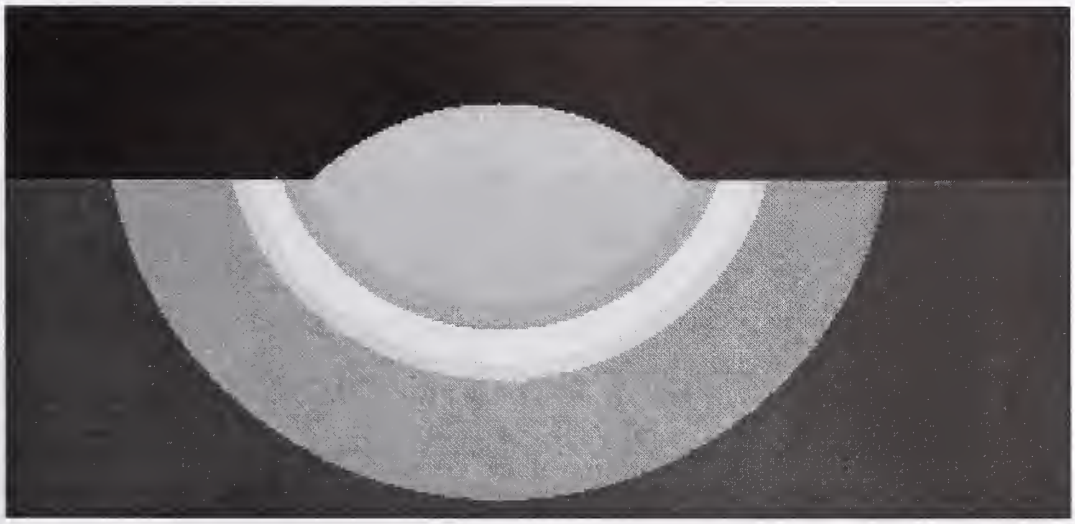

Figure 4. Bead-on-plate weld computed at 1.6 kJ/mm.

obtained in these regions. These temperatures range from above the melting point of the steel down to about 850 °C below which no transformations are expected. The program performs an iterative calculation on the heat input (essentially modifying the efficient of the process) so that good agreement is reached between the depth and width of the weld as calculated from the modified Rosenthal equation and the depth and width of the

Fig.4. Single V weld after one pass.

experimental bead-on-plate welds fabricated at various heat inputs. The program presently allows only a few weld geometries to be calculated: bead-on-plate, single V, and double V. The angle of the V is input for the program.

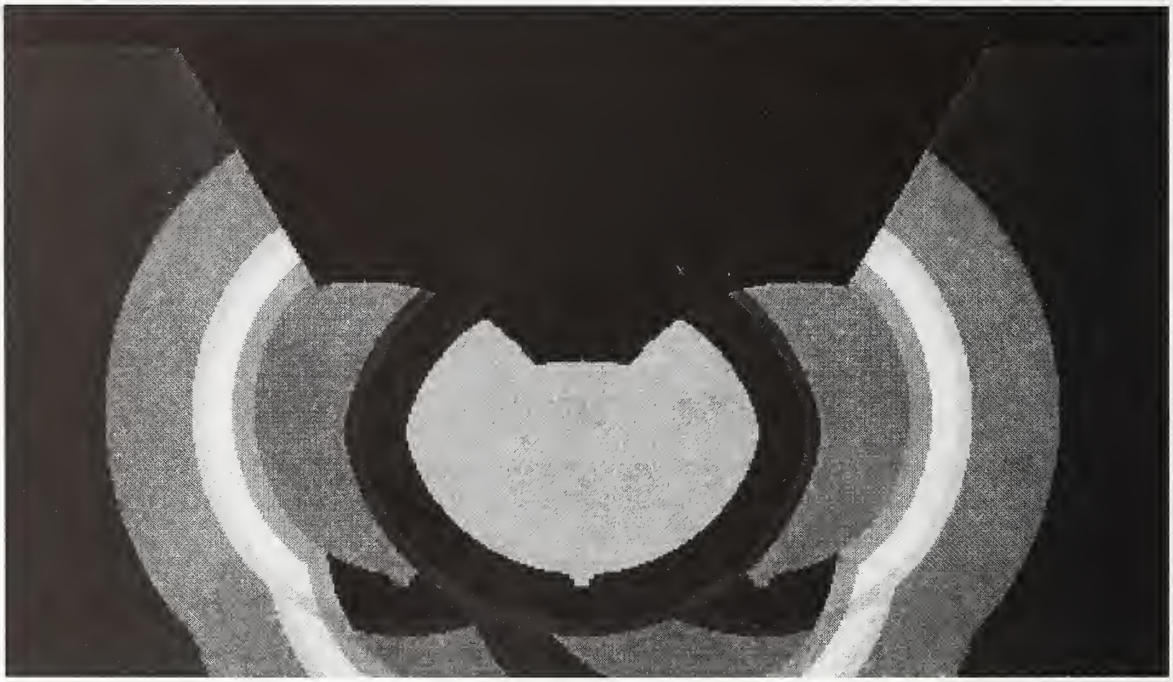

Fig. 5. Single V weld after ten passes.

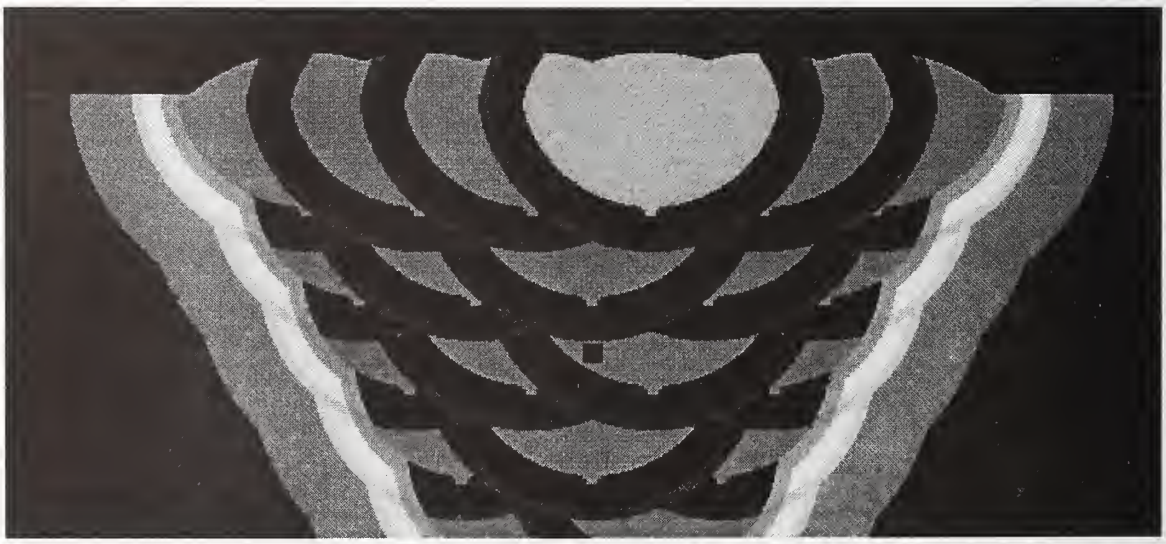

Fig. 6 Single V pass after completion (21 passes).

In calculating a multipass weld, a significant variable is the amount of overlap between adjacent passes. If this input value is incorrect, the resulting cross section will have holes in

A cknowldegemntit. Thus the program has been run with an array of overlaps until the cross section is dense and the number of passes is appropriate. If the overlap is too great, the cross section appears distorted. The geometry of the addition of each pass is critical in filling the single V. The geometrical factors have been explained by Reed and Bhadeshia (1). An example of a single V weld with a heat input of 40 kJ/mm is shown in Fig. 5 after a single pass, in Fig. 6 after 10 passes, and in Fig. 7 after completion (21 passes). Each of these passes contains a finger penetration, which would occur at these voltages, but is artificially added to the calculation. Again the variations in color or shading are an indication of the temperature regimes last experienced in the calculation. The small square in the middle represents the point in the weld where the complete thermal history is known from the program. Figure 8 shows the thermal profile obtained from the program at different peak temperatures. The program can calculate the peak temperature experienced

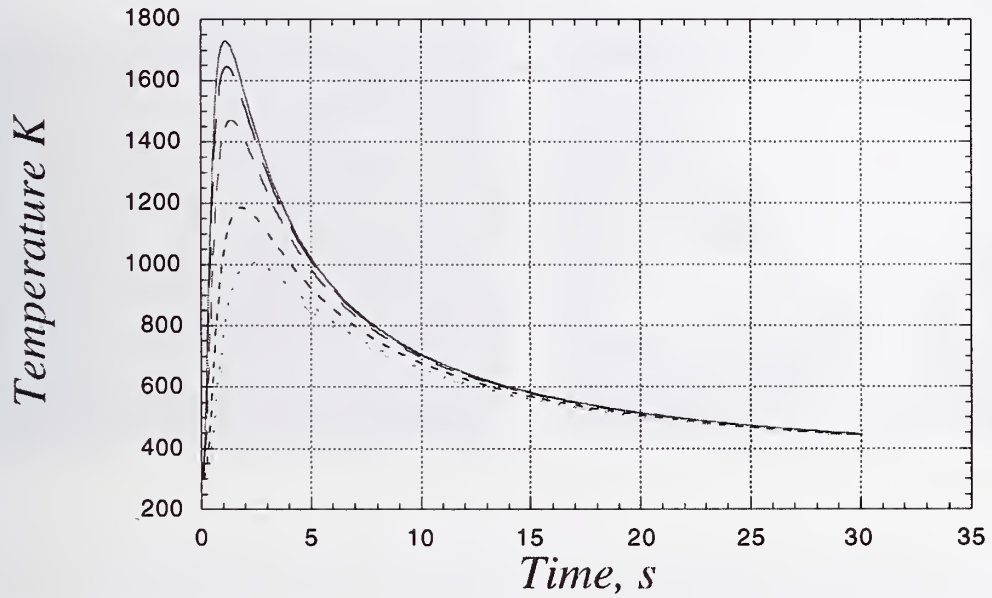

Fig. 8 Thermal profiles based on different peak temperatures.

by any point in the weld. The succession of peak temperatures gives an approximation of the tempering that occurs by subsequent passes. Depending on the location of the point of interest, a subsequent pass may completely austenitize the point.

Future Work

A series of welds of A36, HSAL65 , and HSLA100 have been fabricated at three different heat inputs of 1.0, 1.6, and 2.0 kJ/mm (25, 40, and 50 kJ/in) under the direction of R. Wong at the Naval Surface Warfare Center, Carderock Division. These gas metal arc welds are approximately twenty four inches long, have a single V, 60° configuration and were made such that each subsequent pass was indexed (7) about two inches from the prior pass. In this manner the microstructural evolution of each pass will be examined. Macro and microstructural evaluation of these welds has begun. Hardness maps will be constructed. Tempering will be studied using a dilatometer.

Acknowledgement

This work was supported by the Office of Naval Research.

References

1. R. C. Reed and H. K. D. H. Bhadeshia, *Acta metall. mater.* **42**, 3663 (1994)
2. G. L. Franke, David Taylor Research and Development Center, private communication
3. D. Rosenthal, *Weld. J. Res. Suppl.* **20**, 220s (1941)
4. 4. D. Rosenthal, *Trans. ASME* **68**, 849 (1946)
5. M. F. Ashby and K. E. Easterling, *Acta metall.* **32**, 1935 (1984).
6. J. C. Ion, K. E. Easterling, and M. F. Ashby, *Acta metall.* **32** 1949 (1984)
7. R. Wong, Naval Surface Warfare Center, Carderock Division, private communication

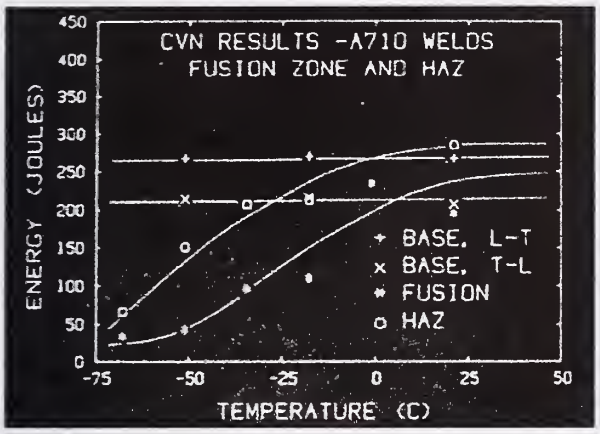

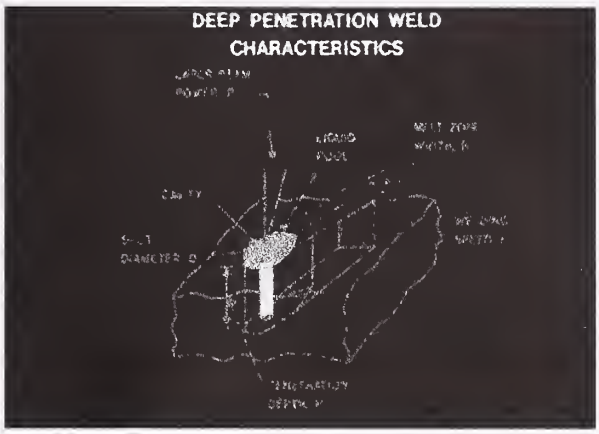

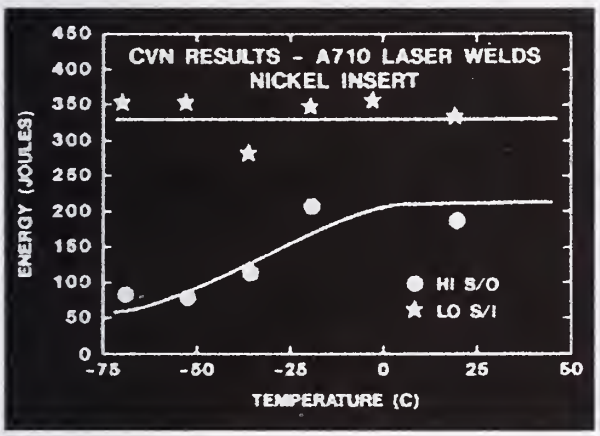

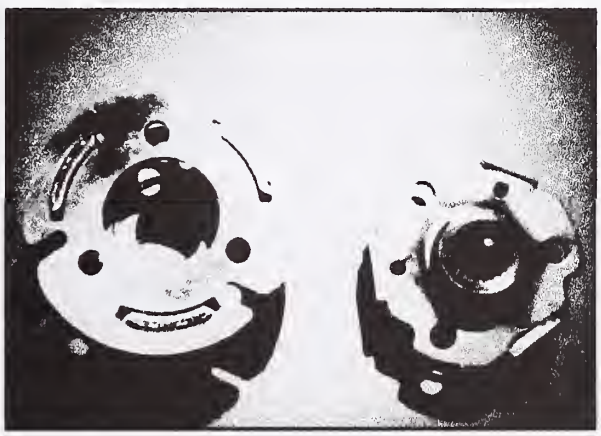

COMPLEX PRECISION HIGH VOLUME ASSEMBLY

requires high speed welding with low heat input
service of the component requires a tough weld
high cooling rate causes a hard and brittle weld
the assembly cannot be bulk heated

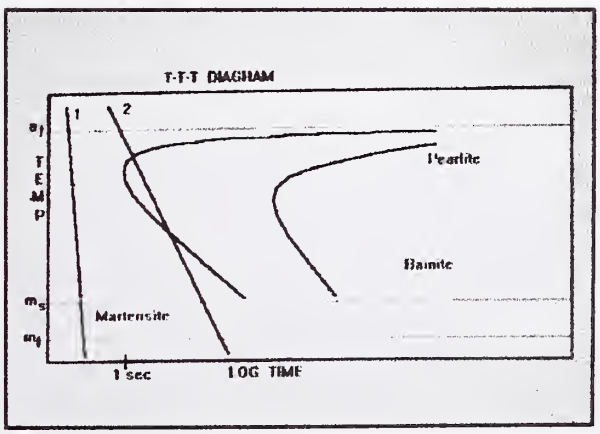

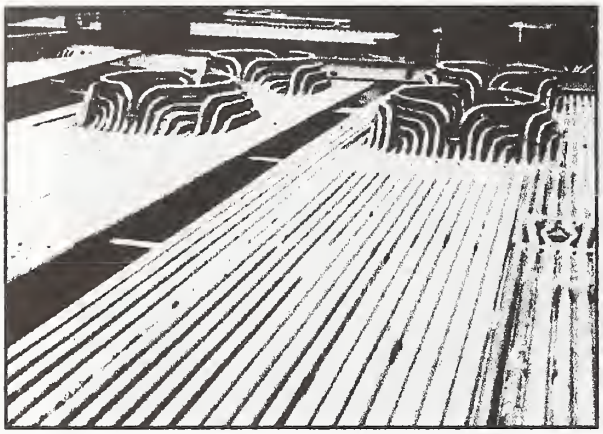

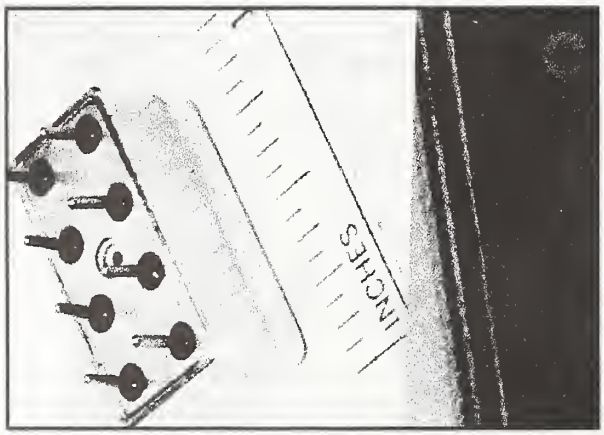
INCHES

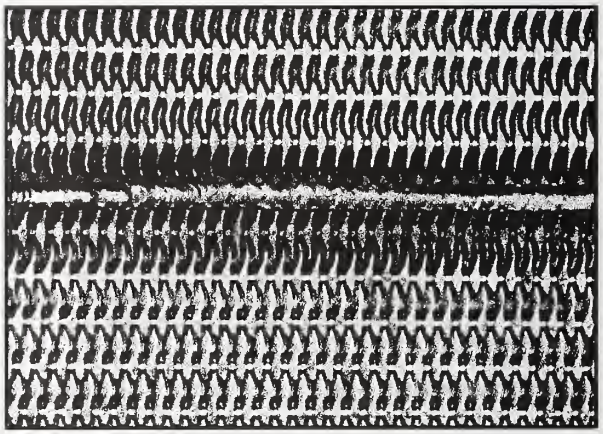

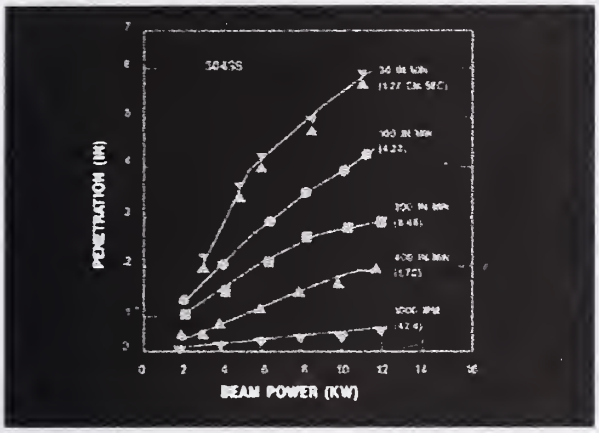

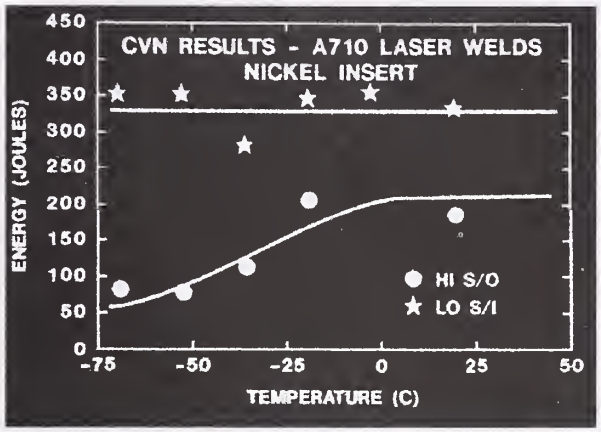

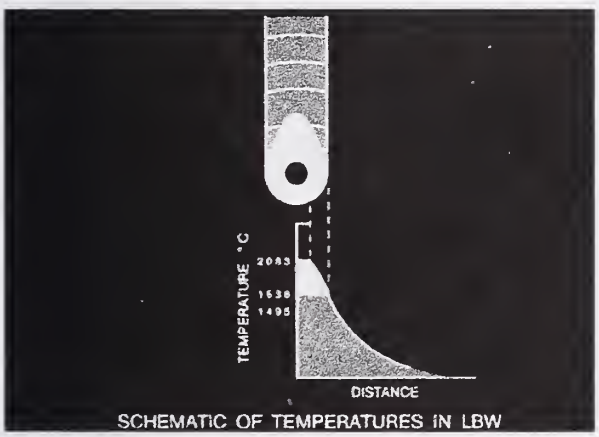

SCHEMATIC OF TEMPERATURES IN LBW

CONCLUSION

The potential cost savings of heavy-section laser welding is significant. The technology appears to be at hand. It is now our challenge to solve the complementary problems to expedite implementation.

LASER BEAM WELDING OF STRUCTURAL ALLOYS

- GOOD PENETRATION
- FAST WELDING SPEEDS
- DEMANDS AUTOMATION
- GOOD MECHANICAL PROPERTIES

- Chemistries of steel affects weld properties
- Reduction of S increases toughness
- Addition of Ni increases low temperature fracture toughness
- Lower strength steels easier to weld
- Distortion is minimal in LBW
- Low C, low S alloys have best mechanical properties
- Can calculate hardness of fusion and heat-affected zones

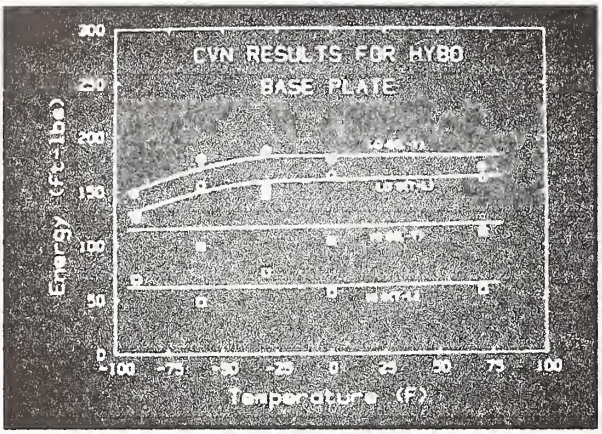

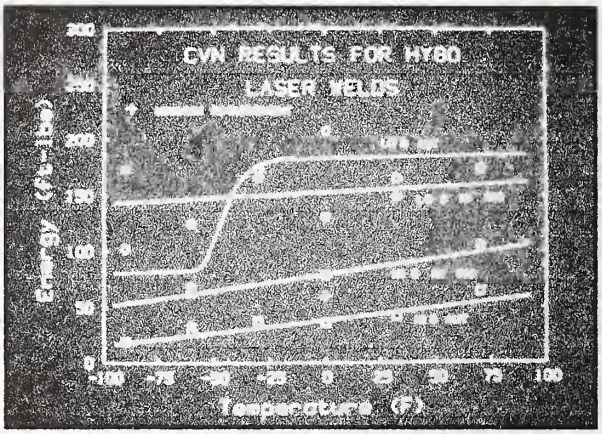

LASER BEAM WELDING PROCESS PARAMETERS

MATERIAL	THICKNESS mm (in.)	POWER kW	SPEED mm/sec (ipm)	HEAT INPUT kJ/mm (kJ/in.)
A-36	6 (.25)	6	21 (50)	.29 (7.3)
	9 (.38)	10	17 (40)	.53 (14.9)
	12 (.50)	13	14 (33)	.93 (23.6)
	15 (.63)	13	6 (15)	2.17 (55.0)
HY-80	6 (.25)	8	26 (60)	.32 (8.1)
	12 (.5)	11	13 (30)	.85 (21.5)
HY-100	6 (.25)	8	23 (55)	.35 (8.8)
HY-130	6 (.25)	8	21 (50)	.38 (9.7)
	12 (.5)	13	13 (30)	1.0 (25.4)
	12 (.5)	10	13 (30)	.77 (19.5)

LASER BEAM WELDING MECHANICAL PROPERTIES

MATERIAL	THICKNESS mm (in.)	YIELD STRENGTH Mpa (ksi)	ULTIMATE STRENGTH Mpa (ksi)	ELONGATION/ HARDNESS % R_C
A-36	6 (.25)	276 (40)	442 (64)	23
	9 (.38)	269 (39)	428 (62)	22 ~10
	12 (.5)	276 (40)	448 (65)	24
	15 (.63)	269 (39)	435 (63)	25
HY-80	6 (.25)	621 (90)	745 (108)	25 42
	12 (.5)	627 (91)	752 (109)	24 43
HY-100	6 (.25)	697 (101)	759 (110)	20 41
HY-130	6 (.25)	966 (140)	1022 (148)	19 40
	12 (.5)	952 (138)	987 (143)	19 40

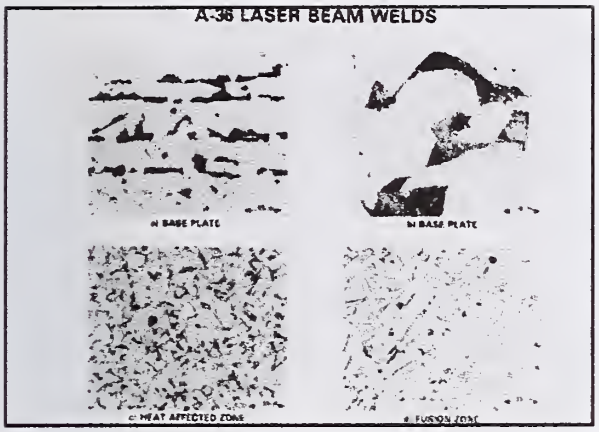

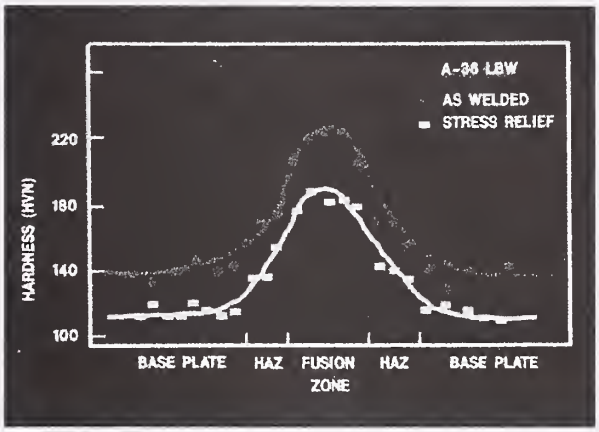

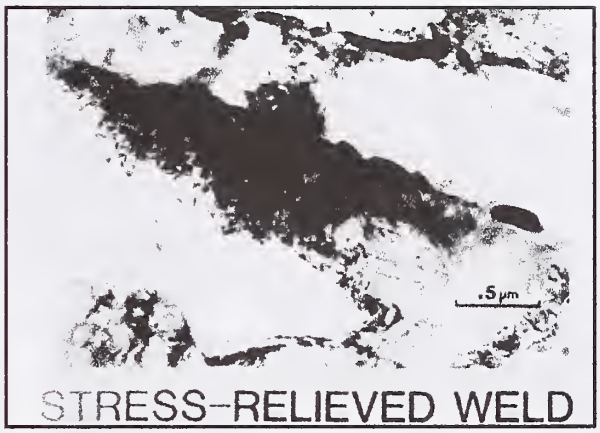

HSLA STEELS

ASTM A633, GRADE E	C/Mn, V, N
ASTM A737, GRADE B	C/Mn, Nb
ASTM A710, GRADE A	LOW C, Cu/Ni PRECIPATION HARDENING

MECHANICAL PROPERTIES ASTM A710

	σ YS ksi (MPa)	σ ULT ksi (MPa)	ELONG %	RA %
BASE PLATE L	89 (613)	98 (675)	29	77
BASE PLATE T	92 (634)	100 (689)	27	67
AUTOGENOUS	73 (503)	91 (627)	19	49
INCONEL	86 (592)	91 (627)	24	70
Ti FOIL	88 (606)	101 (696)	24	65

NRL

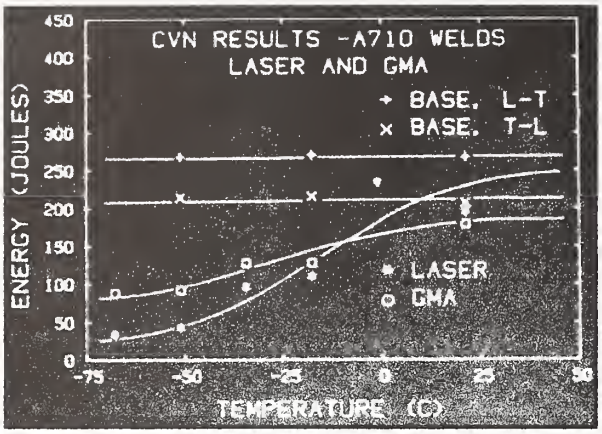
CVN RESULTS -A710 WELDS
LASER AND GMA
+ BASE, L-T
× BASE, T-L
* LASER
o GMA
ENERGY (JOULES)
TEMPERATURE (C)

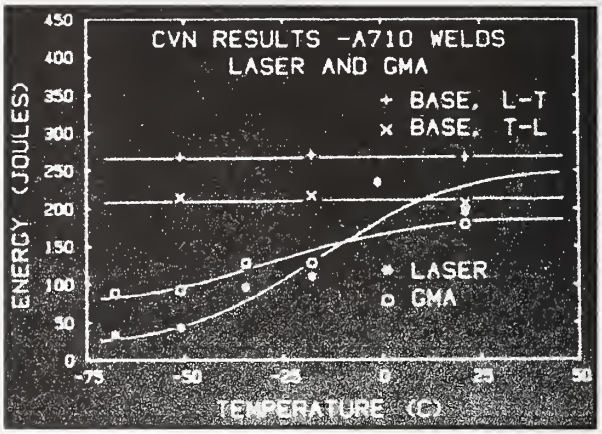
CVN RESULTS -A710 WELDS
LASER AND GMA
+ BASE, L-T
× BASE, T-L
* LASER
o GMA
ENERGY (JOULES)
TEMPERATURE (C)

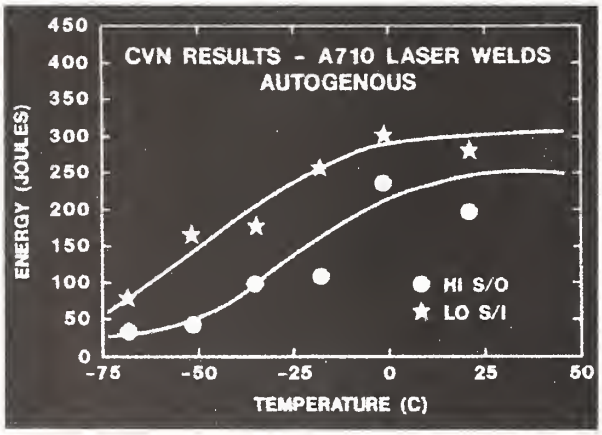
CVN RESULTS - A710 LASER WELDS
AUTOGENOUS
● HI S/O
★ LO S/I
ENERGY (JOULES)
TEMPERATURE (C)

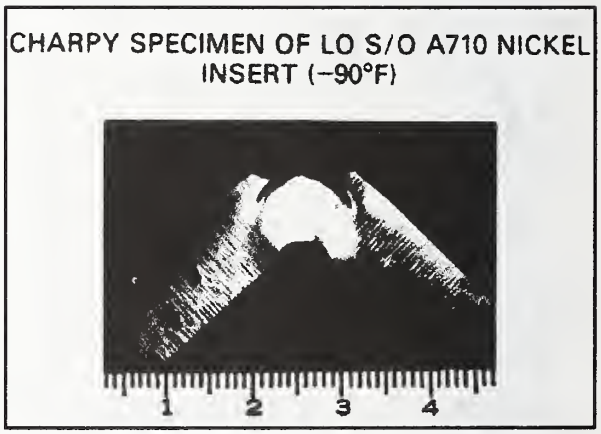
CHARPY SPECIMEN OF LO S/O A710 NICKEL
INSERT (-90°F)

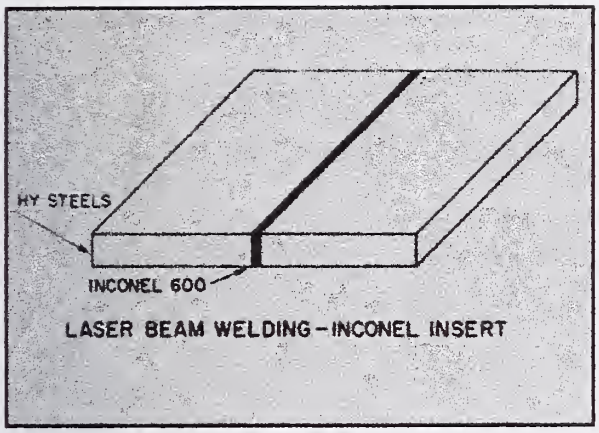
HY STEELS
INCONEL 600
LASER BEAM WELDING – INCONEL INSERT

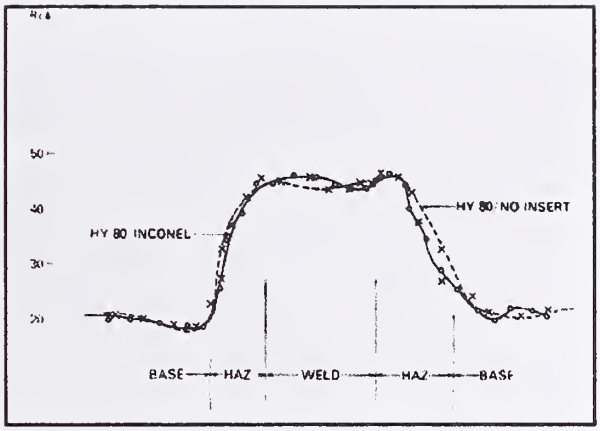
HY 80 INCONEL
HY 80 NO INSERT
BASE
HAZ
WELD
HAZ
BASE

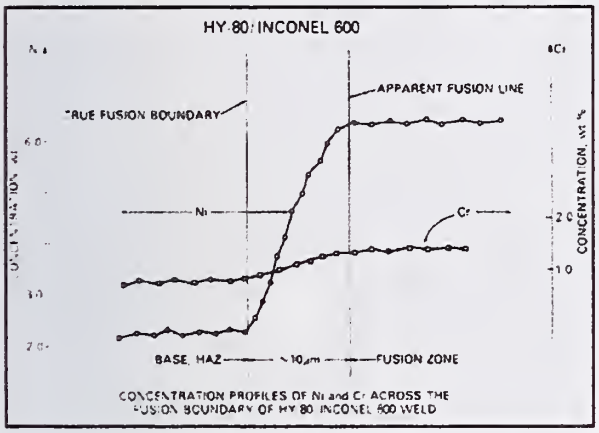
HY-80/INCONEL 600
APPARENT FUSION LINE
TRUE FUSION BOUNDARY
Ni
Cr
CONCENTRATION, wt %
BASE, HAZ
~10 μm
FUSION ZONE
CONCENTRATION PROFILES OF Ni and Cr ACROSS THE FUSION BOUNDARY OF HY 80 INCONEL 600 WELD

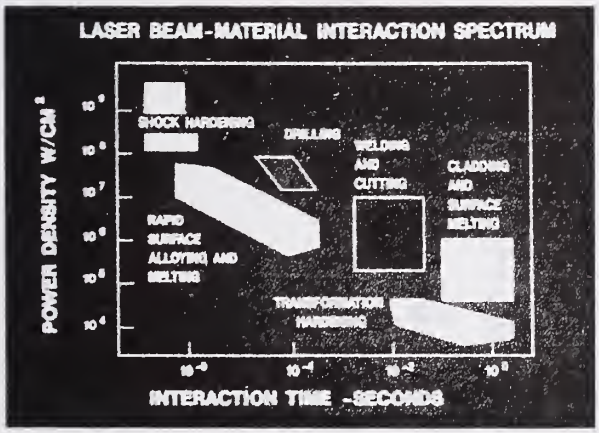
LASER BEAM-MATERIAL INTERACTION SPECTRUM
POWER DENSITY W/CM²
SHOCK HARDENING
DRILLING
WELDING AND CUTTING
CLADDING AND SURFACE MELTING
RAPID SURFACE ALLOYING AND MELTING
TRANSFORMATION HARDENING
INTERACTION TIME - SECONDS

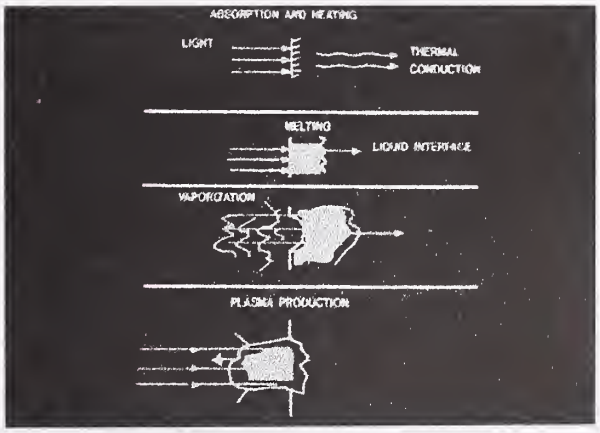
ABSORPTION AND HEATING
LIGHT
THERMAL CONDUCTION
MELTING
LIQUID INTERFACE
VAPORIZATION
PLASMA PRODUCTION

LASER WELDING SPEED

	POWER	THICKNESS	SPEED
Al ALLOYS:	8 kW	½ INCH	70 IPM
HSLA STEELS:	12 kW	½ INCH	40 IPM
O&T STEELS:	14 kW	¾ INCH	25 IPM
LOW CARBON STEELS:	5 kW	SHEET (0.035")	200 IPM
TI ALLOYS:	12 kW	½ INCH	35 IPM
HY-80:	77 kW	2 INCHES	50 IPM
GRADE B SHIP STEEL:	12 kW	1 INCH	30 IPM

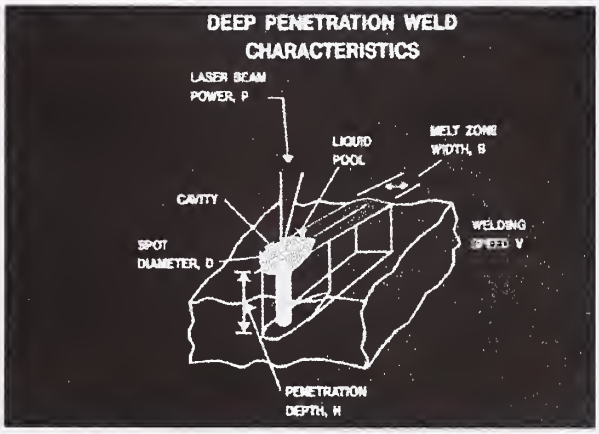

ADVANTAGES OF LASER WELDING

- ULTRA FAST WELDING SPEEDS
- GOOD PENETRATION
- SIMPLE GEOMETRY
- LOW DISTORTION
- GOOD MECHANICAL PROPERTIES
- EXCEPTIONAL FRACTURE RESISTANCE
- DEMANDS AUTOMATION

LASER WELDING SPEED

	POWER	THICKNESS	SPEED
Al ALLOYS:	8 kW	½ INCH	70 IPM
HSLA STEELS:	12 kW	½ INCH	40 IPM
Q&T STEELS:	14 kW	¾ INCH	25 IPM
LOW CARBON STEELS:	5 kW	SHEET (0.035")	200 IPM
TI ALLOYS:	12 kW	½ INCH	35 IPM
HY-80:	77 kW	2 INCHES	50 IPM
GRADE B SHIP STEEL:	12 kW	1 INCH	30 IPM

LASER BEAM WELDS
A633

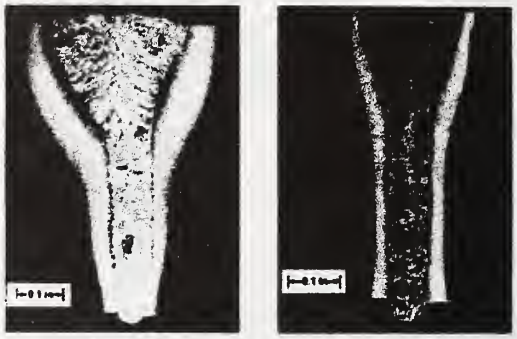

11.5kW, 28 ipm 18kW, 47 ipm

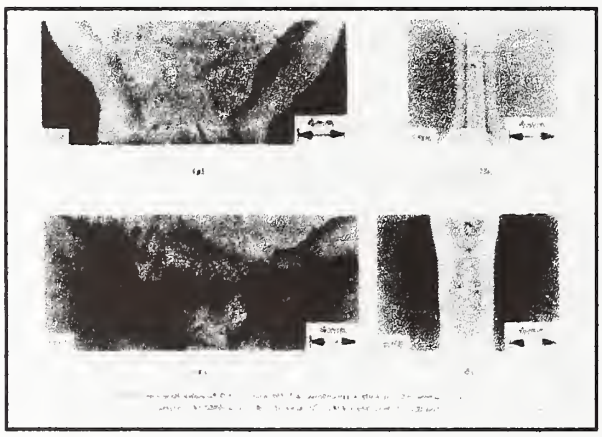

LASER BEAM WELDMENTS of A-36 STRUCTURAL STEEL

MECHANICAL PROPERTIES

σ_{ys} = 37 ksi
σ_{ult} = 65 ksi
elong = 24 %

BEND SPECIMEN

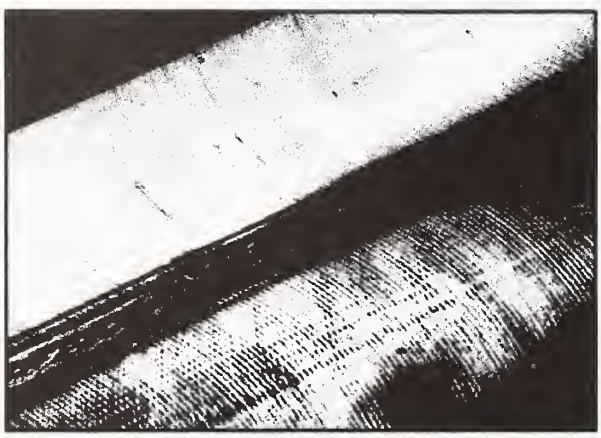

LASER WELDING

MATERIAL SELECTION FOR LASER WELDING

SAMPLE PREPARATION
A) JOINT DESIGN
B) FIT UP TOLERANCE
C) CLEANING OF WORKPIECES

MAJOR LASER PROCESS PARAMETERS
A) POWER AND TRAVEL SPEED
B) WELD PROTECTION GAS
C) FOCUSING OPTICS
D) FOCAL POINT POSITION

POST-WELD INSPECTION
A) DESTRUCTIVE TESTING
B) NON-DESTRUCTIVE TESTING

LASER WELDING

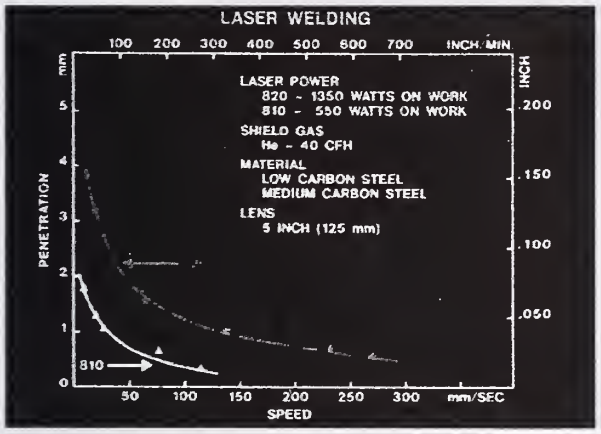

LASER WELDING OF MATERIALS
COMMON STEELS

MATERIAL	SUITABILITY	POSSIBLE PROBLEMS	COMMENTS
LOW CARBON (RIMMED) STEEL	LOW	1. POROSITY 2. BRITTLENESS 3. UNPREDICTABILITY	POOR RESULTS DUE TO INCLUSIONS, DEGASING
LOW CARBON (ALUMINUM KILLED) STEEL	EXCELLENT		LESS THAN 0.3% CARBON CONTENT
MEDIUM/ HIGH CARBON AND ALLOY STEEL	EXCELLENT	1. STRESS CRACKING, CONTROLLABLE BY PRE- AND/OR POST-HEATING	PRE-HEAT TEMP. DEPENDENT ON THICKNESS/PENETRATION RULE OF THUMB: 0.3% < ECC* < 0.6%: 200-500 °C 0.6% < ECC: 400-800 °C
DISSIMILAR STEELS	EXCELLENT	1. STRESS CRACKING, CONTROLLABLE BY PRE- AND/OR POST-HEATING	DEPENDENT ON ECC OF ALLOY IN WELD ZONE AS DETERMINED BY DILUTION ANALYSIS.

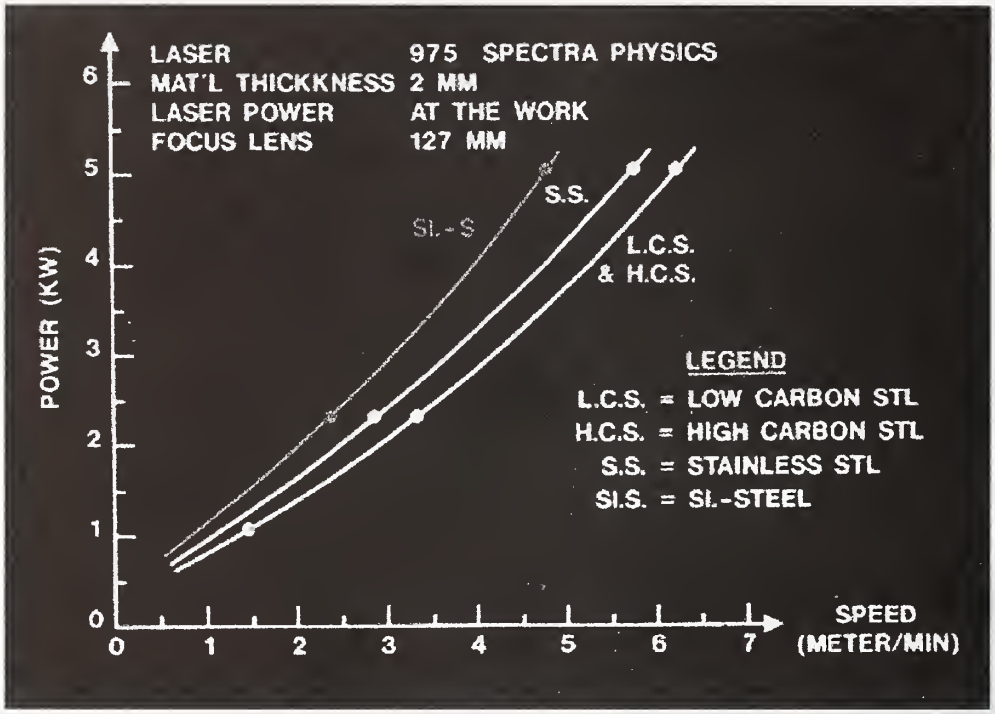

OPTIMIZATION OF LASER WELDING

- POWER DENSITY
- TRAVEL SPEED
- GAS SHIELDING
- PLASMA CONTROL
- WELDMENT PROPERTIES
- FUSION METALLURGY

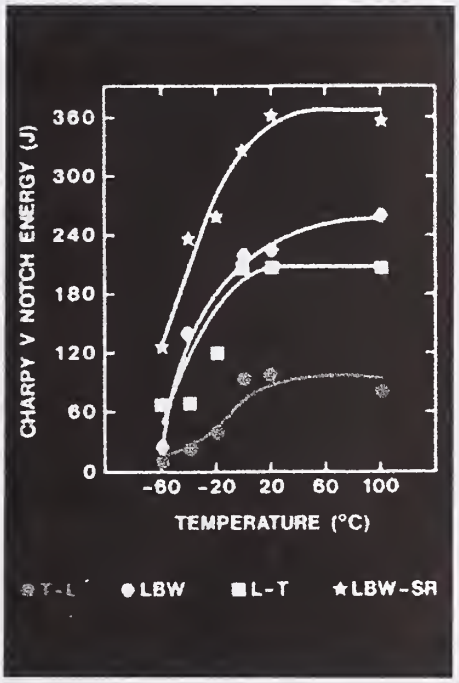
CHARPY V NOTCH ENERGY (J)
360
300
240
180
120
60
0
-60 -20 20 60 100
TEMPERATURE (°C)
T-L
LBW
L-T
LBW-SR

COMPUTER MODELING OF METALLURICAL TECHNOLOGIES

M. Zinigrad[*], V. Mazurovsky[**]

ABSTRACT

The principles of the mathematical modeling of metallurgical welding processes are considered. The essence of the proposed method is the application of fundamental equations of physical chemistry to the analysis of the complex chemical processes that take place between the metallic, oxide, and gaseous phases in weld zone and shape the final composition of the weld metal. The method is used to develop a mathematical model of a flux-core arc welding process. The model permits prediction of the composition of the weld metal (the direct problem) as a function of the composition of the starting materials, i.e., the metal strip, the base metal, and the flux powder components, and as a function of the technological parameters of the process. The solution of the inverse problem, in which the input parameters are the technological characteristics and the composition of the strip, the base metal, and the weld metal, and the output parameter, i.e., the parameter sought, is the ratio between the core materials in the wire, is also possible. In this case, a computer program based on the model yields a new formula for a flux-cored wire over the course of a few minutes.

KEY WORDS

Mathematical modeling, welding and surfacing, flux-cored wire, composition optimization.

INTRODUCTION

The complexity of welding processes stems form the simultaneous occurrence of a large number of physical and chemical processes involving liquid, solid, and gaseous phases. The special features of these processes include a high temperature, intense stirring of the phases, nonstationary mass transport, and thermal fluxes. The course of a process is determined by a large number of parameters, which often depend on one another.

The methods of mathematical modeling are being employed with increasing frequency for just such complex systems (Refs. 1-14). The use of mathematical methods reduces the duration, tediousness, and cost of an investigation. Moreover, computer experiments often provide a result, which is extremely difficult or totally impossible to obtain by empirical means on a real object.

A model is essentially a simplified system, which reflects isolated, but the most significant aspects of the real object. The more parameters the model takes into account, the more universal and faithful to that object it is.

[*] The College of Judea and Samaria, Ariel, Israel
[**] Chisumim Ltd., Ariel, Israel

Modeling involves a search for a mathematical dependence between the input and output parameters of the system being studied. Either industrial welding processes (Refs. 1, 5, 6, 8, 9, and 11), the formation of the weld metal and its properties (Refs. 4, 7, 10, and 12), or the physiochemical and metallurgical processes shaping the composition (Refs. 2, 3, 13, and 14-17) are modeled

ESSENCE OF THE PROPOSED APPROACH

The possibility of predicting the composition of a product is important for any technological process, since it permits prediction of the outcome of a technology already in the planning stage. The solution of this problem takes on special importance for welding technologies because of the high speed of the process, the high temperatures, and the short lifetime of the liquid pool. The principal chemical reactions shaping the final composition of the weld metal take place on the boundary between the metallic and oxide liquid phases, as well as in their interactions with the gas. The interaction between the phases during welding usually represents a large set of parallel and conjugate reactions, whose rates are interrelated. The main problem arising in calculations of the dependence of the composition of phases on time is associated with the difficulty in determining the rates of these reactions. If these rates can be determined, the concentration of any element in a volume of a particular phase can be found using the simple relation

$$V_{E_i} = \pm \frac{dC_{E_i}}{d\tau} \cdot \frac{V}{A}, \tag{1}$$

where V is the volume of the phase in which the element E_i is located, A is the surface area of the interface, C_{E_i} is the concentration of the particular element, and V_{E_i} is the rate of its passage from one phase to another.

The plus and minus signs show the direction of passage of the element: the minus sign corresponds to a decrease in concentration, and the plus sign corresponds to an increase.

If we confine ourselves to small time intervals ($\Delta\tau$), during which the rates can be considered constant, Eq. (1) can be simplified:

$$V_{E_i} \approx \pm \frac{\Delta C_{E_i}}{\Delta \tau} \cdot \frac{V}{A}, \tag{2}$$

This equation permits finding the value of ΔC_{E_i} and, consequently, the concentration C_{E_i} at any moment in time.

Thus, the problem of predicting the composition reduces to selecting a simple and reliable method for calculating the rates of passage of all elements through an interface.

Let us utilize our previously developed method (Ref. 18) for finding these rates. The essential idea of the method is that the entire set of chemical reactions taking place on an interface is described by the equations of chemical reactions with a single common reactant. For metal materials based on iron, we choose iron oxide FeO as such a reactant and write the equation of the reaction in the form:

$$\frac{n}{m}[E_i]+(FeO)\rightarrow\frac{1}{m}(E_{i_n}O_m)+Fe, \qquad (3)$$

where $[E_i]$ is any element in the metallic phase, $(E_{i_n}O_m)$ is its oxide in the oxide phase, and n and m are stoichiometric coefficients.

The method, which was described in detail in Ref. 18, permits determination of the rates of passage of elements through an interface V_{E_i}. It consequently makes it possible to calculate the variation of the concentration of each element $[E_i]$ in the metallic phase and the concentration of the corresponding oxide $(E_{i_n}O_m)$ in the slag phase.

The advantage of such an approach lies in the fact that the calculation results do not depend on which specific reactions among all the possible ones are considered. It is sufficient that they be algebraically independent, include all the necessary components, and contain one common reactant. This is associated with the essence of the method itself, which permits determination of the fluxes of reactants toward and away from the phase boundary, rather than the rates proper.

MATHEMATICAL MODEL OF A FLUX-CORED WELDING PROCESS

This paper discusses the results of the development of a quantitative mathematical model of a flux-core welding (surfacing) process.

Let us consider the sources shaping the composition of the weld metal for the technology chosen. The scheme of the technological process is presented in Fig. 1.

It is expedient to consider the shaping of the composition in two stages of the process: the drop stage and the pool stage.

The final composition of the drop is determined by the concentrations in each of the powdered components in the wire $[E_i]^l_{pd}$ and, accordingly, by the melting rates of these components V^l_{pd}, the concentration of each element the metal cladding $[E_i]_b$ and its melting rate V_b, as well as by the rates of passage of the elements through the interface V_{E_i} of the drop (3) and the slag film (4) on its surface, which can be calculated in accordance with the methods described above. The values of V^l_{pd} and V_b are found from empirical relations as functions of the technological parameters of the process.

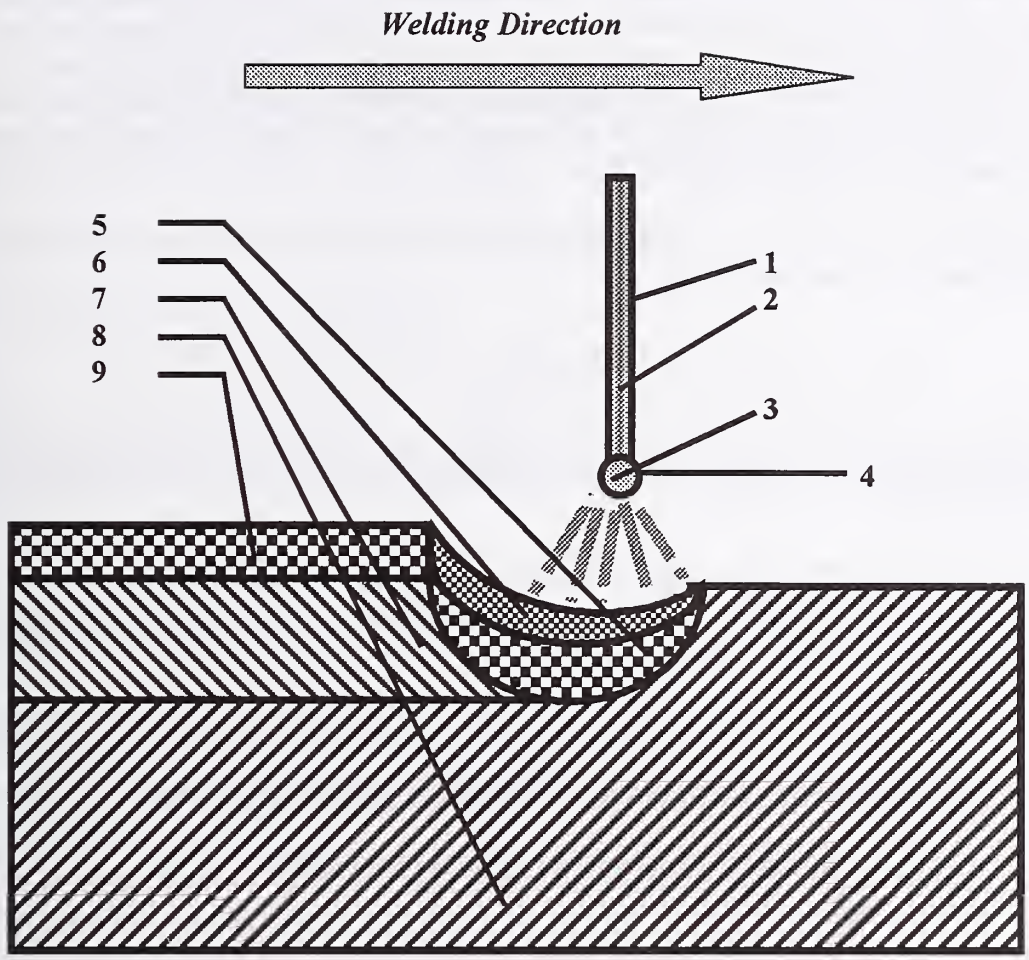

Figure 1. The technological scheme of welding process.
1 – metal tube; 2 – flux (powder mixture); 3 – drop of liquid metal; 4 – slag film; 5 – metal pool; 6 – molten slag pool; 7 – weld metal; 8 – base metal; 9 – slag crust (layer of solid slag)

Thus, the concentration of the *i*-th element in the drop at any moment in time τ $[E_i]_d^\tau$, can be calculated from the equation

$$[E_i]_d^\tau = \frac{V_b \cdot [E_i]_b \cdot \Delta\tau + \sum_{l=1}^{L} V_{pd}^l [E_i]_{pd}^l \Delta\tau + V_{E_i} \cdot M_{E_i} \cdot A_d \cdot \Delta\tau \cdot 100}{m_d^\tau}, \qquad (4)$$

where A_d is the surface area of the liquid drop, l labels the type of powder, L is the number of types, M_{E_i} is the molecular weight of the element, and m_d^τ is the mass of the metal drop at the time τ.

The final drop composition thus calculated $[E_i]_d$ is used to calculate the concentration of the i-th element in the weld pool at any time τ. The composition of the pool and therefore the composition of the weld metal are determined by the concentrations of the elements in the liquid drop $[E_i]_d$ and accordingly by the rate of descent of the drops into the liquid pool V_d, the concentration of each element in the base metal $[E_i]_{bm}$, the melting rate of the base metal, and, as in the case of the drop stage, by the rate of passage of each element through the interface between the metal (5) and slag (6) pools.

In accordance with the foregoing, the expression for calculating the concentration of element i in the weld metal can be written in the form

$$[E_i]^\tau = \frac{V_d \cdot [E_i]_d \cdot \Delta\tau + V_{bm} \cdot [E_i]_{bm} \cdot \Delta\tau + V_{E_i} \cdot M_{E_i} \cdot A_p \cdot \Delta\tau \cdot 100}{m_p^\tau}, \qquad (5)$$

where A_p is the area of the interface between the metal and the slag, and m_p is the mass of the weld pool at the time τ.

The system of equations (4) and (5), together with the expressions for calculating V_{E_i} taken from Ref. 18, comprise a mathematical model, which describes the interaction between the phases in an industrial flux-core welding (surfacing) process.

USING THE MATHIMATICAL MODEL TO DEVELOP NEW FLUX-CORED WIRE COMPOSITIONS

A computer program for PC computers has been written in Microsoft EXCEL and Visual Basic for Windows using the model developed.

This program can be used to determine the composition of a flux-cored wire that ensures the formation of a weld metal with an assigned chemical composition. In this case, the output parameter is the new formula of the flux-cored wire. The input parameters are the chemical compositions of the starting materials, the physicochemical characteristics of the interacting phases and processes taking place between them, and the technological parameters.

Let us analyze the stages of operation of the program in the case of the development of a new formula for a self-shielded flux-cored wire.

We assume that our task is to develop a new electrode for obtaining a welding joint with an assigned composition and required properties. The chemical composition of the base metal, which is needed for the calculation, is stored in the database together with the composition of other standard materials.

At the first step we enter the technological parameters in accordance with the welding procedure selected.

We must ensure that the weld metal has a definite composition. We enter the chemical composition of the weld metal that must be obtained.

Element	C	Si	Mn	Cr	V	Ti	Al	Fe
Concentration, wt. %	0.1	0.15	1.2	0.1	0.012	0.40	0.8	B

Table 1. Required weld metal composition

The next and most important step is optimization of the flux composition. The required weld composition can clearly be obtained with different combinations of components in the flux. The database contains the chemical compositions of various components, which should be utilized in selecting the optimal flux composition.

The program has to establish the flux composition that provides the required weld metal composition and to select the most inexpensive variant among them. The weldability should be optimized as well.

The program also includes a special module, which provides an evaluation and optimization of the mechanical properties of the weld metal having the composition obtained.

This obviously requires a large number of iterations to perform calculations with all possible component ratios.

In particular, four flux compositions were found for the case under consideration, and one of them was specified as flux, which provides the required joint composition with the lowest production costs. The results of the calculation (both the optimal composition and the other three compositions) are stored in the database of the program. The program presents the optimal flux composition. Such a flux provides the solution of the problem posed, i.e., the required joint composition. This composition agrees well with the one we assigned when we posed the problem.

Element	C	Si	Mn	Cr	V	Ti	Al	Fe
Concentration, wt. %	0.09	0.18	1.12	0.09	0.016	0.42	0.71	B

Table 2. Predicted weld metal composition

It would be naive to think that we can get a new electrode just from PC. What we do is narrowing the area of search an extent that by conducting only a few welding experiments we will be able to get the desired composition.

This advantage acquires special importance in the case when we deal with components that have never been used in the welding materials production. In such a case even the most highly skilled and experienced technologist can not know what the influence of this or that component will be.

In the case at hand the approximate time for the calculations and optimization was 15 to 20 min. Very short series of welding experiments was carried out to adjust the composition to the real technological conditions. The result is a new formula for an electrode that provides an assigned joint composition and is 40% less costly than the existing formulas owing to the employment of alternative materials and optimization of the composition.

The flux-cored electrode with a new flux was produced. Welding was carried out. The actual weld metal composition (obtained using a spectroscopic method) is presented in Table 3.

Element	C	Si	Mn	Cr	V	Ti	Al	Fe
Concentration, wt. %	0.08	0.18	1.32	0.11	0.013	0.38	0.62	B

Table 3. Experimental weld metal composition

INDUSTRIAL APPLICATION

In 1997, we founded a new R&D company, Chisumim Ltd., to implement the development techniques described above.

Chisumim specializes in utilizing our unique scientific methods for formulating the optimal composition of welding materials and optimizing welding and hard-facing technologies.

Chisumim is developing new materials for hard-facing machine parts in various industries.

Another of Chisumim's projects (which is being financed by GM-UMI Technology R&D, a joint venture of General Motors and Universal Motors Israel) is the development of a tailor-made flux-cored welding wire intended for improving the course and efficiency of welding processes in GM.

REFERENCES

1. Ducharme R., Kapadia P., Dowden J., Williams K, Steen W. 1994. An integrated mathematical model for the welding of thick sheets of metal with a continuous CO_2 laser. *Laser Inst. Am.* 77: 97-s to 105-s.
2. Boronenkov V., Salamatov A., Zhadkevich M. 1991. A mathematical model of the physico-chemical processes in electron beam remelting. Proc. –All-Union conference,

Novokuznetsk: 21-22.

3. Schwerdtfeger K., Werner W., Pateisky G., Modeling of chemical reactions occurring during electroslag remelting. *Iron and Steel* 3: 135-s to 143-s.

4. Davydov Yu., Boronenkov V., Salamatov A. 1992. Prediction of the weld formation of variable composition based on modeling of metallurgical processes. *Autom. Svarka* 7-8: 23-s to 26-s.

5. Norrish J., Gray D. 1992 Computer simulation and off-line programming in integrated welding systems. *Weld. Met. Fabr.* 60, 3: 119-s to 122-s.

6. Kozlovsky S. 1990. Modeling of the interaction of parts in the contact area in spot welding. *Isv.VUZ. Mashinostr.*9: 89-s to 94-s.

7. Grigorenko V., Kiselev O., Chernyshov G. 1994. Mathematical model and its practical evaluation for weld formation. *Svar. Proizvod.* 2: 30-s to 32-s.

8. Tsybulkin G. 1994. Mathematical models in adaptive control of arc welding. *Autom. Svarka.* 1: 24-s to 27-s.

9. Cerjak H., Easterling K. E. 1993. Mathematical modeling of weld phenomena. 369 London

10. Vitek J., Zacharia T., David S., Rappaz M., Boather H. 1994. Modeling of single-crystal laser-weld microstructures. Proc. Laser mater process symp. TMS, USA: 213-220.

11. Dowden J., Ducharme R., Kapadia P., Clucas A. 1994. A mathematical model for the penetration depth in welding with continuous CO_2 lasers. Laser Inst. Am. 79, 451-460.

12. Grong O., Kluken A.O. 1992. Microstructure and properties of steel weld metals, Key Eng.Mater: 47-93.

13. Mitra U., Eagar T.W. 1991. Slag-metal reactions during welding. *Metall.Trans. (B),* vol.22, No 1: 65-100.

14. Olson D. L., Lui S., Edwards G. R. 1993. Physical metallurgical concerns in the modeling of weld metal transformations. Math. Modell. Weld. Phenom.: 89-108.

15. Zinigrad M., Zalomov N., Mazurovsky V., Aksyutin O. 1997. Creating new welding materials on the basis of metallurgical processes modeling. Proc. 7th int. conf. on computer technology in welding. USA,. ed. T. Siewert: 291-297. NIST spec. publ.923.

16. Zinigrad M., Mazurovsky V. 1996. Modeling of metallurgical welding processes for the purpose of creating new welding materials. Proc. International conf. on modeling and simulation in metallurgical eng. and materials science, Beijing, China. eds. Yu zonsen, Xiao Zeqiang, Xie Xishan: 669-673. Metallurgical Industry Press.

17. Zinigrad M., Mazurovsky V., Zalomov N., Aksyutin O. 1998. Computer approach to the development of welding materials. Proc. 8th International conf. Computer Technology in Welding. pp.S20-1 - S20-9, Cambrige University, TWI.

18. Boronenkov V., Shanchurov S., Zinigrad M. 1979. Kinetics of the interaction of multicomponent metal with slag under diffusion conditions. Izvestiya Ac. Nauk USSR. Metal, 6, 21-27.

Session A5: General Modeling

THE EFFECT OF WELD METAL ON THE GEOMETRY RELATIONS IN C(T) AND SE(B) FRACTURE SPECIMENS

J.R. Donoso* and F. Labbé†

ABSTRACT

The geometry relations in C(T) and SE(B) fracture specimens with weld metal in the ligament are analyzed. For this purpose, ASTM A 588 Grade A steel fracture specimens welded with AWS E8018-G electrodes were modeled by a two-dimensional non-linear finite element code, considering different deformation behavior for the base metal (BM) and the weld metal (WM). A degree of overmatching of 1.4 between weld metal and base metal, various volume fractions of WM, and no dilution effects were also considered in the model. The geometry characteristics analyzed are: the relation between crack-mouth opening displacement (cmod) and load-line displacement; the value of η_{pl} needed for the evaluation of J; and the position of the apparent center of rotation in the ligament, related to the evaluation of CTOD. The numerical results obtained for the modeled specimens were compared to experimental load *vs.* load-line displacement results obtained on blunt-notched, small ligament size ($0.30 \leq b/W \leq 0.50$) weld metal fracture specimens. In addition, a comparison was done with theoretical values of η_{pl} for BM specimens obtained from the Common Format Equation parameters of Donoso and Landes. The effects of crack length and volume fraction of WM on the geometry relations are analyzed and discussed in terms of the constraint imposed by the overmatched weld metal.

KEYWORDS

Elastic-Plastic fracture; fracture toughness; finite element modeling

INTRODUCTION

The application of ductile fracture mechanics to the evaluation of fracture toughness in materials rests primarily upon two widely used approaches: J and CTOD. Both parameters have been extensively used, and become the subject of standards; e.g. ASTM standards E 813 and E 1290 [Refs.1, 2]. Both standards are explicitly intended to be used with homogeneous materials; however, weldments may be included in their scope of application. On the other hand, BS Standard 5762 [Ref. 3] has been followed up with a proposal for the assessment of defects in fusion welded joints [Ref. 4] based on the CTOD approach. Apparently, the evaluation of toughness of welds by using CTOD seems to be more reliable than taking the overall specimen deformation behavior, as does the evaluation of J [Ref. 5].

*** Materials Science Department, Universidad Técnica Federico Santa María, Valparaíso, CHILE**

† Mechanical Engineering Department. Universidad Técnica Federico Santa María, Valparaíso, CHILE.

The latter argument places J in disadvantage in relation with CTOD measurements, when evaluating the properties of a weld. The material property variations in welded joints (base metal, BM; weld metal, WM, and heat affected zone, HAZ) are overcome by making all measurements in the "mouth" of the crack (cmod), thus representing local behavior in the vicinity of the crack. In the case of J evaluations of a transversely loaded weld, measurements of load-line displacement are made that may be affected by the difference in mechanical properties of the various components of the joint (BM, WM and HAZ), much in the sense of a rule-of-mixtures result for the displacement. Such a problem is, obviously, not present in a specimen made of a single (homogeneous) material. Let us recall that The J_{Ic} standard [Ref. 1] requires its evaluation as the sum of an elastic and a plastic contribution:

$$J = J_{el} + J_{pl} \tag{1}$$

where the elastic part is calculated as

$$J_{el} = \frac{K^2}{E}\left(1 - \nu^2\right) \tag{2}$$

for plane strain conditions, and J_{pl} is of the form

$$J_{pl} = \frac{\eta_{pl}}{Bb}\int P dv_{pl} \tag{3}$$

in which b is the uncracked ligament, B is the specimen thickness, η_{pl} is a factor, and the integral term represents the area under the load vs. plastic displacement record.

Recently, Donoso and Landes [Ref. 6] showed that J may be written in one single term as

$$J = \frac{\eta}{Bb}\int P d v_t \tag{4}$$

where v_t is total displacement (elastic + plastic), $\eta_{pl} = \eta_{el} = \eta$, and the area under the curve is the total area. In Eq. 3, the plastic eta factor, η_{pl}, may be computed as [Ref. 7]:

$$\eta_{pl} = \left(\frac{b}{W}\right)\frac{G'}{G} = d\log G / d\log(b/W) \tag{5}$$

where G is the calibration function of the geometry of the specimen employed for the J evaluation. From the Common Format Equation (CFE) analysis of Donoso and Landes [Ref. 8] it may be shown that η_{pl} is equal to the exponent m of the equation for G:

$$G = C\, B\, W\, (b/W)^m \tag{6}$$

In Eq. (6), B and W are the specimen thickness and width, respectively, and C and m are the coefficient and exponent characteristic of the geometry of the specimen. Values of C and m are available for planar fracture testing specimens: C(T), SE(B), SENT, DENT, and M(T) [Ref. 8].

In this context, the accurate description of the behavior of a weld metal fracture test specimen, in terms of both load line displacement, and η_{pl}, should be of great significance for the evaluation of J, as a measure of fracture toughness in welds. On the other hand, the evaluation of the plastic

component of the CTOD relies heavily on geometric models of rigid rotation about an apparent hinge, or center of rotation on the ligament, whose position may depend on load level as well as on the aforementioned variables. The expression employed in the present work is:

$$\delta_{pl} = \frac{r_p(W - a)}{r_p(W - a) + a + z} v_p \qquad (7)$$

where δ_{pl} is the plastic component of CTOD; v_p is the plastic component of the crack mouth opening displacement, cmod; W and a are specimen width and crack length, respectively, and r_p is the plastic rotation factor, defined as 0.44 for SE(B), and between 0.46 and 0.47 for C(T) in the range $0.45 \leq a/W \leq 0.55$ [Ref. 2]. For the case of the numerical evaluations reported here, the parameter z of Eq. (7) has been taken as 0 for SE(B) and 0.25W for C(T). Looking at equation (7), the same arguments discussed above concerning the effects of the physical and geometrical variables on the values of J, can be applied to the evaluation of cmod, and to the determination of the position of the apparent center of rotation in the weld metal fracture specimen. As may be seen in Eq. (7), both parameters, cmod and r_p are needed for the evaluation of CTOD.

The purpose of this work is to assess the effect of the proportion of weld metal in the volume of the test specimen and the crack length, on the following geometric characteristics of weld metal C(T) and SE(B) specimens: the relation between cmod and load-line displacement; the value of η_{pl}, and the position of the apparent center of rotation on the uncracked ligament. A non-linear finite element code was employed in order to solve the various situations modeled, and experimental normalized load *vs.* normalized plastic displacement data was used as a reference for the numerical results obtained, as will be explained presently.

THE FINITE ELEMENT MODELS

A non-linear finite element code was employed in order to model the behavior of the weld metal C(T) and SE(B) fracture test specimens. For this purpose, a 2-dimensional finite element mesh consisting of one-half of the standard C(T) specimen, and one-half of the SE(B) specimen, was constructed. To simulate the welded joint, the mesh was made up of two different sections: one, where the crack is located, has weld metal mechanical properties, whereas the rest of the specimen has base metal properties. In this model no dilution effects were considered, i.e., the properties vary abruptly at the straight WM-BM interface. The fundamental mechanical properties used as inputs for the finite element calculations were the BM yield stress, taken as 400 MPa, and the tangent modulus E_t, taken as being the same for WM and BM, with a value of 2100 MPa (E/100). These values were obtained from tensile tests conducted on ASTM A-588 steel, and its welded joint fabricated with an AWS 8018-G type filler metal. The latter confers the all-weld metal a yield strength of about 480 MPa minimum; experimental values observed for the yield strength of the weld was around 550 MPa. Therefore, the value of overmatching is 1.4, this value being the ratio between 560 MPa and 400 MPa.

On the average, the models employed for the C(T) and SE(B) specimens have of the order of 850 to 1100 4-side elements, with a total of about 925 to 1150 nodes. The elements located around the tip of the crack, about two-thirds of the total, were diminishing in size, down to 0.01 by 0.005

mm. the smallest. The tip of the crack was given a radius of curvature of 0.03 mm. The scheme employed considered von Mises yield criterion, bilinear behavior (i.e., the hardening was considered to be linear beyond limit load), and total Lagrangian formulation. All finite element computations were made under plane strain conditions, for the selected crack lengths employed.

The output generated was load vs. load line displacement; load vs. cmod; displacements of the nodes along the crack, and hoop stresses normal to the ligament. The parameters used to analyze the results were: the ratio of WM to total volume of the specimen, R, and the ligament size, b/W. For the ratio R of WM to specimen volume, values of 1/4, 1/3, and 1/2 were employed, being chosen as representative of most practical cases of manual metal arc weld joints. Finally, in relation to the uncracked ligament, numerical calculations were made for b/W values of 0.5, 0.4, and 0.3. These values represent normalized crack lengths a/W of 0.5, 0.6, and 0.7, respectively, which correspond to what is normally termed "deep cracks".

Figure 1 shows a schematic of both the C(T) specimen and part of the SE(B) specimen. Dimensions are proportional to the standard 1T, with 25 mm thickness (1″), as per ASTM [Ref. 1]. Therefore, W = 50 mm for both geometry. Crack length, a, and ligament size, b, are also shown in this schematic. In Figure 1, p denotes the WM portion of the specimen, whereas q denotes the whole of the specimen. Therefore, the volume ratio has been defined as R = p/q.

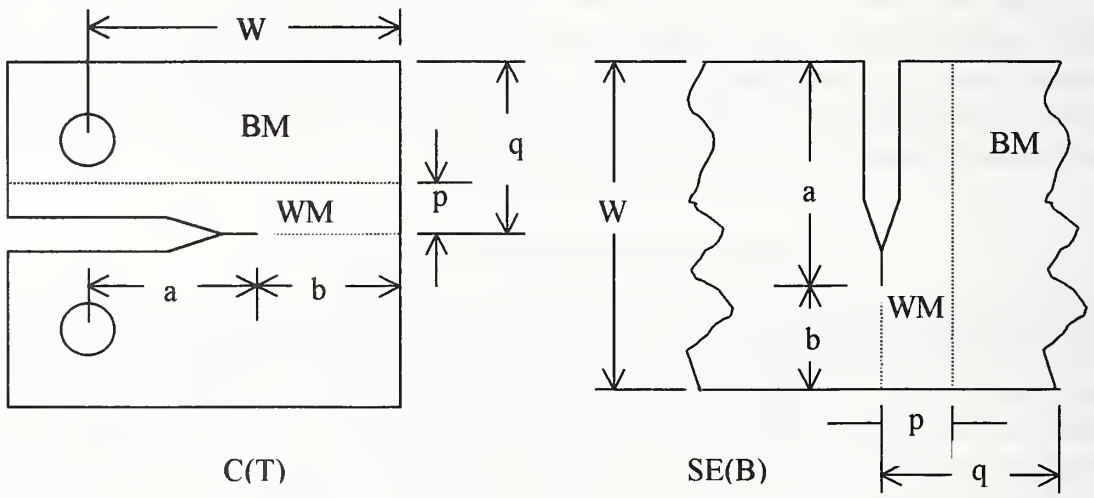

Figure 1. Schematic of the C(T) and part of the SE(B) specimens.

Figure 2, on the other hand, shows the portion of interest of the finite element model for both specimens, with the detail at the crack tip. As pointed out above, the radius of curvature at the crack tip is of the order of 0.03 mm. Elements surrounding the center of curvature are of the order of 0.01 by 0.005 mm.

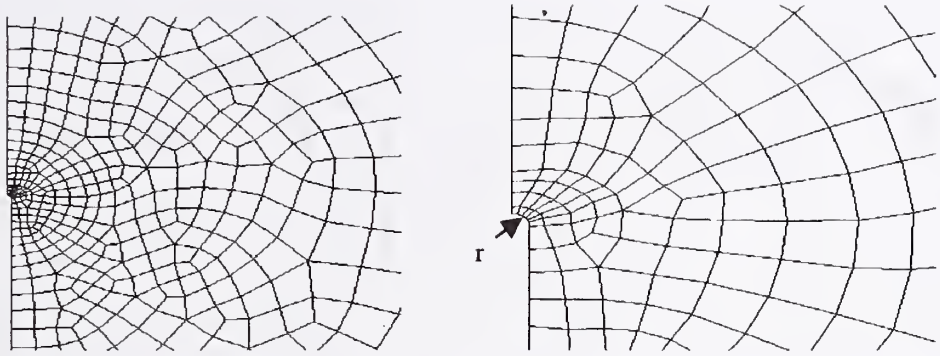

Figure 2. Details of the mesh surrounding the crack tip; r is radius at the tip.

RESULTS AND DISCUSSION

Figure 3 shows plots of normalized load *vs.* normalized plastic component of the load-line displacement for C(T) specimens with b/W = 0.5 (a) and 0.3 (b), respectively. Figure 4 shows similar data for SE(B) specimens. Normalized load is computed from the CFE form for the load:

$$P = \{\Omega^*\}\ \{B\ W\ C\ (b/W)^m\}\ \{\sigma^*\ (v_N)^{1/n}\} \tag{8}$$

from which normalized load, P_N, is:

$$P_N = P/G = (\Omega^*)\{\sigma^*\ (v_N)^{1/n}\} \tag{9}$$

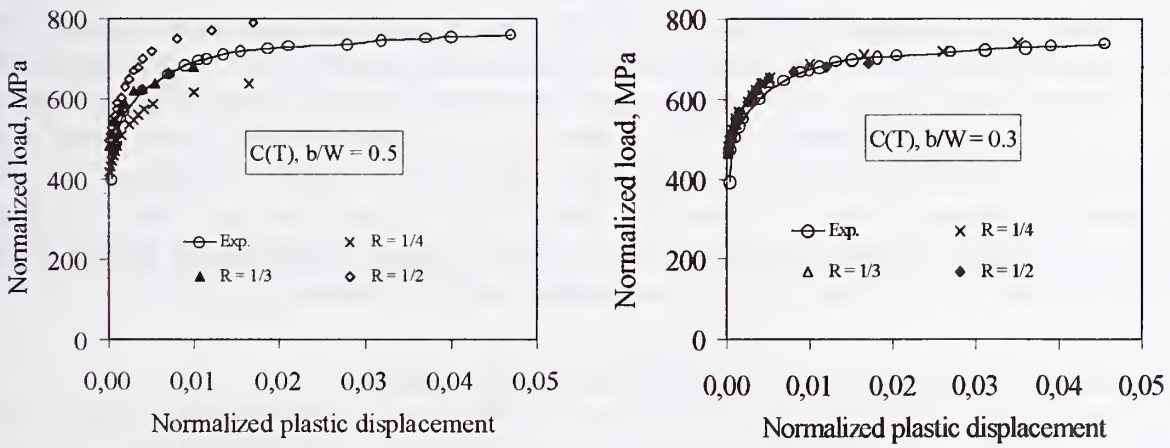

(a) (b)

Figure 3. Normalized load *vs.* normalized plastic displacement, C(T) specimens.

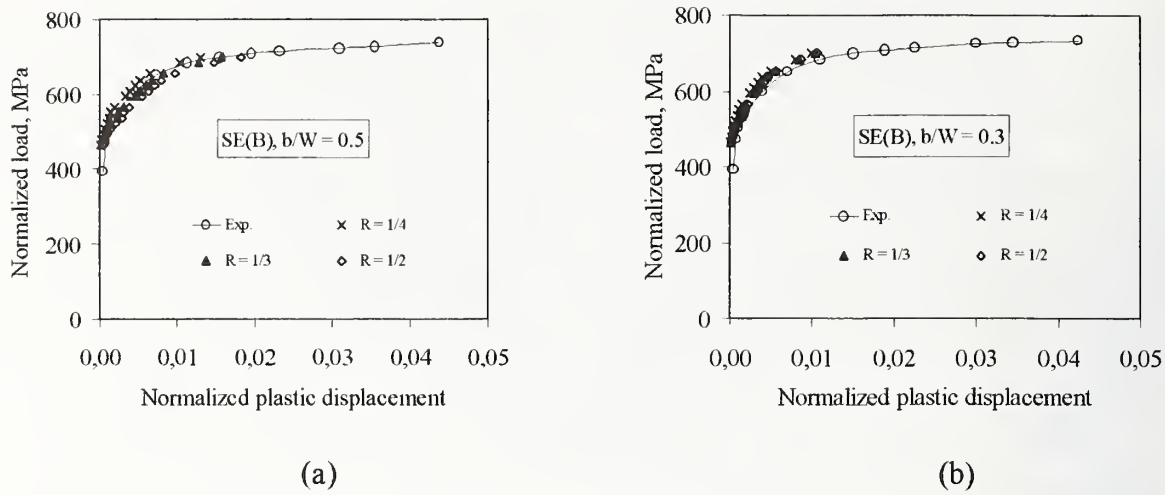

Figure 4. Normalized load *vs.* normalized plastic displacement, SE(B) specimens.

For both geometry, normalized displacement is the plastic component of the load line divided by W. In all four figures there is one experimental curve included for comparison. The main feature of these plots is that whereas the SE(B) data normalize onto one single curve regardless of the ligament size and WM volume fraction, the C(T) data show a distinct difference [Ref. 9]. In fact, for b/W = 0.30 (deeply cracked specimen), all numerical curves are coincident. For b/W = 0.50, however, R plays a dominant role on the behavior. The meaning of this is straightforward: a J computation with a C(T) specimen, for which the load-line displacement is required, may become dependent on the amount of weld metal present in the specimen. The same would not occur when using a SE(B) weld metal fracture specimen.

Notwithstanding the fact that R appears to affect the load *vs.* load-line displacement behavior of the C(T) specimen, the relation between the latter variable and the cmod is not influenced by the presence of weld metal. Figure 5 shows v_{LL} - cmod curves for the C(T) and SE(B) geometries. The C(T) curves are little influenced by the ligament size, and for each value of b/W, there is no influence of R. The SE(B) curves, on the other hand, show a larger influence of ligament size, and no influence of amount of WM. The ratios of cmod to v_{LL}, ζ, are listed in Table 1 for both geometries, obtained by linear regressions. These values are listed together with the GE-EPRI Handbook values for n = 10 [Ref. 10], and the absolute relative differences Δ, in %.

Table 1. Values of ζ = cmod / v_{LL} for WM C(T) and SE(B) specimens

b/W	ζ C(T)	ζ C(T), EPRI	Δ, %	ζ SE(B)	ζ SE(B), EPRI	Δ, %
0.3	1.302	1.300	0.15	0.835	0.843	0.60
0.4	1.315	1.324	1.07	0.766	0.781	1.96
0.5	1.338	1.347	0.67	0.702	0.718	1.70

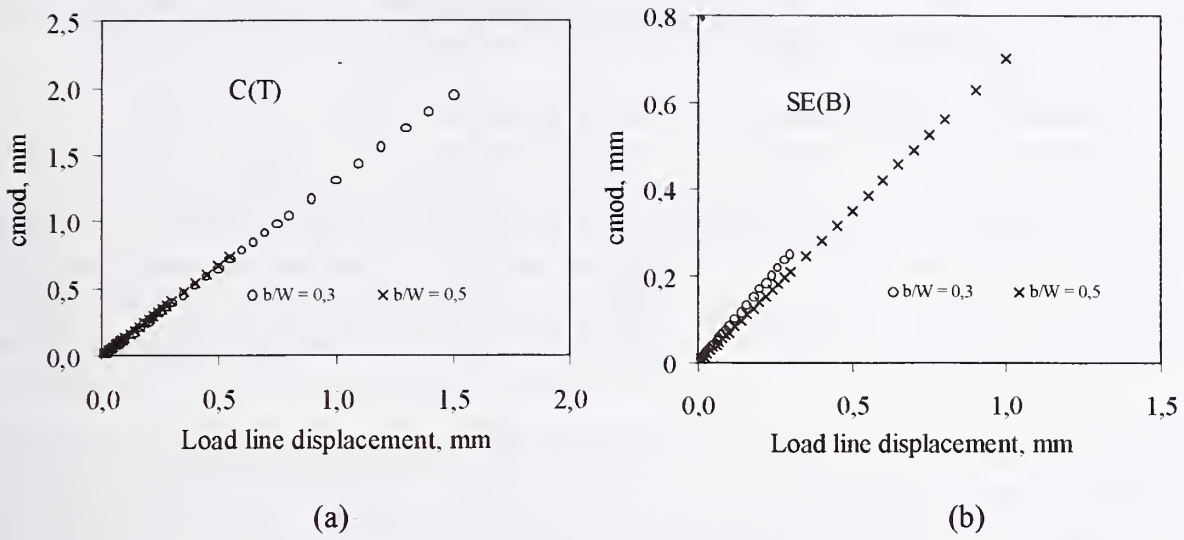

(a) (b)

Figure 5. cmod *vs.* load line displacement, v_{LL}.

The differences between the EPRI ζ ratios and those calculated from the obtained numerical values, are not siginificant, considering that the former are computed with a power law code, and the latter are based on a rigid rotation. Thus, these results could be taken to imply that the presence of weld metal in a fracture C(T) or SE(B) specimen does not alter the ratio between cmod and v_{LL}. However, as was discussed in relation with Figures 3 and 4, the value of R does have an influence on the C(T) load *vs.* load-line displacement behavior, and therefore, may affect the J values.

The relation between cmod and v_{LL} may be further used to determine the location of the apparent center of rotation. The idea of a point about which the two halves of the specimen rotate in a rigid fashion has been employed for a long time in relation with CTOD evaluations, as shown by Eq. (7). For SE(B) specimens and small angles of rotation, Kirk and Hackett [Ref. 11], based on a rigid rotation model, suggest the following relation between cmod and v_{LL}:

$$\zeta = \frac{c\,\mathrm{mod}}{v_{LL}} = 1 - \beta(b/W) \tag{10}$$

where $\beta = 1 - r_p$. On the same grounds, one can propose a similar relation for the C(T) specimen:

$$\zeta = \frac{c\,\mathrm{mod}}{v_{LL}} = \frac{1.25 - \beta(b/W)}{1 - \beta(b/W)} \tag{11}$$

From Eqs. (10) and (11), the following expressions relate β to ζ:

$$\beta = (1 - \zeta)/(b/W) \tag{12}$$

for SE(B), and

$$\beta = \frac{\zeta - 1.25}{(\zeta - 1)(b/W)} \tag{13}$$

for C(T). Table 2 lists the values of β and r_p from the values for each geometry and ligament size, with the E1290 suggested values [Ref. 2] included for comparison.

Table 2. Values of β and r_p for WM C(T) and SE(B) specimens

b/W	β, C(T)	r_p , C(T)	r_p , E1290	β, SE(B)	r_p , SE(B)	r_p , E1290
0.3	0.555	0.445	0.435	0.550	0.450	0.44
0.4	0.515	0.485	0.449	0.585	0.415	0.44
0.5	0.520	0.480	0.465	0.596	0.404	0.44

The r_p values obtained in this work for the WM C(T) specimens are fairly consistent with those used in E1290. For the SE(B) specimens, on the other hand, a value of 0.6 has been used for β [Ref. 11], implying an r_p of 0.4, whereas E1290 suggests a value of r_p of 0.44. In summary, the values obtained in this work seem to indicate that the presence of WM does not affect the position of the apparent center of rotation for either geometry. Thus, the suggested values of r_p given in E1290 may as well be used for evaluating CTOD in weld metal fracture specimens of the C(T) and SE(B) types.

The other issue of importance is the value of η_{pl} for welds: according to Eqs. (5) and (6), η_{pl} is equal to m. Therefore, the evaluation of m serves two purposes: the G function for the geometry, and the coefficient of the J integral of Eq. (3). The value of m is obtained from the variation of limit load with ligament size, according to Eq. (5), expressed in the following form [Ref. 12]:

$$\eta_{pl} = \text{dlog } G / \text{dlog } (b/W) = \text{dlog } (P_0/BW\sigma_0) / \text{dlog } (b/W) \qquad (14)$$

Thus, a log-log plot of normalized limit load, $P_0/BW\sigma_0$ with b/W, will give the value of $\eta_{pl} = m$. Figure 6 show this type of plot, for R = 1/3. For the C(T) geometry, there is a slight effect of R; values are listed in Table 3, in which the CFE value of 2.236 is included for comparison.

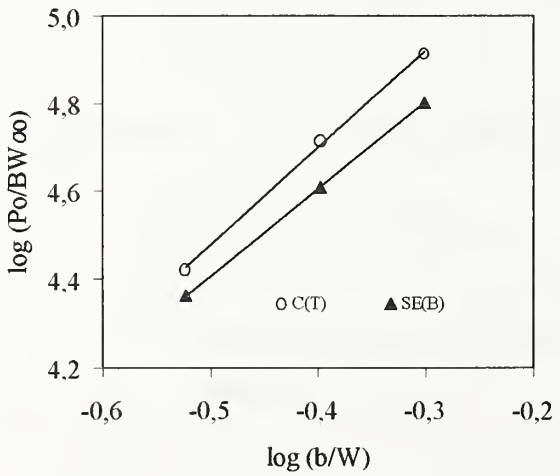

Figure 6. Normalized limit load *vs.* ligament size, C(T) and SE(B) specimens.

Table 3. Values of η_{pl} as a function of R for WM C(T) specimens

R	1/4	1/3	1/2	CFE
η_{pl}	2.135	2.213	2.391	2.236

There is no consistent trend in the η_{pl} behavior as R increases. This is hardly surprising, since one of the shortcomings of the method is the determination of the limit load, especially when dealing with experimental results [Ref. 12]. However, these obtained values are satisfactory if one considers previously reported experimental results of 2.158 and 2.286 for WM C(T) specimens of two thickness [Ref. 12], with an average value of m of 2.222.

The values for the SE(B) specimen, on the other hand, do not depend on R, since the P-v curves are almost all alike. The values of m obtained were: 2.015, 1.989, and 1.990. There can be no doubt that the value representative of the WM SE(B) specimens is 2, equal to the value normally employed for η_{pl} in SE(B) specimens made of homogeneous materials [Ref. 8].

According to these results for the geometries and crack lengths under consideration, there seems to be no effect of the amount of WM on the values obtained for η_{pl}. The values for WM specimens, therefore, are those employed in a standard fashion, like the CFE values of 2.236 for C(T) and 2 for SE(B), or those suggested by E813 [Ref. 1]. The consequences of this are twofold: first, the single specimen J value of Eq. (3) for WM specimens may use the same η_{pl} as for one-material specimens, and second, the G function for a WM specimen keeps the same value of the exponent m as for homogeneous C(T) or SE(B) specimens.

The results obtained by modeling the WM C(T) and SE(B) specimens, with an overmatch of 1.4, several volume fractions of WM present, and crack lengths a/W of 0.5, 0.6, and 0.7, indicate that CTOD evaluations may be made without any influence of the amount of WM present. In fact, since the position of the apparent center of rotation for neither geometry is affected by the presence of WM, the values of E1290 may be used to evaluate CTOD in weld metal fracture specimens of C(T) and SE(B) types.

As to the evaluation of J_{pl} according to the single specimen form of Eq. (3), the value of the coefficient η_{pl} is unaffected by R, in both geometry modeled. However, the amount of weld metal present in the specimen does affect the value of the plastic displacement, v_{pl} for C(T) specimens, and therefore, has an influence on the calculation of J_{pl}. The same is not true for the SE(B) geometry.

In conclusion, while the evaluation of CTOD in C(T) and SE(B) weld metal fracture specimens with an overmatch of 1.4, and $a/W > 0.5$ may be made in a way similar to the evaluation for one-material, homogeneous specimens, without any influence of amount of weld metal or crack length, the evaluation of J_{pl} may be subject to large differences for a given a/W, since v_{pl} is dependent on the amount of weld metal and the ligament size. In this respect, for crack lengths close to $a/W = 0.5$, it is recommended to use specimens with $R > 1/3$. Conversely, if the amount of weld metal is small, $R = 1/4$, deeply cracked specimens, $a/W \approx 0.7$, should be used to obtain J values representative of the weld metal fracture properties.

ACKNOWLEDGMENTS

This work was supported by FONDECYT-CHILE, Project No. 1980169.

REFERENCES

1. ASTM Standard E 813-89, 1991. Standard Test Method for J_{Ic}, A Measure of Fracture Toughness, Annual Book of ASTM Standards, Vol. 03.01, American Society for Testing and Materials, 713-727.
2. ASTM Standard E 1290-89, 1991. Standard Test Method for Crack-Tip Opening Displacement (CTOD) Fracture Toughness Measurement, Annual Book of ASTM Standards, Vol. 03.01, American Society for Testing and Materials, 924-939.
3. BS 5762: 1979. Methods for Crack Tip Opening Displacement (COD) Testing, British Standards Institution, London.
4. BS PD 6493: 1980. Guidance on Some Methods for the Derivation of Acceptance Levels for Defects in Fusion Welded Joints, British Standards Institution, London.
5. International Institute of Welding, 1990. IIW Guidance on Assessment of the Fitness for Purpose of Welded Structures. Draft for Development. IIW/IIS-SST-1157-90.
6. Donoso, J.R.; Landes, J.D. 1998. A Unifying Principle for Evaluating Fracture Toughness in the Elastic and Plastic Regimes with Planar Fracture Specimens, 30th ASTM National Symposium on Fatigue and Fracture Mechanics, St. Louis, MO.
7. Sharobeam M.W. and Landes J.D., 1991. The Load Separation Criterion and Methodology in Ductile Fracture Mechanics, *International Journal of Fracture*, Vol. 37, 81-104.
8. Donoso, J.R.; Landes, J.D. 1994. Common Format for Developing Calibration Curves in Elastic-Plastic Fracture Mechanics, *Engineering Fracture Mechanics*, Vol. 47, 5, 619-628.
9. Donoso, J.R.; Labbé, F.and Mora, C. 1994. The Effect of the Yield Stress Mismatch on the Calibration Curves of Weld Metal Fracture Specimens, International Conference Proceedings on Modeling and Control of Joining Processes, Ed. Thomas Zacharia: 566-573, American Welding Society.
10. Kumar, V., German, M.D., y Shih, C.F. 1981. An Engineering Approach for Elastic-Plastic Fracture Analysis, NP 1931, EPRI Project 1237-1.
11. Kirk, M.T. and Hackett, E.M. 1988. An Evaluation of J-R Curve Testing Using Three-Point Bend Specimens. Fracture Mechanics: Eighteenth Symposium, ASTM STP 945. Eds. D.T. Read and R.P. Reed: 347-373. American Society for Testing and Materials.
12. Donoso, J., Labbe, F. and Mora, C. 1993. Evaluation of Plastic Eta Factors in Weld Metal Fracture Specimens: A Comparison Between Limit Load and Common Format Solutions. *Engineering Fracture Mechanics.* Vol. 44, 4, 515-520.

Session A6: Welding Documentation

VIDEO MONITORING AND CONTROL OF THE LENS PROCESS

William H. Hofmeister[1], Danny O. MacCallum[2], Gerald A. Knorovsky[2]

ABSTRACT

The LENS (Laser Engineered Net Shaping) process has significant potential impact to the manufacturing community in producing near-net shape rapid prototypes, tooling and customized small lot parts. LENS has its roots in stereolithography and weld surfacing. Parts are built up in layers by delivering powder carried in an inert gas stream directed via nozzles to a laser-produced molten pool. A robust implementation of this technology requires a thorough understanding of how the thermal history during part fabrication influences the dimensions, microstructure and properties of the part. This understanding, in combination with effective closed loop feedback control of the process, and modeling of the part to be formed, is required to ensure routine fabrication of components with appropriate properties Thermal behavior at high temperatures (above 800°C) can be readily monitored by visible light radiation pyrometry. In this work a high speed digital camera with a narrow bandpass optical filter was used to obtain thermal images of the LENS process zone. The thermal imaging system was incorporated into the optical path of the laser so that the melt pool and adjacent areas of the part could be monitored without intrusive hardware add-ons at the lens/powder nozzle/process zone vicinity. The output of the digital camera was collected by a frame grabber card in a personal computer (PC). Characteristics of the melt pool were evaluated and then used as inputs to a Proportional-Integral-Derivative (PID) control algorithm also running on the PC. The output of the PID algorithm was then used to control the laser power. Running the closed loop control resulted in significant stabilization of the melt pool size during simulated fabrication experiments. We will describe the equipment, algorithms, experiments and results obtained from LENS-formed simple shapes of 316 Stainless Steel.

INTRODUCTION

LENS (Laser Engineered Net Shaping) is a process for building solid metallic structures by injecting fine powder into a laser-sustained fusion zone. LENS has its roots in stereolithography and weld surfacing. Parts are built up in layers by delivering powder carried in an inert gas stream directed via nozzles to a laser-produced molten pool. The powder (which is preheated by the laser beam) melts in the fusion zone, adding to its

[1] Dept. of Chemical Engineering, Vanderbilt University, Nashville TN 37235

[2] Joining, Coating & Net Shaping Dept., Sandia National Laboratories, Albuquerque, NM 87185-0367

volume, thus building up a solid structure as shown in Figure 1. By tailoring the relative motion of the heat source and the part being built, an almost unlimited variety of solid, hollow, or cavity-containing shapes can be made. Obviously, the larger the pool (limited by laser power), and the greater the rate of powder injected into it, the faster the 'build'. For the work described herein, a 500 W continuous wave (cw) Nd:YAG laser system was used, with powder feed rates of 14 g/min; this suffices to deposit a 12.7 mm cube in about 15 minutes. Since the subsequent mechanical properties are dependent upon atmospheric contamination, the system is run in an enclosed atmosphere chamber containing argon at ambient pressure.

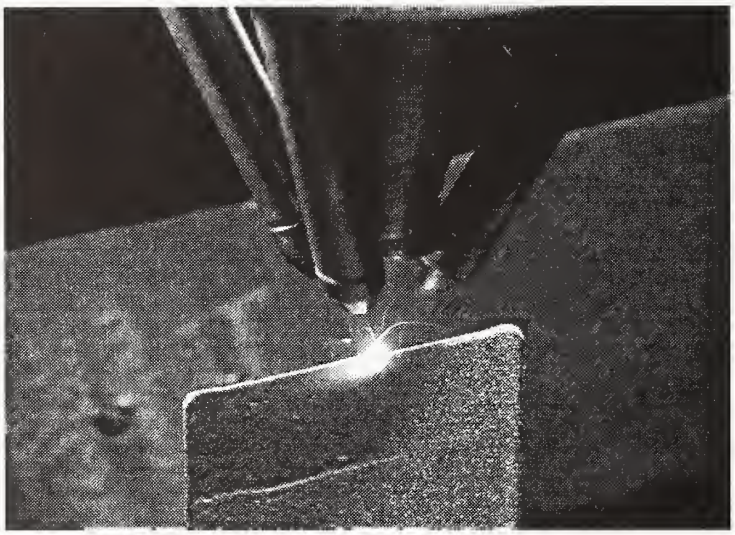

Figure 1: Building a wall of 316 Stainless Steel by the LENS process. The inner laser nozzle is surrounded by four powder injectors. ~1X

The LENS process has significant potential impact to the manufacturing community in producing near-net shape rapid prototypes, tooling and customized small lot parts. A robust implementation of this technology requires a thorough understanding of how the thermal history during part fabrication influences the dimensions, microstructure and properties of the part. This understanding, in combination with effective closed loop feedback control of the process, and modeling of the part to be formed, is required to ensure routine fabrication of defect-free components with appropriate properties.

The first goal of this work was to obtain information about the interaction between process control variables and the resulting object produced. Namely, how much material is deposited at a given laser energy, travel speed and powder feed rate. The thermal distributions are also of interest to determine the thermal history of each volume of material. The dimensions of the resulting shape were compared with the expected shape as well. Since robustness also implies strict repeatability, the characterization parameters

were used in implementation of feedback control of the process, initially to obtain high fidelity shape generation and ultimately microstructural control.

EXPERIMENTAL PROCEDURES

Temperature fields at high temperatures (above 800°C) can be readily monitored by visible light radiation pyrometry.[1] In this work a high speed digital camera with a narrow bandpass optical filter (the laser radiation must be filtered out!) was used to obtain thermal images of the LENS process zone. All pixels of the video camera were calibrated with a NIST traceable tungsten strip lamp to determine the effective wavelength of the camera, lenses, and filter set. During the experiments, an in situ calibration was performed by observing the freezing of a 3 mm ball of the deposited material.The temperature uncertainty is +/-7K. The thermal imaging system was incorporated into the optical path of the laser (as shown in Figure 2) so that the melt pool and adjacent areas of the part could be monitored without intrusive hardware add-ons at the lens/powder nozzle/process zone vicinity. The output of the digital camera was collected by a frame grabber card in a personal computer (PC).

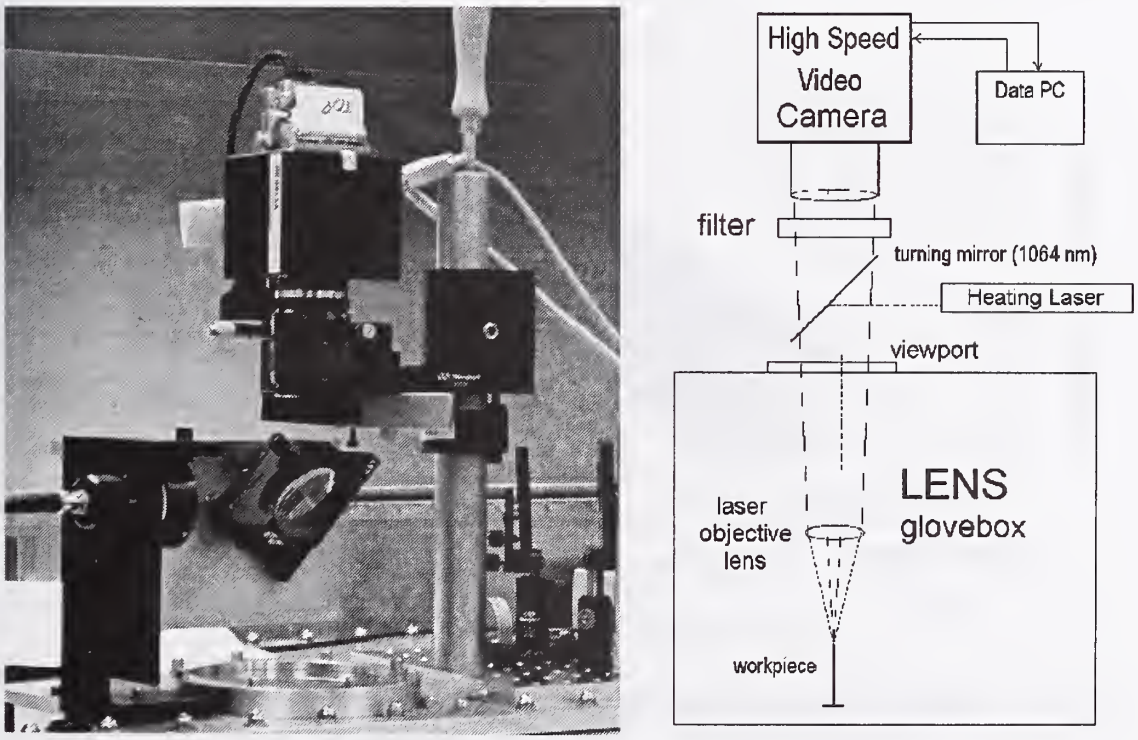

Figure 2: Video monitoring set-up and schematic of optical path modifications.

After converting the intensity data to temperature vs location maps, characteristics of the melt pool and local temperature conditions were evaluated as a function of the build

parameters (laser power and scanning speed). These included the length and width of the molten zone, its area, and temperature gradients at the liquid/solid interface. The area was later used as an input to a Proportional-Integral-Derivative (PID) controller also running on the PC which controlled the laser output power. Additional information was also needed, such as whether a boundary or a fill pass was being made, and whether the laser shutter was open or closed. This information was obtained from the X-Y-Z table/lens height controller, running on a separate PC. The output of the PID algorithm was then used to control the laser power in such a manner as to maintain the projected area of the molten zone constant. All manipulations to the intensity data were performed using LabView software.

The ranges of power and travel speed investigated are shown in Figure 3; where the resulting isotherm area of the melt pool is plotted. As is expected from the different heat sink conditions, the isotherm area for a given set of conditions changes markedly depending upon whether one is building a line, at the border of a solid, or at the interior of a solid. As may be seen, the isotherm area decreased in that order, with the fill condition having less than half the isotherm area of a line build at equivalent conditions.

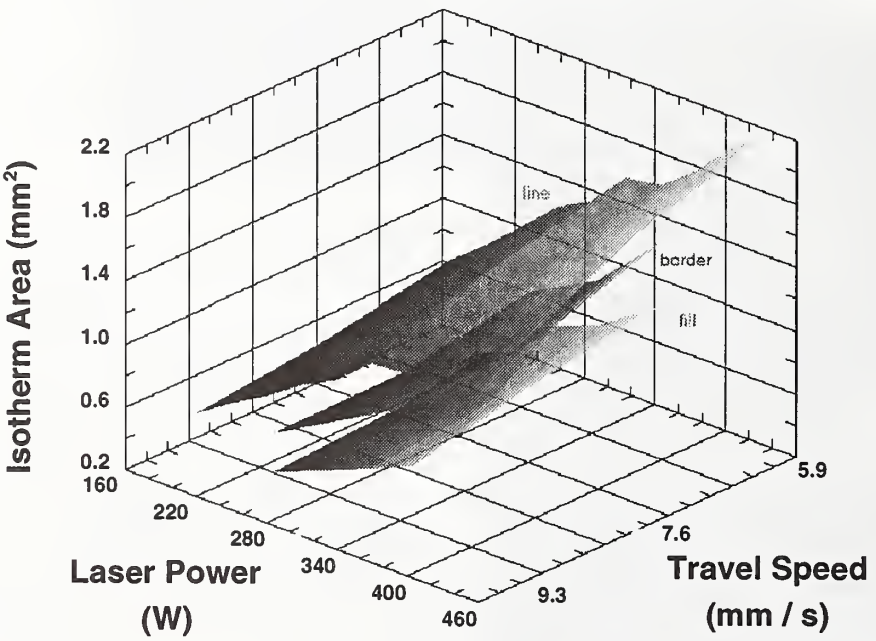

Figure 3: Melt isotherm area as a function of laser power and travel speed.

VIDEO MONITORING RESULTS & DISCUSSION

In order to determine if the melt isotherm video measurements were correctly calibrated, a number of runs were subjected to metallographic verification. These are noted in Figure

4 for the line build data. As can be seen, the video and metallographic pool width results both increase with absorbed laser energy (laser power times absorptivity divided by the travel velocity; with 0.35 used for absorptivity), and are in excellent agreement at low values of absorbed energy; however, at higher values the agreement deteriorates and the width measured by microstructural analysis is smaller than the width indicated by video.

A smooth relation was found for the video-measured pool length shown in Figure 5. The melt pool area isotherm also smoothly increased with absorbed energy as shown in Figure 6, with a linear fit of the relation of the isotherm area to absorbed energy. Metallography of the bead cross-sections for the 7.62 mm/s travel speed builds, allowed calculation of the bead height and volume. This ratio (0.76) was found to be constant at a given travel velocity, independent of laser power. Assuming that the bead height-to-width ratio was constant and 0.73 for the 5.93mm/s builds, and 0.89 for the 9.32 mm/s conditions allowed all three volume vs absorbed energy to be brought into concurrence as shown in Figure 7. This corresponds with having a relatively taller bead at slower speeds. In welding, it is common for slower speed pools to be more isotropic is shape, with faster speeds leading to more elongated pools.

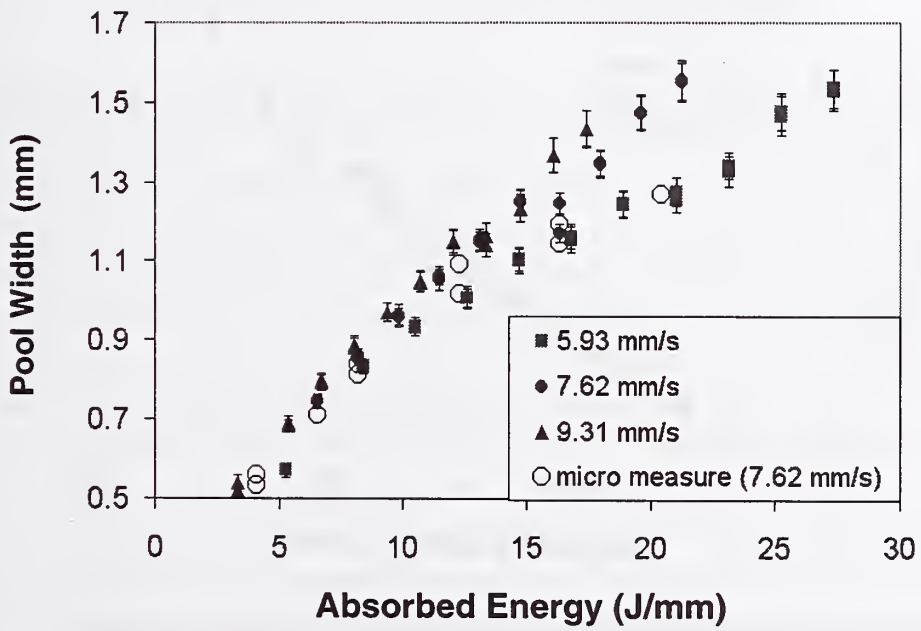

Figure 4: Melt pool width vs absorbed laser energy, line build.

The cooling rate at the liquid/solid interface, derived from the temperature gradient and travel speed product, showed a greater amount of scatter, but generally decreased as the absorbed energy increased. It may be noted that the cooling rate is in excess of 500K/s even at the absorbed energy values. This is conducive to fine solidification structures.

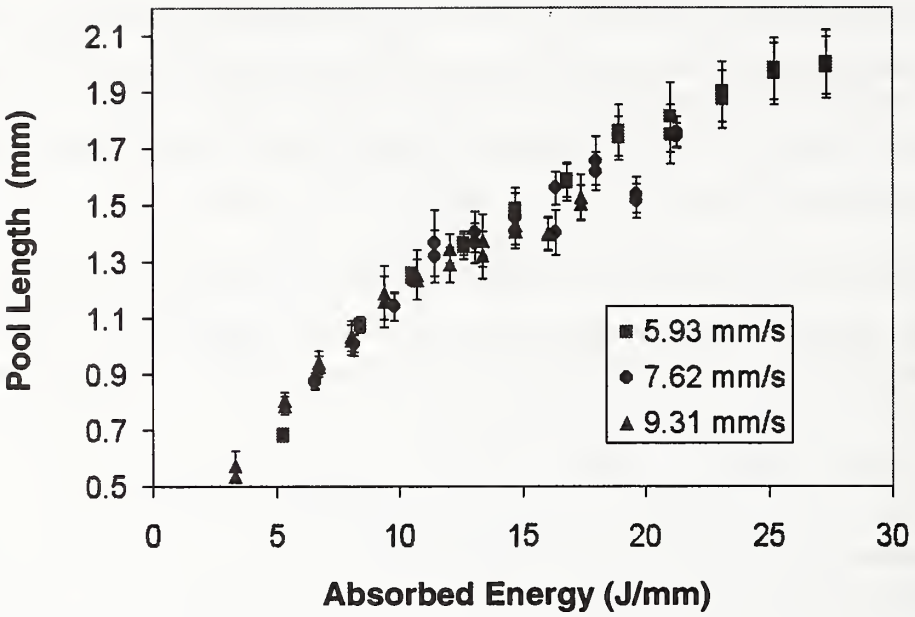

Figure 5: Melt pool length vs absorbed laser energy, line build.

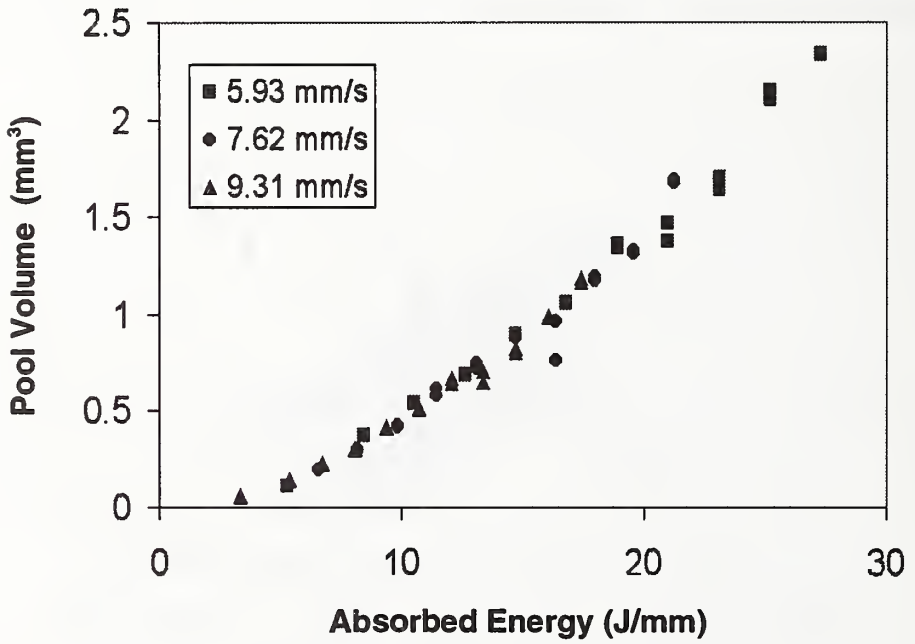

Figure 6: Pool melt isotherm area vs absorbed laser energy, line build.

CONTROL RESULTS AND DISCUSSION

The fusion zone thermal boundary conditions change appreciably during a part build. In the initial stages the substrate is at ambient temperature and is a significant heat sink. As

the build progresses, the substrate and part heat up, generally decreasing the gradient for heat extraction. Thus, unless a preprogrammed decreasing laser power schedule is incorporated into the laser controller, the fusion zone size will increase as the overall part

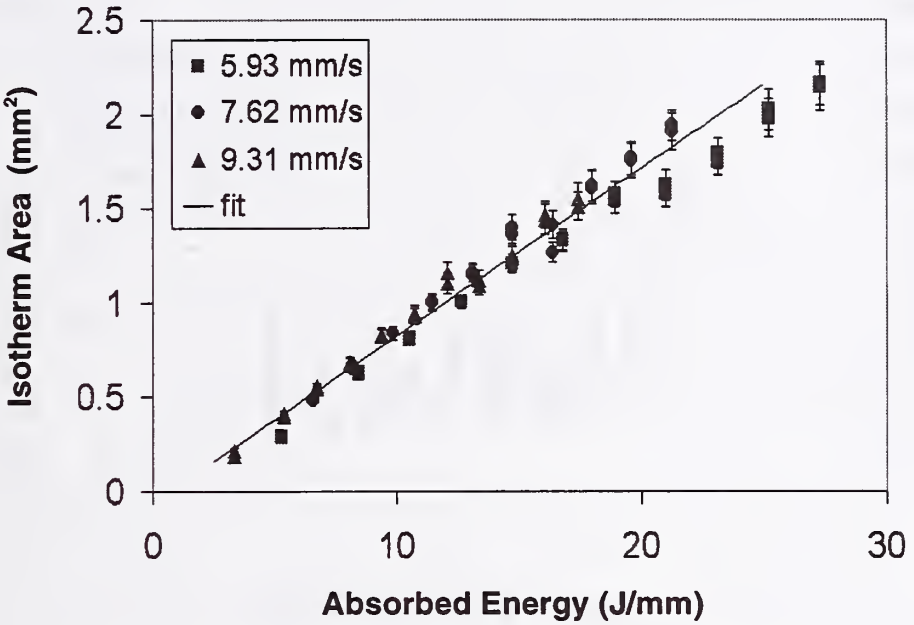

Figure 7: Pool volume vs laser energy density, line build.

temperature increases and the thermal gradients decrease. This is shown by the open loop data sets in Figure 9, where the fusion area pixel size increased by ~60%. Without a comprehensive model of the heat flow involved during the part build, this laser power programming has to be found by experimentation. Alternatively, by incorporating the molten zone area measured by the video system into a control loop, the laser power can be automatically adjusted to keep this area at a set point. The results of such a video-based controller are also shown in Figure 9 as the closed loop data sets. For this hollow square geometry, over the four data sets represented, the laser power decreased by about 10% while maintaining a constant set point area of ~325 pixels or 0.66 mm^2. Similar behavior was also seen when building a solid cube of 12.7 mm edge length, as shown in Figure 10. The open loop data sets vary non-monotonically because they are not at an equivalent distance from the side surface of the cube. Thus, the run 2 data on open loop are closer to an outside surface (and hence are more 2-dimensional) than runs 1 or 3. Clearly the controller is working to decrease both the mean and standard deviation of the molten pool area. The standard deviation of the molten pool area in the control samples was 20% less than the standard deviation on the open loop samples.

Profilometer measurements were taken from four cube shaped samples (12.7 mm per side) to evaluate the efficacy of closed loop control in maintaining dimensional control.

Table 1 summarizes the measurements of cube height for the samples, open loop, closed loop with border set point of 320 pixels and fill set point of 265 pixels, closed loop with a border set point of 200 pixels, and a duplicate of the previous condition with different

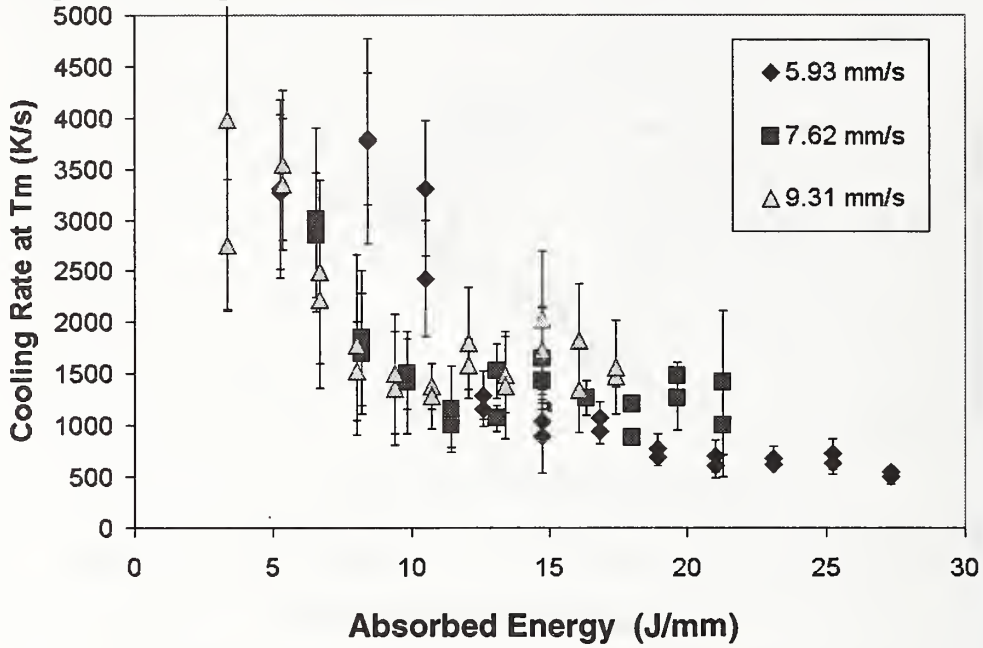

Figure 8: Cooling rate at liquid/solid interface vs energy density

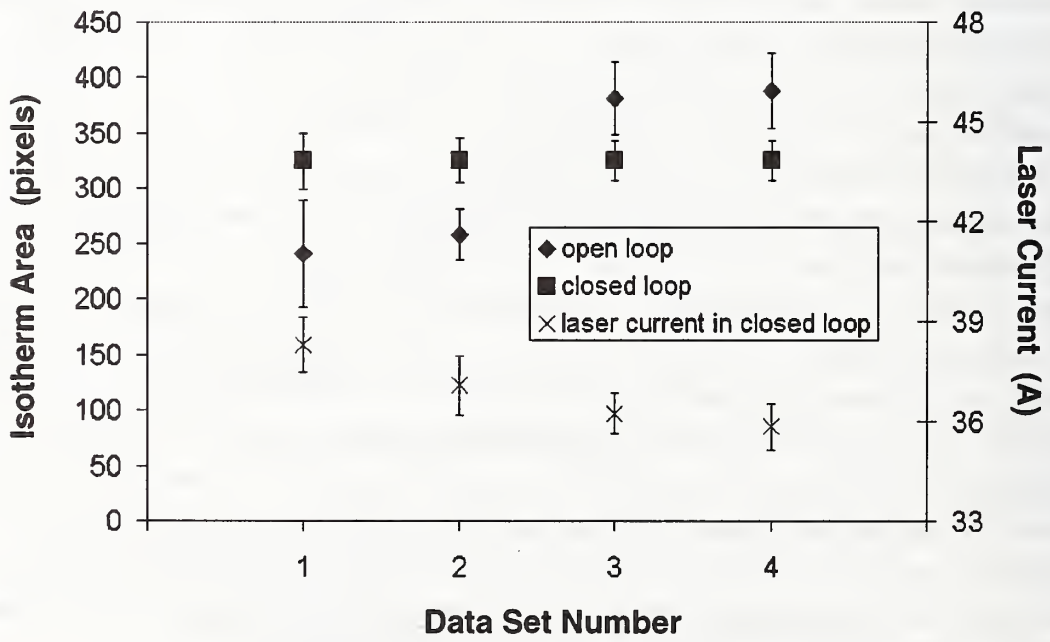

Figure 9: Variability of laser power and molten zone area at various times during open and closed loop builds of a hollow square (wall build). Laser current is proportional to laser power. Each data set averages 20 seconds of data.

control parameters. The flatness and center-edge differences are reduced substantially compared with the open loop case. Flatness is defined as the rms value of deviation from mean, while the center-edge difference is the maximum difference between the center and the outer edge.

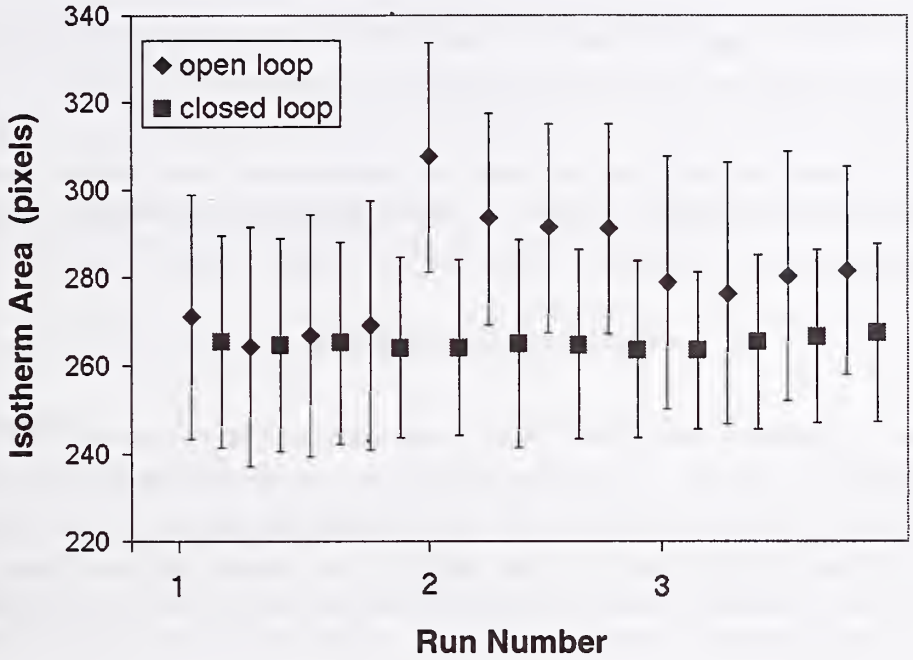

Figure 10: Three open and closed loop runs were evaluated in 5 second increments. The error bars are the standard deviations of each increment.

By controlling the area of the fusion zone, the controller has decreased the difference between the desired true planar surface contour and the as built surface. It is clear that further improvement is necessary. However, the strategy of using isotherm area control shows promise in improving the consistency of build volumes and final shapes.

Table 1: Summary of profilometric results

Control	Isotherm area (pixels)		Flatness	Z height (mm)		ctr-edge difference (mm)	
Case	Border	Fill	(mm)	center	edge	probe	profilometer
open			0.88	14.64	15.40	0.76	1.07
closed	320	265	0.64	14.38	14.90	0.52	0.78
closed	200	265	0.58	14.00	14.38	0.38	0.72
closed	200	265	0.52	14.57	14.90	0.33	0.59

CONCLUSIONS

Thermal video imaging via visible radiation is a powerful tool for understanding gradients, cooling rates, and parameter scaling of the LENS process.

Based upon our monitoring experiments we found that the pool length, width, area and volume scales well with absorbed energy (absorptivity x laser power / velocity).

Control from PC-based thermal imaging based on isotherm area works, giving consistent isotherm areas with less variance. Set point control of the fusion zone area also improved dimensional accuracy of a simple cubic shape relative to open loop process operation.

ACKNOWLEDGEMENTS

This work was supported by the United States Department of Energy under Contract DE-AC04-94AL85000. Sandia is a multiprogram laboratory operated by Sandia Corporation, a Lockheed Martin Company, for the United States Department of Energy. The work was performed for the LENS CRADA. The authors also thank Melissa Wert, John Smugeresky, Joel A. Philliber, Michelle Griffith, Don Greene and Mark Ensz for help in performing the experiments.

REFERENCE

1. G.D. Nutter in Applications of Radiation Thermometry, ASTM STP 895, J.C. Richmond and D.P. DeWitt, Eds., ASTM, Philadelphia, 1985, pp 3-23.

Implementation of a QA/QC system that complies to ISO 3834.

E. Engh, 4X Software, Norway

Introduction.

As the global production scenario is growing and the rapid requirements for high quality products are being focused, most people clearly see the needs for a common QA/QC strategy in their companies.
For global fabricators it is of the utmost importance that their product quality is reliable even if their final product must consist of products from their facilities all over the world.

For medium sized and small companies it is a growing demand or more reliable products and better quality, reduced costs and reduced time to market.

Being able to manage the production and its quality to the right level will be an important competitive factor in the years to come.

Background.

Competitive fabricators in Europe, US and Canada cannot compete on labor intensive fabrication unless this fabrication can have a high degree of technology. We have had an ever lasting story of labor intensive products with low technological content that has been wiped out from our fabrication sphere. Fabrication of standard vessels for crude oil, bulk and so forth. Boilers with low working pressure are another example.
Due to our background and history we must face that we have to add an additional value to the products in form of technology and quality to be able to survive in the competitive marketplace.
The competitive window we can achieve through technology and quality we must use to stretch our goals and limits further on. One of the typical competitive advantages we can have is time to market as one ff production and small series production becomes more typical.

Quality management and quality control in all phases of a product life cycle will therefore be more and more important.

Quality records

Still a lot of fabricators thinks that fabrication records are the same as quality management. To be able to document what has happened is far from being able to monitor the fabrication and taking corrective actions.
With a shorter turn around time it is not of interest to find out three weeks later what happened, you need to know it now so that you can avoid consequential damages or a complete destruction of parts.

Quality Management.

With Quality Management we mean that you should be able to monitor the production constantly so that immediate action can be taken when necessary. In Quality Management

we see a management Dedication to quality in all phases of the production and that this management dedication is understood and accepted at all levels in the organization.

ISO 900 series of standards are a good tool to drive the organization in the right direction. ISO 3834 completes the ISO 9000 series with fabrication expertise and know how. This is of special importance for fabricators where welding is an important fabrication method.

Over the last two to three years we have seen an increasing interest from fabricators to implement the ISO 3834 standard as well as an increasing demand for using this standard as reference in other standard, specification, product standards and European directives.

Implementing a Quality management system.

Two key factors for success has been:

Management focus and dedication to the implementation.
Always an underestimated factor. An implementation will always take time. Costs can be estimated wrong or the time for the implementation can be longer than expected. This is actually quite normal. Unforeseen problems in the organization can take longer time to solve.

Motivation and dedication of the personnel participating in the implementation.
This also a key factor to a success. You cannot order a person to change, you must motivate him or her. Motivated people in the organization will be a driving force for change and a positive resource of knowhow and ideas.
However very often job functions and tasks have to be reorganized. Such changes must be cared for and supported at all levels.

The human factor is the most valuable resource in implementing a Quality Management system and that is very often forgotten. It has to be planned for in such a way that you can utilize this resource.

Tools

A Quality Management system must also consist of the necessary tools that will enable the users to access the data they need fro verification purpose. They also need tools to be able to establish the required routines and procedures.

A set of tools has been developed to cope with the requirements of ISO 3834, XWELD, QMWELD and XQUALITY.

XWELD

This tool enables the welding engineer to create documentation of any PQR (or WPAR) including test documentation. Based on an approved PQR he can develop one or more WPS fro production. Procedures can be stored and retrieved or manipulated fro alterations and so forth. The system have input verification on essential variables as well as a powerful drawing tool for generating weld sequences and layer disposition.

QMWELD

A tool for tracing all activities related to a weld. This means it follows the weld through the production process, from engineering to final product. In this system a weld is connected to a drawing. Then associated information is connected to the weld, like material information, information about extent of control. From production additional information is added, like which WPS was used, which welders carried out the job and at what time.
The qualification of the welder is verified to see if the certificate is valid for the joint. This means that a system for administrating certificates are included as well as a system for updating the certificates.

Coming to the Quality Control department, the welds are controlled with non-destructive methods, like RT, UT ,MT and so forth.
The system is used for this control and reports are automatically generated when a defect is found. The reports must be signed off and they are then stored with reference to the weld.

Since all production data is stored, then a set of valuable statistics can be generated. Like production status, remaining work, scope of work for each department and so forth.

Implementation.

This part of the system will usually involve at least four departments, engineering or design, welding engineering, production and Quality Control.

The implementation will focus on the function and process flow. Usually we carry out an overall training showing the process in order to have full acceptance for the process understanding and process flow. An important factor in this part of the implementation is getting acceptance fro the interdepartemental dependencies and also to highlight any changes in the organization if necessary.

After the first training session, then department oriented training will take place. This means that we follow the fabrication process and carry out a job-function related training. Again, the implementation takes into consideration the effect every department has on the final product and their relations.

Other QA activities.

So far we have been concentration on welding only. But in order to achieve a first class product, the rest of the QA process must be planned and documented. For this purpose we use XQUALITY.

XQUALITY

A tool for generating control plan at different levels. First a main Control Plan is developed to meet the contractual requirements. And agreed to with the client. Then these control plans are broken down to detailed control activities. These activities can span over the whole product development cycles to the material reception.
Logical connections are developed between the control activities to ensure that we have

consistency in the planning activities.
Sign off routines are standardized and reports are generated automatically if the result from a control is not acceptable.

Implementation.

Implementing XQUALITY in an organization means that we suddenly have to train a high number of employees, from material reception to shop floor control. AS training schedule is then developed to cope with the fact that most people in production need to have access to this tool.

Necessary thin clients or other hardware are implemented in the production facilities. We also encourage the client to let people that are responsible for a control activity, also report the result from the control itself.

Conclusion.

Implementing a QA/QC system in an organization has been done in a number of fabrication sites. The implementation has focused on following the production process and thematically concentrating on the tasks for each department. The overall process understanding is important and has to be understood in each department.
Being able to follow the process and as a consequence see their own part in such a process is motivating factor for the user.

An implementation must be based on a management commitment. If this commitment is not present, then an implementation is likely to fail. But the users are also the key factor to success. Their understanding, motivation and cooperation must be stimulated. If we. Through such an implementation, can create a positive teamwork, then the implementation will be a success.

DEVELOPMENT OF ULTRA-NARROW GAP GMA WELDING PROCESS BY NUMERICAL SIMULATION

T. Nakamura* and K. Hiraoka**

ABSTRACT

To obtain high quality welded joints with the HAZ width which is as narrow as possible by controlling the arc heat input distribution, an ultra-narrow gap GMA welding (UNGW) process with less than 5mm gap width has been developed. In the UNGW process, the arc heat pole at the groove wall is made widely oscillate in the direction of thickness. The heat input density is reduced by the UNGW process, and the heat input density is smaller than that of conventional GMA welding. The arc heat pole is dominated by wire melting tip position in GMAW process, and the wire melting tip can be represented by wire extension. The wire extension is a function of wire feed speed and wire melting speed which is determined by welding current and wire polarity. If the wire feed speed is constant, the wire extension can be controlled by DC pulse current or AC current.

In order to determine optimum welding conditions without defects in the UNGW process, a numerical simulation of the wire melting tip behavior is carried out in the pulsed DC and AC arcs. As the results, excellent welding joints with the maximum melted area width 6mm and HAZ width 1～2mm, can be obtained by using the newly developed pulsed-UNGW system.

KEYWORD

Ultra-narrow gap welding	(I)
GMA	(II)
Electrode melting speed	(III)
Oscillation	(IV)
Wire extension	(V)
DC pulse arc	(VI)
AC arc	(VII)
Process simulation	(VIII)

---

* NATINAL RESEARCH INSTITUTE FOR METALS, JAPAN

** NATINAL RESEARCH INSTITUTE FOR METALS, JAPAN

1. INTRODUCTION

Narrow gap welding (NGW) possesses many advantages than conventional welding method such as higher mechanical properties of welded joints, higher productivity, lower residual stress and higher cost effectiveness, and various NGW techniques have been developed.

On the other hand, as decreasing the gap width, weld defects such as incomplete fusion at groove side-wall easily occur. In most narrow gap GMAW processes, therefore, the weaving techniques of the arc heat across the groove gap had been developed. Usually, small current and multi-pass welding process has been applied in NGW with the gap width from 7 to 15mm (Ref.1, Ref. 2).

It can be expected that if the groove gap becomes narrower than the diameter of higher current arc heat source, the mechanical weaving system is not necessary to be applied.

However, narrow gap causes the increase of the hydrostatic head of molten metal, and thus inducing the incomplete fusion at groove side-wall. As the decrease in gap width, the phenomena become seriously. Under 7mm narrow gap the unstable arc phenomena, that the arc irregularly goes up at the groove wall, appears remarkably.

In this report, a new NGW process with less than 5mm gap is proposed by means of the numerical simulation of GMA welding process.

2. ULTRA-NARROW GAP GMA WELDING

2.1 Principle of ultra-narrow gap GMAW process

In the ultra narrow gap welding (UNGW) with less than 5mm gap, the bead height per welding pass increases, and the arc is unstable so that the arc pole irregularly perturbates up-to-downwards along the groove wall. To sustain the arc stable and obtain weld joint without defects such as lucks of fusion and undercuts of bead surface, the arc pole behavior and the arc heat input along the groove wall corresponding with a bead height have to be regularly controlled and distributed respectively.

In this report a new GMA process is proposed to control the arc pole and regularly oscillated up-to-downwards along the groove wall by welding current form (Ref.3).

The arc pole is dominated by wire melting tip position in the GMAW process, and the wire melting tip can be represented by the wire extension. The wire extension L is regarded as a function of wire melting speed v_m and wire feed speed v_f. The relationship between wire extension L and wire melting speed v_m is given by

$$\frac{dL}{dt} = v_f - v_m \qquad (1)$$

In the GMAW process, the wire feed speed is recognizes to be constant as conventional GMA welding. Because the extension is determined by the melting speed which depends on

welding current and the electric polarity of the wire, the position of the melting wire tip corresponding with the arc pole can be oscillated along the groove wall in DC pulse current or AC current welding system.

DC pulse current process is shown in Fig. 1. In the high current pulse period, the wire melting speed v_m, which is larger than the mean wire melting speed, is larger than the wire feed speed v_f. As the dL/dt given by equation (1) becomes negative, the wire extension decreases and then the position of wire tip moves up from position A1 to position A2. Next, in the low base current period, as the wire melting speed v_m becomes smaller than the wire feed speed v_f, the wire extension increases, and the wire tip moves from A2 point to the bottom A3.

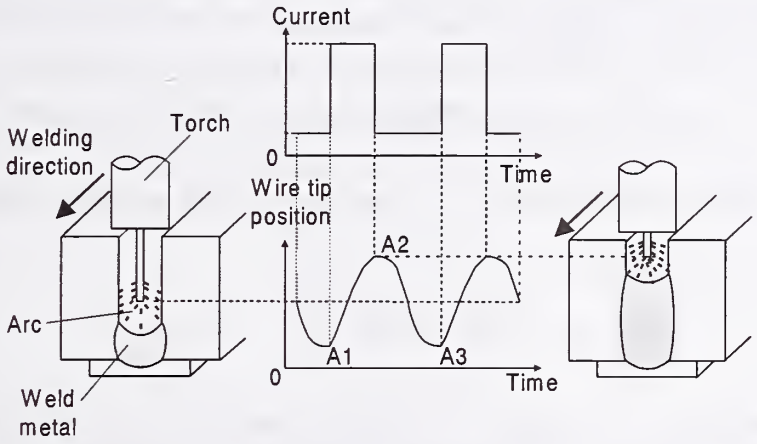

Figure 1. DC pulse arc welding process of UNGW

Figure 2 shows AC arc welding process. The wire melting speed during the electrode negative (EN) is about 1.7 to 3 times the wire melting during the electrode positive (EP) at the same welding current (Ref. 4). In the EN period, the wire melting speed v_m becomes larger than the wire feed speeds v_f, thus the extension becomes shorter and the wire tip moves from the bottom position A1 to the upper position A2. In the EP period, the wire melting speed v_m becomes smaller than wire feed speeds v_f and the wire tip moves from A2 position to the bottom position A3.

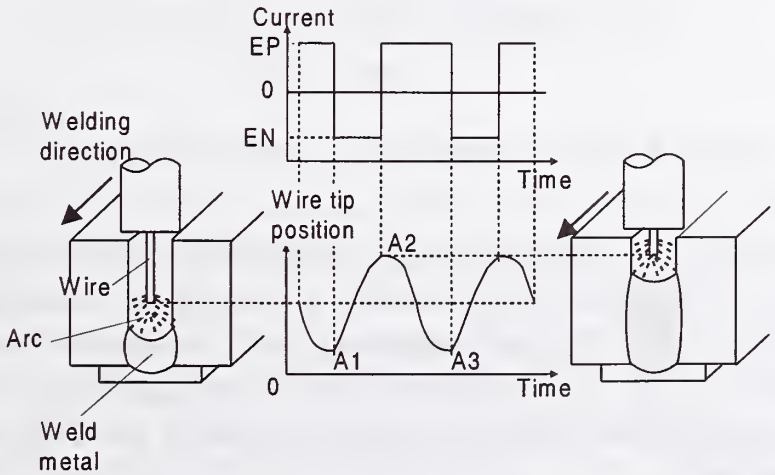

Figure 2. AC arc welding process for UNGW

The results suggest that the position of the melting wire tip corresponding with the arc pole can be oscillated along the groove wall in DC pulse current or AC current welding system.

2.2 Numerical stimulation for ultra-narrow gap welding process

In the numerical simulation, many factors are considered such as the energy balance of droplet, heat input from arc to droplet, heat transfer from droplet to wire, joule's heating at wire extension, hydrostatic potential of molten metal at arc pole above the molten pool, arc pressure and balance of GMA welding electric circuit. Here, the vibration of molten pool and surface profile of the molten metal are not considered. Halmϕy's expressions described in stable state are utilized, although the wire melting behavior is not exactly stable in DC pulse process and AC process.

From equation (2), the welding current is calculated in GMA welding circuit shown in Fig.3.

$$E = V_a + V_L + R_C \cdot I + L_C \cdot \frac{dI}{dt} \qquad (2)$$

Where E is voltage of power supply, V_a is arc voltage, V_L is voltage drop of wire extension, R_c is resistance of welding circuit and L_c is inductance of welding circuit.

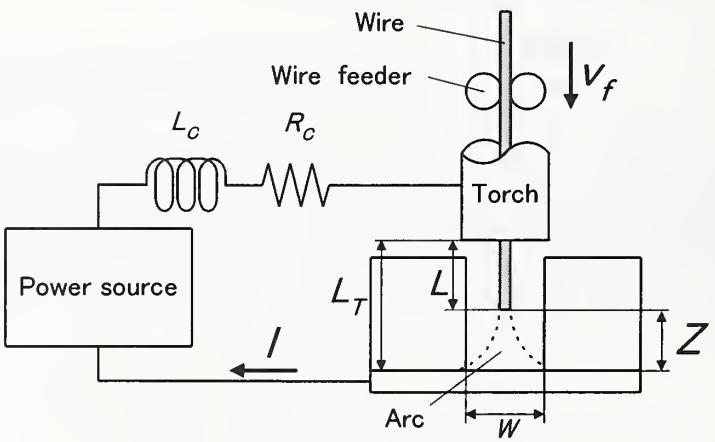

Figure 3. Schematic illustration of GMA welding circuit

The following constrained condition for an ultra narrow gap welding is applied. If the arc length is longer than W/2, where W is the width of groove gap, arc occurs between wire tip and groove wall, and if the arc length is smaller than W/2, arc occurs between wire tip and molten pool. Moreover, in the UNGW process which satisfies equation (2), the arc length is calculated by considering the balance of current determined arc force and hydrostatic potential of molten pool.

Figure 4 shows the flowchart of the ultra-narrow gap welding simulation process by

using equations (1), (2) and Halmϕy's equations (Ref. 5, Ref. 6). In Fig. 4, the voltage drop of wire extension V_L and wire melting speed v_m are derived from Halmϕy's equations.

According to the procedure of the flowchart, the optimum welding conditions for the ultra-narrow gap welding are obtained.

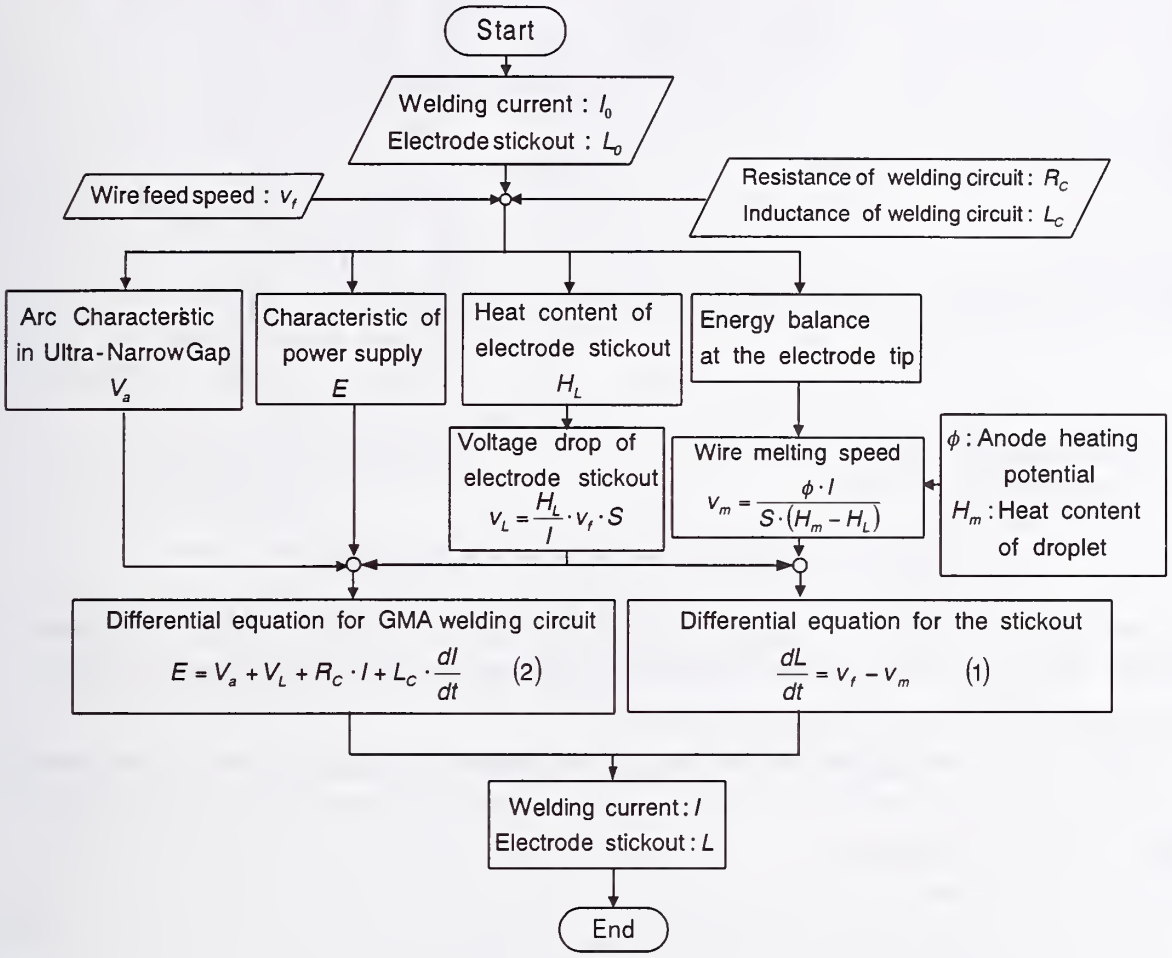

Figure 4. Flowchart of UNGW simulation process

2.3 Simulation results

In order to find out the optimum welding conditions, the relationship between wire tip position and electric current waveform is described by the numerical UNGW simulation.

Firstly, DC pulse process was simulated by means of the square pulse current waveform for the plate 19mm thickness with 5mm I-gap groove. Fig. 5 shows the simulated behavior of the wire melting tip with in the following welding parameters ;

pulse peak duration time T_P = 0.06s, pulse base duration time T_b = 0.3s,

no load voltage of power source for peak voltage is 40V,

no load voltage of power source for base voltage of power source is 34V,

external characteristics of power source is 0V/A,
average current I_{av} is 380A.

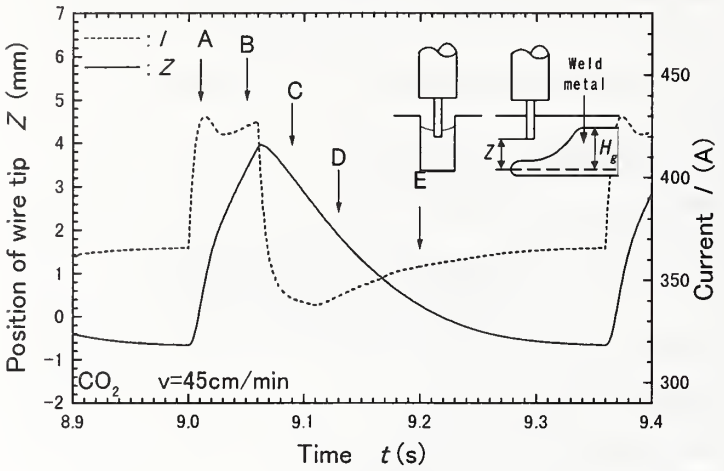

(a) Relationship between pulse current and position of wire tip

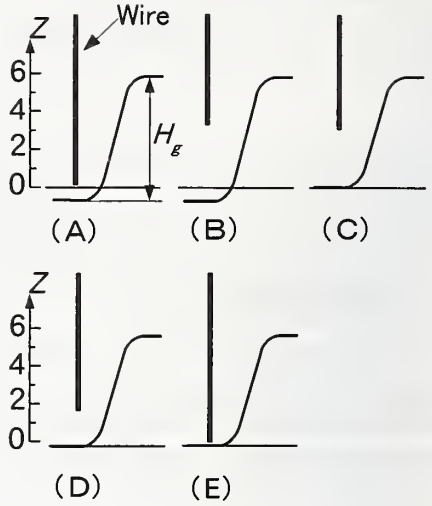

(b) Behavior of wire tip

Figure 5. Results of simulation of wire tip position

From the wire feed speed computed in these welding conditions, the throat thickness of deposited metal is calculated and is about 10mm. The wire tip can be located near the groove bottom from (D), (E) to (A) as shown in Fig. 5(b).

Because the arc pole varies below the groove bottom, the arc heat can be distributed along the groove wall through the throat thickness and the groove bottom can be melt enough.

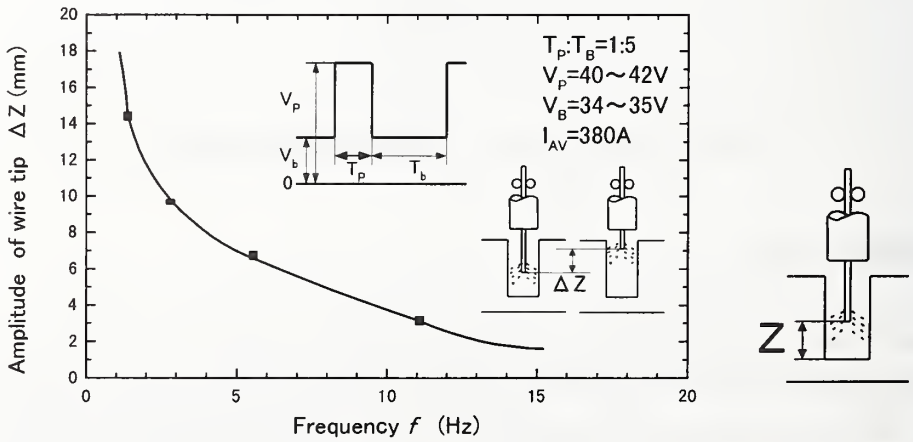

Figure 6. The effect of DC pulse frequency on amplitude of wire tip

Figure 6 shows the relationship between pulse frequency f and oscillation amplitude of the wire tip ΔZ in DC pulse arcs in which the ratio of peak time T_p to base time T_b retains

1/5. The amplitude ΔZ decreases as increasing the pulse frequency. In the UNGW process, the low frequency of less than 5Hz is effective to obtain the amplitude ΔZ corresponding with the throat thickness of the bead.

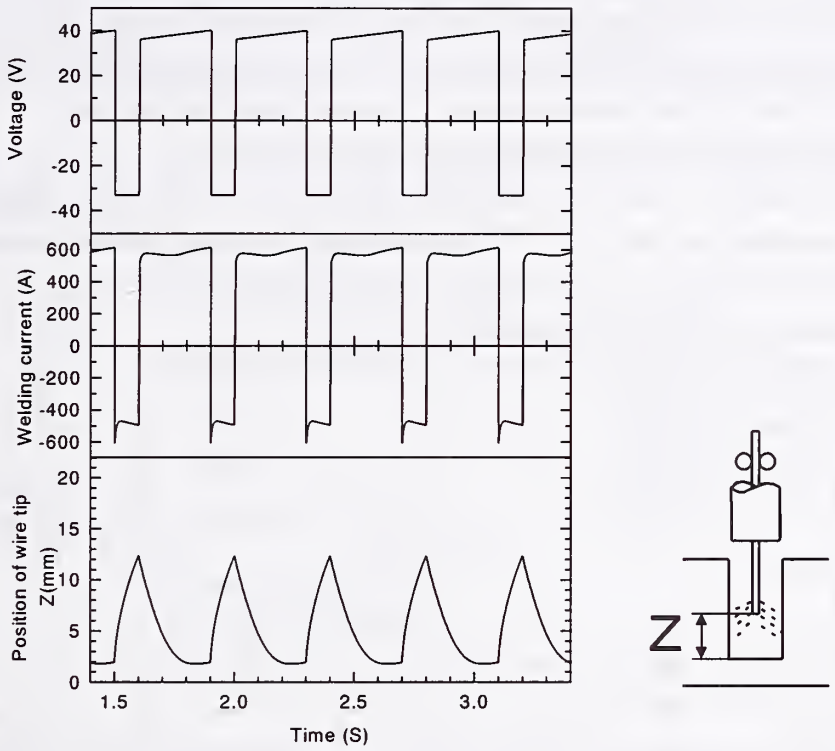

Figure 7. Simulation results of AC arc welding

The UNGW process by AC arc is simulated in Fig. 7. As mentioned in section 2.1, the wire tip can be oscillated along the groove wall as the same as DC pulse process. For the high current 600A during positive wire polarity, further, the wire tip can move to the groove bottom, because the wire melting speed during positive wire polarity is smaller than that during negative wire polarity. The melting efficiency of base metal in negative wire polarity is generally higher than that in positive wire polarity.

AC process, therefore, can effectively transfer the arc heat to the groove bottom and be more effective to prevent of the incomplete fusion at the corner of groove than DC pulse process.

From all the simulated results, the distribution of arc heat input in the new UNGW process can be controlled by selecting electric current waveform.

3. EXPERIMENTAL RESULTS

Figure 8 shows the simulated relationship between the ratio of peak current to base current I_p / I_b and melting wire tip position Z. The ■, ▲ and ● marks show the maximum upper position Z_{max}, the minimum lower position Z_{min} and the mean position Z_{av} in wire tip

oscillation, respectively. From the simulated results, it is found that the position of wire tip increases with I_p / I_b.

The ultra-narrow gap GMA welding with 5mm I-gap is carried out with the welding conditions I_p / I_b = 1.31 and I_p / I_b = 1.47 which are determined by the numerical simulation of UNGW. Fig. 9 shows the cross-section of penetration obtained in case of I_p / I_b = 1.31 and I_p / I_b = 1.47. Compared with the bead for I_p / I_b = 1.31, the position of the maximum bead width for I_p / I_b = 1.47 at first pass moves upwards. Further, in second pass welding of I_p / I_b = 1.47, incomplete fusion lacks occur at both corners of bead bottom.

From the results, it can be experimentally found that the mean heated zone moves upward as increasing the ratio I_p / I_b. This experimental tendency agrees qualitatively with the simulated results. Therefore, the developed numerical simulation is useful to determine many welding parameters in the UNGW process.

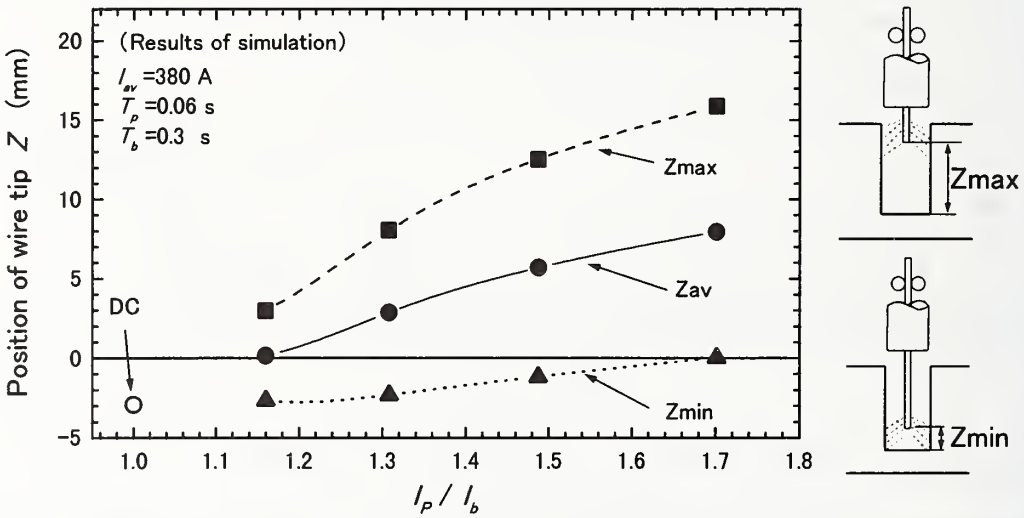

Figure 8. Effect of the ratio of peak current to base current on wire tip position

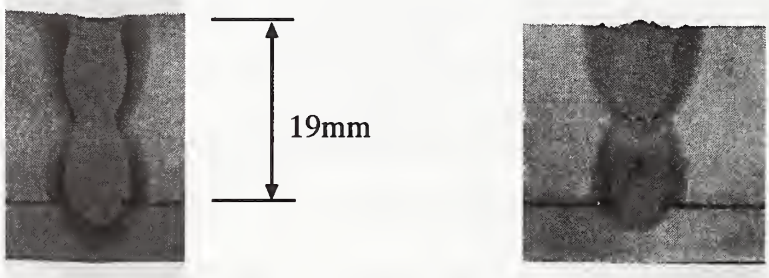

(a) *Ip/Ib* =1.31
Tp =0.06s
Tb =0.3s
Ip =472A
Ib =361A
Iav =380A

(b) *Ip/Ib* =1.47
Tp =0.06s
Tb =0.3s
Ip =522A
Ib =355A
Iav =380A

Figure 9. Bead cross-section of UNGW joints

Figure 10 schematically shows an example of the cross-sections of UNGW joints in optimum welding conditions. Maximum width of molten zone is 6 mm and it is confirmed that the base metal can be slightly melted and the one side width of HAZ can be minimized within 1 to 2 mm. The oscillation control of arc pole along the groove wall by current waveforms reduces the density of arc heat input in the UNGW process.

Furthermore, the welded joint with 10mm in the thickness can be formed by 2 welding passes.

From the all facts mentioned above, a higher-efficient GMA process producing higher-quality joints have been developed.

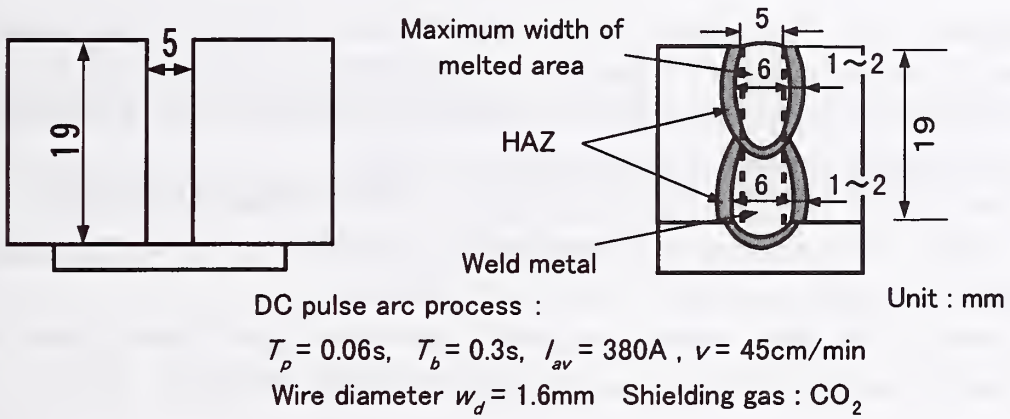

(a) Shape of ultra-narrow gap groove (b) Schematic cross section of welded joint

Figure 10. Results of ultra-narrow gap DC pulse arc welding

4. CONCLUSIONS

The ultra-narrow gap GMAW process with less than 5mm gap width is proposed to obtain high quality welded joints with the HAZ as narrow as possible. In the UNGW process, in order to control the arc heat input distribution and to achieve stable arc welding without weld defects. The behavior of arc pole along groove wall was discussed by the numerical simulation of arc current waveforms. The conclusions are summarized as follows.

(1) It is found from the numerical simulation process that under the correlation between the wire melting speed and wire feed speed, the wire tip oscillating behavior along the ultra-narrow gap groove wall can be controlled by arc current waveform of DC pulse or AC arc. The wire melting speed is dominated by arc current.

(2) Welding parameters determined by numerical simulation leads to good experimental results. The numerical simulation of the new UNGW process in which is effective to find optimal conditions by considering many factors in ultra-narrow gap arc phenomena.

(3) A welded joint with the width of HAZ 1～2 mm and the maximum width of penetration 6 mm can be obtained by the UNGW. The oscillation of arc pole along the groove wall can reduce the density of arc heat input.

(4) Further, a higher-efficient GMA process which can achieve deposited metal height of about 10mm per welding pass without weld defects is developed.

REFERENCES

1. Malinm,V. 1987. Monograph on Narrow-Gap Welding Technology. WRC Bulletin 323
2. Hori,K. and Haneda,M. 1999. Narrow Gap Arc Welding. Journal of J.W.S. 68(3): 41-62
3. Nakamura,T. and Hiraoka,K. 1998. Development of Ultra-Narrow Gap Welding Process. Preprints of the National meeting of J.W.S. 62: 82-83
4. Lancaster, J. F. 1984. The Physics of Welding: 225-226. PERGAMON PRESS.
5. Budapest, 1996. Simulation and Instabilities in GMAW and SAW, The International Institute of welding. Halmϕy, E. IIW Doc.212-895-96
6. London, 1979. Wire melting rate droplet temperature and effective anode melting potential. Conf. on Arc Physics and Weld Pool Behavior. Halmϕy, E. : 49-59.

Session B1: Real-Time Weld Sensing and Control Systems: GMAW Arc Quality Monitoring I

EBSIM -A SIMULATION TOOL FOR ELECTRON BEAM WELDING

Authors: Prof. Dr.-Ing. U. Dilthey, Dr.-Ing. A. Brandenburg, Dipl.-Ing. S. Böhm,
T. Welters
ISF-Welding Institute, Aachen University; Germany,
Dr. S. Iljin, Dr. G. Turichin
State Technical University, St. Petersburg, Russia

Abstract:
During a research cooperation between the ISF Welding Institute Aachen and the St. Petersburg State Technical University a software for forecasting the electron beam welding process with vapour capillary was developed. In this paper the new computer program is presented. All input and output data are described and the simulation algorithms are explained. A short introduction into some physical aspects of the model is also given. It is shown which influence quantities are not neglected in contrast to some other already existing models. In order to evaluate the performance of the simulation algorithm, a comparison between the simulated welding results and real welding experiments is carried out. For some materials the newly developed model gives results with a variation from the real experiments of less than 10%.

1.0 INTRODUCTION

One of the most important characteristics of electron beam welding which helped to increase the industrial acceptance of this welding method is the high reproducibility of the welding results. This is supported by the possibility of controlling the welding parameters automatically. New legal rules concerning quality insurance require extra efforts specially in mass production which are very easy to fulfill for electron beam welding.

Because of the huge amount and type of welding parameters and the complexity of the welding tasks it is necessary to carry out welding experiments to find out the correct parameters. But these experiments are time consuming and therefore, costly. It is impossible to replace these experiments by computer simulations without a physical model. Although different models were developed during the last 30 years industry did not accept these models for practical use.

The problem with all these models is that they are only suitable for a restricted type of materials, certain welding machines and small intervals of parameters. The reason for this is that the welding process itself was not modelled carefully enough until now. To describe the welding process and the melt pool exactly gasdynamical and hydrodynamical processes must be taken into account. It is also necessary to take the absorption and reflection of electrons in the capillary and above the workpiece into consideration.

2.0 MODELLING

overview

It is well known that an electron beam with sufficient beam power is capable of producting a narrow and deep capillary in the workpiece. This capillary is surrounded by liquid metal and is filled with metal vapour which partly escapes from the capillary. Because of the movement of the capillary through the workpiece the weld seam is produced. In the following the process of electron beam welding is divided into separate processes:

- scattering of the beam at the vapour jet above the capillary
- absorption and reflection of the electron beam at the surface of the capillary
- heat transport in the molten metal
- hydrodynamic processes in the molten metal
- dynamic of the vapour

Each single process is described exactly but not all processes are solved satisfactory and the combination of all processes to an overall-model is not yet done sufficiently.

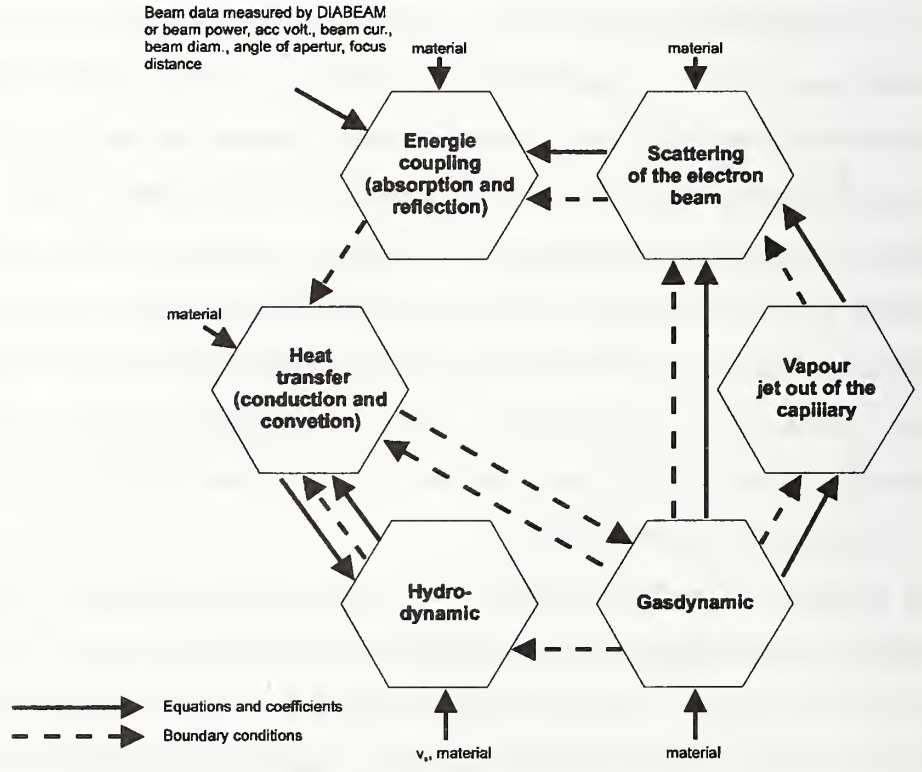

Figure 1: Aspects of the physical model

To sum up it can be said that it is necessary to solve a certain number of single problems which are closely related. By assuming certain parameters it is even possible to solve connected problems analytically (e.g. to calculate the radius of the capillary when solving the heat source problem). The solution of the problem depends in that case on these parameters. By solving all essential separate problems a system of equations for these parameters is generated. This represents a model of the welding process. But only the use of several simplifications which are connected with the physical process leads to a solution of the problem. In the following some separate processes are listed:

scattering above the workpiece

During electron beam welding a vapour-filled capillary is produced inside the workpiece. Because of the different pressures in the capillary and the surrounding vacuum the vapour pours out and accumulates above the workpiece. Due to the scattering of electrons at the vapour atoms the power density distribution and distribution of angles is changed. Therefore, the focussing parameters are also changed. This effect has to be analysed when the vapour density distribution is described. This cannot be reached by making use of the conventional equations for gas dynamic problems because in this case the transition from the gas dynamic fluid to free movement of molecules is not possible. The exact problem can only be solved by using the kinetic Boltzmann equation (1).

scattering in the capillary

The interaction between the electron beam and the vapour above the workpiece and inside the capillary leads to a broadening of the beam (2), a reduction of power density and results in a change of the angle in which the electrons arrive at the surface of the workpiece. On the other hand this results in a change of the absorbed power. For the description of the scattering effect (1) it is helpful to use an approximation of the Boltzmann equation for small and very fast particles and small angles. This assumption can be made because the speed of the gas molecules is much smaller than the speed of the electrons and no kinetic energy is exchanged during the impact, and the electrons are scattered back in a small angle.

energy coupling

The problem of decreasing power density with increasing depth during deep penetration electron beam welding consists of two independent separate problems. In the first part the electron absorption coefficient and the energy of the particle flow in the interval of angles between 1 to 10 degrees have to be calculated. The second part deals with the

determination of the energy distribution at the surface of the capillary which depends on the reflection of electrons.

The first problem can be solved by using the Monte-Carlo method (3). This method can be applied as long as the electron beam responds to classical laws of mechanics and the electrons move on different trajectories. When collisions occur the electrons change their direction of movement and during ionization of the metal atoms and the formation of plasma the electrons loose their energy. The angels at the collisions and the length between the collisions are considered as random variables with probability distributions given by the theory of scattering in quantum mechanics.

The local reflection of the electrons at the capillary wall leads to a new distribution of the delivered energy in the depth and the capillary circumference.

Using the results of the Monte-Carlo method the whole surface of the capillary does not effect the electrons like a mirror. Instead the electrons are distributed at an average reflection angle. At a cylinder shaped reflecting surface, the electron distribution after a multiple reflection and the resulting energy distribution are very difficult to determine. To simplify this the angle between the arriving electrons and the capillary wall increases rapidly after multiple reflections. Therefore the reflection coefficient is also increasing. This means that to obtain a good approximation it is enough to take into account only the first reflection.

gas dynamics

For the model of vapour forming it is assumed that the vapour inside the capillary is saturated. It is also assumed that the momentum of the vapour from the outer limits of the Knudsen-layers is not perpendicular but parallel to the surface. In other words: perpendicular to the surface, the „hydrodynamic" speed at the outer limits of the Knudsen-layer is equal to zero. In that case existing models for vapour forming deliver „zero" for the value of the vapour flow. A one-dimensional approximation is used for the description of the movement of the vapour through the capillary (velocity, pressure, density and temperature of the vapour flow are a function of one coordinate „z" in the direction of the axis of the capillary). The equations of the model are conservation equations regarding mass, impact and energy flow.

heat and mass transport

Heat and hydrodynamic processes in the area of electron beam welding with deep penetration are very complex. The problem consists of two separate problems: on the one

hand the heat transfer and on the other hand the mass transfer. Both problems are closely related. Therefore, the solution of the hydrodynamic problem results into values for coefficients of the equation of heat transfer. The solution of the heat problem determines the boundary conditions for the hydrodynamic equation. The problem is complex because of non-linear physical quantities like viscosity, thermal conductivity etc. There are also non-linear geometric quantities which are directly generated from the solution.

geometry of the workpiece

A completely allocation of the geometry of the workpiece is only possible at the expense of a considerable computational effort. Since the above described calculations are carried out in a personal computer, some simplifications must take place:

According to the division of the workpiece into different calculation layers during the calculation of the capillary the virtual heat sources are also divided because of the heat reflection at the layer boundaries. For the reflection every layer for calculation of the primary heat source is regarded as a 3-dimensional point-shaped heat source which images are calculated. Only the first reflections at the workpiece boundaries are taken into account. To calculate the temperature at a certain point in the workpiece it is necessary to consider on one hand the influence of the primary heat source and on the other hand every single virtual heat source.

3.0 PRACTICAL REALISATION

Development of the simulation software

The simulation algorithm was built with the help of the experience gained during the project. The purpose of this realisation was a strongly modular program. This has the advantage that it can react on new demands also during the development of the program.

User interface

The practical applicability is one of the main aspects of the software. The purpose is to supply the user with a tool which requires no specific knowledge. The complete product can be run on a usual PC. It eliminates the need of investing on expensive hardware. The current program version is fully developed for Windows 95® under the programming environment Borland Delphi 2.0® and is a 32bit program, which can use all potentialities of the graphical environment of Windows 95®. The whole application can be operated to a large extent through a system of object oriented context menus. For instance it is possible to change the system of coordinates by regulating the cut of whole view.

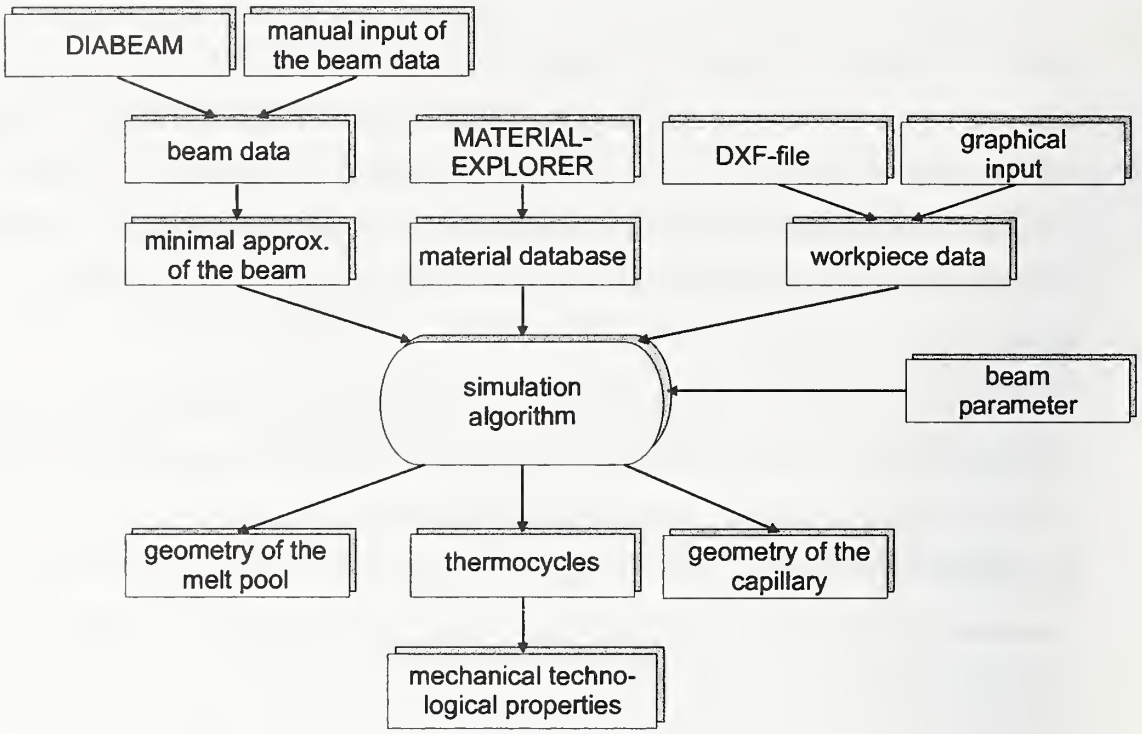

Figure 2: Schematic of the program

In order to increase the user's overview of the simulation process and results, it was attempted to make the program environment possibly modular. One set of input parameters, which consists of materials, beam, some other welding and simulation parameters, leads to only one set of output data. The output also has a modular structure. One part plots dimension and temperature parameters which describe real appearance and behaviour of welding joint. Furthermore, it is possible to output the parameters, that are not connected to the description of the welding joint, but characterize the behaviour of the simulation algorithm.

Input data

The calculation algorithm needs a lot of information concerning material, for example heat conductivity, atomic number or data about chemical compounds. In order to make it easy for the user, specific physical parameters of material are saved in a material database which contains parameters of typical materials. Using a special program, this database can be upgraded. When a new calculation starts, the user chooses from the list of materials the desired material.

In order to calculate the energy distribution it is necessary to have data on the electron

beam, as for example the power distribution or acceleration and the aperture of angle. There are two possibilities: the data can be entered manually on the data come from the output file of the electron beam measuring system DIABEAM®. A numerical description of the beam is built up from measured beams data, i.e. real data are simulated with superposition of some Gaussian distributions. The accuracy of this simulation can be defined by user. There is another set of parameters that constitute an additional category. This set consists of the welding speed, the focus position and the preheated temperature of the material.

In order to increase accuracy of the calculation of the temperature field under the conditions of moving melting pool, alternative calculation of the temperature field under assumption of cylindrical source of heat is possible. For different geometries of the workpiece the corresponding measurements can be graphically entered. It is possible to use data from a „DXF"-file as a source of such measurement.

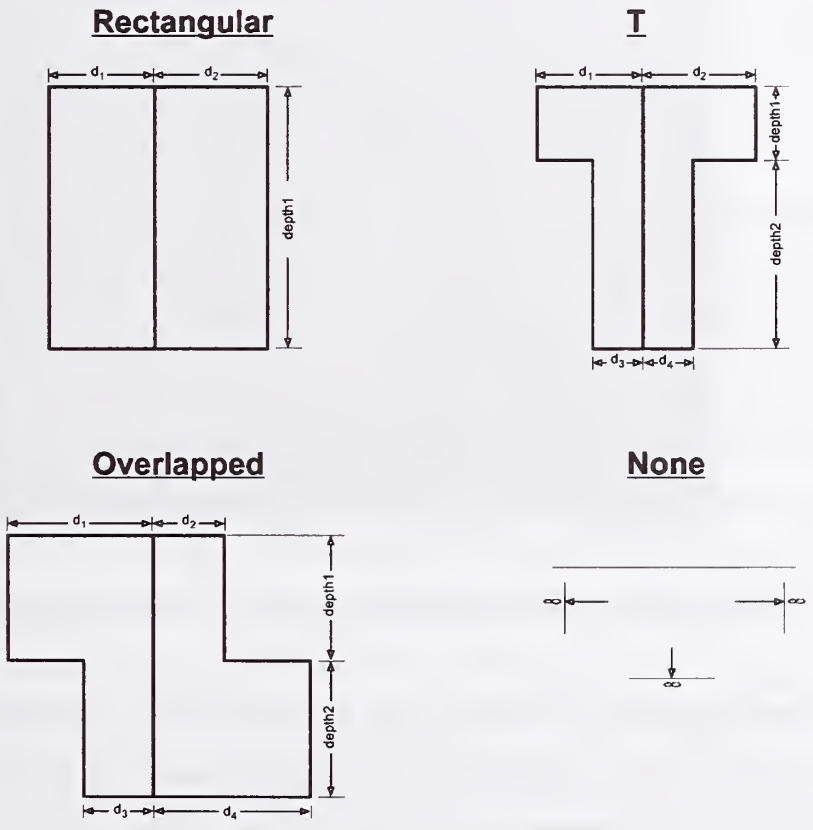

Figure 3: Possible geometries and their dimensions

Output data

The most interesting data obtained during the simulation are plotted on the screen. Plotted data concern the weld geometry or for example the temperature cycles or isotherms. Data referring to the temperature of capillary or the mean convergence of the angle of electron beam which describe the stability and convergence of the algorithm can also be obtained. All output results can be set up and switched on and off in an option's menu, in order to minimise the calculation time and only determine the necessary results.

The application calculates both a side view and a frontal view of the melt pool, so that it is possible to obtain information about the cross and longitudinal dimensions of the melt pool of the stationary heat source, Figure 4. This view and calculation of the dimensions is not limited to the dimension of the melt pool, but it can be used for the determination of any thermo-cycles. Furthermore, it is possible to export the temperature field in various formats like EXCEL® spreadsheets or text files.

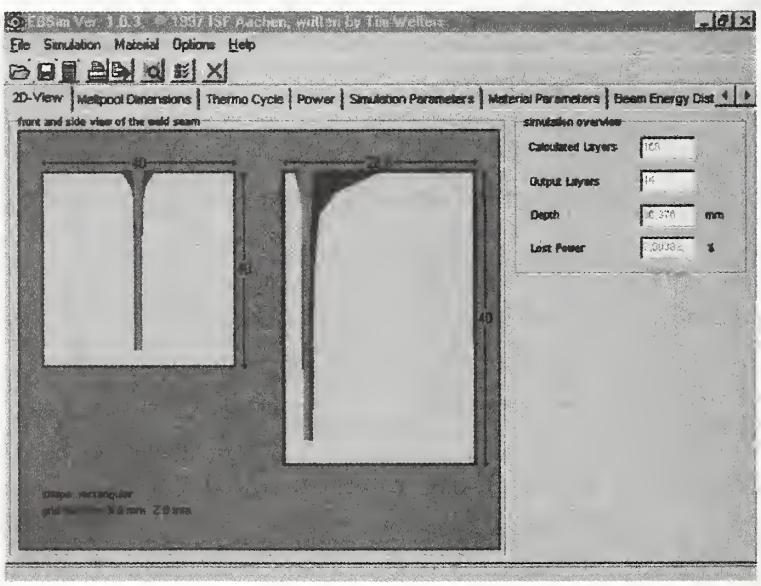

Figure 4: Output of the cross and longitudinal section of a simulated seam

If it is interesting to know the thermo cycle in a special point, for example to obtain the $t_{8/5}$-time the program also calculates the temperature cycle. It is not only possible to fix a time area but also a temperature area. To give the user a clear picture of the geometry of the melt pool it is possible to calculate a 3-dimensional view of the melt pool.

4.0 EXPERIMENT AND RESULTS

Description of the experiments

Experiments of many penetrated weldings and not fully penetrated weldings were carried out. The welding parameters were changed in the area of 6-18kW, 90-150kV and 2-25mm/s. The main materials were high-temperature resistant steel X20CrMoV12.1 and the fine grain steel EStE355. All experiments were performed with an electron beam machine with 150kV/30kW and horizontal gun at the ISF Welding Institute, Aachen.

Description of the simulation parameters used

The parameters used for the simulation are the measured distribution of beam densities, which are read directly from the DIABEAM measurement file (4) and approximated afterwards, the angle of aperture, weld velocity, the acceleration voltage and the beam current. If the measurement of the beam density distribution is not desired or not available, it is possible to input one diameter of the electron beam. In this case it is also necessary to add the percentage of the beam power included in this diameter. The geometry of the workpiece is not so important because simulation and experiments show that the influence of the workpiece borders is not so significant.

Interpretation of the simulation results

Corresponding to the welding experiments and using the welding parameters and the measured beams data from DIABEAM for each case, all weldings were simulated. Due to the differences between the reality and the simulation of the weld depths it is not easy to compare different widths in various weld depths (e.g. the 10%-width at S=45mm not equal to the 10%-width at S=40mm). It should be remarked that in the simulation the penetration depth is higher compared to the weld experiments. The average error is less than 10%. The error occuring at the simulation of the melted area is less than at the simulation of the weld depth. But both simulations lead to bigger quantities. It is obvious that the simulation of the material EStE 355 at 18kW produces an average error about 20%. Such a large error is due to the Humping-Effect and the Spiking-Effect. To reduce the amount of variations of the welding parameters the 18kW weldings experiments were also performed with surface focused beam. However, this leads to an unstable weld pool and a strong Humping-Effect.

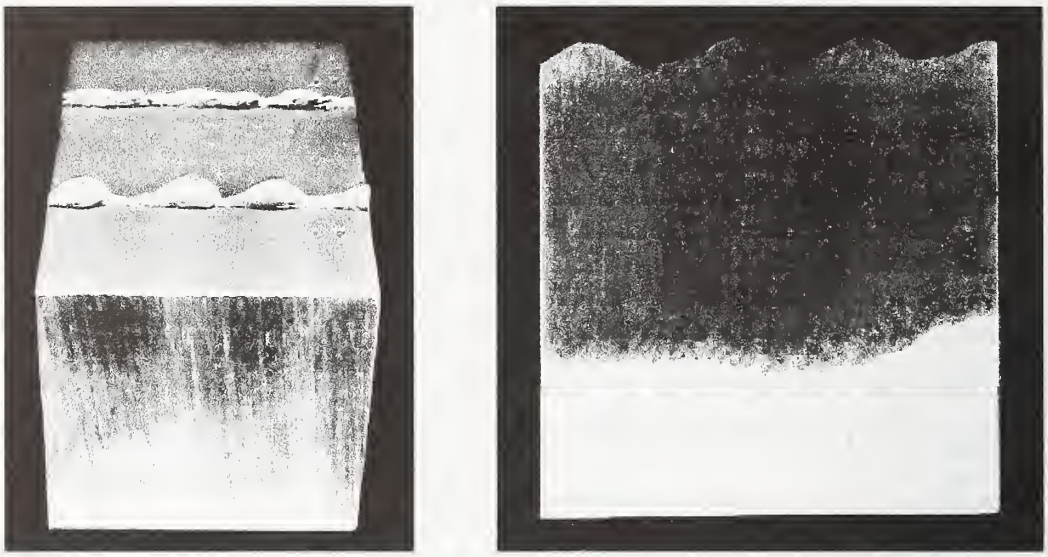

Figure 5: View of the upper bead of a EStE 355 weld sample (l) and view of the longitudinal section (r). The weld parameters are 150kV, 18kW, 15mm/s, surface focused. The Humping-Effect and the Spiking-Effect are good to recognise. The difference between the minimal and maximal depth of the weld is about 7 mm.

The welding experiments with an acceleration of 90kV were not carried out because the beam measurement system could not be used successfully at this acceleration voltage. The simulation results are slightly worse than the error of measurement at the determination of the real seam geometry. At the measurement of the seam geometry problems occur which are produced by the dynamic behaviour of the weldings like Spiking or Humping. The distinction between heat affected zone and melt pool is in spite of a good chemical etching partially possible. In addition inaccuracies of the measurement and of the interpretation do occur. Depending on the material and on the welding parameters, errors can be as large as 20%.

Variation of the material parameters

Although the accuracy of the simulation can be increased, it is interesting to know the relation between material parameters and the results. The material parameters heat capacity, heat conductivity and boiling heat and the consideration of the alloy elements influence the simulation results more strongly than other material parameters. The specification of physical material parameters is critical. The literature gives partly varying values. For parameters of some materials like the surface tension it is not possible to determine the values by experiments or only in a small limited temperature interval. The content of the alloys can also fluctuate. The effects on the welding results are not neglect-

able. The used material parameters should not be interpreted as absolutely fixed values. So it is interesting to analyse the influence of changes in the material parameters on the welding results.

In a first step the values of the heat capacity, the heat conductivity and the boiling heat of the materiel X20CrMoV12.1 were changed in an area of +/- 10%. Here it was possible to see that increasing the value of the boiling heat reduces the weld depth and increases the melted area. Increasing the value of the heat conductivity or heat capacity the simulated weld depth and the melted area decrease. It should be noted that by optimising the material parameters the quality of the simulation can be increased.

5.0 SUMMARY

In the frame of a cooperation project between the Technical University St. Petersburg, Russia and the ISF Aachen, Germany the simulation program EBSim was developed. It combines a simulation algorithm with a user friendly interface. Simulation results like the shape of the melt pool and additional information like the thermo cycles can be obtained graphically. This program makes use of databases that store the large amount of input parameters, specially the material parameters, so it is easy to use for non specialists too.

The comparison of the simulation results of EBSim and experimental results of not fully penetrated welds of the materials X20CrMoV12.1 (1.4922) and EStE 355 (1.1106) showed that the prediction of the weld depth and the melted area is in keeping with the trend. The electron beam welding process is quite good researched in the mostly parts. The combination of the results of the individual physical phenomena is connected with some practical problems. On the one hand, the complete evaluation of all differential equations describing the system is not possible under current computing power. On the other hand, the determination of many boundary values of the simulation like the surface tension in dependency of the temperature is uncertain. Furthermore, the experimental verification of the simulation results is complicated by various factors:

- the simulation of all physical phenomena is very complex. This makes the verification of the individual parts more complex;
- an experimental verification of all parameter dependencies needs thousands of experimental weldings;
- the determination of the experimental values is not error free. For example, the deter-

mination of the weld deepth is influenced by Spiking and Humping-Effects;

- the determination of the geometry of the beam, specially the determination of the angle of aperture, is not error free. The geometry of the beam is important for the process of energy coupling. Small fluctuations of the machine parameters during the welding leads to measurable changes of the welding;
- the presented model solves the physical problem on a static way, so that a prediction of the dynamical behaviour of the capillary and the weld seam is not possible.

In spite of some problems this paper shows that it is possible to develop a fundamental and in a wide area quantitatively correct description (in comparison to the error of the measurement of the experimental results) of the electron beam process. So is the prediction of the welding results for material close to iron better than the prediction of high alloyed materials. This shows that a further development for other materials is necessary.

Acknowledgements:

The model described in this paper is partly accrued in a common project of the ISF Aachen and the CL&PT, TU St. Petersburg, St. Petersburg, Russia. The project was financed by the DFG (Deutsche Forschungsgemeinschaft). Both institutes wish to record their thanks for this funding of the DFG project ('Mathematische Simulation des Elektronenstrahl-Schweißprozesses und der sich einstellenden mechanischen und metallurgischen Kennwerte der Schweißung', Projekt Nr.:436RUS113/55) to the BMBF (Bundesminiesterium für Bildung und Forschung). WINDOWS 95 and EXCEL are trademarks of MICROSOFT and DELPHI 2.0 is a trademark of BORLAND INTERNATIONAL.

6.0 LITERATURE

[1] U. Dilthey, S. Böhm, T. Welters, S. Ilyin, G. Turichin:
EBSIM - New Simulation Software for Electron Beam Welding with Deep Penetration
IIW Doc. No. IV-669-97

[2] V. Bashenko, E. Mitkevich, G. Turichin, D. Ivanov:
Energy absorption law in cavity in EBW
2nd Int. Conf. on EBW, Varna, Bulgaria, 1988, pp460-463

[3] A.F. Akkermann, U.M. Nikituschev, W.A. Botwin:
Problem des Transfers von schnellen Elektronen in Stoffe mit der Monte-Carlo-Methode

[4] U. Dilthey, S. Böhm, M. Dobner, G. Träger:
Comparability, Reproducability and Portability of the Electron Beam Technology Using New Tools of the DIABEAM Measurement Device
IIW Doc. No. IV-650-96

INDUSTRIAL FAULT DETECTION AND ARC STABILITY MEASUREMENT USING WELDING SIGNATURES

P W Hughes, P Gillespie, S W Simpson

ABSTRACT

The use of signature images for on-line analysis of arc welding electrical data in industrial applications is described. Welding signature images are data objects or structures that can be manipulated to yield on-line information about welding processes. Although numerically intensive mathematical processing is required, this is hidden from the end-user. Arc stability is gauged by an inner product comparison of an on-line signature image with the immediately preceding signatures. Similarly, welding quality is gauged by an inner product comparison of a reference signature image with an on-line signature image, and welding faults can be detected. Industrial applications including applications where conditions vary during a weld are described.

KEYWORDS

welding signatures, information processing, on-line fault detection, welding quality, arc stability, WeldPrint.

INTRODUCTION

Signal processing of arc welding data to produce signature images is being used for on-line fault detection and process improvement in fully automatic industrial welding applications. The ability to detect faults in real time without time consuming post production analysis allows the manufacturing process to be halted as soon as a fault occurs. This saves rework and greatly accelerates process improvement.

Compared to other forms of sensing arc conditions such as acoustic or optical, electrical sensing offers distinct advantages in that costly diagnostic equipment is not needed and the necessary equipment can be located remotely. The measurement technique is robust enough for most industrial environments and is non-intrusive.

In the following section, generation of signature images from sampled electrical data is discussed, including the mathematical framework for manipulating the signatures. These signatures are used to quantify the stability of the arc and the quality of the welds produced. Signature tracking, a technique to allow for expected variations in conditions during a welding run, is outlined.

Industrial applications using Stability, Quality and Tracking for fault detection and process improvement are then described.

GENERATION OF WELDING SIGNATURE IMAGES

Welding signature images are statistical data objects generated from blocks of sampled welding data. Data collection is via non-invasive electrical measurement - generally the welding voltage or current. Typically 2000 to 4000 data points are collected in 0.25-0.5 seconds. The data object is filtered to remove statistical noise resulting from the finite sample size, and then remapped and scaled non-linearly to generate a signature image, which enhances the information about the welding arc and weld pool that is available in the data block during that time period.

Vector space operations are defined for the data objects, specifically an inner product that leads to a definition of length and permits manipulation and comparison of signature images.

WELDING ARC STABILITY

The comparison of successive signature images acquired from a welding process allows quantification of arc stability. The stability can be defined as how closely the signature at a given time matches what would be predicted from the signatures recorded immediately before. A perfect match will give an inner product of unity, or 100%.

Until now, welding arc stability has proven difficult to quantify for different welding processes. Stability in the ordinary electrical sense is inappropriate in gas metal arc welding. For example, the well-known process of short arc metal transfer is technically an unstable non-linear (limit cycle) oscillation.

Tests verifying that signature images do in fact give a measure that relates to the phenomena occurring during welding and, in particular, during the metal transfer process, have been performed. A laser shadowgraph arrangement (ref 1) was used to record droplet images with a video camera and computer image analysis was employed to determine the droplet diameter distribution in a gas metal arc weld. Figure 1 plots average stability (open circles) measured for a set of welding runs at different wire feed rates. The welds were steel bead-on-plate with wire diameter 0.9mm, voltage 30V and 20mm contact tip-to-workpiece separation. Approximately 200 droplets were analysed for each run. The mean droplet diameter is also plotted in Figure 1 (solid circles). At wire feed rates from 150mm/s to 160mm/s the average droplet size moves downwards from a size greater than the wire diameter to a size smaller than the wire diameter, and this corresponds to the transition from globular to spray metal transfer.

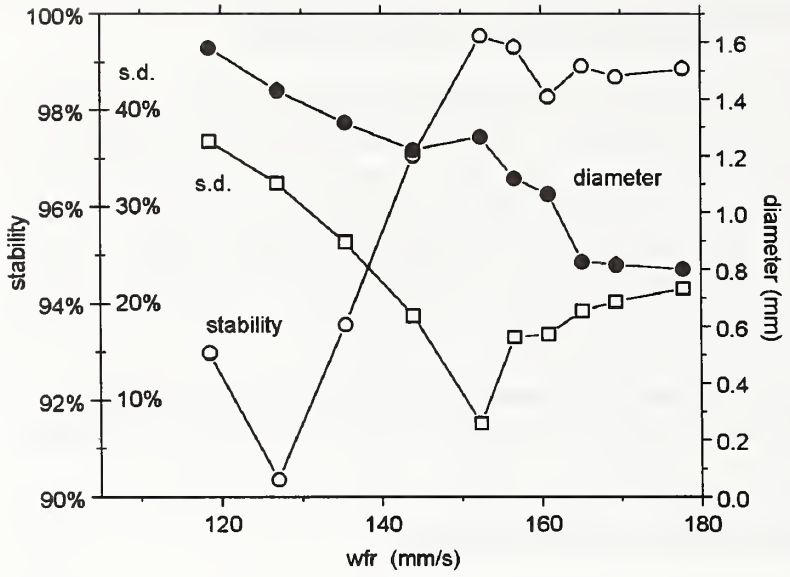

Figure 1. Measured stability (open circles), average droplet diameter (solid circles) and standard deviation of droplet diameters (open squares) as a function of wire feed speed.

Relating the stability measurements (open circles) to the transfer regime as indicated by the droplet diameter (solid circles) in Figure 1, it can be seen that the stability is much lower for globular transfer, around 92%, compared to spray transfer, where it is around 99%. This agrees with common experience in welding. However the stability measurement shows a surprising feature: instead of a smooth increase in stability through the transition from 150mm/s to 160mm/s, there is a stability peak before the transition where the stability rises to 99.5%, still in the globular transfer region. Confirmation that this point does in fact represent a very stable operating condition comes from the calculated standard deviations of the droplet diameter distributions, which measure the spread of droplet sizes in metal transfer. Figure 1 also plots the standard deviation of the droplet diameters divided by the average diameter expressed as a percentage (open squares). The curve shows a pronounced minimum in the standard deviation at 150mm/s, the same point as the stability maximum. The good agreement demonstrates that weld stability measurement correlates closely with the physical phenomena taking place during welding and is a valuable diagnostic welding tool.

Example of Using Stability Measurement for Process Improvement

Figures 2a, 2b and 2c below show the voltage, current and stability average over 5 welds made on an automotive component by a robot using GMAW to make a lap joint between the top and bottom sections. The welding is done with 1.2mm solid wire and Argon/CO2 gas mixture.

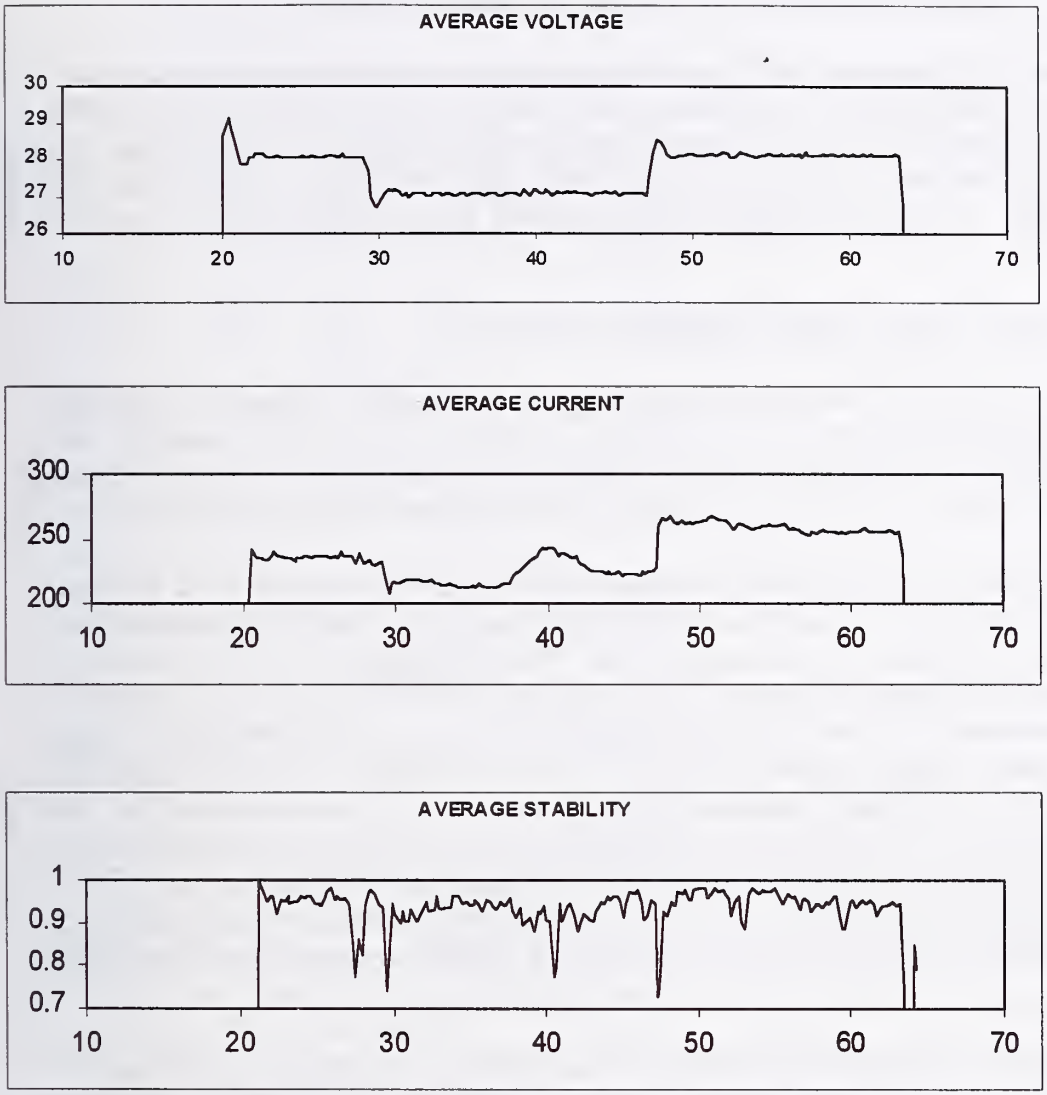

Figure 2. Average over 5 welds made on automotive components by a robot using GMAW. (a) Voltage, (b) Current and (c) Stability

Routine destructive testing has found deficiencies in these welds from time to time, probably associated with fit-up and electrical interference from the stop–start welding being done on the same component by other robots. The procedure is altered at 29 seconds, and again at 47 seconds to minimise these problems, but they still persist.

It is not obvious from examination of the voltage and current traces where these welds will be most prone to problems. The two points where the procedure changes are readily identified. It can be seen from the stability trace that apart from the above two points, the arc is quite unstable at 27 seconds and between 39 and 42 seconds. The arc is also potentially unstable at 53 and 60 seconds. The lack of arc stability means poor reproducibility and an unreliable process. With the information on precisely where this is likely to occur, the fit-up, torch position and earthing arrangements can be altered and improvements verified.

SIGNATURE IMAGES TO MEASURE QUALITY

The simplest approach to measure quality and detect faults is to compare a reference signature image with data collected on-line. The resultant inner product x 100% can be described as the (instantaneous) weld quality, provided the reference is a good quality weld. When the signature images differ, the quality falls below 100% and a sufficient difference can be described as a fault. A typical level below which an event would be described as a fault is 85%.

Laboratory Example of How Quality Measurement Works

Figure 3(a) shows the result of reducing the gas flow in short-arc welding. Here, the reference signature was collected during the first one second of welding after a trigger delay of one second to allow the wire to feed down and a stable arc to be established. The weld is steel bead-on-plate with 1.2mm wire, a 20mm contact tip-to-work separation and a current of 190A.

At time 17s during the run, the gas flow was reduced from 26 litres per minute to 12 litres per minute. Although there is no observable change in the average voltage of each data block (Figure 3b), there is a change in the details of the waveform (Figure 3a). This leads to a difference between the measured signature image and the reference after time 17s, which is indicated by a deterioration in the weld quality (Figure 3c). It can also be seen that the weld quality is not constant, suggesting that the welding is less stable after 17s. A point to note in this comparison with a reference signature image is that there is an assumption that the reference is representative of a good weld, and changes from the reference in any direction in signature image space represent a deterioration in weld quality and eventually a fault. If, for example, a fault were present during the initial one second period when the reference signature image was recorded, subsequent welding would be (incorrectly) compared with the faulty reference.

Nevertheless, using a reference at the start of a long welding run does have advantages in terms of simplicity. A more reliable method of making a comparison is to record a reference signature image or series of signature images for a qualified welding procedure under good welding conditions. In this case it is possible to inspect and test the resultant welds to ensure that the signature images represent good welding. Such reference sequences can then be recalled for comparison on-line during production welding.

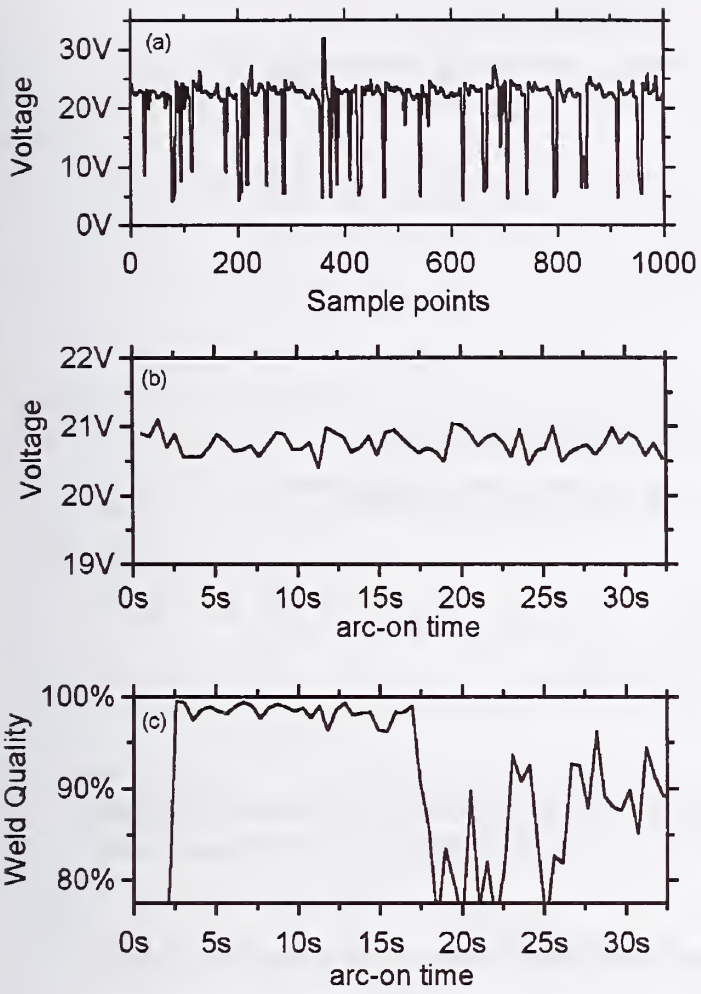

Figure 3. Effect of Gas Flow on Weld Quality. (a) Sampled block of 1000 data points; (b) average voltage for each block through welding run; (c) welding quality calculated from signature images (see text).

Industrial Example of Process Improvement Using Quality Measurement

At a Welded Beam Plant, the signal imaging quality measurement has been used to fine-tune the welding process, which led to a 6% increase in throughput.

The plant uses two H Master welding stations. Two fillet welds are completed on one side of the I beam in one pass through the first station before the beam is turned over and the two fillet welds on the other side are completed in one pass through the other station. All four fillet welds are performed with tandem arc (lead wire AC, trailing wire DC) submerged arc welding.

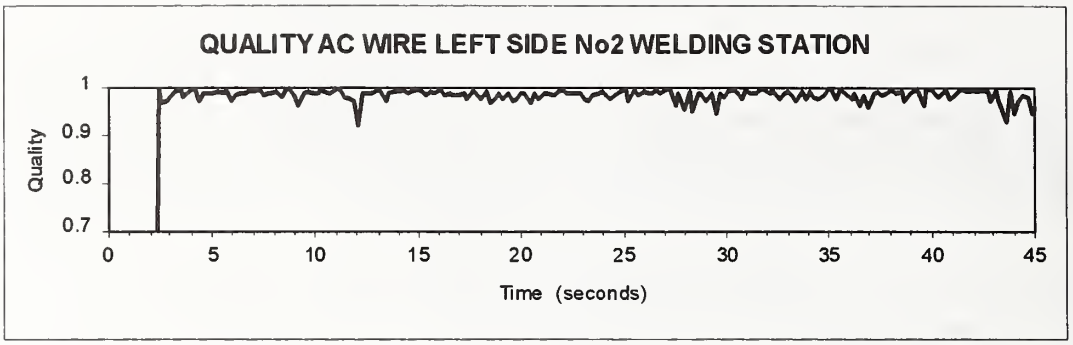

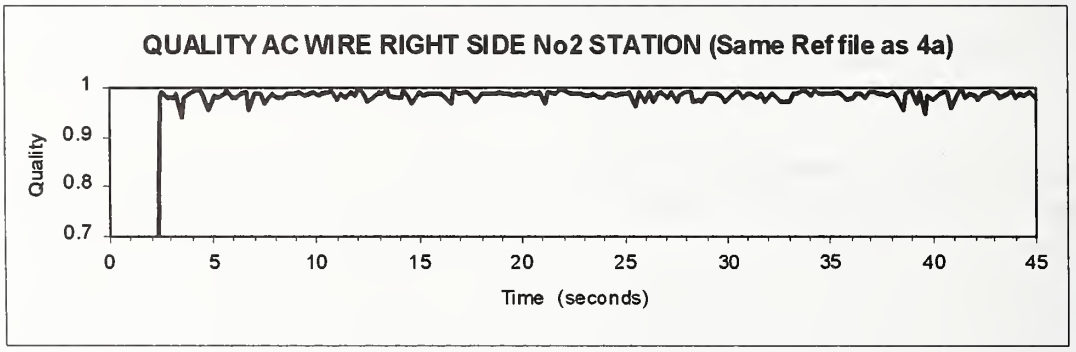

Figure 4 (a) Quality as measured on the AC wire on the left side of the second welding station. (b) Quality as measured on the AC wire on the right of the same station using the same reference file.

As can be seen from the above quality measures, the welding is very consistent on both sides.

This is the result of process improvements made using WeldPrint, the commercially available form of signature image analysis, to identify problems with earthing and voltage control, leading to the redesign of both and the establishment of a maintenance program. This was not possible by simply measuring voltage and current. Changes in the target settings of 0.25 volts were demonstrated to affect the quality measure and the actual welding performance, even though this was only a fraction of the fluctuations occurring during normal welding.

WELD TRACKING USING SIGNATURE IMAGES

Where the intended welding conditions are steady state, the measurement of quality and stability are adequate. However, frequently in industrial situations the conditions are changed by design during the weld. This could be for example where a weld overlaps at the end of a circumferential weld, or due to programmed changes to welding parameters. In these circumstances the changes which are expected should not show as a fault or deterioration in quality. At the same time, the quality needs to be measured for the entire weld.

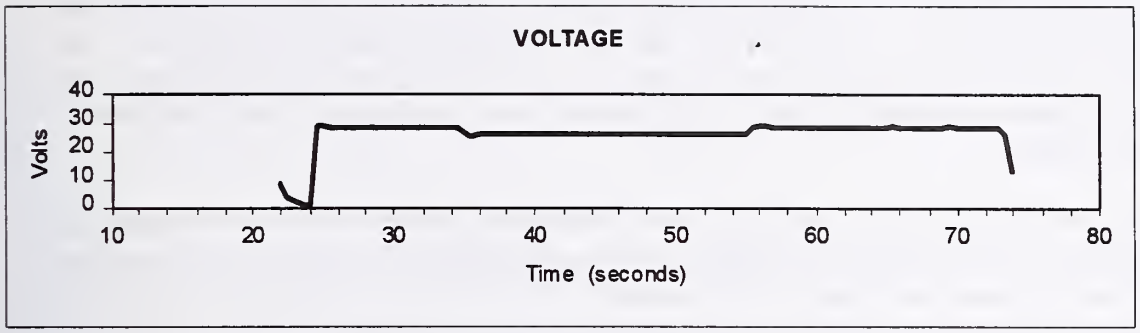

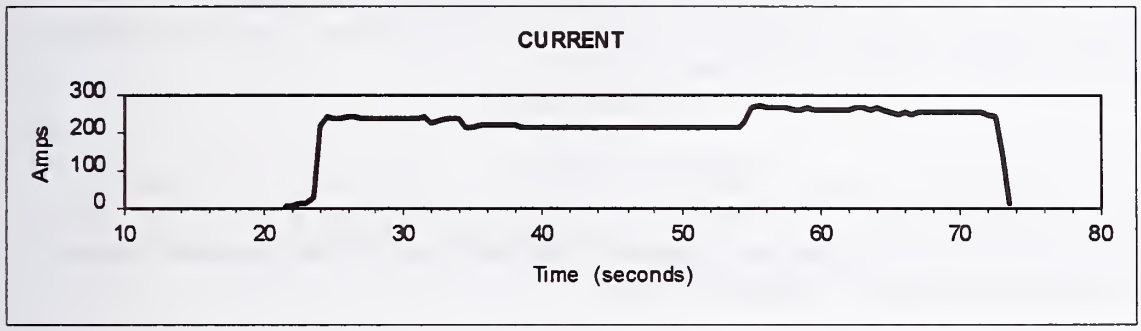

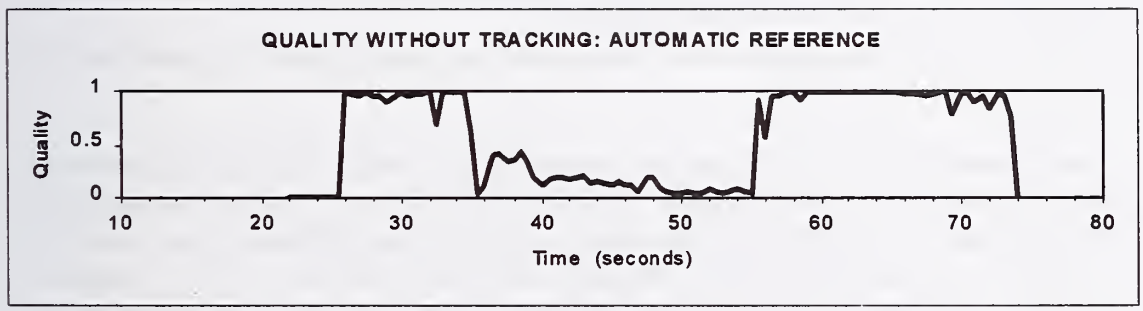

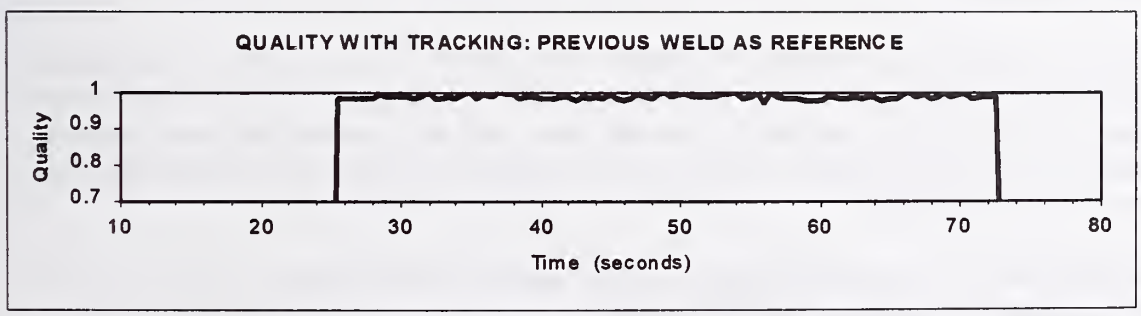

Figures 5 Robotic GMAW on automotive component with two procedure changes (a) Voltage (b) Current (c) Quality measured with automatic reference and without tracking and (d) Quality measured using previous weld as reference and with tracking.

To accommodate this requirement, tracking has been developed. Mathematically, a linear subspace is defined from the acceptable signatures, and the measured signature is divided into a component orthogonal to the subspace and a component within the subspace. Any component orthogonal to the subspace represents an error component, while the component within the subspace represents an error if it does not lie on the line or "track" between the acceptable signatures.

The data in the above figures is again from the automotive industry where components are being welded by robots using GMAW. Figures 5(a) and 5(b) are the current and voltage traces of a weld and the parameter changes at 35 seconds and 55 seconds are apparent. Figure 5(c) and 5(d) show the quality measured without tracking and with tracking.

With the previous weld as the reference, it is possible to measure the quality of this weld relative to the previous weld along the entire length using tracking, even though the welding goes from spray transfer to short arc and back to spray.

CONCLUSIONS

This paper has described several current industrial applications of welding signature images. The key advantages of signature image analysis are:

(i) robustness, ability to extract data features, and immunity from noise since the basis of the inner product operations is cross correlation, and
(ii) it requires only a simple training process (or none at all) and has the ability to generalise to a wide range of industrial situations

Welding signature images offer a fault detection capability in a range of welding processes, including robotic weld sequences where fully automated operation will become increasingly important in coming years. Tracking expected changes during welding allows the technique to be extended from simple welding processes operating under fixed conditions to very complex welding procedures. Welding arc stability from signature images provides a new quantitative process measurement tool, which is being used for process improvement and welding procedure development.

Although the information processing embodied in signature image analysis is relatively sophisticated, this complexity is hidden from the end user. The key to successful application of information technology in welding in coming years will be a convenient user interface which allows the welding engineer to focus on the welding task and not the monitoring and control hardware and software.

Future developments of signature imaging include automatic identification of the cause of faults and interfaces to control the welding process.

ACKNOWLEDGMENT

The authors gratefully acknowledge financial support from the Australian Research Council.

REFERENCES

1. S.W. Simpson, P. Zhu, S. Law, J. Baba, and M. Rados, "Metal Transfer Modes in Gas Metal Arc Welding", International Institute of Welding Asian Pacific Welding Congress - Productivity Beyond 2000, Auckland, 3, 1319-1326, February 1996.

APPLICATION OF VISION SENSOR FOR WELDING AUTOMATION IN SHIPBUILDING

W.-S.Yoo*, S.-J.Na*, J.-W.Yoon, Y.-S.Han*****

ABSTRACT

For welding automation in shipbuilding it is necessary to compensate for such complications as workpiece shape errors, setting errors, jig errors and weldment distortions. At the same time it is also required to track the weld seam accurately to stabilize welding quality and improve productivity. Recently developed automatic welding systems can simultaneously perform both seam tracking and adaptive control of welding conditions based on information obtained from either a single sensor or combined sensors.

Among various sensors the vision sensor is probably the most powerful form of sensory feedback, because it can provide a 3-D geometry information in detail and can be used with workpieces of arbitrary shape without requiring any contact or interfering with the manufacturing process.

In this paper three examples are presented to demonstrate the research effort on application of vision sensor to welding automation for shipbuilding in Korea.

INTRODUCTION

In a variety of robot applications in manufacturing, sensing of the exact location and orientation of a workpiece, and its detailed surface geometry is needed for the robot guidance. Among various sensors of contact and non-contact type, the vision sensor is probably the most powerful form of sensory feedback because it can provide a 3-D geometry information of workpieces. Applications of vision sensors are spreading into many areas of manufacturing processes due to the fact that the price of vision sensor components such as CCD camera, diode laser and DSP board becomes lower and lower.

The active vision sensor based on optical triangulation is classified into two types according to the beam characteristics: projected sheet of light or scanned point beam (Ref. 1). Although the vision sensor with projected sheet of light is largely influenced by arc noise and the preprocessing time of image is considerably long, it is widely used because it is relatively cheap and its construction is simple (Ref. 2-5). In spite of the complex structure and relatively high price, the application of vision sensor with a scanned point beam increases steadily, because the effect of arc noise is low and the preprocessing time of captured image is relatively short (Ref. 6-8). In addition to that, this type of laser vision sensor provides a possibility of real time control of the observation zone.

* Dept. of Mech. Eng., KAIST, Yusong-gu, Taejon, Korea
** Samsung Heavy Ind. Co. Ltd., Shinhyun-up, Kyungnam, Korea
*** Daewoo Heavy Ind. Co. Ltd., Jangseungpo-up, Kyungnam, Korea

VISION SENSOR

Figure 1 shows the classification of 3-D vision sensing methods based on the principle of operation. In the industrial environment, the proximity of objects allows the active direct measurement method based on optical triangulation to be used more widely than other methods including passive stereo vision type or time-of-flight method. Applications of indirect measurement methods are highly limited because of the harsh environment of welding such as high temperature arc plasma, spatter and welding fume.

Active direct measurement systems replace one of the cameras in the stereo vision system with a source of controlled illumination called structured light. The term 'structured light' refers to a pattern of lines, triangles, or grids projected on the surface being measured. Commonly, the structured light may be projected serially on the surface by scanning a collimated laser beam or it can be a sheet of light generated by fanning a laser beam through a cylindrical lens, Figure 2. Many systems based on scanning a beam of light use a mirror attached to a galvanometer whose oscillation is controlled by a microcomputer. 1-D CCD cell is used in this system to capture the light reflected from the object surface, while 2-D CCD cell is used in systems based on a sheet of light.

LASER VISION SENSOR FOR PRE-ASSEMBLING OF STIFFENERS

The block assembly production method, a result of the development in welding technology, is the most common method of shipbuilding today. Common block assembly process is composed of several production phases such as manufacturing of flat and curved panels, pre-assembling of stiffeners on plate, assembling of the pre-assembled parts in sections, assembling of blocks and erection of blocks in the building dock.

One of big shipyards in Korea has devoted a few years to developing an automatic welding system for pre-assembling of stiffeners on plate. The developed system is equipped with a gantry type welding station on which two 6-axis articulated welding robots are suspended to trace two fillet joints of stiffeners simultaneously, Figure 3. This welding gantry covers a working area of 9m x 22m and is designed to allow a positional repeatability of ±0.1mm accuracy. Inverter type welding power sources with 500A/42V capability were integrated into the automatic welding system with flux-cored wire of 1.2mm diameter and shielding gas of 100% CO_2.

The laser vision sensor was designed, manufactured and implemented for automatic welding in pre-assembling of stiffeners by cooperative research effort of the industry and KAIST. It was based on optical triangulation of the projected sheet of light with lateral field of view of 51mm(resolution: 0.03mm – 0.1mm) and depth of field of 143mm(resolution: 0.15mm – 0.24mm). The sensor was mounted on only one of two articulated welding robots, because the geometrical information of one joint can be also used to define the other joint of stiffeners, Figure 4. It was attached to a two-axis device whose motion is controlled to avoid the collision of sensor with weldments.

The developed sensor was calibrated by using a block of predefined geometry and could

process up to 10 image frames per second. The captured image of the sheet of reflected laser beam was thinned to produce lines. The intersection points of lines were then calculated to determine the weld seam point and the size of gap between plate and stiffener. Various joint types such as fillet, V-groove, I-butt and lap joint could be identified according to the geometrical data obtained. Fuzzy logic and neural network algorithms were incorporated into the main program for the adaptive control of welding parameters. The laser vision system could carry out various functions such as seam tracking, recognition of weld start/end point, gap sensing and adaptive control of welding condition, multi-pass welding and weld bead sensing, Figure 5.

LASER VISION SENSOR FOR CORRUGATED MEMBRANES

The development of an automatic welding process of the LNG tanker is necessary to meet demands for consistent weld quality and precise welding, and consequently to provide a secure transport of LNG. The vision sensor is suitable for automatic welding of membrane type LNG tanker because of its high resolution without affecting the surface condition of thin corrugated membranes and its relatively low cost.

The automatic welding system is equipped with a portable robot. It moves in two rectilinear coordinates (horizontal and vertical), and rotates by a torch rotation mechanism, Figure 6. The device of torch rotation has a unique structure to keep the torch tip end at a constant position, while the torch angle changes continuously to maintain the welding torch substantially perpendicular to the surface of workpiece. The vision sensor is mounted at a side of torch holder, and consequently its motion is the same as that of the torch.

The vision sensor was based on optical triangulation of projected sheet of laser beam with lateral field of view of 35mm(resolution at center: 0.037mm) and depth of field of 35mm (average resolution: 0.070mm). The image data of the workpiece surface captured by the vision sensor were processed to give information on the height and slope of corrugated membranes. In this study it was assumed that the corrugated panel has a considerably good straight side, so that the sensor-based weld line tracking can be neglected.

For weldments with complicated shape like the corrugated membrane it is difficult to determine the proper configuration of sensory system because of the rotating motion of torch and sensor which will result in very fast change of laser illumination line. Many of data points can be missed, because they are located out of the field of view of the sensor or the laser beam reflected from the weldment surface does not reach the camera due to the interference with workpiece. The sensor configuration in relation to the relative location of camera and laser, and separate angle between them was optimized to give the best measurement efficiency.

The specular surface of corrugated panels causes the multi-reflection of projected laser sheet, and adversely affects the recognition of weld line height, Figure 7. The image of specular reflection shown in right side of the figure can be brighter than that of original pattern. This phenomenon occurs severely especially at the start and end of steep corrugation. The original pattern of the projected laser beam was extracted from the raw image data by using

the continuity of corrugated panels in height variation. The initial image was that captured just before the start of corrugation, because the flat part did not cause multi-reflection and consequently any disturbances in raw image data.

LASER VISION SENSOR FOR BLOCK ASSEMBLY

Design of a conceptual mobile platform-manipulator welding system is discussed in this section. This system is equipped with a wheeled mobile platform, a manipulator with articulated arms and a laser vision sensor, Figure 8. The mobile platform has two independent driving wheels at the center of each side and two passive castor wheels at the center of front and rear of the platform, while the manipulator has 6 degrees of freedom. The vision sensor attached on the mobile platform has one degree of freedom in vertical direction. Robotic welding operations require trajectory control of the welding torch mounted on the end-effector of the robot. Welding of two vertical plates on a flat plate is considered to investigate the application of a laser vision sensor for automatic seam tracking.

The laser vision sensor is based on optical triangulation of scanned point beam, because its measurement area can be easily controlled according to the welding condition. Its depth of measurement range was 890 mm with average resolution of 0.87 mm. The range of lateral measurement and scanning rate of the sensor are variable with a maximum value of 50 ° and 80 Hz respectively. These two sensor parameters and the sampling rate will determine the sensor resolution in lateral direction.

Figure 9 shows some typical image patterns captured at various sensor positions to find feature points of P1 to P5. At first some characteristic features should be extracted from the image data to identify the pattern categories. For this purpose several parameters were tested and it was revealed that the sum of coordinates of each image pixel and the maximum difference of coordinates of two consecutive pixels are the most appropriate to differentiate the image pattern from each other, Figure 10.

A neural network using two beforementioned parameters as inputs and two hidden layers was developed to find the pattern type as output. Back propagation algorithm was adopted to teach the neural network by using the geometrical patterns determined by simulations. Three image patterns of the weld seam (pattern 1-1, 1-2 and 1-3) were almost identical after the characteristic features, so that they were classified in one group at the stage of neural network, Table 1. For the pattern 2, 3 and 4 the image data were processed using the line segmentation method to determine the distinctive feature. This feature of each pattern can be then used to find the weld seam or its end position for automatic welding system.

For the image pattern 1-1, 1-2 and 1-3, the intersecting point of two line segments was firstly determined. It was then transformed into the three dimensional space to differentiate the pattern type of weld seam. Finally the image data were processed to find the weld line for automatic seam tracking.

CONCLUSIONS

Laser vision sensors with the principle of active direct measurement were developed for automatic welding of shipbuilding industries in Korea. The cooperative research between industry and research institute was essential, since the laser vision sensor should compose the whole automatic welding system.

Two of three laser vision sensors presented in this paper were based on optical triangulation of projected sheet of laser beam. The third one was the type of scanned point beam, because its measurement range and resolution can be easily controlled. The laser vision system could carry out various functions such as seam tracking, recognition of weld start/end point, gap sensing and adaptive control of welding condition, multi-pass welding and weld bead sensing.

REFERENCES

1. Lee, C.W.; and Na, S.-J. 1993. Vision sensor for welding automation. *Journal of the Korean Welding Society* 11(3): 10-21
2. Clocksin, W.F.; Bromley, J.S.E.; Davey, P.G.; Vidler, A.R.; and Morgan, C.G. 1985. An implementation of model-based visual feedback for robotic arc welding of thin sheet steel. *The International Journal of Robotics Research* 4(1): 13-26
3. Richardson, R.W. 1986. Robotic weld joint tracking systems – theory and implementation methods. *Welding Journal* 65(11): 43-51
4. Agapakis, J.E.; Katz, J.M.; Koifman, M.; Epstein, G.N.; Friedman, J.M.; Eyring, D.O.; and Rutishauser, H.J. 1986. Joint tracking and adaptive robotic welding using vision sensing of the weld joint geometry. *Welding Journal* 65(11): 33-41
5. Niepold, R.; and Brummer, F. 1987. PASS – a visual sensor for seam tracking and on-line process parameter control in arc welding applications. Robotic Welding: IFS Ltd.: 129-140
6. Oomen, G.L.; and Verbeek, W.J.P.A. 1987. A real-time optical profile sensor for robot arc welding. Robotic Welding: IFS Ltd.: 117-128
7. Bjorkelund, M. 1987. A true seam tracker for arc welding. Robotic Welding: IFS Ltd.: 167-177
8. Nitzan, D. 1988. Three-dimensional vision structure for robot applications. *IEEE Trans. on PAMI* 10(3): 291-309

Table 1 Output of neural network for captured images

	Output of Neural Network			
	y_1	y_2	y_3	y_4
Captured Image 1-1	**0.989871**	0.000000	0.011705	0.000005
Captured Image 1-2	**0.931313**	0.000000	0.095693	0.000008
Captured Image 1-3	**0.990139**	0.000000	0.011015	0.000005
Captured Image 2	0.006624	**0.920713**	0.016061	0.029989
Captured Image 3	0.009474	0.012195	**0.970208**	0.023555
Captured Image 4	0.014312	0.000000	0.000816	**0.990243**

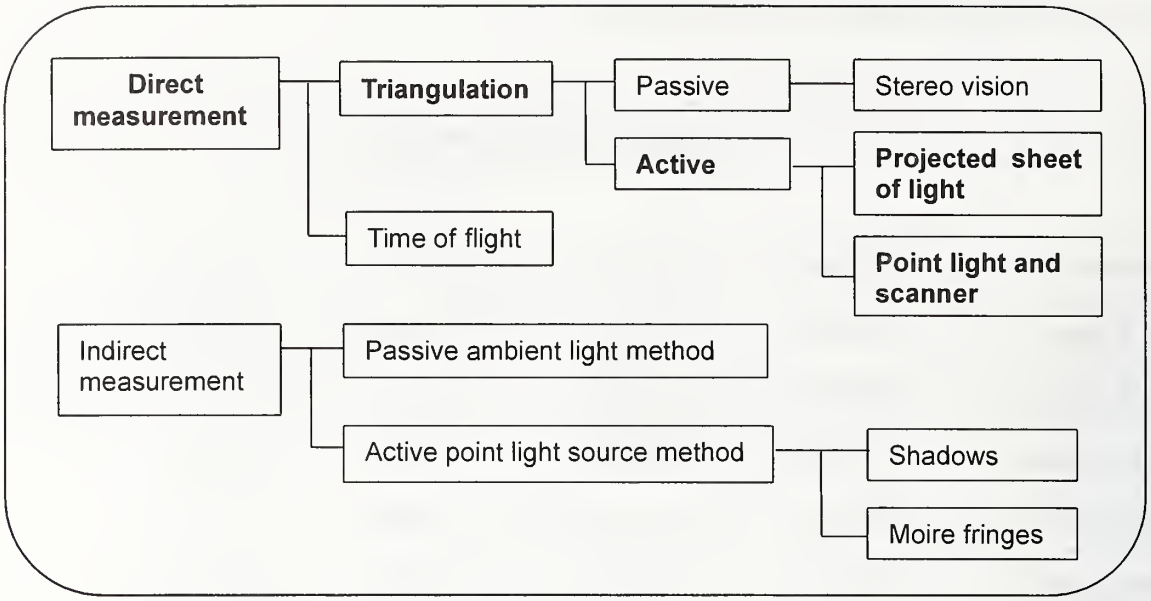

Fig. 1 Classifications of 3-D vision sensing methods

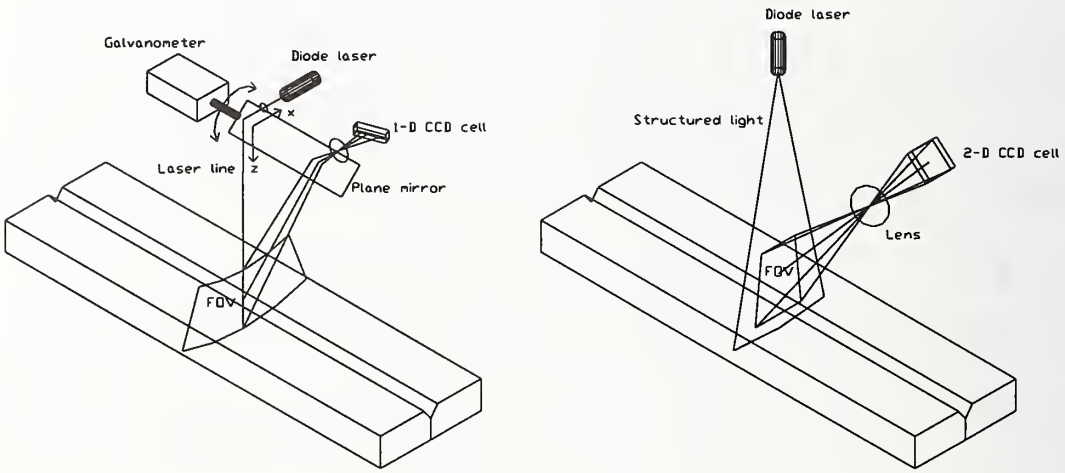

Fig. 2 Principle of optical triangulation of structured light

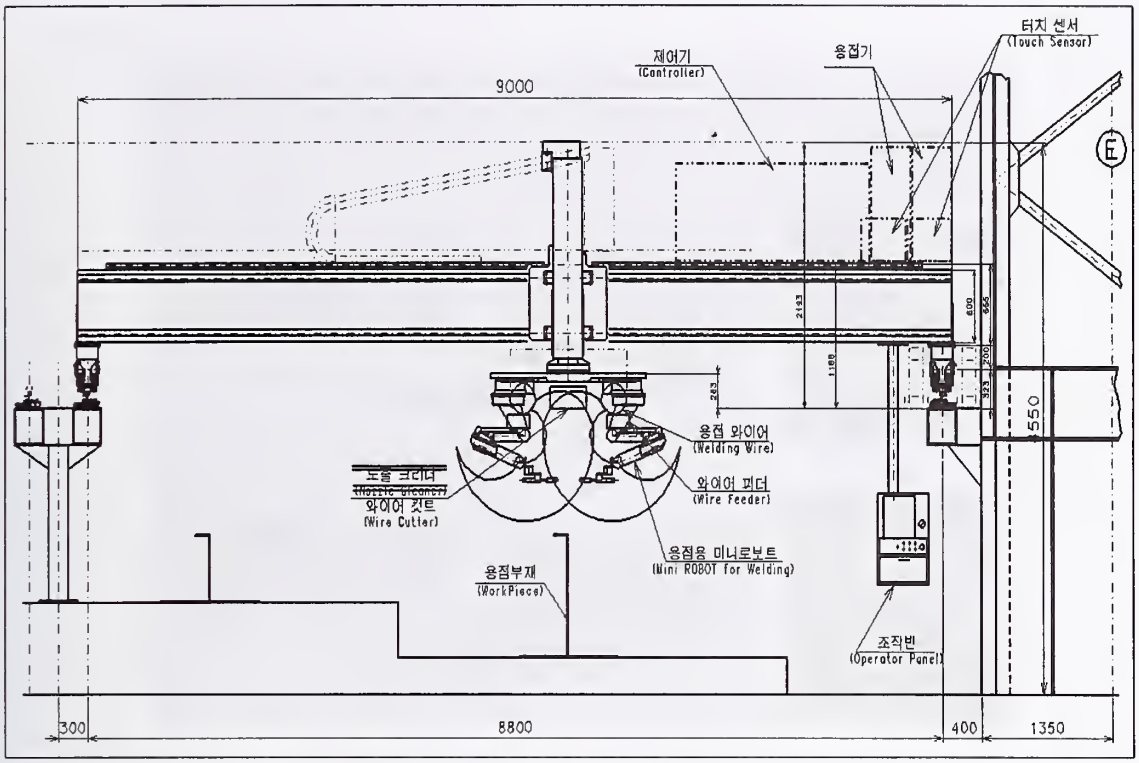

Fig. 3 Schematic diagram of gantry welding station with two articulated robots

Fig. 4 Photograph of automatic welding system for stiffeners

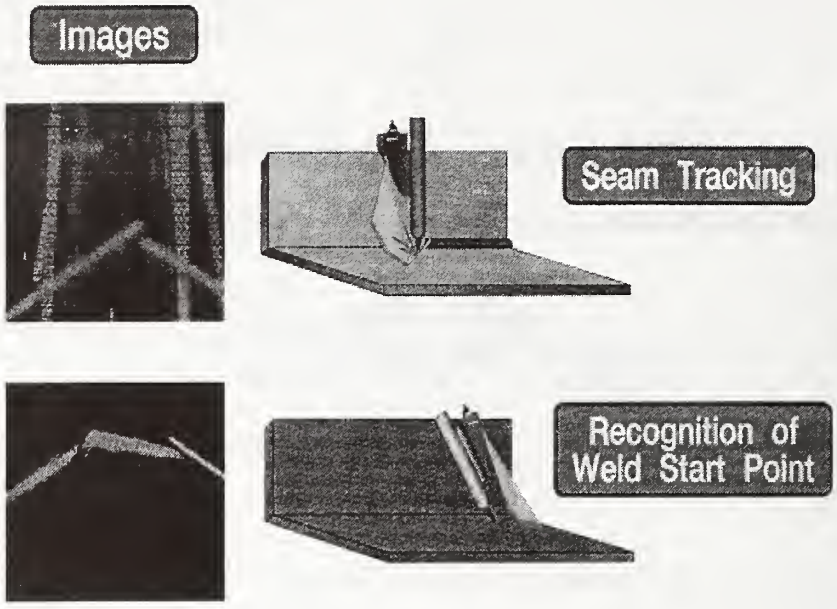

Fig. 5 Functions of laser vision sensor for pre-assembly of stiffeners

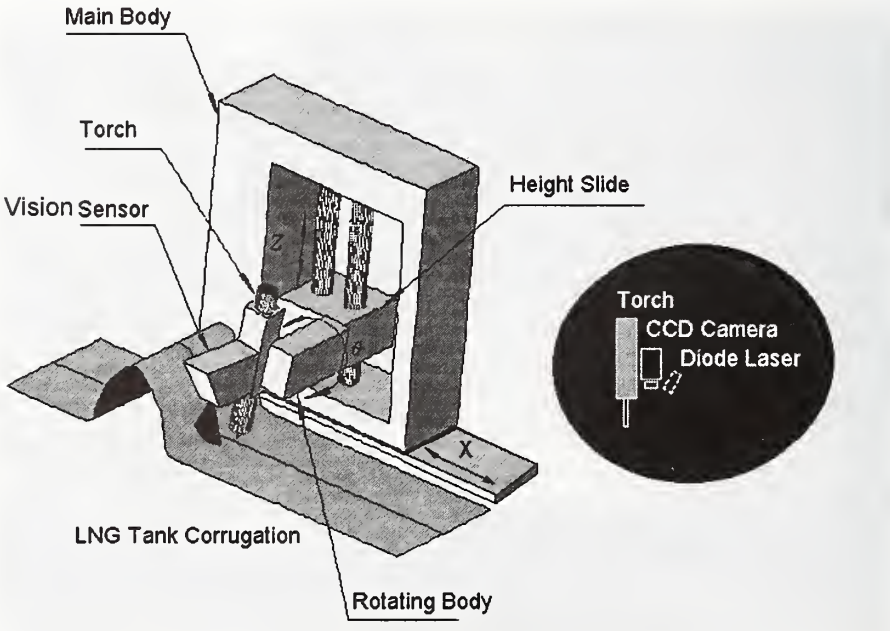

Fig.6 Schematic diagram of the automatic welding system for corrugated membranes

Fig. 7 Multi-reflections on corrugated panel of LNG tank

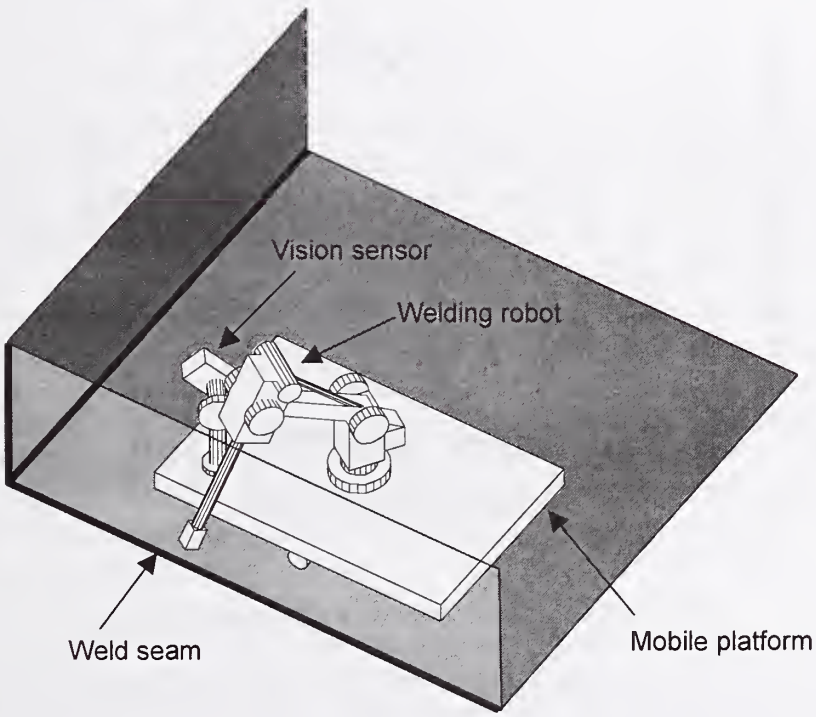

Fig.8 Mobile platform-manipulator welding system using vision sensor

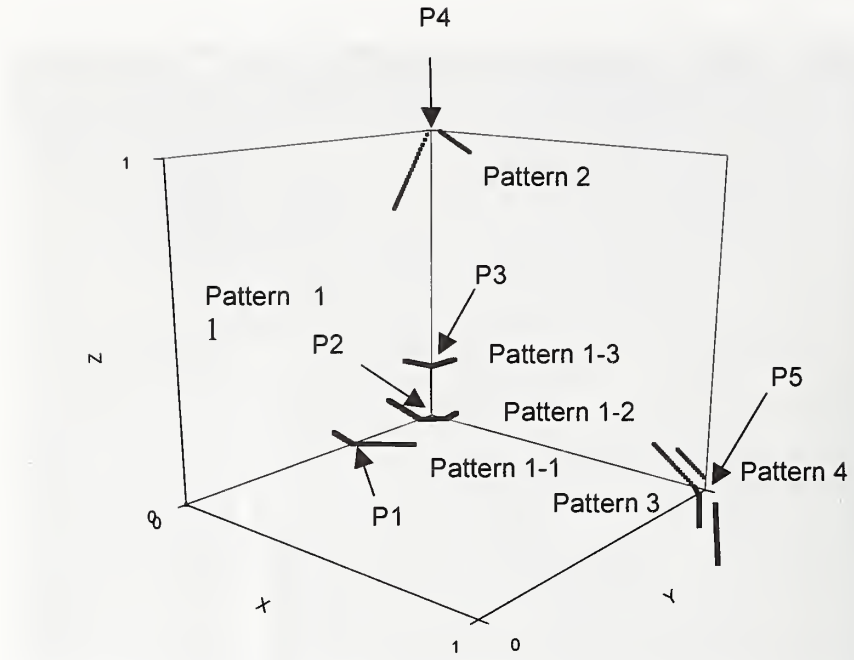

Fig. 9 Feature points and typical images of vision sensor

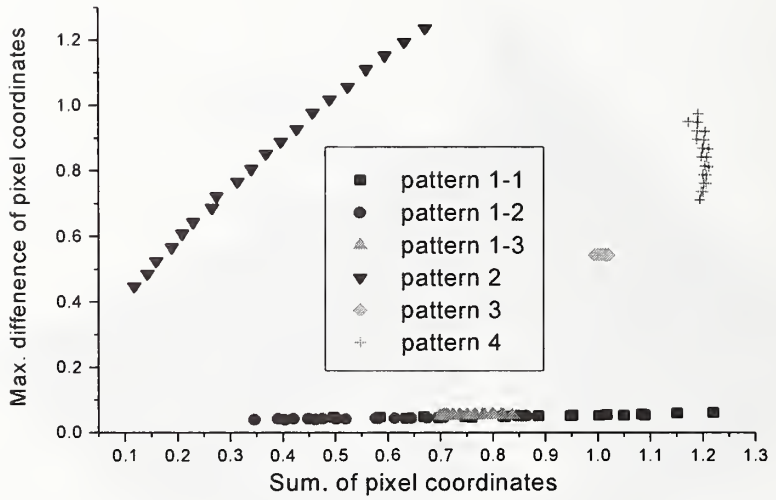

Fig. 10 Characteristic parameters for neural network

INTERNET BASED MANAGEMENT OF DATA FROM WELDING SENSORS[‡]

T.P. Quinn*

ABSTRACT

This paper describes a case study of data management for the data generated during sensing of welding processes. Real-time sensors can produce large amounts of data for weld documentation or control. The data can also be made available to a geographically remote station to allow informed decisions to be made about the productivity of a welding station or to troubleshoot problems of a welding station. The arc sensing monitor (ASM), a through-the-arc sensing system, was used to demonstrate a possible solution. The ASM outputs seven different quality measures thirty-two times a second. Based on the quality measures, the ASM decides whether there has been a defect. The ASM was modified to make the data and defect decisions available via Internet protocols. A data client collected the information and pushed it into a standard database. An applet accesses the database from a web browser or as a stand-alone application. The welding engineer can use the applet to identify the defective welds and plot the quality measures from any location on the Internet, either off-line or as the weld is being made. The scheme of storing the data in a standard database architecture allows simple scripts to be developed to query any aspect of the data.

INTRODUCTION

This paper presents a recipe for managing large amounts of weld-sensing data using Internet technologies. In 1991, the National Research Council (NRC) outlined the needs for manufacturing research (Ref. 1). The NRC decided that one of the principal needs for deployment of intelligent-manufacturing control is the effective acquisition, correlation, and presentation of manufacturing data. Many welding sensors have been developed over the past decade (for examples, see Refs. 2-10), and many produce large amounts of data that can be used to document parts, to do statistical process control, and to troubleshoot welding lines. However, as the NRC pointed out, the data must be presented to the welding engineer in a manner so that s/he can predict when process disruptions are about to occur and can learn from process disruptions if they do occur. If the welding engineer is not located near the welding station, it becomes imperative that the data from the welding station be accessible remotely. The engineer can save down time on the line and can better recognize trends in the data if the data are available at his/her current location immediately.

The growing use of Internet protocols has not bypassed manufacturing. Many equipment suppliers for factory automation now offer Internet communication facilities. Researchers are also developing data management solutions using Internet protocols: Gower *et al.* demonstrated the use of a Internet protocols in controlling a a semiconductor processing cell remotely (Ref.

---

* National Institute of Standards and Technology, Boulder CO 80303

11). Bertocco *et al.* described a client-server system for controlling electronic instrumentation over the Internet (Ref. 12). Adams *et al.* used Internet protocols to control and collect data for toxic exposure tests (Ref. 13).

In the research presented here, I used Internet and database standards to gather and consolidate the data produced by a through-the-arc sensing system of gas metal arc welding.

METHODS

The through-the-arc system has been described in Refs. 5,14. The arc sensing monitor (ASM) calculates seven quality variables and, once every $\frac{1}{32}$ s decides whether defects have occurred. The ASM is a PC-based system that is attached to an Intranet. The ASM can be controlled from the network using Transmission Control Protocol and Internet Protocol (TCP/IP), the standard protocols used for the Internet.

The scheme utilizes four independent modules: the sensor, the database server, the web server, and the engineer's workstation. The sensor in the weld cell (in this case the ASM) connects to a database server located somewhere across the network. The ASM acts as a TCP/IP streaming socket host and listens for connections on a specified port (Ref. 15) – Figure 1. The "database tender," a program running on the database server, connects to the ASM socket, and after each weld, the quality variables are sent over the socket. The database tender also receives the configuration parameters for the ASM. The data are buffered by the database tender so that the ASM can be ready for the next weld. Once the data transmission is complete the database tender parses the data and places it in the database. The database is accessed through an Open DataBase Connectivity (ODBC) manager. ODBC allows the database tender to interact with the database using SQL, a widely used programming language. The database tender can also configure the ASM remotely by changing the configuration parameters of the ASM.

The database is relational and is arranged in four tables: defective welds, quality parameters, graphing indices, and configuration constants. The name of the weld and the time and date of its creation are used as keys for organizing the tables. The defects table shows whether the weld has defects or not. The quality parameters table contains all the time indexed quality parameters for each weld. The configuration table stores the setup parameters needed for the ASM, which includes such things as the sampling frequency and current scale. The graphing indices are used so that the visualization program can quickly plot the quality parameters and the thresholds on the quality parameters without recomputing.

A visualization program written in Java™† runs on the Engineers Workstation but is served from the web server. The visualization program also accesses the database through the ODBC manager.

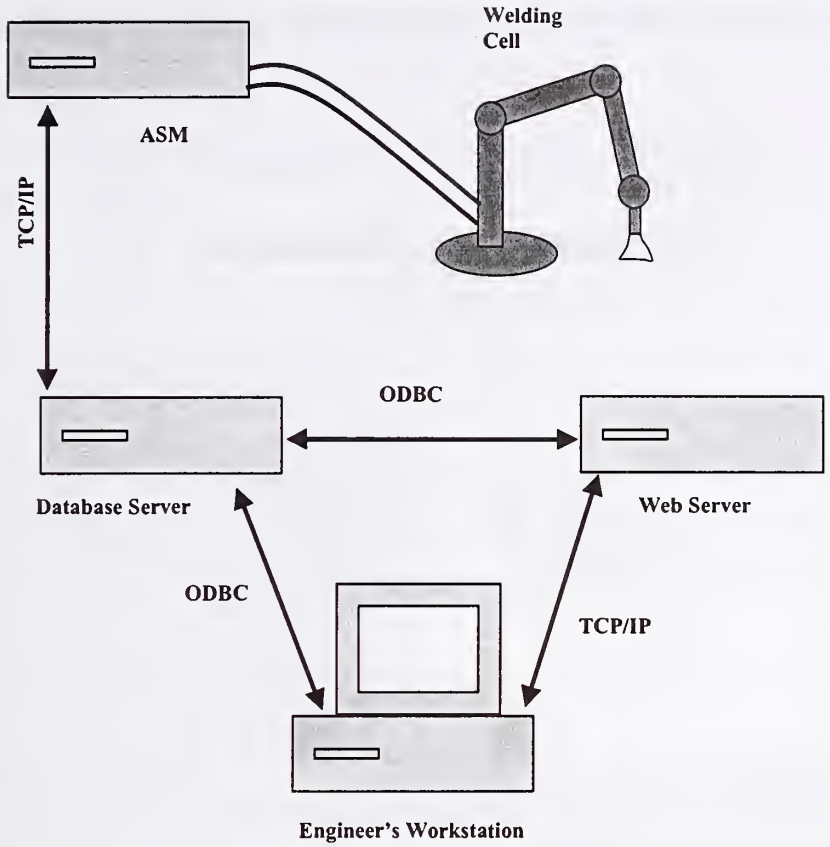

Figure 1: The architecture for the data-handling scheme.

The visualization program can be run as a stand-alone application or in a browser on the engineer's workstation. The program displays to the welding engineer a table of the welds made. The defective welds are checkmarked (Figure 2). The welding engineer can plot a time-series of any of the quality parameters by highlighting the weld s/he is interested in and clicking on the appropriate button.

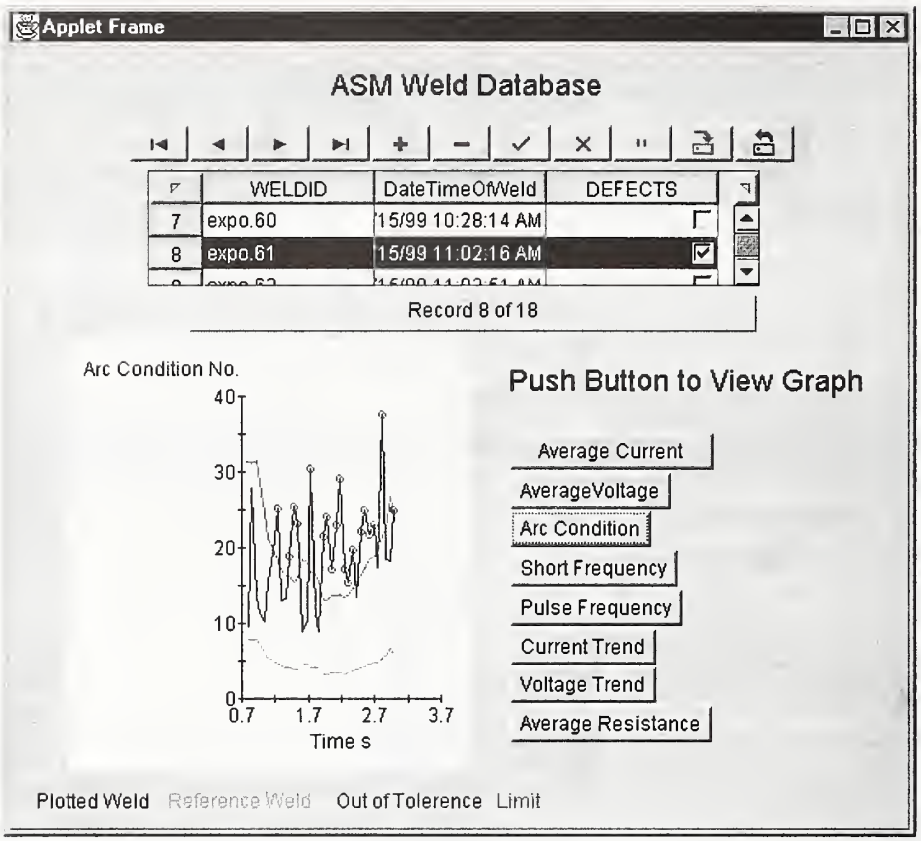

Figure 2: The visualization program's user interface.

RESULTS AND DISCUSSION

The scheme was implemented and used in combination with other web-based technology to demonstrate remote collaboration (Ref. 16). Welds were made in Gaithersburg, Maryland and reviewed in Boulder, Colorado and in St. Louis, Missouri. The welds joined a mounting bracket to the shaft of an automotive suspension strut. Two, 2 s welds were made with an approximately 1 s delay between welds. In both cases, the network speed was adequate to transmit the data between welds and have the ASM be ready to process the next weld. Approximately 3 KB of data need to be transmitted for each second of weld. An Intranet connection implemented at ISDN bit-rates (128000 bits/s) could transmit the data from a 2 s weld in 0.375 s.

The web server, the engineering workstation, and the database server need not be running on three different computers–in this implementation, they all ran on a single PC. The ODBC manager was included in the operating system, and the run-time engine for the visualization program was downloaded from the Internet without cost. Wizards to manage the database were available in common, office-productivity software (Ref. 17). Queries to the database that are not programmed into the visualization tool can easily be constructed using the same software.

The advantages of this scheme are the following: (1) The data are available remotely, allowing production welding lines to be monitored and troubleshot by a central staff. (2) Large amounts of

data generated in the cell can more easily be handled on machines that are designed to be database servers. (3) The process of developing user-specific ways to view the data can take advantage of the large number of relatively low-cost tools already developed for databases. (4) The visualization program can be run on virtually any platform. A disadvantage is that a reliable TCP/IP-based network must be installed in the factory.

SUMMARY

A data-management system was developed for a through-the-arc sensing system. The sensor reports its data over a TCP/IP network to a program that buffers the data, then places it in a database. The database is accessed with the standard ODBC protocol. Weld engineers can use a visualization program that also accesses the database through the ODBC protocol. The engineers can then monitor and troubleshoot the welding station. The visualization program is written in a generic programming language that can run on almost any platform. The large amounts of data are managed easily using generic or specific scripts developed for databases.

REFERENCES

1. Committee on Analysis of Research Directions and Needs in U.S. Manufacturing. 1991. *The Competitive Edge - Research Priorities for U.S. Manufacturing*. Washington: National Research Council, pp. 25-53.
2. Araya, T., and Saukawa, S. 1992. Recent Activities on Sensing and Adaptive Control of Arc Welding. *Proc. 3rd International Conference on Trends in Welding Research*, eds. S. A. David and J. M. Vitek, pp. 833-842, ASM International.
3. Smartt, H. B. 1992. Intelligent Sensing and Control of Arc Welding. *Proc. 3rd International Conference on Trends in Welding Research*, eds. S. A. David and J. M. Vitek, pp. 843-851, ASM International.
4. Sicard, P., and Levine, M. D. 1988. An Approach to an Expert Robot Welding System. *IEEE Transactions on Systems, Man, and Cybernetics* 18 (2):204-222.
5. Quinn, T. P., Smith, C., McCowan, C. N., Blachowiac, E., and Madigan, R. B. 1999. Arc Sensing for Defects in Constant-Voltage Gas-Metal-Arc Welding. *Welding Journal* (in press).
6. Hanright, J. 1986. Robotic Arc Welding under Active Control - A Survey of Current Technology. *Welding Journal* 65 (11):19-24.
7. Richardson, R. W. 1986. Robotic Weld Joint Tracking Systems - Theory and Implementation Methods. *Welding Journal* 65 (11):43-51.
8. Madigan, R. B., Quinn, T. P., and Siewert, T. A. 1995. *Control of Gas-Metal-Arc Welding Using Arc-Light Sensing*. Gaithersburg, MD: National Institute of Standards and Technology, Report No. NISTIR 5037, p. 9.
9. Johnson, J. A., Carlson, N. M., Smartt, H. B., and Clark, D. E. 1991. Process Control of GMAW: Sensing of Metal Transfer Mode. *Welding Journal* 70 (4):91s-99s.
10. Song, J.-B., and Hardt, D. E. 1993. Closed-Loop Control of Weld Depth Using A Thermally Based Depth Estimator. *Welding Journal* 72 (10):471s-478s.

11. Gower, A., Boning, D., and McIlrath, M. 1996. A Flexible, Distributed, Architecture for Semiconducter Process Control and Experimentation. *Proc. Intl. Symposium on Intelligent Systems and Advanced Manufacturing, SPIE Proc.*
12. Bertocco, M., Ferraris, F., Offelli, C., and Parvis, M. 1998. A Client-Server Archetecture for Distributed Measurement Systems. *IEEE Transactions on Intrumentation and Measurement* 47 (5):1143-1148.
13. Adams, D., Swannack, R., and Peterson, M. 1999. Remote Control of Instrumentation Via Ethernet. *Scientific Computing and Instrumentation* 16 (9):46-48.
14. Quinn, T. P., and Madigan, R. B. 1998. Sensing of Arc Welding Process Characteristics for Welding Process Control. United States Patent No. 5,756,967.
15. Quinn, B., and Shute, D. 1996. *Windows Sockets Network Programming*. Reading: Addison-Wesley.
16. Gilsinn, J., Rippey, W., Falco, J., Quinn, T. P., Russel, B., and Stouffer, K. 1999. A Welding Cell that Supports Remote Collaboration. *Proc. Ninth International Conference on Computer Technology in Welding*.
17. Microsoft. 1997. *Microsoft Access*®: Microsoft.

---

† Trade names are used only to specify adequately the techniques used. Such identification implies neither endorsement by NIST that the particular technique is the best available for the purpose.

Session B2: Real-Time Weld Sensing and Control Systems: GMAW Arc Quality Monitoring II

The Use of an Integrated Multiple Neural Network Structure for Simultaneous Prediction of Weld Shape, Mechanical Properties, and Distortion in 6063-T6 and 6082-T6 Aluminium Assemblies

Ø. Gundersen[1], A. O. Kluken[2], O. R. Myhr[2], J. E. Jones[3], V. Rhoades[3], J. Day[3], J. C. Jones[3], B. Krygowski[3]

[1] SINTEF Materials Technology
N-7465 Trondheim, Norway

[2] Hydro Raufoss Automotive Technical Centre AS
P. O. Box 41
N-2831 Raufoss, Norway

[3] Native American Technologies Company
1317 Washington Ave. – Suite 1
Golden, Colorado 80401

ABSTRACT

Neural networks are parameterised non-linear mathematical models well suited for pattern classification and non-linear function approximation. These kinds of models are empirical models and in the training process, the unknown parameters are adjusted until the non-linear response of the network fits the data according to a specified performance criterion. Neural networks offer certain advantages in weld modelling. However, in the past, such models did not provide all of the information that is usually necessary to completely design a welded assembly and optimise the welding operation. In this work, a neural network structure for simultaneous prediction of weld shape, mechanical properties and distortions of welded aluminium assemblies is presented. The experimental approach is well described and extensive information about the neural network concept used in this work is also provided. In a simulation case, it is shown that optimisation of individual weld properties may easily cause other properties to fall outside the acceptable range (SPC-limits). It is also shown that the model can be used for optimisation of multiple properties.

1. INTRODUCTION

As the demands of the manufacturing environment continue to increase and time-to-market for products experiences a continual contraction, better computer tools are necessary. The is need for a design system that is capable of virtual manufacturing to provide the capability to "manufacture" a product in the computer, just as it would be produced on the shop floor. Such a system should provide virtual manufacturing that is simultaneous with the design process, so that the manufacturability of designs can be verified without investment in expensive production equipment.

Higher strength heat treatable aluminium alloys exhibit degradation of the metallurgical properties in the heat affected zone (HAZ) of arc welds. Arc welded automotive space frame assemblies produced using these alloys will have the overall strength limited by the HAZ properties. Additionally, distortions from the welding process can cause difficulties with the fit-up of other components of the automobile.

Robotic welding of aluminium space frame assemblies demands that the process be optimised. Such optimisation should focus not only on the weld engineering shape parameters, such as depth of penetration, or weld size, but also consider to minimise distortions in the final assembly as well as to maximise the strength of the weld HAZ. Previously, each of these has been modelled separately and most frequently by using different kinds of models. Also, there have been no reports of a comprehensive model that allows for complete optimisation of the welding process to meet the specifications of the weld itself, while simultaneously minimising distortions and maximising HAZ properties.

Previous work conducted at Native American Technologies Company (NATech) and by others have shown that neural networks provide certain advantages in weld modelling. Until now, however, neural network models as well as other types of models have not provided all the information that is necessary to completely design the welded assembly and at the same time be used as an aid for optimisation of the welding operation. The present study describes the development of a multiple neural network structure for prediction of multiple properties of aluminium weldments. The study presents results obtained in a project conducted by Hydro Raufoss Automotive Technical Centre (HRTC) in cooperation with NaTech; a company that has specialised in development of neural networks for welding applications. SINTEF Materials Technology (SINTEF) played the role as a third party consultant during the whole project. HRTC's main objective was to study the potentials of using neural network modelling in computer assisted welding procedure development.

The welds were made from extrusions of two aluminium alloys, both in the peak aged temper condition. The extrusions of square tubing were heat treated to the same property levels. Material thickness varied from 2 to 5 mm. Pulsed gas metal arc (GMA) welds were produced according to a set of experiments derived from an experimental design technique optimised for neural network modelling. Included in this part of the work was also some initial screening experiments to become familiar with the operation ranges of the different welding parameters. The screening experiments were embedded into the experimental design matrix. The neural networks were

trained using the P/NA^3 neural network concept developed at NATech [1,4,6]. Each of the neural network prototype models was tested by the use of an exclusive statistical method used for determination of the upper error bound in the models as well as confidence levels for the predicted information. This method, known as guided experimentation was used to generate additional experimental data in regions of the parametric space where refinement of the neural network models was needed.

The refined neural networks are integrated into a single software Graphical User Interface (GUI) that provides the ability to simultaneously observe weld shape, weld mechanical properties and distortions for a T - connection structural assembly. The experimental approach and neural network modelling concept are thoroughly described and the capabilities of the neural network structure as a complete knowledge source for engineering design and process optimisation is demonstrated. The software system also provides a set of exclusion rules which prevents the user and the built in optimisation routine from selecting welding parameters that belong to a region in which the welding process will not operate.

The rest of the article is organised as described in the following. At first, some characteristic features of aluminium space frame weldments along with their traditional modelling approaches are presented. Then, a unified approach to neural network modelling is described and important phases of the development work is classified. Relevant properties of the aluminium alloys and different approaches in experimental design are then described. Also, a brief introduction into neural networks is presented along with a thorough description of the neural network concept used in this work. Then, some general features of the computer model are summarised before the presentation of a simulation study related with optimisation of weldment properties. Finally, some ideas about future use of neural networks in the field of weld modelling are given before the concluding remarks at the end of the paper.

2. SPACE FRAME WELDMENTS: MODELLING OF CHARACTERISTIC FEATURES

In this section, some important problems related to welding of automotive space frame components in aluminium are presented. These include predictions of weld bead shape, strength distribution and weld distortions. For each of these features, the basic mechanisms will briefly be explained along with descriptions of the different modelling approaches that are most frequently used for modelling these phenomena. It will be shown that traditionally, different modelling approaches are used depending on which feature of the weld that is focussed on. This is in contrast with the approach described in this work where the same neural network modelling approach is used to describe different features of the weldment.

2.1 Weld Bead Shape

There is a growing interest for simulation programmes that can predict the detailed geometry of the weld bead. Based on the bead geometry, geometric data of the bead can be defined and used for assessment of weld quality. If such programmes are sufficiently accurate, they can be applied as a tool in welding procedure development. Work with procedure development has traditionally

been a discipline of trial and error, which is costly and time consuming. By bringing simulation tools into use, the task of developing a welding procedure becomes more systematic and predictable. Different techniques based on both empirical modelling techniques and physical principles have been used for describing the weld bead shape or associated bead parameters. The reader should note that most of the references cited in this subsection deals with studies of steel weldments, but the principles discussed will also be applicable in welding of aluminium.

Linear and non-linear regression techniques have been used for modelling the relationship between welding parameters and geometric data for description of the bead [1, 2]. As opposed to these traditional regression type models which have been used for direct prediction of weld geometry parameters, neural networks have been used for prediction of the whole weld bead [4, 5]. Then, weld geometry and engineering parameters can be derived with basis in the predicted whole bead shape. It has been shown that this approach yields a much more accurate prediction since many of the geometry parameters are not continuous as the weld shape varies, but the bead shape varies in a "smooth" way as the welding parameters are varied [Klein 94; obtain ref. from JJ]. The neural network which is used as a non-linear empirical model is capable of sufficient multi-dimensionality to describe the entire weld bead shape; the neural network concept used in this work is described in section 5.0 on neural networks.

Physical modelling techniques have also been used for modelling the shape of the weld bead. The mechanisms that determine the weld pool shape are very complex and include fluid flow, droplet detachment and metal transfer phenomena. For the majority of cases, the Peclet number is high enough to introduce significant effect from the convective heat transfer on the weld pool shape [7]. The driving forces for convection in the weld pool depend on the kind of heat source used. In arc welding, electromagnetic forces will contribute to the weld pool circulation but in laser driven welds such forces are absent. Thus, in arc welds, forces due to the surface tension temperature gradient (Marangoni effect), the buoyancy force, the electromagnetic body (Lorenz) force and aerodynamic drag forces contribute to the convective flow in the pool [8, 9, 10,11]. Models of this kind are frequently based on finite volume and finite difference techniques but finite element approaches are also applied in modelling of weld pool convection.

Finite element based models have been extensively used for prediction of residual stresses in welds. Details of the weld may have impact on the residual stresses in regions close to the weld but are not critical for proper prediction of the residual stresses in the heat affected zone. In such models, the approximate shape of the weld is implemented by using an appropriate heat source model to account for the heat power distribution in the weld pool [12]. In an even simpler approach, analytical models with distributions of elementary point heat sources and the method of images have been used for a qualitative prediction of weld bead shape [13].

Even though physically based models have become increasingly sophisticated and can account for several of the mechanisms that influence weld shape, they are still not useful for most production applications since they usually require many hours to run, which is far too slow for real-time simulations. If experimental data for weld shape are available, neural networks offer an alternative method for modelling the weld shape since these models are capable of capturing all of the

complexity of the manufacturing process. Such empirically based models represent a completely different approach to weld bead modelling compared with the physically based models.

2.2 Weld Mechanical Properties

The structural strength of 6XXX (i.e. Al-Mg-Si) alloys can not be fully utilised in welded automotive space frame assemblies since the HAZ is significantly softer than the unaffected base material. This strength loss is caused by a sequence of unfavourable metallurgical reactions taking place in the HAZ as a result of the high temperatures imposed by the welding arc.

During welding, reversion of hardening β"(Mg_2Si)-precipitates will occur to an increasing extent within the peak temperature range from about 220-500°C. At the same time, non-hardening β'(Mg_2Si) precipitates can nucleate and grow at dispersoids. Fig. 1(a) shows the corresponding hardness drop across the HAZ immediately after welding. It follows from Fig. 1(b) that this strength loss is not permanent, but will gradually become smaller as excess solute starts to recombine and form GP-zones during subsequent natural aging. The recovery process is almost completed after 1-2 weeks, and the resulting hardness profile will then be as shown in Fig. 1(b) from which it is apparent that the minimum hardness will be located at some distance from the weld fusion line. The corresponding yield stress at this position is an important value in engineering design since it defines the overall strength of the assembly.

Different types of models can be applied to predict the HAZ strength distribution. Myhr and Grong have derived physically based models which simulates the microstructure evolution during welding, and these have been successfully applied to predict the effect of different welding and material combinations on the resulting HAZ strength [8-11, 14, 15]. The microstructure model is derived by considering the β" particle dissolution (*particle reversion model*) during welding which leads to strength loss. A natural ageing model accounts for the subsequent reprecipitation of GP-zones during storing at room temperature which leads to strength recovery. In the model, equations are established for the relative volume fraction $f_p/f_{p,o}$ of the strengthening particles; f_p is the actual volume fraction of precipitates and $f_{p,o}$ is the volume fraction of precipitates in the (artificially aged) base material. In the next paragraph, it is shown that the quantity $f_p/f_{p,o}$ can be related to the strength of the weldment.

The high strength values of AA6XXX alloys are due to the presence of the β'' particles. The net precipitation strength increment $\Delta\sigma_p$ due to artificial hardening can be calculated from an equation originally derived by Kelly and Nicholson [16] that states:

$$\Delta\sigma_p \propto f_p \tag{1}$$

Now, if the relative volume fraction $X_p = f_p/f_{p,o}$ is introduced, the strength increment can be expressed by

$$\Delta\sigma_p \propto X_p f_{p,o} \tag{2}$$

$\Delta\sigma_p$ reaches its maximum when $X_p = 1$; i.e. when the maximum number of precipitates are present in the aluminium matrix. Thus

$$\frac{\Delta\sigma_p}{\Delta\sigma_{p,\max}} = \frac{\sigma_p - \sigma_{p,\min}}{\sigma_{p,\max} - \sigma_{p,\min}} = X_p \qquad (3)$$

$\sigma_{p,min}$ denotes the intrinsic strength of the aluminium matrix after complete particle dissolution while $\sigma_{p,max}$ is the original base material strength in the artificially aged condition. As a rough estimate, the yield strength can be estimated from the hardness value by a linear relationship [17] for certain alloys. For AA6082 alloys of the kind studied in this work, the following relationship between hardness and yield strength can be used [15]:

$$\sigma = 3.0HV - 48.1 \qquad (4)$$

This kind of linear relationship cannot in general be expected to be valid for all types of AA6XXX alloys. *In principle, however, we see that hardness, strength and volume fraction of strengthening precipitates are related properties and information about strength and precipitation reaction kinetics can be obtained via hardness measurement.* Such measurement are much easier to perform than measurement of the actual particle volume fractions. Hardness measurements constitute the experimental basis for the microstructure model. In this work, hardness measurements are used as the basis for calculation of the minimum strength in the HAZ of the weldment.

2.3 Weld Distortions and Residual Stresses

Thermally induced distortions caused by the steep thermal gradients associated with welding may represent a serious problem in keeping the dimensional tolerances within the specified limits of welded automotive components. Fig. 2 shows schematically the sequence of deformations taking place during welding of a typical T-joint of a space frame assembly. The vertical displacement is initially in the upward direction as shown in Fig. 2(a). This is due to thermal expansion of the heated material adjacent to the weld. The direction is however reversed during cooling when the material contracts, and the final deformation will usually be as shown in Fig. 2(b).

Finite element (FE) modelling techniques can be applied to calculate such deformations. Accurate predictions require that the softening of the HAZ, as described in Section 2.2, is accounted for in the mechanical model which calculates the evolution of stresses and strains during welding. If this effect is ignored, the result will be a significant overestimation of the residual stress level in the HAZ [18]. FE-models where the microstructure evolution is accounted for by internal state variables have recently been developed for different types of aluminium alloys [19,20,22,23]. These models have been demonstrated to be capable of predicting how different base materials, welding parameters and sequences affect the resulting deformations, and they are also very flexible with respect to the geometric design which can readily be changed for each new simulation. The disadvantage is, however, that each simulation requires a substantial computer time that implies that such models at present cannot be used as an interactive tool.

The cornerstone in these simulations is the microstructure model. Myhr et. al use only the reversion model to describe the evolution of microstructure over the weld cycle; the natural ageing modelling is needed to describe strengthening processes in the material after welding is completed. The reversion model operates together with a constitutive equation for the mechanical behaviour of the material. The constitutive equation relates the effective flow stress σ also to other critical parameters in the system:

$$\sigma = \sigma\left(\frac{f_p}{f_{p,o}}, T, \dot{\varepsilon}_p, \right) = F(T)G\left(\frac{f_p}{f_{p,o}}, T\right)\left(H(\phi, \frac{f_p}{f_{p,o}})\right)^{n(T)}\left(\dot{\varepsilon}_p\right)^{m(T)} \qquad (5)$$

Myhr et. al used this constitutive equation which takes into account the dependency of the flow stress on the effective (equivalent) viscoplastic strain rate. Also, strain hardening is taken into account by a separate function that depends both on microstructure and the strain hardening parameter ϕ. Above a certain temperature T_f during heating, the subsequent deformation during cooling will have no memory about its initial deformation. Thus, pure creep (ϕ = 0) is assumed until the temperature falls below T_f. Below a lower temperature T_o, the hardening parameter evolves in the same way as the effective (equivalent) viscoplastic strain rate. Between temperatures T_o and T_f there is a linear decay of ϕ to zero. Isotropic elastic-viscoplastic material behaviour was assumed in the calculations [20].

3. A UNIFIED APPROACH TO NEURAL NETWORK MODELLING

The concept used for developing the neural networks presented in this work constitutes a part of a systematic approach to neural network modelling. As basis for this approach, it is realised that *the prediction performance of the neural networks is dependent on the quality of the experimental data. Data of satisfactory quality is a prerequisite for the development of a successful neural network model.* Also, it is realised that experimental work most frequently is an expensive part of a modelling project and it should be aimed to keep to number of experiments to a minimum as well as exploiting already available information in an optimal manner. Finally, it should be possible to return to the experimental planning phase and add new input parameters without having to redo the previous work done in experimental planning. Next, training of the neural networks should be as efficient as possible and modifications of the neural network model should be done without having to redo the work already spent during initial training of the neural networks. This has lead to the development of a methodology for neural network modelling that typically involves the following phases (tasks):

1. *Brainstorming and Planning*: The objective of this phase is to gain understanding of the process to be modelled. This involves discussions to decide which are the relevant input and output parameters to be considered. Decisions about the discretisation (number of levels) of the input parameters will also be taken.
2. *Experimental Design*: Based on the information provided in the previous phase, a *design of experiments* (DOE) will be performed by the use of suitable software. This gives a matrix of experiments listed in randomised order to be conducted in the next

phase. If experimental information already is available, the software can be loaded with this information. Then, a design matrix is generated which includes the already available experiments.

3. *Experimental Work*: This phase involves the main part of the experimental work and preparation of the weld samples. This usually includes a set of screening experiments. Such experiments are needed to become familiar with the operation range of the input parameters. Due to such information, one may sometimes need to involve more input parameters to extend the experimental design matrix.
4. *Sample Preparation:* This may involve metallographic preparation of the samples and different types of materials testing.
5. *Preparation of Data for Neural Network Training*: The samples and information obtained from the previous phase are used to generate a neural network training - file in electronic format.
6. *Training & Analysis of the Prototype Model*: This phase involves both initial training and testing of the prototype model to point out domains in the input parameter space that gives predictions with an error larger than accepted for the current application. Then, guided experiments are planned to generate additional information to improve the performance of the model in the uncertain regions of the input parameter space. Also, at this stage, work will start with development of a Window's based *Graphical User Interface* (GUI) for the neural network software model.
7. *Execution of "Guided Experiments":* This phase involves execution of the guided experiments and preparation of the samples.
8. *Refinement of the Neural Network Model*: The information obtained from guided experiments is used for refinement (improvement) of the prediction performance of the neural network.

At best, guided experimentation only has to be executed once. In general, however, several stages of guided experimentation may be needed to achieve a neural network model with the desired predictive capabilities.

The following two sections of this study include descriptions of the experimental approach and the neural network concept (training and testing) respectively. Information about the guided experiments is given in section 4.3 although guided experimentation may be considered to belong to the task of testing the neural networks as described in section 5.6.

4. MATERIALS, EXPERIMENTAL DESIGN AND WELDING PROCEDURE

This section is related with the experimental approach used in this study. A thorough description of the experimental planning methodology is given along with information about the welding procedure applied during the experiments.

4.1 Materials

The welds studied in this work were made from hot extrusions of two aluminium alloys AA6063 and AA6082; each alloy in the peak aged temper condition (T6). These alloys belong to the

AA6XXX series that contains on the order of (0.5-1.3)% magnesium and (0.4-1.4)% silicon. AA6082 has a significantly higher yield strength than AA6063 (typically 300 MPa and 220 MPa, respectively). Such alloys are made by DC-casting and subsequent homogenisation at temperatures between 530 and 580°C. Subsequently, the metal is extruded and cooled. Then, for the extrusions to achieve the desired properties, the extrusions are age hardened at temperatures between 160 and 185°C for 3 to 6 hours. Age hardening is performed over a limited period of time to avoid overaging; i.e. reduction of the strength of the material. *The hardening process during ageing of hot extruded AA6XXX alloys is described in Appendix A.*

4.2 Introduction to Experimental Design

The following subsection gives a review of the principles of experimental design. The material presented is mainly based on [24, 25, 26].

Experimental design (Design Of Experiments; DOE) deals with methods for experimental planning that support the user in efficiently obtaining the relevant characteristics of the process. The ideas involved in experimental design are relatively simple but in many cases the statistics involved can be quite difficult. However, such methods are also available to the non-expert via software packages that have built – in routines for a wide variety of design techniques. The output from this process is an experimental design matrix with information on the set of experiments to be conducted.

The keyword in experimental design is planning. Typical decisions that have to be made include:

- Specify the goal of the experiment
- Classify input- and output variables
- Clearly specify assumptions about the process

This is in contrast with the technique often used in traditional experimentation: Frequently, one tends to vary the process input parameters in an unsystematic way; using the results of one run to give guidelines for how to perform the next run. By following this approach, no insight into the coupled influence of the input parameters on the process outputs can be achieved. Thus, when there is no systematic planning of the experiments, there is always a risk of loosing knowledge about a certain important feature of the process and may result in reinforcing false assumptions due to confounding effects in the non-randomized data.

Most experimental designs allow for the estimation of the desired coefficients in the model with fewer (*less than full factorial*) than the full set of experiments that would be included in a *full factorial* design. There is, however, a trade-off between the number of runs, the number of estimated terms and the quality of the estimation (i.e. the estimated model parameters).

In the literature, two groups of experimental designs are classified. *Classical designs* have desirable statistical properties that make the analysis of the experimental data quite easy. Unfortunately, these designs are applicable only to certain problems and they are inflexible about the number of runs and the factor settings they need. *Taguchi* designs, *full factorial* designs,

fractional factorial designs, *Box-Behnken* designs, *central composite* designs and *orthogonal arrays* belong to the classical designs. Constraints on the region of operability of the factors and other special features of the design situation may prevent the use of classical designs. In such cases, the use of an optimal design technique is the only alternative. The *optimal designs* constitute to the second group. These designs are non-orthogonal. There are several types of optimal designs (A, D, G and V optimal) each named after the optimisation criterion used to determine the set of experimental runs. According to the criterion, the amount of information in the experiments is maximised.

In this work, experimental design was used to support the process of establishing a complex model based on neural networks. NATech has long experience in using experimental design for neural network modelling. In a study performed at NATech, several classical design methods and optimal designs were examined to determine the best experimental approach for neural network modelling. The initial study included a two level Box-Behnken design and a Taguchi design with three levels. The result of this work clearly indicated that the Taguchi design provided a much better model than the Box-Behnken design.

As part of a continuing overall plan for testing and verification of neural networks, a series of tests were conducted to evaluate the effectiveness of various other experimental designs, currently used for statistical modelling. These designs included both three and four level D-Optimal designs. Depending on the number of factors, these designs required similar numbers of experiments as the Taguchi designs. The neural networks generated with the four level D-Optimal designs performed better than neural networks generated from other designs.

However, based on the results of the tests, it was concluded that there could be an improvement on the D-Optimal design of experiments. The result of this work was an "N-Optimal" design method that is optimised for neural network development.

4.3 N-Optimal Experimental Design

A refined D-optimal design technique called N-optimal design optimised for neural network applications was developed [1]. The N-optimal design provides the maximum likelihood of minimising the error in the neural network while simultaneously using a minimum number of experiments. Cost of experimentation can often be a significant part of the development cost of a neural network, so reduction of the number of experiments is a primary criterion in the N-Optimal design method. When combined with Guided Experimentation (described in Section 4.4), a neural network can be trained to an acceptable error level. Also, the N-optimal design gives the user the opportunity to add factors and add data from new experiments without having to redo the whole design. Furthermore, the design method is capable of excluding parts of the input parameter space which correspond to possible invalid parameter settings for the process. In the neural network software, these socalled exclusion rules keep track of these omitted regions of the input parameters.

In addition to using a good design of experiments, it is important to carefully document each conducted experiment. One should keep track of error sources and also register special features

observed during the experiments. Based on this documentation, sources of error can be traced and possible bad experiments removed from the data set used to train the neural network. Also, accurate and repeatable measurements are necessary to derive a neural network model that provides an accurate representation of the process that is modelled.

Much effort has been spent at NATech to develop an experimentation methodology in which the objective is to minimise the amount of experimental work. This can be achieved if one is able to select *only* the specific data points that completely represent the underlying process. This reduces experimentation costs, network training difficulties and the risk of network overtraining (overfitting) and hidden node generation. This experimentation methodology is called *Guided Experimentation*. The method includes three steps. At first, an N-optimal design gives the least possible number of experiments that is needed to train the neural network model. However, one may often need to perform some screening experiments but these experiments may be included in the set of N-optimal experiments. Secondly, another group of experiments is selected based on the value of a statistical parameter called the S-parameter. The S-parameter described in section 5.6 is a specially designed maximum likelihood estimator that has shown to be conservative; the error in the S-parameter is never less than the error in the neural network. Also, it conforms to the student t statistical distribution. Depending on the accepted error level in the neural network, the value of the S-parameter as evaluated on the original N-optimal data set can be used to pinpoint the regions in the parameter space that needs more information about characteristics of the process. The experimental data obtained during the guided experimentation stage are used for so-called refinement of the neural network model to embed into the model the new amount of information represented by the guided experiments. In reality, this is an iterative process that in practical work only has to be repeated once. Then, training, testing and verification of the neural network model is based on the original N-optimal data set and the additional guided experiments. This is a unique feature of the Guided Experimentation methodology that contributes to reducing the amount of experimental work.

4.4 Guided Experimentation

A neural network can be thought of, in an analogy, as a "wet blanket" that is to be draped over a set of data points in space. It is pinned at each of the points, but is free to conform to any shape in the regions between points. Using this analogy, it is clear that the first logical conclusion would be that the better "pinned" the neural network, the more accurate will be the resulting model. Stated differently, "if a large set of data points will produce a good neural network, a very large set of data points will produce an even better neural network". "This "more is better" syndrome is generally accepted throughout the neural network community.

However, on closer analysis, the problem is really one of selecting the specific data points that represent the underlying process completely. There are actually two methods of achieving this "completeness" of coverage of the process operating space. The first is based on the premise that if there are a sufficiently large number of data points, then the probability is higher that all of the process behaviours will be represented in the neural network training set. This approach is often cited as the only approach that is useful for training neural networks.

However, if it was possible to select only the data points that exactly represented the process, and no more, then several advantages would accrue. First, since experiments are always costly, this approach will yield a cost reduction. Secondly, the neural network training time and difficulties will be reduced if the training data set is smaller. Third, as the number of training examples increases, the likelihood of over training also increases as well as the likelihood of too many hidden nodes required to map the training examples. *Guided experimentation* provides a method for achieving these results by near optimum selection of the necessary training data points while also minimising the number of unnecessary data points.

The technique developed for this guided experimentation approach consists of a set of steps. First, an initial neural network is developed using the data generated from a very small experimental design. In the second step, the next experiment or group of experiments to be conducted is selected. The selection criterion is to maximise the amount of expected decrease in overall error of the neural network. The S-parameter method for testing the network is described in the next section. Third, by using the refinement technique of the P/NA^3 neural network structure (see description in the next section) together with the associated training algorithm, the network is modified to represent the new data without disturbing the basic neural network structure that was already trained. Fourth, this process is repeated until the neural network is within an error bound that is reasonable for the problem (considering experimental error, cost trade-off, etc.). Usually one loop of Guided Experimentation gives a model with satisfactory prediction performance.

4.5 Experimental Design in this Study

For derivation of the model presented in this work, screening experiments were performed to determine the exclusion regions in the input parameter space and determine the operation ranges for the critical factors. Also, the screening experiments contributed to determine the significant input parameters to be considered. The exclusion regions correspond to parameter combinations that do not work in practice during welding. As an example, it was shown that welding of thin materials (thickness 2 and 3 mm) has to occur at different parameter settings than the parameters used for the thick materials (thickness 4 and 5 mm). The ability to treat such exclusion regions is a unique feature of all of the Optimal design methodologies. In this study, approximately 150 experiments were included in the set of N-optimal experiments and 20 additional experiments were recommended by the use of guided experimentation. Altogether thirteen input parameters were considered and seven of these were four level parameters.

4.6 Welding Procedure

The parts used in the weldments were produced from extrusions of square tubing. The gage thickness of the extruded profiles varied between 2.0 mm and 5.0 mm. The weld was a T-fillet joint around the circumference of a butted tube end in a T-connection of a square tubular structural assembly. The weld configuration is shown in Fig. 3. The welding experiments were conducted in a robotic welding fixture, in which weld distortion was monitored during the welding process by using a LVDT (*Linear Variable Displacement Transducer*) to determine the amount of deflection of the chord. The weld was produced as two fillet welds, one starting at one

corner of the abutting hollow profile, along one side, around an adjacent corner and along a second side to the opposite corner. The second weld started at the same point as the first weld and progressing along the sides not included in the first weld and terminating at the same point as the first weld as shown in Fig. 4. The welds were deposited using a 4043 (AlSi5) filler wire and two different shielding gas compositions (pure argon and 70%Ar/30% He, respectively). The welding parameters included wire feed rate, weld travel speed, voltage, pulsing parameters, torch offset and a "ramp parameter" which represented a decreased heat input set of parameters for the second weld to accommodate the pre-heat caused by the first weld. All of the welding parameters were recorded electronically during each welding experiment. As noted before, the experiments were conducted in two phases. The first phase included the screening experiments and the set of experiments as suggested by the experimental design software. Then, the guided experimentation procedure was performed according to judgement of the S-parameter to provide data for refinement of the neural network model in regions of the parameter space where the model predictions are not within the accepted error bounds.

All of the welds were sectioned at eight locations along the length of the weld producing nearly 900 samples. These samples were metallographically prepared and the etched weld cross-section was captured using a video camera into a PC computer. The weld shape was quantified and stored electronically, using a special multiple spline fit program, to produce data for the neural network models. The graphical measurement screen used for capturing the weld cross section images is shown in Fig. 8.

To be able to monitor the degradation of the mechanical properties in the heat affected zone of the welds, the method described previously in section 2.2 of this paper which relates hardness to strength was applied. The method has been previously published and shown good correlation when used for weld strength prediction. Microhardness profiles were taken on multiple sections of each weld, to determine the hardness through the HAZ, as a function of the distance along the centerline of the material progressing away from the location of the. The resulting data set included approximately 10000 hardness readings.

5. FEATURES OF NEURAL NETWORK MODELS

This section is devoted to the neural networks. After the introduction, some features of perceptrons, feedforward neural networks and the backpropagation training algorithm are reviewed. Then, some limitations of the standard backpropagation method are stated before presentation of NATech's neural network concept applied in this work. Finally, testing of neural networks is discussed before the section is closed with a description of the neural networks developed in this study.

5.1 Introduction

A neural network is an empirical approach to process modelling. Such empirical models may be developed from various sources of data, both real and virtual. In general, however, experimental data from actual process operation is the best source of information for developing a neural network model to be used in planning and controlling the production process. Therefore, the

quality of the neural network model is a direct function of the quality of the data set. Carefully designed experiments are the key to producing high quality neural network models.

Neural networks are not a new technology, but a newly applied technology. This work does not intend to give a survey of different kinds of neural networks; the reader is referred to other publication for this kind of discussion [1, 3 - 9]. A brief review, however, of some of the most widely used networks is given in the next subsection. Neural networks (NN)[i] are an attempt to develop computer systems that emulate the neural reasoning behaviour of biological neural systems (e.g. the human brain). As such they are, mathematically, loosely based on the internal functioning of biological neural networks. For the interested reader, Chapter 1 in Bose and Liang's book [27] gives a description of the relationships between (artificial) neural networks and neuroscience.

Numerous examples of the application of neural networks can be found in the literature [30, 31, 32, 33]. In aerospace, neural networks have been use in applications like autopilots and aircraft control systems. In banking and finance, where neural nets are used very extensively they have been used for check reading, currency price predictions, loan approval, and for buy/sell decisions for stocks and other securities. Several applications like visual quality inspection systems, dynamic modelling, analysis of weld quality and chemical products can be mentioned in manufacturing. Other important application areas are defence, robotics, telecommunications and entertainment.

A neural network consists of a series of nodes (neurons) and weighted connections (axons) that, when presented with a specific input pattern, can associate specific output patterns. The operation characteristics of a neuron are shown in Fig. 5 and a typical architecture of a neural network is shown in Fig. 6. In essence, the neural network represents a highly complex, non-linear, mathematical relationship or transform. However, it is not necessary for the developer of such a system to understand the basic underlying physical or scientific principles of a process in order to develop an accurate ANS based process model. Thus, in this way it is quite different from other mathematical modelling approaches such as the Finite Element Analysis (FEA) method and more like the traditional statistical or regression type models. The primary difference between neural networks and statistical methods, however, is that neural networks are efficient at extracting patterns from data sets and the data need not be structured in orthogonal arrays. Usually, mathematical functions that resemble step functions have been used as transfer functions in neural networks. Due to computational reasons, the sigmoid function shown in 11Z has frequently been used.

The challenges in neural network development are to decide how many nodes and connections are needed to model a specific process, how to configure them, and to determine the specific values of the connection weights and the transfer functions that exist within the network. There is no direct known correspondence between the network parameters, it's operation, and the problem to be modelled by the network. One of the most successful approaches that has yielded reasonable results in developing networks is known as the "backpropagation" method. This method is described in sections 5.3 and 5.4 below.

---

[i] Sometimes also known as Artificial Neural Systems (ANS) or Artificial Neural Networks (ANN).

5.2 Perceptrons and Feedforward Neural Networks

Neural networks may be classified into static- and dynamic networks. Static networks are characterised by node equations that are without memory and delays; i.e. the output of the neural network is only dependent on the current input value to the node. Among others, the perceptrons (single and multilayered layered) neural networks belong to the group of static networks:

In the simplest form, perceptrons are one-layered neural networks with nodes that have a hard limit transfer function. This simple architecture places limitations on the computational power of the perceptron. The perceptron learning rule is used to train these single layered networks. Perceptrons may be coupled in series to form multilayer perceptrons (MLP). If one allows the transfer function to be more general than the hard limit function, such MLP networks are also denoted multilayer feedforward neural networks. Among the static networks, the MPL - or feedforward neural networks are most widely used. Such multilayer networks often use a log-sigmoid transfer function. If a linear transfer function is used at the output neurons, the network is capable of generating outputs of any value.

If a linear transfer function is used, training can be done by using the Widrow-Hoff algorithm. It should be noted that any multilayered network with linear transfer functions can be represented by an equivalent single layered network with linear transfer functions. This is an inherent property of the linear functions.

The backpropagation training algorithm was created by generalising the Widrow-Hoff learning rule to multiple layer networks with nonlinear differentiable transfer functions. Standard backpropagation is a gradient descent algorithm. By *using the standard backpropagation training rule, it may be difficult to obtain a solution. Even more, if one is able to find the optimal set of weight parameters, the convergence may be slow.* Numerous modifications of the standard backpropagation method can be found in the literature.

The learning rules described so far belong to the group of supervised learning rules. This means that they are presented with a set of example input-output pairs (x_i, d_i) and then trained to implement a nonlinear mapping that matches the training examples (datapoints) as close as possible.

During learning, the outputs of a supervised neural net are used to approximate supplied target (output) values from supplied input variables. *By generalization, however, is meant the ability of the neural network to approximate output data from input variables that are not in the training set.* Generalization is a measure of how well the neural network performs on the actual problem once training is completed; i.e. how good is the prediction performance of the network? The following conditions are typically necessary (but not sufficient) for good generalization:

- The function that the network tries to learn is in some sense smooth.
- The training data set must be a sufficiently large and representative subset of all cases that the network is supposed to generalize over.
- The network is large enough.

In a MLP (feedforward) network, the number of training samples should be approximately ten times the number of weights to achieve satisfactory generalization properies (i.e. avoid overtraining/overfitting). Other features of generalization are discussed by Hush [34].

Since, in general, a neural network performs a highly non-linear transformation from inputs to outputs of the network, it is possible also to 'overfit' the training data: The network behaves correctly for the training data but prediction based on test data may lead to very bad prediction properties. Such a network is unable to generalize properly; the situation is denoted overtraining or overfitting. Overtraining can be handled by Bayesian regularisation theory. Application of Bayesian neural networks is described by Cool and MacKay [35], [36]. Another method used to improve generalization is the Early-Stopping technique described in section 5.6.

A neural network that is not sufficiently complex can fail to detect fully the signal in a complicated data set. This leads to underfitting; i.e. the model performs badly for the training data points as well as for the test points.

5.3 The Back Propagation Training Algorithm

In the back propagation method, "training" of the neural network is a search for a network configuration that offers minimum error for all of the data points (examples) in the "training set". The method assumes that the search in weight space for a functioning network configuration can be accomplished as an iterative search using the error gradient (i.e. slope of the error surface). That is, a series of moves are accomplished on the multi-dimensional error surface using approximately the maximum mean squared error gradient direction as the move direction to a new set of weight values, at each iteration (training cycle). The error in the network is defined as the difference between the desired output representation and the actual output given the current weight matrix values. By calculating the maximum gradient of the mean squared error for any given training example (set of input and corresponding output patterns), the weights are adjusted so that the net moves along that gradient direction in each presentation of the training example to the network. Using this procedure, the network slowly "learns" to associate all of the training example input patterns with the correct corresponding output patterns by finding a global minimum on the error surface. A mathematical formulation of the backpropagation algorithm can be found in Hush's article [34].

5.4 Limitations of Back Propagation

This "basic" back propagation learning process has several significant drawbacks. *First, the optimum configuration* (i.e. number and relative location of hidden layers of nodes) *cannot be pre-determined by any known method and, yet, needs to be pre-assigned by using an "educated guess" in order to use this procedure*. Since the node configuration can significantly affect the operation of the network, this will at best lead to a long series of training re-starts and at worse to no useful network at all. *Secondly, the training process is very slow and no known method for predetermining the learning rate (gain term) will consistently choose an optimum value*. As with any search approach, taking steps that are too large will result in overshoot and an inability to find the minimum and steps that are too small will lead to very long search times. *Third, it has been*

shown that it generally requires a larger network to "learn" a problem than is required to solve the problem. There are techniques for trimming nodes or connections from a large network, but there is no known method of reducing the size the size of the network after training that will guarantee optimal net performance. Finally, *learning instabilities* exist in nearly every problem that will cause the network to stop learning (converging); *at least three types of learning instabilities have been shown to exist.* One of these instability types is known as a local minimum. This occurs when a "low" spot is reached on the error surface that is not the lowest error position. Using a geographic analogy, if you are sitting at the bottom of a lake, your local surroundings appear to go up in every direction. If your objective is to always move downward, you will be stuck. However, if you stop at that point, you will never find the bottom of the ocean (i.e. the absolute minimum error point on the surface). This problem has been studied, but for complex processes, it is often difficult to overcome this problem when using the traditional back propagation method.

5.5 A Novel Neural Network Concept

A new method developed at NATech for training neural networks has been shown to overcome many of the known problems with the back propagation method described above. The mathematical construct of a neural network is inherently good at zero-one or on-off, type problems (e.g. signal classification). Although the functions typically used as the nodal transfer function in a neural network are continuous functions, they are designed to produce output values that are not close to one or zero only in a very small range of input values. This problem persists in making it difficult to produce accurate continuous valued functional relationships with neural networks. Fig. 7 shows a neural network trained using an error gradient descent type method (e.g. back propagation). This neural network contains a relationship that is very similar to that of the underlying function that was used to generate the training points. However, there is some error in the neural network due, in part, to the transfer function - particularly at points located some distance from the training points. For many modelling applications, particularly where the slope of the response surface is important, this neural network has an unacceptably high error rate.

When the back propagation neural network is "pushed" to converge to very low error levels, or when an excessive number of hidden layer nodes are added in an effort to produce low error, the result is "over training". Fig. 8 illustrates the condition of over training. For many real problems, particularly complex process models, the back propagation method will produce either a low accuracy neural network, similar to the example shown in Fig. 7, or an overtrained (overfitted) neural network similar to the example shown in Fig. 8.

A new neural network architecture was developed that permits the development of highly accurate continuous valued models. This new neural network configuration, known as the Progressive Neural Network (P/NA), has a completely different hidden node structure than that of the commonly used networks. It is not possible to train this type of neural network using back propagation. The third type of this Progressive Neural Network, known as P/NA^3, is capable of highly accurate representation of continuous valued functions, as illustrated in Fig. 9.

Also, a new training algorithm (the D/NA; Delta/Neural-Activity Algorithm) [37] has been developed for the P/NA^3 neural network structure to provide accurate modelling of continuous valued processes and very fast convergence of the neural network during training. *By combining dynamic self - configuration of the neural network together with avoidance of learning instabilities, an operating network is virtually guaranteed for all problems. The network's ability to dynamically configure itself during training will produce a network size nearly optimal for the problem under study.* Finally, the P/NA^3 networks have good generalization properties and are not hampered with the over-training problems. The resulting neural network structure is ideally suited for all complex non-linear modelling problems, and provides a universal solution to empirical modelling with accurate prediction capabilities.

The P/NA^3 neural network structure with the D/NA training algorithm also has the ability to "refine" the neural network. That is, additional data points can be used to make minor adjustments to the neural network without affecting the overall network structure and without having to re-start the training process. When approximate models of the process already exist, the neural network can be trained to emulate the behaviour of the existing models (e.g. the finite element models) by using outputs from the existing models as basis for neural network training. Then the network can be refined using a very small number of additional data points from experiments (see guided experimentation below), reducing the cost of experimentation.

5.6 Testing of Neural Networks

In order to develop a level of confidence for a neural network model, it is necessary to thoroughly test the network. Testing and verification provide information that can be used in design and production process planning.

A variety of testing methods are currently used to test and verify the performance of neural network models. Three principal techniques are frequently applied alone or in combination. The first method, known as Train-Test-Verify requires three independent data sets. The first data set is used to train the neural network, the second data set is used to determine the effectiveness of the training process and determine when over training is eminent, and the third data set is used to verify the performance of the neural network. Training is stopped when the prediction error related to the test data set starts to increase while at the same time the error related to the training set still is decreasing. This situation is demonstrated in Fig. 10. This method of training neural networks is referred to as Early-Stopping.

The Jack-Knife and Boot-Strap methods require less excess data than the Train-Test-Verify method, but all three techniques require additional data in excess of that necessary to train the neural network. All experimentation costs resources, both fiscal and personnel, so the more excess data that is required, the higher the cost of developing the neural network.

NATech's methodology for training, testing, and verifying the performance of a neural network, does not require any additional data, other than the original neural network training set. This method, when coupled with the N-Optimal experimental design and Guided Experimentation to

pinpoint the specific data needed to characterise the process, offers the most cost effective approach to producing an accurate neural network model.

This method involves the use of a maximum likelihood estimator of the neural net predicted outputs, called the S-Parameter. This estimator has been shown to be a conservative estimator; that is, the error in the S-Parameter values is never less than the error in the outputs of the neural network. Additionally, it has been possible to show mathematically that the S-Parameter is a statistic that is t-distributed; it conforms to the student t statistical distribution. *Finally, the calculation of the S-Parameter does not require any additional data beyond the amount necessary to train the neural network.*

Fig. 11, 12 and 13 illustrates the use of the S-parameter. Fig. 11 shows a neural network developed specifically to have a very poor representation of the underlying function used to generate the training samples. Fig. 12 shows a neural network for which the confidence level is approximately 2 σ. The confidence level is approximately 99.5% as determined expected for that size of the confidence interval. Note that the value of σ is estimated by sampling the output prediction of the neural network at random positions and comparing those values to the values of the known underlying function. This approach is used in testing the S-parameter, but in practice one does not know the underlying function (i.e. the process response) since that is the objective of using the neural network. Fig. 13 shows a neural network developed using the N-optimal experimental design method, applying Guided Experimentation, and trained with the P/NA^3 neural network exhibits high accuracy and a corresponding high level of confidence predicted by the S-parameter test.

5.7 Development of the Neural Networks in this Study

The neural networks were trained using the P/NA^3 neural network described previously in this section. Each neural network was tested using the statistical S-parameter method, to determine the upper bound of the error in the model, and confidence levels for the predicted information. Then the multiple neural networks were integrated into a single software interface that provides the ability to simultaneously observe the weld shape, weld mechanical properties, and weld distortion predictions for the T-joint structural assembly. The software system also includes a search engine for simultaneously optimising the weld shape parameters and weld strength, while minimising distortion in the welded assembly. One should be aware that the multiple neural network structure consists of individual networks for the weld shape, weld mechanical properties, and weld distortion predictions. It has been more flexible to perform the model development by considering stand alone network structures for the individual phenomena rather than developing one comprehensive structure for all the different outputs. For the user, however, it appears as if one is dealing with only one neural network structure.

Training of the neural network for weld shape was relatively straight forward; NATech has long experience with neural networks for prediction of weld shape. Also, the use of a specially developed spline based (Windows compatible) software NAMeS for capturing the weld cross section pictures makes it possible to efficiently generate the weld shape training file. The

performance of the weld shape network is very good. Figure 14 shows the NAMeS software interface used for producing the weld shape data for training the neural network model.

Training of the hardness neural network was challenging. In general, the position in HAZ for the minimum value of hardness is varying. Initially, the network was trained to predict both position of the minimum hardness value as well as the value itself. This was very difficult to achieve; in fact even more data would have been needed to accomplish this. The problem was solved by associating the minimum value of hardness with a fixed position and let one of the output parameters of the hardness neural network be the shape of this normalised hardness curve. The actual position of the minimum value is easy to determine from the measurements and this position is modelled as the second output variable of the hardness neural network. Then by coupling this information with the predicted (i.e. normalised) hardness curve, it is possible to display a modified hardness curve that takes into account the actual position of the hardness minimum value as well as the correct minimum value. Also, this modification of the hardness neural network made significant improvement of the convergence rate of the training process for the hardness network.

The simplest network to train was in fact the deformation neural network. The predictions are very close to the measured deformation curves and the mean prediction-error is in the order of 4%. The network is able to predict the time dependent deformation during progress of the welding cycle. The time axis is discretised such that 512 outputs are used in the deformation neural network. The LVDT used to measure the displacement of the part during and following the welding process produced a signal that contained a significant amount of noise. Additionally, the LVDT was not set at zero for the start of each weld, due to variation in the exact shape of the square tube profiles that were welded. Consequently, for the training process to operate well, some pre-processing of the deformation data was needed. The deformation curves were corrected with a certain offset value; individually determined for each curve. Sudden jumps on the curve (i.e. obvious outlier points caused by noise in the LVDT data) were removed from the database and moving average filtering was done on the resulting curve by taking into account five points on each side of the actual time position along the curve. Training of the neural network was simple and convergence was obtained within 5 minutes of the onset of training.

Is it in general possible to determine when the training process should be stopped? Obviously the error in the neural network can never be less than the error in the experimental data themselves; i.e. the quality of the network predictions depends on the quality of the data. Therefore, there is a certain threshold value for the prediction error of the network; the error should not be reduced below this threshold since one then starts to correct errors that are intrinsically present in the data themselves. Thus, the training process is stopped according to experience gained through a number of neural network modelling - projects. Replicates are included in the designed experiment, and statistical analysis of the results from those replicates is used to produce an estimate of the error inherent in the experimental data.

6. THE COMPUTER MODEL

A standardised Microsoft Visual C++ based graphical usér interface has been designed for use with neural network based empirical models. This kind of graphical user interface was used for presentation of the simulations performed by the suite of neural network models discussed in this work. The interface allows the user to execute model simulations in an intuitive manner and also makes it possible for the user to have an excellent overview of the model outputs at any time. The standard graphical user interface is designed in a flexible manner that makes it possible to fit the tools in the interface to different kinds of neural network based models tasks. Work is continuously done to improve the flexibility of the standard graphical user interface. In the following, some features of the graphical user interface are described with focus on graphical issues and a search facility used for optimisation of weldment properties.

6.1 The Graphical User Interface

As shown in Fig. 15, the interface consists of four windows that can be individually resized and moved around on the computer display. The bottom window is the "Slide Bar Input Window" which allows the user to control the setting of the welding parameters and other input parameters for the neural network models. The use of slide bars facilitates the handiest way of entering input data to the models. Due to the rapid execution time of the neural network models (i.e. in the order of milliseconds), the user will see an immediate response of changes of the input variables in the "Output Window" and the "Visual Display Window". The output window contains a number of engineering parameters for classification of geometric features of the weldment. The green and red colour coding signals that the computed output variable is within or outside the SPC limits respectively. In the "Visual Display Window", the user may view the weld shape, the hardness distribution or the deflection of the weldment respectively. In the upper part of the compound window can be seen the a window with a set of scroll-down menus designed in the same way as one may recall from standard Windows-based computer programs; note the presence of the "File", "Options" and "View" menus. Under these menus the user will find menu selections comparable with the ones usually present in Windows based software.

6.2 Search Optimisation and Graphical Features

The search optimisation facility is operated by using the items under the "Search" menu in combination with tick-marking of the relevant parameters in the "Input Parameter Window" that are supposed to be actively used in the search. One should note that a "S"-marked check box is associated with each of the slide bars for the input parameters. If an input parameter is allowed to vary during the search, the "S"-box should be checked. All the other input parameters will then stay at the current values of the slide bars. Under the "Search"-menu, allowable ranges for the output parameters (SPC-limits) and target values may be specified along with specification of output parameter weights i.e. the relative importance of the output parameters during the search. Allowable ranges of the input parameters as well as their costs may also be specified. The SPC limits can be adjusted by using scroll bars as shown in fig. 16. In this way, the objective function for the search may be specified. The search resolution may also be set and finally, the search operation may be invoked. The search is performed by first evaluating the performance criterion

over the whole input parameter domain according to the selected resolution. Then a gradient-based search is executed in the part of the input domain that so far has got the most optimal solution. When the search is completed, the input parameters are set to the optimal values and the optimal solution presented in the "Output-" and "Visual Display" windows.

The graphical features under the "DynaGraph (TM)" menu may then be used to display the result of the search. Menu items for setting of SPC-limits and resolution are also available here. Also, the type of surface to be displayed can be selected and it is possible to select the axes of the graph. Then by invoking the "Generate Graph" item under the "DynaGraph (TM)"-menu, the response surface corresponding to the current input parameter setting will be presented. Note that the "DynaGraph (TM)" menu may be used for graphical display of the outputs of the neural networks at any stage during exercise with the software. An example of such a response surface is displayed in Fig. 17.

7. APPLICATION OF THE MODEL

The search engine of the neural network model was applied for optimising the properties of the welded T-joint. In order to carry out a search, the SPC-limits for each separate output parameter must be defined. In the present work, the SPC-limits for the weld bead shape were set according to an internal weld quality standard. The other SPC-limits were approximated from typical performance requirements for similar types of welded aluminium joints. Additionally, an output weight number can be devoted to each separate output parameter in order to rate their relative importance in the performance criterion.

7.1 Optimisation of Individual Properties

First, the model was used to optimise individual properties. This was done by assigning a high value of the output weight number for the specific property to be optimised. Similar searches were then successively performed for the individual properties listed below:

Case 1: Optimisation of productivity (maximise weld travel speed).
Case 2: Optimisation of fatigue properties (maximise weld toe angles).
Case 3: Optimisation of HAZ strength (maximise yield and tensile strength).
Case 4: Optimisation of distortions (minimise weld distortion).

The results from these search operations are summarised in Table 1. It is evident from the table that optimising just one property at a time is not a method that can be recommended since other properties than the optimised one will be neglected in the search and, as a result, they will easily fall outside the defined SPC-limits.

7.2 Overall Optimisation of Properties

In practice, welding of aluminium space frame assemblies demands that the process be optimised for a number of different properties. In the present case, this means that one has to seek the best trade-off between the different output parameters in the neural network model. This can be

Table 1. Results from the neural network models search engine. Plus and minus signs indicate that the specific property is within or outside the defined SPC-limits, respectively.

Property	Case 1	Case 2	Case 3	Case 4	Case 5
Weld shape	+	-	-	-	+
Fatigue	-	+	-	-	+
HAZ strength	-	-	+	-	+
Distortion	-	-	-	+	+
Productivity (m/min)	1.26	0.99	0.99	0.99	1.05

achieved by investigating the response surfaces of the output parameters to obtain a better impression of the sensitivity between different input and output parameters. Also manipulation with the output weight numbers for the different properties is an efficient way of "compromising" between the different properties. By utilising these techniques, Case 5 in Table 1 was obtained. As can be seen, this specific combination of welding parameters results in properties that are all within the SPC-limits. Moreover, a slight increase in productivity is also observed for this case compared with case 2, 3, and 4.

Figs. 18, 19 and 20 show examples of visual outputs from the graphical user interface which display the weld shape, the weld distortions, and the HAZ strength distribution. All figures are from Case 5. As seen from Fig. 18, the actual choice of the interactive changeable control parameters will produce a weld where all the critical geometrical shape parameters are within the defined SPC-limits (i.e. green colours).

Figure 19 shows two different curves for the HAZ hardness distribution across the brace and cord, respectively. These curves are qualitatively very similar to the schematic diagrams shown in Fig. 3, which indicates that dissolution and reprecipitation of hardening particles are the governing mechanisms determining the HAZ strength as explained in Section 2.2. The important strength parameters from an engineering design point of view are the minimum values for yield and tensile strength which are both within the specifications for the chosen set of control parameters.

Figure 20 shows the time variation of the vertical deflection of the chord during welding. A positive value on the y-axis corresponds to thermal expansion of the material adjacent to the weld during heating and a corresponding global deflection as shown schematically in Fig. 2(a). Contrary, a negative value corresponds to the situation shown in Fig. 2(b) and is associated with thermal contraction during cooling. The two peaks in the curve arises because the material is given enough time to cool significantly in the 10 seconds time period after the first weld is finished and before the second weld is started. As seen from Fig. 20, the selected set of process parameters yields an end distortion of only 0.098 mm which correspond to 0.51 mm/meter length of the profile.

8. FUTURE APPLICATIONS OF NEURAL NETWORK MODELS

Traditionally, neural network models are trained with basis in data sets provided from experimental work performed in the laboratory. Neural networks, however, are also capable of using data generated by other sources of information. A very interesting possibility is to use the results from FE-calculations as the basic input data for training neural network models. Such FE-calculations may take hours to complete, but when the data provided from such calculations are used for training of neural networks one will obtain a model that is capable of providing the same results within milliseconds of execution time. Such a combination of models utilises the neural network model's advantage of rapid calculations with the FE-modelling technique's capability to test completely new geometric designs. Examples of neural network models based on FE-calculations already exist in the literature [39], and others must be expected to arrive in the future.

Another application of neural networks is their use in control. The neural network is a non-linear model, that can be operated in real-time on very fast digital signal processor (DSP) hardware. The neural network is often generated as a feedforward model; that is, the inputs are the controlled or measured parameters of the process operation, and the outputs are the outcome of the process. Generally, model based controllers are developed by inverting a feedforward model to produce a feedback model, which is then used to set the operating parameters of the process. In many cases, it may not be possible to construct a feedback model because of the relationships that exist in the process data. For example, if two different sets of input parameters can produce identical outputs, it is easy to produce a feedforward model, but will be impossible to produce a complete feedback model. Methods have been developed to operate a control system, using a feedforward model, and these are being applied with neural network based control system for welding [40].

9. CONCLUSIONS

In this work, the powerful non-linear prediction capability of neural networks is exploited in a neural network based computer model for simultaneous prediction of shape, properties and distortions of aluminium weldments. The model includes a search engine for optimisation of these characteristics of the weldment. A set of exclusion rule assist during usage of the software both in manual operation as well as automatic search to generate output only from combinations of input parameters that are physically realistic. However, the quality of the model predictions relies entirely on quality of the experimental data used as basis for training and testing the neural networks. Accurate work during the data collection is therefore a prerequisite for a model of acceptable prediction performance.

To assist in the data collection part of the work, an experimental design methodology specially formulated for neural network model development was used to suggest the set of experiments to be conducted. This technique of experimental planning is based on the theory of optimal designs with an objective to minimise the number of experiments needed to derive the empirical neural network based model. This is very attractive since in most cases, experimental work in the industry is costly and time consuming.

It should also be noted that all the information generated during experimental work is used for training the socalled P/NA^3 neural networks; i.e. there is no need to divide the database into test- and verification datasets in addition to the training set. In fact, this is an exclusive feature of the neural network concept used in this work. In the concept, testing and verification of the neural networks are done by the use of a novel statistical method that determines the upper error bound in the model predictions. In this way, the analyst will be informed about possible sub-domains in the input parameter space that causes predictions with an error outside the accepted error bound. Then it is possible to collect more experimental data in this domain and continue training of the neural network to improve the prediction performance in this (these) domain(s). Note that training of the network can be continued with basis in the solution that so far has been determined. Thus, there is no need to start retraining the network with the weights reinitialised to all random numbers.

The use of the neural network has shown that simultaneous optimisation of weldment properties is possible but also that other properties may fall outside the SPC-limits if optimisation is focussed on only one weldment property. This kind of neural network based computer model puts new perspectives into the use of computer based tools as basis for virtual design and manufacturing as used in the industry. This is due both to the systematic approach used for derivation of the models as well as the short runtimes and powerful prediction capabilities of such models. Costs of model development efforts are predictable and as the model becomes available it virtually allows the user to weld on the computer. Finally, one should also be aware that the data used for training the neural networks can be obtained from traditional experimental works as well as be generated from the output of finite element based simulations. In this way, the rapid runtimes of empirically based neural network models is exploited to generate predictions that could also be obtained from first principles finite elements models but then usually after hours of execution time.

ACKNOWLEDGEMENTS

The authors are grateful to Hydro Raufoss Automotive Technical Centre AS for giving the opportunity to publish the results presented in this work

APPENDIX A
The AA6XXX Aluminium Alloy Series

The welds studied in this work were made from hot extrusions of two age hardenable aluminium alloys AA6063 and AA6082; each alloy in the peak aged temper condition (T6). These alloys belong to the AA6XXX. Age hardening of such alloys is performed over a limited period of time to avoid overaging; i.e. reduction of the strength of the material.

According to the phase diagram these alloys will in the single - phase region (at high temperature) consist of the phase α which contains aluminium with a mixture of Mg and Si in solid solution. The two phase region (at lower temperature) is a mixture of α and an intermetallic phase β. The solubility of Mg and Si in the aluminium matrix decreases with temperature but the elements will remain in solid solution if the alloy is rapidly quenched from the higher temperature down to room temperature. If then, the alloy is heated to a certain temperature, artificial ageing of AA6XXX alloys will occur according to the following (ageing) sequence:

Supersaturated $\alpha \rightarrow$ GP1 zones $\rightarrow \beta''(Mg_2Si)$ needles $\rightarrow \beta'(Mg_2Si)$ rods $\rightarrow \beta$ equil.

This operation leads to precipitation hardening of the alloy. GP1 represents the socalled Guinier-Preston zones which most possible are spheres of Mg and Si. β'' represent an intermediate very fine needle shaped precipitate structure along the <100> directions in the aluminium matrix. β''precipitates are the main strengthening contributing particles in the AA6XXX-alloys. The next intermediate β' precipitates are more coarse, partly coherent rods which do not contribute to strengthening of the material since their number density is too low. The maximum strength is achieved for a certain number density and size of β''. If the alloy is held (aged) for very long times at a given temperature, strength will be lost due to formation of completely incoherent equilibrium precipitates β (i.e. the interparticle spacing is increased). This effect is known as overageing. The presence of the very fine, needle shaped β'' precipitates contributes to high yield strength values in the artificially aged T6 condition. The AA6XXX alloys are weldable, but as discussed in section 2.2, they suffer from severe softening in the heat affected zone because of dissolution of the β'' precipitates during the weld thermal cycle. Total recovery of the strength of the HAZ is not possible (without performing a completely new solution heat treatment) due to formation of non-strengthening β' particles during the cooling leg of the thermal cycle. However, strength recovery after welding may be enhanced by artifical ageing.

APPENDIX B
EXPERIMENTAL DESIGN

A typical exercise in experimental design has to go through the following phases:

Define the problem
Specify the type of model to be used
Select type of Experimental Design
Run the experiments
Analyse/ use the data (to determine the unknown model parameters)
Interpret the results

In this appendix, items one to four on the list are discussed in sequence. Then, some features of Taguchi and D-optimal designs are discussed.

B.1 Define the problem

It is of great importance to have knowledge about the behaviour of the process and also to decide which features of the process that one wants to study. Typical ingredients in this step are as follows:

1. Identify input variables (input parameters, factors)
2. Classify the nature of the input variables:
   - *Qualitative* parameters, i.e. parameters that only can take *discrete values*.
   - *Quantitative* parameters, i.e. parameters that *varies continuously*.
3. Which factors (input variables) can be controlled in an experiment?
4. Decide the level of each factor (i.e. select values for the qualitative parameters and discretise the qualitative parameters).
5. Identify process output parameters (output parameters are called response variables).

In a process with a lot of input parameters, it may be a challenge to extract the important ones. This can be done by screening - experiments to obtain information of the process. Also, these screening experiments can help as an aid to determine the operation range for each factor. The screening experiments performed in the T-joint project served both these purposes: Due to the result of the screening experiments, it was decided to introduce the voltage as an input variable. Screening experiments were also needed to set the right values for the range of the parameters (i.e. the minimum and maximum values of the input parameters). Even more, the range of a typical quantitative parameter (i.e. voltage, wire feed rate etc.) was dependent on the value of typical qualitative parameters like material thickness.

It should be noted that there is a trade-off between the number of factors to be included in the model and the number of experiments.

B.2 Select the Model

The number of levels for each factor (i.e. the number of values that are considered for each parameter) must be determined according to the type of model we want to use and the nature of the process that is studied. To determine second order effects, one at least needs three levels for each factor. In the N-Optimal design, a minimum of at least four levels is recommended for each quantitative (continuous) factor.

The type of model depends on the characteristics of the process. If second order effects are present in the process, a second order (quadratic) model must be used. In some cases, even higher order models are needed; i.e. cubic models or higher. It should be noted that the size of the experimental design matrix depends on the complexity of the chosen model.

In general, the simplest possible model should be selected. Quite frequently linear models with possible interaction terms are used. Nonlinear models may also be applied but often a nonlinear transformation is used so that linear regression still can be used to obtain the unknown coefficients in the model.

B.3 Select Experimental Design Methodology

The experimental design methodology is an aid for determining the actual set of experiments to be performed. The following has impact on the selection of the experimental design technique:

- The experimental objective
- The number of factors
- The type of factors
- The terms in the model

Quite frequently, the levels of a factor are *scaled* for ease of use in designing the experiments. The scaling is a linear transformation and is also called a *standardisation*. Two level factors are often coded by (–1) for the low level and (+1) for the high level respectively. For three level factors, codes –1, 0 and +1 (or 0, 1 an 2) are used.

A special feature of some experimental designs is that they are *orthogonal*, i.e. the correlation between the factors is zero. Orthogonality lets the desired effects be measured independently of each other. This means that the influence of each factor can be tested without the influence from other factors.

The number of possible experimental designs that may be chosen in a certain case may depend on whether the factors are qualitative or quantitative.

Experimental designs can be described by the ability to identify the effects considered in the model (i.e. distinguish between the different terms in the model). *Confounding* happens when two effects cannot be distinguished from one another. In a design of *resolution* **R**, no *p*-factor effect is confounded with any other effect containing less than *(R-p)* factors. A design of resolution R=III

does not confound main effects (i.e. terms depending linearly on one factor) with one another but does confound main effects with two factor interactions. A design of resolution R=IV does not confound main effects and two-factor interactions but does confound two-factor interactions with other two factor interactions. Characteristics for higher order resolutions may also be specified.

B.4 Run the Experiments

The result of the experimental design is a matrix of experiments. The execution of the experimental matrix should be randomized to minimize the chance of obtaining experimental results that are biased by possible factors that are not considered in the experiment. Often, the experimental design software package will give a list of randomized runs for the experiment.

B.5 Taguchi Designs

Taguchi designs [39] belong to the classical designs. These designs, originally developed by Genichi Taguchi, were primarily designed for identification of significant process factors i.e. main effects. The designs rely heavily on orthogonality. Thus the designs are simple and allow for reproducibility and cost effective conduction of experimental work. Unfortunately, these designs do not allow for identification of all interaction terms due to confounded effects since the designs generally have resolution R = III. The Taguchi analysis generally can be used to determine the settings for the process that results in the best outcome. The prediction equations generally associated with Taguchi designs basically gives an overall predicted value by using differences from the mean value.

Research performed at NATech, has shown that Taguchi type of designs are the second best alternatives for performing experimental designs to be used in association with neural network modelling. This is probably due to the fact that the designs are well suited for determining the main effects in the process. Also the cost efficiency and reproducibility of the method are important factors which makes the Taguchi design suited for designing experiments to be used with neural networks.

B.6 Optimal Experimental Designs

Classical experimental designs are often the most elegant and powerful tools for solving practical engineering problems. They are based on a standard geometrical formulation or they constitute a subset of all possible designs (i.e. fractional factorial design). Unfortunately, restrictions on sample size (i.e. sample size; number of experiments, should be as low as possible), constraints on the region of operability for the factors and other special features of the design situation may prevent the use of the classical designs. In such cases, the use of an optimal design technique is the only alternative. According to a certain criterion, these designs maximise the amount of information in an experiment. It should be noted that the optimality of an optimal design is closely linked to the criterion used for the design. If the criterion is changed, redesign according to the new criterion has to be done to achieve optimality.

B.6.1 D Optimal Design

D-optimal design is based on a design criterion that maximises the amount of information in the design. The criterion is expressed as finding the maximum value of the determinant of the matrix X^TX where X is the design matrix. A definition of the design matrix X is given below. How does the determinant of X^TX, measure the information in a design? The mathematical objective of D-optimal design is to determine good values of the unknown model parameters (contained in the vector $\underline{\beta}$; described in the next subsection). The noise in the process introduces uncertainty in the estimated values of the parameters. One way to express this uncertainty is by a region in the space of the parameters, which is likely to contain the true but still unknown parameters $\underline{\beta}$. The idea in D-optimal design is to minimise the volume of this region.

D-optimal designs can handle mixed level experiments; i.e. the factors do not need to run with the same number of levels. D-optimal designs are also attractive in that they often need fewer runs compared to standard classical designs. The reduced number of runs is a very important feature in industrial settings where the runs may be very expensive.

Two effects of using the determinant as the criterion for D-optimal design should be stated. Firstly, in design situations were all the factors are quantitative (i.e. varies continuously), the D-optimal design places the experimental runs on the edges and vertices of the factors' region of operability.

Once there are enough runs to completely determine the unknown parameters in the model, the algorithm for D-optimal design tends to replicate runs that are already included in the design rather than adding completely new experiments. Then, there is generally very few runs that can be used to assess the possible lack of fit of the apriori model and the experimenter relies heavily on the correctness of the model. In the standard D-optimal design, the data are mostly taken from the boundaries of the factors' operation range. Obviously then, interpolation inside the operation ranges of the factors may give predictions which do not compare well to reality if the model is invalid.

B.6.2 Mathematical Theory for Optimal Designs

St. John [26] gives a very brief introduction to the field of optimal design by the use of a mathematical formalism for stating the optimal criterion used for G- and D- optimal design. In the simplest case, a linear regression model of the following type is considered [26]:

$$y_i = f^T(\underline{x}_i)\underline{\beta} + \varepsilon_i \qquad (1)$$

where i= 1, ..., n. n is the number of experiments (observations). y_i is the responses (observations). $f(\underline{x}_i)$ (p x 1) is a vector that depends on the form of the selected response function. $\underline{x}_i$ (q x 1) a vector of predictor variables. ε_i is a noise term; the process noise is assumed to be noncorrelated (i.e. the variance is σ^2) and have zero mean value. $\underline{\beta}$ (p x 1) is a vector of unknown model parameters. The model can be expressed in matrix notation as follows

$$\underline{y} = X\underline{\beta} + \underline{\varepsilon} \qquad (2)$$

Now, $\underline{y}$ (n x 1) is a vector of the process responses (process observations). X (n x p) is the design matrix where the i'th row contains the vector $f^T(\underline{x}_i)$. Again, $\underline{\beta}$ (p x 1) is the parameter vector and $\underline{\varepsilon}$ is independently and identically distributed random variables with mean zero and variance as specified above. The experimental region is denoted by χ; i.e. the vector has to belong to χ. A typical example of the vector $f(\underline{x}_i)$ may be

$$f^T(\underline{x}_i) = (1, x_1, x_2, x_1x_2, x_1^2) \qquad (3)$$

We see that in this model, two factors (input parameters) x_1 and x_2 are considered. The model is quadratic since terms x_1^2 is included. We also see that the model contains a constant and the linear terms x_1 and x_2. Finally, an interaction term x_1x_2 is included. In this model, q = 2 (i.e. $\underline{x}_i = [x_1\ x_2]^T$) and p = 5. If $x_1 = 0.8$ and $x_2 = 0.5$ for the i'th experiment, the design matrix will contain the line (1, 0.8, 0,5, 0.4, 0.64) in the i'th row. Thus, the design matrix is the collection of these rows for every run in the experiment.

At a point $\underline{x} \in \chi$, the predicted response is:

$$y_p = f^T(\underline{x})\beta_e \qquad (4)$$

The least squares estimates of the parameters is given by

$$\beta_e = (X^T X)^{-1} X^T \underline{y} \qquad (5)$$

where y_p is the predicted response and β_e is the vector of estimated parameters.

In optimal design, the design problems consists of selecting vectors x_i (i=1,2, ... ,n) such that the design defined by these n vectors (i.e. the experimental design matrix X) is in some sense optimal. In D-optimal design, the criterion is related with maximising the determinant of the matrix X^TX. The matrix X^TX needs to be non-singular (i.e. no linear dependent rows or columns in the matrix) for the design to be optimal.

For polynomial regression, this is comparable to minimising the maximum variance for the selected model. To state the criterion by using the linear model notation, we may write:

$$\left[x_i(i = \overset{\min}{1,2,\mathrm{K},n})\right]_{x\in\chi}^{\max}\left(\mathrm{var}(y_p)(x)\right) \qquad (6)$$

where var(y_p) is the variance of the process response y_p. The regression model presented above is very restrictive since it assumes that the response function is linear in the parameters. St. John [26] discusses how the optimal design theory can be extended to also include nonlinear response functions.

REFERENCES

1. D. R. WHITE and J. E. JONES: 'The use of Neural Networks for Automotive Body Applications', *IBEC'96: International Body Engineering Conference & Exposition*, 1996.

2. L. J. YANG, M. J. BIBBY and R. S. CHANDEL: 'Modelling the submerged -arc welding process using linear regression equations' in S. A. David and J, M. Vitek ed., *International Trends in Welding Science and Technology: Proceedings of the 3rd International Conference on Trends in Welding Research*, ASM International, Gatlinburg, Tennessee, USA, June 1-5, 1992, pp. 411-415.

3. I. S. KIM and A. BASU: 'A study of influence of welding process variables on GMAW', *Transactions of Mechanical Engineering, Australia*, 1995, **20**(1), 35-41.

4. J. JONES: 'Weld Parameter Modelling', in S. A. David and J, M. Vitek ed., *International Trends in Welding Science and Technology: Proceedings of the 3rd International Conference on Trends in Welding Research*, ASM International, Gatlinburg, Tennessee, USA, June 1-5, 1992, pp. 895-899.

5. X. XU, et. al.: 'The use of Neural Network Technology in Welding and Materials Applications', in T. Zacharia ed., *Modelling and Control of Joining Processes,* American Welding Society, Orlando, Florida, December 8-10, 1993, 203-214.

6 KLEIN, C. F., "Case Study of a Neural Network Model of a Automobile Seat Structural Weld",T. A. Siewert ed., 'Computerization of Welding Information IV. Proceedings, International Conference', November 3-6, 1993, Orlando, Florida, USA

7. J. SZEKELY: Keynote address: 'The mathematical modeling of arc welding operation', in S. A. David and J, M. Vitek ed., *Advances in Welding Science and Technology: Proceedings of the 3rd International Conference on Trends in Welding Research*, ASM International, Gatlinburg, Tennessee, USA, 18-22 May, 1986, pp. 3-14.

8. Y. H. WANG and S. KOU: 'Driving forces for convection in weld pools', in S. A. David and J, M. Vitek ed., *Advances in Welding Science and Technology: Proceedings of the 3rd International Conference on Trends in Welding Research*, ASM International, Gatlinburg, Tennessee, USA, 18-22 May, 1986, pp. 65-70.

9. T. ZACHARIA, A. H. ERASLAN, D. K. AIDUN and S. A. DAVID: 'Three dimensional model for arc welding process', *Metallurgical Transactions*, 1989, **20B**, 645-659.

10. A. MATSUNAWA and S. YOKOYA: 'Fluid flow and its effect of penetration shape in stationary arc welds', in S. A. David and J, M. Vitek ed., *Recent Trends in Welding Science and Technology: Proceedings of the 2nd International Conference on Trends in Welding Research*, ASM International, Gatlinburg, Tennessee, USA, 14-18 May, 1989, pp. 31-35.

11. MATSUNAWA, A., Keynote Address: 'Modeling of heat and fluid flow in arc welding', in S. A. David and J, M. Vitek ed., *International Trends in Welding Science and Technology: Proceedings of the 3rd International Conference on Trends in Welding Research*, ASM International, Gatlinburg, Tennessee, USA June 1-5, 1992, pp. 3-16.

12. J. GOLDAK: Keynote address: 'Modeling Thermal Stresses and Distortions in Welds', in S. A. David and J, M. Vitek ed., *Recent Trends in Welding Science and Technology: Proceedings of the 2nd International Conference on Trends in Welding Research*, ASM International, Gatlinburg, Tennessee, USA, May 14-18, 1989, 71-82.

13. A. KELLY and R. B. NICHOLSON: '*Precipitation Hardening*', Progress in Materials Science, Vol. 10, Pergamon Press, London, 1963.

14. O. R. MYHR, Ø. GRONG: 'Process Modelling Applied to 6082-T6 Aluminium Weldments-I. Reaction Kinetics', *Acta Metall. Mater.*, 1991, **39** (11), 1991, 2693-2702.

15. O. R. MYHR, Ø. GRONG: 'Process Modelling Applied to 6082-T6 Aluminium Weldments-II. Applications of the Model, *Acta Metall. Mater.*, 1991, **39** (11), 1991, 2703-2708.

16. O. T. MIDLING: M.Sc. Thesis, The Norwegian Institute of Technology, Trondheim, 1988.

17. Ø. GRONG: 'Metallurgical Modelling of Welding', 2nd Ed.' The Institute of Materials, The University Press, Cambridge, 1997.

18. O. R. MYHR, Ø. GRONG, S. KLOKKEHAUG, H. G. FJÆR and A. O. KLUKEN: 'Process Model for Welding of Al-Mg-Si Extrusions. Part I: Precipitate Stability', *Science and Technology of Welding and Joining*, 1997, **2** (6), 245-254.

19. O. R. MYHR, S. KLOKKEHAUG, Ø. GRONG, H. G. FJÆR and A. O. KLUKEN: 'Modelling of Microstructure Evolution, Residual Stresses and Deformations in 6082-T6 Aluminium Weldments', *Welding Journal*, **77** (7), July 1998, 286-292

20. O. R. MYHR, S. KLOKKEHAUG, H. G. FJÆR, Ø. GRONG and A. O. KLUKEN: 'Modelling of Microstructure Evolution and Residual Stresses in Processing and Welding of 6082 and 7108 Aluminium Alloys', *The 5th International Conference on Trends in Welding Research*, Georgia, USA, 1-5 June 1998.

21. G. O. RADING and J. T. BERRY: 'A Model for Heat-Affected Zone Hardness Profiles in Al-Li-X Alloys', *Welding Journal*, **77** (9), September 1998, 383-387.

22. E. SARRAZIN: Ph. D. Thesis, Ecole Polytechnique, Palaiseau, France, 1995.

23. D. RADAJ, H. HAEUSER and S. BRAUN: Numerische Simulation von Eigenspannungen und Verzug bei Schweissverbindungen aus AlMgSi-Legierungen, *Konstruktion*, 1998, **50**, 30-38.

24. A. C. ATKINSON and A. N. DONEV: '*Optimum Experimental Design*,' Clarendon Press, Oxford, 1992.

25. S. R. SCHMIDT and R. G. LAUNSBY: '*Understanding Industrial Designed Experiments*' 4th Edition, Air Academy Press, Colorado Springs, 1997.

26. R. C. ST. JOHN and N. R. DRAPER: 'D-optimality for Regression Designs: A Review', *Technometrics*, **17** (1), 1975.

27. X. N. K. BOSE and P. LIANG: Neural Network Fundamentals with Graphs, Algorithms, and Applications, McGraw-Hill International Editions, Elecrtical Engineering Series, 1996.

28. R. IRVING: 'Successful Welding Operations: Aren't They Top Management Responsibility', *Welding Journal*, May 1994, 33-35.

29. W. W. McCULLOCH and W. PITTS: 'A Logical Calculus of the Ideas Imminent in Nervous Activity', *Bulletin of Mathematics Biophysics*, **5**, 1943, 115-133.

30. B. WIDROW and M. E. Hoff: 'Adaptive Switching Circuits', 1960 IRE WESCON Convention Record, part 4, New York Institute of Radio Engineeris, pp. 96-104, 1960.

31. K. ASAKAWA and H. TAGAKI: 'Neural networks in Japan', Communications of the ACM, 1994, 37 (2), 106-112.

32. H. DEMUTH and M. BEALE: 'Neural Network Toolbox for use with MATLAB', Version 3, User's Guide, January 1998.

33. DARPA Neural Network Study, Lexington, MA: M.I.T. Lincoln Laboratory, 1988.

34. D. R. HUSH and B. G. HORNE: 'Progress in Supervised Neural Networks, IEEE Signal Processing Magazine, 8-36, January 1993.

35. T. COOL, H. K. D. H. BHADESHIA and D. J. C. MACKAY: 'Modelling the Mechanical Properties in the HAZ of Power Plant Steels I: Bayesian Neural Network Analysis of Proof Strength', in H. Cerjak ed., 'Mathematical Modelling of Weld Phenomena 3, Materials Modelling Series, The Institute of Materials , The University Press, Cambridge, UK, 1997, pp. 403-442.

36. D. C. J. MACKAY: 'A Practical Bayesian Framework for Backprop Networks', J. E. Moody, S. J. Hanson and R. P. Lippman ed., *Advances in Neural Information Processing Systems*, **4**, 839-846, 1997.

37. JONES, J, "A Radar Signal Processing Application of Neural Networks", Report, Colorado School of Mines No. TI8604, submitted to Texas Instruments, May 1986.

38. JONES, J., "A Neural Network Model of the Friction Soldering Process", Report, N. A. Technologies Co. #94231, submitted to Ford Motor Company, February, 1996.

39. R. K. ROY: 'A Primer on the Taguchi Method', Society of Manufacturing Engineers, 1990.

40. D. WHITE, J. A. CHARMEIN, J. E. JONES, K. LIU: 'Integrated Control of Welding with Neural Network based Process Control Methods', T. A. Siewert ed., 'Computerization of Welding Information IV. Proceedings, International Conference', November 3-6, 1993, Orlando, Florida, USA, 310-324.

41. W. W. McCULLOCH and W. PITTS: 'A Logical Calculus of the Ideas Imminent in Nervous Activity', Bulletin of Mathematics Biophysics, 5, 1943, 115-133.

42. F. ROSENBLATT: *Principles of Neurodynamics*, Spartan Books, New York, 1962.

43. D. E. RUMELHART, D. E. HINTON and R. J. WILLIAMS: 'Learning Internal Representation by Error Propagation', in Parallel Distributed Processing, Vol. 1, MIT Press, Cambridge, MA., pp. 318-362, 1986.

44. D. B. PARKER: 'Learning Logic', Invention Report S81-64, File 1, Office of Technology Licensing, Stanford University, Stanford, CA, 1982.

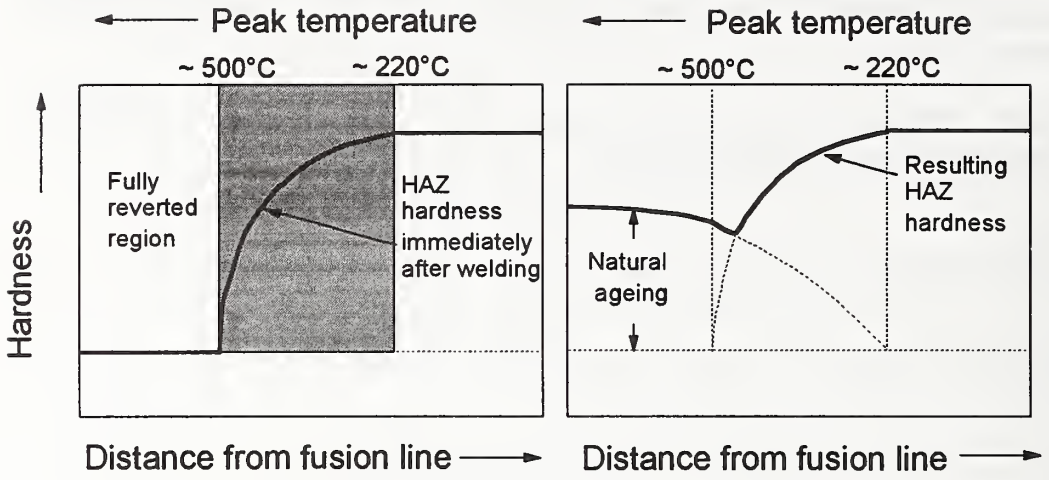

(a) *(b)*

Figure 1. Schematic diagrams showing the HAZ hardness distribution immediately after welding of peak aged (T6) Al-Mg-Si alloys; (a). Hardness distribution following prolonged room temperature aging; (b). (From Ref /6/).

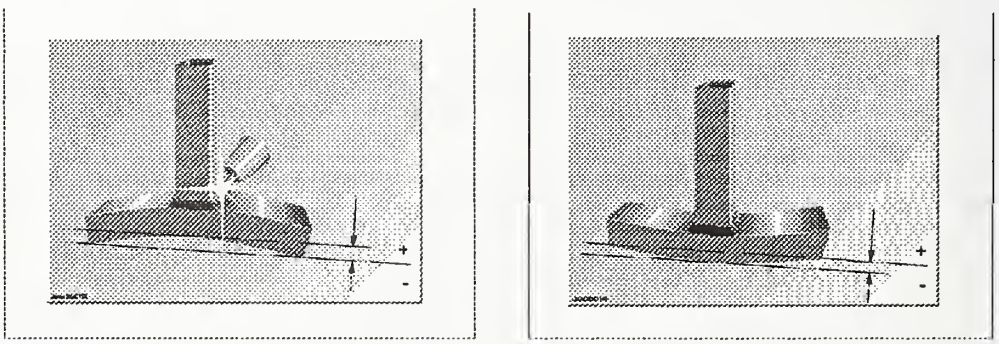

(a) *(b)*

Figure 2. Schematic diagram of deformations in welding of a T-joint. (a) During welding, and (b) after welding is completed.

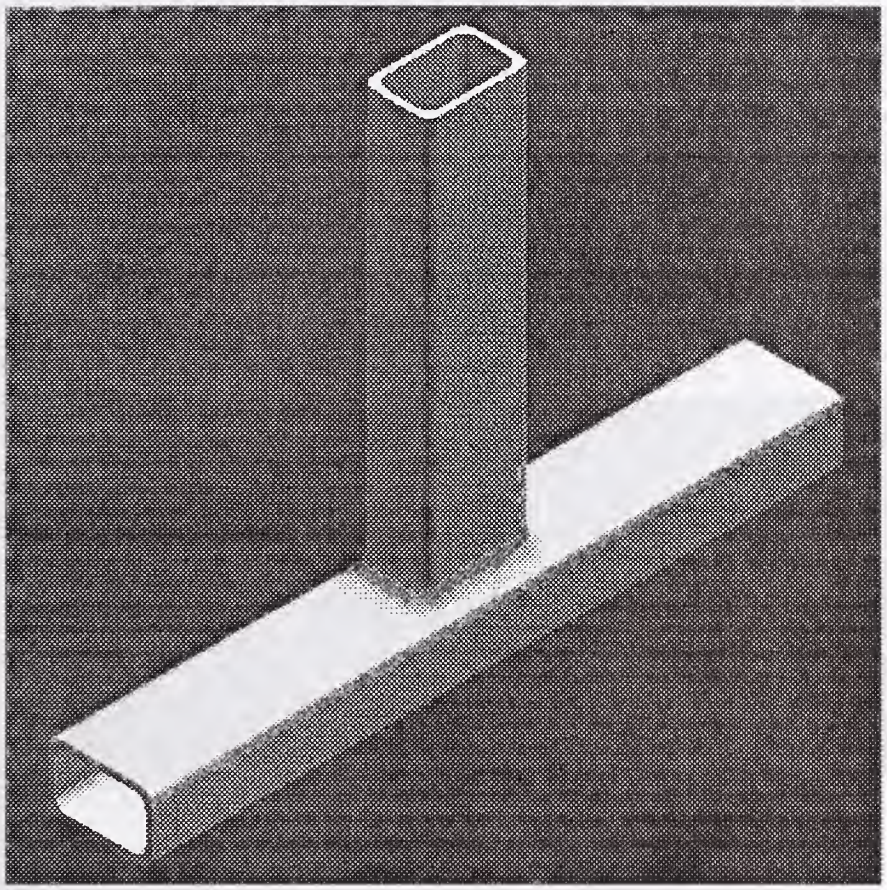

Figure 3: The weld configuration used in this work.

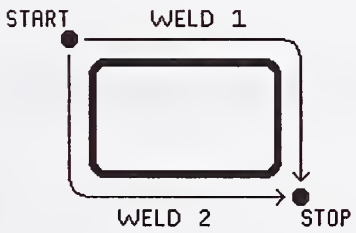

Figure 4: The 2D welding path used in this work.

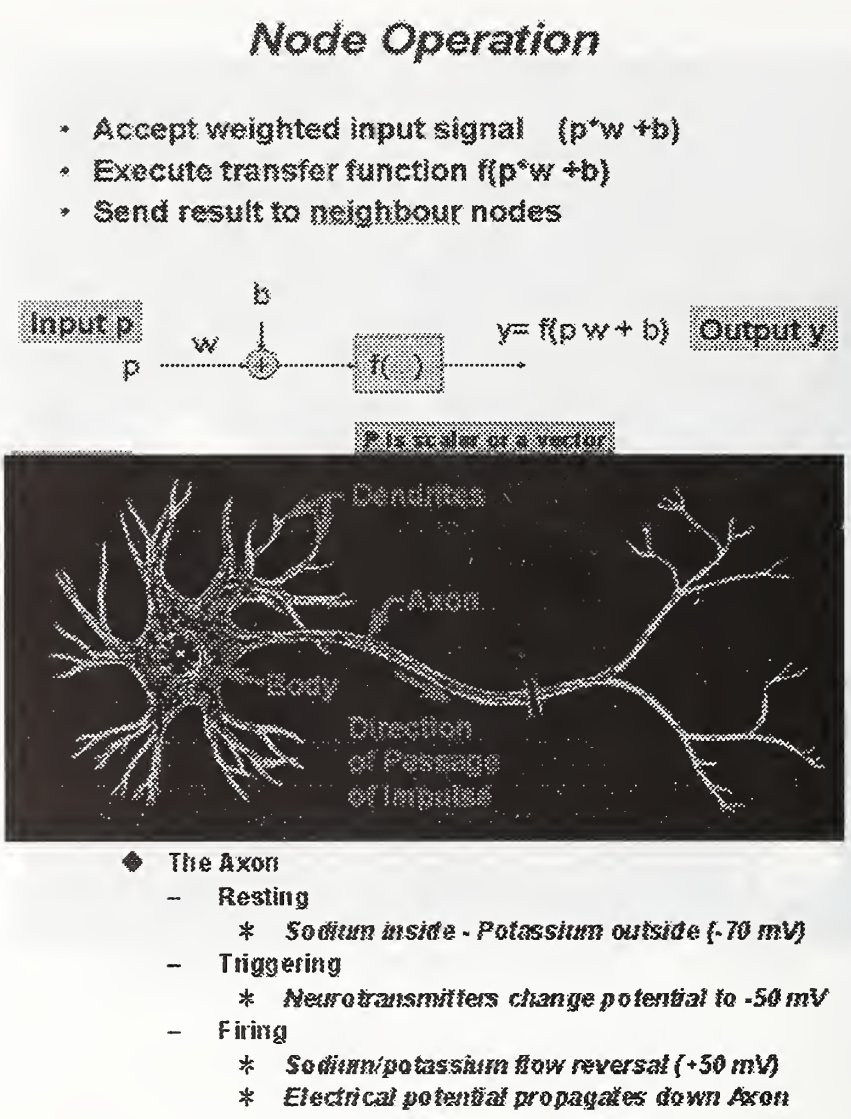

Figure 5: The operation characteristics of a neuron.

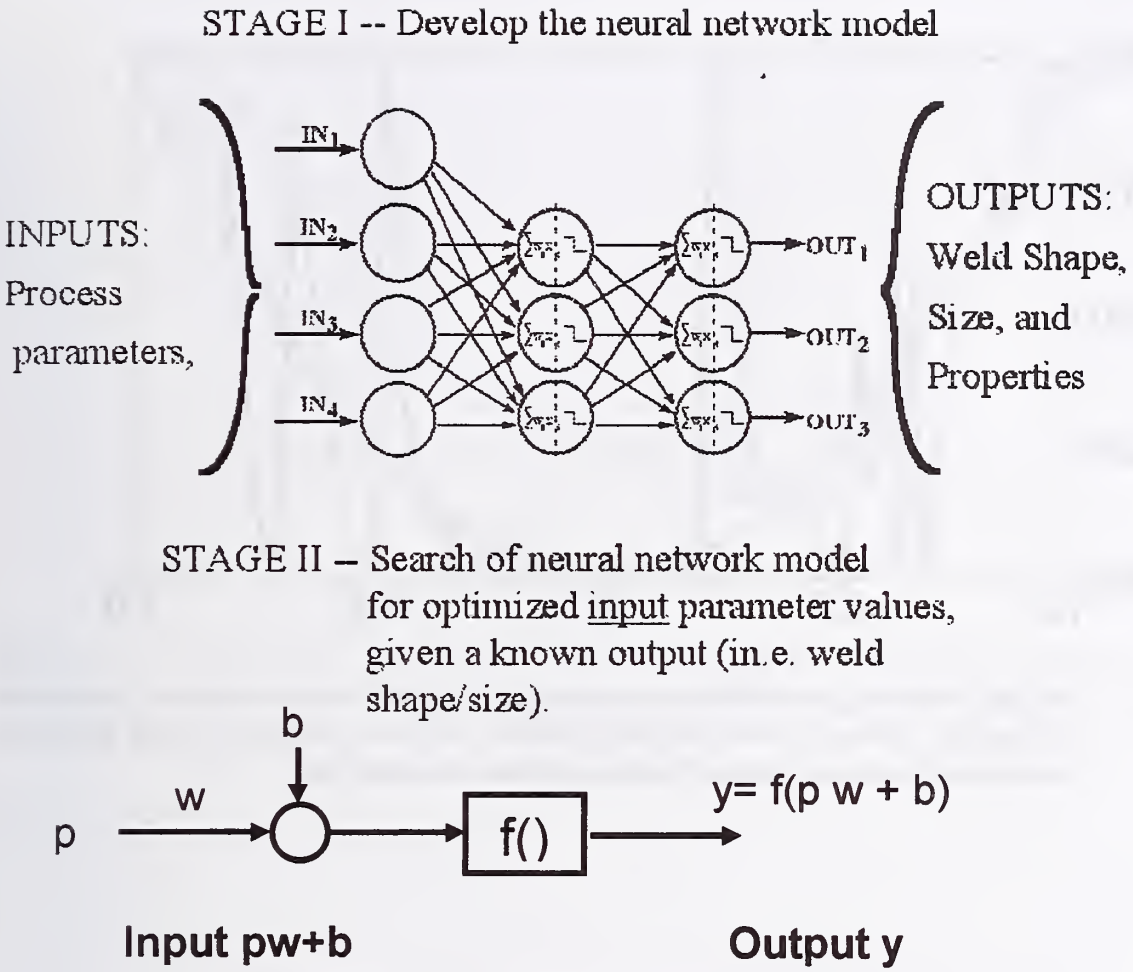

Figure 6: The architecture of a typical feed forward neural network.

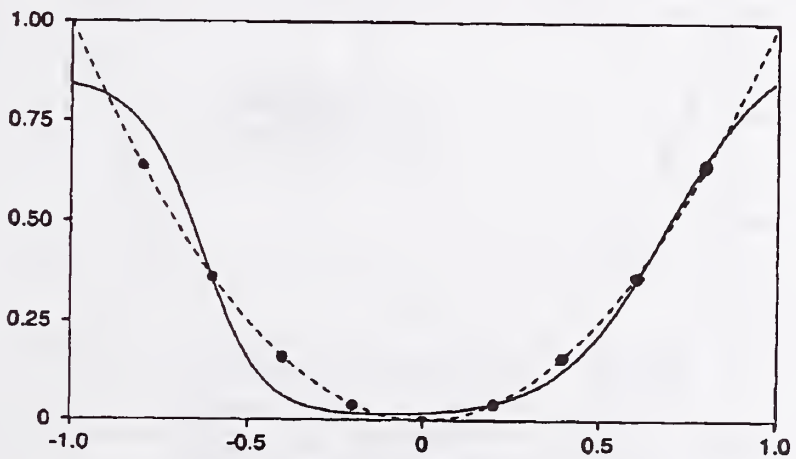

Figure 7: Neural network trained by the backpropagation training algorithm. The solid line is the neural network model, the dashed line is a function that the neural network is supposed to emulate, and the black dots are the data points used to train the model.

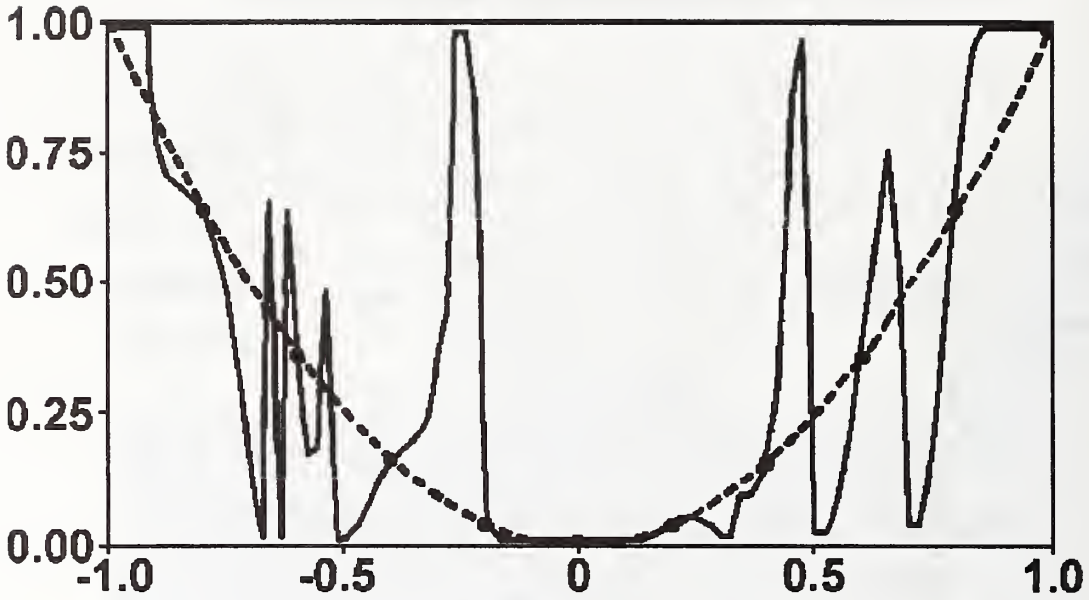

Figure 8. Diagram showing the performance of a backpropagation neural network trained to 4 % error. The overtraining effect is present. This is expressed by good fit in the datapoints but the overall performance of the network is bad.

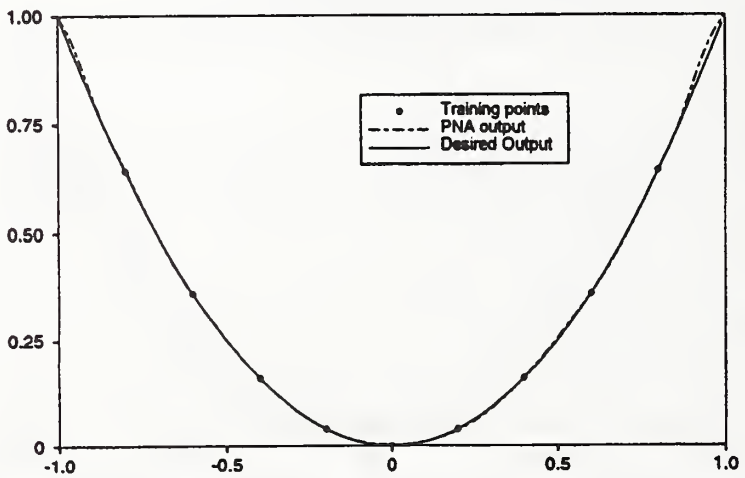

Figure 9: P/NA^3 neural network. The underlying function and training data are the same as for the neural networks shown in figures 7 and 8. The neural network model was trained using the N. A. Technologies P/NA^3 algorithm to a mean error of approximately 1%.

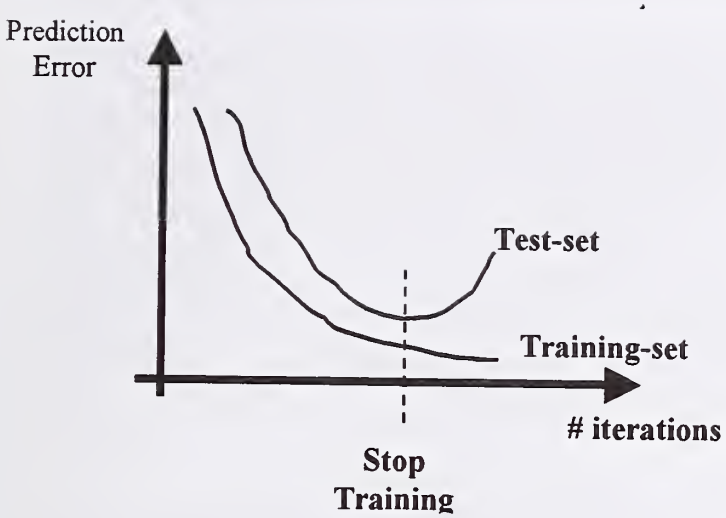

Figure 10. Neural network prediction error for training and test data sets as a function of the number of training cycles. Training eventually leads to a low prediction error for the training data set. At the same time, the prediction error increases for the test set and the generalisation capability of the neural network starts to decrease.

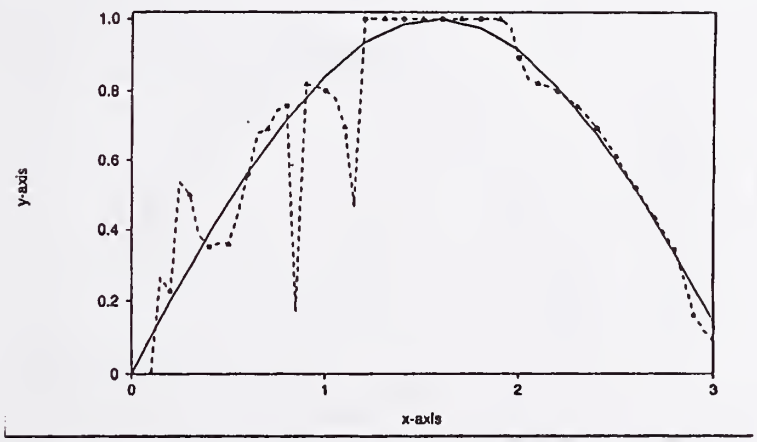

Figure 11: A neural network developed specifically to have a very poor representation of the underlying function used to generate the training samples.

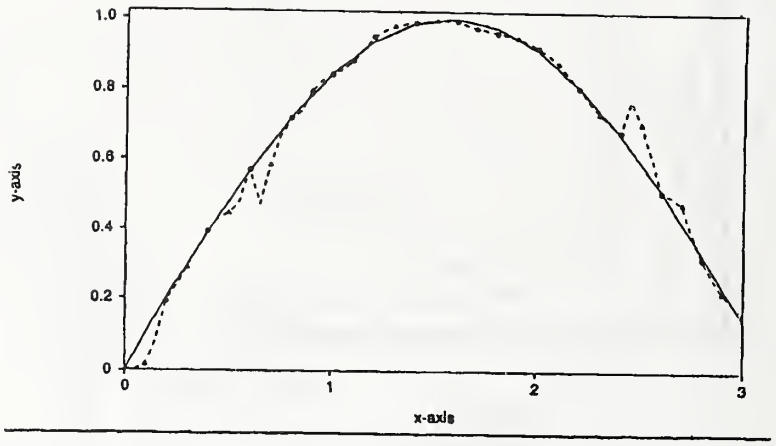

Figure 12: A neural network for which the confidence level is approximately 2σ. The confidence level is approximately 99.5% as determined expected for that size of the confidence interval.

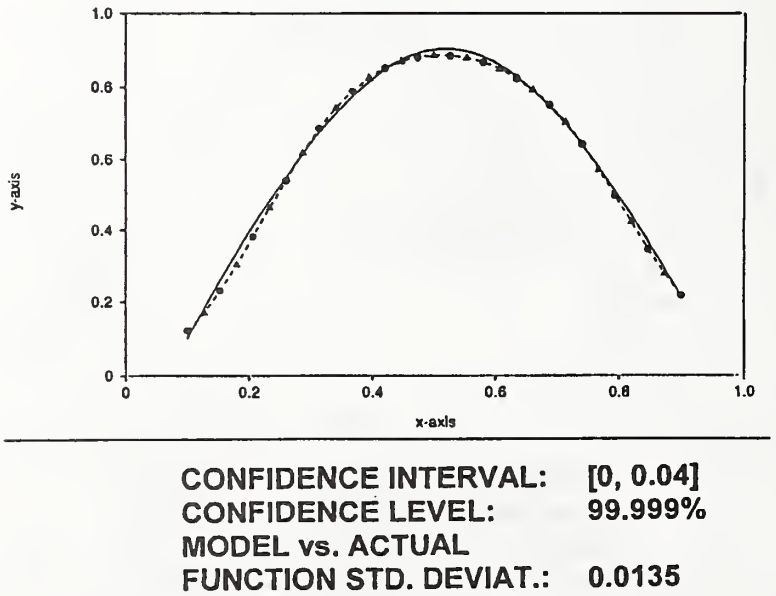

Figure 13: A neural network trained with the P/NA^3 neural network exhibits high accuracy and a corresponding high level of confidence predicted by the S-parameter test

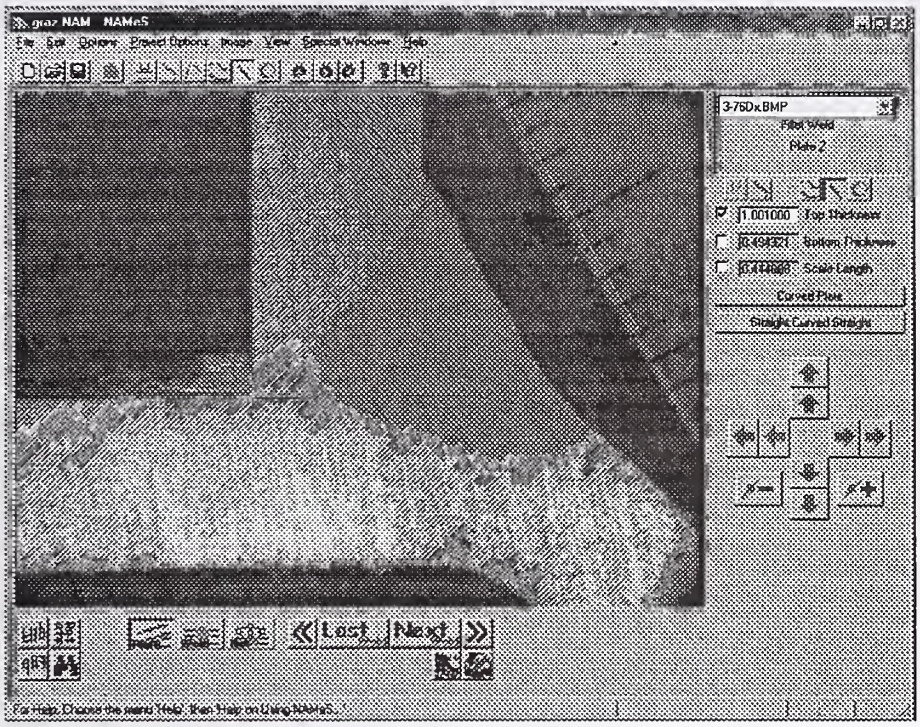

Figure 14: The NAMeS GUI for measurement of weld shapes.

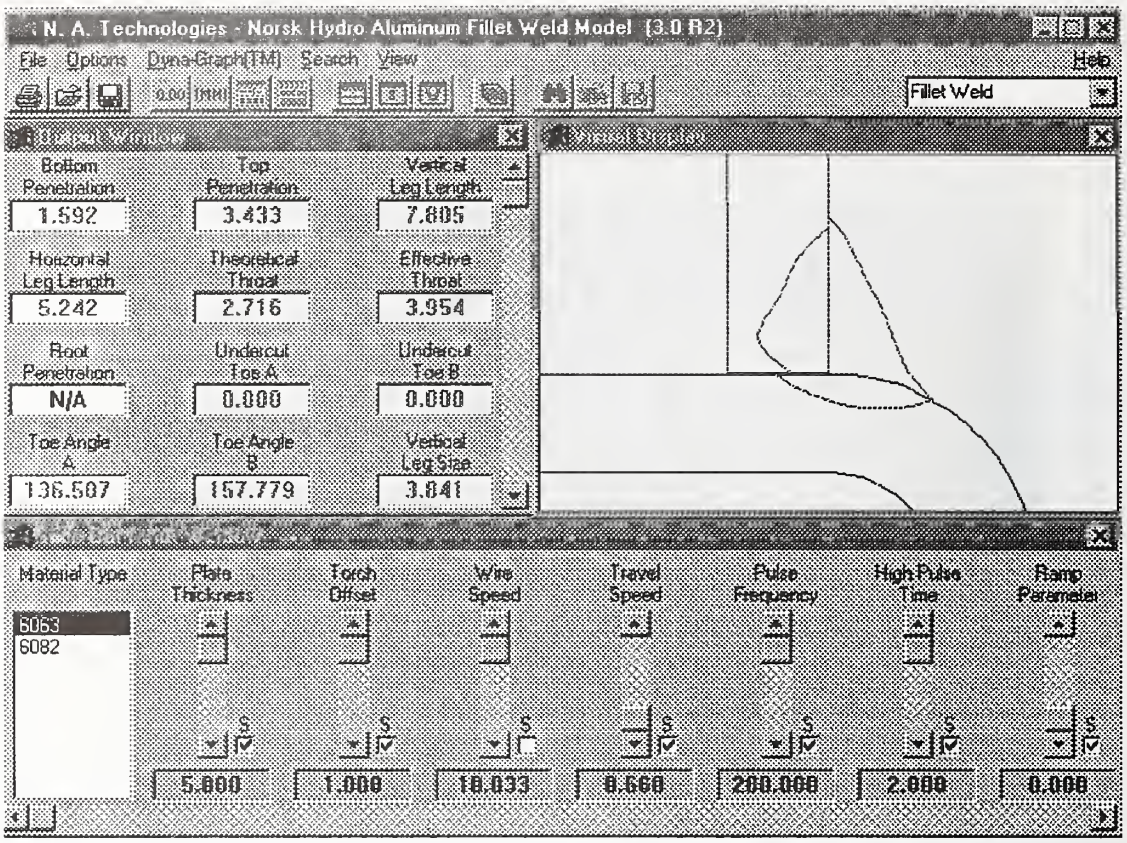

Figure 15: Screen dump of the GUI software for the model presented in this work. Compare this model prediction to the shape of the actual weld in figure 14.

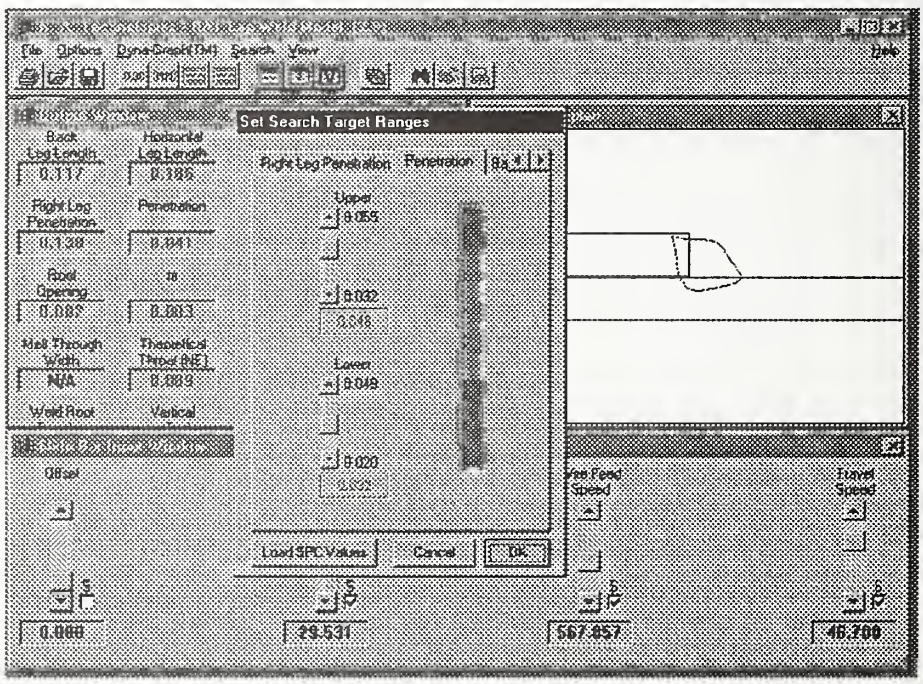

Figure 16: Screen dump of the GUI with dialog box for setting of the ranges of the input and output parameters.

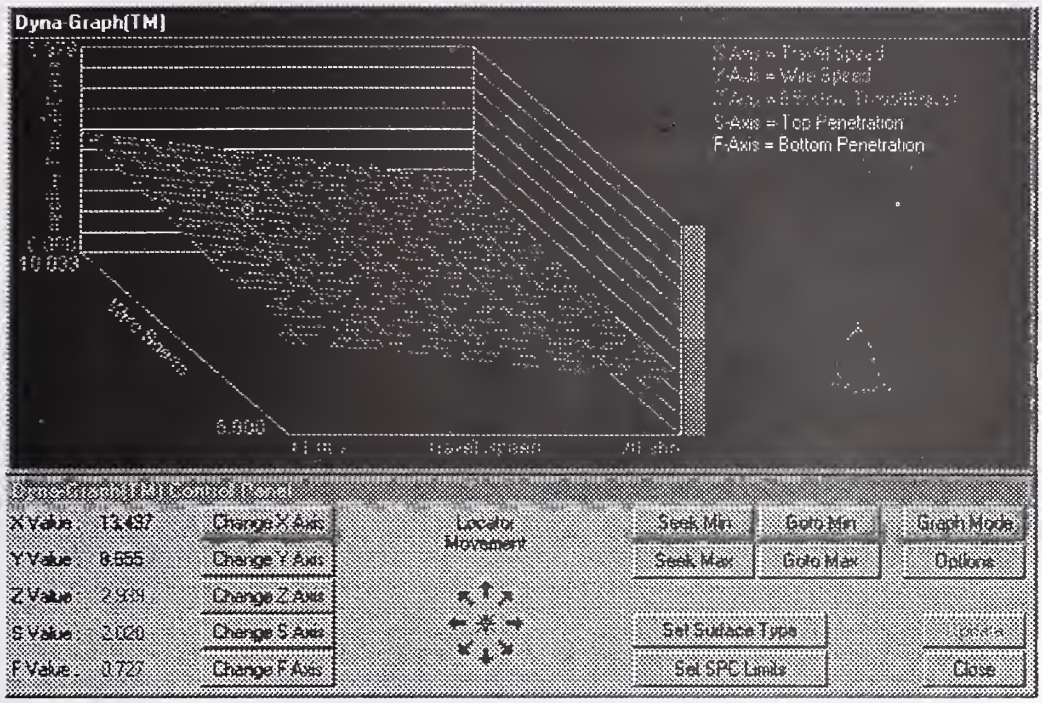

Figure 17: Screen dump of a typical response surface window. The red colour represents values of the response variable (effective throat) not within the specified SPC-limits.

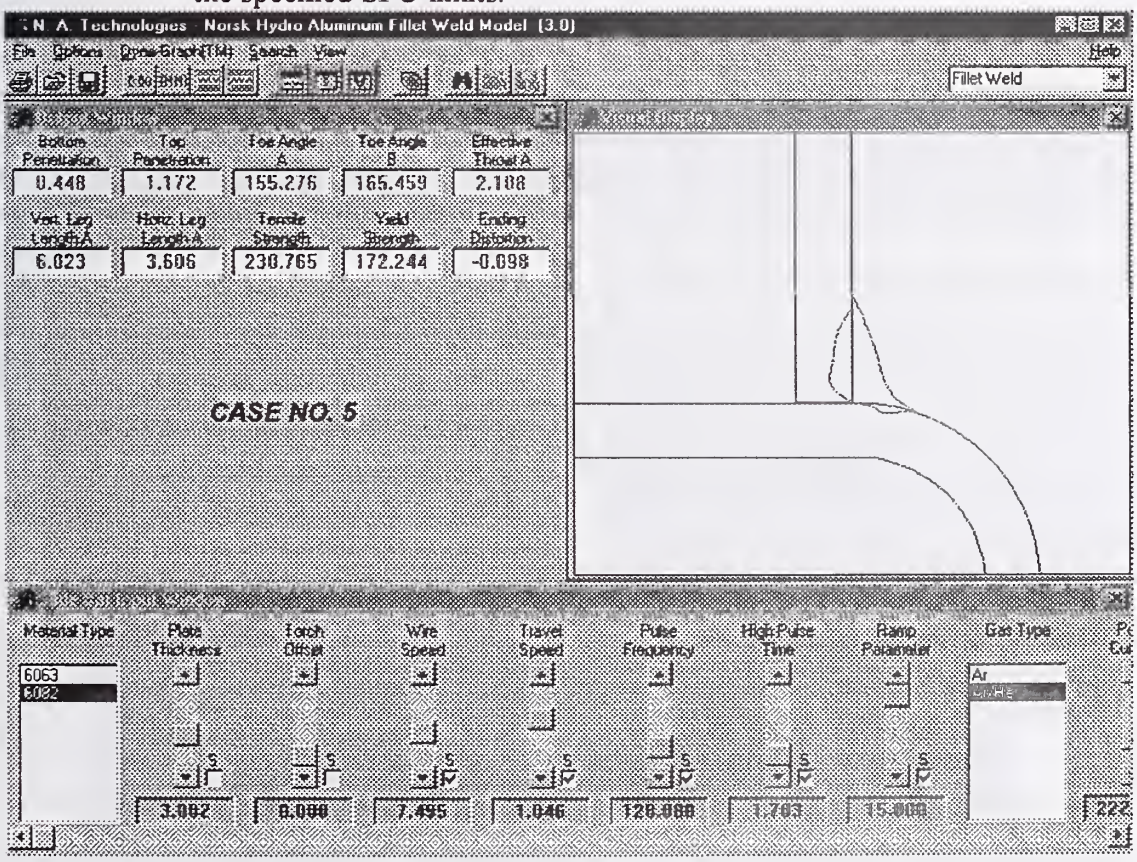

Figure 18. Screen dump of the graphical user interface that visualises the weld bead shape and selected output values.

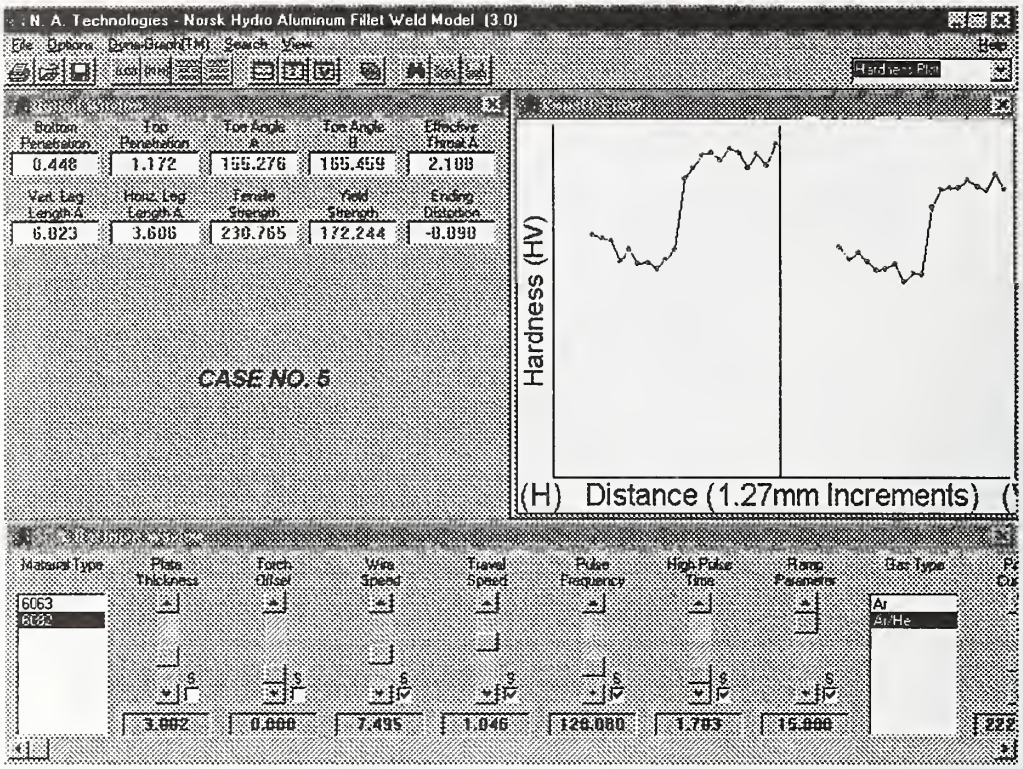

Figure 19: Graphical interface visualising the HAZ hardness distribution along the chord (left hand side curve), and the braze (right hand side curve).

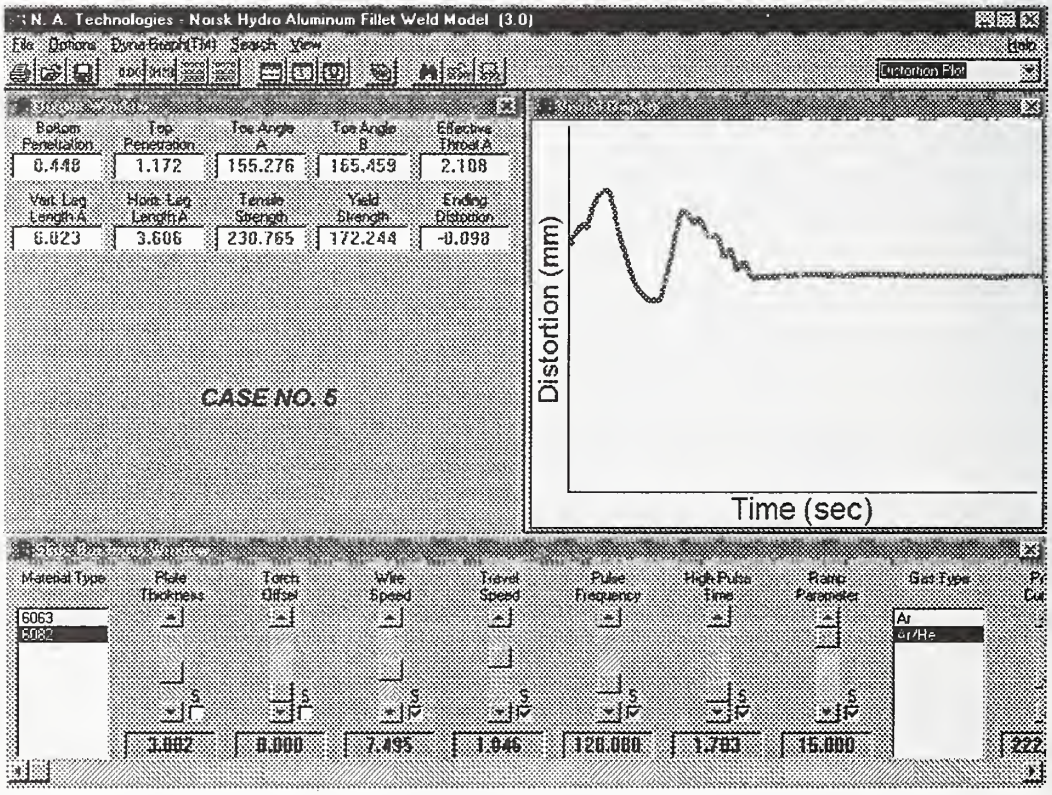

Figure 20: Graphical interface visualising the thermally induced distortions of the chord as a function of time after start of welding.

SPATTER MONITORING FOR SHORT CIRCUIT METAL TRANSFER IN GMAW

S. K. Kang* and S.-J. Na*

ABSTRACT

Quantitative analysis regarding the effect of waveform parameters of arc welding current on spatter generation was conducted using a microcomputer-based experimental data analyzing system. Statistical data derived from welding experiments showed that qualitative relationships can be obtained between spatter generation and some parameters of welding current. By using the multiple regression analysis method, two indices predicting the spatter and big spatter generation during a fixed welding time were developed. Neural networks were also used to estimate the spatter and big spatter generation. It was revealed that the indices and the neural networks could predict the spatter and big spatter generation to a certain extent in comparison with experimental data of spatter generation.

INTRODUCTION

In recent years the development of semi-automation, automation and robotization techniques for welding has been remarkable. GMAW with active shielding gas such as CO_2 and Ar-CO_2 using these developments now has a major role in arc welding practice as an alternative to manual metal arc welding, although it still has some problems such as spatter and fume generation. The occurrence of spatter in GMA welding has a number of detrimental effects such as: 1) obstruction of the shielding gas due to its adhesion at nozzle inside, 2) increase in number of operations because of the need to remove spatter, and 3) danger of burns and fires. Consequently various preventive measures are considered in terms of many factors such as welding conditions, filler wire materials and welding power sources.

Spatter reduction in pulsed CO_2-shielded arc welding has been studied with special reference to waveform control of the power source and chemical composition of the welding wire (Ref. 1). Inverter-controlled power source with high-speed control capability was used in one study to control the welding current and voltage for spatter reduction in CO_2 arc welding (Ref. 2-3). Using a newly developed inverter controlled pulsed MAG welding machine, a new current waveform control system was developed to reduce spatter (Ref. 4). Other studies were conducted on spatter reduction in MAG welding from the viewpoint of welding materials such as filler wire and shielding gas (Ref. 5-6).

A great amount of work has been done to investigate the phenomena and mechanisms of spatter generation in short circuit metal transfer mode (Ref. 7). The mechanisms of spatter generation obtained can be summarized as follows: 1) Electric explosion - Under the action of magnetic force produced by high short circuit current, the metal bridge shrinks in cross section and the density of short circuit current increases further. The metal bridge is

*Dept. of Mech. Eng., KAIST, Yusong-gu, Taejon, Korea

overheated and evaporated, resulting in metal explosion. 2) Gas explosion - Surplus oxygen and carbon in the melted metal react intensively with each other in high temperature arc, which results in violent evolution or explosion of CO gas. 3) Gas impact - Atmospheric gas heats and expands due to abrupt arc initiation after short-circuiting. The melted metal in the weld pool and remaining drop are blown off through this gas impact. 4) Instantaneous short-circuiting - Instantaneous short-circuiting refers to short-circuiting of a very short duration without metal transfer. As the thin metal bridge breaks, a small quantity of spatter may be produced.

In this paper, the parameters affecting spatter generation were selected based on previous papers and tested by preparatory welding experiments. Spatter indices and neural networks were developed to estimate the spatter and big spatter generation during a fixed welding time.

EXPERIMENTAL PROCEDURE

Experimental Equipment

Figure 1 shows the experimental apparatus composed of three parts. The first part consists of several welding machines having different characteristics. The second one is a welding table to move the welding torch in three directions. The third is a microcomputer to acquire and analyze the welding current and arc voltage signal through a PC-Lab card with 330 kHz sampling frequency. Programs were developed to analyze the waveform of welding current and arc voltage.

Welding Experiments

Bead-on-plate welding was carried out on the workpiece of 12 mm thickness using inverter controlled power sources. Solid wire of 1.2 mm diameter was used with a stick-out length of 15mm. The shielding gas was Ar 80% and CO_2 20% with a flow rate of 20 liter/min, and the welding speed 360 mm/min. The range of welding current was between 150 A and 250 A, and that of arc voltage between 20 V and 32 V, which covers the range of short circuit metal transfer mode. Welding experiment was conducted by varying the welding voltage, while the welding current was fixed. Figure 2 shows the typical relationship between arc voltage and spatter and big spatter generation, which reveals that spatter and big spatter generation increases with increasing arc voltage. The sampling frequency for waveform data was 10 kHz, and data were measured during 0.8 sec. intervals.

Parameter Selection

There are several parameters to be considered for estimating the spatter generation At short circuit breakage, metal vapor explodes and spatter occurs. If peak current is high, the amount of metal vapor will be large and heavy spatter will be caused by explosion. If the short-circuiting time is long, the peak current will become large, resulting in increase of spatter generation. When short-circuiting bridge is formed, the complete contact is not made immediately after contact due to surface disturbances such as oxidants. Welding current passes through small points of real contact, which will cause overheating. It was shown that

the welding current at short circuit start and its increasing rate after short-circuiting are related to spatter generation (Ref. 6).

While the welding arc exists, the electrode melts and droplet is formed at the end of electrode. If the arcing time is long, a lot of electrode will melt and the electrode droplet will become large. The large droplet can be the source of instability and result in spatter generation.

Based on the above explanation, five parameters were selected to analyze the spatter generation. They are peak current (I_p), arcing time (T_a), short-circuiting time (T_s), current slope at short circuit start (S_s) and current at short circuit start (I_s), as shown in Figure 3.

RESULTS AND DISCUSSION

Relationship between Waveform Parameters and Spatter Generation

Figure 4 shows the common relationship between I_p and spatter generation. Spatter generation increases with increasing I_p, which coincides with the previous research (7). Figure 5 shows that spatter generation increases with increasing T_a. The main mechanism of spatter generation is believed to be the explosion of metal vapor. Because metal vapor explosion is less influenced by T_a than by I_p, the correlation coefficient between T_a and spatter generation is lower than that between I_p and spatter generation, Table 1. Figure 6 reveals that spatter generation increases with increasing I_s, while it shows the highest correlation coefficient with spatter generation.

Figure 7 shows that spatter generation increases with increasing S_s. This is probably due to the fact that the longer the period of controlling I_s to a low value, the more regular and uniform the short circuit state becomes. Figure 8 shows the relationship between T_s and spatter generation, which reveals no particular correlation. While short circuit is formed, many factors - the inductance of welding machine, T_s and the diameter of short-circuiting bridge - influence the welding current rise. It seems to be difficult to analyze the influence of T_s on spatter generation in general.

A big spatter was defined as a spatter whose diameter is larger than the electrode diameter (1.2 mm). Big spatters adhere strongly to the nozzle and base metal while small spatters are easily removed with a blow or touch. Figure 4 shows the relationship between I_p and big spatter generation. Big spatter generation is more dependent on the size of droplet than the explosion of metal vapor. Therefore the correlation coefficient between I_p and big spatter generation is lower than that between T_a and spatter generation.

Figure 5 reveals that big spatter generation increases with increasing T_a. It is generally considered that the size of shattered particles is dependent on that of droplets. A big droplet generates shattered particles larger than those of a small droplet. Therefore it is considered that a large amount of big spatter is generated from a large diameter of short-circuiting bridge. The main parameter resulting in a large diameter of short-circuiting bridge is large T_a, and consequently the correlation coefficient of T_a with big spatter is the highest among the parameters considered, Table 2. Figure 6 and 7 show the relationship between big spatter

and I_s and S_s respectively. It was also revealed that the effect of I_s and S_s on big spatter generation is less than that on spatter generation. Figure 8 shows that there is no particular correlation between T_s and big spatter generation, like that between T_s and spatter generation.

Index and Neural Network

By analysis of the relationships between parameters and spatter generation, it was found that the parameters tested are influencing the spatter and big spatter generation in various ways. For spatter generation I_p and I_s are the dominant parameters, and S_s and T_a are the secondary ones, while for big spatter generation T_a is the dominant parameter, and I_p and I_s are the secondary ones. In order to estimate spatter and big spatter generation, it is necessary to analyze and synthesize the contribution of each parameter. In this purpose, the indices and neural networks were developed for spatter and big spatter generation. The index expresses the direct relationship between parameters and spatter generation, while the neural network possesses the robustness and ability to extract an underlying pattern from noisy or erratic data. The ability of neural networks to train on representative test data enables the complex and nonlinear relationships to be interpreted, without time consuming construction of a complete model of the process.

Spatter

Multiple regression analysis was performed to develop an index of I_p, T_a, S_s and I_s to estimate the spatter generation during a fixed time. The developed spatter index is as follows.

$$S = 7.9446 \cdot 10^{-4} \cdot I_p + 3.46523 \cdot 10^{-3} \cdot T_a + 0.0045 \cdot S_s + 0.00578 \cdot I_s - 0.82705$$

The neural network consisted of 4 inputs (I_p, T_a, S_s and I_s), 2 hidden layers and 1 output (spatter generation). 53 representative conditions were selected from welding experiments to teach the neural network. In order to test the performance of the neural network, the experimental data not used in teaching stage were used.

Figure 9 shows the relationship between real spatter generation and spatter generation estimated by the index and neural network. The correlation coefficient of the index was 0.80, while that of the neural network was slightly higher (0.86).

Big Spatter

The big spatter index was developed by multiple regression analysis, neglecting the effect of short circuit time (T_s) and current slope at short circuit start (S_s). The developed big spatter index is as follows.

$$B = 1.02871 \cdot 10^{-4} \cdot I_p + 5.07155 \cdot 10^{-3} \cdot T_a + 9.89649 \cdot 10^{-5} \cdot I_s - 0.03696$$

The neural network consisted of 3 inputs, 2 hidden layers and 1 output. I_p, T_a and I_s are the input variables and big spatter generation is the output. 56 representative values were

selected to teach the neural network, and the data not used at the learning stage were used to test its performance.

Figure 10 shows the relationship between the real big spatter generation and big spatter generation estimated by the index and neural network. The correlation coefficient of big spatter generation was 0.77 and 0.76 for the index and neural network respectively, which were slightly lower than those for spatter generation

CONCLUSIONS

To investigate the spatter generation, a waveform analysis system for welding current and arc voltage was developed using a microcomputer. Based on previous studies related to spatter generation, five waveform parameters of welding current were selected. Using these parameters, the indices and neural networks were developed to quantitatively estimate the spatter and big spatter generation for short circuit metal transfer in CO_2 welding.

Spatter and big spatter generation were influenced by current waveform parameters in various ways. Peak current and current at short circuit start were the dominant parameters for spatter generation, while arcing time was dominant in big spatter estimation. Short-circuiting time could be neglected in estimating the spatter and big spatter generation, because its correlation coefficient was substantially low. For big spatter generation, the current slope at short circuit start could be additionally neglected.

The indices and neural networks could predict the spatter and big spatter generation to a certain extent in comparison with the experimental data. Especially spatter generation estimated by the neural network developed was in fairly good agreement with experimental data. In general, the estimation accuracy of big spatter was relatively low, both by the index and neural network, when compared to that of spatter generation.

REFERENCES

1. Ito, T.; Koshiishi, F.; Sato, M.; Suga, T.; and Ushio, M. 1998. Study of spatter reduction in pulsed CO_2 shielded arc welding. *Welding International* 12(5): 366-371.
2. Mita, T. 1988. Reducing spatter in CO_2 gas shielded arc welding - waveform control. *Quarterly Journal of the Japan Welding Society* 6(2): 209-214.
3. Maruyama, Y.; Sato, M.; and Hida, Y. 1990. Waveform control in gas shielded arc welding. *Welding International* 4(9): 677-683.
4. Yamamoto, H.; Harada, S.; and Yasuda, T. 1990. The development of welding current control systems for spatter reduction. *Welding International* 4(5): 398-407.
5. Suga, T. 1992. Spatter reduction in MAG welding - consumables aspects. *Welding International* 6(1): 16-19.
6. Mita, T. 1991. Spatter reduction - power source consideration. *Welding International* 5(11): 847-850.
7. Chen, J.H.; Sun, J.C.; and Fan, D. 1996. Study on the mechanism of spatter produced by basic welding electrodes. *Welding Journal* 75(10): 311s - 316s.

Table 1. Correlation coefficients between parameters and spatter generation

Parameters	Correlation coefficient
Peak current, I_p	0.674750
Arcing time, T_a	0.405783
Short-circuiting time, T_s	-0.219596
Current slope at short circuit start, S_s	0.357295
Current at short circuit start, I_s	0.738757

Table 2. Correlation coefficients between parameters and big spatter generation

Parameters	Correlation coefficient
Peak current, I_p	0.352940
Arcing time, T_a	0.776558
Short-circuiting time, T_s	-0.142999
Current slope at short circuit start, S_s	0.173930
Current at short circuit start, I_s	0.303819

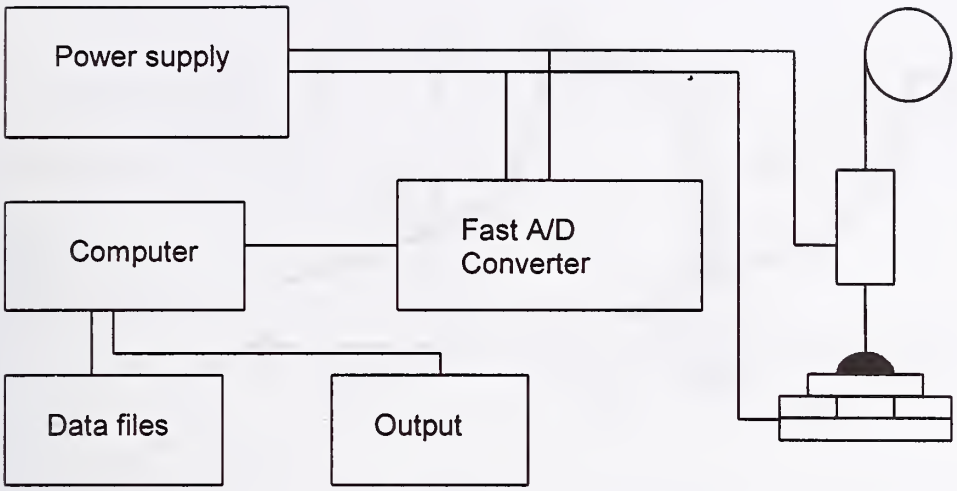

Figure 1. Welding waveform analysis system

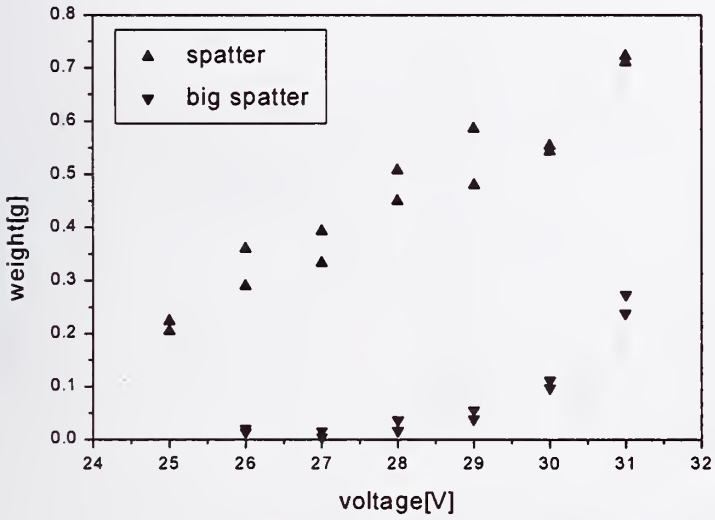

Figure 2. Relationship between spatter and big spatter generation and arc voltage

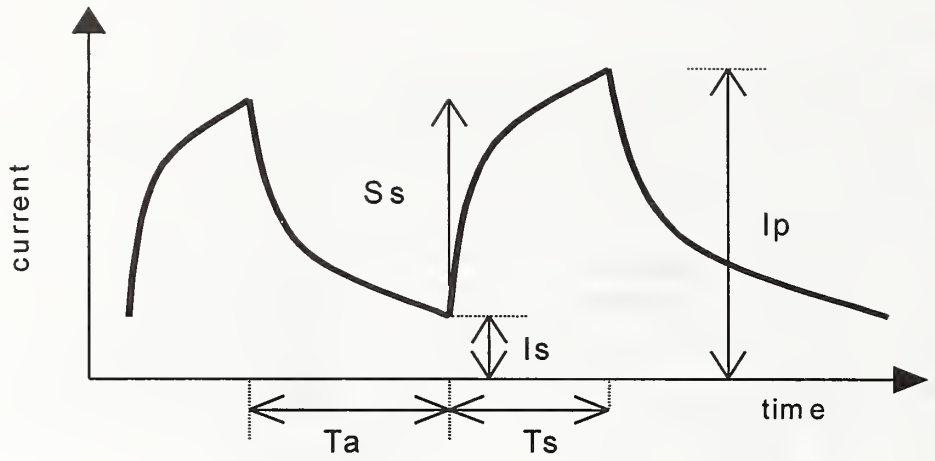

Figure 3. Waveform parameters for analysis

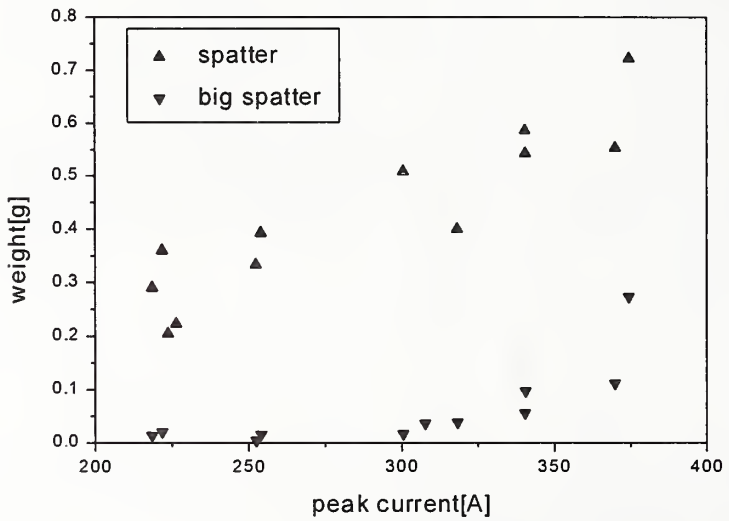

Figure 4. Relationship between spatter and big spatter generation and peak current (I_p)

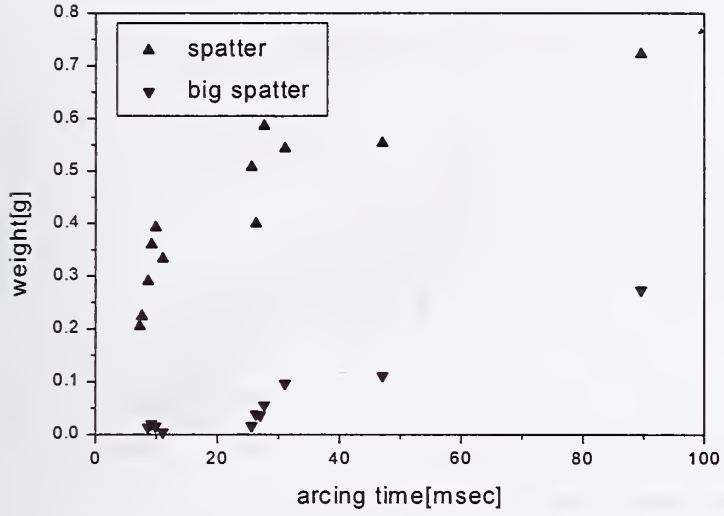

Figure 5. Relationship between spatter and big spatter generation and arcing time (T_a)

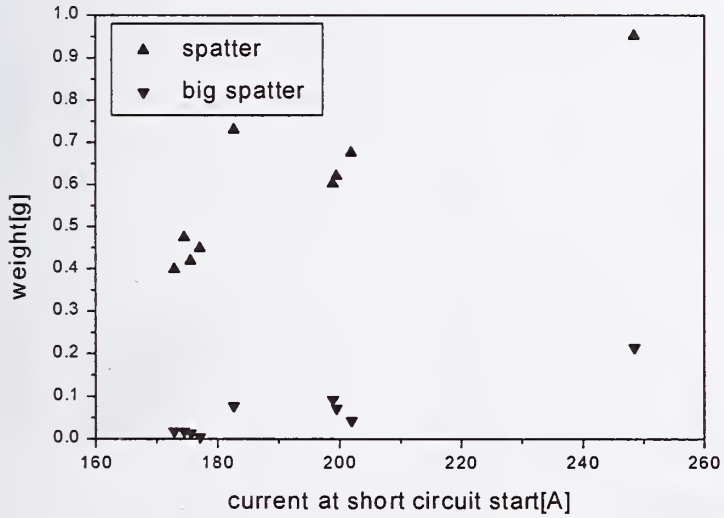

Figure 6. Relationship between spatter and big spatter generation and current at short circuit start (I_s)

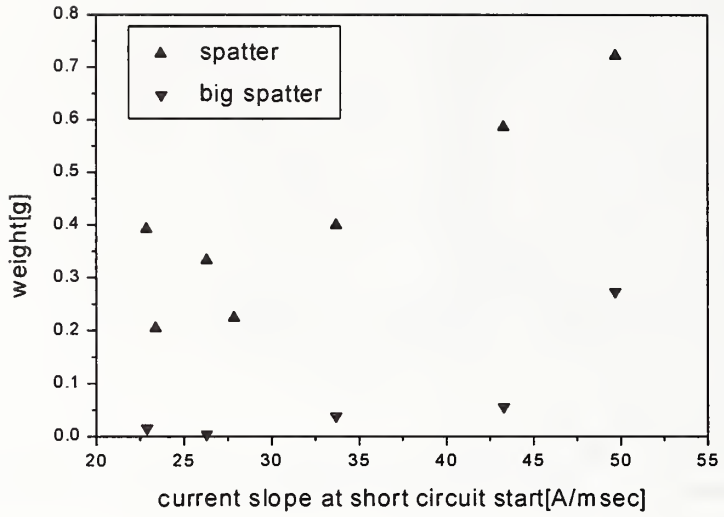

Figure 7. Relationship between spatter and big spatter generation and current slope at short circuit start (S_s)

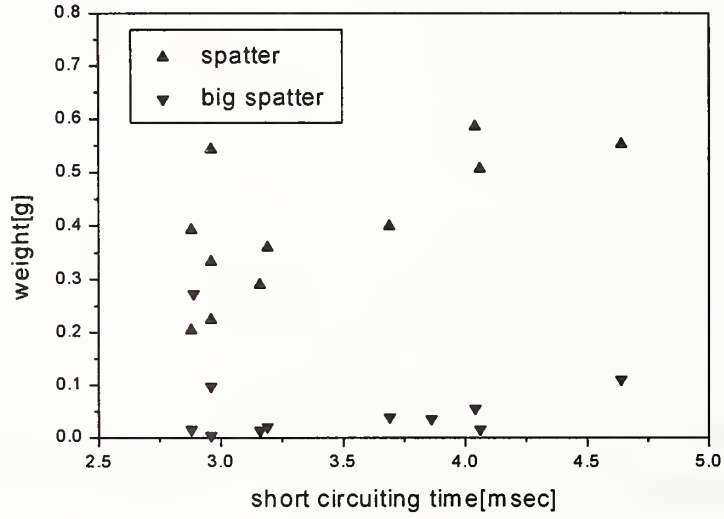

Figure 8. Relationship between spatter and big spatter generation and short-circuiting time (T_s)

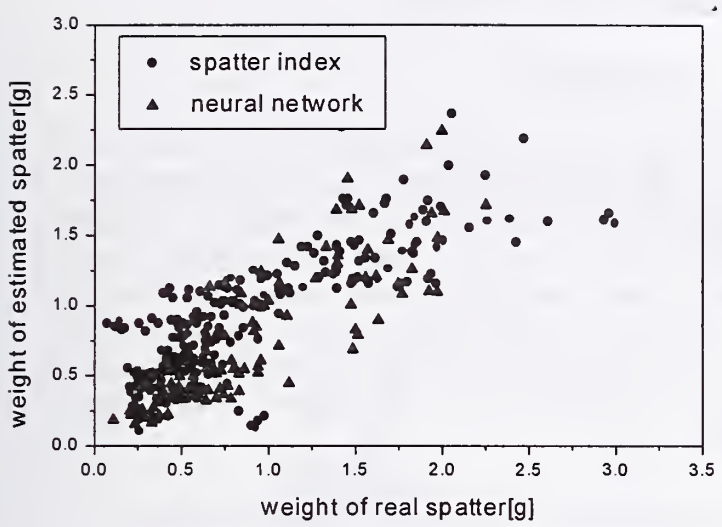

Figure 9. Relationship between estimated and real spatter generation

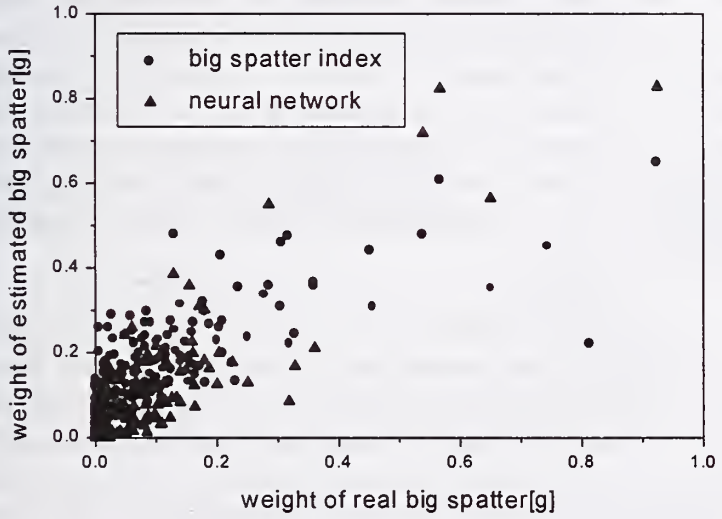

Figure 10. Relationship between estimated and real big spatter generation

ACOUSTIC IDENTIFICATION OF THE GMAW PROCESS

A.M. Mansoor[1] & J.P. Huissoon[2]

ABSTRACT

In this study, a high speed data acquisition system was developed to record and analyse the arc sound produced during GMA welding. The recorded data was processed to obtain time domain, frequency domain and time-frequency domain descriptors. Relationships between these descriptors and the originating weld parameter levels and metal transfer mode were investigated, as were relationships between the electrical power supplied to the weld and the arc sound. Results indicate that the arc sound exhibits distinct characteristics for each welding mode. The occurrence of spatter and short circuits was also found to be clearly detectable in the arc sound record.

Keywords: Arc acoustics, automation, metal transfer mode, sound spectra

INTRODUCTION

The automation of Gas Metal Arc welding applications is often desirable due to the somewhat unpleasant working conditions that the process creates. If properly implemented, automation can increase productivity and weld quality while simultaneously improving the work environment. However in general, automation efforts are usually most successful in applications where relatively little skill is required for the manual operation, and least successful when a high level of skill is required. The skill level required is often related to hand-eye co-ordination (sensing and feedback control) and the experience necessary to be proficient at the job (learning the appropriate controller "transfer function"). Gas Metal Arc welding can be difficult to automate properly, since replicating the level of skill required to produce a quality weld by an automatic machine relies heavily on an understanding of the relationship between feedback from the process and actions to be taken in response.

Skilled manual welders represent extremely sophisticated and effective feedback control systems. Visual, audio and tactile feedback cues are sensed, and a sophisticated non-linear adaptive controller processes these data and recruits muscles in response. In developing feedback control systems for automated welding, it is useful to study the sources of feedback utilised by skilled manual welders. One such source of feedback is the arc sound produced during welding [1,2]. This study was undertaken in an effort to determine if and how this sound can be used as a source of feedback in automated GMA welding.

EXPERIMENTAL SETUP

The experimental equipment is comprised of a computer controlled GMA welding system, synchronised with a data acquisition system for collecting acoustic data while welding. This system is depicted schematically in Figure 1.

---

[1] Ainsworth Technologies, Cambridge, Ontario; [2] Dept. of Mechanical Engineering, University of Waterloo

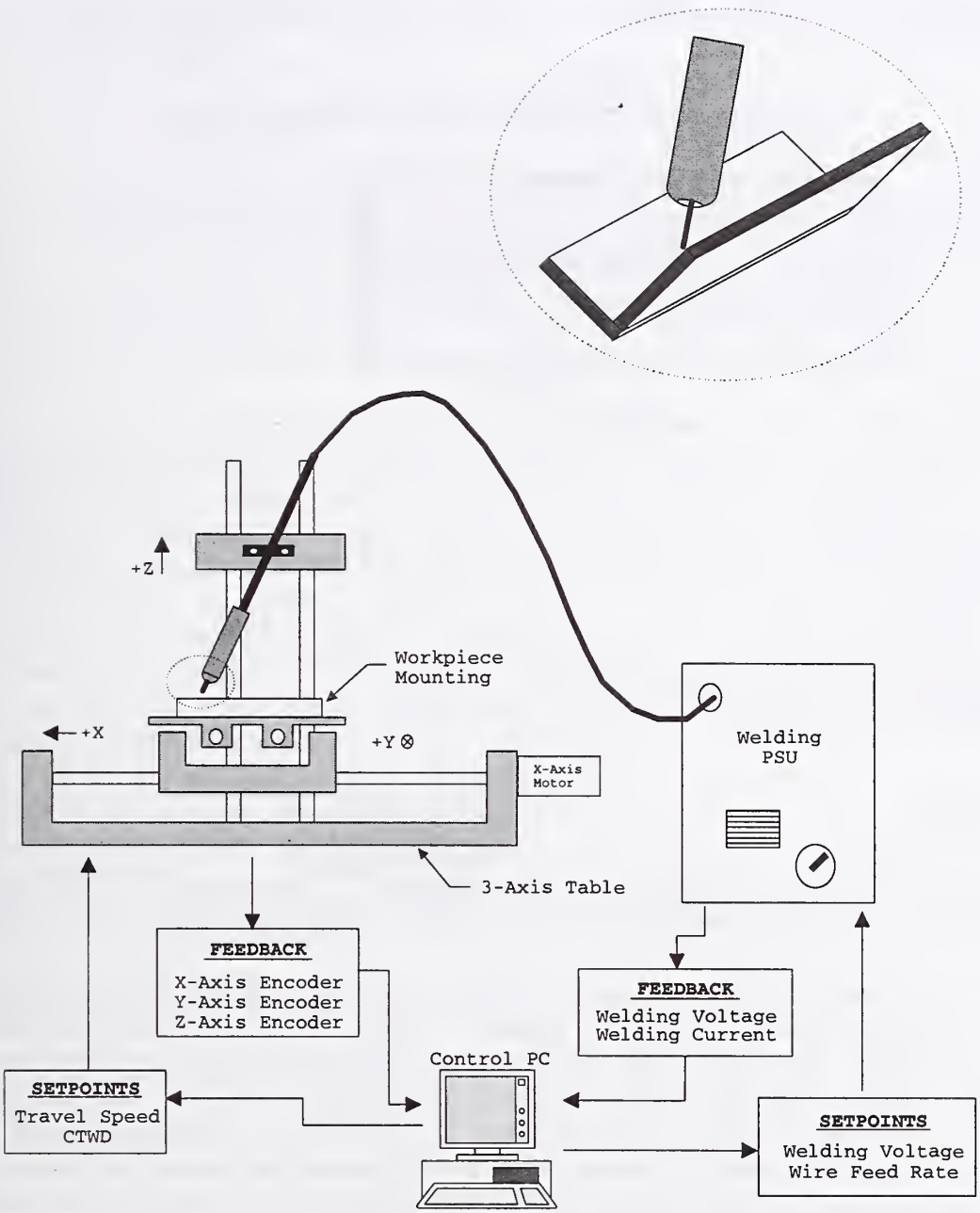

Figure 1. Schematic of experimental test equipment

The welding system consists of a Fronius 500A welding power source and wire feed unit, and a three axis motion control system. This welding system provides computer control of the wire feed rate (WFR), the torch travel speed (TS), the contact tube to workpiece distance (CTWD) and the welding voltage at the contact tube. The shielding gas flow rate (SGF) was manually set, and a standard Ar-15 shielding gas composition was used.

The data acquisition system consists of sound level meter (SLM) with an analog output, low pass anti-aliasing filtering and pre-amplification circuitry, shielding for the SLM and circuitry, a Datel® PC-414A high-speed multi-channel analog input board, and a host 80486 based PC. The data acquisition system is depicted in Figure 2.

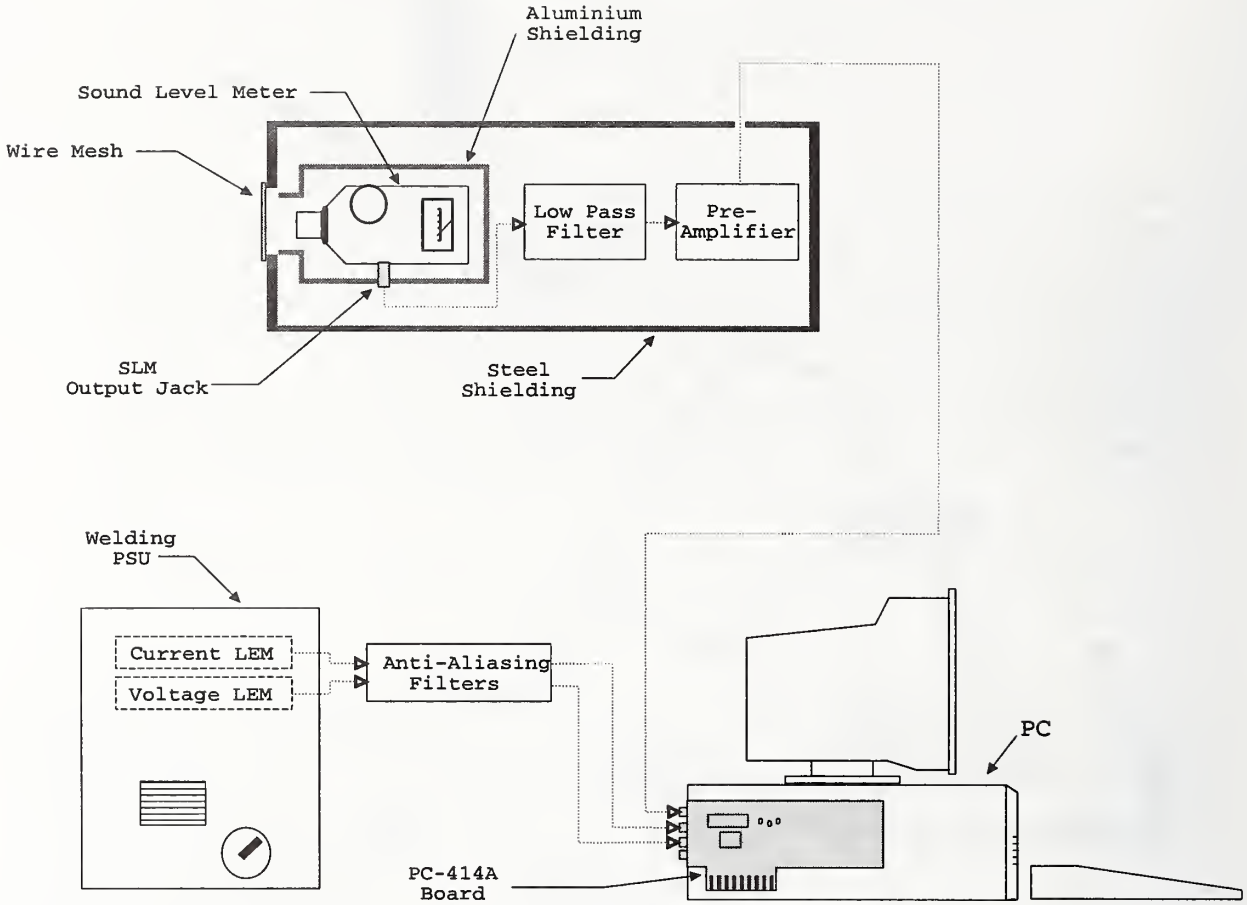

Figure 2. Schematic of Sound Level Meter (SLM) and data acquisition system

The sound level meter (SLM) can measure sound levels from 50dB to 126dB with an accuracy of ±2dB, and was set to the C weighted frequency response. The output from the SLM is conditioned with a 6th order Butterworth low pass filter with a break frequency of 10kHz, so that the frequency range considered is 32Hz to 10kHz. The conditioned SLM analog output was connected to one channel of the analog input board. The SLM and conditioning circuitry were shielded from RF and EM noise by placing these in an electrically grounded steel casing. The SLM was positioned 2m behind the welding torch, and at a height of 20 cm above the seam of the weld. Since the 3-axis welding table moves the workpiece with respect to the stationary welding torch, this arrangement maintains the SLM at a constant distance from the arc.

Voltage and current measurements were obtained using LEM® isolation sensors, and connected to the analog input board. The PC-414A analog input board simultaneously samples the input channels and provides 12-bit resolution at up to 350kHz per channel. In this application, the acoustic, welding voltage and current signals were sampled at 40kHz. An 8Mb RAM drive enabled up to 35 seconds of continuous data to be recorded.

In preliminary experiments, it was found that there were significant noise sources besides the welding arc. These included the power supply unit, the motors on the 3-axis table, ventilation and shielding gas flow. The sound from these background sources was measured and found to

have very constant characteristics, with a mean level of 68.33 dB and a very consistent time averaged frequency response.

EXPERIMENTAL PROCEDURE AND RESULTS

Experiments were performed by welding at prescribed conditions while acquiring the sound signal, weld voltage, and weld current as described above. All welds were 90° fillet geometry on two pieces of 2" x ¼" hot rolled flat steel cut to 2 ft. lengths. All analyses were performed on 3021 frames of 1024 samples, with an overlap of 960 samples between frames and using rectangular windowing (this corresponds to 5.1456 seconds of weld data). This data sample was taken 2 seconds into the data record, so that any transients due to arc initiation would be avoided.

To provide a base-line, nominal welding conditions were chosen to be 27V, 6.0m/min wire feed rate, 20mm CTWD, 8.0mm/s travel speed, and 50cfm gas flow rate. A set of experiments to investigate the primary effects of the five controllable parameters on the resulting acoustic signal was performed. Twenty-two welds were made, using the parameter combinations indicated in Table 1. The welds for group I were intended to characterise the effect of weld voltage, as these welds were produced at varying levels of contact tip voltage while the remaining weld parameters were held constant. Similarly, the welds from group II investigate the effect of wire feed rate, and those from group III the influence of CTWD (stand-off). The welds for group IV consider the effect of travel speed, while those from group V should show the effects of inadequate shielding gas flow rate. As shown in the experimental layout of Table 1, five of the 22 welds were conducted under the same nominal welding conditions; this was done so that the repeatability of the measured data could be evaluated. The time averaged frequency spectra for these five welds are shown in Figure 3, while the associated time domain descriptors are tabulated in Table 2. There is clearly significant variation in the sound spectra and descriptors for this specific set of weld parameter values. This is likely caused by a transitioning metal transfer mode, but it does indicate that the arc sound is a poor descriptor of the weld parameter levels.

Group	Weld #	Voltage	WFR (m/min)	CTWD (mm)	TS (mm/s)	SGF (cfm)
I	1	21	6.0	20	8.0	50
	2	24	6.0	20	8.0	50
	3	27	6.0	20	8.0	50
	4	30	6.0	20	8.0	50
	5	33	6.0	20	8.0	50
II	6	27	3.6	20	8.0	50
	7	27	4.8	20	8.0	50
	8	27	6.0	20	8.0	50
	9	27	7.2	20	8.0	50
	10	27	8.0	20	8.0	50
III	11	27	6.0	16	8.0	50
	12	27	6.0	20	8.0	50
	13	27	6.0	24	8.0	50
	14	27	6.0	28	8.0	50
	15	27	6.0	32	8.0	50
IV	16	27	6.0	20	6.5	50
	17	27	6.0	20	8.0	50
	18	27	6.0	20	9.5	50
	19	27	6.0	20	11.0	50
	20	27	6.0	20	14.0	50
V	21	27	6.0	20	8.0	50
	22	27	6.0	20	8.0	5

Table 1. Experimental Layout

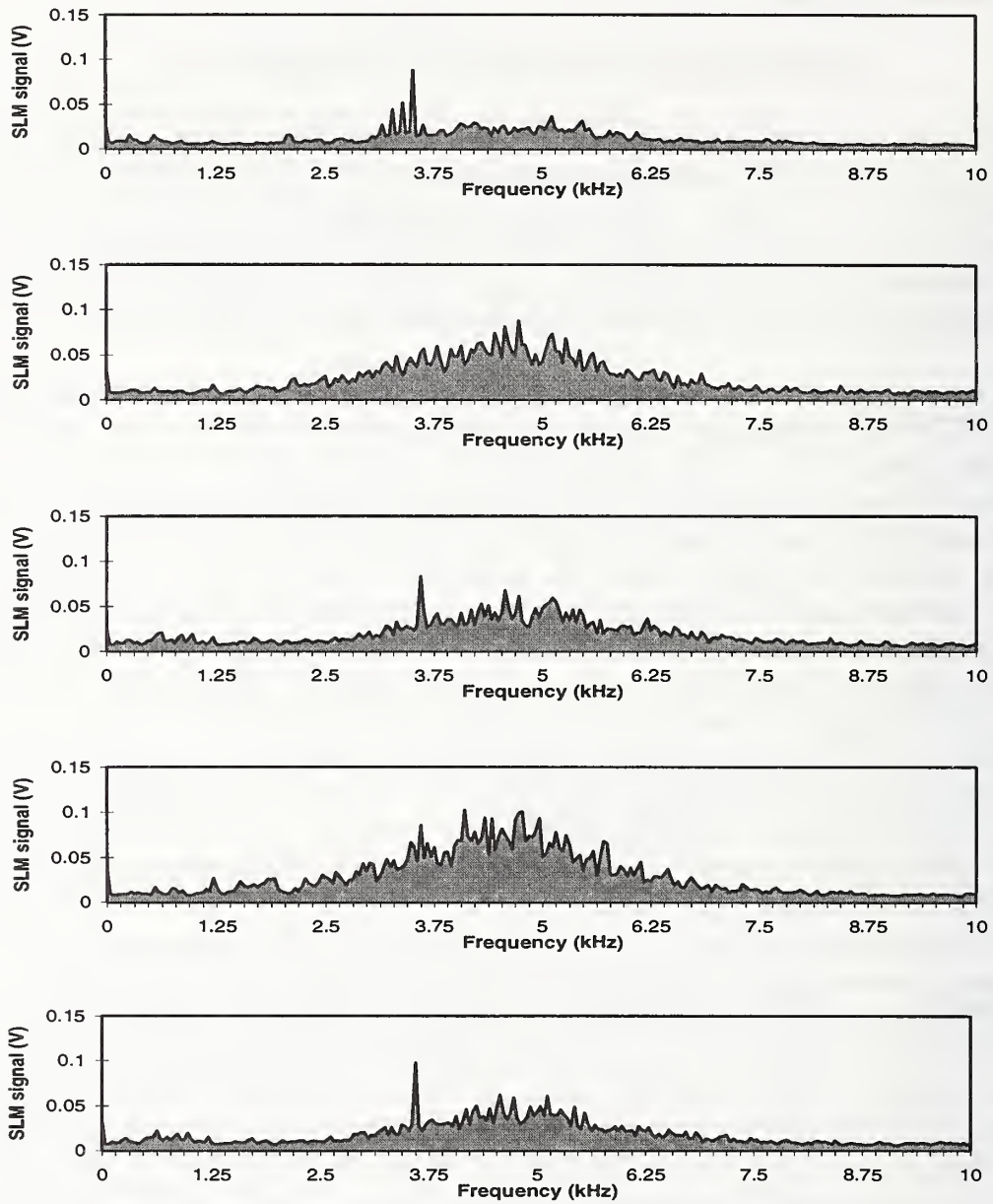

Figure 3. Time averaged frequency spectra for five welds at the nominal parameter levels

	Weld				
	3	8	12	17	21
Mean Sound Level (V)	0.147	0.231	0.363	0.225	0.326
Peak Sound Level (V)	2.28	3.83	3.83	3.37	3.2
Standard Dev. (V)	0.128	0.209	0.321	0.198	0.278
Coeff. of Variation (%)	87.1	90.5	88.4	88	85.3
Mean Sound Level (dB)	79.43	83.29	86.96	83.01	86.28
Peak Sound Level (db)	107.08	111.57	111.59	110.47	110.02

Table 2. Time domain sound descriptors for five welds conducted with the same parameter levels

Arc Sound vs. Metal Transfer Mode

The metal transfer mode is the characteristic most commonly associated with arc sound. Three sets of welding parameters that resulted in spray transfer, globular transfer and short arc transfer were experimentally determined. Using these parameters, five welds were performed in each transfer mode. Typical sound records for each transfer mode are shown on a compressed time scale in Figure 4. These records are consistent with those reported in other studies [3,4].

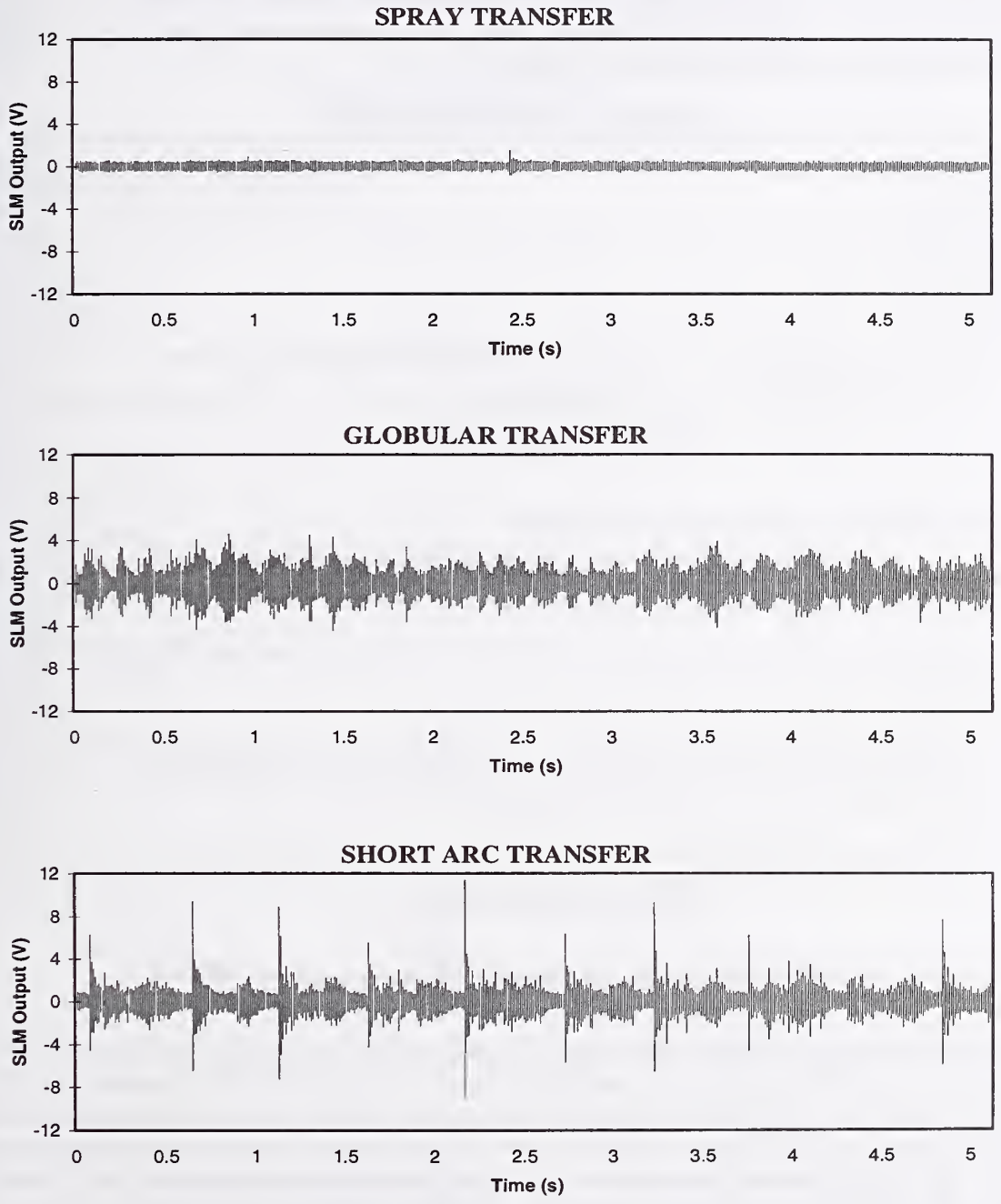

Figure 4. Typical Compressed Sound Records for each Transfer Mode

From Figure 4 it is clear that the time domain characteristics vary significantly with transfer mode. Spray transfer produces a low amplitude signal, while globular and short arc transfer produce louder signals. The sound from short arc transfer is distinguished from that of spray and globular transfer by abrupt short spikes in the sound signal, these spikes being associated with the occurrence of a short circuit. In order to summarise the nature of the acquired sound signals, time domain descriptor values were calculated. Three of these descriptors: Peak Sound level, Coefficient of Variation and Maximum Rise are plotted versus transfer mode in Figures 5, 6 and 7. The Maximum Rise is found as the largest absolute difference between consecutive samples in a sound record. These Figures show that the values of all three of the plotted time descriptors increase from spray to globular to short arc transfer.

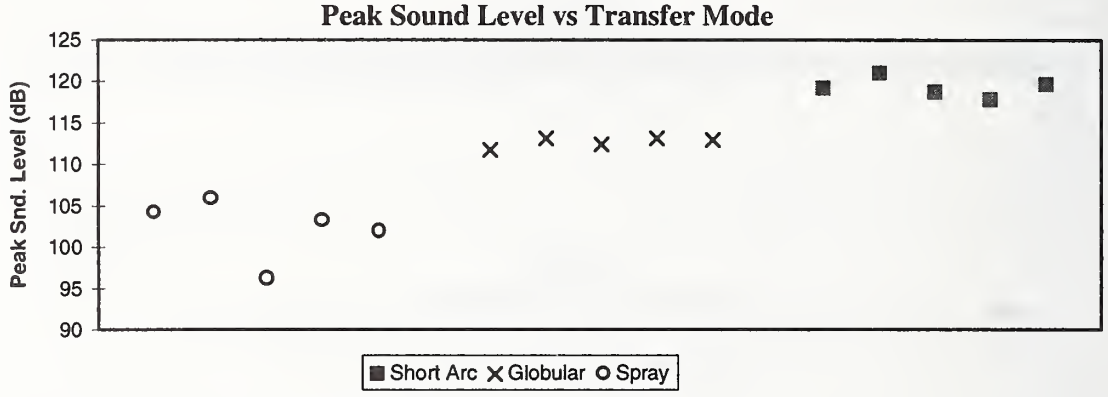

Figure 5. Peak Sound Levels vs. Transfer Mode

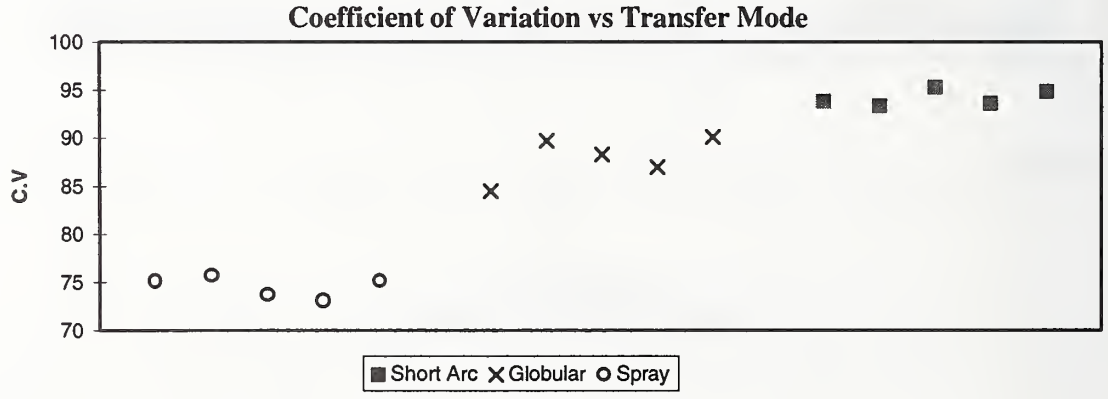

Figure 6. Coefficient of Variation of Sound Level vs. Transfer Mode

Time averaged frequency spectra were found for each of the five sound records associated with each transfer mode. These spectra are plotted in Figures 8, 9 and 10. From these plots it can be seen that even though the frequency spectra from a given transfer mode exhibit some variation, the general shape of the spectra is quite consistent. Spray transfer exhibits an almost monotone spectrum, while globular and short arc transfer exhibit more broad-band signals. The spectra for globular and short arc transfer are similar, but smaller amplitudes and spectra with a more trapezoidal shape can distinguish the short arc spectra.

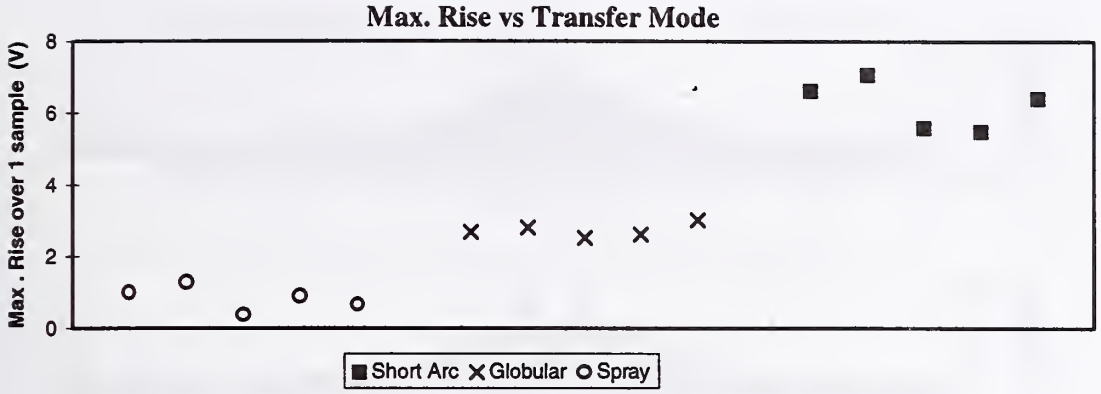

Figure 7. Max. Rise vs. Transfer Mode

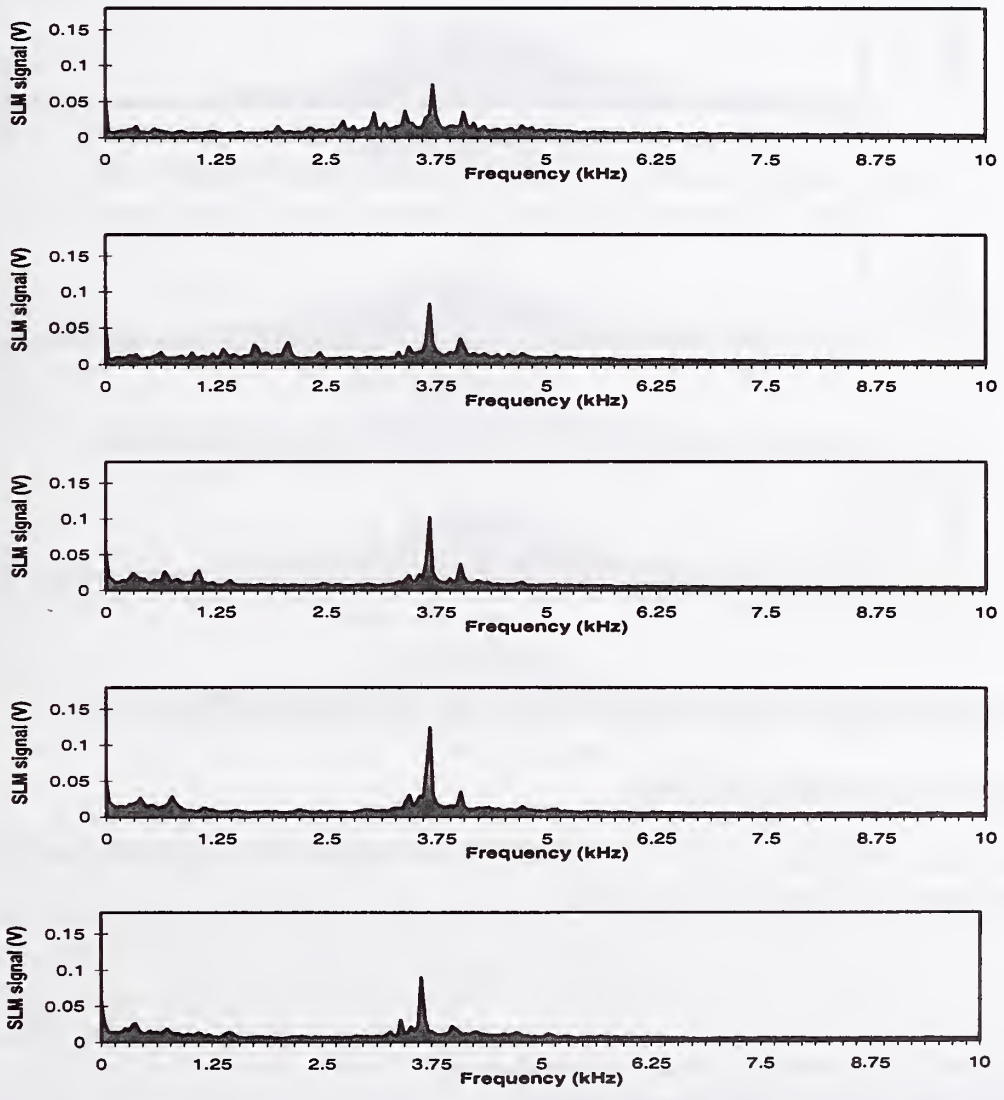

Figure 8. Time Averaged Frequency Spectra for Sound from Spray Transfer

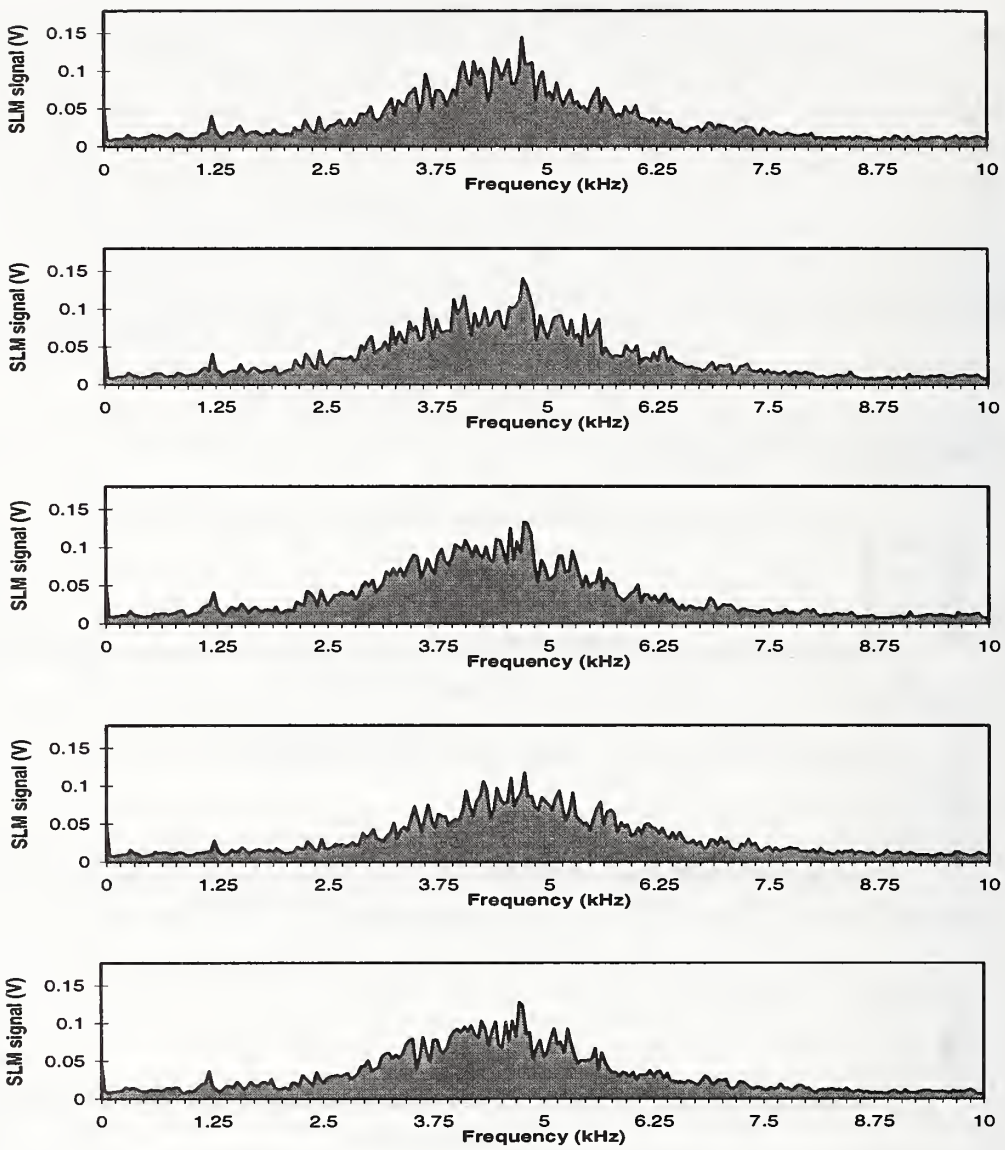

Figure 9. Time Averaged Frequency Spectra for Sound from Globular Transfer

Comparison of Arc sound and Power

The relationship between the sound produced by an electrical arc and the electrical power supplied to the arc can be expressed as [5,6] :

$$S_a(t) = k\frac{d}{dt}\big(V(t)I(t)\big)$$

where $S_a(t)$ is the amplitude of the sound signal at time t,
$V(t)$ is the voltage across the arc at time t,
$I(t)$ is the current flowing through the arc at time t,
k is a constant of proportionality .

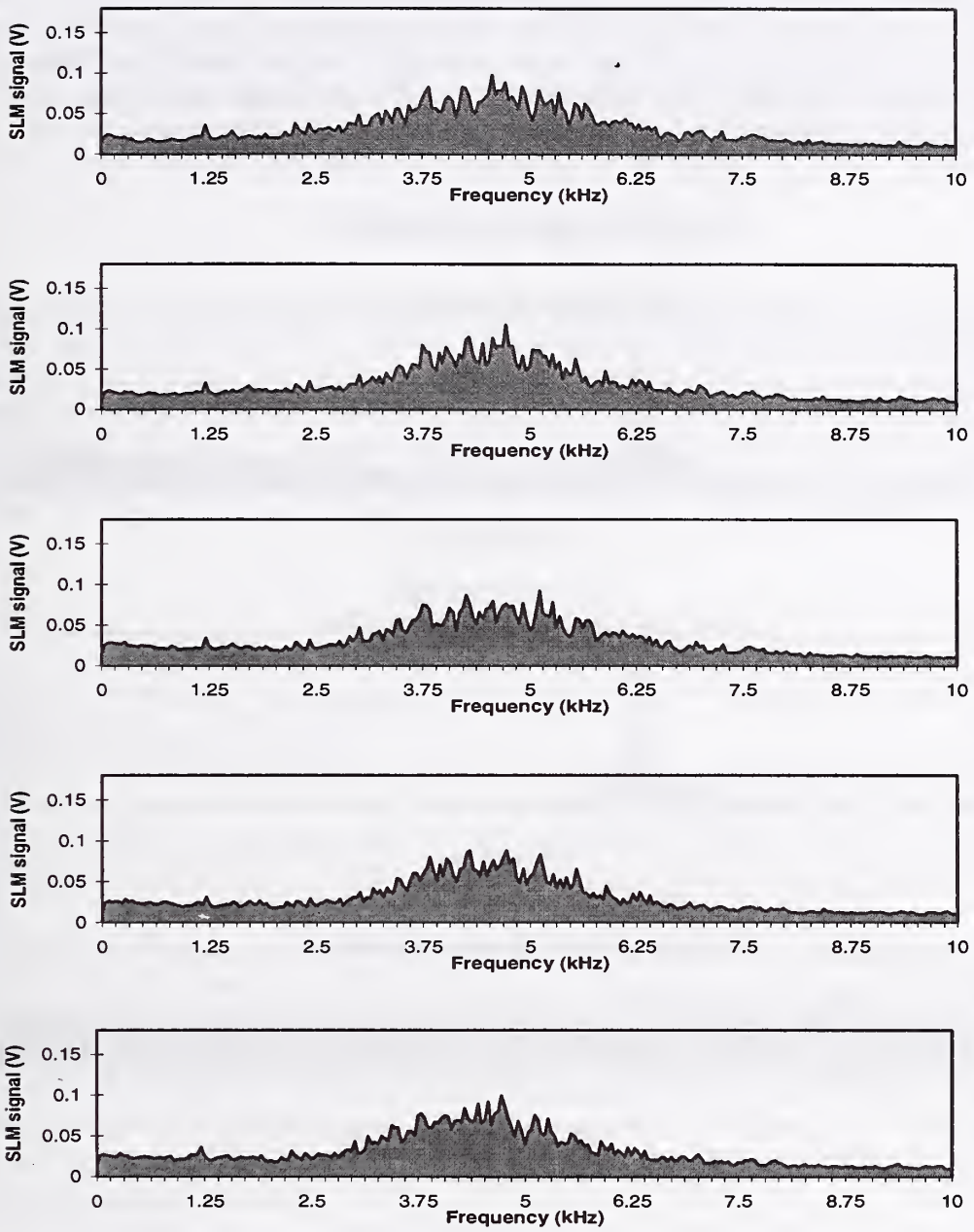

Figure 10. Time Averaged Frequency Spectra for Sound from Short Arc Transfer

There is evidence that this relationship also holds for the GTA welding arc [7]. To investigate this relationship for the GMA welding arc, the sound and power derivative signals for welds were compared in the time and frequency domains. The electrical power supplied to the arc was calculated as the product of the measured welding current and voltage (an over-estimate since the voltage was measured at the contact tube). The power signal was then differentiated using a 2nd order backward finite difference equation. The time domain sound and electrical power derivative signals did not exhibit a great deal of similarity for either spray or globular transfer, although for short arc, a similar periodicity was evident. As seen in Figure 11(a), the power

derivative spectrum exhibits higher frequency components, which arise from the numerical differentiation. To reduce any masking effect that this differentiation 'noise' may have introduced in the time domain comparison, the power derivative signal was low pass filtered using a finite impulse response filter with a corner frequency of 4kHz. The resultant signal shown in Figure 11(c) shows some of the fluctuation exhibited by the sound signal (Figure 11(d)).

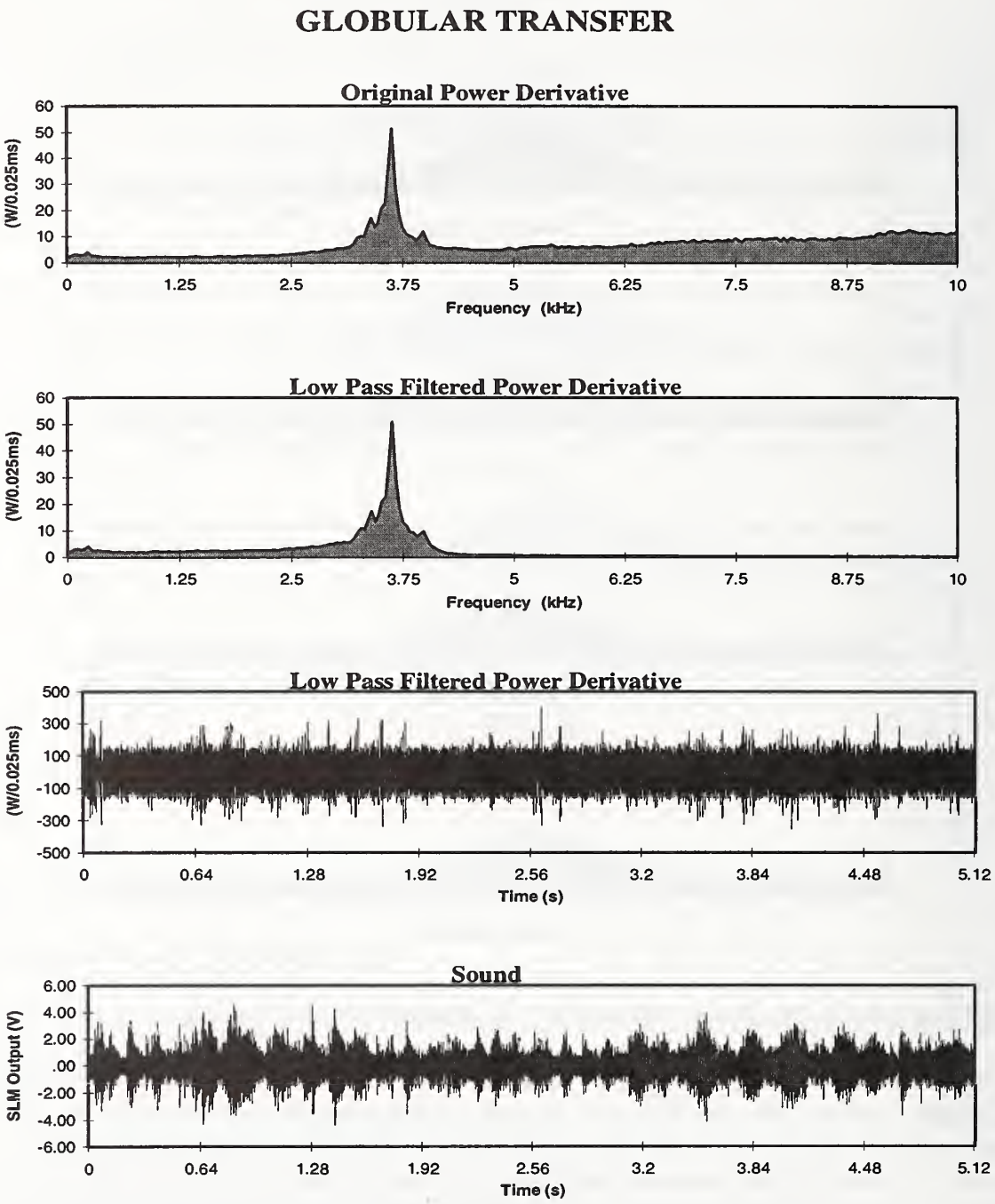

Figure 11. Low Pass Filtered Power Derivative for Globular Transfer

CONCLUSIONS

The results of this study indicate that the arc sound produced during the GMA welding process can be used as a source of process feedback. Specifically, this study has shown that the metal transfer mode, and events such as the occurrence of spatter or short circuit can be discerned from the arc sound. Such feedback has potential applications in monitoring the GMA welding process.

FUTURE WORK

Further work in this area will concentrate on incorporating the arc sound descriptors developed in this study into a weld monitoring system. This system would acquire the sound from the arc and calculate time domain, frequency domain and frequency-time domain descriptors. These descriptors would then be further analysed using a set of heuristics or a pattern recognition tool such as a neural network to extract useful information about the weld process. Possible applications are spatter detection and automatic arc tuning.

REFERENCES

1. Arata, Y.; Inoue, K.; Futama, M.; and Toh, T. 1979. Investigation on Welding Arc Sound (Report II), Evaluation by Hearing Acuity and Some Characteristics of Arc Sound. *Transactions of JWRI* 8(2): 3-38
2. Wu, C. 1992. Microcomputer Based Welder Training Simulator. *Computers in Industry* 20: 321-325.
3. Morita, T.; Ogawa, Y.; and Sumitomo, T. 1995. Analysis of Acoustic Signals on Welding and Cutting. Proc. 14th Int. Conf. on Offshore Mechanics and Arctic Engineering (ASME), Part 3: 547-52.
4. Blumschein, E.; Werner, C.; Blumschein, J.; and Schik, U. 1996. A Concept for Cognitive Control of Welding Processes. Proc. 6th Int. Conf. on Computers in Welding, paper 33
5. Dadgar, H.; Pilorget, A.; and Fitaire, M. 1977. Acoustic Noise Excited by Electric Arcs. IEEE Int. Conf. on Plasma Science: Conference Record - Abstracts, R.P.I., 117.
6. Drouet, M.; and Nadeau, F. 1982. Acoustic Measurement of the Arc Voltage Applicable to Arc Welding and Arc Furnaces. *J. Phys E: Sci. Instrum*. 15.
7. Kaskinen, P.; and Mueller, G. 1986. Acoustic Arc Length Control. Proc. Int. Conf. on Trends in Welding Research, 763-765.

Session B3: Real-Time Weld Sensing and Control Systems: GMAW Arc Quality Monitoring III

DEVELOPMENT OF ADAPTIVE CONTROL OF ARC WELDING BY IMAGE PROCESSING

T.Maeda, Y.Ichiyama

ABSTRACT

Sensing welding circumstances during welding is essential for seam-tracking and in-process controls of automatic arc welding. Among many types of sensing, visual sensing is influenced to a less extent by the change in welding conditions and provides much more information than other sensing. However, miss-operation in processing of visual sensing may take place due to noises caused by arc light and others, and visual sensing devices are costly. From these reasons, the use of visual sensors have been less popular than arc sensors.

The authors have developed a system of image measuring of a weld molten pool. The newly developed system has enabled to avoid the external interference such as arc light fluctuation and spattering during welding. This development has been achieved by, 1) reduction of relative intensity of arc light through improved optical processing; 2) detection of the location of the electrode wire through processing images by the camera with a trigger high-speed shutter; 3) averaging images by integration and stabilization of data processing through an algorithm using a weighting function.

A control of the shape of a back-bead reinforcement in one-side narrow gap welding is important. This image processing has accomplished not only preferable seam-tacking but also the improvement of quality of deposited weld metal through a control of the surface shape of a molten pool. The in-line control system with this image processing is to be applied for one-side GMAW narrow gap welding in which a control of the shape of a back-bead reinforcement is significantly important.

INTRODUCTION

There has been an increasing demand for an in-line control of automated arc welding in steel welded constructions. Laser sensors have recently been used to measure the groove shape and control the position of a welding torch so that the preferable quality of deposited metal can be

obtained. However, some difficulties arise in controlling the torch position when the welding condition fluctuates. For example, it is almost impossible for the laser sensor to correct the torch position when the welding wire is bent. Furthermore, the laser sensing is inappropriate in optimizing back-bead welding such encountered with pipe girth welding.

This study is dealt with a technology of image processing and an in-line control in narrow gap arc welding with a torch weaving with high speed. This technology is featured by a computer-aided vision system enabling in-process detection of the electrode wire position and the geometry of a molten weld pool. This system is ready to be applied to automatic all-position welding such as pipeline construction welding.

IN-LINE WELDING DATA ACQUISITION SYSTEM

An in-line data acquisition system equipped with a visual sensor consists of a CCD camera, an image processor and sensors other than the CCD camera. The real time data acquisition is essential in in-line sensing of dynamic welding situation. The system presently studied enabled to concurrently acquire images of the molten pool, arc light, welding sound, arc voltage, and welding current. Because of their huge data size, image data of the molten pool were compressed into a moving picture format (MOTION-JPEG) and then the compressed data were stored as a Video for Windows format (AVI file) in the computer. The image data of the molten pool and acquisition data for arc light, welding sound, arc voltage, and welding current were stored in a precisely synchronous manner as a text file in the computer.

Fig. 1 shows the composition of a multiple-sensing system for the in-line processing developed in the present study. The software in the system enabled to display pool images and measured data either graphically or in an image manner (still picture or moving picture), and either independently or synchronously. The text data of arc voltage, welding current, welding sound and others were analyzed by some application software (e.g. EXEL, MATLAB). The development of the visual sensing method and the image measurement of the molten pool is mainly focused in the present paper.

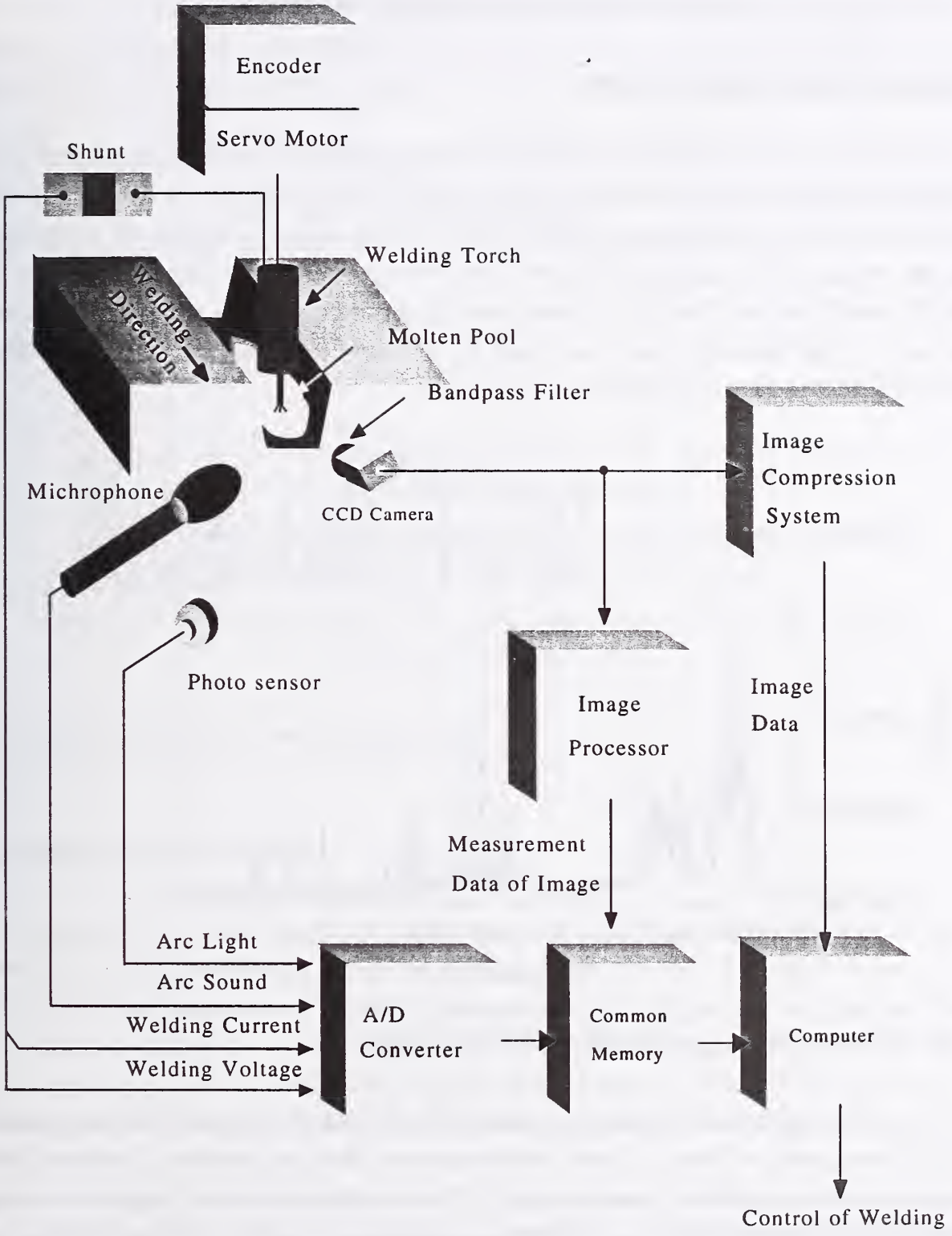

Fig.1 Multiple Sensing System of Welding Process

IMAGE PROCESSING OF MOTLEN POOL

Selection of Optical Band-Pass Filter

A visual sensor, which acquires the image of a molten pool and a weaving electrode wire, was installed at an angle forward a welding torch as shown in Fig. 1. Brightness of arc light is much more intense than radiation from the molten pool. It is, thus, difficult to acquire the processing-possible images of the molten pool unless some measures are taken. The arc spectrums of GMAW with 80%Ar and 20% CO_2 mixture shielding gas were measured and it was found that there are two high intensity groups: one around 400 to 500nm wavelength due to Fe and another from 700 to 900nm due to Ar as shown in Fig. 2.

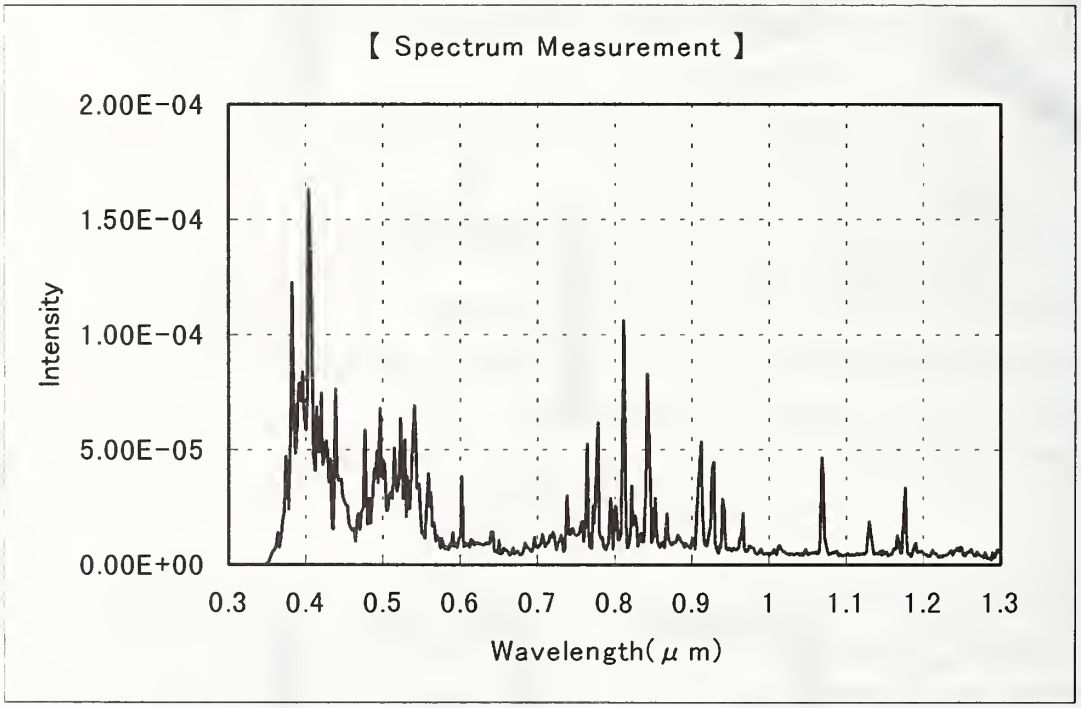

Fig.2 Measured Spectrum(GMAW, Ar 80%+CO2 20%)

For a comparison purpose, a detailed spectrum of Ar according to the database(Ref.4) as shown in Fig.3 was referred to. From a Plank's radiation formula, the peak intensity of radiation from the molten pool is considered to range between 1,200 and 1,600nm. However, the sensitive range of the CCD device is not higher than 1,000nm. So, it is desired to view a weld region through an optical band-pass filter whose the center wavelength is near 1,000nm.

However, when the center wavelength of a band-pass filter is too close to 1,000nm, the

sensitivity of the CCD drops and poor acquisition of pool images results. Finally, a filter with the center wavelength of 955nm was used in the present study and the significant interference with detectable spectrums of the molten pool due to Ar spectrum could be avoided.

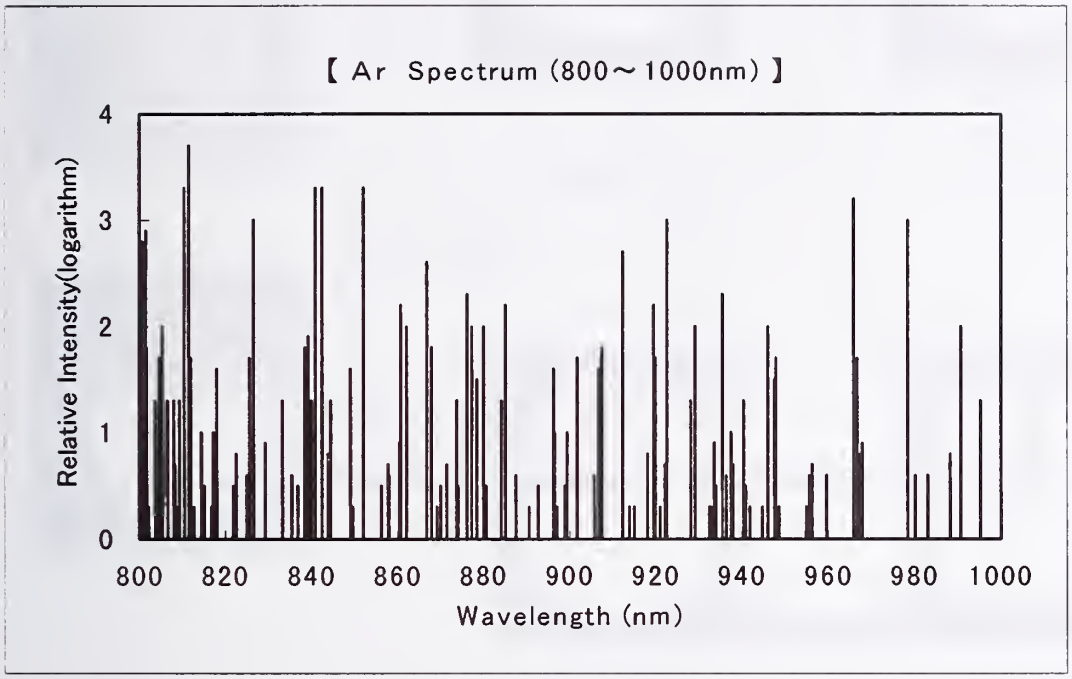

Fig.3 Spectrum data from "Wavelength Table"

Acquisition of Molten Pool Image

A CCD camera with an electronic trigger shutter was used to apply the present system to in-line processing of welding with an electrode wire weaving as fast as 10 to 50Hz speed. The camera with a normal synchronous shutter is unable to acquire the images of the pulsating pool and the fast weaving electrode wire. In this study, a CCD camera was employed which was provided with an electronic shutter operating with external trigger signals at arbitrarily selected timing. The timing was selected so as to coincide with the center position of wire weaving.

Fig. 4 shows trigger shutter timing in this system. Then, it became possible to obtain still images even under the condition of high speed weaving and detect the wire position in a weld groove and the wire shape within the molten pool image. Through keeping the distance between the wire position and the center of the molten pool zero, the torch position was satisfactorily controlled at the center of the welding pool all the time.

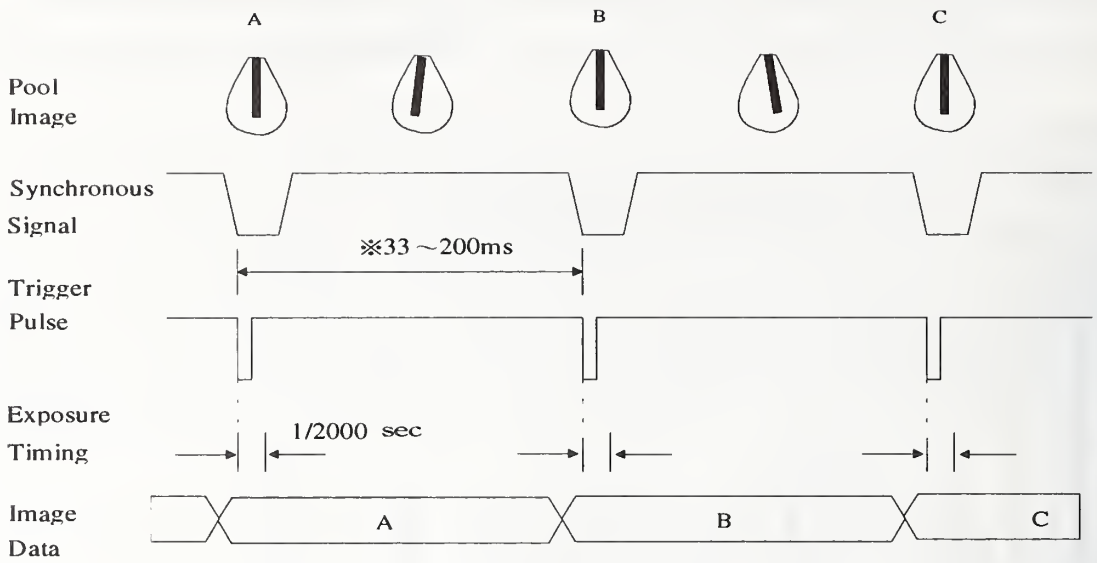

Fig.4 Exposure Timing and External Trigger synchronized with torch weaving

Algorithm of Image Acquisition and Image Analysis

The algorithm of image acquisition of a molten pool is divided into three stages: an averaging process by image integration; detection of characteristic points of a welding pool; and analysis of the shape of a welding pool.

Arc light intensity fluctuates very often due to droplets transfer into the molten pool and the brightness of molten pool images frequently changes because the molten pool is reflected by arc light. Fig. 5 shows a dark arc image with pool radiation alone and a bright arc image with pool radiation and arc reflection. This brightness fluctuation results in incorrect acquired images. To solve this problem, a frame averaging process by image integration was introduced.

As shown in Fig. 6, the integration of several video frames followed by bit shifting made it possible to average noise images and reduce disturbing images. The image integration processing was done in real time by the image processor.

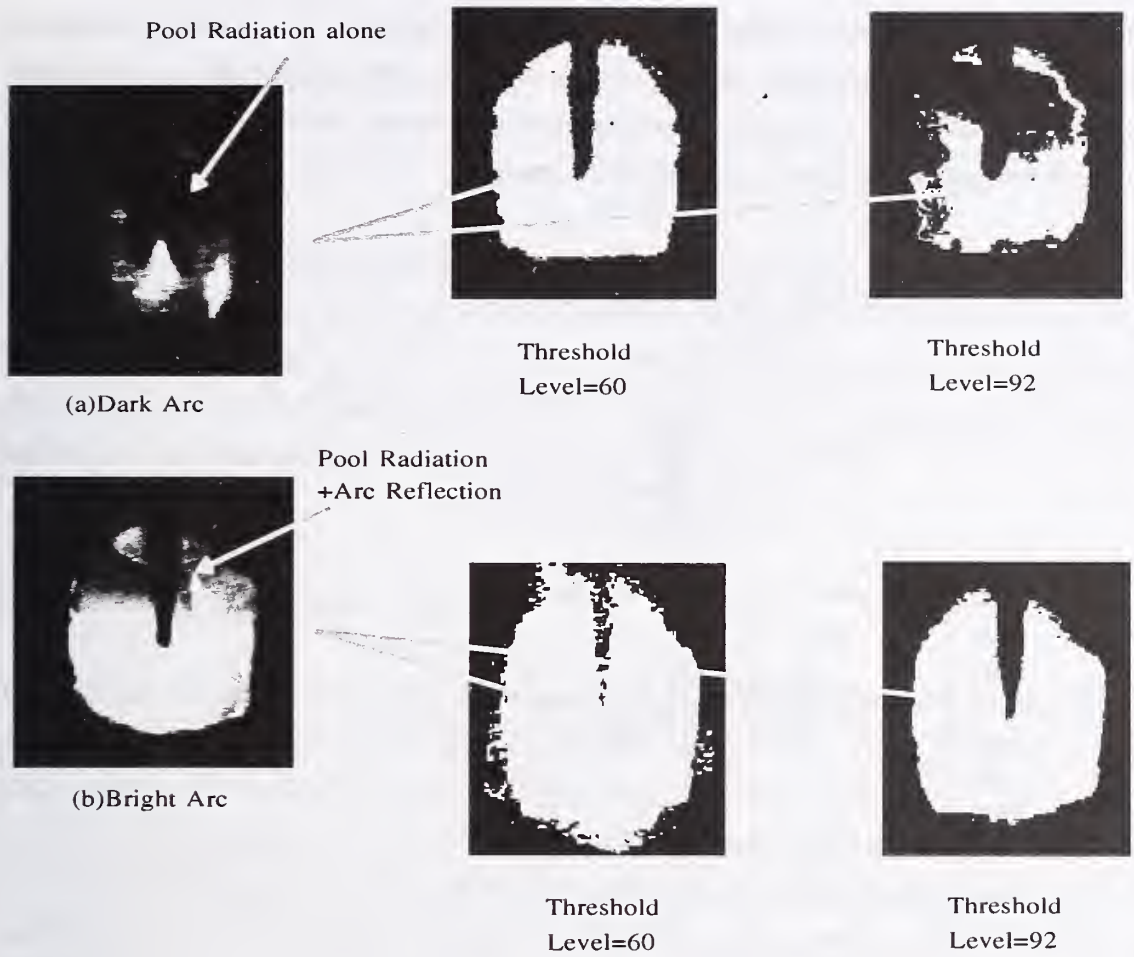

Fig.5 Binary Images Depending on Threshold Level

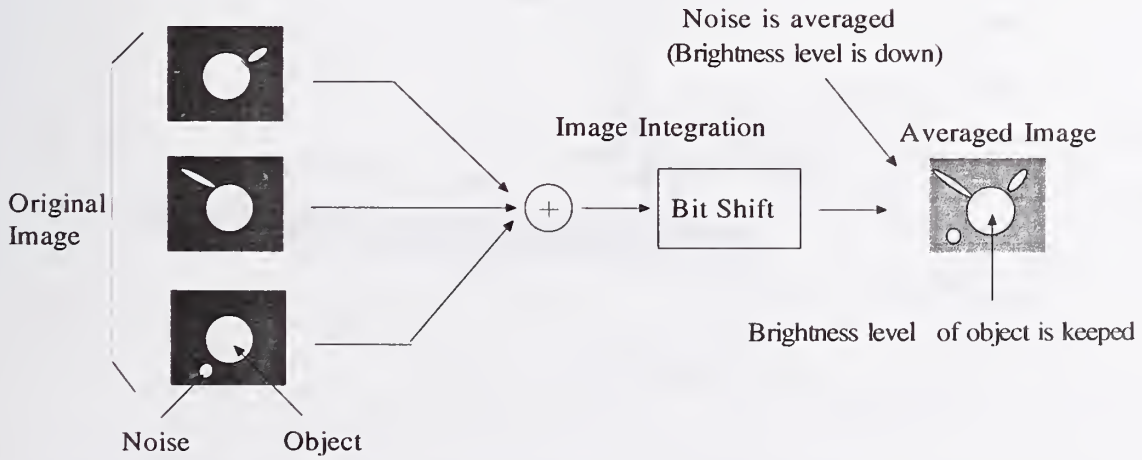

Fig.6 Averaging Operation (Image Integration)

The images of a weld region were acquired by the CCD camera and then, the position of the side edges of a molten pool and the center of an electrode wire were determined by the smoothed differentiation of the brightness along the line perpendicular to the welding direction. Fig. 7 shows a newly developed image processing algorithm.

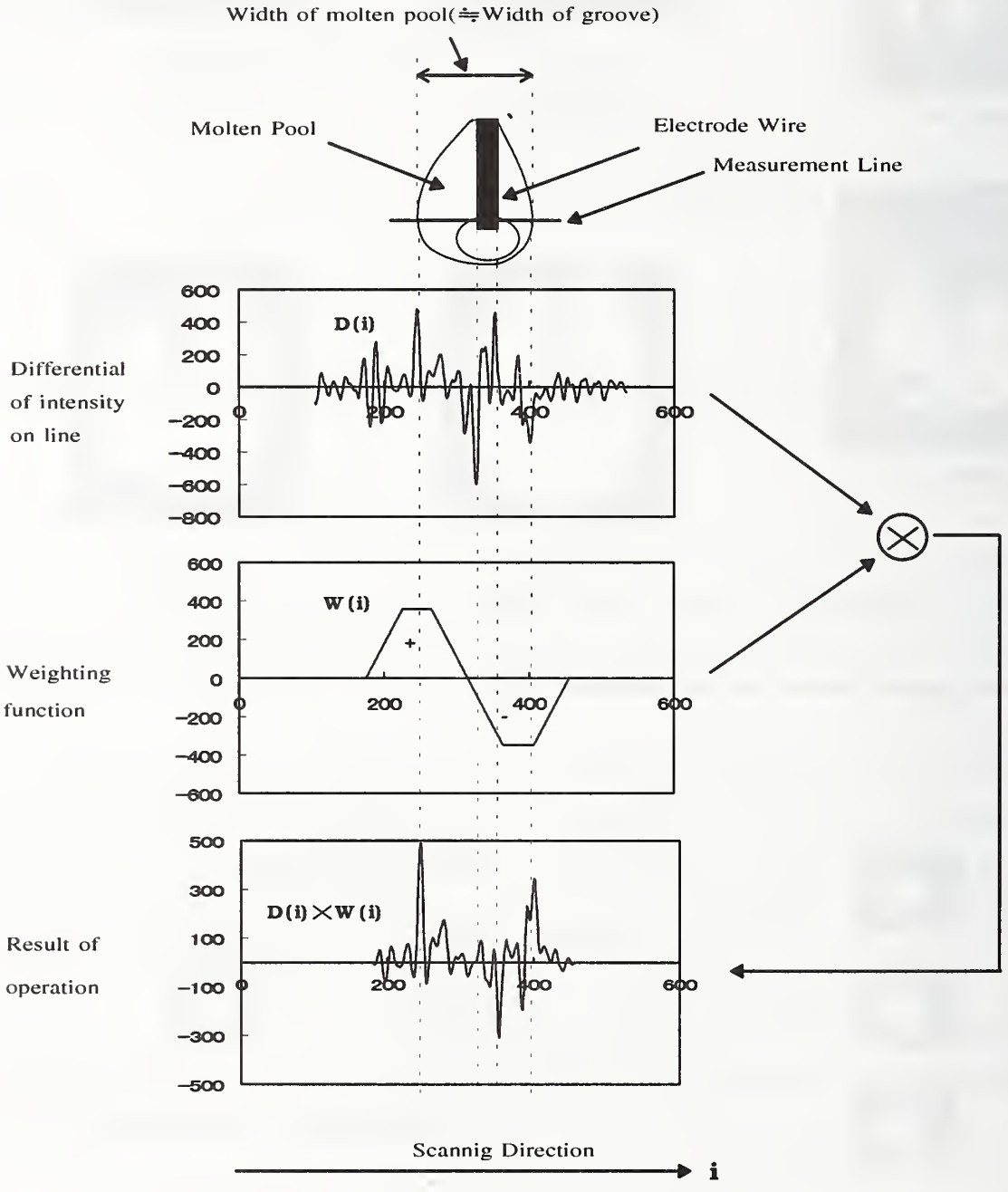

Fig.7 Pool Edge Detection with Weighting Function

As mentioned above, acquired images by the CCD camera equipped with a high-speed shutter considerably fluctuates in their brightness. In order to accomplish stable detection of the characteristic points of the pool image, a dynamic threshold level or gray level in the data acquisition was set up instead of a fixed threshold level.

Furthermore, the weighting function, W(x) corresponding to the groove size was prepared as shown in Fig.7 and then the values of differentiated brightness, D(i) and W(x) were multiplied. This multiplication facilitated the avoidance of external interference due to arc light and spatters. As a result, the developed algorithm enabled stable detection of the characteristic points of a molten pool so that satisfactory seam tracking could be performed.

Result of Seam-Tracking Control Test

The authors conducted seam-tracking tests using the image-processing algorithm developed in the present study. A work piece was machined with a narrow gap with a bevel angle of 10 degree and a root gap of 7mm. It was set at an angle toward the travel direction, i.e., 2.5mm per 170mm-travel direction, as shown in Fig. 8. GMAW was conducted under the conditions of 80%Ar and 20%CO_2 shielding gas, solid electrode wire, 20cm/min of travel velocity and 30Hz weaving frequency. During testing, zero distance was kept between the wire position and the center of a molten pool, and it was found that the torch position was constantly controlled at a satisfactory level along the groove center line, as shown in Fig. 9.

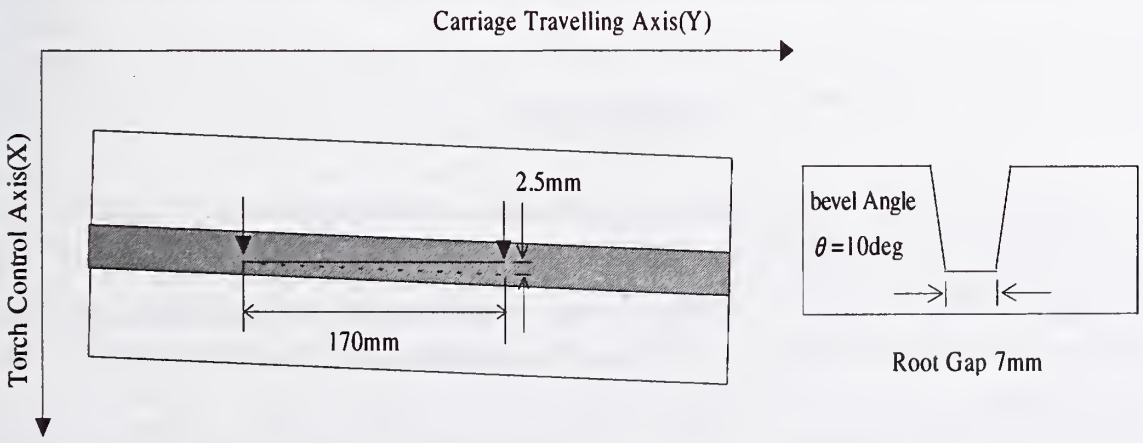

Fig.8 Relative Directions of Carriage Travel and Welding Groove

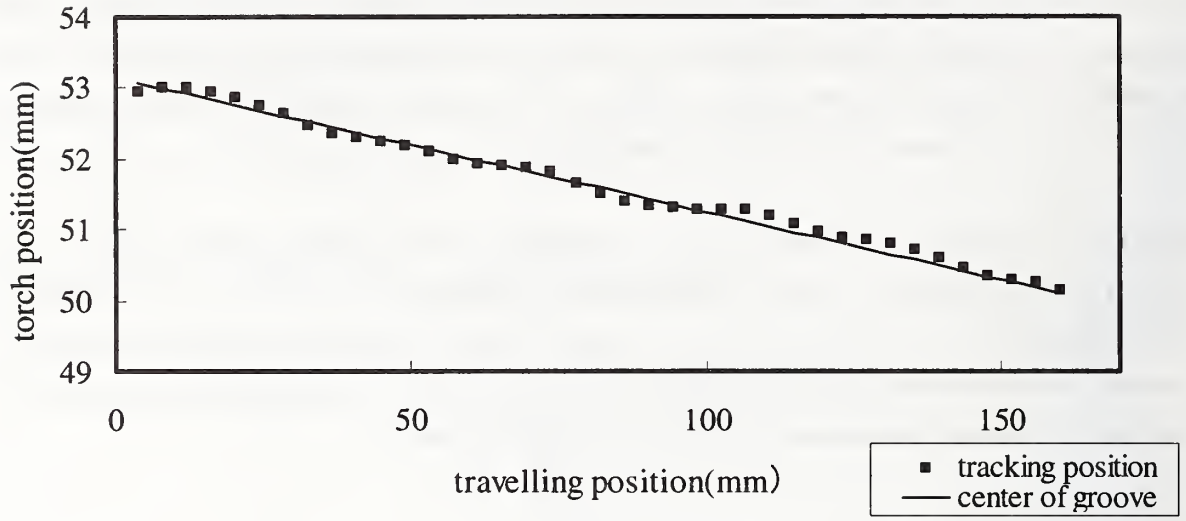

Fig.9 Result of Seam-Tracking Control by Image Processing

SUMMARY

An in-line control system for all-position narrow gap welding was developed, which measures images of a molten weld pool. The image measurement developed in the present study was characterized by being less susceptible to the external influences such as spattering during welding. This development was achieved by: 1) reduction of relative intensity of arc light through improved optical processing; 2) detection of the location of the electrode wire through processing images by the camera with a high-speed trigger shutter; 3) averaging images by integration and stabilization of data processing through an algorithm with a weighting function.

REFERNCES

1. Inoue,K.1981. Image processing for on-line detection of welding process(2nd report). Yousetsu gakkai shi/ VOL.50,NO.11, 1118-1124
2. Li,Y.,Wu,L.,Middle,J.E.,1993. Machine Vision Analysis of the Welding Region and Its Application to Seam Tracking in Arc Welding. Proc Inst Mech Eng Part B/VOL.207, NO.4,275-283
3. Maeda,T.,Makabe,T.,Ichiyama,Y.,1997. Development of an On-line Visual Sensing System for Molten Pool Measurement , Yousetu gakkai kouen gaiyou/VOL.61,8-9
4. Phelps,F.M.,1982. M.I.T. wavelength tables. vol.2 2 ed. 4 ed.

ADAPTIVE VOLTAGE CONTROL IN GTAW

P. Koseeyaporn [*], G. E. Cook [*], A. M. Strauss [#]

ABSTRACT

Automatic voltage control (AVC) systems are commonly used in gas tungsten arc welding (GTAW) to maintain constant arc length. Although AVCs usually perform adequately in most operating circumstances, there are conditions during which the traditional systems cause problems because the arc voltage-to-arc length gain, K_{arc}, a feed forward gain, is not constant but varies with the nominal values of the arc current and voltage. Thus, an AVC that has a fixed voltage set point will not maintain a fixed arc length if the arc current changes. In this paper an adaptive controller is introduced that is capable of "identifying" the arc sensitivity characteristic and adjusting the controller in real time for optimum response without any a priori knowledge of the current/gain relationship.

INTRODUCTION

Automatic voltage control (AVC) systems are commonly used in gas tungsten arc welding (GTAW) to maintain constant arc length. Although AVCs usually perform adequately in most operating circumstances, there are conditions during which the traditional systems cause problems and sometimes fail totally in providing acceptable position control. Bjorgvinsson [1] has traced these problems to two significant characteristics of the welding arc that are not accounted for in traditional AVCs:

1) The arc voltage-to-arc length gain, K_{arc}, is not constant but varies with the nominal values of the arc current and voltage. In the closed-loop AVC system, this arc sensitivity affects the dynamic response of the system since it is one of the parameters forming the forward loop of the AVC.
2) The arc voltage-to-gap relationship is not constant but varies with current. Thus, an AVC that has a fixed voltage set point will not maintain a fixed arc length if the arc current changes.

The unstable phenomena frequently observed with AVCs occur primarily at the operating conditions that are significantly different from "normal" welding conditions, such as when the welding current is pulsed between primary and secondary current levels or at low currents experienced during upslope and downslope. If an AVC is tuned for the optimum response at normal welding current levels, then at the lower currents experienced during upslope and downslope the position control may become oscillatory sometimes driving the torch into the weld pool. To avoid these instability problems the AVC is frequently turned off in practice during the critical current sloping portions of the weld cycle. However, it is widely known that control of the cooling rate of the weld during termination is important if cracks in the weld seam are to be avoided. A simple disabling of the AVC during welding initiation and termination deprives the welder of full control over the welding heat during that period. Although the

[*] Department of Electrical & Computer Engineering, Vanderbilt University, Nashville, TN 37235
[#] Department of Mechanical Engineering, Vanderbilt University, Nashville, TN 37235

welding current is sloped down, voltage is not as well controlled, and the result is the so-called "tail-out" cracking. Therefore, a means of maintaining control of the arc gap, independent of current, is needed. Bjorgvinsson, Cook, and Andersen address the first characteristic by introducing a gain scheduling adaptive control law [2]. This system is based on use of a lookup table or empirical relationship between arc sensitivity and current. While the gain scheduling adaptive controller employed by Bjorgvinsson has been demonstrated to work well under controlled conditions, the functional relationship between arc sensitivity and current is dependent on a number of parameters that are difficult to preprogram. In this paper an adaptive controller is introduced that is capable of "identifying" the arc sensitivity characteristic and adjusting the controller in real time for optimum response without any a priori knowledge of the current sensitivity relationship. It is thus capable of providing stable operation at all points. Ability to control the arc voltage in a stable manner at all welding currents also permits addressing the second characteristic. The voltage reference is varied as the current changes, e.g., decreases during weld termination, in such a manner as to maintain an appropriate weld pool width to depth ratio and maintain an optimum weld pool shape [3-4]. In this research, fuzzy logic control was used to estimate the required voltage reference setpoint to maintain the weld pool geometrical characteristics [5]. While both characteristics of the welding arc are accounted for in the results described in this paper, the adaptive control aspect of the first characteristic is the paper's primary focus.

TRADITONAL CLOSED-LOOP SYSTEM VERSUS ADAPTIVE CONTROL

To control the gas tungsten arc welding (GTAW) system with a constant current power source (see Figure 1.), an automatic voltage control (AVC) is typically used to control the arc voltage in order to maintain a desired arc length. However, it is known that the arc voltage-to-gap relationship is not constant but varies with current [1,2]. Thus, an AVC that has a fixed voltage set point will not maintain a fixed arc length if the arc current changes. The traditional AVC design uses a fixed arc voltage-to-arc length gain, K_{arc}, as shown in the closed-loop AVC block diagram in Figure 2. Although not shown in the simplified block diagram, rate feedback would normally be employed for improved response characteristics. To prevent the system from being unstable when the arc current changes, adaptive control [6] is used to identify the arc voltage gain in the closed-loop system, as shown in Figure 3, and produce compensatory changes in the controller.

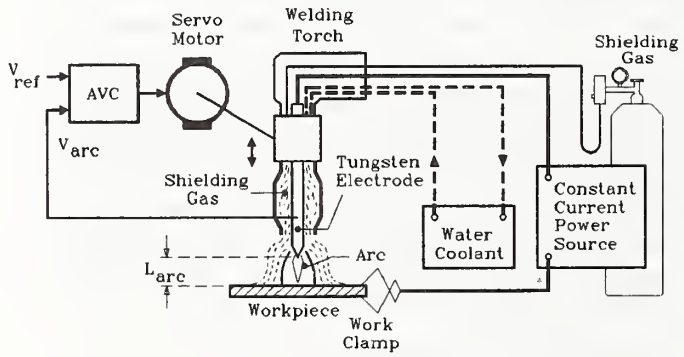

Figure 1. GTAW system with AVC.

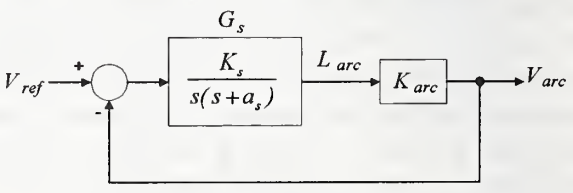

Figure 2. Traditional closed-loop AVC.

DESIGN OF THE ADAPTIVE CONTROL

In this paper, the adaptive controller, shown in Figure 3, is used to identify the gains in the model-based portion of the partitioned control system [7] used to control the arc voltage. The adaptive controller provides stable control of the system even when the input current is changed over a wide range.

The transfer function of the dc servomotor used for control of the arc length (and hence arc voltage) is given by

$$G_s(s) = \frac{L_a}{V_m} = \frac{K_s}{s(s+a_s)}. \tag{1}$$

Using $L_a K_{arc} = V_a$ in (1), we may express the corresponding differential equation as $\ddot{v}_a + a_s \dot{v}_a = K_s K_{arc} v_m$

Letting $c_2 = \frac{1}{K_s K_{arc}}$ and $c_1 = \frac{a_s}{K_s K_{arc}}$, we may rewrite the open-loop equation as,

$$c_2 \ddot{v}_a + c_1 \dot{v}_a = v_m. \tag{2}$$

Both c_1 and c_2 vary inversely as K_{arc}, which is a nonlinear function of the welding current and arc voltage. Thus, when the current/voltage dependence of K_{arc} is taken into account, the open-loop dynamics of the system relating arc voltage to servo drive voltage is a nonlinear second-order differential equation.

The partitioning scheme [4] employed here partitions the controller into a model-based portion and a servo portion. The model-based portion appears in a control law of the form

$$v_m = \alpha v_m' + \beta, \tag{3}$$

where α and β are functions or constants chosen such that if v_m' is taken as the *new input* to the system, the system appears as a simple *linear* second-order system,

$$v_m' = \ddot{v}_a. \tag{4}$$

Equating (1) and (2),

$$c_2 \ddot{v}_a + c_1 \dot{v}_a = \alpha v_m' + \beta. \tag{5}$$

Clearly, in order to make the system appear as the linear system given by (3) at the v_m' input, α and β must be chosen as

$$\begin{aligned} \alpha &= c_2 \\ \beta &= c_1 \dot{v}_a \end{aligned} \tag{6}$$

Referring to Figure 3, $\hat{c}_1$ and $\hat{c}_2$ are estimates of c_1 and c_2, respectively. We choose the proportional-plus-derivative control law

$$v_m = \hat{c}_2 v_m' + \hat{c}_1 \dot{v}_a, \tag{7}$$

where $v_m' = \ddot{v}_{ref} + K_v \dot{e} + K_p e$, and $e = v_{ref} - v_a$. From Figure 3, we see that

$$v_m' = \ddot{v}_{ref} + K_v \dot{e} + K_p e, \tag{8}$$

and

$$v_m = \hat{c}_2 v_m' + \hat{c}_1 \dot{v}_a. \tag{9}$$

Equating (9) to the open-loop dynamics of the system, as expressed by (2), and substituting (8) into the right-hand side of (9), we obtain

$$c_2 \ddot{v}_a + c_1 \dot{v}_a = \hat{c}_2 [\ddot{v}_{ref} + K_v \dot{e} + K_p e] + \hat{c}_1 \dot{v}_a.$$

Rearranging,

$$\hat{c}_2 \ddot{v}_{ref} + \hat{c}_2 [K_v \dot{e} + K_p e] = c_2 \ddot{v}_a + (c_1 - \hat{c}_1) \dot{v}_a.$$

Subtracting $\hat{c}_2 \ddot{v}_a$ from both sides,

$$\hat{c}_2 (\ddot{v}_{ref} - \ddot{v}_a) + \hat{c}_2 [K_v \dot{e} + K_p e] = (c_2 - \hat{c}_2) \ddot{v}_a + (c_1 - \hat{c}_1) \dot{v}_a$$

or

$$\hat{c}_2 \ddot{e} + \hat{c}_2 [K_v \dot{e} + K_p e] = \tilde{c}_2 \ddot{v}_a + \tilde{c}_1 \dot{v}_a,$$

where the parameter errors are $\tilde{c}_2 = c_2 - \hat{c}_2$ and $\tilde{c}_1 = c_1 - \hat{c}_1$.

The desired error equation is then,

$$\ddot{e} + K_v \dot{e} + K_p e = \hat{c}_2^{-1} [\tilde{c}_2 \ddot{v}_a + \tilde{c}_1 \dot{v}_a]. \tag{10}$$

If the model-based portion of the controller equals exactly the system parameters, then $\tilde{c}_1$ and $\tilde{c}_2$ are zero, and the error disappears. In this case, K_p is chosen to provide the desired closed-loop stiffness and K_v is chosen to provide the desired damping, e.g., critical damping, $\zeta = 1$. When the model parameters are not known exactly, the mismatch between actual and modeled parameters will cause servo error, possibly resulting in an oscillatory or unstable system, in the absence of adaptive control. With adaptation, the servo error may be used to drive the adaptation scheme, as shown in Figure 3, which attempts to update the values of the model parameters until the error disappears. Equation (10) may be rewritten in the form,

$$\ddot{e} + K_v \dot{e} + K_p e = \hat{c}_2^{-1} W(\dot{v}, \ddot{v}) \Phi \tag{11}$$

where $\Phi = \begin{bmatrix} c_2 - \hat{c}_2 \\ c_1 - \hat{c}_1 \end{bmatrix} = \begin{bmatrix} \tilde{c}_2 \\ \tilde{c}_1 \end{bmatrix}$, and $W(\dot{v}_a, \ddot{v}_a) = \begin{bmatrix} \ddot{v}_a & \dot{v}_a \end{bmatrix}$

The adaptive law computes how to change the parameter estimates as a function of the *filtered* servo error signal (see Figure 4),

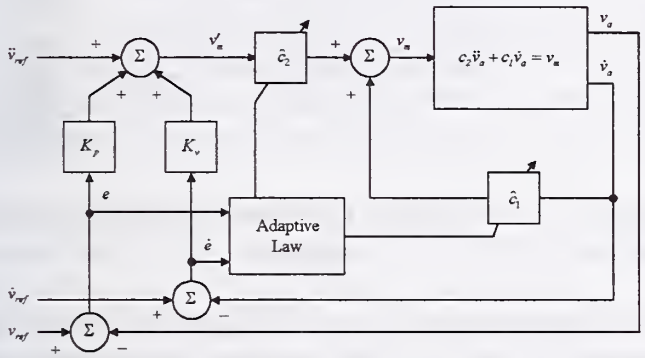

Figure 3. The welding system with an adaptive controller.

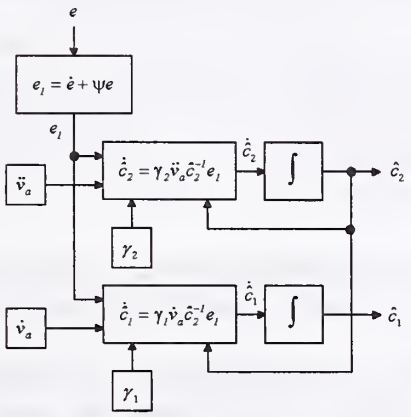

Figure 4. The adaptive law.

$$E_1(s) = (s + \psi)E(s), \tag{12}$$

where ψ is a positive constant.

Substituting the Laplace transform of the error equation (11),

$$E_1(s) = \frac{s + \psi}{s^2 + K_v s + K_p} \hat{c}_2^{-1} W \Phi. \tag{13}$$

Based on the strictly positive real (SPR) lemma [8] and Lyapunov stability theory [9], we choose

$$\dot{\Phi} = -\Gamma W^T \hat{c}_2^{-1} e_1, \tag{14}$$

where $\Gamma = diag(\gamma_1 \quad \gamma_2)$ and γ_i is nonnegative.

Equation (14) provides the parameter updates in the "identification paradigm" of the adaptive system. The adaptation law, including the error filter, is shown in the block diagram of Figure 4.

FUZZY LOGIC SELECTION OF VOLTAGE SETPOINT

During initiation of the weld, the welding current is typically ramped linearly from a low value, e.g., 10 amperes, or less, to the weld value, e.g., 50-400 amperes, or more. During termination of the weld, the welding current is typically ramped linearly from the weld value back down to a low value. During both of these critical portions of the weld, it is important that desired

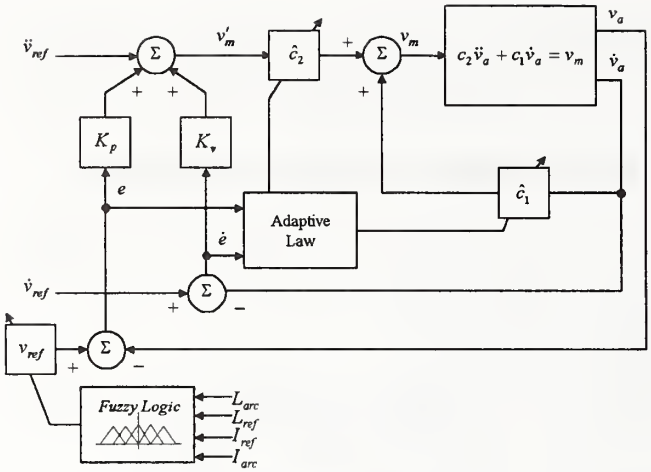

Figure 5. The welding system with an adaptive controller and FLC for setpoint selection.

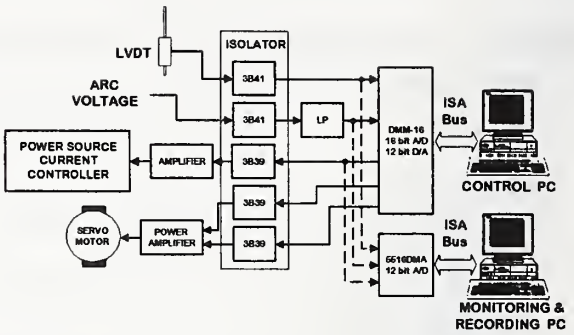

Figure 6. Hardware interfacing block diagram.

geometrical characteristics of the weld pool are maintained [10-13]. To accomplish this, it is not only necessary that the AVC be operative and stable, but it is also necessary that the reference (setpoint) voltage be changed as the current changes. This is because the arc voltage-to-gap relationship is not constant but varies with current [1]. Since the arc length can not easily be measured, it is difficult to continuously set the voltage reference to the correct value to obtain a specific arc length required for the desired weld pool geometry. The required relationship could be determined experimentally [3-4], but this relationship varies as a function of a number of variables. In this research the required voltage was chosen by means of a fuzzy logic control (FLC) system.

The FLC is only operative when the welding current I_{arc} is below a reference value I_{ref}. In addition to I_{arc} and I_{ref}, inputs to the FLC are the *relative* arc length error (L_{ref} - L_{arc}) and the derivative of the error. The relative arc length error was measured with a linear transducer connected between the AVC servo mount and the welding torch.

Membership functions of the FLC were composed of the input error, the velocity error, and an output (v_{ref}). The shape of the membership functions was selected as triangular for faster control. A center-of-gravity defuzzification scheme was applied [14]. Each of the negative and positive fuzzy sets was assigned three values (large, medium, and small), so there was a total of forty-nine rules. Example rules are as follows:

*If the **error** is **negative large** and the **velocity error** is **negative large**, then the **output** is **negative large**.*

*If the **error** is **positive small** and the **velocity error** is **negative small**, then the **output** is **positive small**.*

When $I_{arc} < I_{ref}$, the FLC increases or decreases the arc length by adding its output to the fixed weld voltage level. When $I_{arc} > I_{ref}$, the FLC has no output, and the system operates in the constant arc voltage mode. The adaptive AVC with FLC selection of voltage reference is shown in Figure 5.

IMPLEMENTATION

To implement and test the adaptive AVC system, both software and hardware components were required. The control algorithms were written in C++ on a personal computer (PC) allowing the user to conveniently change the parameters during the experiments under a Graphic User Interface (GUI) environment. Monitoring and recording programs were also required to obtain data from the system during its real-time control.

The hardware used in the research included a data acquisition system, isolator, welding power supply, control PC, monitoring and recording PC, and linear variable differential transformer (LVDT). The hardware interfacing block diagram is shown in Figure 6. The hardware can be classified into two groups: interfacing devices, and power and control devices.

Referring to Figure 6, the DMM-16 data acquisition board [15] was used to send and receive the data composed of the arc voltage, the relative arc length (LVDT) and the arc current to the control PC. Two input channels were connected to the voltage pickup for arc voltage measurement and the LVDT for relative arc length measurement. An output channel was linked to the power source current controller. Two of the output channels were employed to drive the reversible servomotor, one used for positive output and another for negative output. All of the input channels have 16-bit resolution with a 2 kHz maximum sampling rate per channel for single mode operation. The output channels have 12-bit resolution with the same sampling rate.

Another data acquisition board, 5516DMA [16], was used to capture the analog signals for use by the monitoring and recording PC. Three channels of this board were employed. One is linked to the arc length signal, and the others are connected to the arc current and arc voltage signals.

Magnetic isolators [17] were utilized to prevent the power signals from disturbing sensitive devices such as the PCs and data acquisition boards. A class-H welding power source [18-19] provided constant current output control. The power source can deliver output current from 0 to 500A at a voltage from 0 to 45 volts.

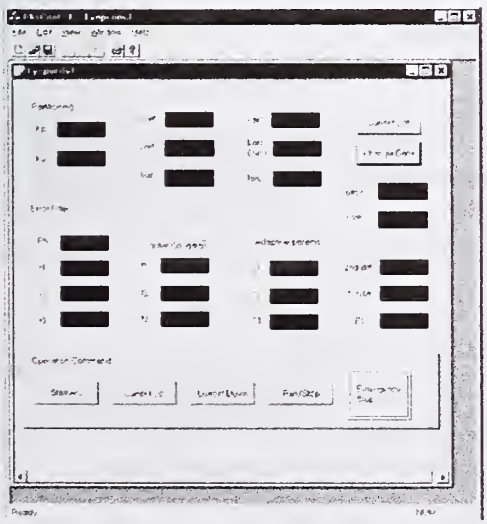

Figure 7. The dialog-based control program.

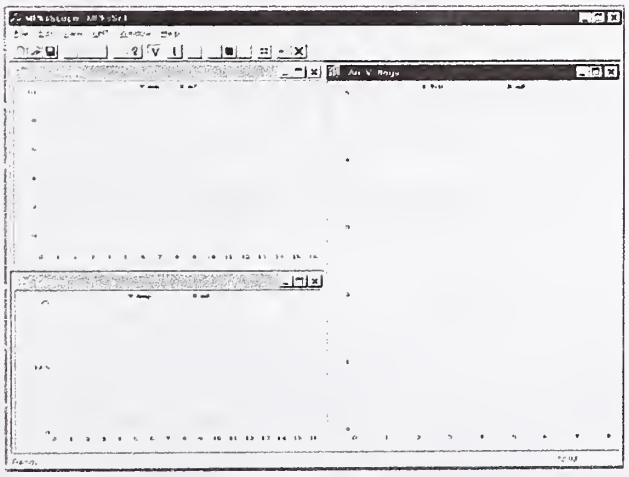

Figure 8. Monitoring/recording program.

All of the control schemes, including a digital non-adaptive AVC and adaptive AVC, were implemented by programming under a graphic user interface (GUI) based on Microsoft's Visual C++ platform language [20]. For some programs in which an algorithm was needed to run concurrently with other tasks, the thread program feature was applied [20]. The dialog features were used for conveniently allowing the user to adjust the parameters during experimental implementation (see Figure 7). The document and viewing features were used to graphically display the input/output signals and to enable data recording with adjustable resolution (see Figure 8). Control programs used for real-time control consisted of an automatic arc starter program, a digital non-adaptive AVC program, an adaptive AVC program, and a utility program used to move the welding torch to a specified position [5].

EXPERIMENTAL RESULTS

Dynamic response tests

To test the dynamic response of the AVC system with and without adaptive control, a copper stepped-plate was used, as shown in Figure 9. Tests were conducted at 30 amperes and 100 amperes. The travel speed was 2.12 mm/sec. The shielding gas was argon with a flow rate of 25 cfh. The tungsten electrode was 1.65-mm diameter. The gain of the digital non-adaptive AVC was set for optimum response at 100A. The response is shown in Figure 10. With the same gain setting, the experiment was repeated at 30A. The results are shown in Figure 11. As can be seen, the response at this lower current was quite oscillatory. This is consistent with experimental results that show the arc voltage-to-arc length, K_{arc}, increases at the lower currents [1]. The increase in K_{arc} reduces the damping ratio according to (see Figure 2)

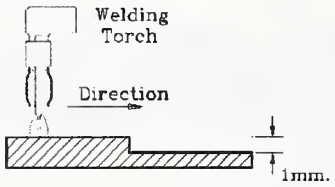

Figure 9. Step-plate experiment.

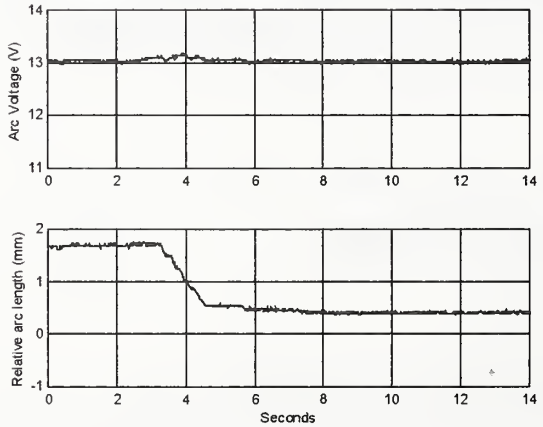

Figure 10. Digital non-adaptive AVC response with I_{arc}=100A.

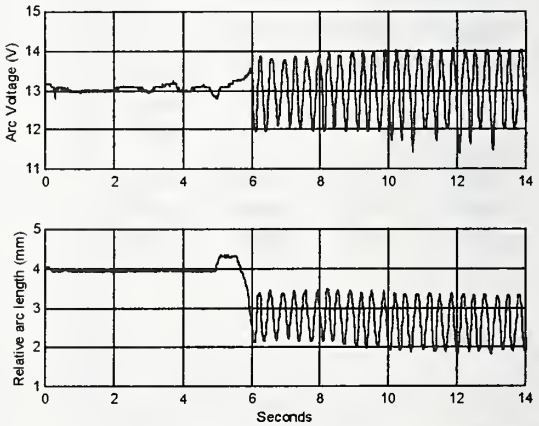

Figure 11. Digital non-adaptive AVC response with I_{arc}=30A.

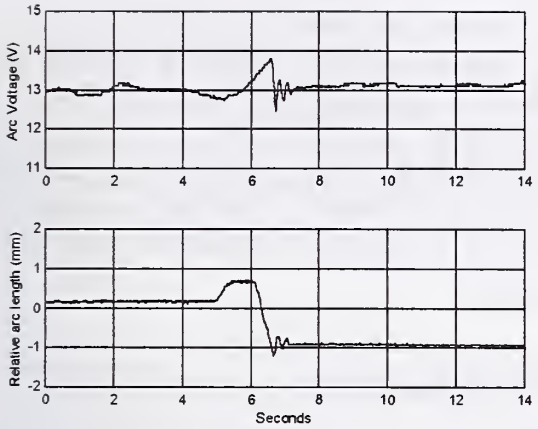

Figure 12. Adaptive AVC response with I_{arc}=30A.

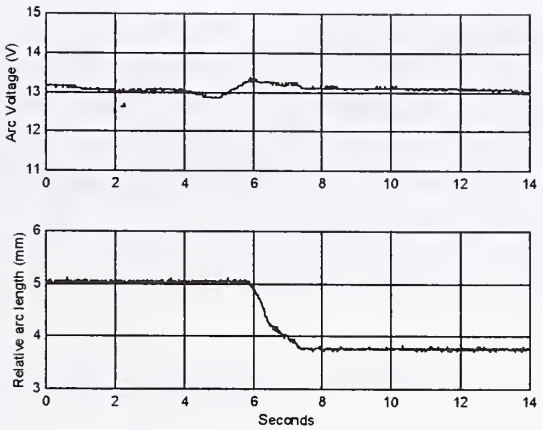

Figure 13. Adaptive AVC response with I_{arc}=100A.

$$\zeta = \frac{a_s}{2\sqrt{K_s K_{arc}}}$$

leading to the oscillatory response observed in Figure 10. The response of the adaptive AVC system is shown in Figure 12 for 30A and in Figure 13 for 100A. As can be seen, at 30A, there is an initial oscillation but that is quickly damped out as the adaptive system adjusts the model-based parameters to match the system. At 100A, the response is optimum as in the non-adaptive case.

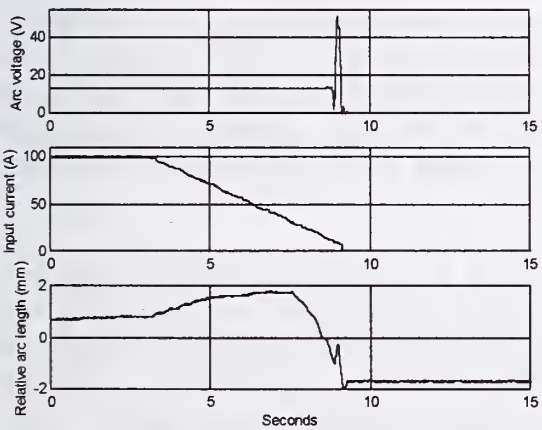

Figure 14. AVC ramping down current result.

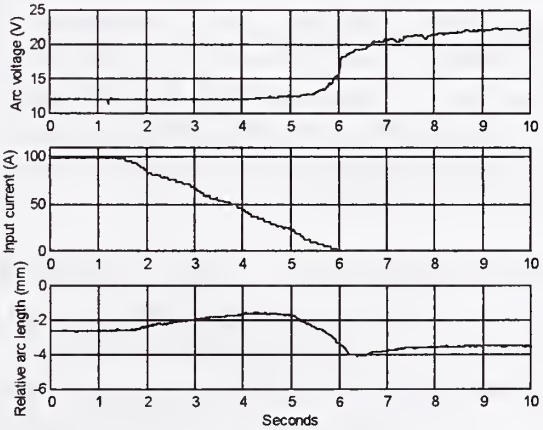

Figure 15. Adaptive ramping down current result.

Ramping down current tests

These experiments were conducted to test the ability of the non-adaptive AVC and the adaptive AVC to control the arc voltage when the welding current varied from 100A to a minimum level at weld termination. The tests were conducted with an arc voltage of 13V at the welding level of 100A. A copper test plate was utilized without travel speed. The results of the non-adaptive AVC

tests are shown in Figure 14. As can be seen, when the current decreased to a sufficiently small value, the welding torch was uncontrollable and the tungsten electrode suddenly touched the workpiece. This behavior was due to the oscillatory state of the closed-loop system at the low current. In comparison, the result of the same test with the adaptive AVC is shown in Figure 15. In this case stability is maintained throughout the downsloping period. Furthermore, below a preset reference current of 70A, the FLC system varied the arc voltage in a manner necessary to maintain a reasonably constant energy density at the arc resulting in consistent weld pool geometry throughout the downsloping period.

DISCUSSION AND CONCLUSIONS

The primary focus of this paper was on design of an adaptive AVC system that would provide stable voltage control over the full range of expected operating currents for the GTA welding process. This is important in many welding applications where it is essential to control the arc voltage throughout the current upsloping period at the weld initiation and the current downsloping period at weld termination. Traditionally designed AVCs have been unable to meet this requirement, simply being switched off during the ramping periods of the weld program. For many applications, this is unacceptable because it results in weld cracking, particularly at the weld termination. Ability to control the arc voltage throughout the ramping periods is also important because it is necessary to vary the reference (setpoint) voltage in such a manner as to maintain approximately constant energy density during these critical periods of the weld in order to maintain a weld geometry that is least susceptible to cracking.

The adaptive control system design presented in this paper, in combination with the fuzzy logic voltage setpoint controller, proved to robustly satisfy both of the requirements for full-range arc voltage control. In tests in which the current was ramped down from a 100A weld level to a minimum level of approximately 5A, the adaptive controller maintained stable control, and the fuzzy logic setpoint varied the setpoint voltage in such a manner as to maintain a reasonable arc length. This results in maintenance of the desired weld pool geometry for minimum susceptibility to cracking.

For argon shielding gas, as employed in this research, the arc voltage-to-arc length gain, K_{arc}, increases by a factor of approximately six when the current decreases from 100A to 5A [1], as in the weld termination tests reported in this paper. Without adaptive control this would lead to an approximate twenty-five percent overshoot for a step change in input. Additionally, a traditional AVC would attempt to maintain constant voltage throughout the ramping down period. With a voltage of 13V at 100A the arc length would be approximately 4 mm. At 5A, a 13V arc is approximately 0.9 mm long. When this short arc length requirement is coupled with the oscillatory state of the feedback system, it is understandable that the traditional AVC design fails. The adaptive AVC system reported in this paper maintains optimum dynamic response characteristics throughout the range of current. The FLC setpoint controller increases the reference voltage at the low currents to realize a more reasonable arc length. The two systems act in combination to provide greatly improved weld initiation and termination control.
In conclusion, the application described in this paper requires adaptive control for proper operation. This is because of the large changes in system gain as operating conditions change.

While gain-scheduling adaptive control has been shown to work [2], the many variables that affect the gain schedule render this method problematic for general usage. The adaptive control scheme proposed in this paper provides the real-time idéntification and control needed for trouble-free operation. The authors have no doubt that other adaptive control schemes, such as a model reference adaptive system (MRAS) approach, would work also.

REFERENCES

1. Bjorgvinsson, J. B., Adaptive Voltage Control in Gas Tungsten Arc Welding, M.S. Thesis, Vanderbilt University, 1992.
2. Bjorgvinsson, J. B., Cook, G. E., and Andersen, K., "Microprocessor-Based Arc Voltage Control for Gas Tungsten Arc Welding Using Gain Scheduling," IEEE Transactions on Industry Applications, Vol. 29(2), pp 250-255, March/April 1993.
3. Yizhang Liu, George. E. Cook, R. Joel Barnett, and James F. Springfield, "PC-Based Arc Ignition and Arc Length Control System for Gas Tungsten Arc Welding," IEEE Trans. On Industry Applications, vol. 28, 5, pp. 1160-1165, Sept./Oct. 1992.
4. R. Joel Barnett, Kristinn Andersen, George E. Cook, and Alvin M. Strauss, "Weld Quality Enhancement Using Precision Multi-Parameter Control in Gas Tungsten Arc Welding," International Trends in Welding Science and Technology, S. A. David and J. M. Vitek, Eds. Materials Park, Ohio: ASM International, 1993, pp. 981-985.
5. Poolsak Koseeyaporn, Adaptive Voltage Control in Gas Tungsten Arc Welding, M.S. Thesis, Vanderbilt University, May 1999.
6. Astrom, K.J. and Wittenmark, B., Adaptive Control, Addison-Wesley, Reading, Massachusetts, 2nd Edition, 1995.
7. Craig, J.J., Adaptive Control of Mechanical Manipulators, Addison-Wesley, Reading, Massachusetts, 1988.
8. Kumpati S. Narendra and Anuradha M. Annaswamy, Stable Adaptive Systems, New Jersey: Prentice Hall, 1989, pp. 63-65.
9. William L. Brogan, Modern Control Theory, New York: Quantum Publishers, Inc., 1974, pp. 262-282.
10. M. Lu and S. Kou, "Power and Current Distributions in Gas Tungsten Arcs," *Welding Journal*, vol. 67, no. 2, pp. 29s-34s, 1988.
11. W. F. Savage and A. H. Aronson, "Preferred Orientation in the Weld Fusion Zone," *Welding Journal*, vol. 45, no. 2, pp. 85s-89s, 1966.
12. L. A. Weeter, C. E. Albright, and W. H. Jones, "Development of a Weldability Test for Pulsed Laser Beam Welding," *Welding Journal*, vol. 65, no. 3, pp. 51s-62s, 1986.
13. Fukuhisa Matsuda, "Solidification Crack Susceptibility of Weld Metal," Recent Trends in Welding Science and Technology, S. A. David and J. M. Vitek, Eds. Materials Park, Ohio: ASM International, 1990, pp. 127-136.
14. B. Kosko, Fuzzy Engineering, New Jersey: Prentice Hall Inc., 1997.
15. Diamond-mm-16 PC/104 Format 16-bit Analog I/O Module User Manual V1.0, California: Diamond Systems Corporation, 1997.
16. User Documentation for 5516DMA Multi-Function Data Acquisition Board, Massachusetts: American Data Acquisition Corporation.

17. *User's Manual*: The 3B Series Signal Conditioning I/O Subsystem, Massachusetts: Analog Devices Inc., 1986.
18. Hussam El-Dean E. H. Eassa, Electric Arc Welding Control with a High Performance Power Source," Ph.D. Dissertation, Vanderbilt University, 1983.
19. Kristinn Andersen, George E. Cook, Robert J. Barnett, and E. H. Eassa, "A Class-H Amplifier Power Source Used as a High-Performance Welding Research Tool," Recent Trends in Welding Science and Technology, S. A. David and J. M. Vitek, Eds. Materials Park, Ohio: ASM International, 1990, pp. 973-978.
20. Microsoft Visual Studio 97 Development System - Enterprise Edition.

WELD SURFACE UNDULATION CHARACTERISTICS IN THE PULSED GMA WELDING PROCESS

S. Rajasekaran

ABSTRACT. The weld surface quality in pulsed current gas metal arc welding (GMAW-P) process is mainly influenced by the pulse parameters. Selection of the most suitable combination of pulse parameters is very difficult due to the complex interdependence of the parameters of pulsed current. Therefore effect of the pulse parameters on weld surface characteristics has been studied for different types of droplet detachments, namely background detachment, one droplet detachment per peak, two droplets detachment per peak and three droplets detachment per peak. The suitable type of droplet detachment for welding, using 1.2 mm diameter of ER 5356 filler metal, has been selected on the basis of measuring the surface characteristics of the weld using a computerized measuring system based on a Linear Variable Differential Transformer. One droplet detachment per peak was considered to be capable of providing smoother weld surface than other types of droplet detachments. The peak energy was found to be low for background detachments.

KEY WORDS: Al-Mg Alloys Welding, Droplet Detachment, Pulsed Current Gas Metal Arc Welding, Pulse Parameters, Weld Surface Undulation, Weld Characteristics, Weld Quality.

INTRODUCTION

Aluminium and its alloys are widely used in the transportation industry, where lightweight, corrosion resistance and high fatigue strength are the desired properties. Pulsed current gas metal arc welding process (GMAW-P) is widely used to weld many Al-Mg alloys components of spacecraft, automobile, ship, air craft, rail road, bridges, oil tanks, pipe lines, structures, cryogenic storage tanks, marine, unfired pressure vessels, T.V towers, missile components and drilling rigs. Al-Mg alloys offer maximum resistance to atmospheric, salt water and alkaline corrosion (Ref. 1). The GMAW-P may be considered a potential process for the welding Al-Mg alloys, where the dilution can be controlled more precisely than other conventional welding processes.

The pulsed current gas metal arc welding process has recently gained wide attention in welding industry, due to its comparatively low heat input and precise control over the thermal cycle (Ref. 2). Because, In pulsed current gas metal arc welding process, spray transfer or more precisely controlled droplet transfer is obtained at low average current. This condition provides a smaller and controlled weld pool, which allows welding of thin materials in all positions (Ref. 3,4). Detachment of molten metal droplets from the filler metal, its transfer across the arc and its flow

S. RAJASEKARAN, formerly a Research Scholar, Department of Mechanical Engineering, Indian Institute of Technology-Bombay, Mumbai 400 076, India, is presently an Assistant Professor, Department of Production Engineering, Amrita Institute of Technology and Science, Coimbatore 641 105, Tamil Nadu, India.

into the weld pool are defined as metal transfer characteristics. Droplet detachment characteristics are defined as (a) the size of molten droplet (b) instance and duration at which detachment takes place and (c) number of droplet detachments per pulse.

The superiority of the GMAW-P process is mainly related to the nature of metal deposition governed by the pulse parameters viz. peak current (I_P), peak duration (T_P), background current (I_B) and background duration (T_B) (Ref. 5). Selection of the most suitable combination of pulse parameters is very difficult due to the complex interdependence of the above parameters of pulsed current (Refs. 3, 6-8). To resolve this problem, studies have been carried out for different types of droplet detachments, namely background detachment, one droplet detachment per peak, two droplets detachment per peak and three droplets detachment per peak, by varying pulse cycle time.

Depending on the parameters of GMAW-P (Fig. 1) process either a single droplet or multiple droplets may get detached. If it is a single droplet, this detachment may occur either in peak duration or background duration and if it is multiple droplet detachment, the same may occur in peak duration. This difference in the timing of droplet detachment affects the uniformity in weld surface undulation and overall quality of the weld (Ref. 9). These characteristics have been investigated in this study. Experiments were conducted at fixed value of W_F, I_B and T_B to establish the relationship between I_P and T_P for different types of droplet detachments. In order to obtain different type of droplet detachments, pulse cycle time was allowed to vary. For this, it was not assumed that the molten droplet diameter is equal to the diameter of weld metal. In addition to obtaining the above relationship between I_P and T_P, further studies have been carried out to select a suitable type of droplet detachment to obtain good quality welds.

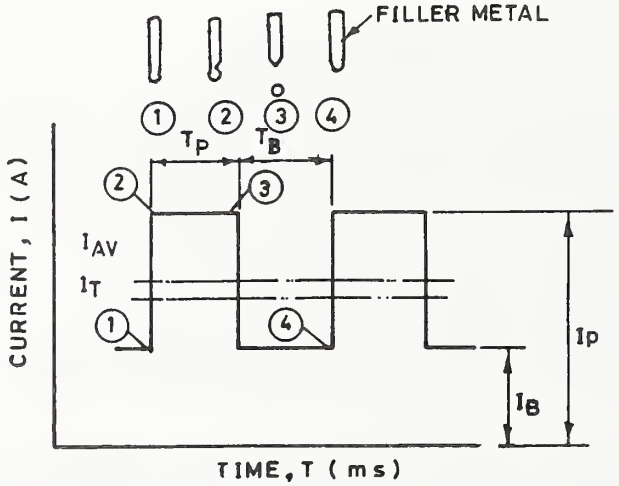

I_P-Peak current (A); I_B-Background current (A)
T_P-Peak duration (ms); T_B-Background duration (ms)
T-Pulse cycle time (ms); $T=T_P+T_B$; Pulse Frequency, $F_{PU}=1/T$
I_{AV} -Average current (A); $I_{AV} = (I_P T_P + I_B T_B) / (T_P + T_B)$
I_T-Spray current level (A); Above I_T-Spray metal transfer
Below I_T- Globular metal transfer
1,2,3 and 4- Stages of metal transfer

Fig. 1 Pulsed current metal transfer

Objective

The objective of this investigation was to determine the suitable combination of pulse parameters to obtain a good quality weld surface.

EXPERIMENTAL WORK

Materials

The welding was carried out with a diameter of 1.2 mm ER 5356 Al-Mg wire. To study the weld surface characteristics of the ER 5356 Al-Mg alloy, welding was done on the compatible AA 5083 Al-Mg alloy of 6.0 mm thickness base metal. Argon gas having a commercial purity of 99.97 % and a flow rate of 20 L/min was used throughout the welding as shielding gas.

Welding Equipment

Fig. 2 shows the schematic layout of the experimental set-up of GMAW-P. A transistorized welding power supply - Transarc Fronius 500 was used for carrying out welding operations in pulsed current, operating with a constant voltage output characteristics. In the pulsed current mode, peak voltage, background voltage, peak duration, cycle time and wire feed speed can be varied over a range of 10 to 40 V, 10 to 30 V, 1 to 15 ms, 3.3 to 50 ms and 0 to 300 mm/s, respectively.

Directly setting the levels at peak and background current is not possible in the above welding power supply. Hence, levels of peak and background voltage were adjusted by trial and error to obtain the desired peak and background current levels, and measured using a high-speed double channel digital storage oscilloscope. Wire feed speed, peak duration and cycle time could be independently adjusted using the power supply control.

Filters for Voltage and Current Signals

The problem of high frequency noise and process noise in the signals of voltage and current was discussed with the manufacturer of welding power supply and eliminated from the signals using two 5 kHz low-pass passive filters as shown in Fig. 2. These filters permit frequencies below 5 kHz to pass and reject all other frequencies, which are above 5 kHz. Since expected molten droplet frequency is well within 5 kHz, droplet detachment phenomena could be clearly studied from the blips on the waveform of pulsed voltage.

Instrumentation

Currents during welding were sensed from the RTR-B control PCB - plug x - 102 of power supply as shown in Fig.2. Voltage levels were sensed between the base metal and the contact tip and they are used as measure of arc voltage (Ref. 10, 11). Sufficient time was allowed during

welding to reach a stable welding condition. For this, delay time was set in the oscilloscope and then instantaneous current and voltage were monitored and recorded simultaneously with a high speed double channel digital storage oscilloscope (Gould 4072) through 5 kHz low-pass passive filters (Fig. 2).

Levels of peak current were measured on the pulsed current waveform for every pulse cycle time and average peak current level was taken as a measure of peak current. Levels of background current were measured on the captured pulsed current waveform for every pulse cycle time and the average background current level was taken as a measure of background current. Droplet detachment was observed from the blips on the waveform of pulsed voltage. There are variations in the peak voltage values along peak duration except those due to the intentional pulsing. The reason for variations is that when the droplet is transferred, the instantaneous arc voltage will momentarily increase and form blips on the peak voltage levels along the peak duration (Ref. 6, 12). Droplet detachment time and the number of droplet detachments were obtained from pulsed voltage traces.

The total area of the captured waveform of the pulsed current was measured by using a waveform processor of the oscilloscope. Average current was calculated by dividing the total area of the current waveform by total time duration, which corresponded to the measured area of the waveform. Similarly, average voltage was calculated by dividing the total area of the pulsed voltage waveform by the corresponding total time.

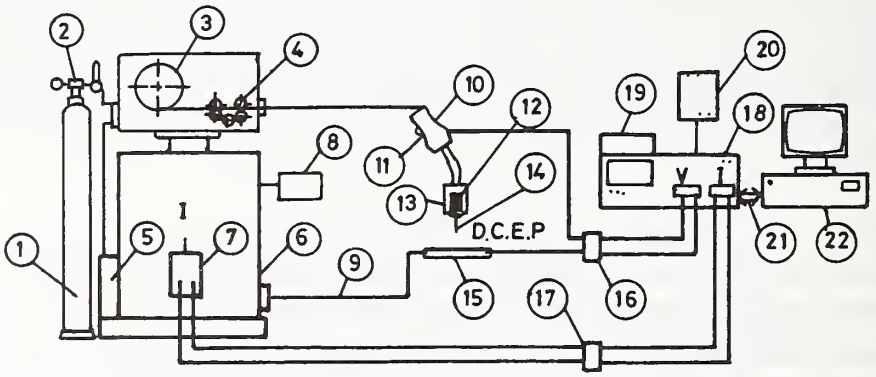

1) Argon gas cylinder
2) Regulator with flow meter
3) Filler metal reel
4) Filler metal feed rollers
5) Water cooling unit
6) Transistorized welding power supply
7) RTR-B control PCB plug x 102
8) Power supply control unit for setting parameters
9) Workpiece lead
10) Torch
11) Torch switch
12) Contact tip
13) Gas nozzle
14) Filler metal
15) Base metal
16) 5kHz low pass passive filter for voltage signal
17) 5 kHz low pass passive filter for current signal
18) Double channel digital storage oscilloscope
19) Internal color digital plotter
20) Waveform processor
21) GP - IB interface
22) Personal computer

Fig. 2 Experimental set-up of the pulsed current gas metal arc welding

Welding Procedure

Filler metal was connected to the direct-current-electrode-positive (DCEP) polarity. Prior to welding, the base metal surface was mechanically cleaned. Welding torch was mounted on four-wheeled variable speed tractor (Esab A2 Mini trac). It was moved above the base metal and welding was carried out (down hand type) in the rolling direction of base metal. The torch-to-work-angle was maintained at 90^0 and contact tip-to-work distance at 15 mm. Proper guiding was ensured and proper alignment was made for moving the variable-speed tractor with welding torch over the base metal. This set-up ensures constant gap between the contact tip and base metal throughout the welding operation; this ensures that the current levels are the same throughout the length of a weld. The suitable parameters of the pulsed current and the type of droplet detachment were selected on the basis of weld surface quality. Method of measurements of this quality parameter is detailed below:

Quality Parameters and their Measurements

Measuring the surface characteristics of the weld using a computerized measuring system based on a Linear Variable Differential Transformer (Sylvac) (Fig. 3) carried out a quantitative evaluation of the quality of weld. The workpiece was mounted on an X-Y measuring table using a specially designed and fabricated fixture. The workpiece was aligned properly and moved under a LVDT probe, in the direction of welding. LVDT probe with a standard contact point of 2 mm diameter carbide ball was used (Fig. 3). A sample length of weld used was 25 mm. Fluctuations on the top of the weld surface were displayed numerically on the digital-indicating unit of a LVDT (1 micron accuracy). All the displayed digital output values were transferred to a personal computer through a data acquisition card and analyzed statistically to calculate the standard deviation (σ) and coefficient of variation (C.V). The weld surface undulation profile with lesser standard deviation and coefficient of variation was considered to be good from the standpoint of smooth weld surface.

RESULTS AND DISCUSSION

Limiting Peak Current (I_P) and Peak Duration (T_P)

Experiments were conducted at fixed value of W_F = 100 mm/s, W_S = 10 mm/s I_B = 20 A and T_B = 6 ms to establish the relationship between I_P and T_P for different types of droplet detachments, namely background detachment, one droplet detachment, two droplets detachment and three droplets detachment per peak, respectively (Ref. 13). For this, levels of I_P were kept above the spray current level (Refs. 14-17), and I_P and T_P were allowed to vary (Figs. 4-7). To obtain the above types of droplet detachments, pulse cycle time was allowed to vary. For this, it was not assumed in this study that molten droplet diameter would be equal to the diameter of weld metal.

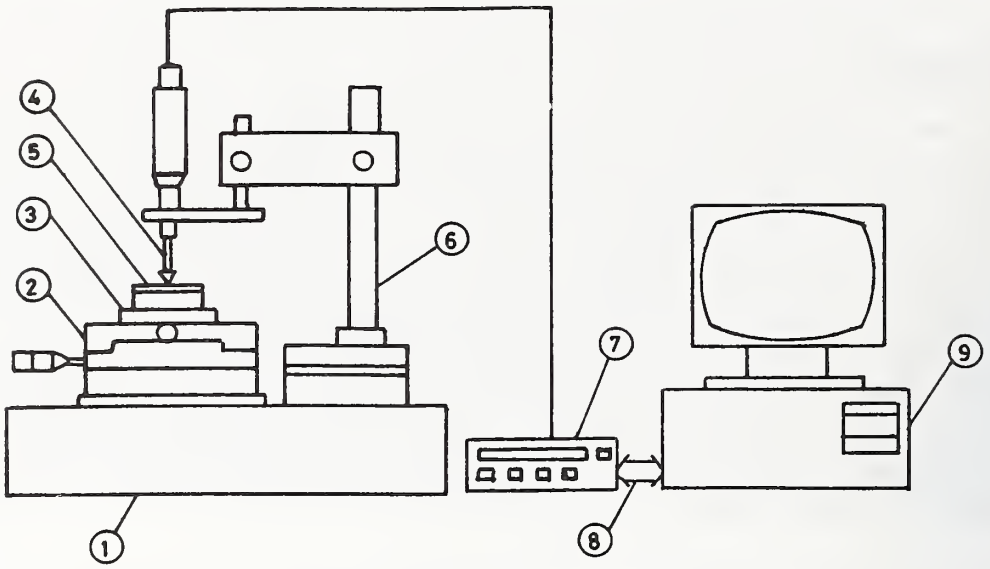

1) Base
2) X-Y measuring table with micrometer
3) Fixture
4) LVDT probe (P 25)
5) Welded workpiece
6) Measuring stand
7) LVDT Digital indicating unit (D 50)
8) Interface (PCL 208)
9) Personal computer

Fig. 3 Schematic layout of the linear variable differential transformer (LVDT) experimental set-up to measure weld surface undulations.

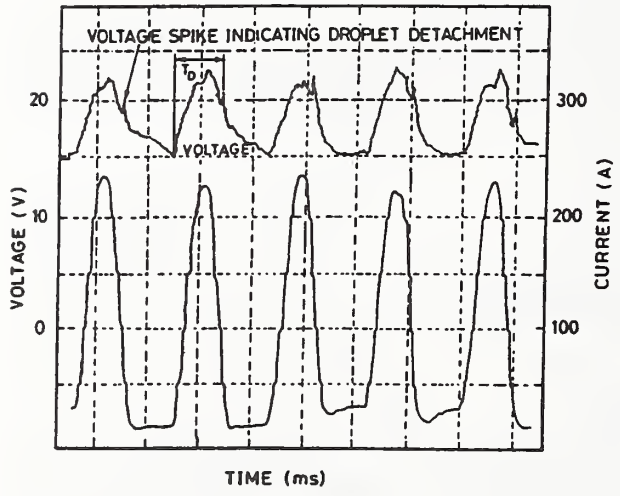

I_P = 240.5 A; T_P = 3.0 ms; I_B = 20 A;
T_B = 6 ms (Weld No: WE 1);
Scale: X-axis: 5 ms/div;
Y-axis: 5 V/div and 50 A/div

Fig. 4 Typical arc voltage and current traces, indicating background detachment.

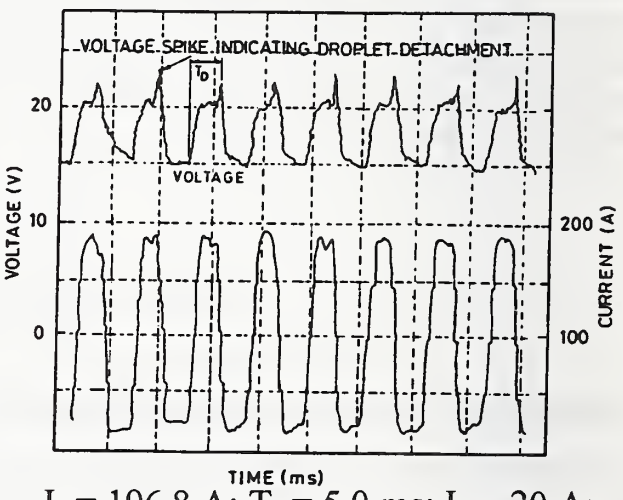

I_P = 196.8 A; T_P = 5.0 ms; I_B = 20 A;
T_B = 6 ms (Weld No: WE 4);
Scale: X-axis: 10 ms/div;
Y-axis: 5 V/div and 50 A/div

Fig. 5 Typical arc voltage and current traces, indicating one droplet detachment per peak

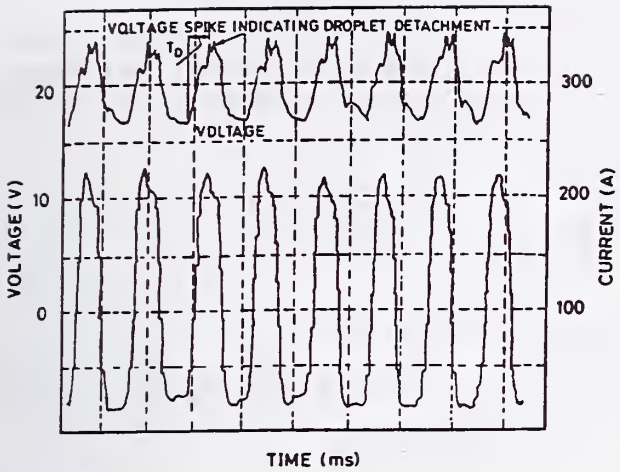

I_P = 230.3 A; T_P = 5.0 ms; I_B = 20 A;
T_B = 6 ms (Weld No: WE 6);
Scale: X-axis: 10 ms/div;
Y-axis: 5 V/div and 50 A/div

Fig. 6 Typical arc voltage and current traces, indicating two droplets detachment per peak.

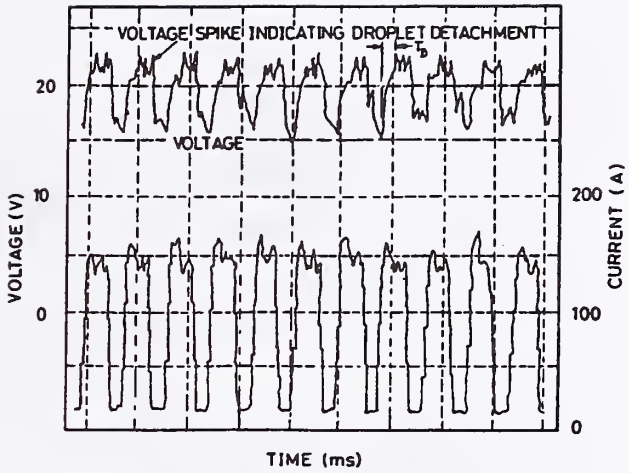

I_P = 172.7 A; T_P = 10.0 ms; I_B = 20 A;
T_B = 6 ms (Weld No: WE 11);
Scale: X-axis: 20 ms/div;
Y-axis: 5 V/div and 50 A/div

Fig. 7 Typical arc voltage and current traces, indicating three droplets detachment per peak

The values of I_P and T_P were grouped according to the type of droplet detachment and plotted on the logarithmic scale (Fig. 8). Slope between I_P and T_P was found to be -1.7 for all type of droplet detachments, i.e. $T_P \alpha I_P^{-1.7}$. Amin (Ref. 6) found the slope as -2.3 for 1.6 mm diameter of pure aluminum filler metal, and Trindade and Allum (Ref. 14) found the slope as -2.0 for the filler metal diameter of 1.2 mm pure aluminum. However, Araya, Endo, Imamiya, Ando and Sejima (Ref. 18) found the slope as -1.54 for the filler metal diameter of 1.6 mm ER 4043 Al-Si alloys. This shows that the slope varies depending on chemical composition and diameter of filler metal. The relationship between I_P and T_P can be expressed as follows:

$$I_P^{1.7} T_P = K_V \quad A^{1.7} s \quad \text{equation (1)}$$

Where K_V is a constant called detachment parameter. The values of constant vary depending on the droplet volume to be detached from a given filler metal and diameter. In this investigation, Al-Mg alloy weld surface characteristics, produced by the GMAW-P process were studied with respect to the pulse parameters viz. peak current (I_P), peak duration (T_P), background current (I_B) and background duration (T_B).

Selection of Suitable Pulse Parameter Combinations and Suitable Type of Droplet Detachment

Weld surface undulation criterion has been considered for selection of the suitable pulse parameter combinations to obtain good quality weld. Also, on the basis of the above criterion, the suitable type of droplet detachment was recommended among the four different types of droplet detachments viz. background detachment, one droplet detachment, two droplets detachment and three droplets detachment per peak (Figs. 4-7) (per peak is applicable only to one droplet detachment, two droplets detachment and three droplets detachment).

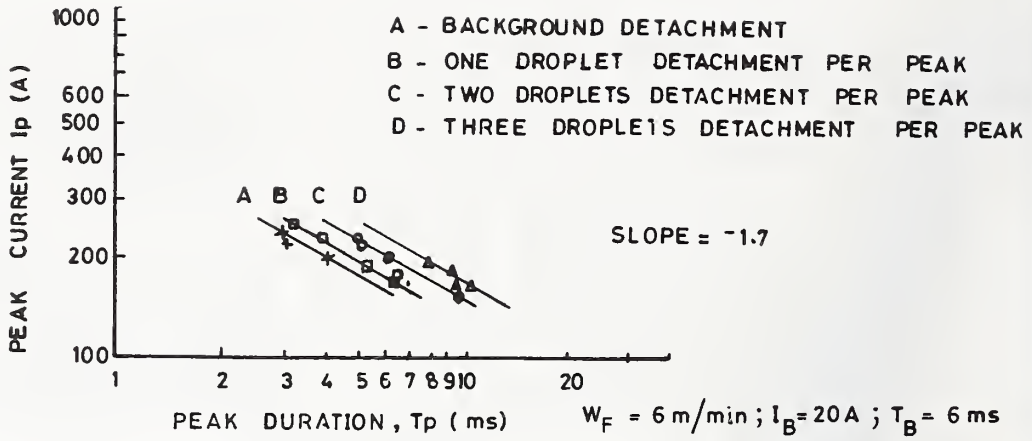

Type of droplet detachment	Relationship
A- Background detachment	$I_P^{1.7} T_P = 34\ A^{1.7}\ s$
B- One droplet detachment per peak	$I_P^{1.7} T_P = 40\ A^{1.7}\ s$
C- Two droplets detachment per peak	$I_P^{1.7} T_P = 50\ A^{1.7}\ s$
D- Three droplets detachment per peak	$I_P^{1.7} T_P = 62\ A^{1.7}\ s$

Fig. 8 Relationship between I_P and T_P for different types of droplet detachments.

Uniformity in Weld Surface Undulation

Typical weld surface undulation as revealed by LVDT traverse is shown in Fig. 9. The standard deviation and the coefficient of variation of the weld surface undulation were calculated for four types of droplet detachments viz. background detachment, one droplet detachment per peak, two droplets detachment per peak and three droplets detachment per peak and given in Table 1. Different types of droplet detachments were produced at various combinations of pulsed current. The lowest standard deviation and the lowest coefficient of variation were observed for the weld nos. WE 1, WE 4, WE 6 and WE 11 which were produced at different welding conditions viz. background detachment, and one droplet detachment, two droplets detachment and three droplets detachment per peak, respectively. Among these four types of droplet detachments, the lowest standard deviation (0.0553) and the lowest coefficient of variation (0.0252) were found for the weld made with one droplet detachment per peak (Weld No. WE 4). Smaller the standard deviation and the coefficient of variation, the smoother the weld surface. Hence, one droplet detachment per peak was considered to be capable of providing smoother weld surface than other types of droplet detachments. Based on this, the following corresponding parameters of the pulsed current were found to be more suitable than other combinations of pulsed current. I_P = 196.8 A; T_P = 5.0 ms; I_B = 20 A; T_B = 6 ms; W_F = 100 mm/s; I_{AV} = 99.7 A and W_S = 10.0 mm/s. However, standard deviation and coefficient of variation of the weld made with background detachment (Weld No. WE 1) was found to be second in the order of smooth weld surface.

Peak Energy

The peak energy was determined for the various droplet detachment conditions and given in Table 1. Peak energy required for background detachment is less, but one droplet detachment per

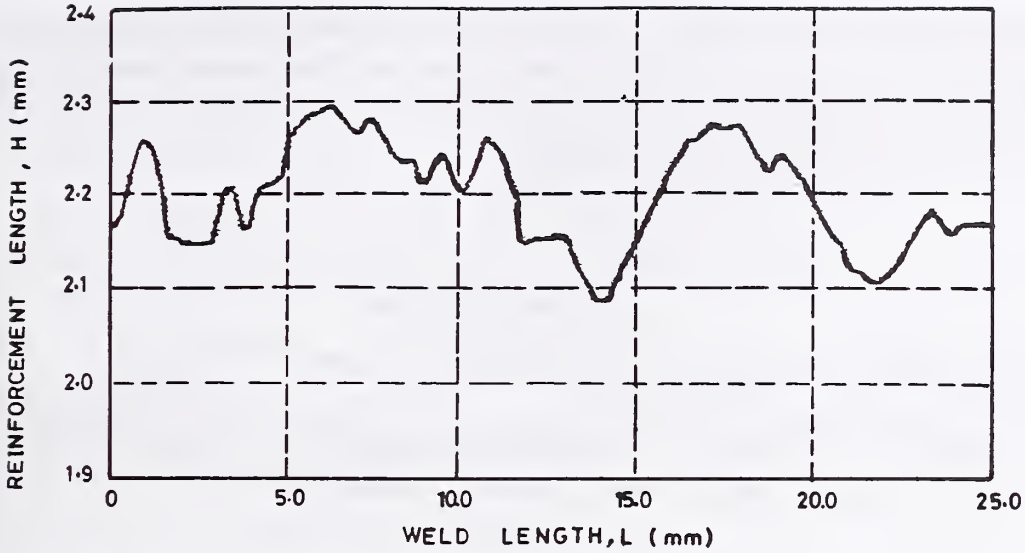

Minimum value: 2.077 Standard deviation : 0.0553
Maximum value: 2.292 Coefficient of variation : 0.0252
Arithmetic mean: 2.197
I_P = 196.8 A; T_P = 5 ms; I_B = 20 A; T_B = 6.0 ms;
W_F = 100 mm/s; W_S = 10.0 mm/s

Fig. 9 Typical weld surface undulation recorded by LVDT (Weld No: WE 4);

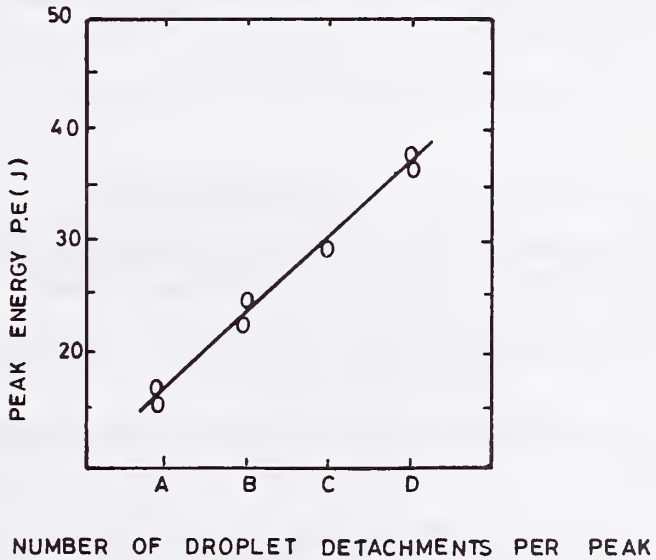

A - Background detachment
B - One droplet detachment per peak
C - Two droplets detachment per peak
D - Three droplets detachment per peak

Fig. 10 Relationship between peak energy and number of droplet detachments per peak

peak, two droplets detachment per peak and three droplets detachment per peak conditions require high peak energy, in increasing order. The reason is that the combination of the highest I_P and the lowest T_P is used during background detachments and results in low peak energy. Hence, background detachment is preferable (Fig. 10).

CONCLUSIONS

The most significant findings of this study can be summarized as follows:

1. The slope between I_P and T_P was found to be -1.7 for all type of droplet detachments. i.e. $T_P \alpha I_P^{-1.7}$. Slope varies depending on chemical composition and diameter of weld metal. The relationship between I_P and T_P can be expressed as follows:

$$I_P^{1.7} \; T_P = K_V \qquad A^{-1.7} \; s$$

   Where K_V is a constant called as detachment parameter. The values of constant vary depending on the droplet volume to be detached from a given filler metal and diameter.

2. A smoother weld surface was observed for the welds made with one droplet detachment per peak (Weld No. WE 4) than background detachment, two droplets detachment per peak and three droplets detachment per peak conditions.

3. Peak energy required for background detachment is less, but the peak energy required for other types of droplet detachments is high, i.e. one droplet detachment per peak, two droplets detachment per peak and three droplets detachment per peak conditions require high peak energy, in increasing order.

REFERENCES

1. Donald S. C.; and Wilbur, R. V. 1986. Physical metallurgy for engineers: Second Edn, 423-439 New Delhi: Affiliated East-West Press Private Limited.

2. Smillie, S. 1989. Corrosion resistant synergic MIG overlaying. *Joining and Materials* Aug: 387 to 389.

3. Brosilow, R. 1984. Welding better with pulsed power. *Welding Design and Fabrication*. 57 (10): 57 to 70.

4. Pixley, M. 1999. The microprocessor revolution-synergic pulsed MIG/MAG welding. *Welding and Metal Fabrication* 67, (2): 17-18.

5. Ueguri,S; Hara,K; and Komura, H. 1985. Study of Metal Transfer in Pulsed GMA Welding. *Welding Journal*, 64 (8): 242-s to 250-s.

6. Amin, M. 1983. Pulsed current parameters for arc stability and controlled metal transfer in arc welding. *Metal Construction* 15 (5): 272 to 278.

7. Kim, Y.S; and Eager, T.W. 1993. Metal transfer in pulsed current gas metal arc welding. *Welding Journal* 72 (7): 279-s to 287-s.

8. Pan, J.L; Zhang, R.H; Ou, Z.M; Wu, Z.Q; and Chen, Q. 1989. Adaptive control GMA welding - A new technique for quality control. *Welding Journal.* 68 (3): 73 to 76.

9. Wang, Q.L; Li, P.J; Zhang, L; Li, Q; and Jiang, W.Y. 1994. A new close - loop droplet transfer control system in the pulsed GMAW. Advanced Techniques and Low Cost Automation. 217 - 226. Beijing.

10. Needham, J.C 1985. What do you mean by voltage?. *The Welding Institute Research Bulletin.* Sept: 311 to 316.

11. Street, J.A. 1987. Practical measurement of voltage and current in arc welding. *Metal Construction* . 19 (11): 646 to 648.

12. O'brien R. L. (Editor). 1991. Welding handbook. Vol.2:115-123, Miami: American Welding Society.

13. Trindade, E.N; and Allum, C.J. 1984. Characteristics in steady and pulsed current GMAW. *Welding and Metal Fabrication.* 52 (8): 264 to 272.

14. Allum, C.J. 1985. Welding technology data: Pulsed MIG welding. Sheet no:65. *Welding and Metal Fabrication.* 53 (1): 24 to 30.

15. Daggett,E.H; and Zircher,W.E. 1970. New developments in pulsed spray welding. *Welding Journal.* 49 (10) : 780 to 787.

16. Needham, J.C. 1966. Pulsed current for gas shielded arc welding. *IEEE Transactions on Industry and General Applications.* VIGA-2, (3): 225 to 233.

17. Middleton, P; and Norrish, J. 1990. Progress in controlled transfer welding. *Welding and Metal Fabrication.* 58 (9): 497 to 504.

18. Araya, T; Endo, T; Imamiya, H; Ando, B; and Sejima,I. 1981. Transistor-controlled pulse MIG welding of aluminium alloys. IIW Doc. XII-C- 19-81: 1 to19.

LIST OF SYMBOLS

C.V	Coefficient of Variation	T	Pulse cycle time
DCEP	Direct Current Electrode Positive	T_B	Background duration
		T_D	Droplet detachment time
GMAW-P	Pulsed Current Gas Metal Arc Welding	T_P	Peak duration
		V	Voltage
I	Welding current	V_B	Background voltage
I_B	Background current	V_D	Droplet volume
I_P	Peak current	V_P	Peak voltage
I_{AV}	Average current	V_{AV}	Average arc voltage
K_V	Detachment parameter	W_F	Wire feed speed
LVDT	Linear Variable Differential Transformer	W_S	Welding speed
		σ	Standard deviation
Mg	Magnesium		

Weld No.	I_P (A)	T_P (ms)	(a) I_{AV} (A)	(a) V_{AV} (V)	TY	W.S.U	P.E (J)
WE 1	240.5	3.0	96.0	18.6	A	0.0611[(c)]	16.7
						0.0283[(d)]	
WE 2	211.5	4.0	96.4	19.1	A	0.0714	19.5
						0.0334	
WE 3	226.0	4.0	101.8	18.2	B	0.0616	21.3
						0.0300	
WE 4	196.8	5.0	99.7	18.1	B	0.0553	22.5
						0.0252	
WE 5	180.5	6.0	99.4	18.6	B	0.1540	24.7
						0.0657	
WE 6	230.3	5.0	109.4	18.3	C	0.0756	26.5
						0.0352	
WE 7	207.8	6.0	109.5	18.3	C	0.0976	29.6
						0.0406	
WE 8	160.0	9.0	105.7	18.7	C	0.0792	32.8
						0.0320	
WE 9	192.9	8.0	109.8	19.9	D	0.0736	36.9
						0.0291	
WE 10	180.2	9.0	109.2	19.6	D	0.0992	38.3
						0.0432	
WE 11	172.7	10.0	104.6	20.2	D	0.0740	40.8
						0.0318	

Table 1. Types of Droplet Detachment, and Statistical Analysis of Weld Surface Undulation

(a)Measured value
(b)Average value
(c)Standard deviation
(d)Coefficient of variation;
I_B=20 A
T_B = 6 ms
W_F = 100 mm/s
W_S = 10 mm/s

TY:Type of droplet detachment
A:Background detachment, $I_P^{1.7} T_P = 34.0\ A^{1.7} s$
B:One droplet detachment per peak, $I_P^{1.7} T_P = 40.0\ A^{1.7} s$
C:Two droplets detachment per peak, $I_P^{1.7} T_P = 50.0\ A^{1.7} s$
D:Three droplets detachment per peak, $I_P^{1.7} T_P = 62\ A^{1.7} s$
P.E: Peak Energy = $I_P \times T_P \times V_P$ (J)
W.S.U: Weld Surface Undulation

Session B4: Real-Time Weld Sensing and Control Systems: GMAW Droplet Control and Weld Process Automation

A Novel Control Approach

for the Droplet Detachment in GMA Welding of Steel

Bing Zheng and Radovan Kovacevic

Southern Methodist University, Dallas, TX 75275

ABSTRACT

Projected spray in one droplet per pulse (ODPP) mode in combination with closed loop feedback control of droplet detachment is the most effective approach to guarantee high weld quality for gas metal arc welding (GMAW) of steel in argon-rich shielding. Three groups of experiments are performed according to the different welding current wave forms in this paper: pure square wave, square wave combined with sine wave (combined wave), and pure sine wave. Compared with the pure square wave form, the combined wave form can generate a weld bead with narrower and shallower penetration (the width and depth are respectively 3.048 mm and 0.228 mm). The direction of the droplet is still very straight even though the corresponding frequency of the droplet transfer is as low as 18 Hz. In pure sine wave form pulsed GMAW, the droplet is forced to oscillate once (the oscillation cycle equals the pulse cycle) at the wire tip and then detaches smoothly. The process is accompanied with a harmoniously characteristic sound. The images also show that the droplet is forced to oscillate twice (the oscillation cycle equals half of the pulsed cycle) at the wire tip and then detaches in square wave form or combined wave form pulsed GMAW. Careful selection of parameters is also required to generate more oscillations for the droplet at the tip of the wire before it detaches. The cross section of a weld bead show that the penetration profile can be greatly improved using a combined waveform. The results achieved are beneficial for the investigation of the mass and heat control in GMA welding of thin materials.

Key Words: GMAW, Penetration profile, Droplet detachment, Metal transfer, Oscillation, Projected spray

INTRODUCTION

In a gas metal arc welding (GMAW) process with argon-rich shielding, a consumable electrode wire is fed, melted, and transferred to the weld pool to form a weld bead. This technology featuring different metal transfer modes of globular, projected spray, streaming, and rotation [1] is one of the most attractive arc welding technologies in manufacturing industry due to its high deposition rate, deep penetration, and low cost. If the welding material is steel, the above metal transfer modes can be observed in sequence when the welding current increases [2-4]. The critical welding current making the metal transfer mode changeable is defined as transition current, such as spray transition current [2]. Usually, the high weld quality can be achieved using the projected spray transfer mode of one droplet per pulse (ODPP) because of that mode's flexible controllability of the droplet detachment and the better adjustability of the operational process parameters in pulsed GMA welding [2, 5-8]. However, as the parameters are

selected mainly for control of the droplet detachment, regulation of the penetration profile of a bead is usually unachievable.

According to the static force balance theory [9-11], the forces promoting the droplet detachment in flat welding position consist of electromagnetic force resulting from the welding current, gravity, and plasma gas drag force; while the force resisting the droplet detachment is the surface tension. When the forces promoting the droplet detachment are equal to or greater than the surface tension, the droplet will detach from the tip of the electrode wire. Based on this theory and the analysis of the approaches used, the controlling strategies may be categorized into two types: electrical and mechanical. Previous research on feedback control for the droplet detachment is electrically or mechanically implemented using voltage, current, light, or vision sensing of an arc [5-8, 12]. Since electrically controlling the electromagnetic force inside the droplet and arc is reliable and fast, most of the investigations on droplet detachment control focused on this approach. With the electrical approach, the droplet detachment is controlled mostly by the adjustment of the dynamic parameters, such as the pulse current, background current, pulse duration time, and pulse frequency. According to the theories of both the static force balance and the pinch instability, the ODPP approach characterizing approximately the same droplet diameter as that of a wire can be electrically achieved only when the welding current during a pulse period is above the transition current. The droplet may detach during the period of the pulse current or during the period of the background current in a cycle, depending on different combinations of the parameters. The melting rate of the electrode wire (or wire feeding speed) is directly proportional to the frequency of the welding current pulse: the higher the frequency, the higher both the average welding current and the melting rate. Therefore, the mass and heat transferred to the workpiece may be flexibly controlled by the regulation of the average welding current. The mechanical approach applies the inertia principle in physics for a moving object: the droplet at the wire tip will keep moving along its axis towards the weld pool because of the action of inertia generated when the wire feeding speed is suddenly reversed or stopped. The inertia force acting on the droplet is beneficial in promoting its detachment [14-17,18]. For the mechanical approach, the droplet detachment occurs even if the welding current is below the transition current. So, the heat transferred to the workpiece is even lower than that of the electrical approach because of the lower average current used. However, compared with the electrical approach, besides the bulky wire feeder and limited applications, the mechanical approach has a slow control response and short wire feeding length from a wire feeder to the torch.

In ODPP of GMA welding of steel, during the pulse period, the droplet gradually grows to a certain size. This length of time may be defined as the growing period. Besides growth, the droplet at the tip of the electrode wire may also oscillate vertically (or with a horizontal component oscillation) at random frequencies (multi-resonant oscillation) because of the forces acting on the droplet. Previous researches paid almost all attention to the droplet growth and detachment, but little attention to the oscillation of the droplet at the tip of the wire in the range of projected spray transfer. However, the investigation of this oscillation may be beneficial to both the droplet detachment control and the penetration profile regulation.

This paper intends to: 1. explore new approaches for controlling the droplet detachment in GMA welding of steel, which may improve the GMA welding process for rapid prototyping of metallic parts; 2. examine the droplet oscillation using different welding current wave forms in the range of ODPP, which may be beneficial to the welding of thin materials.

EXPERIMENT PROCEDURE

A PC-controlled, inverter welding power source with a data acquisition system and a wire feeder are used. A high frame rate digital camera with adjustable frame rate and a frame grabber is used for monitoring the droplet based on the principle of the back-illuminating light from a He-Ne laser. Current and voltage sensors, as well as a computer controlled spectrometer are integrated with the system. A CNC three-linear positioning system with three-dimensional movements is also controlled by another PC-Pentium II.

Due to the fact that the droplet at the wire tip may oscillate before detachment, a sine wave form signal with a widely adjustable range of frequencies is integrated with the developed computer controlled pulse generating circuit. This can make the droplet oscillate under a given frequency that is the same as the frequency of a sine wave form current during the background period of a cycle. The schematic for the welding current control wave form is shown in Fig. 1. The electrode wire is 1.2-mm-diameter steel (AWS standard ER 70S) and the shielding gas is argon-rich (Ar-CO_2). Bead-on-plate welds are made on 6.0 mm thick mild steel plates.

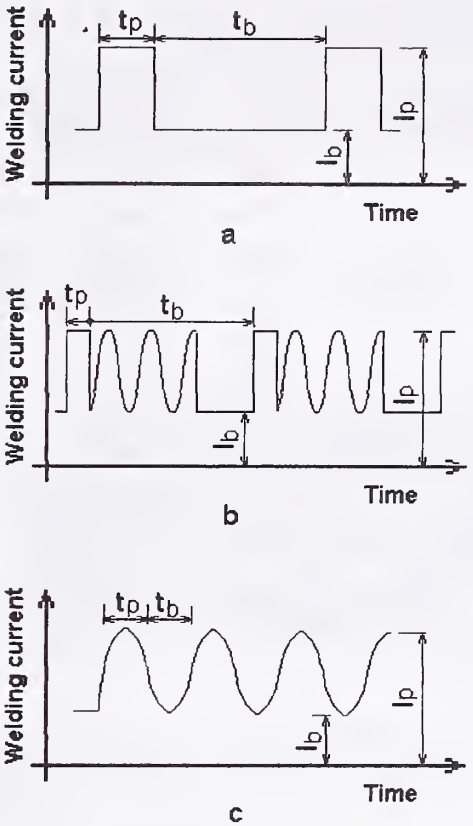

Fig. 1 Schematic of Welding Current Control Wave Form

a. pure square wave
b. square wave combined sine wave
c. pure sine wave

RESULTS and DISCUSSION

The evaluation of the difference between the pure square wave form and the combined wave form is done by using the ODPP transfer mode with the same droplet detachment frequency, while maintaining as little energy input from the welding power source as possible. Three groups of experiments with droplet detachment frequencies of 50 Hz, 25 Hz, and 18 Hz are made respectively according to the five groups of parameters in Table 1 (from No. 1 to No. 5). The corresponding images for the droplet detachment in a cycle of pulse are shown respectively in Fig. 2, Fig. 3, and Fig. 4. For the droplet transfer frequencies of 50 Hz and 25 Hz, the detachment instant of the combined wave form is during the period of a pulse (t_p in Fig. 1) in a cycle, which is the same as in the case of the corresponding pure square wave form applied. This can be verified by the step increase of the arc light intensity on the consecutive images. The detachment instant for the combined wave form with the frequency of 18 Hz is also during the pulse period. The photo of a weld bead with the detachment frequency of 18 Hz using the combined wave form is shown in Fig. 5. Since the energy input is low, the ODPP approach with a detachment

frequency of 18 Hz can not be applied to the pure square wave form. The curves in Fig. 6, based on the data in Table 2, show that the penetration, width, and height of a weld bead with the combined wave form are smaller than those of the pure square wave form.

Table 1. Experimental Parameters for GMAW of Steel

Test Number (N)	Wire Diameter (mm)	Pulse and Base Current (A)	Wire Feeding Speeds (cm/min)	Square Wave Pulse Frequency (Hz)/(ms)	Square Wave Pulse Width (t_p) (ms)	Sine Wave Frequency (Hz)/(ms)	Remarks
1	1.2	260/40	290/300*	50/20	3.00	465/2.15	Combined wave form
2	1.2	260/40	290/300	50/20	5.00	N/A	Pure square wave form
3	1.2	260/40	230/245	25/40	3.00	62.5/12	Combined wave form
4	1.2	260/40	230/245	25/40	5.00	N/A	Pure square wave form
5	1.2	260/40	190/230	18.51/54	1.60	465/2.15	Combined wave form
6	1.2	250/40	335/360	50/20	1.60	465/2.15	Forced osclillation with combined wave form, oscillating twice in a cycle of a pulse
7	1.2	210/40	380/390	50/20	12.00	N/A	Forced osclillation with pure square wave form, oscillating twice in a cycle of a pulse
8	0.8	160/40	660/700	N/A	N/A	78/12.82	Oscilating once in a cycle of a pulse of a pure sine wave form
9	1.2	160/40	220/240	25/40	2.0	500/2.00	Forced oscillation of four or five times before detachment in a cycle of a pulse combined with a sine wave form

* The numbers following the back slash in this column represent the values of wire-feeding speed when a welding process is stopped.

Also, for both of the approaches, as the average welding current increases, the geometrical sizes of a weld bead and the detachment frequency of a droplet increase while the average droplet diameter decreases. These phenomena can also be observed from the images of the droplet at the tip of the wire.

The sine wave form, combined with the square wave form in Fig. 1b, has the following effects: improvement of the penetration profile and maintenance of a bigger droplet. These can be seen from the curves in Fig. 7a and the photos of the cross sections of the corresponding weld beads (shown in Fig. 10). According to the well-known conclusion for the GMA welding of steel, the streaming mode of the droplet transfer often results in a finger shaped penetration

a b

Fig. 2 Images of Droplet Detachment with Frequency of 50 Hz (frame rate: 409 frames/second)

a. combination of square wave form with sine wave form for current control
b. pure square wave form for current control

a b

Fig. 3 Images of Droplet Detachment with Frequency of 25 Hz (frame rate: 409 frames/second)

a. combination of square wave form with sine wave form for current control
b. pure square wave form for current control

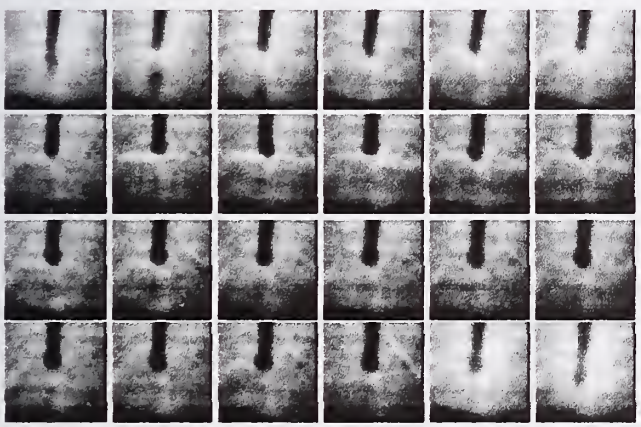

Fig. 4 Images of Droplet Detachment with Frequency of 18 Hz (frame rate: 409 frames/second)

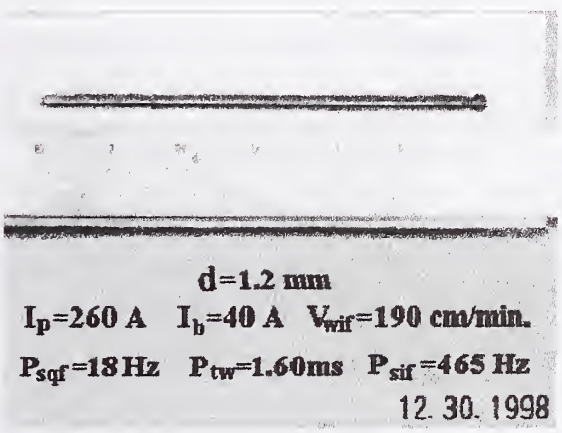

Fig. 5 Photos of Weld Bead with Detachment Frequency of 18 Hz

profile, compared with the projected spray transfer mode. So, the projected spray transfer mode is preferred and widely applied to production. However, it was found in our work that a finger shaped, deep penetration can also be generated if the detachment frequency in ODPP mode is above 50 Hz, even though it is not as severe as in the case of streaming mode when the average

welding current is below 100 A. When the droplet transfer frequency decreases to 25 Hz, the penetration profile is much more uniform and shallow using the combined wave-form approach. The probable reason for this is that the bigger droplet, associated with the applied higher average welding current and long background time, will bring more heat to the molten pool without deeper and stronger droplet impingement to the molten pool. The heat convection in the weld pool may also make the heat inside it more evenly be distributed. From the above results, it can also be observed that in order to improve the penetration profile, the droplet transfer frequency in ODPP mode has to be below 25 Hz, which is very crucial to the parts made in the GMAW based rapid prototyping.

Table 2 Sizes of Weld Bead, Average Current, and Average Droplet Diameter

Test Number (N)	Penetration depth (mm)	Width (mm)	Height (mm)	Average welding current (A)	Wire length per droplet (mm/d)	Diameter of the droplet (mm)
1	0.6858	5.4356	1.6256	97	0.9668	1.014
2	0.7366	5.3594	1.7272	95	0.9668	1.014
3	0.2524	3.9116	1.4224	90	1.5364	1.154
4	0.2686	4.1500	1.6764	84	1.5364	1.154
5	0.2280	3.0480	1.2700	56	1.7235	1.230
6	1.0668	6.0452	1.8288	80	1.1170	1.206
7	1.5240	7.1120	1.7780	142	1.2667	1.110
8	0.9144	6.0452	1.8796	120	1.7600	1.587
9	N/A	N/A	N/A	58	0.7333	1.166

The random oscillation of the droplet was observed and analyzed mostly in the range of globular transfer mode where the droplet suspends at the tip of the wire for a comparatively longer time because the electromagnetic force inside the droplet is smaller than the surface tension [9-11]. This type of oscillation is not controllable and thus not a candidate for droplet detachment control. A so-called active control for the droplet detachment was developed by Radovan Kovacevic and his research team at the University of Kentucky using a high frame rate camera as a vision sensor to detect the vertical coordinate of the droplet along the axis of the wire [12-13]. This process first experiences a growth period preset in advance to develop a droplet with a certain size at around 240 A for a 1.2-mm-diameter wire, which is higher than the transition current. Then the current is cut down to a low level (40 A) to excite a damped droplet oscillation at the tip of the wire. When the droplet nearly finishes the oscillation of a first cycle and goes down-wards, a high welding current pulse (higher than 250 A) is applied. Thus, the inertia generated by the oscillation and the electromagnetic force generated by the high welding current both act on the droplet to promote it to detach from the tip of the wire. After the above high current pulse is applied, the background period of a preset time is initiated with a current of 40 A. When the background period terminates, the next cycle repeats the same process.

Actually, in a pulsed GMA welding process with the ODPP mode, the droplet can detach in the range of either the pulse period or the base period. There is a possibility that the droplet is forced to detach at the instant of the front edge of the next welding current pulse. Thus, a current pulse is not only used as a growth period for providing the arc with the heat to melt the wire and

form a new droplet, but also as a detachment pulse by generating electromagnetic force for the previous droplet to promote it transfer to the weld pool. To verify this, two approaches of an open loop control with induced oscillation are examined: pure square wave form and combined wave form. The images of the electrode-droplet in a pulse cycle of 50 Hz are shown in Fig. 8.

The results show that each droplet will oscillate twice before it detaches at the instant of the front edge of the next welding current pulse (verified by the intensity increase of the arc light from the images) and that the combined wave form can generate a more stable droplet transfer process and an improved penetration profile. For instance, in the Fig. 8b, the first frame shows that the droplet is ready to detach. After it detaches at the instant of the second frame, a new droplet forms and moves upward and downward from frame 2 to frame 6. This is the first cycle of the oscillation for this new droplet. From frame 7 to frame 12, the droplet has another cycle of oscillation, and then detaches at the instant of frame 14. The droplet at the tip of the wire will be forced to oscillate at this frequency. During the droplet oscillation, although the heat generated in the acting period of a sine wave-form current is less than that of a square pulse with the same magnitude and acting time as a sine wave pulse, it still continuously melts the wire. This type of melting effect should be considered when the dynamic parameters are selected for the forced multiple oscillations. The droplet oscillation using pure sine wave form can also been observed from Fig. 9.

A natural oscillation frequency for a given droplet depends on its size. When this natural oscillation frequency equals that of a periodically varied external force applied on the droplet, a resonance may occur. In this case, the droplet may detach if the magnitude of the resonance is high enough.

The experiment is designed to verify the feasibility of a droplet resonance-based detachment control. The corresponding parameters and the images of the droplet are given for the experiment No. 9 in Table 2 and in Fig. 11, respectively. The wire is melted under the heating of the pulse current of 160 A to form a certain size droplet, and then the current is cut down to the base current of 40 A. After that, a sine wave-form current is applied to the droplet with the magnitude of 260 A and the frequency of 500 Hz.

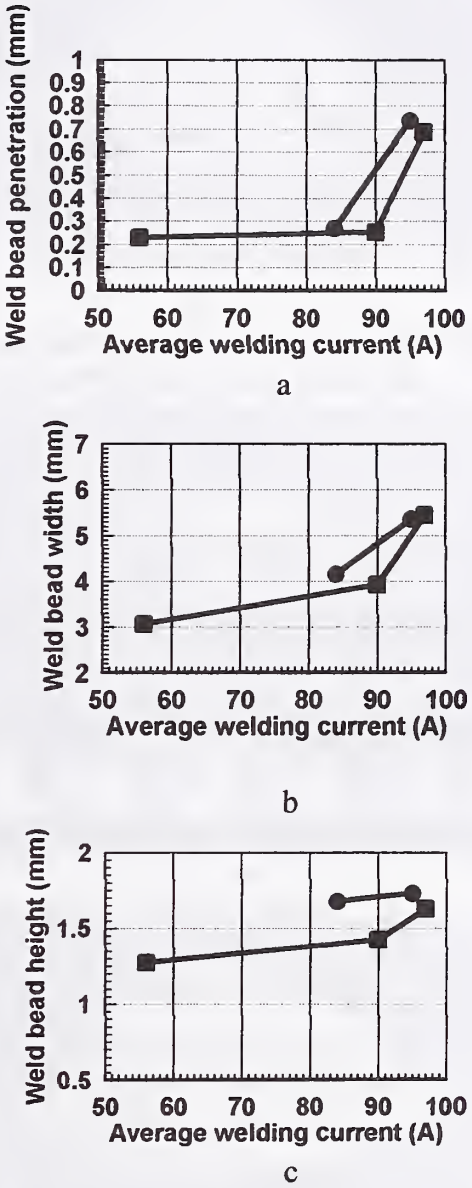

Fig. 6. Geometrical Sizes of the Weld Bead versus Average Welding Current (corresponding to the experiments of No. 1-5 in Table 2)

a. weld penetration b. weld bead width c. weld bead height
● pure square wave form
■ combined wave form

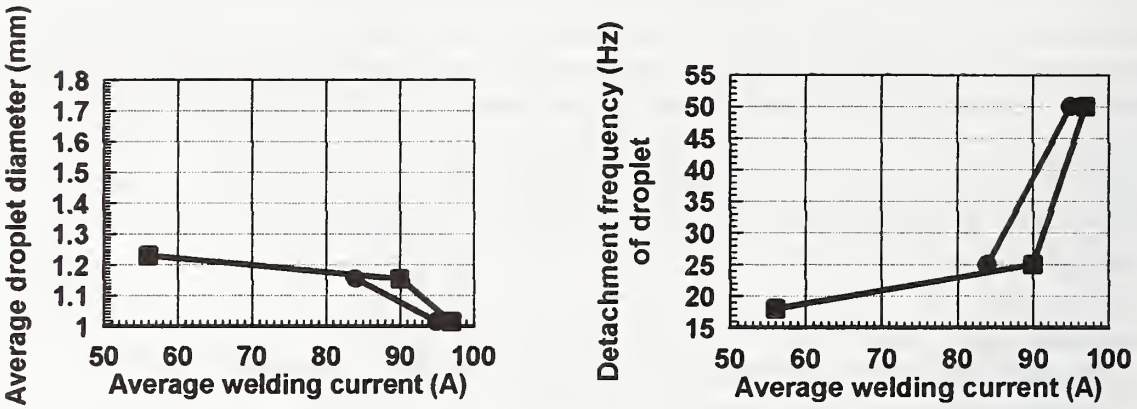

a b

Fig. 7 Droplet Diameter and Detachment Frequency versus Average Welding Current (for the Experiments of No. 1-5 in Table 2)

a. average droplet diameter b. droplet detachment frequency
● pure square wave form ■ combined wave form

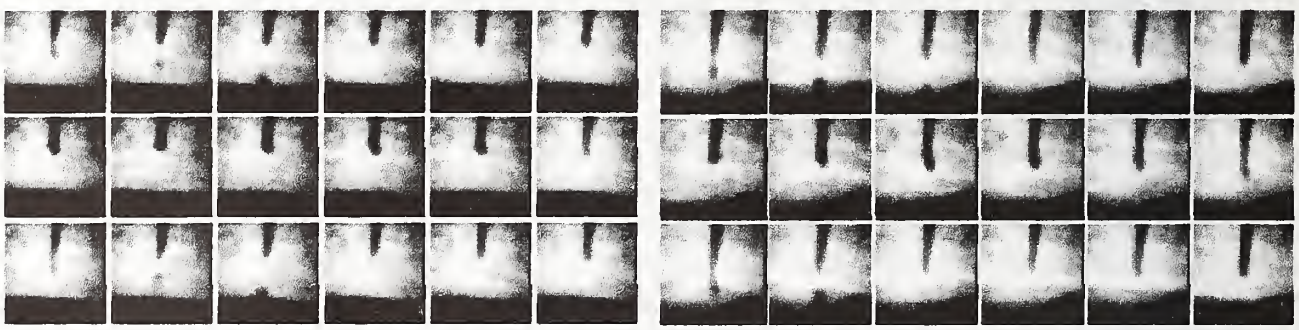

a b

Fig. 8 Images of Forced Droplet Oscillation with Detachment Frequency of 50 Hz Corresponding to Fig. 11 (frame rate: 606 frames/second)

a. combination of square wave form with sine wave form for current control
b. pure square wave form for current control

This promotes the droplet to continuously grow as it oscillates. When the droplet detaches, the welding current is cut down to the base current. At the end of base current period, a new following cycle repeats the same process. It can be seen from Fig. 11 that the arc is maintained and the wire melted from frame 1 to frame 7. From frame 8 to frame 12, the droplet finishes the first cycle of oscillation.

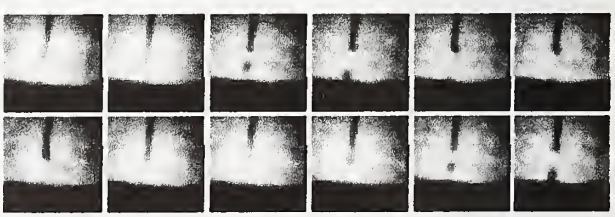

Fig. 9 Images of Forced Droplet Oscillation with Detachment Frequency of 75.5 Hz (frame rate: 606 frames/second)

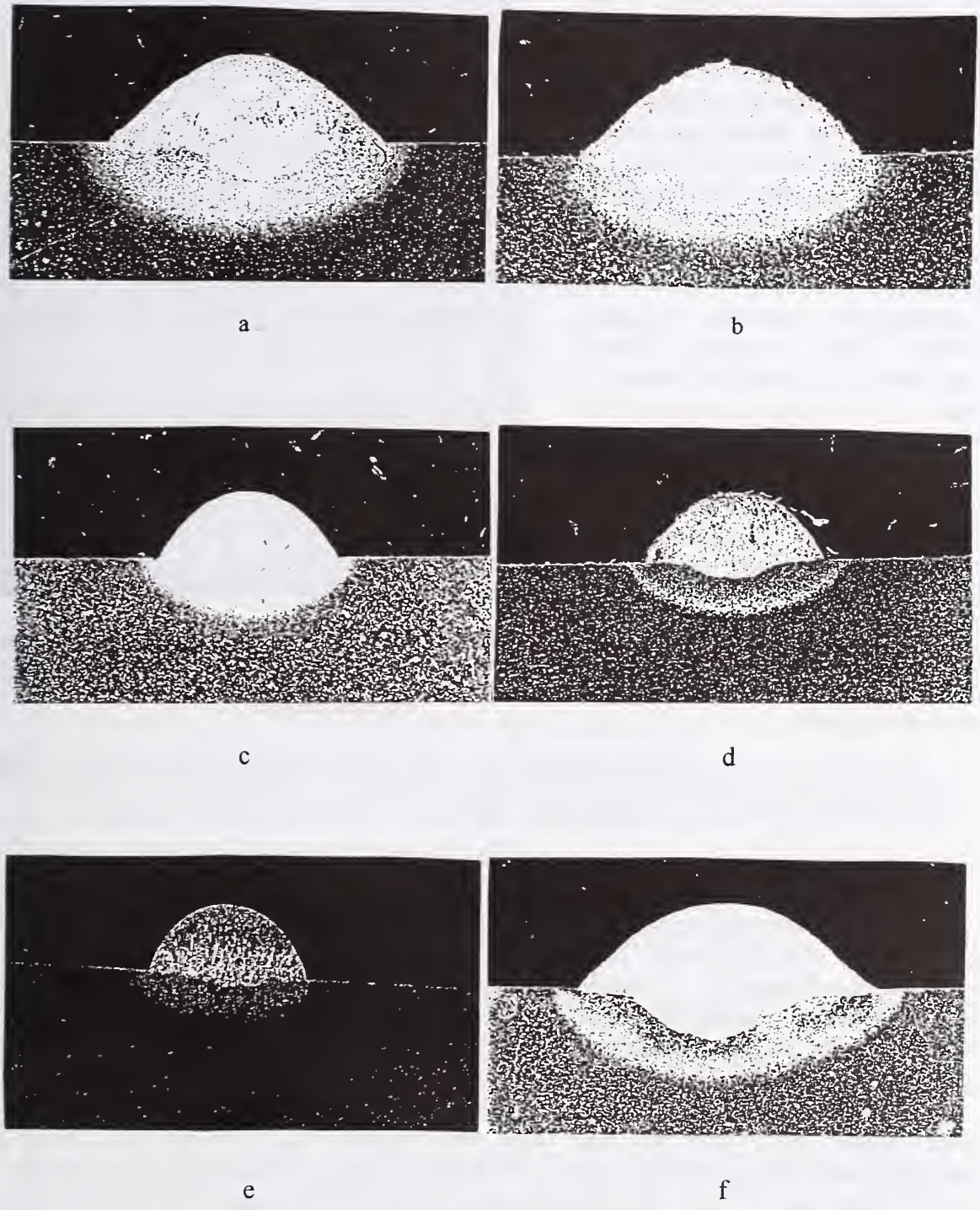

Fig. 10. Cross Sections of the Weld Bead for the Experiments of No. 1-5 and No. 8 in Table 2

a. combined wave form of 50 Hz b. pure square wave form of 50 Hz
c. combined wave form of 25 Hz d. pure square wave form of 25 Hz
e. combined wave form of 18 Hz f. pure sine wave form of 75 Hz

From frame 12 to frame 15, the droplet makes the second oscillation. During the time from frame 15 to frame 18, the droplet oscillates the third time. The droplet also makes the fourth oscillation from frame 18 to frame 21, and then detaches at the instant between frame 22 and frame 23. The frequency of the droplet oscillation (496 Hz, acquired by counting the numbers of image frames and making simple calculation) is nearly the same as that of a sine wave form pulse (500 Hz). Compared with the droplet oscillation, the sine wave-form current has just two and a half cycles. Therefore, in this case, the droplet can oscillate only twice based on the sine wave-form frequency and one induced oscillation resulting from the cutting down of the current after the square wave-form pulse.

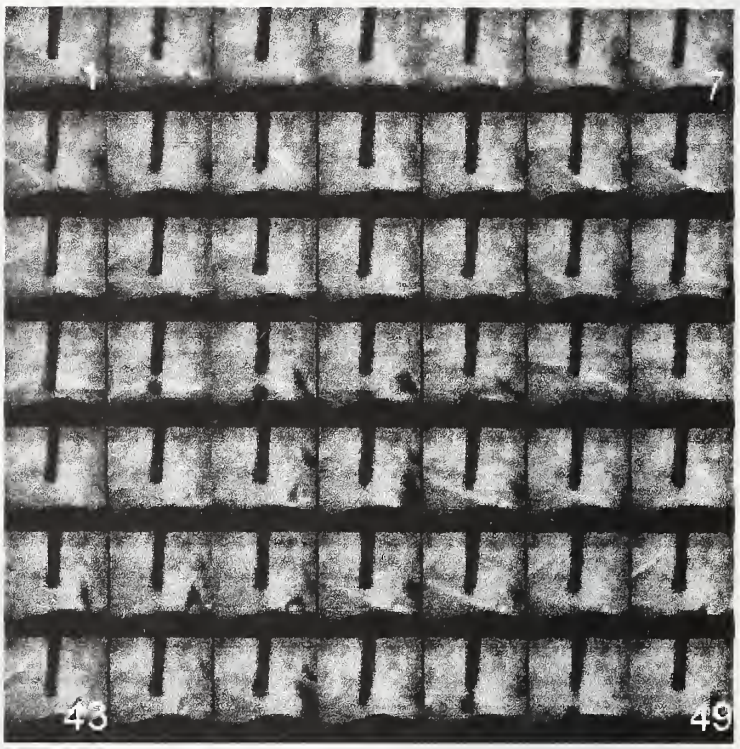

Fig. 11 Images of Droplet Resonance Oscillation Corresponding to Fig. 15 (frame rate: 595 frames/second)

The fourth oscillation and the detachment of the droplet indicate that the droplet resonance occurs because of the effect of the inertia generated by the forced multiple oscillation.

CONCLUSION

Droplet detachment control is crucial to control the mass and heat transferred to the parts in gas metal arc welding process. To maintain a stable welding process, the one droplet per pulse mode for metal transfer is recommended. An output current with the shape of a square wave form combined with a sine wave form can widen the operational range of the welding parameters for one droplet per pulse mode and highly improve the weld penetration profile. To achieve optimal results, the droplet transfer frequency should be maintained below 25 Hz.

Droplet oscillation can be implemented and controlled in the range of the one droplet per pulse transfer mode. The pure sine wave form approach can generate one forced droplet oscillation before its detachment, which is associated with a harmoniously characteristic sound. The welding current with the pure square wave form can generate two forced droplet oscillations. The larger number of forced droplet oscillations can be beneficial using the combination of the square wave-form current with the sine wave-form current with which the control of the droplet detachment and the regulation of the penetration profile can be guaranteed.

REFERENCE

[1] Lancaster, J. F., Ed. The Physics of Welding, 2nd ed. Edition. New York, Pergamon Press. 1986.

[2] AWS. Welding Handbook. Vol. 2. American Welding Society, Miami, Fla. 1991

[3] Y.S. Kim and T. W. Eagar. Analysis of Metal Transfer in Gas Metal Arc Welding. Welding Journal, 6: 269-278. 1993.

[4] L. A. Jones, T. W. Eagar, and J H. Lang. Images of a Steel Electrode in Ar-2%O2 Shielding during Constant Gas Metal Arc Welding. Welding Journal, 4: 269 to 278. 1998.

[5] Q. L. Wang and P. J. Li. Arc Light Sensing of Droplet Transfer and Its Analysis in Pulsed GMAW Process. Welding Journal, 11: 458s to 469s. 1997

[6] J. A. Johnson, N. M. Carlson, and H. B. Smartt. Detection of Metal Transfer Mode in GMAW. Proc. 2nd International Conf. on Trends in Welding Res., 5: 377 to 381, Gatlinburg, Tenn. 1989.

[7] R. B. Madigan, T. P. Quinn, and T. A. Siewert. Sensing Droplet Detachment and Electrode Extension for Control of Gas Metal Arc Welding. Proc. 3rd International Conf. on Trends in Welding Res., 11: 999 to 1002, Gatlinburg, Tenn. 1989.

[8] ESAB Group. Size and Shape of the Liquid Droplet at the Molten Tip of an Arc Electrode. Journal of Physics, 4: 1433 to 1442. 1994.

[9] J. C. Amson. An Analysis of the Gas-shielded Consumable Metal Arc Welding System. British Welding Journal, 41(4): 232 to 249. 1962.

[10] J. W. Greene. An Analysis of Transfer in Gas-shielded Welding Arcs. Trans. AIEE Part 2, 7:194 to 203. 1960.

[11] J. H. Waszink and L. H. J. Graat. Experiment Investigation of the Forces Acting on a Droplet of Weld Metal. Welding Journal, 62(4): 109s to 116s. 1983.

[12] R. Kovacevic, L. G. Er, and Y. M. Zhang. Achieving Projected Spray Based on Excited Droplet Oscillation. The Second World Congress on Intelligent Manufacturing Progresses and Systems, Budapest, Hungary. 6: 10 to 13. 1997.

[13] Y. M. Zhang, L. G. Er, and R. Kovacevic. Active Metal Transfer Control by Monitoring Excited Droplet Oscillation. Welding Journal, 77(9): 388s to 395s. 1998.

[14] Z. Dubon. A Device for Interrupted Electrode Wire Feed during Arc Welding. Czechoslovakian Priority Certificate No. 116243. 10, 1965.

[15] B. E. Paton et al.. Controlling the Arc Welding Process by Programming the Electrode Wire Feed Rate. Automatic Welding, 30(1): 1 to 4. 1977.

[16] V. P. Dmitrienko. Calculation of the Speed of Movement of the Electrode Tip during Welding with Mechanical Control of Metal Transfer. Automatic Welding, 32(2): 1 to 4. 1977.

[17] L. A. Jones, T. W. Eagar, and J. H. Lang. Investigation of Droplet Detachment Control in Gas Metal Arc Welding. Proceedings of the 3rd International Conference on Trends in Welding Research. Gatlinburg, TN. 6: 1009 to 1013. 1992.

[18] S. Y. Yang. Projected Droplet Transfer Control with Additional Mechanical Forces (AMF) in MIG/MAG Welding Process. Ph. D. Dissertation, Harbin Institute of Technology. 1998.

HIGH PERFORMANCE PARALLEL DIGITAL SIGNAL PROCESSORS APPLIED TO WELDING

*D.A. Hartman and G.E. Cook ‡‡

ABSTRACT

Increasingly affordable digital signal processors are providing engineers with expanded capabilities and design flexibility when developing a process monitoring or control system. Microprocessors, and digital signal processors (DSP) in particular, are narrowing the performance gap between analog- and software-based implementations of control systems. In addition to bandwidth improvements, microprocessors afford the engineer with additional benefits, such as environmental invulnerability, reproduceability, and adaptability. Finally, a software-based approach allows an engineer to supplement and enhance new or existing control algorithms with intelligent techniques.

This paper presents the development of a parallel DSP platform for weld process monitoring and control. Four Texas Instrument's TMS320C40 parallel DSPs are interconnected to provide hard real-time process monitoring and control. A Pentium class PC serves as the host computer for the parallel-based platform. Real-time control, on-line process data visualization (time and frequency), data logging, and dynamic reconfigurability are just a few of the benefits available in this system.

An application involving the control of penetration in the gas tungsten arc (GTA) welding process is discussed. Intelligent methods, such as neural networks and fuzzy logic, applied to control and signal detection are presented. The system provides an excellent development, test, and verification platform prior to implementing on an embedded processor.

INTRODUCTION

Digital signal processing continues to extend the functionality and capabilities of software-based control systems. Although it may not be obvious why it is desirable to migrate from analog-based control applications to software-based systems, consider the following advantages:

- *Environmentally invulnerable*: In general, analog circuitry is subject to behavior variations depending on environmental factors, such as temperature. Digital systems, on the other hand, are essentially immune to such environmental effects.
- *Reproducible*: Analog circuitry depends on the combination of interconnected components each of which deviates to some degree from its nominal behavior. Consequently, expensive and hard to find

*This work was supported, in part, by the American Welding Society Foundation under a graduate research fellowship, 1995-1998. The author gratefully acknowledges an AWS Nashville section gift from Kirby Welding Supply.

†D.A. Hartman is a technical staff member of the Metallurgy Group in the Materials Science and Technology Division of Los Alamos National Laboratory, P.O. Box 1663, Mail Stop G770, Los Alamos, New Mexico 87545. E-mail: hartman@lanl.gov.

‡G.E. Cook is with the Welding Automation Laboratory at Vanderbilt University, Electrical and Computer Engineering Department, Box 1824-B, Nashville, Tennessee, 37235.

components, such as precision resistors, are necessary if the design engineer must duplicate an analog-based circuit to within very tight tolerances.

- *Adaptable*: Modifying the characteristics of an analog circuit, such as a filter, is not easily accomplished. Implementing a filter digitally, however, using a microprocessor enables the engineer to quickly and easily change the characteristics of the system.

Analog-based systems will always exceed their digital counterparts in terms of speed. However, microprocessors, and digital signal processors specifically, are narrowing the performance gap such that more and more applications are easily and effectively accomplished in software.

This paper presents the development of a parallel digital signal processing system for weld process monitoring and control. Information regarding the difficulty of automating the welding process, the objectives for feedback control of the welding process, and intelligent techniques that can help overcome some of the difficulties is presented in the Background section. A brief introduction into parallel hardware architectures is then provided. Finally, the framework for and the implementation of a distributed GTAW penetration control system is presented.

BACKGROUND

Manual vs. Automated Welding

In a typical manual welding situation, a human operator can observe the sights and sounds emanating from the welding process, assess the weld pool with respect to its desired state, and make minor changes in the weld parameters under his immediate control (weld current, voltage, travel speed and electrode orientation with respect to the joint path) in an effort to maintain the desired state of the weld. Adapting these sight and sound inputs to machine control and making the appropriate decisions is a challenging task. The human operator makes decisions from his inputs based primarily on past learned experience. For instance, when a weld is performed in the vertical position a seasoned welder knows that when the weld pool gets too large the liquid will run out of the pool leaving a crater. Acquiring the skill and knowledge to perform complicated tasks, such as full-penetration vertical-up or overhead welds, are the result of countless hours of practice through acquired rule of thumb techniques. Explaining this knowledge verbally involving precise visual cues to another human being or to a knowledge engineer is practically impossible.

Attempting to emulate the flexibility and adaptability of the human welder though mechanization is a non-trivial task. Providing a weld controller with sight and sound input is straightforward; however, making appropriate decisions from these inputs concerning control of the weld is not. In an attempt to circumvent a machine's lack of human intuition and decision-making capabilities, in-process welding control systems have incorporated feedback of welding characteristics which are unobservable to humans, such as thermography or ultrasonics, and utilized sophisticated control algorithms that involve accurate sensing feedback in an effort to maintain a tight tolerance on the welding process conditions.

Ultimately, most welding automation techniques did not evolve from traditional manual methods. Instead control engineers have applied conventional quantitative techniques of system analysis through the use of difference, differential, and integral equations to model and control the mechanized aspects of welding. Such an approach requires mathematical formalism and formal truths.

Applications involving through-the-arc sensing, such as automatic voltage control and seam tracking, have been met with a great amount of success such that they have found their way into commercial use. These

systems, arc voltage control and seam tracking in particular, have been successful for a variety of reasons. Clearly, the sensing technique is low cost, reliable, and nonintrusive. Their success, however, is directly correlated to their performance. Both of these systems are mechanistic systems, that is, they are physical systems that are governed, in this case, by electromagnetic laws. These laws are well understood and are therefore strategically and efficiently applied to both the sensor feedback information and to the control laws within the closed-loop feedback path.

More complex systems such as bead geometry or penetration control are well understood phenomena that can be accurately modeled from a theoretical standpoint; however, there are simply too many parameters involved in the models that require precise process feedback information that in-process implementation is impractical. As the complexity of the system increases the ability for the control technique to make precise and significant statements about its behavior decreases. Conventional quantitative techniques are inherently unsuitable for such complex systems.

The ability of a skilled human welder to assess and control bead geometry, for example, is not due to a fundamental understanding of the laws of physics. Instead of applying a mechanistic approach to the control of the weld pool, a seasoned welder applies a more humanistic approach in which the feedback information is not based on precision and formal truths but rather on imprecision and partial truths. Clearly, fully automated welding robots will require a marriage between mechanistic approaches for phenomena that is physically well understood and mathematically feasible for both sensors and control algorithms and humanistic approaches for phenomena that are otherwise infeasible to implement using conventional control techniques due to the required complexity resulting in a diminished accuracy.

Feedback Control of Fusion Welding

The objectives for feedback control of fusion welding are to continuously sense and control (1) the placement of the heat source with respect to the joint, (2) the geometry of the weld reinforcement and fusion zone, (3) the mechanical properties of the completed weld, (4) the microstructural evolution during solidification and cooling, and (5) the discontinuity formation (Ref. 1). The first objective, more commonly known as seam or joint tracking, is a well established and commercially successful adaptation to the mechanized fusion process (Refs. 2–5). Difficulties in sensing and controlling the geometry of the weld reinforcement and fusion zone area is an ongoing research topic (Ref. 6). Furthermore, regulating the geometrical properties of the welded joint will, in turn, influence the mechanical properties of the joint. Sensing and controlling the mechanical properties and the microstructure, such as centerline cooling rate and the heat affected zone, are topics of current, albeit relatively new, research interest (Refs. 7–9). Finally, the on-line identification of discontinuities, such as porosity and incomplete sidewall fusion, have been investigated in (Refs. 10–12).

The replacement of the human operator by a welding robot is particularly susceptible in its ability to handle process variations and disturbances. The flexibility and judgement inherent in a human welder has yet to be transferred successfully to a mechanical system. Nevertheless, techniques such as neural networks, fuzzy logic, expert systems, and genetic algorithms; multiple feedback sensing; and distributed, autonomous, and hierarchical control coupled with conventional control methods are the first step in an attempt to mimic human intuition and capabilities.

Intelligent Techniques for the Control of Complex Systems

Although intelligent techniques have been successfully demonstrated to effectively replace and, in certain cases, even exceed conventional control methods, intelligent techniques can, more importantly, complement,

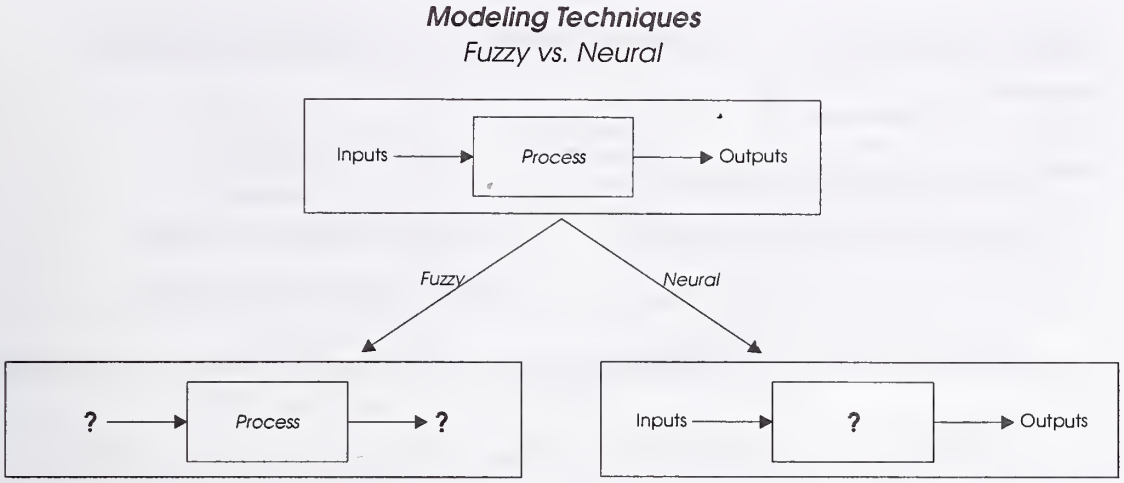

Figure 1: Fuzzy or neural modeling techniques should be chosen depending on what type of knowledge is available about the process.

enhance, and extend conventional control methods through the use of supervisory agents (Refs. 13–16) and through the use of hierarchical (Refs. 17–19), distributed (Refs. 20,21), and autonomous (Refs. 22,23) control methods. Processes that (1) were too complex to understand or represent simply, (2) contained large unpredictable environmental disturbances, or (3) involved nonlinear, time varying, or stochastic characteristics are now being approached with intelligent control methods in a practical and viable manner. Furthermore, unlike conventional methods which rely on mechanistic approaches, intelligent techniques can emulate humanistic approaches in an attempt to control non-deterministic processes.

Although other equally effective intelligent techniques are available, this paper will limit its focus to the application of fuzzy and neural network methods for the control of a complex process, and specifically the control of the depth of penetration in gas tungsten arc welding (GTAW). Choosing between a neural or fuzzy modeling technique should be based on what type of knowledge is available about the process (see Figure 1). Questions, such as, "Is the process well understood and the inputs and outputs of the system hard to quantify?" or "Is the process ill-defined and the inputs and outputs of the system precise and easily quantifiable?", must be addressed prior to committing to an intelligent technique.

In general, fuzzy modeling techniques excel when an intuition-based, or humanistic, understanding of the process is available. Consequently, precise information regarding the process's inputs and outputs is not required. Fuzzy logic attempts to solve a problem in the same manner that a human might typically solve a problem: linguistically using rules of thumb. That is, when a human is asked to explain the solution to certain types of problems they (1) quantify the information used to make decisions in terms of imprecise values or categories and (2) they justify their actions in terms of if-then rules. For example, the amount of pressure that a person applies to the brakes of a car while approaching a stop sign at an intersection is based on information such as speed, distance, visibility, and road traction. Instead of mapping exact values, such as 45 MPH and 72.5 feet to speed and distance, respectively, in order to determine the brake pressure a human applies imprecise concepts such as "fast" or "slow", "near" or "far", "clear" or "foggy", and "good" or "bad" to quantify speed, distance, visibility, and road traction respectively. Furthermore, concepts such as visibility and road traction which are extremely hard to quantify precisely are nonetheless critical to ensuring that the car will stop at the proper location. Conventional control techniques that are typically applied to computer decision making processes would inevitably fall short in achieving a robust design due to the inability to

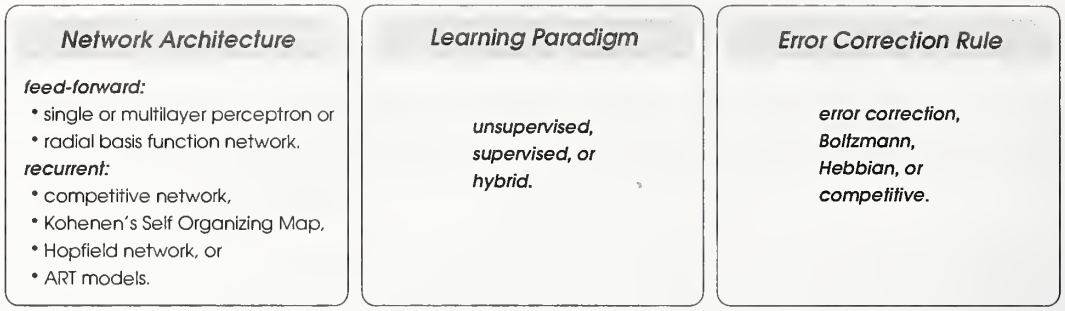

Figure 2: Commonly used methods for network architecture, learning paradigm, and error correction rules.

formulate an exact mathematical relationship for brake pressure involving all the necessary variables.

Neural networks, on the other hand, are well adept at mapping the input-output relationships of a process when the process is not well understood or too complex to implement using an analytical solution. Unlike fuzzy logic which employs ambiguity, a neural network requires precise values for both its input and its output nodes. Developing a neural network involves selecting a network architecture, a learning paradigm, and an error correction rule. Figure 2 illustrates some of the more commonly used methods for each of these selections. Clearly, extensive knowledge of the problem is required to in order to match the problem with the architecture, the learning paradigm, and the error correction mechanism (Ref. 24). Furthermore, constructing a training set that appropriately represents the problem to be modeled can be rather challenging, if not impossible, to obtain. Finally, ensuring that the training data and the training mechanism produce a network mapping capable of generalizing rather than memorizing is critical to the successful application for modeling and control.

When compared to other modeling methodologies, neural networks have certain drawbacks as well as advantages. The most notable drawback is the lack of comprehension of the physics of the process. Relating the qualitative effects of the network structure or parameters to the process parameters is usually impossible. On the other hand, most physical models resort to substantial simplifications of the process and therefore trade accuracy for comprehensibility. The advantages of neural models include relative accuracy and generality. If the training data for a neural network is general enough, spanning the entire ranges of process parameters, the resulting model will capture the complexion of the process, including nonlinearities and parameter cross couplings, over the same ranges. Model development is much simpler than for most other models. Instead of theoretical analysis and development for a new model the neural network tailors itself to the training data. Finally, the neural network can calculate its result relatively fast, as the input data is propagated once through the network in the application mode.

Microprocessor-Based Monitoring and Control

When high speed, deterministic control is required most control engineers resort to a programmable logic controller (PLC). PLCs fit a very large class of control problems very well; in particular, PLCs excel at mechanistic processes, such as machine control. Most importantly, the simple and specialized nature of a PLC enables it to perform most tasks effectively, cheaply, and reliably.

A traditional PLC-based design is inappropriate when developing a control system for a complex, nondeterministic process, such as those found in welding. A microprocessor-based development environment, on the other hand, presents an ideal platform for the investigation and deployment of modeling and control

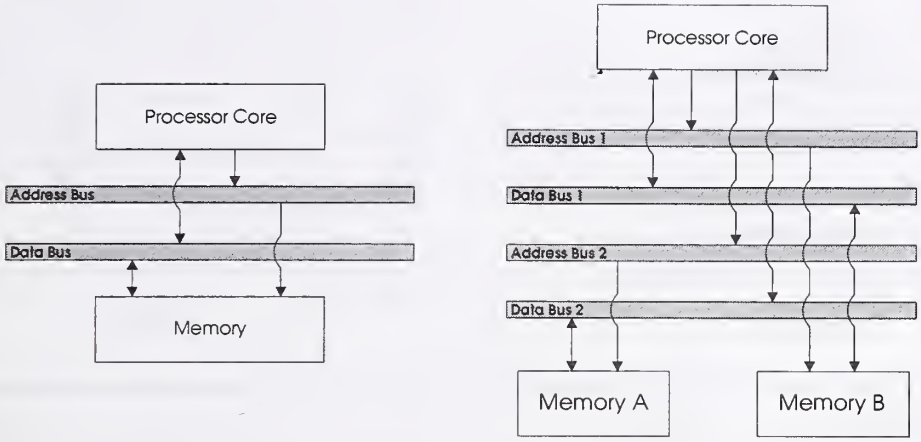

(a) Von Neumanm memory architecture. (b) Harvard memory architecture.

Figure 3: Microprocessor architectures.

techniques that extend beyond conventional control-based methods. In addition to providing an operator interface in which valuable process information can be viewed in real time, microprocessor-based control environments can provide software reconfigurability enabling different control strategies to be created, debugged, and evaluated.

PARALLELISM AND HIGH-PERFORMANCE COMPUTING

Parallelism can be architecturally characterized as a spectrum of different hardware configurations or designs involving, in one extreme, distributed network computing and, in the other extreme, simple bit-serial multiprocessing. Distributed network computing involves the loose interconnection of isolated and separated computing systems through a communication transport mechanism, such as Ethernet or, more recently, asynchronous transfer mode (ATM) networks. At the other extreme, the bit-serial processor, although of little value by itself, when coupled together into upwards of tens of thousands of processing elements (PEs) can achieve massive processing power (Ref. 25).

An intermediate approach to parallelism, and the path chosen for this research, involves using a microprocessor device as a building block with other microprocessor devices to construct a parallel computing network. Rather than waiting on a single processor to accomplish a set of tasks in series, we can distribute these tasks to a number of different processors. Each processor can execute its operations concurrently. Unlike a uniprocessor implementation, this results in a more accurate reflection of the real world in which many activities, or "processes", are happening concurrently.

Introduced in the late 1980's, the first commercially successful, general-purpose microprocessor that addressed the issues of parallel processing (communication, scheduling, scaling) was the Inmos Transputer (Ref. 26). The Transputer chip is a single-chip computer with a processor, local memory, and communication link interfaces. This general purpose processor (GPP) uses a von Neumann architecture in which the central processor is connected by a single data bus to memory (see Figure 3(a)). Concurrency within the single processor is handled by a processor scheduler implemented into the chip's microcode for fast

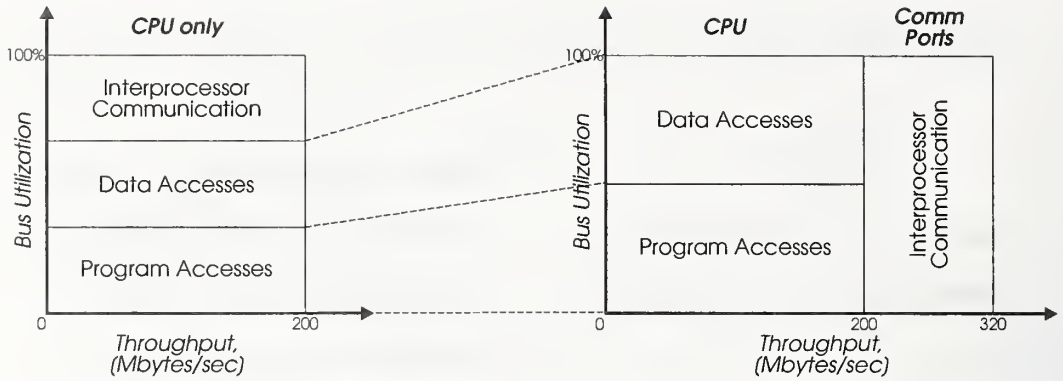

Figure 4: TMS320C40 throughput increase through the use of communication ports (Ref. 30).

task switching. An underlying direct memory addressing (DMA) controller supports both send and receive events enabling inexpensive interprocessor communication (Ref. 27).

Although fundamentally related, DSPs are significantly different from GPPs. Probably the most significant difference between DSPs and GPPs is the architecture. Unlike a von Neumann architecture, a Harvard architecture, most commonly found in DSPs, utilizes two memory spaces and two bus sets allowing two simultaneous accesses to memory per instruction cycle (see Figure 3(b)). Four memory accesses in a von Neumann architecture would require a minimum of four instruction cycles. A Harvard architecture, however, would only require a maximum of two cycles, thus increasing the processor's memory bandwidth.

Consistent with the adaptation of the Harvard memory architecture, other enhancements found in a DSP that enable efficient execution of common signal processing functions, such as signal filtering and fast Fourier transforms, include the following: single-cycle multiplication, specialized multiply-accumulate (MAC) hardware, specialized addressing, such as circular and bit-reversed addressing, zero-overhead looping, and execution time predictability. The distinction between GPPs and DSPs is becoming less clear as major microprocessor vendors incorporate the enhancements traditionally found in DSPs into their own processors (Refs. 28, 29).

The processor platform chosen for the research presented in the next section is the TMS320C40 floating point processor (commonly known as the C40) from Texas Instruments (Ref. 30). The C40 incorporates the multiprocessing capabilities of the Transputer and the execution efficiency of a DSP. A commercial DSP accelerator card, the SPIRIT-40 from Sonitech International, Inc., was used in this research. The SPIRIT-40 houses two C40 processors running at 40 MHz, 12 high speed communication ports (6 ports per C40), and an ISA bus interface to the host PC (Ref. 31).

At the heart of the C40 is six parallel bidirectional communication ports. An on-chip DMA coprocessor supports all interprocessor communication concurrently with calculations being executed by the CPU. Although a common bottleneck with any parallel or distributed processing system, the six communication ports (capable of asynchronous transfer rates of 20-Mbytes/sec per port) alleviate the CPU's dual data buses from interprocessor communication thus improving processor throughput, which is illustrated in Figure 4.

The C40 uses a modified Harvard architecture in which two identical, 80-pin parallel interfaces provide asynchronous access to two memory banks, commonly referred to as global and local memory. The buses can be placed in a high-impedance state for multiprocessor bus sharing in parallel systems. Using the C40 device as a building block, virtually any architecture, including both distributed and shared memory, can be

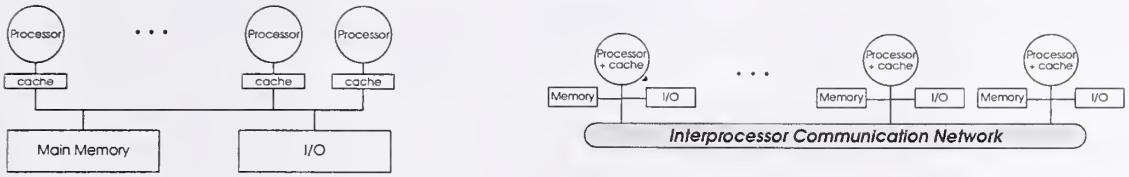

(a) Centralized shared memory.

(b) Distributed memory.

Figure 5: Memory architectures.

defined to solve computationally intensive problems (Ref. 32). Any number of C40 processors can be linked together through the communication ports or the multi-port data bus interfaces thereby enabling an engineer to custom tailor the size of the processing system and its level of performance.

The interconnection of microprocessors can fall into two classes depending on the memory organization and the interconnect strategy (Ref. 33). What constitutes a small or large number of processors will inevitably change over time. Therefore, parallel machines are typically referred to by their memory organization: shared or distributed.

A centralized shared-memory architecture (see Figure 5(a)) can be classified in many ways. At its most basic level, a centralized shared-memory architecture involves multiple processors[1] sharing a single centralized memory via a bus. However, such an architecture is not restricted to public memory rather it may also involve some public and some private memory. Because a single main memory must share access to a group of processors, the scale of a centralized shared-memory parallel machine is limited.

A distributed-memory architecture (see Figure 5(b)) can support larger processor counts by physically distributing the memory among the processors. Memory bandwidth increases and the latency between accesses decreases because each processor has access to its own private memory. Transmitting data between processors is more complex and has a higher latency in a distributed memory architecture because the processors no longer share a single centralized memory. Consequently, the key disadvantage for a distributed-memory architecture is interprocessor communication.

Although a vast array of memory configurations and system architectures using the C40 can be configured to solve virtually any kind of computationally intensive problem, the parallel architecture chosen for this research was restricted to a distributed-memory architecture which is hard-wired into SPIRIT-40. In particular, the SPIRIT-40 houses two C40s (labeled 0 and 1) that are hardwired through communication ports 3 and 0, respectively. Two single cycle dual-access RAM blocks (global and local) are accessible privately to each processor. The global RAM block is also accessible to the host PC through the ISA bus. A functional block diagram detailing the configuration is provided in Figure 6.

[1]Most computer scientists draw a distinction between multiprocessors and multicomputers. A parallel machine consists of multiprocessors if the replication of processors within the parallel framework does not alter the relationship between the processor(s) and other components, such as memory or I/O. A multicomputer system consists of individual, whole microprocessors (processor and memory) in which some form of communication network must be added to exchange data.

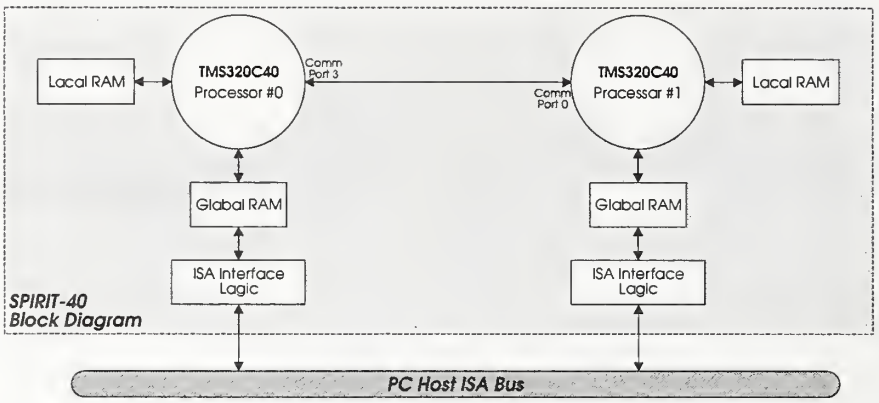

Figure 6: Simplified SPIRIT-40 block diagram.

WELD POOL OSCILLATION MONITORING AND PENETRATION CONTROL

Weld pool oscillation sensing was first proposed by Hardt, et al. (Ref. 34) as a method of sensing pool geometry, and hence penetration, for closed-loop feedback control of the depth of penetration. The fundamental concept is based on the fluid dynamics of the molten region in the weldment which is constrained by a solid container (i.e., the unmelted workpiece) and by surface tension forces. External excitation of the weld puddle's surface will result in pool oscillations that are a function of (1) the external force, (2) the properties of the molten region, (3) the surface tension, and (4) the shape of the container.

Implementing penetration control using pool oscillation sensing involves (1) excitation, (2) detection, and (3) control. Excitation of the weld puddle is most commonly initiated through the modulation of the welding current which thereby induces a change in the arc pressure on the pool's surface. Detection of the pool's fundamental mode of vibration requires (1) sensing the fluctuations in either the arc voltage or arc light and (2) extracting the fundamental mode of oscillation from the sensed fluctuations. Finally, control of the total heat input, either through current or travel speed or both, into the the workpiece can take on many different control algorithms involving either traditional, adaptive, or intelligent techniques or some combination thereof (Ref. 6).

System Objectives

The successful implementation of the closed-loop, single input (weld pool oscillation frequency), single output (welding current) controller requires not only the implementation of each of these functionally independent components, but also the ability for each of the components to cooperatively interact with one another. The system was modeled after work performed by Andersen in (Ref. 35). The following three items detail the requirements set forth by Andersen:

- *Excitation*: An improved method for inducing the molten weld pool into motion using a phase-locked loop (PLL) technique was developed by Andersen. The synchronized pulsing scheme provided a reliable means of sustaining weld pool vibration without introducing surface wave interference or compromising the response time of the controller. Although the design was sufficient for preliminary feasibility studies, a more robust excitation system was needed to accommodate changes in pool frequency, harmonic mode competition, and chaotic surface wave interaction. A software-based, dynamically reconfigurable, PLL was implemented enabling superior tracking performance over a wider range of resonant frequency conditions (Ref. 36).

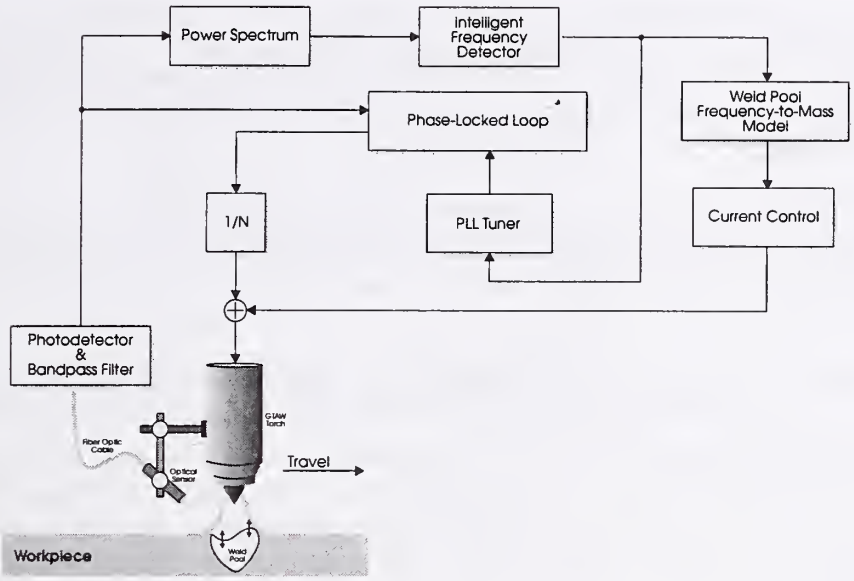

Figure 7: Penetration control using weld pool oscillation sensing.

- *Detection*: Detection of the weld pool's fundamental frequency requires (1) sensing the pool's vibrations, (2) converting the time-domain signal into the frequency domain, and (3) extracting the fundamental frequency from noise and other harmonics. Sensing pool oscillation was accomplished by collecting the specular reflection of the welding arc from the weld pool's mirror-like surface. The fast Fourier transform (FFT) and other higher order spectrum analysis methods were employed to convert the time-domain signal into the frequency domain. Frequency-domain conversions were performed anywhere between 5 and 20 times per second depending upon the welding parameters, the welding process, and the material employed (Ref. 37). Finally, both a neural network and a fuzzy logic method were developed to extract the fundamental mode of oscillation from the weld pool's power spectrum. Noise and modal dominance fluctuations prevented the determination of the fundamental frequency from being straightforward.

- *Control*: The control of the fusion zone by adjusting the total heat input into the weldment is a non-linear, time-varying, asymmetric problem. Conventional methods require an analytical technique based on the fundamental laws of physic to describe the dynamic and static behavior of the process. Consequently, several intelligent control techniques were investigated to regulate the current under varying thermal conditions (Ref. 38).

Figure 7 is a grand view illustration of the approach taken to the penetration control problem. PLL tuning and current control rely on the timely completion of the calculation of the power spectrum and the extraction of the fundamental frequency. However, the software-based PLL routine can run in parallel.

System Requirements

A number of requirements for a weld pool oscillation monitoring and penetration control system have been identified. They each put constraints on the possible control implementations that can be employed. They are identified as follows.

- *Extensibility*: The system should evolve as the researcher gains additional insight into and knowledge of the physical process. Therefore, modifications and improvements to the system throughout the development cycle can be expected. Furthermore, the system should be capable of hosting a variety of different detection and control algorithms. Extensibility can be facilitated through careful planning and modular design.

- *Speed*: The system must be fast. The reaction time of a typical GTAW process requires that the system respond within a 10 Hz frequency window (Refs. 1, 39). More importantly, power spectrums, intelligent frequency detection, current control, and phase-locked loop activities all must be performed within this window.

- *Visual Feedback*: A thorough understanding of the physical process is essential in developing an accurate, responsive, and reliable control system. Although an extensive amount of research has been conducted in the area of weld pool oscillation and penetration control there are still unresolved issues. In particular, Andersen notes that the PLL circuit fails to perform adequately during the transition from partial to full penetration. Real-time observation of the physical process through time and frequency-based analysis of the feedback signals can provide insight that off-line viewing of the data might otherwise fail to uncover.

- *Reliability and Fault Tolerance*: The system must operate in a manufacturing environment.

- *Safety*: The system must be safe. The welding operator must be able to manually override any process parameters or controller decisions. Consequently, the controller's interface must provide the operator with intimate details of the process and control information.

- *Cost*: The system must be economically feasible.

Achieving real-time monitoring and control in addition to fulfilling the previously mentioned requirements must involve a combination of hardware and software components. A parallel digital signal processor platform built around the Texas Instrument's TMS320C40 (C40) processor was used to facilitate modularity, hence extensibility, and to provide the response time, hence speed, necessary from a GTA welding control system.

Rather than relying on one serial processor to handle all of the operations of each component within our system, we can distribute the operations to a number of different processors. Therefore, using a modular design approach in conjunction with a parallel microprocessor environment enables the researcher to add and subtract components from the system without disrupting the entire system as a whole. Consequently, the development process can be naturally decomposed into a variety of functional components. Each component can be tested and verified to ensure both accuracy and reliability, hence ensuring a robust system.

An Intel-based Pentium computer was used to host the graphical user interface (GUI) necessary for the welding operator. The interface enables real-time display (time and frequency) of process parameters and feedback signals. Most importantly, the GUI contains numerous controls which allow the operator to manually control and override (if necessary) any process parameters or control variables.

Parallel DSP Platform

Table 1 summarizes the actions required, the methods employed, and the response time objectives needed in order to implement the controller. In addition to the functional components listed in Table 1, the parallel

Table 1: Real-time control actions for penetration control.

Requirement	Method Employed	Response Time
Excitation	Software-based PLL	400 - 2000 Hz
	On-line tuning of the PLL	5 - 20 Hz
Detection	FFT or other spectrum analysis method	5 - 20 Hz
	Extracting the fundamental frequency	5 - 20 Hz
Control	Fuzzy or neural control method	5 - 20 Hz

DSP platform must be able to interface with a data acquisition card for I/O and a personal computer (PC) for data logging, operator interface, and data visualization. In addition to real-time data display, the welding engineer must be able to manually override all computer controlled welding operations.

Clearly, the requirements imply very high computational costs. Consequently, a single processor implementation would be infeasible. Therefore, in order to guarantee a system-wide, real-time response from the controller the tasks were distributed onto separate microprocessors.

Two SPIRIT-40 boards were used in this research providing a total of four (4) C40s. The decomposition of the problem was therefore limited to only four DSP processors and one host (Intel Pentium) processor. Since shared memory only exists between the host PC and a C40, a message passing dichotomy was used to exchange information between the DSP processors.

The parallel machine design was based on a collection of loosely-coupled processes. The processes are therefore statically bound to a processor at compile-time. Consequently, parallelization was achieved using a functional decomposition of the problem (see Figure 8). The communication ports were hard-wired between C40s to facilitate communication between the processes.

Although a loosely coupled system is generally more difficult in ensuring optimal throughput of the system (Ref. 40), the primary objective in the design of the system was performance. Other factors such as maximizing processor utilization, cost, and programmability are important, however, they were not the primary objective. Therefore, in order to guarantee a real-time response the tasks were distributed across the four DSP processors in such a manner to ensure that all processing take place within some specified amount of time at every instance. Figure 8 illustrates the functional decomposition of the problem taken in this research.

Ultimately, the system performance as a whole depends on the timely completion of each individual task. Due to the sequential nature of the problem, any shortcoming in performance of an individual task (i.e. decreased response time) will inevitably result in deteriorated system performance as a whole. Therefore, careful attention was taken in determining the required CPU time necessary for completing each task.

PC Host Interface

Due to the nondeterministic nature of the welding process, the asymmetric behavior of the heat transfer characteristics, and the chaotic interaction of the surface waves of the molten weld pool a PC-based interface, capable of real-time display of the process's measurable variables, was deemed necessary. On-line interrogation of most aspects of the penetration control system provided a debugging environment for the excitation, detection, and control algorithms of the system. Although off-line (or post process) inspection of the data is necessary for sufficiently validating the reliability and stability of the control system, on-line process monitoring enabled the control engineer to not only watch the process data but to correlate it with

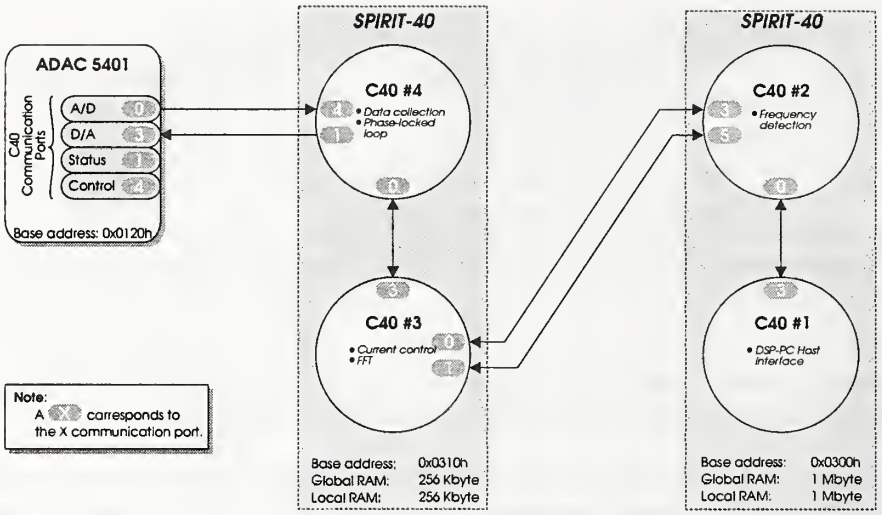

Figure 8: Interprocessor communication layout.

the sights and sounds emanating from the process.

Unlike a deterministic control system in which an analytical model is available, an intelligent control technique relies on either extensive training data, such as a neural network, or human-based intuition, such as a fuzzy logic approach, in order to derive a model. The PC-based interface facilitated this need by (1) being capable of storing large amounts of data and (2) serving as a learning tool for the development of human insight into the complex nature of the process.

Figure 9 is a typical screen capture during a penetration control welding experiment. Both time- and frequency-domain information of all the measurable process variables can be displayed in real-time. Most importantly, the control engineer can change different parameters of the process, such as the welding current, pulse frequency, travel speed, etc., and watch their effect upon the process. Experimenting in this manner can enable one to extend their understanding of the process beyond a traditional model-based understanding that one might obtain strictly through a mathematical presentation of the process.

Figures 10(a) through 10(f) illustrate the different control views available to the operator. The fuzzy logic control (FLC) view and the FLC tuner view (see Figures 10(a) and 10(b), respectively) enable the operator to change the controller's set-point, gain, etc. and compare the overall performance of the controller relative to its desired performance. The PC interface also empowers the operator with control over the synchronized pulsing capabilities (see Figure 10(c)). Presented in Figure 10(d), manually changing the PLL's configuration can be performed on-line. Finally, both the frequency-to-mass model and the fundamental frequency detection method can be modified on-line (see Figures 10(e) and 10(f), respectively).

CONCLUSIONS

The advent of microprocessors and PC-based control environments has enabled engineers in all disciplines to employ control methods that extend beyond those of conventional-based control. Intelligent techniques, such as fuzzy logic, neural networks, etc., can provide an engineer with additional tools to tackle complex processes that can not be represented in a tractable and analytical fashion. Furthermore, intelligent control methodologies, such as hierarchical, distributed, and autonomous control, can complement and enhance,

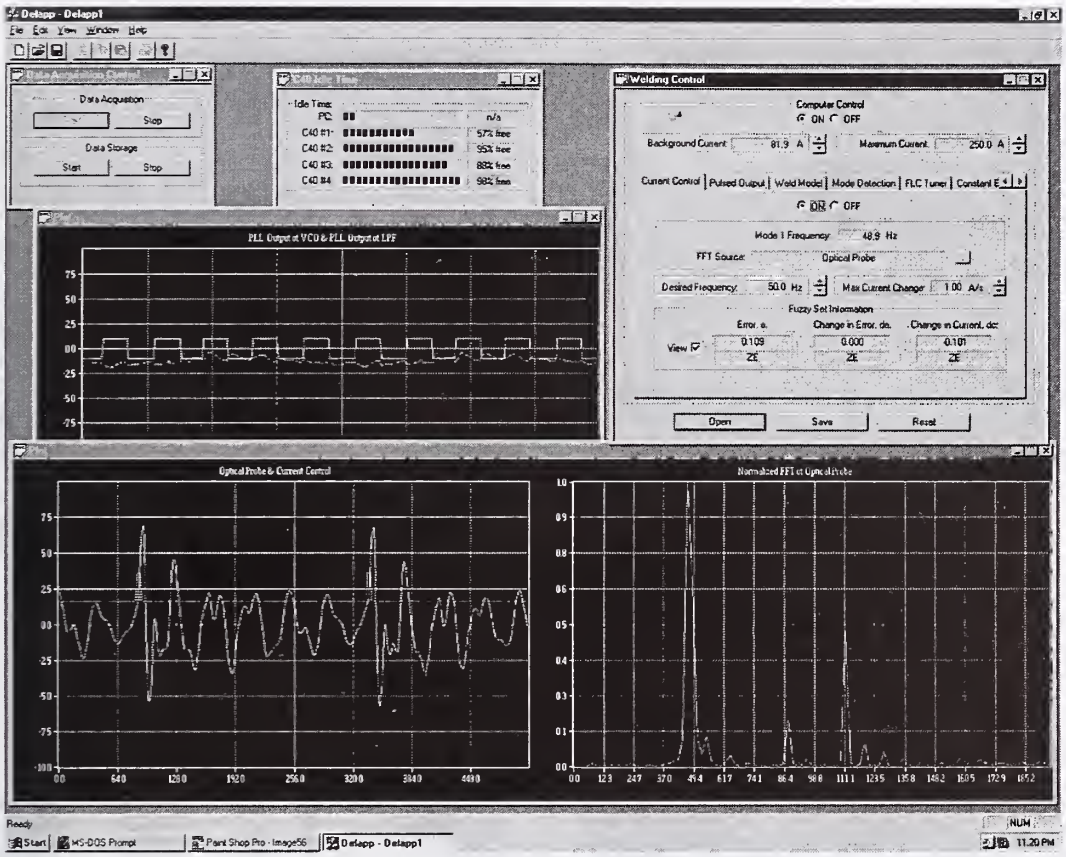

Figure 9: Penetration control main window.

rather than replace, conventional-based control algorithms in an attempt to improve the robustness and dynamic range that a controller can perform within.

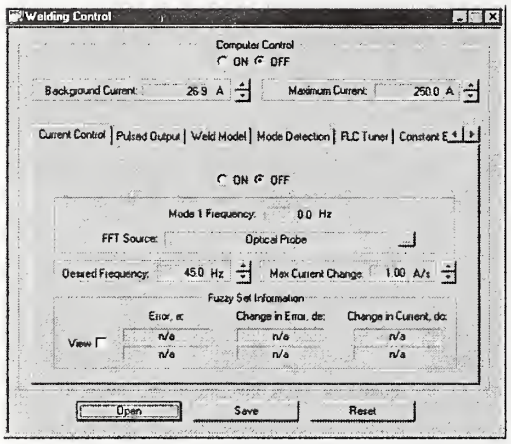

(a)

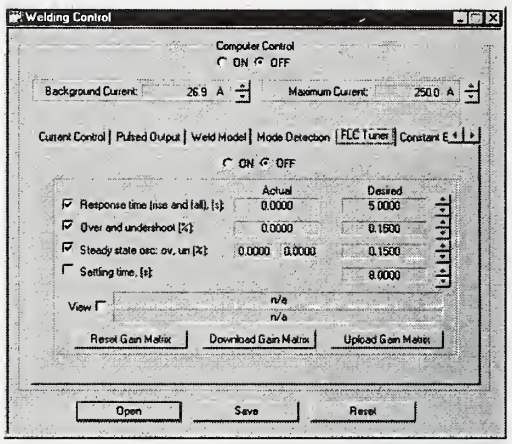

(b)

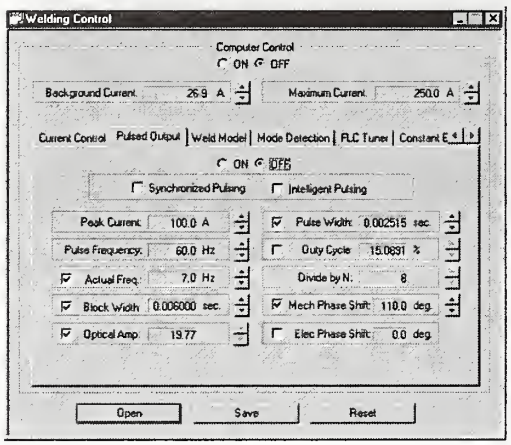

(c)

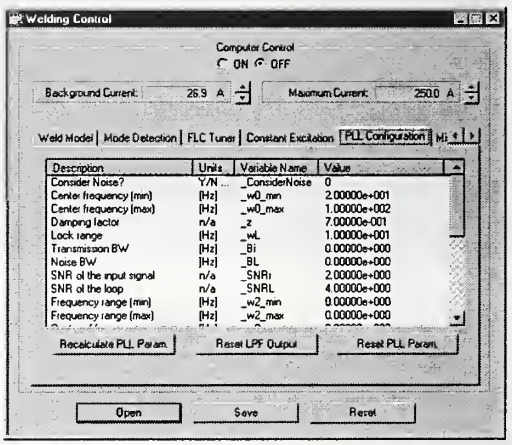

(d)

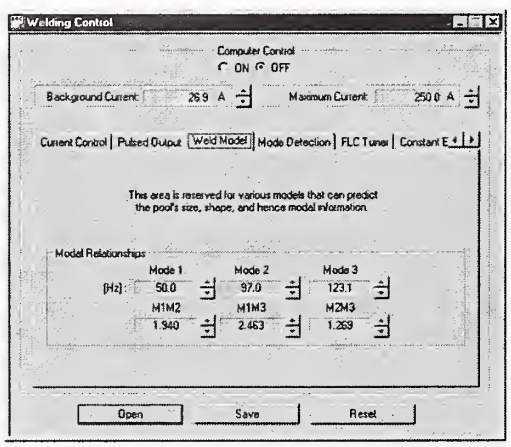

(e)

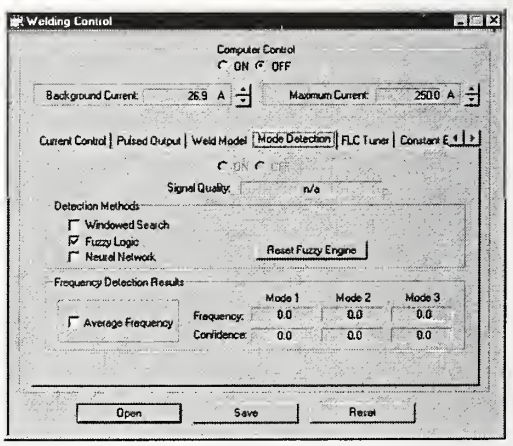

(f)

Figure 10: Penetration control interface.

References

[1] G.E. Cook, K. Andersen, and R.J. Barnett. Feedback and adaptive control in welding. In S.A. David and J.M. Vitek, editors, *Recent Trends in Welding Science and Technology, Proceedings of the 2nd International Conference on Trends in Welding Research*, pages 891–903, Gatlinburg, Tennessee, USA, May 14-18, 1989. ASM International.

[2] G.E. Cook, G.M. Merrick, U.A. Schneider, and W.R. Rosenberger. Weld tracking/electric arc sensing. United States Patent 4,336,440. Westinghouse Electric Corporation, Pittsburg, Pennsylvania, June 22, 1982.

[3] G.E. Cook. Apparatus and method for sensing a workpiece with an electrical arc. United States Patent 4,531,192. CRC Welding Systems, Inc., Nashville, Tennessee, July 23, 1985.

[4] B. Butler. Joint tracking automation triples propane cylinder production. *Welding Journal*, 71(8):61–63, August 1992.

[5] Joint tracking robot system transforms company's welding production. *Welding Journal*, 73(3):68–69, March 1994.

[6] Daniel Anthony Hartman. *Modal Analysis of GTA Weld Pools for Penetration Control*. PhD thesis, Vanderbilt University, December 1999.

[7] W.E. Lukens and R.A. Morris. Infrared temperature sensing of cooling rates for arc welding control. *Welding Journal*, 61(1):27s–33s, January 1982.

[8] C.C. Doumanidis and D.E. Hardt. A model for in-process control of thermal properties during welding. *Transactions of the ASME: Journal of Dynamic Systems, Measurement, and Control*, 111(1):40–50, March 1989.

[9] D.R. DeLapp, R.J. Barnett, G.E. Cook, A.M. Strauss, and D.A. Hartman. An investigation into the local solidification rate of the GTA weld pool. In H.B. Smartt, J.A. Johnson, and S.A. David, editors, *Trends in Welding Research, Proceedings of the 5th International Conference*, page to be published, Callaway Gardens, Georgia, USA, June 1–5, 1998. ASM International.

[10] N.M. Carlson, J.A. Johnson, and D.C. Kunerth. Control of GMAW: Detection of discontinuities in the weld pool. *Welding Journal*, 69(7):257s–263s, July 1990.

[11] C.D. Sorensen and T.W. Eagar. Digital signal processing as a diagnostic tool for gas tungsten arc welding. In S.A. David, editor, *Advances in Welding Science and Technology, Proceedings of an International Conference on Trends in Welding Research*, pages 467–472, Gatlinburg, Tennessee, USA, May 18-22, 1986. ASM International.

[12] T.P. Quinn, R.B. Madigan, C.B. Smith, and E.G. Blachowiak. Weld defect decisions using through-the-arc sensor data. In T. Siewert, editor, *NIST Special Publication 923, Seventh International Conference on Computer Technology in Welding*, pages 496–502, San Fransisco, California, July 8-11, 1997. National Institute of Standards and Technology.

[13] Jon Zumberge and Kevin M. Passino. A case study in intelligent vs. conventional control for a process control experiment. In *Proceedings of the 1996 IEEE International Symposium on Intelligent Control*, pages 37–42, Dearborn, Michigan, September 15-18 1996.

[14] K.M. Passino. Toward bridging the perceived gap between conventional control and intelligent control. In M.M. Gupta and N.K. Sinha, editors, *Intelligent Control Systems: Theory and Applications*, pages 3–27. IEEE Press, New York, NY, 1996.

[15] S. Chiu. Developing commercial applications of intelligent control. *IEEE Control Systems*, 17(2):94–97, April 1997.

[16] S. Chiu. Using fuzzy logic in control applications: Beyond fuzzy pid control. *IEEE Control Systems*, 18(5):100–105, October 1998.

[17] G.V.S. Raju, Jun Zhou, and Roger A. Kisner. Hierarchical fuzzy control. In C.J. Harris, editor, *Advances in Intelligent Control*, pages 243–258. Taylor & Francis, London; Bristol, PA, 1994.

[18] V.G. Moudgal, K.M. Passino, and S. Yurkovich. Rule-based control for a flexible-link robot. *IEEE Transactions on Control Systems Technology*, 2(4):392–405, December 1994.

[19] M. Sugeno, I. Hirano, S. Nakamura, and S. Kotsu. Development of an intelligent unmanned helicopter. In *Proceedings of the 1995 IEEE International Conference on Fuzzy Systems, Part 5 (of 5)*, pages 33–34, Yokohama, Japan, March 20-24 1995.

[20] S.A.K. Zaidi and A.H. Levis. Algorithmic design of distributed intelligence system architectures. In Madan M. Gupta and Naresh K. Sinha, editors, *Intelligent Control Systems, Theory and Applications*, pages 101–126. IEEE Press, New York, NY, 1996.

[21] R.R. Brooks and S.S. Iyengar. Robust distributed computing and sensing algorithm. *Computer*, 29(6):53–60, June 1996.

[22] K.M. Passino. Intelligent control for autonomous systems. *IEEE Spectrum*, 32(6):55–62, June 1995.

[23] P.J. Antsaklis, M. Lemmon, and J.A. Stiver. Learning to be autonomous. In M.M. Gupta and N.K. Sinha, editors, *Intelligent Control Systems: Theory and Applications*. IEEE Press, New York, NY, 1996.

[24] M. Brown and C.J. Harris. Neural networks for modelling and control. In C.J. Harris, editor, *Advances in Intelligent Control*, pages 17–55. Taylor & Francis, London; Bristol, PA, 1994.

[25] K.E. Batcher. Design of a massively parallel processor. *IEEE Transactions on Computers*, C-29(9):836–840, September 1980.

[26] D. Pountain. The transputer strikes back. *Byte*, (8):265–275, August 1991.

[27] Inmos, Berkeley, CA. *The Transputer Databook*, 1989.

[28] Microprocessors return to DSP: The technology battle. *EDN*, pages S31–S35, June 20, 1996.

[29] T. Fliegel. Trimedia: Separate but better? *MacWorld*, 14(2):46, February 1997.

[30] Texas Instruments, Inc., Houston, Texas. *TMS320C40 User's Guide*, 1992.

[31] Sonitech International, Inc., Wellesley, Massachusets. *SPIRIT–40 ISA User's Guide, Revision 3.0*, 1995.

[32] R. Simar, Jr., P. Koeppen, J. Leach, S. Marshall, D. Francis, G. Mekras, J. Rosenstrauch, and S. Anderson. Floating-point processors join forces in parallel processing architectures. *IEEE Micro*, 12(8):60–69, August 1992.

[33] D.A. Patterson and J.L. Hennessy. *Computer Architecture: A Quantitative Approach.* Morgan Kaufmann Publishers, Inc., San Fransisco, California, 1996.

[34] D.E. Hardt, K.M. Masubichi, H.M Paynter, E. Unkel, J. Converti, and M. Zachsenhouse. Improvement of fusion welding through modeling, measurement, and real-time control. In *International Conference on Welding Technology for Energy Applications*, pages 281–299, Gatlinburg, Tennessee, USA, May 1982.

[35] Kristinn Andersen. *Synchronous Weld Pool Oscillation for Monitoring and Control.* PhD thesis, Vanderbilt University, May 1993.

[36] D.A. Hartman, D.R. DeLapp, G.E. Cook, and R.J. Barnett. Intelligent fusion control throughout varying thermal regions. In *34th Annual Meeting - IEEE Industry Applications Society*, page to be published, October 3-7, 1999.

[37] G.E. Cook, K. Andersen, and R.J. Barnett. Welding and bonding. In R.C. Dorf, editor, *The Electrical Engineering Handbook*, pages 2223–2237. CRC Press, Inc., Boca Raton, FL, 1993.

[38] D.A. Hartman, D.R. DeLapp, G.E. Cook, and R.J. Barnett. Intelligent control in arc welding. In Cihan H. Dagli, Joydeep Ghosh, Anna L. Buczak, Okan Ersoy, and Mark J. Embrechts, editors, *Smart Engineering System Design: Neural Networks, Fuzzy Logic, Evolutionary Programming, Complex Systems and Data Mining*, page to be published, New York, NY, November 7-10, 1999. ASME Press.

[39] A. Suzuki, D.E. Hardt, and L. Valvani. Application of adaptive control theory to on-line GTA weld geometry regulation. *Transactions of the ASME: Jounral of Dynamic Systems, Measurement, and Control*, 113(1):93–103, March 1991.

[40] R.N. Ibbett and N.P. Topham. *Architecture of High Performance Computers, Volume II: Array Processors and Multiprocessor Systems.* Springer-Verlag New York, Inc., New York, NY, 1989.

WAVE DESIGNER™: PULSED GMAW ONLINE WAVEFORM EDITOR AND SOFT OSCILLOSCOPE

C. HSU*

ABSTRACT

A Java™ powered GMAW tool is introduced which allows graphical manipulation of current waveforms and arc characteristics with a live welding arc. Objectives of arc stability weld quality and productivity can be balanced and optimized for given welding conditions and manufacturing requirements.

In pulsed GMAW process and surface tension transfer® (STT®) process, the tool is used to refine arc starting, short clearing, droplet growth and detachment, pinch force control, heat input, arc length, bead profile, puddle following, and arc end tip conditioning.

The program also can monitor and analyze the actual waveforms of critical welding parameters at high resolution, including directly measurable electrical signals (such as arc current and voltage), derived signals (such as arc impedance, power and energy), and process state switching conditions (such as short circuit clearing and plasma boost). Furthermore, the apparatus is capable of recording welding signals and signatures in a data acquisition system without special sensors or instrumentation.

KEYWORDS

Process control, waveform control, pulse welding, GMAW, Surface Tension Transfer, short-circuiting, droplet transfer, arc start, arc end, data acquisition, heat input, arc physics, microprocessor controlled welding, arc signals, arc monitor

INTRODUCTION

Waveform Control Technology™ in gas metal arc welding such as advanced pulse welding and low spatter, controlled short-circuiting process produces high quality welds in broader operating conditions than traditional constant potential (CV) and short-circuiting process. However, the flexibility of waveform control introduces a large set of parameters to make a good weld with a stable process. These parameters must be adjusted for given welding conditions and joint design to meet weld specification and production rate.

Welding conditions and specifications vary depending on industry, application, plant location, work center layout, etc. For example, a procedure optimized for 90% Argon and 10% CO2 gas blend does not well work in Europe, where the common gas mix has 18% CO2 or other gas blends. A boom mounted wire feeder has longer cables, which affects output inductance and actual pulse ramp rate at the arc. Wire type, size and its manufacturing affect the transition

* Lincoln Electric, Cleveland, Ohio

between globular and spray transfer. Higher welding speeds require shorter arc lengths, for puddles to follow. Other examples include position (effect of gravity), material type, weldment surface treatment, joint design, preparation and accessibility, heat sinking condition, grounding, tooling and fixture, etc. Weld specifications are application dependent, which include penetration profile, surface profile, tolerance of defect and discontinuity, distortion, and mechanical properties. Trade-offs are often made between quality and productivity.

In order to make the "controls" or the user interface friendly, commercial equipment manufacturers offer "synergic" or "one-knob" procedures for selected materials and wire sizes, with limited flexibility for adjustments. Due to factorial explosion of possibilities, it is not practical to offer a procedure for every combination of welding condition and requirement. Therefore, these procedures are developed with "typical" welding conditions, and with the goal of seeking process compromise for wide coverage instead of optimization. Additionally, hard-wired or hard-coded power sources are not ready to take advantage of new materials or new consumables coming to the market, in terms of cost savings and quality improvements.

Wave Designer is tool to put the degree of flexibility back into the hands of a welding engineer. It is a graphical program to harness Waveform Control Technology and to customize arc characteristics, in order to achieve optimum weld quality and productivity. It is first implemented on Lincoln Electric PowerWave® 455 and 455/STT system.

GRAPHICAL WAVEFORM EDITOR

Wave Designer allows graphical manipulation of waveform while welding. It starts with a pre-built template (Fig. 1). This template is drawn on the screen and contains a set of "hot spots", which can be picked up or selected by an input device (such as a mouse or keyboard). These hot spots can be moved around on the screen by the input device and dropped or placed to a new location on the screen. As the hot spots are moved about on the screen, new waveforms are plotted on the screen to reflect the altered wave shape, and the new set of welding parameters are calculated and sent to the power source, which are reflected in the arc immediately.

The graphical editor also contains a panel of individual variables to manipulate the controlling parameters discretely. The variable field list contains characteristics of the waveform and other process parameters. Each field has a numerical window where the parameter can be typed in directly and a scrollbar where the parameter can be slid or incremented in small and large steps, and a "soft lock" mechanism to lock out unintentional altering. There are also relationships between these parameters such as that one parameter can not exceed the other, and frequency is a function of peak time and background time, etc. The editor ensures that when a change is made, all the minimum/maximum limits are met with the target and spontaneous parameters and all internal relationships are held valid. The waveform and the parameter panel are linked to each other so that changes made to one automatically update the other.

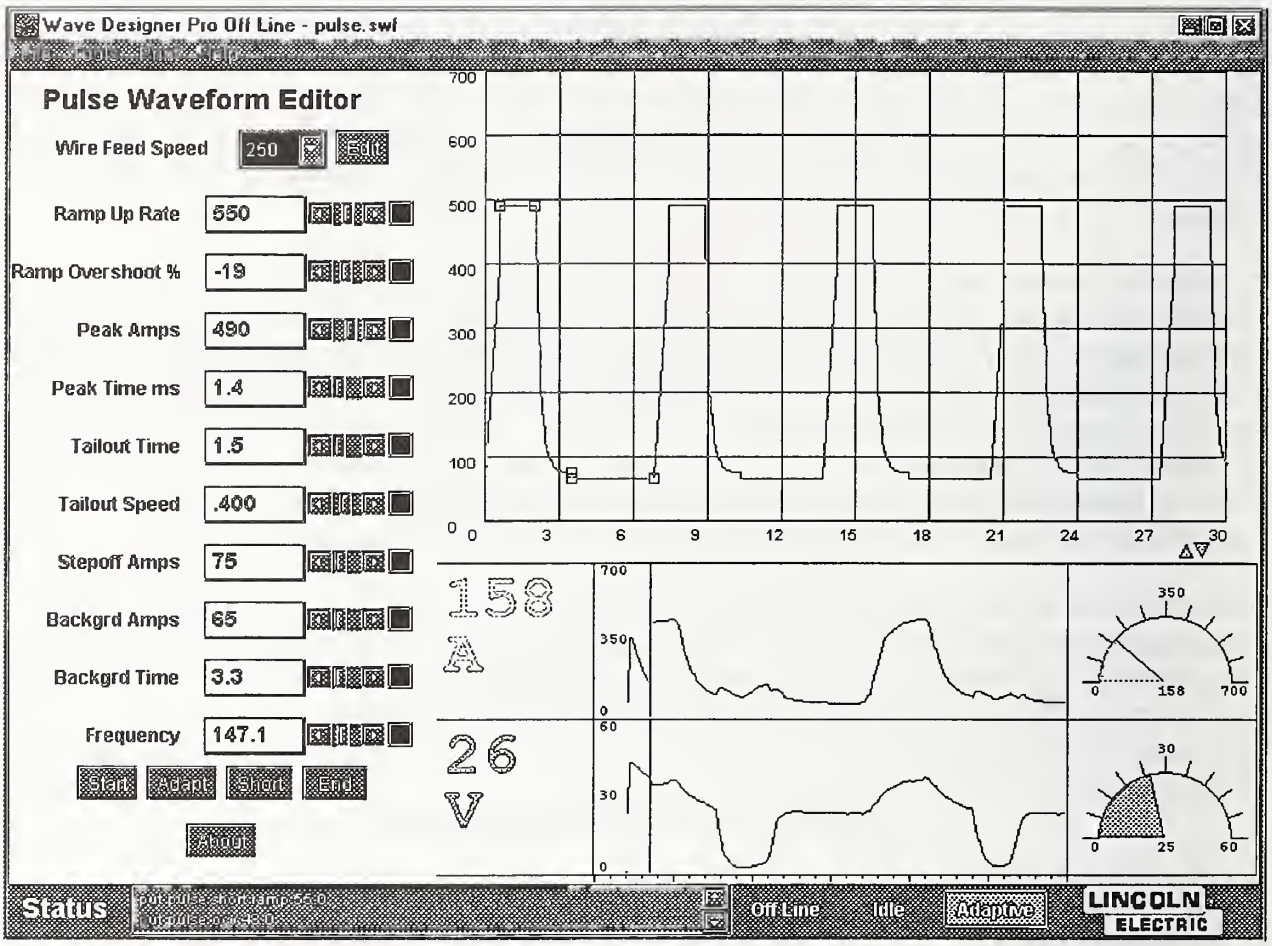

Fig. 1 OnlineWaveform Editor

SOFT OSCILLOSCOPE AND ANALYZER

The program also accomplishes functions of an oscilloscope (ArcScope™) without additional sensors, probes or special I/O boards (e.g. A/D converter). It uses the welding power source itself to sample the data. Arc signals such as current and voltage are sampled at 40 KHz by the power source, filtered at 10 KHz, and plotted on the screen during welding. High quality arc signals are acquired with special mechanism to block out inverter switching noise. In addition to physical signals, ArcScope also captures software signals such as estimated arc length, machine control logic, current and voltage regulation, etc.

FIG. 2 shows a simultaneously sampled or computed group of signals of a pulse process. Five simultaneously sampled traces are displayed: arc voltage, arc current, voltage derivative, impedance, and current derivative. The time scale is displayed in milliseconds.

ArcScope extends traditional scope functions by computing and plotting derived signals on the fly. Examples include the arc impedance and instantaneous power. The behavior of adaptive loop to contact tip to work distance (CTWD) variations is also sampled and displayed. Such behavior scales the dynamics to adapt to the changes in CTWD. Actual pulse frequency in a

pulsed GMAW or shorting frequency in a short-arc or surface tension transfer process is also calculated and displayed in real-time. Average current and voltage are sampled at a fixed rate and the welding time and accumulated energy input are displayed on the left.

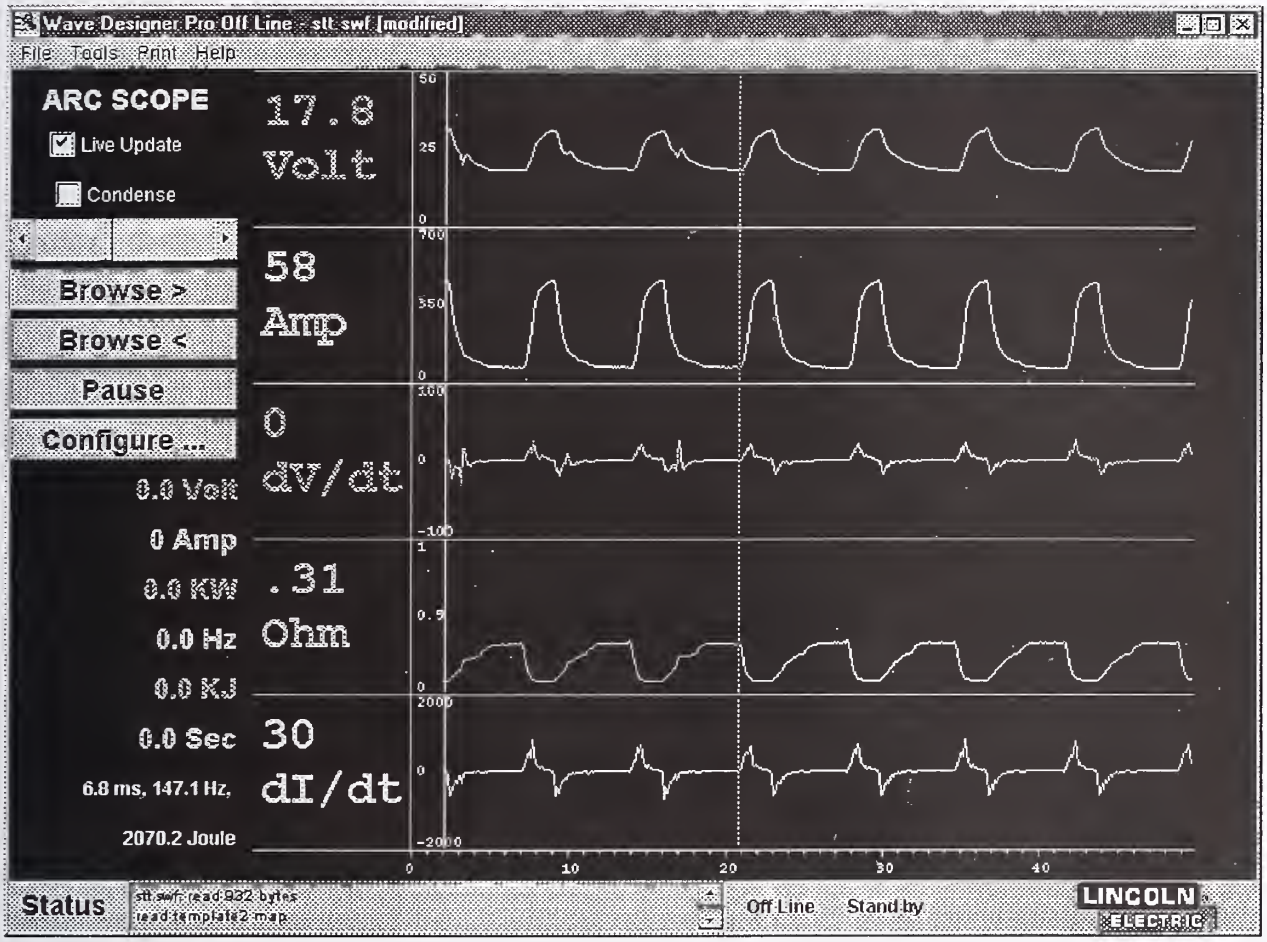

Fig 2. ArcScope is a soft oscilloscope using welding equipment to sample process signals

ArcScope provides an on-screen measurement and analysis tool. A reference bar (near 20 ms mark in Fig. 2) can be picked up and moved across the sampled waveform and the numerical data of all channels are updated. Furthermore, if the mouse is pressed at a spot near the reference bar, the differential time to the reference bar, the frequency and joule energy integrated under the power curve are computed and displayed.

Traces of voltage, current, power, and machine control logic can be logged, and waveform parameters can be exported, to text and html files. It provides the storing of welding signals and signatures of waveform for documentation, viewing and analysis, with Wave Designer or other tools such as spreadsheets and web browsers.

DEVELOPING PULSED GMAW WAVEFORM

Waveform is developed at a specific wire feed speed called "work-point". First, a base waveform is designed at a fixed CTWD. Secondly, dynamics to adapt to CTWD variations are chosen. Many work-points make up a table of waveforms. Waveform for a wire speed that falls in between work-points will be linearly interpolated from the table by the machine. Fig. 3 illustrates a basic waveform for pulsed GMAW process.

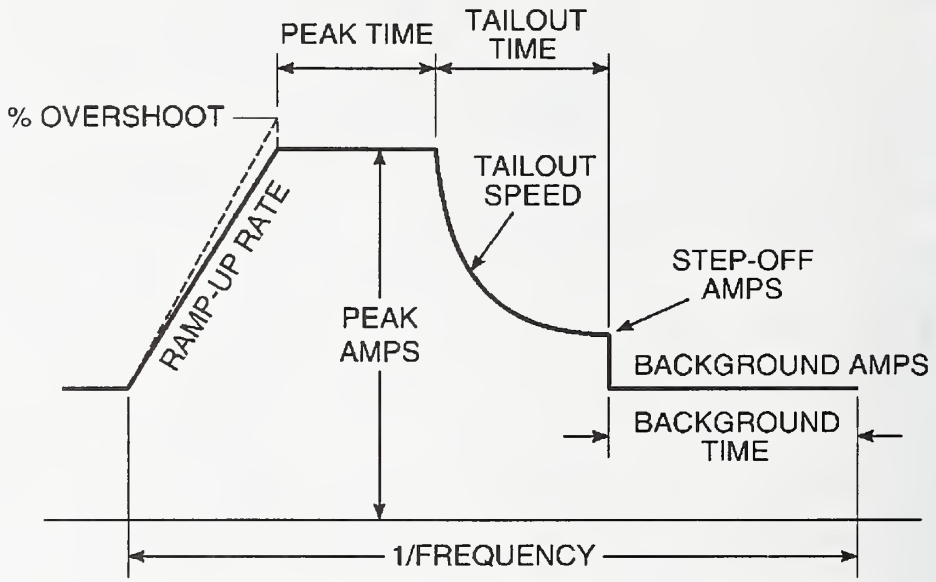

Fig. 3 Pulsed GMAW parameters to define a base waveform

Waveform variables are adjusted with objectives of process stability, arc length, heat input, bead profile, and defect elimination. Ramp up rate contributes to the formation of droplet, arc force applied to the weld pool, and ability to cut through mill scale. Peak current is set to be higher than the spray transition current. Together with peak time, they facilitate melting and pinching off the droplet and propel it towards the weld pool. Tail-out speed and time offer control of heat input. Background current keeps the arc lit. Between pulses, frequency is usually set to achieve single droplet transfer per pulse, with droplet size compatible with wire size to avoid spatter. The ratio of peak and background current affects power density, which in turn can affect weld width to depth aspect ratio and weld susceptibility to defects. Area under the waveform must be properly set to achieve desired melt-off rate.

Adaptive control parameters determine how waveform is adjusted to compensate for a change in stickout. The variables subject to CTWD adaptation include peak current, peak time, step-off and background current, and background time. Wire feed speed has a great influence on droplet forming and transfer physics and thus CTWD adaptation strategy. At low speeds, frequency may be used. At high speeds, peak current may be used. Both may be used in the midrange of wire speeds.

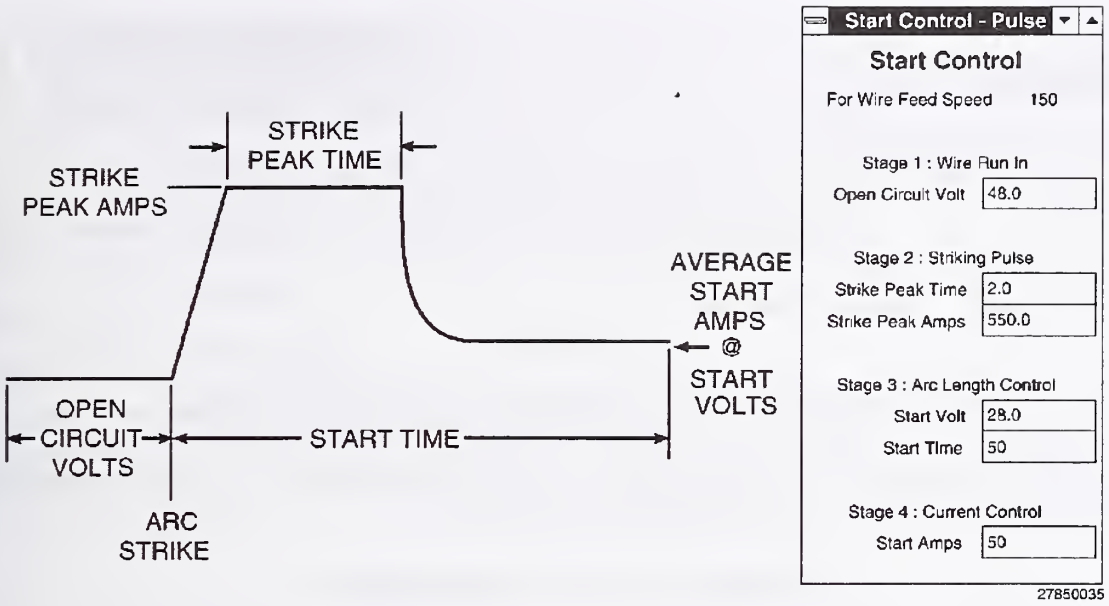

Fig. 4 Arc start control for pulsed GMAW process

Arc start, short clearing and arc end behavior can also be tailored to specific welding conditions. Fig. 4 shows start control, which is broken down into four stages. First is wire run in at open circuit voltage. Second a striking pulse is applied when the wire touches the workpiece. In stage 3 it regulates on voltage to establish an arc length and finally it switches over to current regulation. Fig. 5 shows a simple short clearing cycle, where voltage is used to detect a short, followed by electromagnetic pinch current ramp, and voltage is monitored for arc re-establishment. Fig. 6 shows the last pulse applied to eject any droplet before extinguishing the arc, so that the wire tip is conditioned for reliable arc start next time.

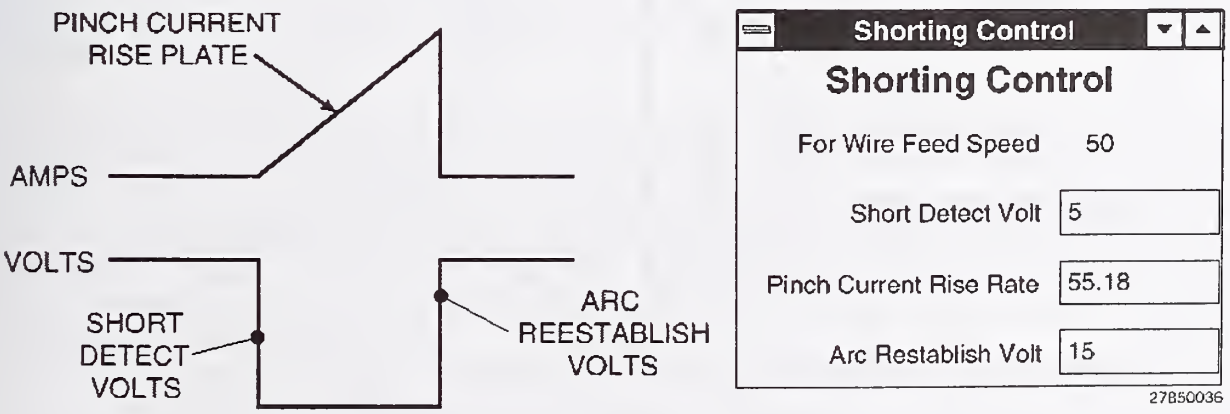

Fig. 5 Short clearing control for pulsed GMAW process

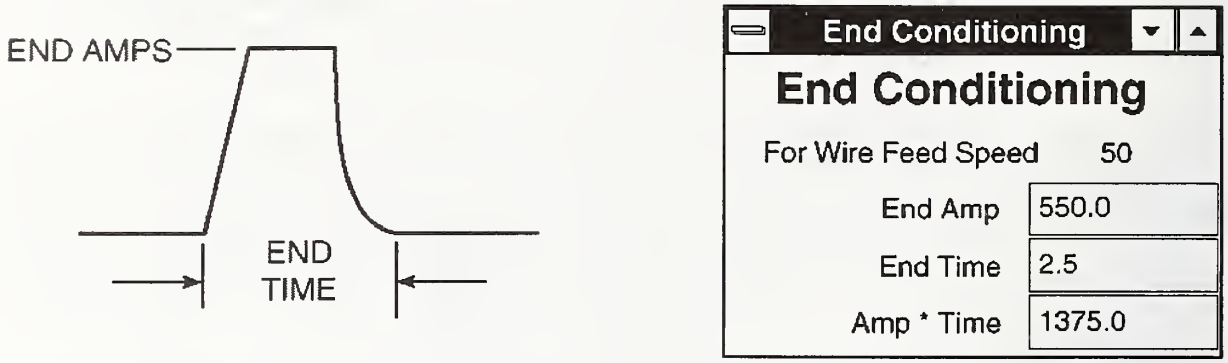

Fig. 6 End tip conditioning control for pulsed GMAW process

From a "global" perspective, Wave Designer provides productivity tools, such as parameter interpolation and extrapolation among selected work-points.

DEVELOPING STT WAVEFORM

Key parameters of an STT waveform are shown in Fig. 7. As in the case of pulsed GMAW, the waveform is developed for a given wire feed speed and CTWD.

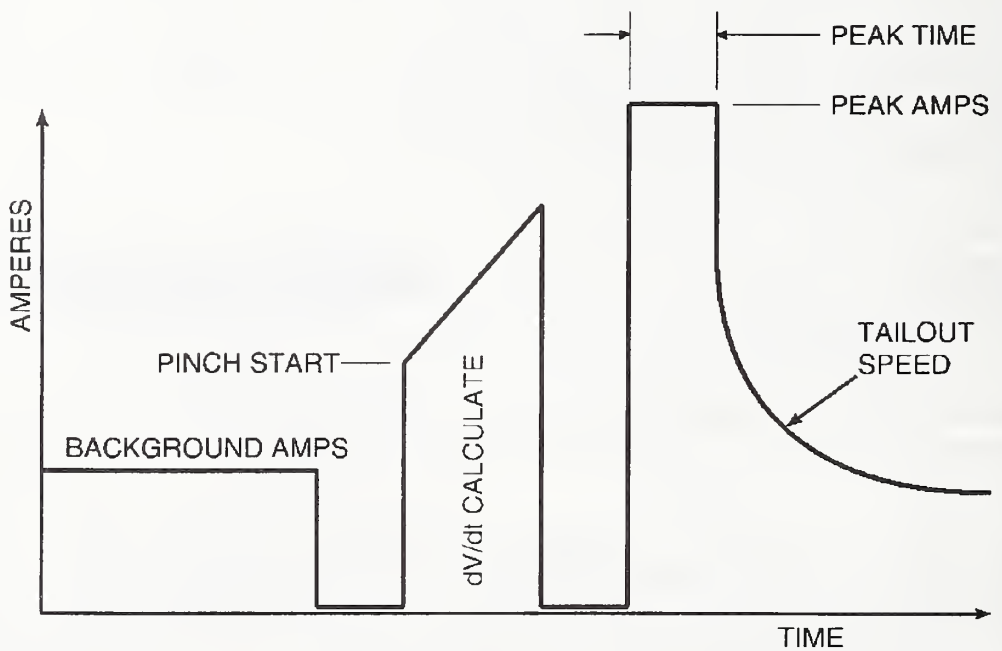

Fig. 7 STT parameters to define a base waveform

STT is a low spatter short circuiting transfer process that cuts back pinch force when liquid bridge is about to break into an arc (Ref. 1). A background current between 50 to 100 amps

maintains the arc and contributes to plate heating. After the electrode initially shorts to the weld pool, the current is immediately reduced for about 0.75 millisecond to ensure a solid short. Pinch current is then applied to squeeze molten metal down the pool while monitoring derivative of voltage (dV/dt). When liquid bridge is about to break, dV/dt increases sharply and power source reacts by cutting back current to 50 amps. Immediately following the arc establishment, a peak current is applied to produce plasma force pushing down the weld pool. Finally exponential tail-out and background are adjusted to regulate heat input.

SUMMARY

This paper introduces a Java program designed for pulsed GMAW and Surface Tension Transfer (STT) welding process development. It includes graphical online editors for controlling power source waveform and dynamics while welding, and an integral software oscilloscope to monitor actual welding signals.

In order to optimize for weld quality and process stability, the dynamics of welding power source must be developed for given welding conditions, such as material, wire size, wire feed speed, gas composition, cable inductance, and travel speed, etc. The dynamics of pulsed GMAW process are the commanded current waveform, the arc start behavior, the adaptive response to CTWD fluctuations, the reaction to a short, etc. A simple waveform is consisted of ramp up rate and time, peak amps and time, ramp down rate and time, and background amps and time. Since these large number of parameters are interrelated and difficult to master, equipment manufacturers often provide sets of pre-defined dynamics for specific conditions. Unfortunately, these factory-set characteristics often do not meet the needs of changing conditions in your welding applications.

To expedite pulsed GMAW weld development, Wave Designer is used to modify commanded wave shapes and monitor actual wave shapes, online with a computer controlled welding power source. A welding engineer can use a mouse to alter the waveform by grabbing and moving many graphical elements of a template and the results is shown both on screen and in the arc instantly. When one parameter is changed, many interrelated parameters are spontaneously changed to maintain a valid waveform.

While controlling the output of the power source, Wave Designer also serves many functions of an oscilloscope at the same time. It uses the power source itself as sensors, and graphically plots welding signals sampled at 10 KHz. The signals include arc current, voltage, instantaneous power, CTWD indicator, arc impedance, and the time derivative of above signals. It has mouse driven measurement capability. On a per weld basis, it also keeps track of average voltage, current, power, pulse or shorting frequency (for pulse or short-arc welding respectively), and accumulated weld energy and time.

Once a waveform is properly designed for a custom application, it can be stored in the non-volatile memory of the welding power source for production. It can also control and monitor a power source at a remote location, by employing two modems and telephone service. It has import and export features to work with commercial programs such as spreadsheets and Web browsers.

ACKNOWLEDGMENTS

The author wishes to express his sincere appreciation to Steve Peters and Bruce Fulmer for their work on pulsed GMAW; Russ Myers on ArcScope; Heath Suraba on STT; Dave Barton, Jeff Nadzam and Lisa Rini on field beta tests; and George Blankenship for his support and contribution to the project. All are Lincoln Electric employees.

REFERENCES

1. Stava, E. K., "The Surface-Tension-Transfer Power Source: A New Low-Spatter Arc Welding Machine", Welding Journal, January 1993, pp. 25-29

FULLY AUTOMATIC GMAW INSTALLATION

A. Kolasa*, P. Cegielski*

ABSTRACT

The general concept of a welding robotic installation, that has been designed and implemented in industries in collaboration of the Department of Welding Engineering of Warsaw University of Technology and Zakłady Automatyki Przemysłowej ZAP S.A. in Ostrów Wlkp. is described. The installation consists of commercially available two major component parts: industrial robot Irp-6 and synergic, microprocessor controlled MIG/MAG equipment Optymag 500R and is additionally equipped with a number of auxiliary units. All the system components have been manufactured in Poland. Some examples of an industrial applications in Polish industries are also presented.

INTRODUCTION

Automation of manufacturing and/or assembly processes used to be thought to be most applicable to the automotive industry and other highly productive industries, but it is now realised that it can be a feasible means of increasing productivity and quality in many types of manufacturing operations. In recent years, it has become particularly attractive to the welding operations. Beside a number of advantages resulted from an automated welding system application, such as increased productivity and high repeatability, a significant improvement of an operator natural environment is a vital factor. A human labour from the role of a direct manufacturer is replaced by the role of operator and/or supervisor. In the case of welding processes the removal of man from dangerous and hazardous environment is of great importance. On the other hand an automation of welding processes creates high requirements to be met by both personnel and the equipment used. The most significant of them are:

- high dimensional accuracy of parts to be joined,
- high professional skill of personnel involved,
- high accuracy, repeatability and stability of welding parameters and welding conditions.

The optimal solution of an automated welding system should be simple in operation, reliable, safe for operators and equipment, as well as of low cost. The MIG/MAG welding robotic system being presented in this paper meets all the above requirements. The system has been designed, manufactured and implemented as a result of the co-operation between Department of Welding Engineering of Warsaw University of Technology and Zakłady Automatyki Przemysłowej ZAP S.A. in Ostrów Wielkopolski

*** Department of Welding Engineering, Warsaw University of Technology, Narbutta St. 85, 02-524 Warsaw, Poland**

ROBOTIC WELDING SYSTEM CONFIGURATION

Preliminary assumptions

The basic configuration of the MIG/MAG welding installation consists of the following component parts: industrial robot Irp-6 with the robot control unit USR-6, welding MIG/MAG equipment Optymag 500R, positioning table PH-2-100 with work fixtures, torch cleaner and other necessary accessories, that make the entire system fully productive. All component devices are controlled from the robot controller by the use of digital input/outputs. In case of complex application or the use of the installation as a part of a flexible manufacturing system a central master controller can be easily applied.
The robot that was used in the presented installation is of an anthropomorphic type, manufactured by Zakłady Automatyki Przemysłowej ZAP S.A. in Poland. It consists of three major component systems: the supplying system, the mechanical system (manipulator), and the controller. It has five servo-driven motion axes (fig. 5) with repeatability less than ± 0.20 mm and the handling capacity of 6.0 kg. Its controller consists of microcomputer, memory units and binary input/outputs for connection with other system devices and motion axes control modules.

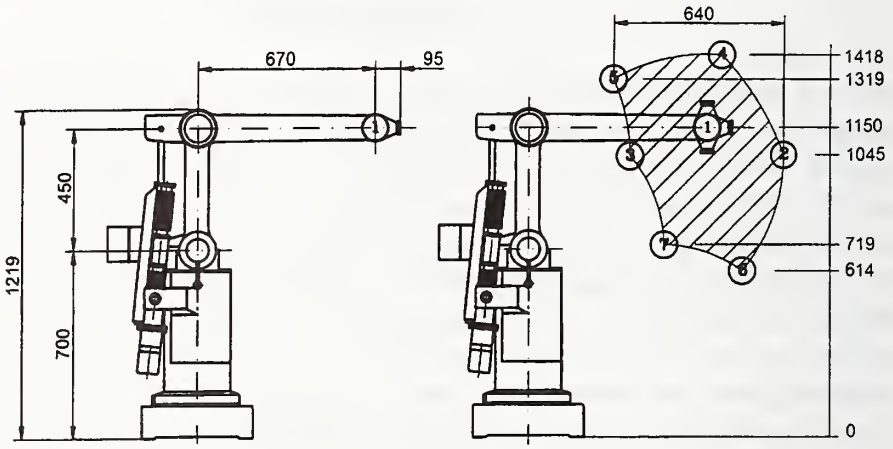

Fig. 1. Dimensions and working range of Irp-6 robot [2].

The semiautomatic synergic MIG/MAG welding equipment, of the commercial name Optymag 500R [3], manufactured by Zakłady Urządzeń Technologicznych Bester in Bielawa, Poland has been selected and adopted for the installation. It can be used for welding low-carbon and low-alloyed steels with an active shielding gases as well as stainless steels and aluminium alloys with inert shielding gases. The microprocessor controlled synergic power source can supply both constant and pulsed welding current up to 500 amps with an option to store up to 49 sets of welding parameters, referred to as welding programs. The power source is equipped with separate wire feeder PDE-3W and water cooled machine welding torch.
These two commercial machines, i.e. the robot and the welding equipment have been connected together as well as the constructed installation has been equipped with all necessary auxiliary devices to make it fully productive. Additionally it has been assumed that the installation should be simple in both construction and operation, be reliable, be low-cost, and be safe for the operator, all installation equipment and welding processes performed. To reach these project objectives, the following tasks have been undertaken:

- the adaptation of welding equipment for continuous duty and the design and implementation of an interface connecting it with the robotic controller,
- the completion of auxiliary devices, such as positioning table, torch cleaning device, electrode wire cutter, etc.
- the design and manufacturing of a positioning table,
- the design and manufacturing of necessary auxiliary devices, such as a torch cleaner, electrode wire tip cutter, etc.

The installation has been presented on the 7th conference of this type in 1997 and described in the conference proceedings. Since than the rebuilding of the robot as well as updating changes of other installation components have been done.

The rebuilding of the robot Irp-6

Comparing to the former structure of the robot [1], the significant changes of the control system, the software and the manipulator structure have been implemented. The entire electronic package has been modernised and the widely used standard of an open VME bus has been applied. The system is controlled by 32-bit microprocessor. Due to these changes the number of advantages have been achieved, such as: increased reliability, non-failure operation, noise immunity as well as easier operation of external axes, that enables both their simple connection in any flexible manufacturing systems and operation in a network. As a result the dynamics of the robot manipulator has been improved and motion speed of each axe has been increased around 20%.
The new control system is based on real-time operation system, the enables the robot reaction with no delay, multipurpose and concurrent operation of the entire system. In order to visualisation and control the programme being just running, the touch-screen has been applied, Independently of the standard programming unit it enables alternatively the edition of another control programme. Both programme software can be run together or separately, depending on the choice of the operator.

Control system of the installation

The basic component parts of the robotic arc welding system are an industrial robot and welding apparatus. All industrial robots are equipped with a microprocessor control system owing both programming and data memory units. Similarly, recent welding power supplies are also controlled by microcomputer systems with its own programming and memory units. Therefore modern robotic welding installations become integrated multicomputer systems [4]. In order to assure proper communication between these microcomputer controllers, they must be connected with an interface using their own input and output systems [1, 5, 6].
The interface is used to transmit signals between them, that control and supervise the welding process. Those signals could be of either control and/or alarm mode. Signals of the first kind are used to select proper welding parameters and directly control tool and work motion devices, while signals of the second kind have to warn each of the components against any malfunctions that might occur and cause a defence reaction. usually the interface is located in and integrated with the robot controller or welding equipment controller.
The control unit of the welding power source allows a direct access to any set of parameters stored in a memory by simply pointing out the number of the welding program. The robotic

controller was equipped with 16 digital output/inputs that could be easily used for this purpose. Such a solution made the interface structure simple and low-cost in manufacturing. The designed interface uses two-directional digital signals for mutual communication between the robotic controller and the welding equipment. Assisted with relevant software the robotic controller played the master role in the controlling and the supervising of the system operation. Control signals are limited to the most significant for the MIG/MAG process (fig. 2) as follows.

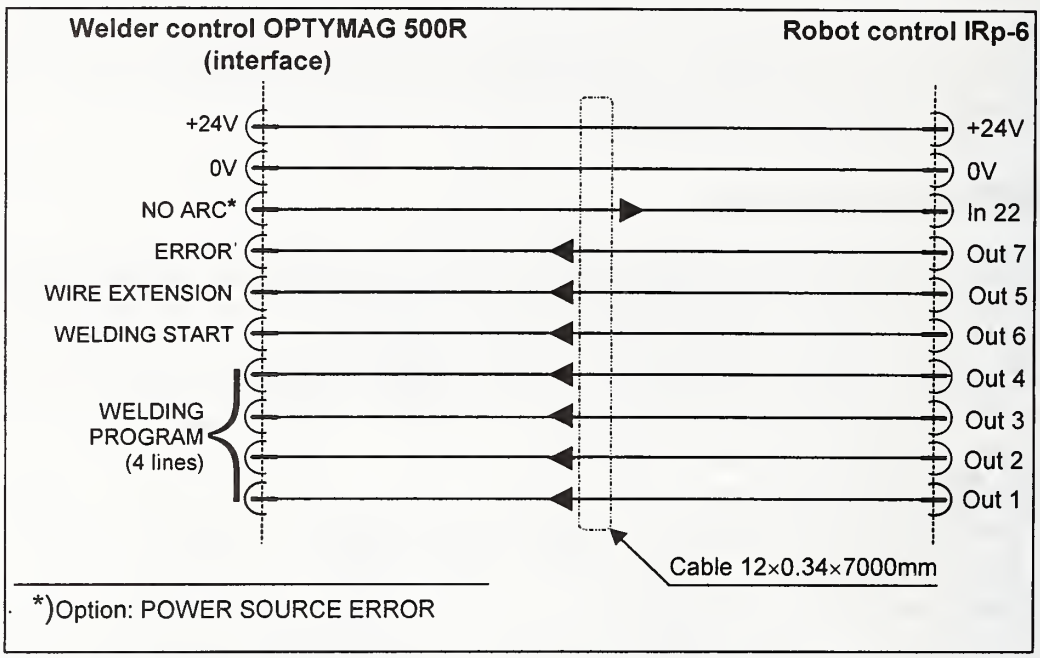

Fig. 2. Block diagram of the robot controller and welding equipment controller interface.

The *"No arc"* signal is generated by the currant flow sensor after a sudden welding arc extinguishing and effects a reset of both the power source and the wire feeder. This signal is also used as a confirmation signal of the arc ignition while the welding operation is being initiated. The „time out" is set on 2.2 sec.

The *"Error"* signal is sent from the robotic controller that monitors all malfunctions and resets the power source and the wire feeder, i.e. the welding operation may be resumed once the error has been remedied and a new start instruction has been given. This signal may be generated by any of the following malfunctions:

(i) *overtemperature*; if the duty cycle is exceeded or if the cooling system malfunctions,
(ii) *no program*; if the program selector does not act correctly or the parameters set is incomplete,
(iii) *power on reset*; for 2 sec. after the power source is switched on,
(iv) *robot reset*; if an emergency stop command is given for the robot.

The *"Wire extension"* signal is used for wire inching after the welding operation in order to cut off the end of the wire to a required length by an automatic wire cutting unit.

The *"Welding start"* signal actuates the power source, the wire feeder and the shielding gas valve.

The *"Welding program"* signal is used for selection by the robot control unit through the interface of one out of fifteen sets of parameters which are stored in the welding power source memory. This signal is coded on four lines and decoded on one-out-of-fifteen basis.
Additionally to the *"no arc"* signal, it is planned to increase the number of welding equipment emergency signals for such signals as *"no water", "no gas", "no wire", and "thermal overloading"*. After modification this join signal will be called the *"power source error"*.

Continuously controlled positioning table

The two-stand positioning table PH-2-100 (fig. 3) is used for spatial positioning of the work to the position most convenient to welding and turn it when required with the welding speed, The stand change of 180 deg. is done by the pneumatically driven rotation around the vertical axe of the positioner while the work rotates around the horizontal axe driven by the electrical motor. The positioning table design allows for assembling other positioner structures using the same component subassemblies. The hoisting capacity of the positioning table is 100 kg, positioning accuracy ±0.2 mm, dimensions 2400 x 1800 x 1775.

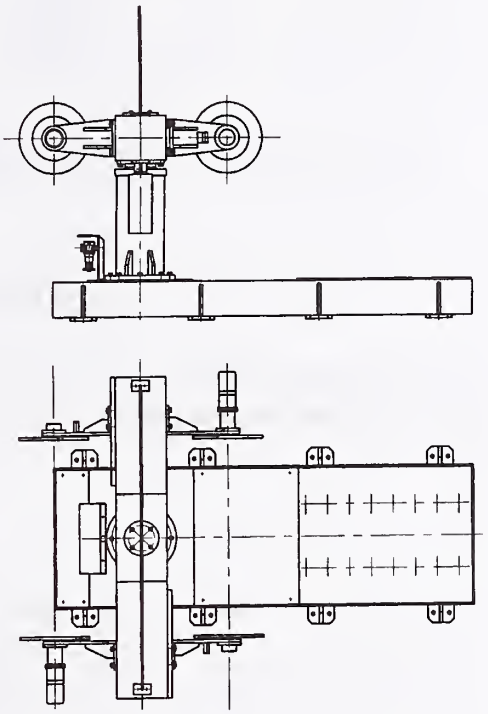

Fig. 3. Positioning table PH-2-100

Together with described above updating changes of the component parts of the installation, the controller of the positioning table has been improved as well. Two new options have been added, i.e. *"partition"* and *"rotation"*. Both enable the partition of one turn of the table into as many as up to 99 parts, the option that can be used in all cases when the same kind of parts are manufactured repeatable and they can be located round the table. By rotating the table from one part to another the manufacturing programme is repeated for each manufacturing part.

Auxiliary devices

The robotic welding installation requires a number of component devices, such as electrode wire tip cutter (fig. 4a), mechanical torch cleaner with lubrication of the gas nozzle or anticollision torch holder (fig. 4b). The installation can be optionally equipped with a base trunk traverse, band conveyors for works transportation or other auxiliary devices regarding to a certain application and arrangement of the job being done.

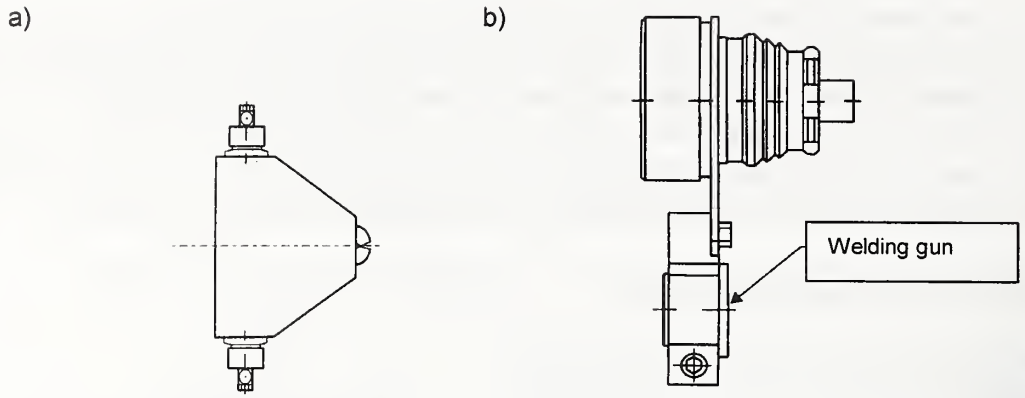

Fig. 4. Auxiliary devices: a) electrode wire tip cutter UT-2, (b) anticollision welding torch holder

EXAMPLES OF APPLICATION

Fig. 5 shows the basic arrangement of the robotic MIG/MAG welding system. Such arrangement has been implemented in one automobile factory for welding the rear bridge housing of a delivery truck.

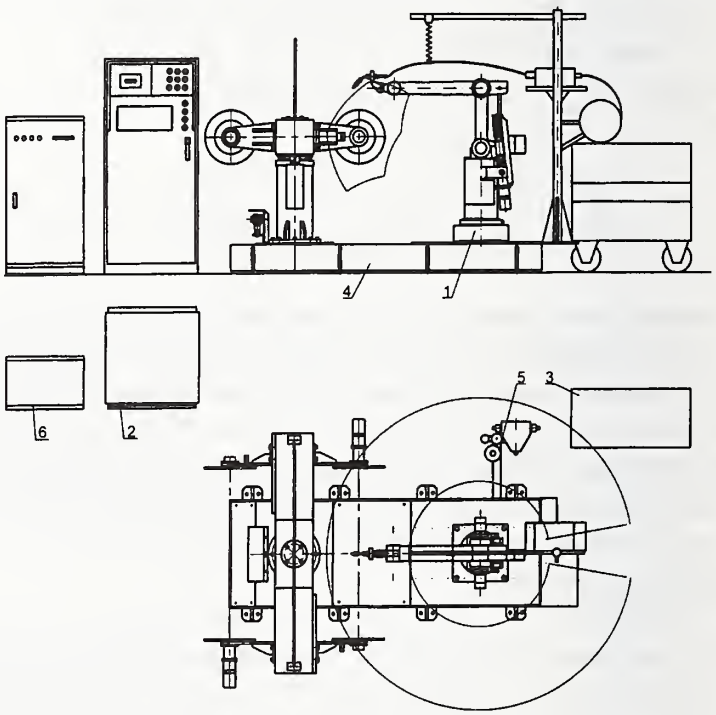

Fig. 5. Typical robotic MIG/MAG welding arrangement:
(1) Irp-6 robot,
(2) robot controller USR-6,
(3) welding power source Optymag 500R,
(4) positioning table PH-2-100,
(5) welding torch cleaner,
(6) positioning table controller.

Another, interesting example of not typical application of the robotic welding system is automatic rebuilding of worn-out parts (fig. 6). In this case the system is controlled and supervised by the master controller. The work is fixed on the positioning table 3. Next, the laser scanner placed in the robot wrist identifies the part and by scanning its surface measures the depth of worn out material. The measurement data is compared by the master controller with the reference contour of the part and the system automatically generates the surfacing programme

and next supervises it until the part gains its nominal dimensions. Once the job is done, the next part is fixed and the process is being repeated.
The several application of given above kind have been already implemented in Polish industries.

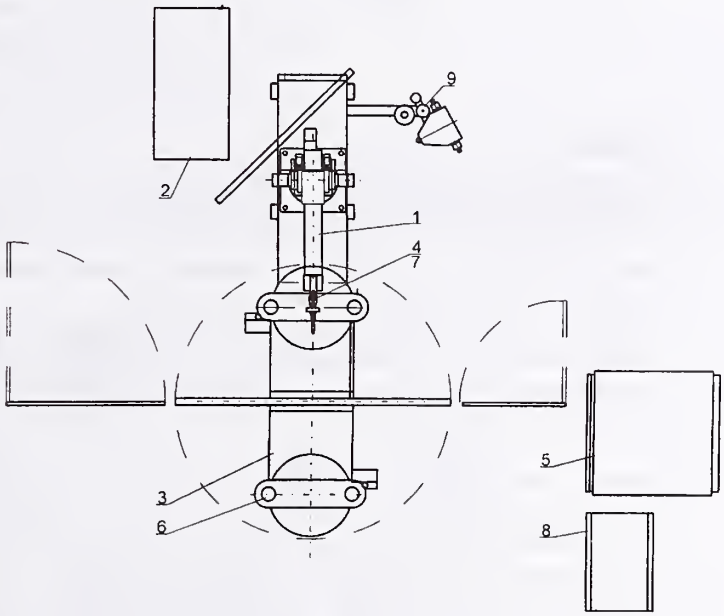

Fig. 6. Robotic surfacing arrangement for automated rebuilding of machine parts:
(1) Irp-6 robot,
(2) welding power source Optymag 500R,
(3) positioning table PZP-3-150,
(4) anticollision torch holder,
(5) robot controller USR-6 with master controller SN-1,
(6) work fixture,
(7) laser sensor SLS 5000,
(8) positioning table controller,
(9) torch cleaner with wire tip cutter.

SUMMARY

Presented here the concept of the robotic installation is a compromise between the requirements concerning the industrial robot - welding equipment system employed to a typical welding application and the technical specification of these two component parts. The implementation of the installation done so far approved the correctness of the design assumptions and practical solutions. The flexibility of the installation allows various kind of application since any modification of the system components is very simple and can be easily implemented.
The presented here automatic GMAW installation due to its programming abilities, visualisation of the job being performed and relatively low price seems to be interesting proposal not only for industrial application but for teaching purposes as well.

REFERENCES

1. Kolasa A., Cegielski P. "Fully Automatic GMAW System", Proceedings of Seventh International Conference on Computer Technology in Welding, San Francisco 8-11. 07.1997.
2. Industrial Robot Irp-6. Operating manual, Zakłady Automatyki Przemysłowej ZAP S.A. Ostrów Wielkopolski (in Polish).
3. Optymag 500. Operating manual, Zakłady Urządzeń Technologicznych Bester, Bielawa (in Polish)
4. Misiurewicz P. "Podstawy techniki mikroprocesorowej" WNT, Warsaw, 1991 (in Polish).
5. Roboter Interface TSST 153. Operating manual, Fronius Schweissmachinen, Austria.
6. Robot Welding System A30A. ASEA Pamphlet, Västeras, Sweden.

A Welding Cell That Supports Remote Collaboration

Jim Gilsinn, Bill Rippey, Joe Falco, Tim Quinn, Bob Russell, Keith Stouffer
National Institute of Standards and Technology
Intelligent Systems Division
http://www.isd.cme.nist.gov/

Abstract
Discrete part manufacturers using robotic arc welding cells often have several more geographically distributed plants than welding experts. This ratio often leads to costly downtimes due to both logistic and communication deficiencies between weld engineers and the production site. The ability for engineers to remotely access welding cells from their home office to anywhere in the world can yield several benefits. These include quicker response time to problems, improved weld quality, increased production line reliability, and reduced travel time for weld engineers. We describe the NIST testbed technology and infrastructure for remote manufacturing that has been applied and demonstrated on a robotic welding cell where valuable process data can be made available to remotely located engineers in real-time or near real-time.

Remote access to cell information is made possible by open-architecture interfaces that tie the robot controller, weld controller, and cell controller together. The welding cell allows remote access through the internet via: an audio/video system for communicating with the operator, a pan/tilt/zoom camera inside the welding cell for viewing the cell in operation and inspecting parts after a weld, a real-time display for welding process data, a web-based graphic simulation of the robot arm driven by real-time motion commands, and an intelligent monitoring system with an internet accessible welding database. The cell incorporates multiple weld monitoring systems with data logging capability to capture process variables during a weld.

Keywords
weld cells, monitoring, remote collaboration, World-Wide-Web, internet, weld sensing, interface specifications

INTRODUCTION

Discrete part manufacturers using robotic arc welding cells often have several more geographically distributed plants than welding experts. This ratio often leads to costly downtimes due to both logistic and communication deficiencies between weld engineers and the production site. The ability for engineers to remotely access welding cells from their home office to anywhere in the world can yield several benefits. These include quicker response time to problems, improved weld quality, increased production line reliability, and reduced travel time for weld engineers. The NIST testbed enables remote collaboration by providing access to the weld cell information via the internet. The data can be accessed remotely with close to the same ease an on-site.

Data produced by cell controllers and dedicated weld monitors can be accessed and displayed over the internet using a combination of general purpose web browsers and special-purpose programs. The welding cell allows remote access through the internet via: an audio/video system for communicating with the operator, a pan/tilt/zoom camera inside the welding cell for viewing the cell in operation and inspecting parts after a weld, a real-time display for welding process data, a web-based graphic simulation of the robot arm driven by real-time motion commands, and an intelligent monitoring system with an internet accessible welding database.

The cell incorporates multiple weld monitoring systems with data logging capability to capture process variables during a weld.

WELD CELL ARCHITECTURE

Figure 1 shows the current architecture of the NIST Gas Metal Arc Welding (GMAW) cell. Three controllers form the framework of the cell: a robot controller that controls the robot, an intelligent welding controller that controls the welding process, and a cell controller that oversees the welding cell and interprets the weld program. Other elements of the architecture deal mostly with monitoring sensors and storing weld data.

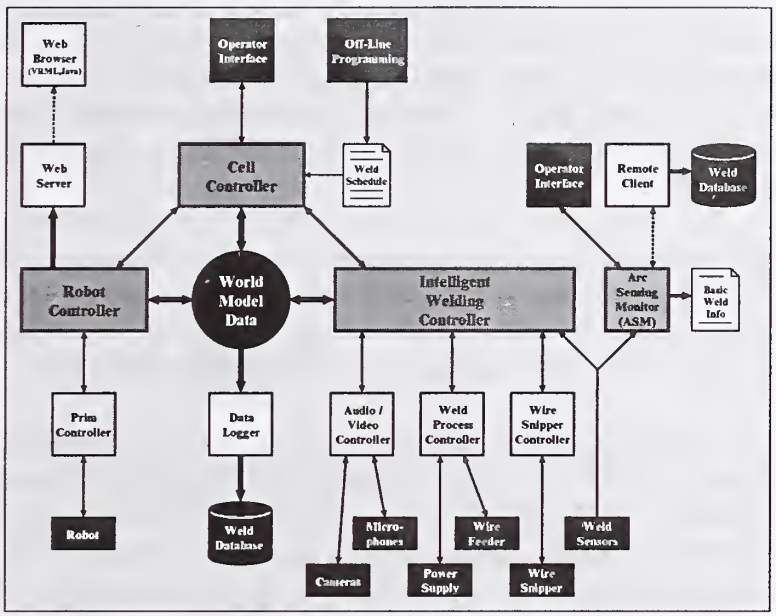

Figure 1 - NIST GMAW Cell Architecture

The **robot controller** controls the robot joint actions to produce the commanded torch path and orientation. The robot controller also makes some of its internal control data available to the World Model [1] and to a web server though open architecture interfaces. Real-time torch location and orientation data is useful when combined with weld process data to relate weld process variables to part geometry.

The **intelligent welding controller** has three sub-controllers: the audio/video controller, the weld process controller, and the wire snipper controller. The audio/video controller handles the microphones and cameras for observing the weld from remote locations. The weld process controller operates the welding equipment to produce the desired weld. The wire snipper controller trims the welding wire to a known length. Through-the-arc sensors feed weld process data back to the intelligent welding controller.

The **cell controller** supervises the welding cell. It interprets the weld program and sends commands to the robot and intelligent welding controllers and monitors their status. It also

handles the operator interaction. All commands from the user to cell components go through the cell controller.

The other cell elements monitor sensors and log data to local files. The world model data consists of all data in the welding cell that is shared between controllers and elements. These include torch position, arc voltage, arc current, error states, etc. The data logger accesses all of this data and stores it in local welding data files.

Monitoring Systems

Monitoring systems gather sensor data at high rates (1-10 kHz), and at minimum, store the data. Filtering and averaging calculations reduce the amount of data that needs to be supplied to other systems, both in real-time and in database files. Some monitors compare real-time data to limits and report alarms when the limits are exceeded. The primary sensors used in weld monitoring systems measure arc voltage and current. Additional sensors may measure wire feed speed, shielding gas flow rate, coolant flow, etc. Data from these sensors are used to model weld quality.

The NIST GMAW cell architecture in Figure 1 shows weld sensors that feed into an embedded monitoring system. NIST's monitoring system uses arc voltage and current sensors to determine weld quality. The voltage sensor is attached to the power supply output terminals. The current sensor is a hall effect current transducer surrounding the electrode cable.

We also incorporate two standalone monitoring systems into our GMAW cell: the Arc-Sensing Module (ASM) [4] developed by the Materials Reliability Division at NIST, and the ARCAgent-2000 [2] developed by Impact Engineering*. Both systems measure voltage at the power supply output terminals. The ASM uses the same hall effect sensor data as the embedded monitoring system, but the ARCAgent uses a current sensor in-line with the power cable. The ARCAgent-2000 also has the capability to use wire feed speed and gas flow sensors, but neither is used in this implementation.

While a weld is being performed, the embedded system records voltage, current, and torch position. The ASM records voltage, current, and time. After the weld has been completed, it computes a modeled arc quality index. The ARCAgent records voltage, current, and time. It filters the data and produces average values and analysis of the electrical characteristics of the weld such as pulse frequency and average voltage.

All three monitoring systems store their data to their own respective files. These files can be stored and retrieved at a later time if a particular weld needs to be analyzed. Currently all three are implemented on different PC platforms and store to local disks. A near future issue is to improve the integration of these files.

* DISCLAIMER: Certain commercial equipment, instruments, or materials are identified in this paper to specify the experimental procedure adequately. Such identification is not intended to imply recommendation or endorsement by the National Institute of Standards and Technology, nor is it intended to imply that the materials or equipment identified are necessarily the best available for the purpose.

Intra-Cell Communications

Real-time communications between processes in the cell employ a NIST communications utility called the Communications Management System (CMS) and a software API called the Neutral Message Language (NML). [9] CMS uses a shared memory model of communications that has been implemented over many different media, including shared memory, dual port RAM, and ethernet. NML is a software interface that utilizes CMS communications, allowing a user to send messages between software modules easily. In addition to allowing intra-cell communications, NML also allows servers to access the data from anywhere over the internet.

Internet Interfaces

Figure 2 shows how the welding testbed interfaces to the internet. The pan/tilt camera is a commercial product that has an embedded web server. It exports images at about 1 Hz, and can accept aiming and zooming commands. A web-based interface to the server is used to communicate with the weld cam. Anyone on the internet running a general purpose browser can view images and control the camera. Figure 3 shows a top view of the welding table and robot arm with torch.

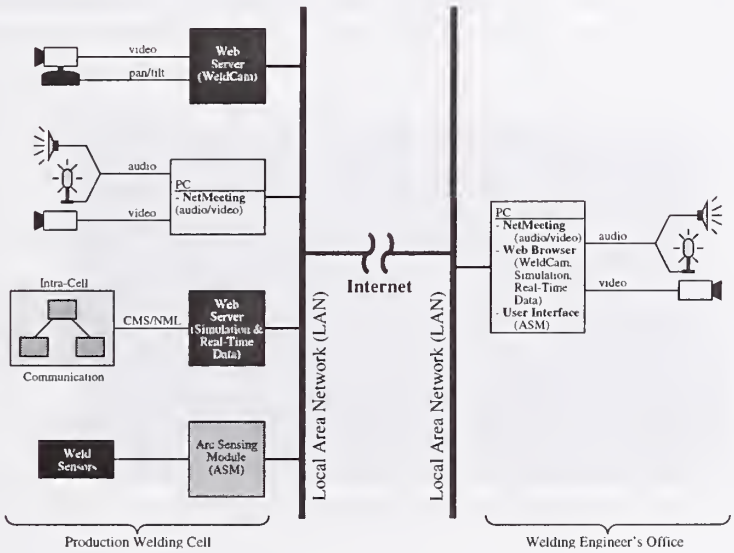

Figure 2 - Internet Interfaces to the NIST Welding Testbed

The stationary camera is attached to a low cost commercial video board. NetMeeting software from Microsoft® integrates video from the board and audio from a microphone. Two way communication is possible with someone else anywhere on the internet via NetMeeting.

The cell web server connects to the intra-cell NML interfaces, and makes their information accessible. This allows internet processes to read intra-cell data using TCP/IP protocol. Typical data rates are 20 Hz for torch position and process data.

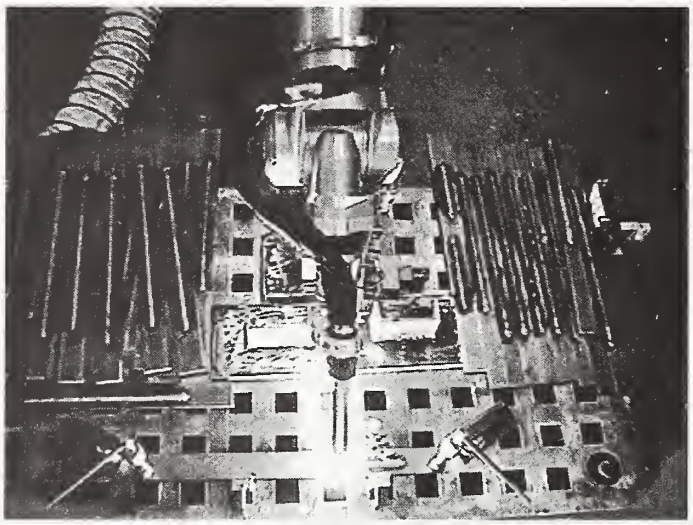

Figure 3 - Live Video Feed from Weld Camera

The Arc Sensing Monitor has a custom interface to the internet that employs TCP/IP socket protocol. The remote user interfaces to this custom interface, allowing them to download a database of welding information. This weld database contains raw sensor data as well as processed data such as weld quality and estimated pulse frequency. Due to the ASM's custom interface, it is not possible to access the weld database through a general purpose web browser at this time.

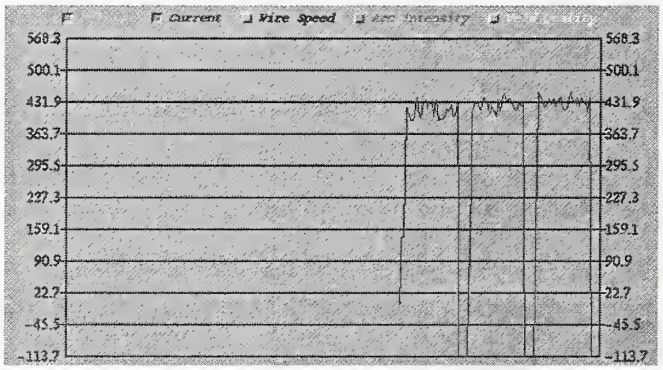

Figure 4 - JAVA Strip Chart Graph

The embedded monitoring system has added capabilities to remotely access to the data. While a weld is being performed, the system allows the process variables to be remotely viewed in real-time with a JAVA strip chart graph as seen in Figure 4. This graph shows real-time data that can give an experienced welder a feel for what is happening with the weld as it is being performed.

NIST has also developed technology to overlay recorded process data onto a three dimensional model of the part to give the operator a better view of where possible defects may have occurred. Figure 5 shows an automotive strut part with voltage and current displayed as lines in a 3D plot. This display is possible due to sharing of data between the welding and robot controllers and the synchronization of the two data streams by the cell controller.

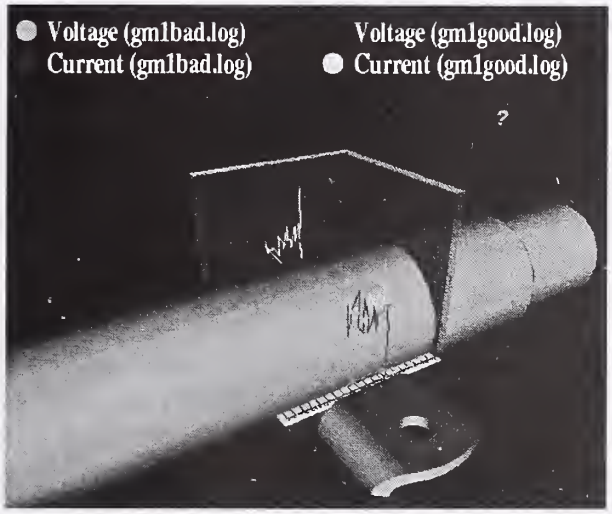

Figure 5 - VRML Plot of Voltage & Current Overlaid on Part Geometry

All of the above technologies discussed above can be seen at the project web site http://www.isd.cme.nist.gov/projects/awms/ .

REMOTE COLLABORATION SCENARIO

A weld engineer establishes audio and video communications with operators at the welding cell. The weld engineer can remotely examine ASM settings and change them if needed. The engineer operates the weld cam to survey the cell, and to see close up views of the part to be welded, fixtures, robot torch, etc. The engineer readies the ASM for monitoring and the operator initiates a welding sequence at the cell. The audio link allows the engineer to hear the weld at reduced fidelity due to bandwidth limitations. The engineer watches the strip chart display for instantaneous voltage and current and the robot simulation for robot motion and process events.

The engineer operates the weld cam to get a close up view of the completed weld. He connects to the ASM and downloads the weld data for the completed weld. The ASM remote program enters the data in the database and filters it to detect events and to model weld quality. The engineer and shop floor operator discuss the results of the experiment, and decide to try a new test. The interactions of the engineer and operator occur almost as if the engineer was on the shop floor.

NEXT STEPS

NIST will be looking into internet security issues of remote access to welding information. Proprietary information that may need protection from remote access includes CAD data for weldments, video data, weld programs, and data from the completed welds.

In the near future, we will pursue the following issues to improve remote capabilities:
- Increasing video frame rates for internet images;
- Automating audio and video recording;
- Synchronizing data streams from different controllers and monitors;

- Centralizing world model data acquisition to simplify interfaces for external access;
- Integrating the testbed with higher level collaborative tools [10];
- Automating co-display of part geometry and sensor model data (Figure 5);
- Incorporating the commercial monitor in remote access, either by adapting interfaces ourselves or using modifications made by the vendor;
- Exploring standard interfaces both for integration of cell components and for remote access;
- Editing the weld program remotely; and
- Initiating cell events, like cycle start, remotely.

NIST is working as a member of the AWS-A9 committee on Computerization of Welding Information to develop a specification for the exchange of welding information between intelligent systems. The NIST testbed will be used to test specifications while they are still in draft stages. One current working document is the Arc Welding Activity Model (available at http://www.isd.cme.nist.gov/projects/awms/aws/).

REFERENCES

[1] Albus, J., "A Reference Model Architecture for Design and Implementation of Intelligent Control in Large and Complex Systems," International Journal of Intelligent Control and Systems, Vol. 1, No. 1, 15-30, 1996.

[2] Impact Engineering, ARCAgent-2000 Networking Overview, 1998.

[3] Madigan, R.B., Quinn, T.P., Siewert, T.A., Control of Gas-Metal-Arc Welding Using Arc-Light Sensing, NIST Internal Report 5037, 1995.

[4] Quinn, T.P., Madigan, R.B., Sensing of Arc Welding Process Characteristics for Welding Process Control, U.S. Patent Number 5,756,967, 1998.

[5] Quinn, T.P., Madigan, R.B., Siewert, T.A., "An Electrode Extension Model for Gas Metal Arc Welding," Welding Journal, Vol. 73 (10): 241s-248s, 1994.

[6] Quinn, T.P., Madigan, R.B., Smith, C.B., Blachowiak, E.G., "Weld Defect Decisions Using Through-The-Arc Sensor Data," Proc. of Seventh International Conf. on Computer Technology in Welding, NIST Special Publication 923, ed. Siewert, T., 1997.

[7] Rippey, W.G., Proceedings of NIST Workshop: Industry Needs in Welding Research and Standards Development, NIST Internal Report 5822, 1996.

[8] Rippey, W.G., Falco, J.A., "The NIST Automated Arc Welding Testbed," Proc. of Seventh International Conf. on Computer Technology in Welding, 1997.

[9] Shackleford, W., Proctor, F., Real-Time Control Systems Library - Software and Documentation, Online Documentation, http://www.isd.cme.nist.gov/projects/rcs_lib/ .

[10] Steves, M., Knutilla, A., "Collaborative Technologies for Global Manufacturing," Proc. Of ASME International Mechanical Engineering Congress and Exposition (IMECE): Symposium on Manufacturing Logistics in a Global Economy, 1999.

Session B5: Real-Time Weld Sensing and Control Systems: Weld Process Automation – Communication and Interfaces

ON-LINE SENSING OF LASER SURFACE MODIFICATION PROCESS BY COMPUTER VISION

D. Hu, M. Labudovic and R. Kovacevic

ABSTRACT

Laser surface modification with alloying or re-melting often has unstable results. To achieve on-line control, process sensing is the key technology. This paper introduces molten pool imaging as laser processing feedback. Well-contrasted molten pool images are acquired in experiences eliminating the strong light from spatter and plasma. The image shows a clear correlation with laser power absorbed by bulk material, which can be used to provide molten depth on-line estimation in laser surface modification with constant scan velocity. An algorithm for real time image processing is developed. The algorithm shows a robust and high-speed performance.

Keywords: Laser surface modification, Computer vision, Image processing, Neural network.

INTRODUCTION

Laser surface modification comprises a family of methods such as transformation hardening, melting, alloying and cladding. It allows a user to build a part with totally different properties in surface layer from bulk material. The surface layer can obtain high wear, fatigue or erosion resistance while the bulk material can still keep its original properties such as good strength.

The theory of laser surface modification is based on rapid thermal cycling due to the excellent characteristic of laser that can produce more concentrated heat energy on the part. A high cooling rate can be reached while the heat conducts into the cold bulk material, which results in a self-quenching process. This self-quenching process produces microstructure refinement, phase transformation or formation of supersaturated solid solution [1].

One typical application of laser surface modification is the thermochemical treatment to the surface of titanium which has excellent mechanical and chemical properties such as high strength, good biocompatibility and high corrosion resistance but with low resistance to sliding and abrasive wear. When nitrogen is blown into the molten pool produced by laser on titanium material a thin golden layer of titanium-nitride forms which shows great hardness (HV=2000-3000 kg/mm^2), high melting temperature, high temperature stability and low electrical sensitivity[2]. But irregular qualities are often produced because the processes are too sensitive to the processing parameters, such as input laser power and scanning velocity. For example, under certain conditions a 10% fluctuation in laser absorption will cause a 50% change in molten depth. Therefore, real-time control of the process is required to produce more stable and repeatable molten depth and adapt to the complex shape of the part.

Accurate and reliable process sensing and feedback is the key to achieve such successful control. Owing to the complex interaction between laser and material, there are several kinds of sensors to be used in laser welding to monitor the welding process (e.g., plasma detector, acoustic sensor,

Department of Mechanical Engineering, Southern Methodist University, PO Box 750337, Dallas, TX, 75275

spatter detector, temperature probe and keyhole imager [3]) to estimate the welding penetration. A few works also have been done in laser surface modification in which thermal pictures are acquired and analyzed to estimate molten depth [4, 5]. Still, sensing the laser process is a problem to be solved. Due to the high light of plasma and spatter, no direct molten pool image can be acquired as an efficient sensing to the laser surface modification process.

In this study, an ultra-high speed shutter camera with pulsed laser illumination (named Laser Strobe vision system) has been used as laser process monitor - which is able to acquire well-contrasted images of the molten pool. The experiment shows that there is a clear correlation between molten depth, molten pool size and geometric shape during constant scan velocity processing. A real-time algorithm of image processing and recognition has been developed to calculate the molten pool's geometric parameters - which will be utilized for feedback of the surface modification process in further close-loop control.

In the next section, a system set-up and preliminary experiment results are illustrated - which provide a rough correlation between molten depth and the molten pool's geometric shape. A real-time algorithm of image processing is discussed in section 3. In section 4, conclusions are presented.

PRELIMINARY EXPERIMENTS

In order to certify whether the image of the molten pool is an efficient information source to reflect the molten depth - while trying to find the potential correlation between molten depth and the molten pool's geometric shape, a series of preliminary experiments have been done using different pairs of laser powers and scan velocities as processing parameters. Nd: YAG laser is the laser source operated in CW mode. Stainless steel is chosen as the treatment material at the beginning.

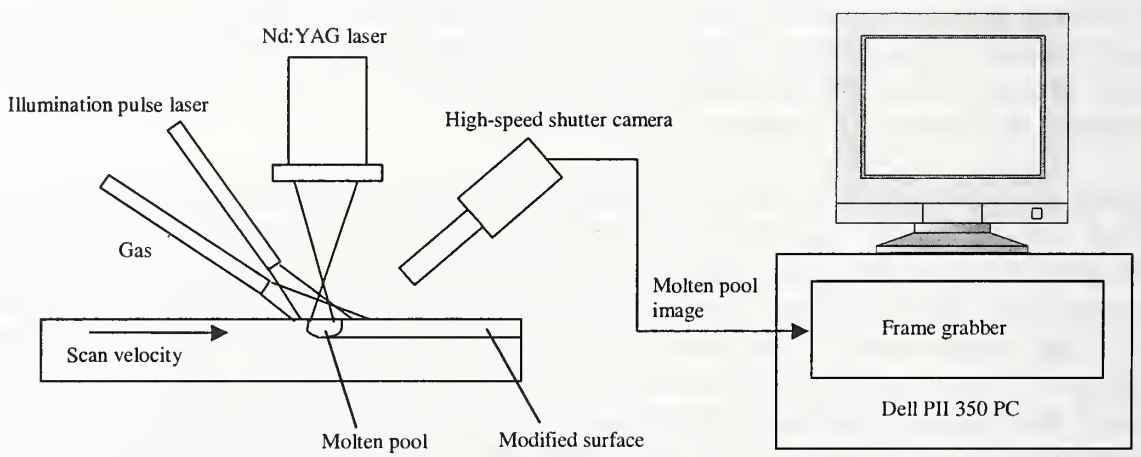

Figure 1. Experience system set-up.

Figure 1. gives the experiment system set-up. Laser fiber conducts a 337nm near the UV laser to illuminate the Nd:YAG laser treating area. The illuminating laser is a pulse laser with a 5 ns pulse duration synchronizing with the high-speed shutter of the camera. The camera also is installed an UV filter only allows light near 337nm wavelength to pass. Whenever the

illuminating laser is triggered, the camera shutter is open 50 ns to capture an image. During the illumination period, the intensity of the illuminating laser can cover the spatter and plasma light. Due to reflecting of the mirror-like molten pool, a well-contrasted image of the molten pool can be obtained. Nitrogen is used as the alloying gas while it also blows away the plasma generated from the molten pool.

A frame grabber installed on a PII 350 PC computer acquires images from the high-speed shutter camera at 30 Hz. Real-time image processing, recognition, molten depth estimation and close-loop control will be completed on the same computer. The experiment results are shown in Figure 2. and Figure 3.

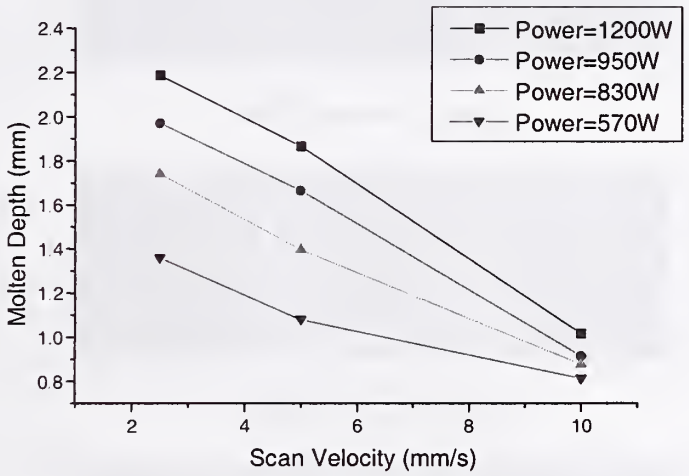

(a) Depth of the modified surface vs. scan velocity for different laser output power.

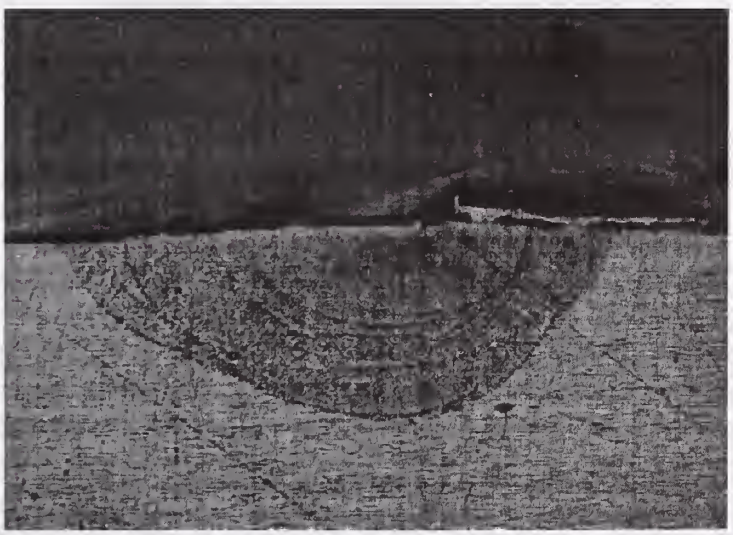

(b) Structure of modified surface.

Figure 2. Laser surface modification results.

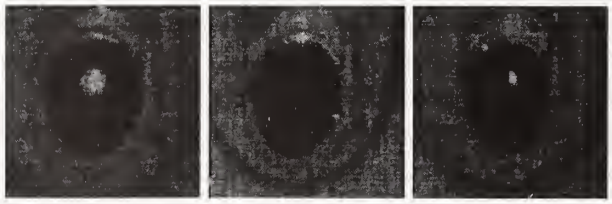

Laser power=1200W

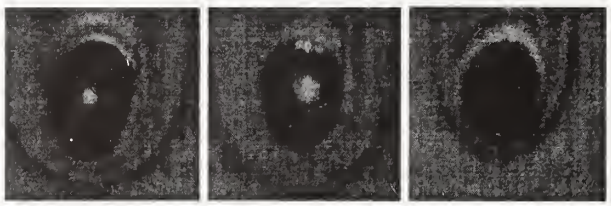

Laser Power=950W

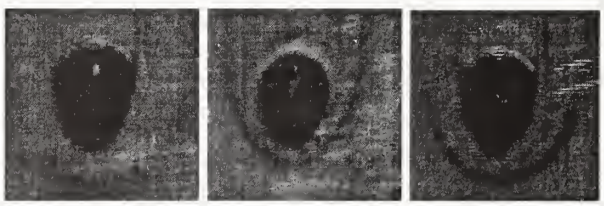

Laser Power=830W

Laser Power=570W

v=2.5 mm/s v=5mm/s v=10mm/s

Figure. 3 Images of the molten pool under different laser powers and scan velocities.

By a laser strobe lighting camera, well-contrasted molten pool images can be acquired whose qualities are good enough for further image processing. From data in Figure 2, the depth of the modified surface shows more sensitivity to absorbed laser power than to scan velocity. For example, processing started with parameters of 1200W laser power and 2.5mm/s scan velocity. Decreasing the laser power 50% or increasing the scan speed 3 times will form almost the same variation of depth in the molten pool. Comparing the images in Figure 3 with data in Figure 2, the molten pool images are also seen to reflect more signs of variation in laser power than in scan velocity. Using constant scan velocity in processing, the geometric shape of the molten pool changes prominently with the variation of laser power. When laser power is decreased, the size of the pool shrinks and the angle at the front end is smaller. In contrast, changing the scan

velocity while keeping the laser power constant will cause only a small difference in the pool's image although the molten depth has changed dramatically. Thus, for surface modification with variable absorbed laser power and scan velocity, images of the pool can not reflect the molten depth very well. But for constant scan speed processing (which is the common method in surface modification) those images can provide sufficient feedback of molten depth for close-loop control. In the following study, we assume that constant scan speed will be utilized during laser processing. In order to extract molten depth feedback from the molten pool's geometric information, a real-time algorithm of image processing will be the next problem to be solved.

REAL-TIME ALGORITHM FOR IMAGE PROCESSING

Real-time image processing includes two steps to find the relationship between the molten pool geometric shape and laser processing power: edge detection and pattern recognition.

1. Edge detection

Edge detection serves to simplify the analysis of the image by preserving useful structural information about object boundary. There are several research results on edge detector (four well known are Canny, Nalwa-Binford, Sarkar-Boyer, and Sobel [5]). Due to the excellent performance of the Canny edge detector (high signal noise ratio, good edge localization and elimination of multiple response), and the features of the image we got, the Canny edge detector for step-edge is used with modification to serve as the front-end edge detector.

In order to decrease the noise effects, Gaussian smooth is applied to the image first described as following:

$$I_s = G * I$$

where G is a two-dimension Gaussian filter, I represents the image array, and * denotes convolution.

$$G = \exp(-\frac{x^2 + y^2}{2\sigma^2})$$

According to Canny [6], the first derivative of the Gaussian operator is an efficient approximation to the optimized operator for step-edge with a 20 percent performance decrease. Thus, the following operation is applied to the image smooth result

$$I_r = G_n * I_s$$

where

$$G_n = \frac{\partial G}{\partial \mathbf{n}} = \mathbf{n} \bullet \nabla G$$

n should be the normal to the direction of an edge to be detected and can be estimated from the smoothed gradient direction

$$\mathbf{n} = \frac{\nabla(G * I)}{|\nabla(G * I)|}$$

An edge candidate I_e is a local maximum of I_r. A function (F) of non-maximum suppression is built to substitute for calculating the second derivation Gaussian operator.

$$I_e = F(I_r)$$

Two edge magnitude thresholds, T_{e1} and T_{e2} ($T_{e1} > T_{e2}$), are selected with hysteresis [6] to classify I_e and to form the edge set E. The processing result is shown in Figure. 4.

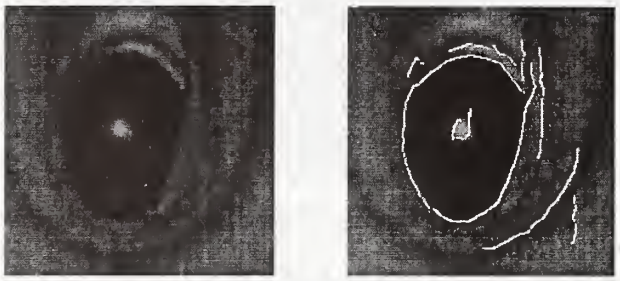

Figure 4. Processing result of the edge detector.

In order to eliminate the edges caused by the heat-effected zone, two gray level thresholds, T_{g1} and T_{g2} ($T_{g1} < T_{g2}$), also with hysteresis, are used combined with edge magnitude thresholds, based on the original image histogram analysis. The process is defined as following:

If $I_e(x, y) > T_{e1}$ and $I(x, y) < T_{g1}$, $(x, y) \in E$, break=FALSE, $x \pm \Delta$, $y \pm \Delta$; Δ is a small increase.
If $I_e(x, y) < T_{e2}$ or $I(x, y) > T_{g2}$, $(x, y) \notin E$, break=TRUE;
If $T_{e1} > I_e(x, y) > T_{e2}$ and $T_{g2} > I(x, y) > T_{g1}$ and break=FALSE, $(x, y) \in E$, otherwise break=TRUE;

Figure 5 shows that the extra edges are greatly reduced. The edge set E is the data source of next step recognition.

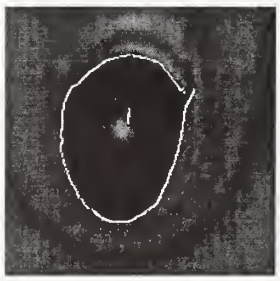

Figure 5. Final processing result of the edge detector.

2. Pattern recognition

The purpose of the molten pool recognition is to classify the geometric shape of the pool according to molten depth. In this study, a template-matching method is selected to satisfy the requirements of real time. Because the positions of laser head and camera are fixed, one dimension optimization searching which has very fast recognition speed is enough for two-dimension recognition. For each processing of certain segment laser power, one template must be built. Then a look-up table can link template and molten depth. Because it is difficult to extract one accurate analytic model for the geometric shape of the molten pool, Self-Organized Feature Map (SOFM) is utilized to construct such a recognition template by the associate learning neural network, due to the good performance of SOFM in distributing weight according to training patterns.

The structure of neural network is shown in Figure 6. The input patterns (p) are 2×1 vectors, which are positions of the edges of one set of the molten pool detected in the above section. A weight matrix will be trained to distribute weight vectors according to the position of the edges and to be the recognition template of that set of molten pool.

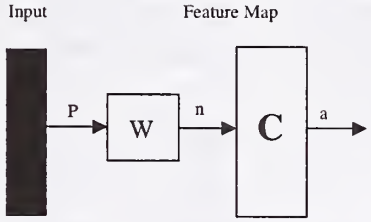

Figure7. Structure of the neural network of SOFM.

Here the set of images with processing parameters of 1200W-laser power and 5mm/s scan velocity is selected to illustrate the template training process in detail. N images of this set are chosen as the training input pattern. The 2-D positions of the edges of the molten pool will be operated by OR set operation to construct input pattern set. The input pattern set is described as follows:

$$P_j = \bigcup_{i=1}^{N} E_i$$

where P_j is the input pattern set for one segment of laser processing power and E_i is edge set of one image.

A program is developed to train the SOFM using the Kohonen rule with neighborhood. The training algorithm is described in the following equation [7].

$$_i w(n) = (1-\alpha)_i w(n) + \alpha p(n) \quad i \in N_{i^*}(d)$$

where $N_i(d) = \{j, d_{ij} < d\}$, i^* represents the wining neuron, and α is the learning rate.

The trained weight matrix (w) will be the recognition template. Because the weight matrix w classifies the edges according to their position, in order to get correct template that can fit the contour of edges of N images, enough number of initial classifications must be selected to avoid the "average" effect. The training result (template) is shown in Figure 8. The template constructed by SOFM can represent the geometric shape of the molten pool very well.

The algorithm combining the modified Canny and template matching constructed by the SFOM neural network method shows good performance in time consuming and robust. On the computer described in section 2, it will take 60ms to complete such image processing. It can classify images formed by different segments of laser processing power, from which sufficient information can be extracted by building a look-up table.

CONCLUSION

Well-contrasted molten pool images of laser surface modification can be obtained by a Laser Strobe vision system. Both images and molten depth are more sensitive to the change of laser

power absorbed by bulk material than by scan velocity. The computer vision can be used as an efficient method for sensing laser surface modification with constant scan velocity. An algorithm for real-time image processing is developed combining modified Canny and template matching constructed by SFOM neural network method. The algorithm shows very robust performance and fast speed in testing on different images. Molten depth estimation modeling and close-loop control for laser surface modification will be the further research.

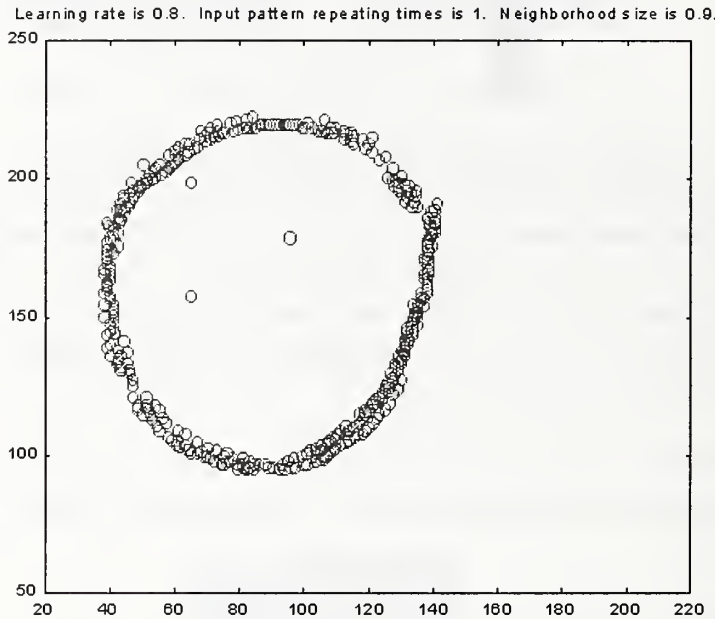

Figure 8. Recognition template trained by SFOM
(Laser power=1200W, scan velocity=5mm/s).

REFERENCE

1. Heuvelman, C.J.; Konig, W.; and et al. 1992. Surface treatment techniques by laser beam machining. *Annals of the CIRP* 41(2): 657 to 666.
2. Romer, G.W.; Hoeksman, M.; and Meijer, J. 1997. Industrial imaging controls laser surface treatment. *Photonics Spectra* 31(11): 104-109.
3. Tu, J.F.; Lankalapalli, K.N.; Gartner, M.; and Leong, K.H. 1997. On-line estimation of laser weld penetration. *Transaction of the ASME: Journal of dynamic system, measurement, and control* 119: 791-801.
4. Derouet, H.; Coste, F.; Sabatier, L.; and Fabbro, R. 1996. Real time control of surface treatments with liquid phase (molten depth on-line estimation). *Proceedings of SPIE* 2789: 264 to 272.
5. Heath, M.; Sarkar, S.; Sanocki, T.; and Bowyer, K. 1998. Comparison of edge detectors-A methodology and initial study. *Computer vision and image understanding* 69 (1): 38 to 54.
6. Canny, J. 1986. A computational approach to edge detector. *IEEE transactions on pattern analysis and machine intelligence* PAMI-8 (6): 679 to 698.
7. Hagan, M. T.; Demuth, H. B.; and Beale M. Neural Network Design 1995. PWS publishing company, USA.

American Welding Society's Committee on the Computerization of Welding Information (A9)

Ninth International Conference on Computer Technology in Welding

Lance Flitter

September 29, 1999

A9 Mission Statement

- The development of standards, specifications, recommended practices, and guidelines relevant to the collection, storage, retrieval, and transfer of computerized welding information.

Organizational Structure

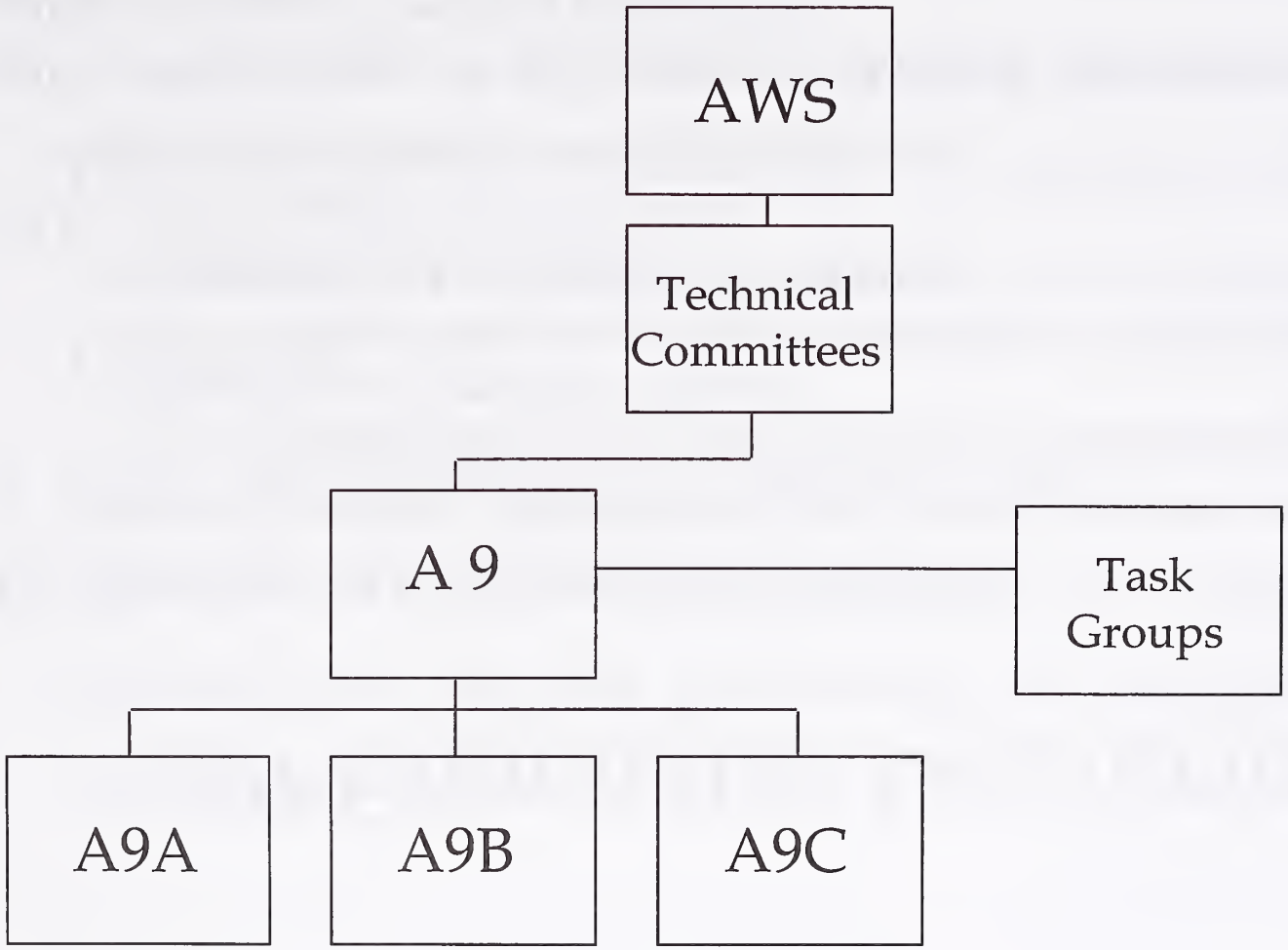

A9 Committee Descriptions

- A9 - Committee on Computerization in Welding
  - 2 Previous Standards - being retracted and to be replaced with new standard A9.1
    - A9.1 - Standard Guide for Describing Arc Welds in Computerized Material Property and Nondestructive Examination Databases
    - A9.2 - Standard Guide for Recording Arc Weld Material Property and Nondestructive Examination Data in Computerized Databases
- A9A - Subcommittee on Conference
  - Plans Computerization in Welding Conference.
- A9B - Subcommittee on the Exchange of Welding Information - Deals with the digital exchange of welding information.
- A9C - Subcommittee on Weld Data Logging
  - Currently "unemployed". Previous projects rolled into A9B. May be dissolved.

A9B Mission

- To provide a forum in which the issues relevant to the exchange of computerized welding information can be examined and resolved.
- The development of standards, specifications, recommended practices, and guidelines for the exchange of welding information.

Current A9B Activities

- Working on three documents
  - AWS A9.1, *Guide for a Data Dictionary for the Electronic Exchange of Arc Welding Information*
  - AWS A9.3, *Specification for the Exchange of Arc Welding Information Between Intelligent Systems*
  - AWS A9.4, *Specification for Data Structures and Protocols for the Exchange of Intra-cell Welding Information*

A9.1- Guide for a Data Dictionary for the Electronic Exchange of Arc Welding Information

- Combination and reworking of old A9.1 and A9.2 documents.
- Describes the data fields considered necessary to uniquely define an arc weld and their relationships.
- Purpose: Provide a common structure for welding databases for ease of information retrieval and exchange; used as input for A9.3 document.
- Three primary sections:
  - Design & Planning
  - Process Execution
  - Evaluation

A9.3 - Specification for the Exchange of Arc Welding Information Between Intelligent Systems

- Purpose: provide a standard method for the exchange of arc welding related information between the systems that use that information.
- To be used by system developers, integrators and end users of arc welding related products to more easily develop interfaces for the exchange of arc welding related information between the various components of the welding environment.
- Implemented as library of classes and objects with their attributes and methods for access.

Conceptualization of Automated Welding Environment

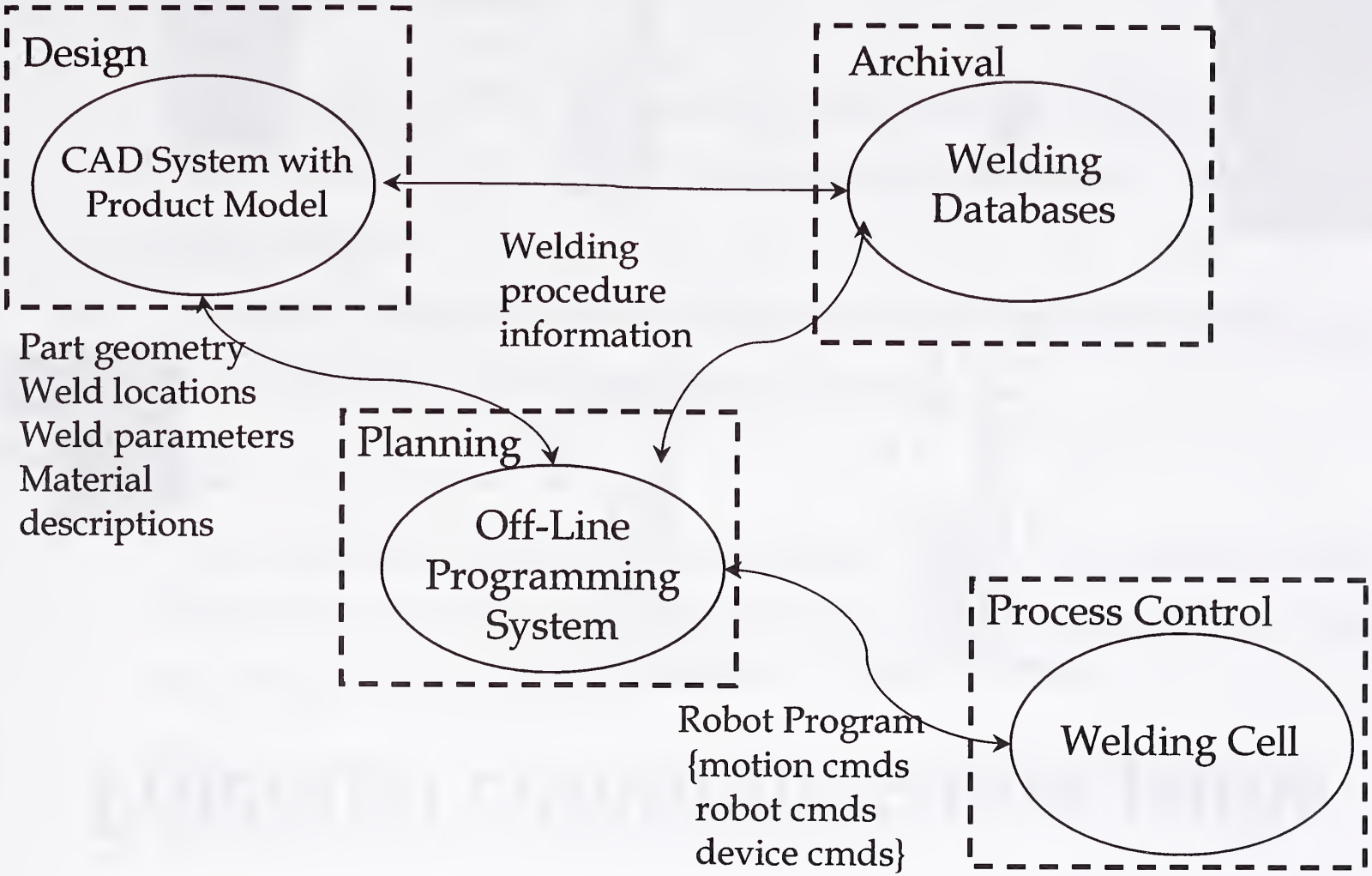

Potential communication paths

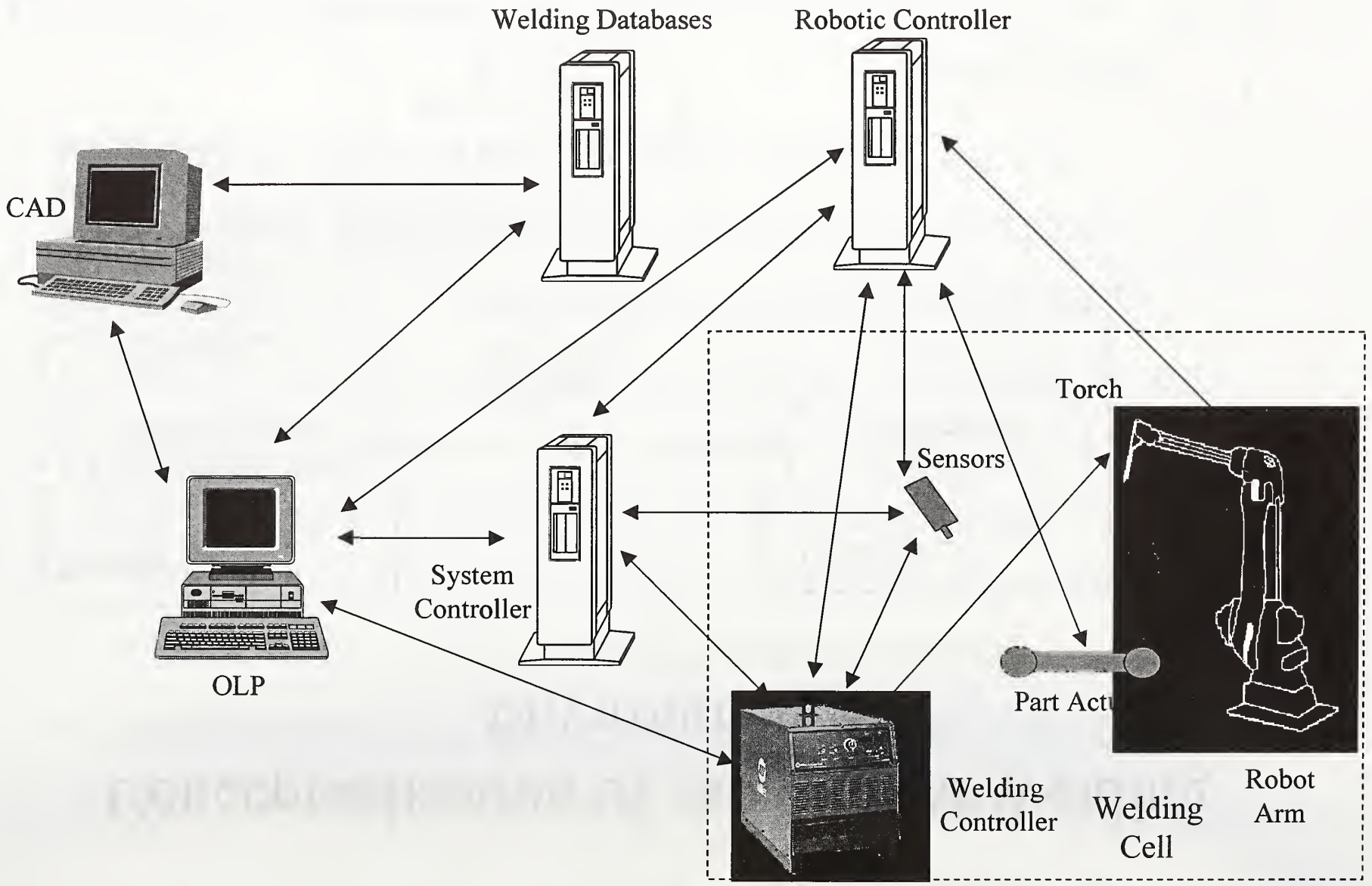

Problem & Need

- Problem
  - Not cost effective to develop advanced welding capabilities in many environments due to the cost of integration.
  - Traditional solutions require the development of unique interfaces for each implementation.
- Need
  - Cost efficient means of providing open communications between systems employed in automated/computerized welding environments.
  - Non-invasive communications standard acceptable to the automated welding community.

Approach

- Use object-oriented techniques in specification
- Start by developing conceptual model of automated welding. Develop IDEF0 activity model.
- Develop object model (specify in UML)
  - **Identify data to be exchanged based on activity model**
  - Identify objects and their relationships
  - Map data to be exchanged to objects in object model
  - Specify methods for exchanging data with objects

IDEF0 Activity Model

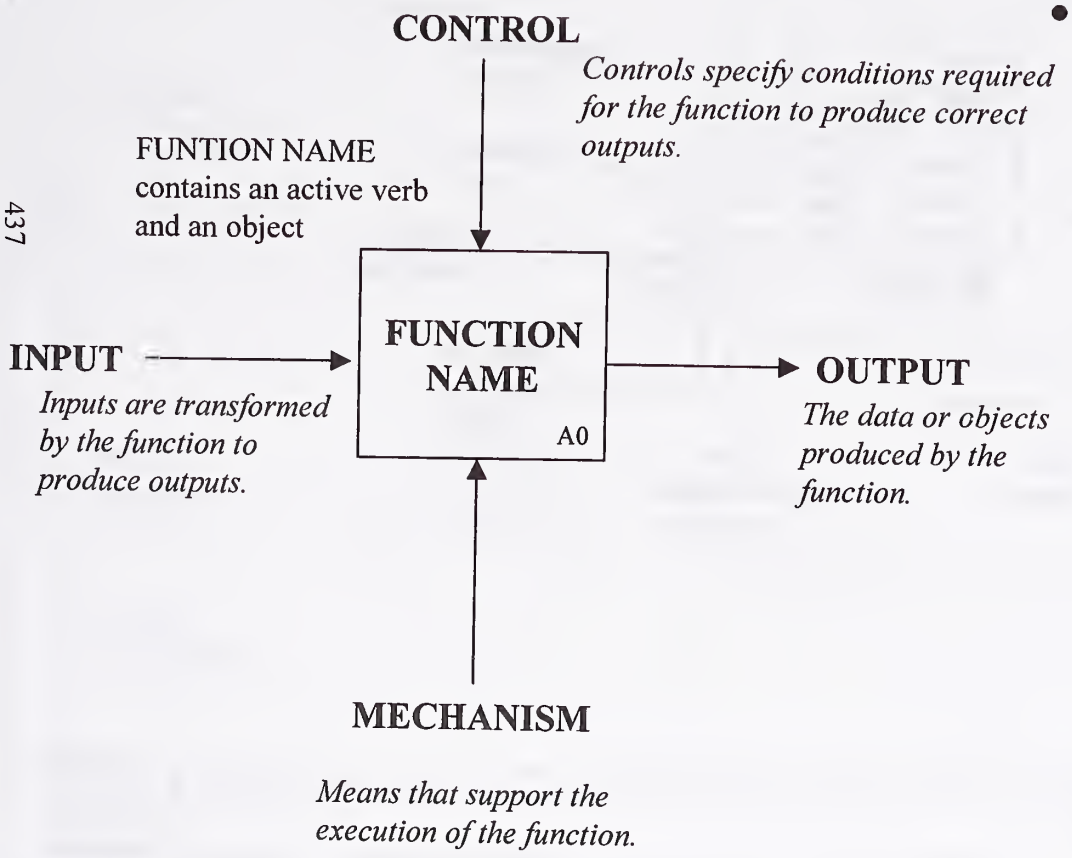

- An activity model is a conceptual tool. It should guide efforts at identifying technical areas to be considered for standards development. Helps assure that all participants in standard development have same conceptual understanding of terms and processes.

USED AT:	AUTHOR: Bill Rippey, editor, 301-975-3417	DATE: 28-Jan-99	X	WORKING	READER DATE	CONTEXT:
American Welding Society	PROJECT: A9B Activity Model	REV: 1.2		DRAFT	Lance Flitter	Top
	NOTES: 1 2 3 4 5 6 7 8 9 10			RECOMMENDED	Chris Pollock	
				PUBLICATION	American Welding Society	

NOTE: This is a working document under consideration by an AWS Committee. It is made available solely to solicit comments from interested parties, and may not be relied upon or utilized for any other purpose. Draft documents may change significantly in subsequent versions.

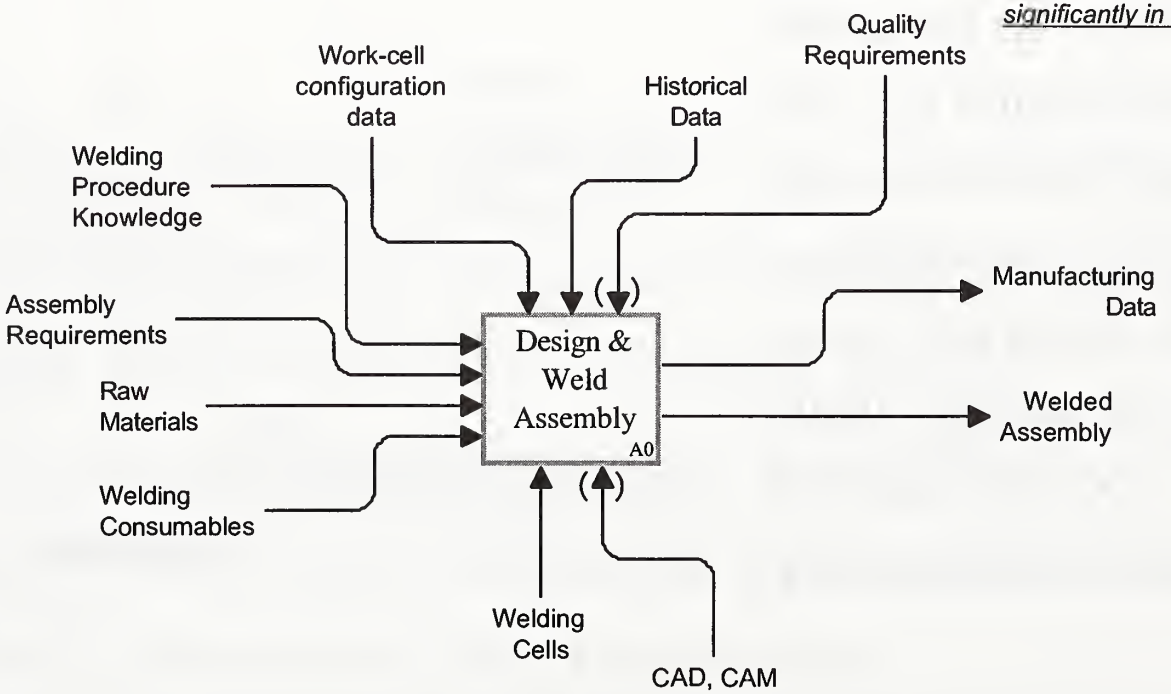

438

Rev 1.2: Changed Product Req to Assembly Requirements

Key: blue activity boxes have further decompositions, black boxes have no further decomposition.

NODE: A-0	TITLE: A9B Arc Welding Manufacturing Activity Model	NUMBER: P. 1

USED AT:	AUTHOR: Bill Rippey, editor, 301-975-3417	DATE: 28-Jan-99	X	WORKING	READER DATE	CONTEXT:
American Welding Society	PROJECT: A9B Activity Model	REV: 1.2		DRAFT	Lance Flitter	
	NOTES: 1 2 3 4 5 6 7 8 9 10			RECOMMENDED	Chris Pollock	
				PUBLICATION	American Welding Society	

NOTE: This is a working document under consideration by an AWS Committee. It is made available solely to solicit comments from interested parties, and may not be relied upon or utilized for any other purpose. Draft documents may change significantly in subsequent versions.

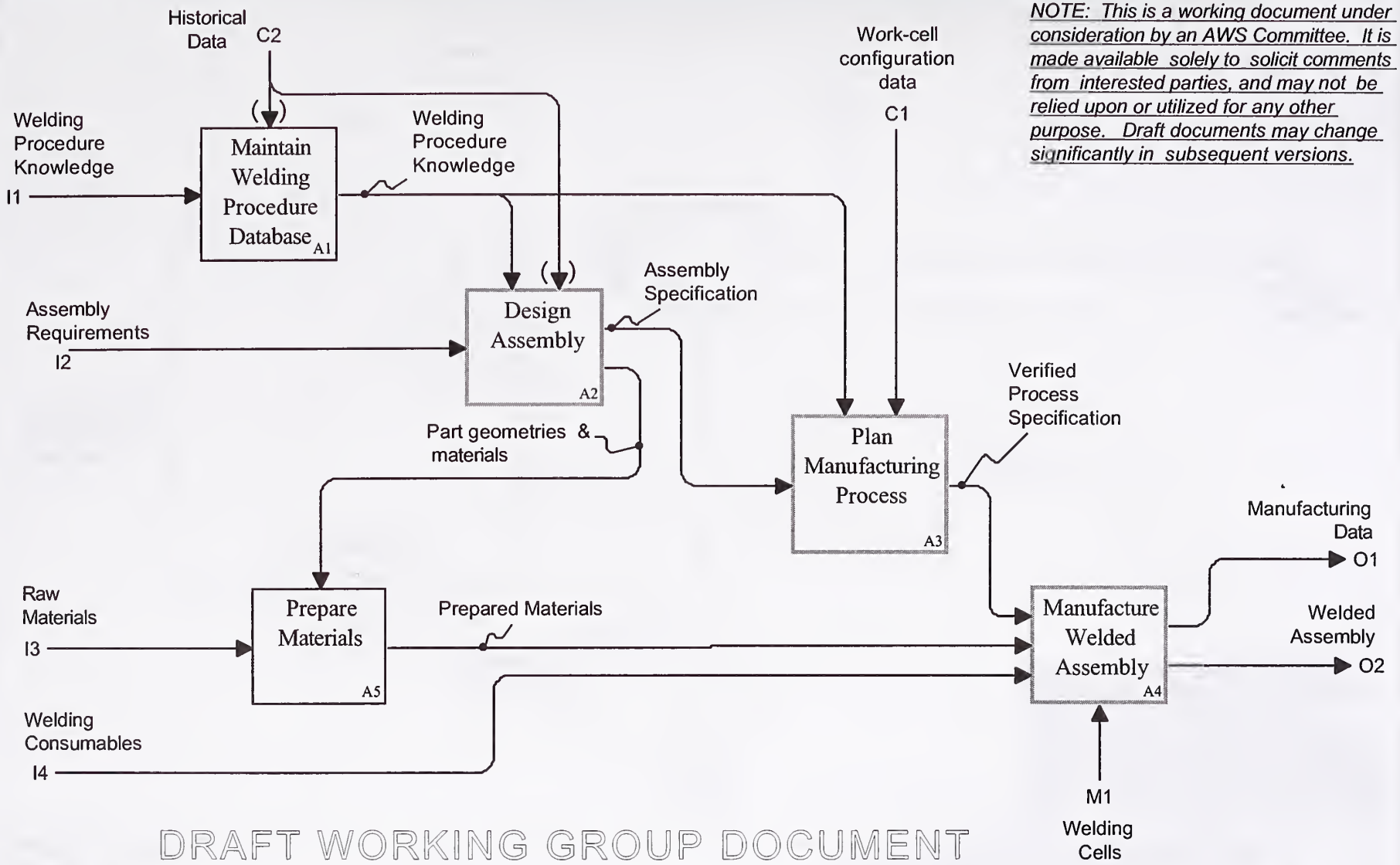

DRAFT WORKING GROUP DOCUMENT

NODE: A0	TITLE: Design & Weld Assembly	NUMBER: P. 2

USED AT:	AUTHOR: Bill Rippey, editor, 301-975-3417	DATE: 28-Jan-99	X	WORKING	READER DATE	CONTEXT:
American Welding Society	PROJECT: A9B Activity Model	REV: 1.2		DRAFT	Lance Flitter	
	NOTES: 1 2 3 4 5 6 7 8 9 10			RECOMMENDED	Chris Pollock	
				PUBLICATION	American Welding Society	

NOTE: This is a working document under consideration by an AWS Committee. It is made available solely to solicit comments from interested parties, and may not be relied upon or utilized for any other purpose. Draft documents may change significantly in subsequent versions.

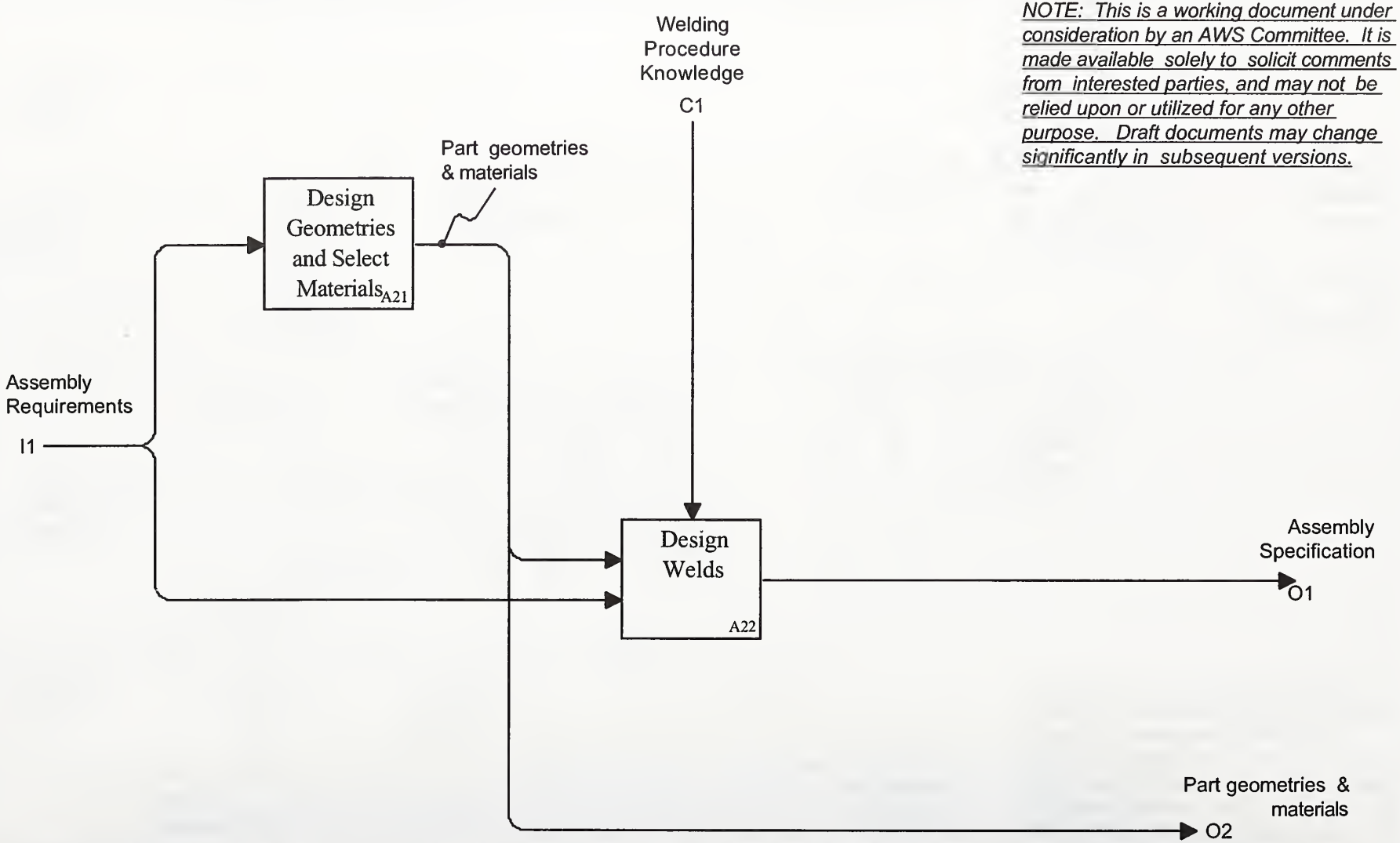

NODE: A2	TITLE: Design Assembly	NUMBER: P. 3

USED AT:	AUTHOR: Bill Rippey, editor, 301-975-3417	DATE: 28-Jan-99				CONTEXT:
American Welding Society	PROJECT: A9B Activity Model	REV: 1.2	X	WORKING	READER DATE	
				DRAFT	Lance Flitter	
	NOTES: 1 2 3 4 5 6 7 8 9 10			RECOMMENDED	Chris Pollock	
				PUBLICATION	American Welding Society	

NOTE: This is a working document under consideration by an AWS Committee. It is made available solely to solicit comments from interested parties, and may not be relied upon or utilized for any other purpose. Draft documents may change significantly in subsequent versions.

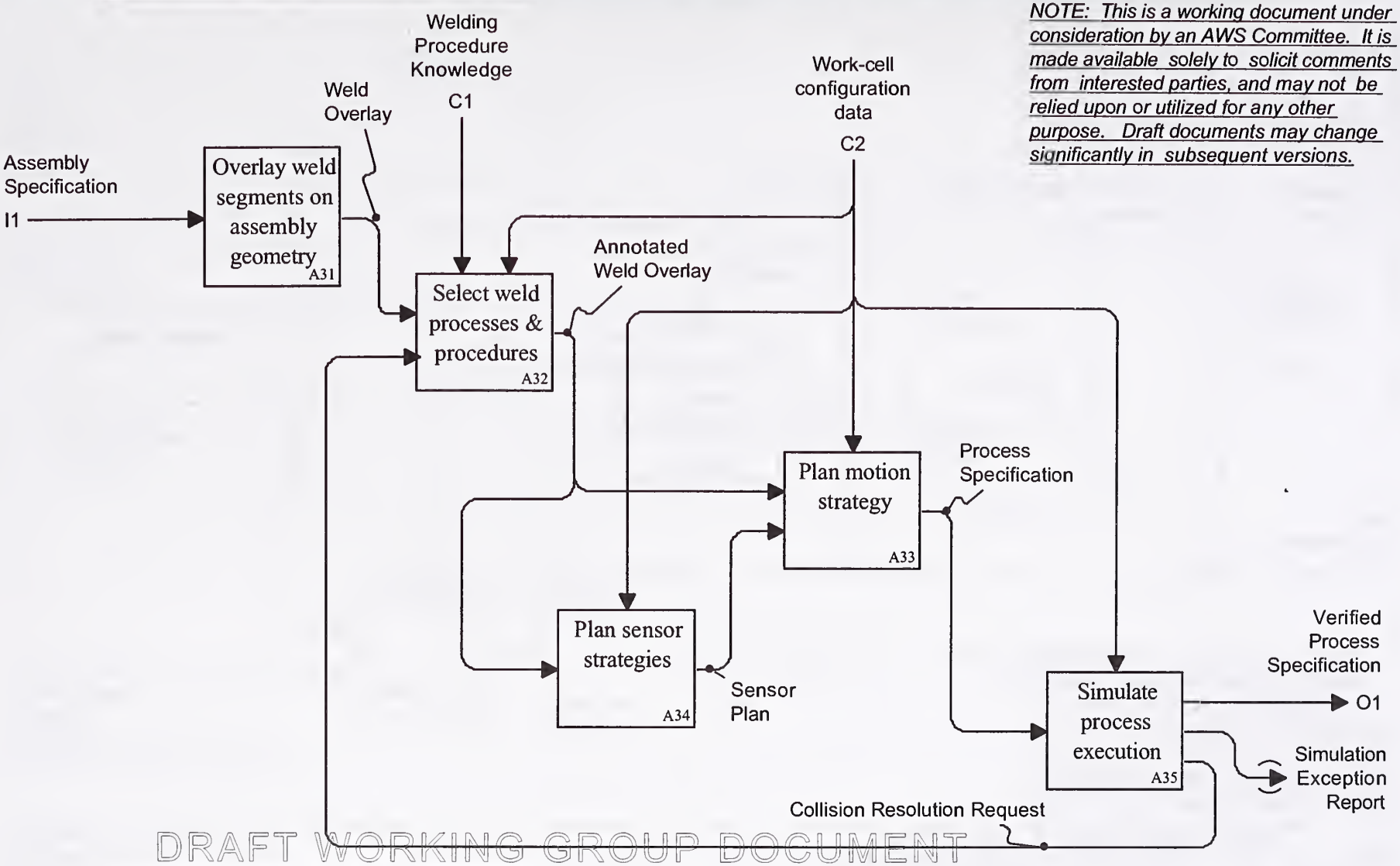

NODE: A3	TITLE: Plan Manufacturing Process	NUMBER: P. 4

USED AT:	AUTHOR: Bill Rippey, editor, 301-975-3417	DATE: 28-Jan-99	X	WORKING	READER DATE	CONTEXT:
American Welding Society	PROJECT: A9B Activity Model	REV: 1.2		DRAFT	Lance Flitter	
	NOTES: 1 2 3 4 5 6 7 8 9 10			RECOMMENDED	Chris Pollock	
				PUBLICATION	American Welding Society	

NOTE: This is a working document under consideration by an AWS Committee. It is made available solely to solicit comments from interested parties, and may not be relied upon or utilized for any other purpose. Draft documents may change significantly in subsequent versions.

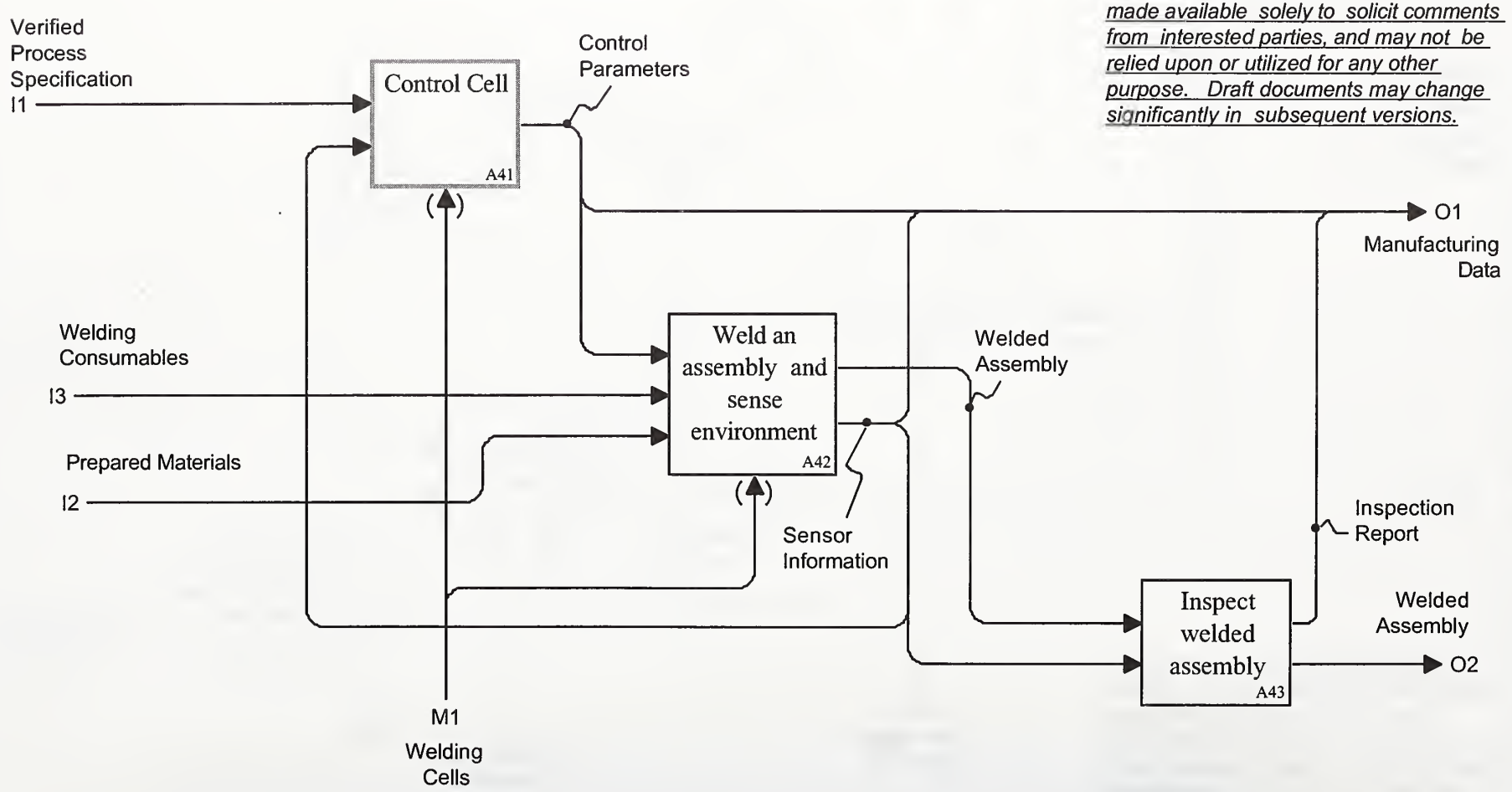

NODE: A4	TITLE: Manufacture Welded Assembly	NUMBER: P. 5

USED AT:	AUTHOR: Bill Rippey, editor, 301-975-3417	DATE: 28-Jan-99	X	WORKING	READER DATE	CONTEXT:
American Welding Society	PROJECT: A9B Activity Model	REV: 1.2		DRAFT	Lance Flitter	
	NOTES: 1 2 3 4 5 6 7 8 9 10			RECOMMENDED	Chris Pollock	
				PUBLICATION	American Welding Society	

NOTE: This is a working document under consideration by an AWS Committee. It is made available solely to solicit comments from interested parties, and may not be relied upon or utilized for any other purpose. Draft documents may change significantly in subsequent versions.

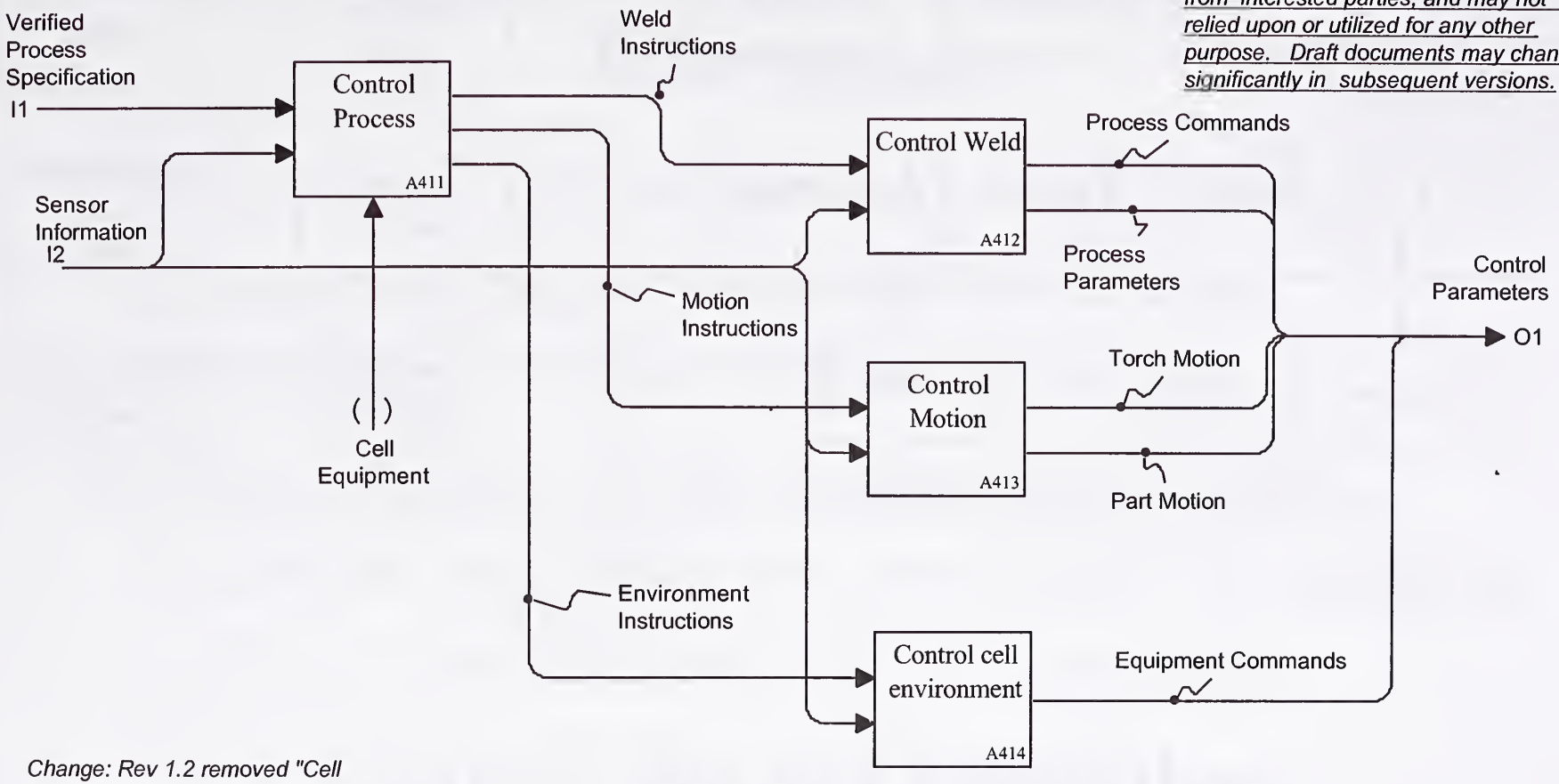

Change: Rev 1.2 removed "Cell Environment Status" control to A411.

NODE: A41	TITLE: Control Cell	NUMBER: P. 6

Object Model Example

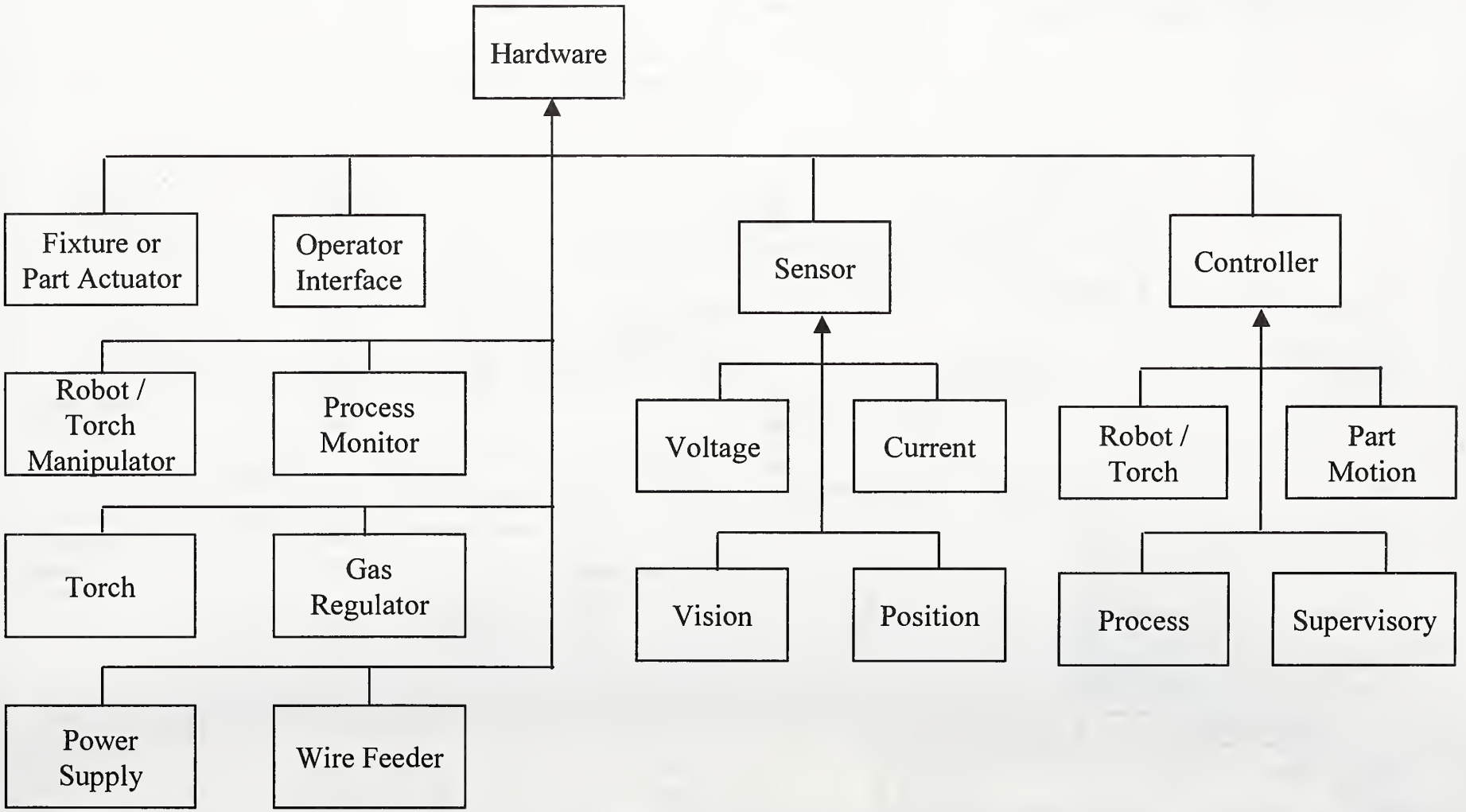

A9.4 - Specification for Data Structures and Protocols for the Exchange of Intra-cell Welding Information

- Purpose: To allow for easy configuration of an automated welding cell by adding, swapping, or removing components.
- A description of the mechanisms, both hardware and software, necessary for passing information between the components typically found in a welding cell.
- "Plug and play" welding

Potential communication paths

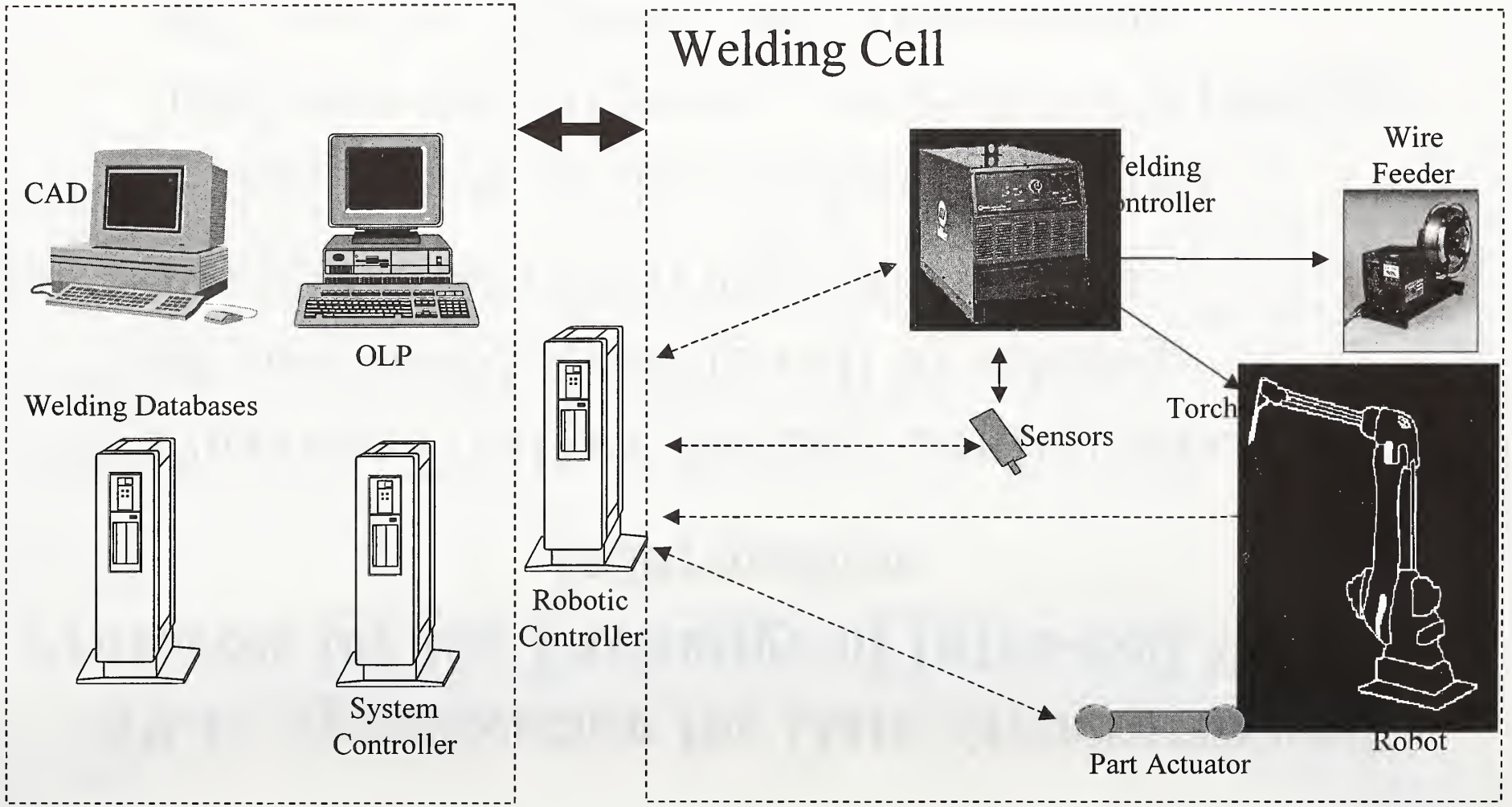

Problem & Need

- Problem
  - Most robotic welding cells bought by manufacturers use proprietary interfaces between the various components of welding cells.
  - Once system is in place it is difficult to change components because of the lack of standard interfaces and data exchange methods. Even simple configurations can incur large integration costs.
- Need
  - An open standard to reduce integration costs, to allow for component interchangeability, and to reduce maintenance and training expenditures.

Approach

- Examine potential standards and products already available
- If an existing product is suitable or close to suitable, use a basis for standard. If no suitable product found, start from scratch.
- Tailor specification to welding community needs.

Status

- Evaluating available products and specifications

- DeviceNet
- ControlNet
- ArcLink

Committee Participants

- AT&T - Vector Research Division
- ABB Robotics
- Carderock Division - NSWC
- Deneb Robotics
- Edison Welding Institute
- FANUC Robotics
- Impact Engineering
- Lincoln Electric
- Miller Electric
- NA Technologies
- NIST - Systems Group
- NIST - Materials Group
- PHT, Inc.
- Poly-Weld
- **AWS D16 Committee**

Points of Contact

- A9B Chairman - Lance Flitter

Carderock Division - Naval Surface Warfare Center

FlitterLA@nswccd.navy.mil (301)227-3161

- A9 Chairman - Tim Quinn

National Institute of Standards and Technology

quinn@boulder.nist.gov (303)497-3480

- A9 Secretary - Chris Pollock

American Welding Society

cpollock@aws.org (800) 443-9353, Ext. 304

A9B web site -

http://www.isd.cme.nist.gov/projects/amws/aws

A METHOD FOR OPTIMIZING WELDING PROCESSES

P. E. Murray*

ABSTRACT

Arc Welder, a Windows-based software application, is developed to accurately, efficiently, and reliably simulate the gas metal arc welding process, and to select welding parameters for optimal control of the process variables that affect weld quality. In this paper we describe *Arc Welder* and how it is used to select welding parameters. We also describe plans to integrate *Arc Welder*, drawing software, and an optimization algorithm into a comprehensive software product for ensuring weld quality and enhancing productivity in the welding industry.

INTRODUCTION

Ensuring weld quality and enhancing productivity are important in the welding industry, especially for automatic and robotic welding used in the automotive and ship building industries. Optimal welding procedures and parameters ensure the quality of the weld and reliability of the welding process while minimizing the cost of fabrication. Currently, designing the joint, selecting the welding technique, choosing the welding consumables, and optimizing the welding parameters are independent tasks. Furthermore, welding procedures are often developed with the aid of handbooks and manufacturers' recommendations that are based on a large amount of empirical data, and welding parameters are often found by a process of trial and error. Consequently, the welding process may not be optimal in regard to weld quality and cost. To integrate these disparate design processes, we are developing a method to select the optimal welding procedure and parameters for satisfying the numerous constraints on the weld process.

Currently, analytical models, simplified numerical models, and empirical methods are used to establish relationships between welding parameters, weld bead geometry, weld quality, and productivity, and to select welding parameters leading to an optimal process. Several notable examples may be found in Refs. 1-4; a related approach that is entirely empirical is described in Ref. 5. But all of these models are based on simplifying assumptions and empirical data—analytical models have deficiencies stemming from simplifying assumptions and empirical models are valid only for the processes and consumables used to validate the model. Nonetheless, empirical models have an important function in welding engineering, because the complexity of the weld process usually precludes detailed numerical simulation. Recently, a numerical approach has been used to simulate thermal phenomena occurring during welding, and to optimize welding parameters for controlling weld bead geometry and productivity (Ref. 6). Although numerical modeling has gained acceptance in the welding research community, empirical modeling is still the current practice in welding engineering.

* Applied Materials and Technology Department, Idaho National Engineering and Environmental Laboratory, Idaho Falls, ID 83415-2210.

In this paper, we report on the first phase of a project to accurately, efficiently, and reliably simulate the gas metal arc welding process. We developed a computer program called *Arc Welder* that can find the operating conditions that lead to a desired weld process and thereby identify the optimal welding procedure. *Arc Welder* performs the calculations in an integrated and efficient manner; provides menu items to select the base metal, type of joint, welding consumables, and welding parameters; and includes a graphical user interface for Windows 95/98/NT operating systems (Figure 1). *Arc Welder* may be used to identify a range of operating conditions, establish limits on welding parameters, assess the effect of changes in welding consumables, find the welding parameters that lead to desired operating conditions, and optimize the parameters to satisfy constraints on the process variables that affect weld quality and productivity. These constraints stem from the need to reduce weld defects, reduce the extent of distortion, meet the requirements on mechanical properties, and to increase productivity by reducing the number of passes needed to fill the joint and increasing the rate of deposition. Optimization is done by simulating the welding process for selected welding consumables and a range of welding parameters, and applying the constraints to find the optimal welding procedure. In this paper, we show examples of determination of welding parameters for optimal control of arc length and depth of fusion to ensure arc stability and adequate joint penetration.

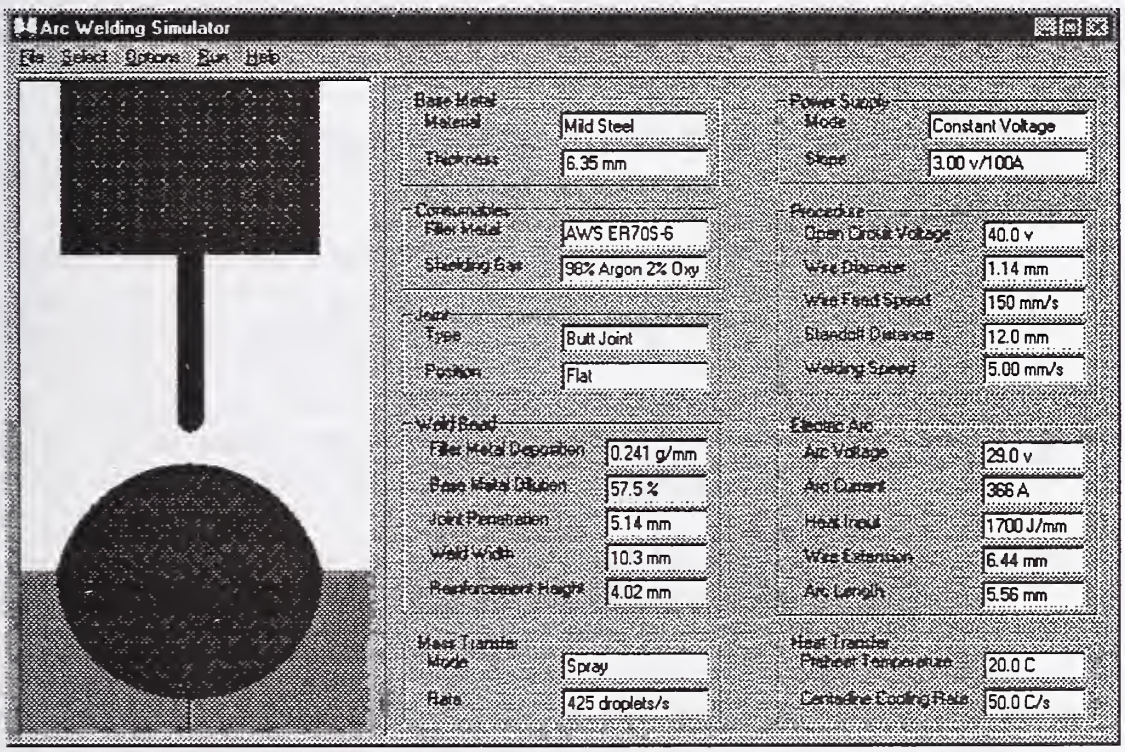

Figure 1. The user interface of *Arc Welder*.

DESCRIPTION OF *ARC WELDER*

Arc Welder simulates gas metal arc welding using a constant voltage power supply. Several models are used to assess the relationship between welding parameters and process variables that affect weld quality, using controllable operating conditions and welding consumables as inputs to the models. Welding parameters include voltage, current, travel speed, wire feed speed, wire diameter, and standoff distance; process variables include heat input, cooling rate, weld metal geometry, base metal dilution, rate of transfer of droplets, arc length, and electrode extension. The rate of transfer of droplets is used to ascertain the mode of mass transfer, i.e., short arc, globular, or spray.

The relationships between voltage, current, arc length, melting rate, and electrode extension are included in *Arc Welder*. As an example, consider a welding procedure using a stainless steel electrode and gas shielding consisting of 98% Ar_2 and 2% O_2. The correlation between voltage, current, and arc length is shown in Figure 2, and the correlation between melting rate, current, and electrode extension given by Lesnewich (Ref. 7) is shown in Figure 3. These relationships are used to compute the arc voltage, current, arc length, and electrode extension. *Arc Welder* also identifies the limiting conditions of "short" and "long" arc length and thereby checks for a stable arc. In this manner, *Arc Welder* may be used to determine the welding parameters that lead to a stable operating condition.

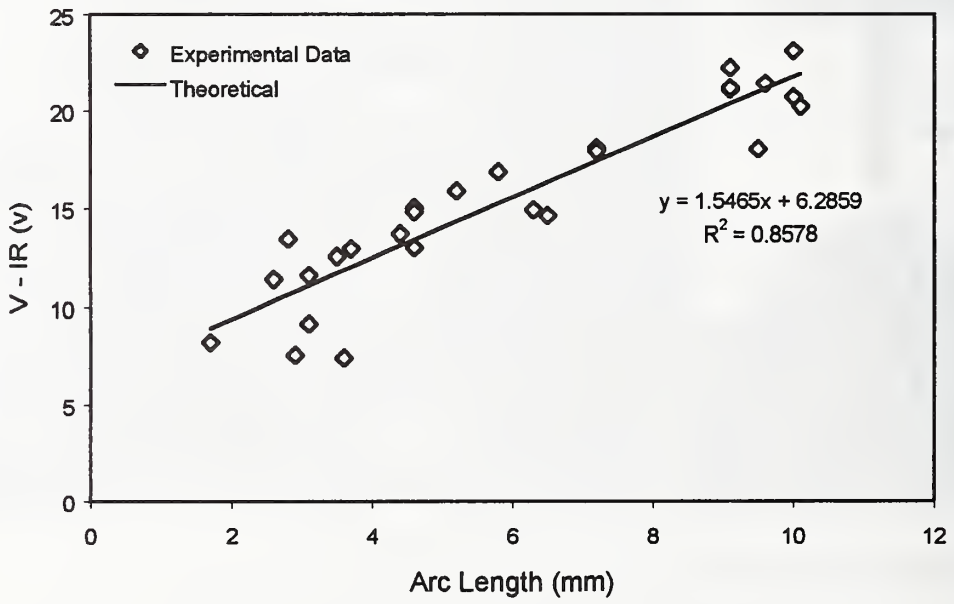

Figure 2. Correlation between arc length, voltage, and current, using stainless steel electrodes (0.9 and 1.2 mm diameter), and 98% Ar_2 and 2% O_2 shielding gas.

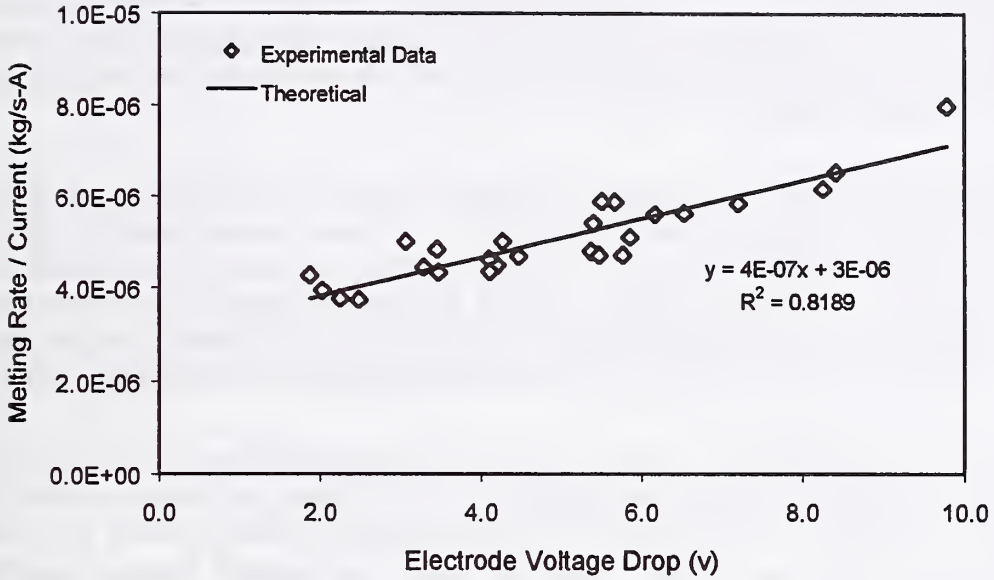

Figure 3. Correlation between melting rate, current, and electrode extension using stainless steel electrodes (0.9 and 1.2 mm diameter), and 98% Ar_2 and 2% O_2 shielding gas.

Arc Welder also includes a model of the depth of fusion, which is used extensively in the examples given in the next section. A complete description of this model and the validation performed in the case of stainless steel base metal may be found in Murray and Scotti (Ref. 8). Other models in *Arc Welder* include a correlation between welding parameters and the rate of transfer of droplets by Murray (Ref. 9), the heat transfer solution of Rosenthal (Ref. 10) as expanded upon by Christensen et al. (Ref. 11), and the centerline cooling rate formula of Adams (Ref. 12). *Arc Welder* may be used to compute joint penetration, weld width, reinforcement height, and base metal dilution.

The current version of *Arc Welder* is for a butt weld in the flat position, but it will be extended to include other joint designs. The user may select mild steel, stainless steel, or aluminum; an option to select other alloys may be provided in a later version. *Arc Welder* has been validated only for selected consumables, but will be extended to include other filler metals and shielding gases. The program provides a view of the base metal, weld metal, arc, electrode, droplet, and contact tip, as shown in Figure 1. The user has the option to "run" the process by simulating transfer of droplets from the consumable electrode. The user also has the options to save a given set of welding parameters in a file, open a file containing welding parameters saved previously, and print a bitmap image of the client area of the window. A future version of *Arc Welder* may include additional base metals, consumables, power supplies, joint designs, and welding techniques.

SELECTING PARAMETERS WITH *ARC WELDER*

As an example, consider the problem of computing the welding parameters that lead to a stable arc. The short arc limit for a 1.2 mm diameter stainless steel electrode is shown in Figure 4; the long arc limit is shown in Figure 5. These limiting conditions determine the range of arc voltage needed to sustain a stable arc. Using these results, the user may select the welding parameters that lead to a desired arc length.

Next consider the problem of computing the depth of fusion to ensure that joint penetration is adequate. The depth of fusion in stainless steel, using a 1.2 mm diameter stainless steel electrode, gas shielding consisting of 98% Ar_2 and 2% O_2, and a filler metal deposition equal to 0.2 g/mm is shown in Figure 6. We assume that 4 mm is the desired depth. The operating conditions needed to obtain the desired depth are shown in Figure 7. The simulations identify the range of voltage, wire feed speed, and standoff distance, and their effect on arc length and heat input.

To identify the optimal operating conditions, the user selects particular objectives and constraints that must be satisfied. For example, suppose that the user wants an arc length equal to 6 mm. The results shown in Figure 7 may be used to find the optimal operating points. In particular, we select specific values of arc voltage, wire feed speed, and standoff distance that lead to the desired arc length while maintaining desired values of filler metal deposition and depth of fusion. A few of these operating points and the effect on current are computed and given below.

Arc Voltage (v)	Wire Feed Speed (mm/s)	Standoff Distance (mm)	Current (A)
25.3	155	13	257
27	170	16	248
28.5	185	19	240

In the preceding example, *Arc Welder* was used to identify a range of stable welding parameters, and to find the welding parameters that lead to desired operating conditions. Specific welding parameters were found by controlling arc length, depth of fusion, and filler metal deposition, leading to arc stability, adequate weld bead size, and adequate joint penetration. *Arc Welder* may be used to select welding parameters for controlling other process variables that affect weld quality. In this manner, *Arc Welder* may be used to develop optimal welding procedures.

FUTURE WORK

Arc Welder is the basis for comprehensive software that the welding industry can use to obtain an optimal weld process specification. The comprehensive software will incorporate simulation and optimization methods to compute the optimal weld process; these methods will satisfy requirements on accuracy, validity, and performance that are essential for improving quality and productivity in welding. In the next phase of this project, we will explore ways to achieve an efficient simulation and optimization of the gas metal arc welding process. We are especially interested in determining welding parameters for controlling arc length, weld metal geometry, and rate of metal transfer because these process variables are important factors in weld quality. Other variables that affect weld quality include heat input, cooling rate, and base metal dilution.

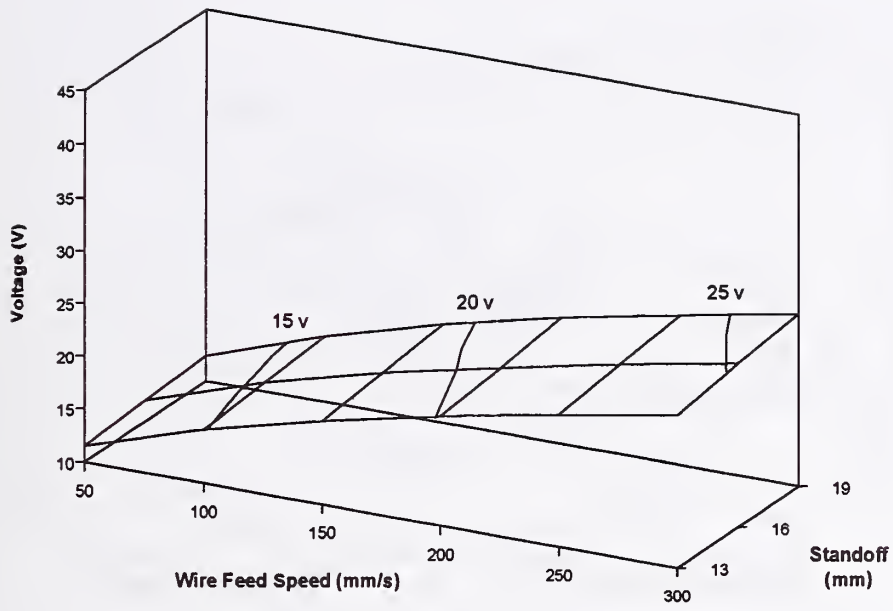

Figure 4. Short arc limit for 1.2 mm diameter stainless steel electrode.

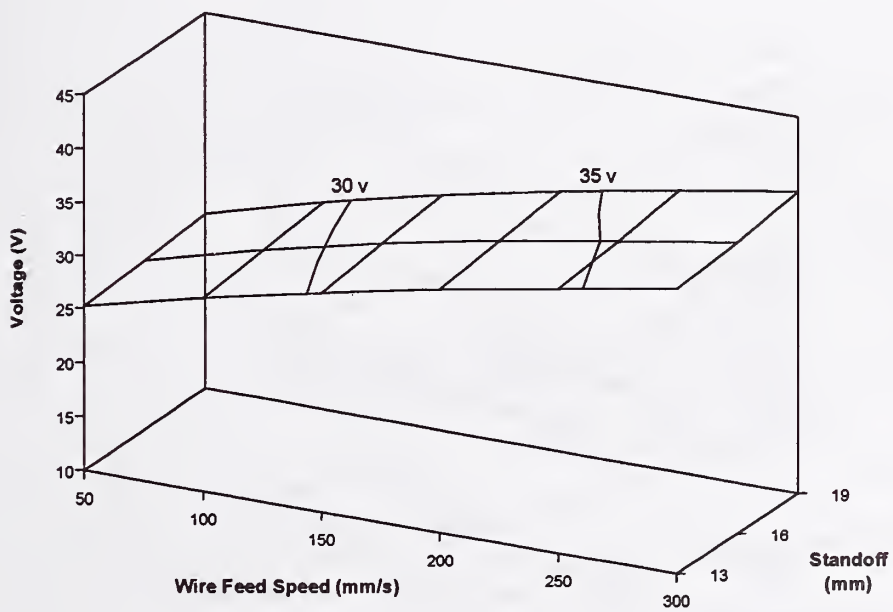

Figure 5. Long arc limit (10 mm arc length) for 1.2 mm diameter stainless steel electrode.

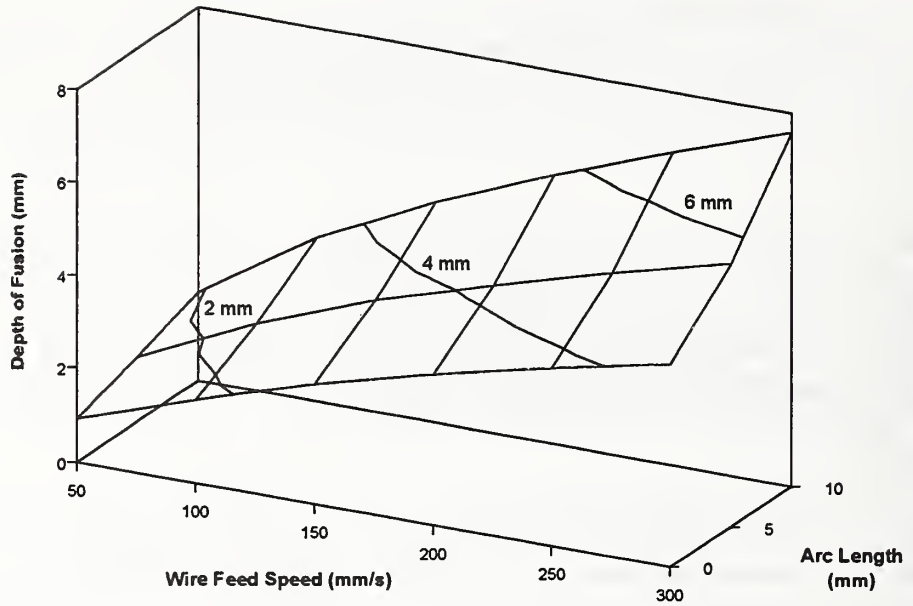

Figure 6. Depth of fusion in stainless steel, using 1.2 mm diameter stainless steel electrode, 16 mm standoff, 0.2 g/mm deposit.

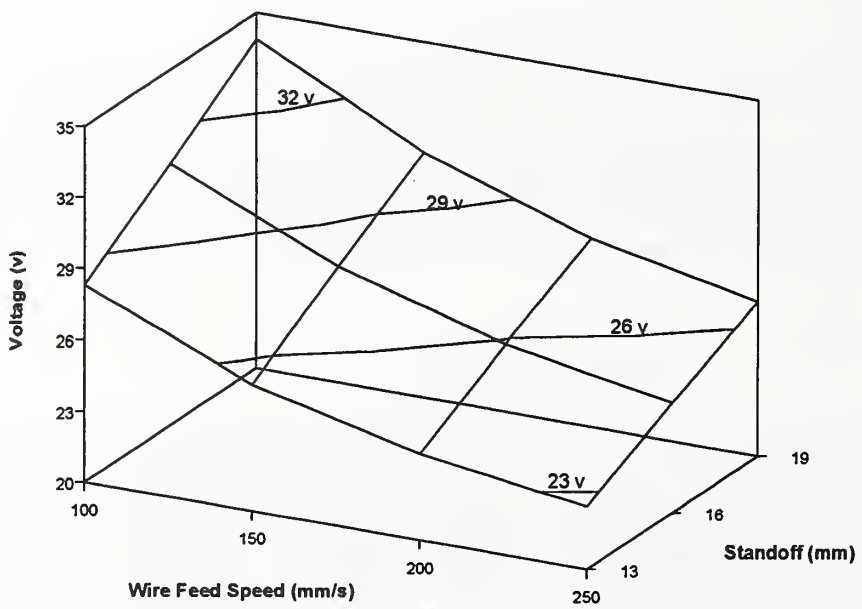

(a) Voltage, wire feed speed, and standoff.

Figure 7. Operating points needed to obtain 4 mm depth of fusion, using 1.2 mm diameter stainless steel electrode, 0.2 g/mm deposit.

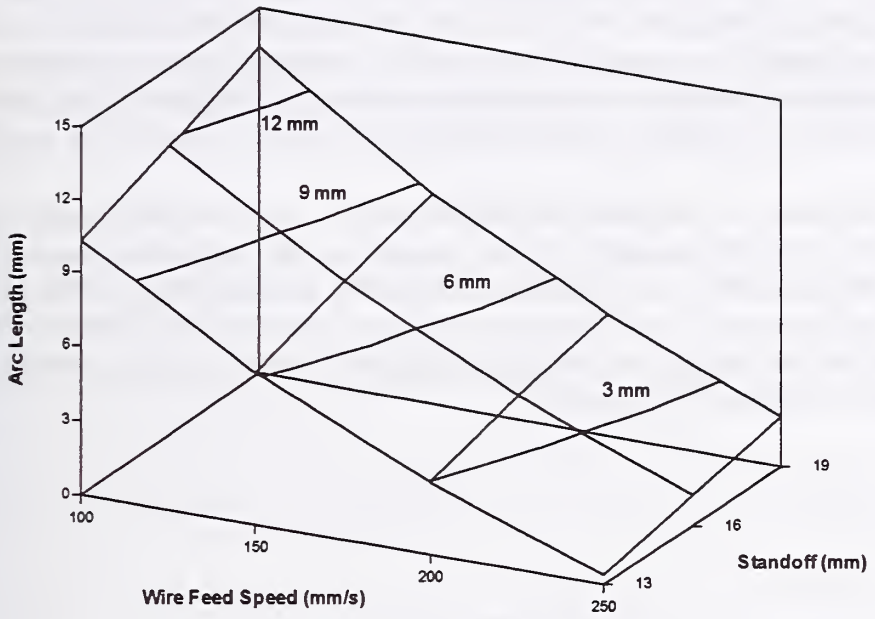

(b) Arc length, wire feed speed, and standoff.

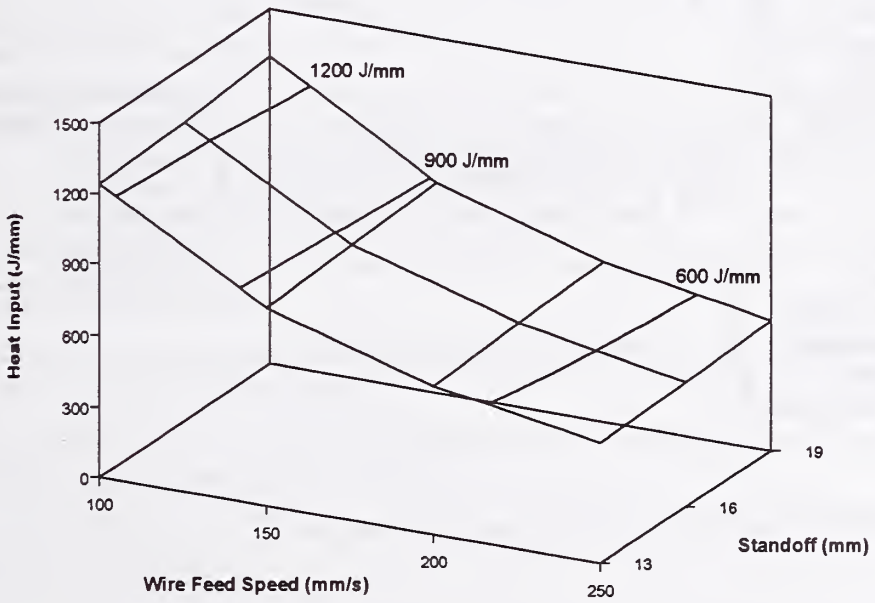

(c) Heat input, wire feed speed, and standoff.

Figure 7. Continued.

In the next phase of the project, we will develop a method of optimization in the manner of inverse design. That is, we will specify constraints on the process variables affecting weld quality, such as minimum and maximum weld bead size and maximum heat input, and find the welding parameters that satisfy these constraints and maximize productivity. A diagram of the flow of data in weld process simulation and optimization is shown in Figure 8. This approach will lead to reduced occurrence of defects, enhanced productivity, and improved weld quality.

We also plan to build software that integrates *Arc Welder* and a computer-aided-design method for drawing a weld joint. The implementation will be compatible with common drawing objects such as bitmaps and will include a user interface compatible with Windows 95/98/NT. We envision engineering software used on a desktop workstation in which *Arc Welder*, drawing software, and an optimization algorithm are used in an efficient manner to obtain a weld process that is optimal in regard to quality and productivity.

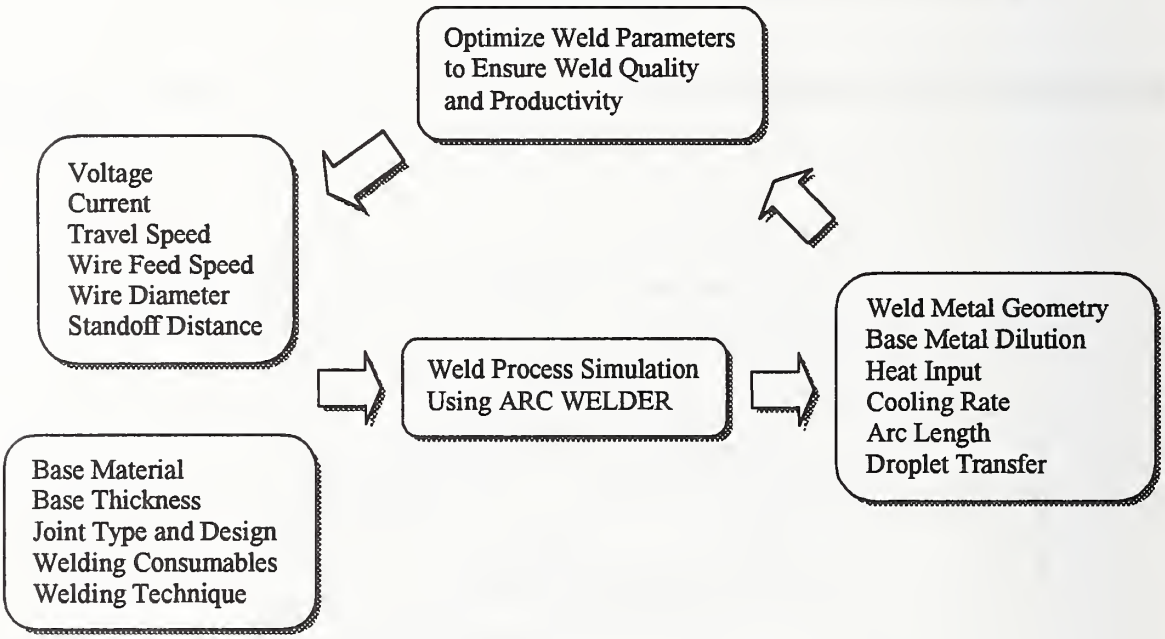

Figure 8. The flow of data in weld process simulation and optimization.

ACKNOWLEDGMENT

This work was supported by the U.S. Department of Energy, Office of Science, Office of Basic Energy Sciences, under DOE Idaho Operations Office Contract DE-AC07-94ID13223.

REFERENCES

1. Salter, G. R., and Doherty, J. 1981. Procedure Selection for Arc Welding. *Metal Construction* 13(9): 544-550.
2. White, D., and Jones, J. 1997. Process Modeling with Neural Networks for Pulsed GMAW Braze Welds. *JOM* 49(9): 49-53.
3. Eisler, G. R., and Fuerschbach, P. W. 1997. SOAR: An Extensible Suite of Codes for Weld Analysis and Optimal Weld Schedules. *Proc. 7th Intl. Conf. on Computer Technology in Welding*, July 9-11, San Francisco, CA. Ed. T. A. Siewert, pp. 257-268. NIST.
4. Mitchiner, J. L.; Kleban, S. D.; Hess, B. V.; Mahin, K. W.; and Messink, D. 1995. SmartWeld: A Knowledge-Based Approach to Welding. *Technical Report SAND-96-1372C.*
5. Harwig, D. D. 1997. The ARCWISE Technique for Increasing Productivity in Arc Welding. Presented at the International Conference on Advances in Welding Technology, Sept. 17-19, Columbus, OH.
6. Dilthey, U., Roosen, S., and Sudnik, V. 1997. MAGSIM and SPOTSIM: PC Aided Simulation of GMA and Spot Welding Processes. *Proc. 7th Intl. Conf. on Computer Technology in Welding*, July 9-11, San Francisco, CA. Ed. T. A. Siewert, pp. 548-561. NIST.
7. Lesnewich, A. 1958. Control of Melting Rate and Metal Transfer in Gas Shielded Metal Arc Welding: Control of Electrode Melting Rate. *Welding J. Res. (Suppl.)* 37: 343s-353s.
8. Murray, P. and Scotti, A. 1999. Depth of Penetration in Gas Metal Arc Welding. *Science and Technology of Welding and Joining* 4(2): 112-117.
9. Murray, P. 1999. Stability of Droplets in Gas Metal Arc Welding. *Science and Technology of Welding and Joining*: in press.
10. Rosenthal, D. 1946. The Theory of Moving Sources of Heat and its Application to Metal Treatments. *Trans. ASME* 68: 849-866.
11. Christensen, N.; Davies, V. de L.; and Gjermundsen, K. 1965. Distribution of Temperatures in Arc Welding. *British Welding J.* 2: 54-75.
12. Adams, C. M. 1958. Cooling Rates and Peak Temperatures in Fusion Welding. *Welding J. Res. (Suppl.)* 37: 210s-215s.

Session B6: Welding Documents and Database Applications

BENEFITS TO BE GAINED FROM COMPUTERIZING THE MANAGEMENT OF FABRICATION

A D Brightmore and M Bernasekˆ

ABSTRACT

Welding engineers have managed welding procedures and welder performance qualifications using computers for some years now and have been gaining benefits such as :

- readily accessible information : no more searching through large amounts of paper.
- easy development of procedures and qualifications through on-screen editing.
- professional looking documentation.
- advance warning of expiry.

Most fabricators now have local or wide area networks and sharing information between key personnel is easier than it has ever been. This paper describes the benefits that can be gained from use of computers to integrate management of procedures and qualifications with production weld information and quality control data. Such integrated systems can give :

- instant progress reporting, important perhaps for stage payments.
- automatic assignment of procedures and personnel, ensuring qualifications are up to date.
- automatic generation of progress reports, including testing percentages and repair rates, etc.
- automatic update of WPQs, based on satisfactory production welds.
- automatic generation of documentation packs.
- instant traceability between production welds and procedures, qualifications and QC data.
- efficient archiving of fabrication information.
- satisfaction of QA requirements.

The paper also describes some of the difficulties in developing such systems, and the pitfalls to be wary of.

KEYWORDS

WPS, PQR, WPQ, Welding procedure, ASME IX, EN 288/287, Software, Production welding

INTRODUCTION

Computers have always been good at storing large amounts of data and sorting and searching through that data, making them suitable for pure database applications. Such applications have depended on the user being able to identify parameters for searching easily, or with minor help from the software. In welding, such systems have been used for managing welding procedures and welder performance qualifications and to date, most have had limited, if any, 'expertise'.

The problem with building expertise into software is that it is necessary to have a deep understanding of both software development, and the technology being computerized. In our

industry, this might include a knowledge of many subjects, including metallurgy, engineering, production, quality control and standards. Standards are particularly important as many aspects of fabrication are specified via national and international standards, such as ASME IX, AWS D1.1, EN 287/288 and ISO 9000.

Software houses with no depth of welding expertise or engineers with no depth of software development skills both find it difficult to develop expert welding systems. It may be possible for individual engineers to develop software, but long term support is at best difficult, and in most cases impossible. For storage of large amounts of information, where considerable time is invested in entering the data, long term support is critical.

In addition, most existing software systems in the fabrication industry are tools for individuals, not large parts of organizations, because until recently, most organizations have simply not had the infrastructure to allow information to be distributed electronically. The widespread use of email has been one of the main driving forces behind the move of most fabricators to use local and wide area networks. It is now possible to share welding procedures or welder approvals across a company via a multi-user software system.

Even so, welding procedures and welder performance qualifications are usually managed by one or two key personnel. The information may be made available across a company, but usually only in a read-only form. By using local and wide area networks, it is now possible to computerize, and integrate database systems, so maximum benefits can be gained. This paper describes the benefits of computerizing welding procedures and performance qualifications, as well as the integration of these with systems of wider scope to manage all aspects of fabrication. Practical examples are used to illustrate how such software can be used in practice.

Welding Procedures and Welder Performance Qualifications

The management of welding procedures is one of the most time-consuming jobs of a welding engineer. Creating, verifying and approving new procedures, and checking, adapting and approving existing procedures takes a long time. Consequently, this was one of the first welding engineering tasks to be computerised. TWI's Weldspec and Computer Engineering's Welding Pro-Write are examples of such software.

Much of this job is administrative. That is, the management of paper welding procedures involved a lot of time with a typewriter and liquid paper. Creating or modifying procedures was very cumbersome. Searching for existing procedures for new production welds was a very time-consuming task and required expert skills.

The first welding procedure database management systems were simply electronic filing cabinets. They used the speed of data-sorting that computers could offer to make searching for existing procedures much quicker. The ease with which documents could be copied and edited to create new documents meant that this task could be undertaken much faster. What they could not do very easily, however, was to give the welding engineer much help when creating new procedures for new applications.

The problem was that the sources of such information are wide and disparate. They comprise standards (welding and application), consumable and parent material handbooks, technical literature and, most difficult of all to computerise, experience. To build all this into a computer program would be, at best, very time-consuming, and impossible without a wide knowledge of the sources available.

TWI and C-spec have collaborated to develop a new version of Weldspec (version 4). Weldspec 4 has been designed to give the welding engineer help in writing and drafting new welding procedures while still giving the benefits of speed and editing of existing procedures, in a full 32-bit Windows application. The development of the program has required expertise in a large number of factors, including :

World-wide welding and application standards, from such organizations as ASME, AWS, European Standards, API etc.

Industry practice in developing, qualifying and using welding procedures.

Typical interactions between customer, fabricator and inspector.

Welding engineering and metallurgy.

Software development and knowledge representation techniques.

The representation of knowledge is important because software based on knowledge and recommendations from standards needs to be frequently updated (ASME IX is updated every year). Knowledge that is hard coded within software is difficult to change. Weldspec's knowledge-base is stored externally to the main program in an easily modified format, making updating more simple.

Management of welder performance qualifications is very similar to welding procedures, in that their administration is defined by standards. Thus, the variables which must be recorded, the extent of approval given by a test and the destructive and non-destructive test regimes are specified in national and international standards.

However, unlike welding procedures, WPQs are only valid for a specified time without practice or additional testing. Certificates expire, so the date of expiry becomes another key variable, so the fast sorting capability of computers is even more beneficial.

TWI and C-spec have collaborated in development of Welderqual 4, which integrates seamlessly with Weldspec 4. For example, the two programs use a shared database of welder details and WPQs can be created directly from welding procedures.

Production Welding and Quality Control

The management of welding procedures and performance qualifications, as described above, can give great benefits in saving time and reducing errors. However, if this is integrated with software to manage production welding and quality control, the benefits can be multiplied.

The Problems

Most fabricators work in a compartmentalized way. The functions of design, engineering, production and quality control are discrete and communication is often difficult. This can give a number of problems :

It is accepted that any error in the design stage of a fabrication can be very expensive to rectify once a weld has been completed. The concept of simultaneous engineering, where all personnel can contribute at all stages of manufacture, is particularly relevant to fabrication.

It is difficult to monitor fabrication, as paperwork can take a long time to circulate. This means that problems can become serious before they are identified.

The sheer weight of paperwork can make it very difficult to update welder performance qualifications based on satisfactory production welds. Many fabricators retest welders unnecessarily. Also, it can be very difficult to identify those welders whose qualifications are close to expiring.

Similarly, it can be very difficult and extremely time consuming to collate project data books, simply because of the amount of paper.

The Solution

An integrated software system such as Welding Co-ordinator can overcome all the problems listed above. Welding Co-ordinator is designed to be used live to manage fabrication as it is progressing. It is usually based around an electronic 'weld map', or 'weld data sheet' or 'weld schedule', into which data are entered as welds are designed, engineered, welded and tested. The weld map would also usually have some space for approval, either weld by weld, or once a project or structure has been completed. Figure 1. shows an example of part of a weld map, for a fabricator in the power generation industry, and figure 2. shows an example of the system as used in the chemical process industry.

Data are usually entered into the system from four functions :

At the design stage, where information such as the weld ID number and other design parameters (material type, thickness, joint type, etc) are entered.

At welding engineering, where a procedure is assigned. It may also be possible to identify suitable welders or classes of welders qualified to make the weld, although this is more likely to be done at the production stage.

At production, where the completion of a weld is registered (usually by entering the date) and visual inspection carried out and approved.

At quality control, where acceptance of the weld is registered. This may be simply by typing test report numbers into the system, or it may be done with live links to NDTspec or similar systems.

It should be stressed that these data should be entered live into the system, as fabrication progresses.

As well as solving the problems identified above, the system can give a number of other benefits, including the following :

Instant progress reporting. Anyone with access to the system can see how fabrication is progressing. This may be simply by looking at the weld data sheet on screen, or by explicitly-programmed progress reports. These can identify bottlenecks (e.g. by comparing the number of welds completed with the number of welds radiographed), or help to produce reports for stage payments in large projects.

Automatic assignment of welding procedures and welders. If enough information is supplied at the design stage, the system has everything it needs to automatically search through Weldspec's database of procedures for suitable WPSs. This may be a single WPS or a number from which to choose. It is important to recognise that this can be done simply with a click of a mouse button. Also, having chosen a suitable WPS, the system can search through Welderqual's database of WPQs to identify suitably-qualified welders. If necessary, the system can list welders in order of expiry date of their certificates so maximum benefit can be made of extending their qualifications.

Automatic production of test requisitions. The system illustrated in figure 2 automatically produces NDT requisitions, based on the NDT requirements for the project. These can be selected either manually, or the system could 'randomly' select welds for testing.

Automatic generation of test percentages and repair rates. The system can produce reports on repair rates per welder (to identify training requirements) by procedure (to highlight defect-prone procedures) or any other measure, providing the relevant data are recorded. Figure 3 is a printed report showing the number of welds of different sizes produced by each welder on a project.

Automatic update of WPQs. This is a very time consuming task on paper and may be impossible due to the amount of paperwork. However, it is ideally suited for computerisation because it is a simple data sort and test function. The integration between Welding Co-ordinator and Welderqual makes it possible for the system to update all WPQs in a project, based on satisfactory production welds.

Automatic generation of document packs on completion of a project. This can also be a very time-consuming task manually, but again is ideally suited for computerisation. On the click of a button, the system can print the weld data sheets for a project, along with all the WPSs used (with backup PQRs if necessary) and all the WPQs. In addition, if NDTspec has been used to

report testing, the system can print relevant NDT reports as well. Alternatively, this information can be archived on CD, which obviously takes less space.

Instant traceability between production welds information and the back-up information. Thus, if the inspector wants to see a WPS that was used on a weld, or wants to see proof that the welder was suitably qualified, this can be done on the click of a button. This facility can also be useful after a number of years of service. If a defect is found in a structure, it is possible to access the original WPS (for repair purposes), or the NDT report (to see if evidence of the defect was present at testing).

Satisfaction of QA requirements. There can be no doubt that the use of a system such as Welding Co-ordinator can help to satisfy the most stringent of QA requirements.

Problems and Pitfalls

If all the above seems too good to be true, there are paybacks and pitfalls, as described below :

For any customised software, it is critical to get the requirements of all personnel who will use the system identified at an early stage, and approved by all concerned. In practice, the software developer and the fabricator will collaborate in producing a list of requirements (WHAT the system will do) and both parties will sign this document. This is a base line from which the system is designed and developed, and is used to measure the quality of the software produced. It works for both the fabricator and the system developer.

The production of a requirements document can be a time-consuming process, and the timescale and cost of the system can only be estimated after this has been generated, so it is an important stage in development.

A system such as Welding Co-ordinator affects may people, as it is, by its nature, a multi-user program. Any form of change is often resisted, so it is important to identify all the potential users of the system and involve them in the requirements analysis stage. Any users not involved in this stage can claim the system does not do what they want. This may be because it makes their job harder, or can be used an excuse to avoid change.

From a system developer's point of view, it is important to find a champion of the system within the fabricator's organisation. This person can help to promote the system in the absence of the developer. This person should either have a senior position, or be well respected.

It is very tempting to develop the system to be too prescriptive. For example, it is possible to develop the Welding Co-ordinator system to only allow the selection of welders who are registered in Welderqual as being qualified. In practice, however, the qualification test may have been taken, but the NDT results may not have been received. Prohibiting selection of that welder would not be correct in such circumstances.

Arguments often arise between QA/QC personnel and engineering staff on how prescriptive to make the system. Experience shows that it is preferable to err on the non-prescriptive side, at least in the early stages of system implementation. It is always possible to modify the system.

ACKNOWLEDGEMENTS

The authors would like to thank ABB Power Construction Ltd (Derby, UK) for their permission to reproduce parts of their system within this paper.

FIGURES

Figure 1. A Weld Data Sheet from a Welding Co-ordinator used by a fabricator in the power generation industry.

Figure 2. A Fabrication Inspection Record from a fabricator in the chemical process industry.

Figures 3. A printed report showing numbers of welds of different sizes produced by welders on a project.

New Construction Weld Case History

Site	PETERHEAD REPOWERING PROJECT			System N°	11-LEL-2IP2A002A	Drawing N°/Spec	LEL-2IP2A002A	File/Section	/	Pressure Test	
Contract	HRSG ERECTION	P Number	P0767-11	System	IP EVA D COMER, IPEVA IN, IP EVA FEED	Sheet	1	ISO Ref	NA	Total Welds	33
Client		Client Ref	6EB1-2668-CO1			Description	IP DOWNCOMERS	Quality Plan N°		Report Date	28-Oct-1999

Material Parameters						Weld Parameters									Inspection And Test							
Weld Number		Parameters				Root/Fill/Cap Weld							Weld Procedure		Report Number And Verdict							
Weld	TQ N°	Material A	Material B	Dia	Thk	Joint	State	ID	Weld Date	Type	Batch	Size	WPS	Process	PWHT	Radiograph	Ultrasonic	DPI	MPI	Ferritic	Hardness	Final
01		A105	106B	323.90	9.53	BW							C/044/AS	GTAW SMAW								
02		106B	106B	323.90	9.53	BW							C/044/AS	GTAW SMAW								
03		106B	106B	323.90	9.53	BW							C/044/AS	GTAW SMAW								
04		106B	106B	323.90	9.53	BW							C/044/AS	GTAW SMAW								
05		106B	106B	323.90	9.53	BW							C/044/AS	GTAW SMAW								
06		106B	106B	323.90	9.53	BW	R	438	16-Jun-1999	PZ6500	123263	2.40	C/044/AS	GTAW SMAW		A 086						
							F/C	438	16-Jun-1999	7018S	503577	3.20										
07		106B	106B	323.90	9.53	BW	R	435	16-Jun-1999	PZ6500	123263	2.40	C/044/AS	GTAW SMAW		A 077						
							F/C	435	16-Jun-1999	7018S	503577	3.20										
08		106B	106B	323.90	9.53	BW							C/044/AS	GTAW SMAW								
09		106B	106B	323.90	9.53	BW							C/044/AS	GTAW SMAW								
10		106B	106B	323.90	9.53	BW							C/044/AS	GTAW SMAW								
11		106B	106B	323.90	9.53	BW							C/044/AS	GTAW SMAW								
12		A105	106B	323.90	9.53	BW							C/044/AS	GTAW SMAW								
13		106B	106B	273.10	12.70	BW	R	420	19-Jun-1999	PZ6500	123263	2.40	C/044/AS	GTAW SMAW		A 086						
							F/C	420	19-Jun-1999	7018S	503577	3.20										
14		106B	106B	273.10	12.70	BW	R	438	18-Jun-1999	PZ6500	123263	2.40	C/044/AS	GTAW SMAW		A 086						
							F/C	438	18-Jun-1999	7018S	503577	3.20										
15		106B	106B	273.10	12.70	BW	R	420	19-Jun-1999	PZ6500	123263	2.40	C/044/AS	GTAW SMAW		A 086						
							F	420	19-Jun-1999	7018S	503577	3.20										
16		A234-WPB	106B	141.30	6.55	BW	R/F/C	346	21-Aug-1999	PZ6500	133713	2.40	C/043/AS	GTAW								
17		A234-WPB	106B	141.30	6.55	BW							C/043/AS	GTAW								
18		A234-WPB	106B	141.30	6.55	BW							C/043/AS	GTAW								
19		A234-WPB	106B	141.30	6.55	BW	R/F/C	346	21-Aug-1999	0PZ6500	133713	2.40	C/043/AS	GTAW								
20		A234-WPB	106B	141.30	6.55	BW	R/F/C	346	21-Aug-1999	PZ6500	133713	2.40	C/043/AS	GTAW								
21		A234-WPB	106B	141.30	6.55	BW	R/F/C	346	21-Aug-1999	PZ6500	133713	2.40	C/043/AS	GTAW								
22		A234-WPB	106B	141.30	6.55	BW	R/F/C	447	20-Aug-1999	PZ6500	133713	2.40	C/043/AS	GTAW								
23		A234-WPB	106B	141.30	6.55	BW	R/F/C	447	20-Aug-1999	PZ6500	133713	2.40	C/043/AS	GTAW								
24		A234-WPB	106B	141.30	6.55	BW	R/F/C	447	20-Aug-1999	PZ6500	133713	2.40	C/043/AS	GTAW								
25		A234-WPB	106B	141.30	6.55	BW							C/043/AS	GTAW								
26		A234-WPB	106B	141.30	6.55	BW							C/043/AS	GTAW								
27		A234-WPB	106B	141.30	6.55	BW	R/F/C	447	20-Aug-1999	PZ6500	133713	2.40	C/043/AS	GTAW								
28		A234-WPB	106B	141.30	6.55	BW	R/F/C	234	20-Aug-1999	PZ6500	133713	2.40	C/043/AS	GTAW								
29		A234-WPB	106B	141.30	6.55	BW							C/043/AS	GTAW								
30		A234-WPB	106B	141.30	6.55	BW							C/043/AS	GTAW								
31		A234-WPB	106B	141.30	6.55	BW	R/F/C	234	20-Aug-1999	PZ6500	133713	2.40	C/043/AS	GTAW								
32		A234-WPB	106B	141.30	6.55	BW	R/F/C	234	20-Aug-1999	PZ6500	133713	2.40	C/043/AS	GTAW								
33		A234-WPB	106B	141.30	6.55	BW	R/F/C	234	20-Aug-1999	PZ6500	133713	2.40	C/043/AS	GTAW								

FABRICATION INSPECTION RECORD

W.O.N: won 1a
PLANT: Innovex planta
PLANT ITEM NUMBER: 34a
DESCRIPTION: Repair to boiler heada
CRITICALITY LEVEL: 1a
DRAWING NUMBER: 12345a

DATE RECEIVED: 01/01/1998
DATE DUE: 01/02/1998

SHEET NUMBER: 1 of 1
JOB PACK/FILE NUMBER: QA/99-0001
PMP NUMBER: 1234
REPAIR SHEET NUMBER: 1234
WELDING STANDARD: EN288a
COST CODE: 1234a

										1	2	3	4	5				6	7				8
										PRE-WELD NDT	SETUP	PREHEAT	POST WELD VISUAL ACCEPT	NDT				POST-HEAT	POST WELD HEAT TREATMENT NDT				PRESSURE TEST
														MPI	DPI	RADIOGRAPHY	ULTRASONIC		MPI	DPI	RADIOGRAPHY	ULTRASONIC	
Spool Number	Weld Number	Dia/Sch.	Material	Process	Joint configuration	PWHT	WPS Number	Welder ID	Consumable batch number	Report Number	Initials	Chart Number	Initials	Report Number	Report Number	Report Number	Report Number	Chart Number	Report Number	Report Number	Report Number	Report Number	Report Number
			A1 A1 A1 A1	01 01	02 02	No																	
1	1					No			1					Req	Req	Req	Req						
1	10	1 Sched 5S 1.651	A1 A1 A1 A1	02 02	02 02	No								Req	Req	Req	Req						
1	11		A3 A3 A3 A3	03 03	02 02	No								Req	Req	Req	Req						
1	2	1 Sched 5S-1.651	A3 A3 A3 A3	01 01	01 01	No			2														
1	3		A1 A1 A1 A1			No			3														
1	4					No			4														
1	5	3/4 Sched 5S-1.651	A1 A1 A1 A1	01 01	01 01	No	2000							Req	Req	Req	Req						
1	6	3/4 Sched 5S-1.651	A3 A3 A3 A3	06 06	06 06	No								Req	Req	Req	Req						
1	7	3/4 Sched 5S-1.651	A1 A1 A1 A1	01 01	01 01	No	2000	BPC 12						Req	Req	Req	Req						
1	7	3/4 Sched 5S-1.651	A1 A1 A1 A1	01 01	01 01	No	2000	BPC 12						Req	Req	Req	Req						
1	7	3/4 Sched 5S-1.651	A1 A1 A1 A1	01 01	01 01	No	2000	BPC 12						Req	Req	Req	Req						
1	7	3/4 Sched 5S-1.651	A1 A1 A1 A1	01 01	01 01	No	2000	BPC 12						Req	Req	Req	Req						
1	8	1/2 Sched 5S-1.651	A4 A4 A2 A2	03 03	01 01	No								Req	Req	Req	Req						
1	9		A2 A2 A2 A2	02 02	02 02	No								Req	Req	Req	Req						

WELD SUMMARY

Spool No	Weld No	Process	WPS
1	1		
1	10	02	
1	11	03	
1	2	01	
1	3		
1	4		
1	5	01	2000
1	6	06	
1	7	01	2000
1	8	03	
1	9	02	

NDT REQUIREMENTS

WELD PREP MPI/DPI	n/a	RADIOGRAPHY	n/a
MPI	n/a	ULTRASONIC	n/a
DPI	n/a	PRESSURE TEST MEDIA	n/a
		TEST WITNESSED	n/a
PWHT		TEST PRESSURE	

HOLD POINTS

HOLD POINT	1	2	3	4	5	6	7	8
TICK								
ACTIONED BY								

ADDITIONAL INFORMATION

thisis some etst

WORKSHOPS DIMENSIONAL ACCEPTANCE		INDEPENDANT INSPECTION AUTHORITY ACCEPTANCE		ENGINEERING INTEGRITY ACCEPTANCE		WORKSHOPS QA ACCEPTANCE	
SIGNATURE	DATE	SIGNATURE	DATE	SIGNATURE	DATE	SIGNATURE	DATE

REPORT CRITEREA

WON: won 1a

PLANT ITEM NUMBER: 34a

DRAWING NUMBER: QA/99-0001

SEARCH RECORDS: No, based on all records

REPORT PERIOD: No range specified

WELDER PRODUCTIVITY REPORT

Welder ID	GTAW					SMAW					OTHER					TOTALS				
	Weld Length	No. Welds	No. Rad	No. Repaired	% Repair Rate	Weld Length	No. Welds	No. Rad	No. Repaired	% Repair Rate	Weld Length	No. Welds	No. Rad	No. Repaired	% Repair Rate	Weld Length	No. Welds	No. Rad	No. Repaired	% Repair Rate
	9.43	1	1	0	0%	0.00	0	0	0	0%	0.00	0	0	0	0%	9.43	1	1	0	0%
BPC 12	37.71	4	4	0	0%	0.00	0	0	0	0%	0.00	0	0	0	0%	37.71	4	4	0	0%

Total Weld Length (all processes)	47.14
Total No. Welds (all processes)	5
Total No. Radiographed (all processes)	5
Total No. Repaired (all processes)	0
% Repair Rate (all processes)	%

HEAT AND MATERIAL FLOW MODELING OF THE FRICTION STIRWELDING PROCESS

C. B. Smith[*], G. B. Bendzsak[#], T. H. North[#], J. F. Hinrichs[@], J. S. Noruk[*], R. J. Heideman[^]

ABSTRACT

To gain an improved understanding of the friction stir welding (FSW) process, a heat and material flow model has been developed to determine the material flow, temperature distribution, and process loads (forces and torque) during the FSW of aluminum. Inputs to the model are the weld tool geometry, tool position, travel speed and rotation speed. Pursuant to the development of the FSW model, there was no information regarding material properties of aluminum at elevated temperatures (e.g. viscosity and boundary conditions). These material properties are essential information for the model to accurately predict the heat and material flow.

The first phase of model development was to determine these unknown material properties. This paper describes the specific model development and experiments used to determine these material properties. Further experiments are also described, which were used to confirm the accuracy of the model. The second phase of the modeling effort used the material property and boundary condition information acquired from the first phase to develop a full three-dimensional model of the friction stir welding process.

INTRODUCTION

Friction stir welding is a solid phase joining process that was invented in 1991 by TWI (The Welding Institute) in Cambridge, U.K. (Ref. 1, 2). FSW has been primarily used to join Aluminum alloys, but has also been used to join numerous other materials (Ref. 3). For joining aluminum alloys, FSW has several advantages over fusion joining processes, which are most commonly used to join aluminum. These advantages include; 1) FSW is an autogeneous process requiring no consumables, 2) improved tensile joint efficiency, 3) improved fatigue strength, 4) reduced distortion as a result of lower heat input, 5) safety improvements (no arc radiation, fumes, etc.), and 6), improved process uptime as a result of being a more robust process (Ref. 3). However, these advantages do not come without any challenges. The two most prohibiting challenges are the relatively large forces required and the slower travel speed when compared to a fusion joining process, such as Gas Metal Arc Welding (GMAW).

For the automotive industry, the advantages of FSW represent a chance to significantly lower aluminum joining costs. The cost advantage can be fully realized, if travel speeds are increased

[*] Tower Automotive, Advanced Technology - Process, Milwaukee, WI, USA
[#] University of Toronto, Toronto, ON, Canada
[@] The Welding Link, Menomonee Falls, WI, USA
[^] A.O. Smith Corporate Technology, Milwaukee, WI, USA

and process loads are decreased (reduces capital costs). In the initial development of the FSW process, travel speeds have been reported to be in the range of 0.25 meters / minute (10 IPM) for 6 mm thick butt welds of 6061 Aluminum (Ref. 4). Whereas, travel speeds of 0.75 to 1.5 meters / minute (30 – 60 IPM) in lap welds of 3 to 4 mm material are common for the GMAW process, which is the most common joining process for aluminum in the automotive structures business. Although, the compared travel speeds are not for the same material thickness nor joint configuration, a FSW tool to perform a butt weld on 6 mm thick material is similar in geometry to an FSW tool for a lap penetration weld on 3 to 4 mm thick material.

Decreasing the process loads of FSW is also an important goal, as there is a need to be able to perform FSW on an industrial robot. There are two critical reasons for being able to perform FSW on a robot; both are related to decreasing the costs of FSW. First, there is a definite need to be able to perform FSW along three-dimensional paths. Industrial robots are ideal for generating three-dimensional paths; however, their load capability is limited. Still, it has been shown that a low-cost standard industrial robot can indeed perform three-dimensional FSW (Ref. 5). However, FSW can only be performed on aluminum within a limited thickness range (up to 3 mm). Thus, custom machines will likely be required, if loads are not decreased. Unfortunately, custom equipment costs are much higher than standard industrial robot costs. Secondly, there is the automotive industry's familiarity with industrial robots. New and unknown equipment raises operating, maintenance, and training costs.

Furthermore, GMAW is the preferred alternative to FSW and is generally performed by industrial robots. Thus, when comparing FSW to GMAW, the limitation of only being able to perform FSW on a custom machine may mean GMAW is more cost competitive, especially considering the added cost of FSW will be primarily in capital equipment. Therefore, load reductions are necessary for FSW to be performed on a standard industrial robot. This will make FSW more cost competitive and will allow for wider acceptance in the automotive industry.

It was perceived that tool design (tool material, tool geometry, coatings) was the most promising area for process optimization to achieve the goal of reducing the loads and increasing the travels speeds during FSW welding. One approach to solve this problem is a trial and error tool design process. Due to the significant cost of testing, even one tool design, it can be prohibitively expensive to exhaustively study a wide range of tool designs for their FSW feasibility. Testing of one tool design would include a weld parameter development study, tensile testing, and fatigue testing. Secondly, there is little guarantee that an optimal tool design has been achieved.

Another approach is to develop a completely theoretical model. This has the obvious problem of not having any validation and can easily yield incorrect results. Therefore the project team at Tower Automotive decided the best approach was to develop a process model of the friction stir welding process with a significant amount of experimental validation. With an accurate and valid process model, optimal weld parameters and tool designs could be determined.

It is also noted that relatively little information is available regarding material flow characteristics, which control weld quality. Again, a trial and error experimental approach followed by metallurgical analysis of many welds could yield information about these aspects,

but the effort could also be overwhelming. It was perceived that a process model could also yield more information about material mixing, defect presence, and retained oxide films.

The specific objective was to develop a model, which was physics based, with no assumptions regarding heat generation and material flow characteristics. This was based primarily on the fact that in FSW welds, the area of material flow is relatively small. If broad assumptions were made regarding the heat generation or material flow, then we were likely to miss important characteristics of FSW welds. The inputs to the model include tool design, tool position, tool rotation speed, and travel speed. The outputs include required forces and torque, temperature distribution, and material flow profiles. It was also decided that this model development should entail significant experimentation to aid in model development and confirmation of model output.

The model development was divided into two distinct phases. The first phase was to develop unknown material properties and boundary conditions that would be required to accurately predict the flow profiles in actual friction stir welds. To determine these properties a two-dimensional system (physical experiment and model) was setup, which is equivalent to an infinite sea viscometer. The second phase was to develop a three-dimensional model of the actual welding process. This paper describes results obtained from the first phase of the project, including the material properties of aluminum that are critical to the successful implementation of a full three-dimensional model of the friction stir welding process. The three-dimensional modeling effort is also briefly described.

TEXT

When investigating a specific approach to modeling of the friction stir welding process, two basic approaches were considered. The first approach is to model the heat generation through friction and subsequently model the material flow. An alternative is to develop a physics based model using equations of fluid mechanics to describe the material flow. Heat generation is then assumed to be via viscous heat dissipation of mechanical energy.

Both approaches to the modeling of the friction stir welding process were investigated. It was concluded that the use of fluid mechanics to model material flow and the heat generation via associated viscous heat dissipation was most likely to achieve positive results. Questions arose as to how and whether friction could be used to explain high temperature phenomena (Ref. 6, 7) and the details of the material flow that occurs during FSW. In a literature review, it was determined that the rotary friction welding (FW) process has been modeled using a fluid mechanics approach (Ref. 8, 9, 10), as well as the aluminum extrusion process (Ref. 11). It was determined that observed material flow patterns could be replicated using fluid mechanics, lending credence to this approach. One material flow pattern that could be observed in rotary friction welding in both the model and the actual process is spiral defect formation, indicating that a fluid flow based approach could be used to model the material flow in actual welds. Another important aspect of the rotary welding research was the geometry of the actual samples in relation to the geometry of the FSW tool that is effective for joining aluminum between 3 mm

and 6 mm. In the work by North and Bendzsak, the rotary friction welded tubes were 19 mm in diameter and were welded at 1000 to 2000 RPM, which is in the neighborhood of the tool diameter and parameters used for FSW of aluminum in the above thickness range.

Since it was known that the principles of fluid mechanics had been successfully employed to model the FW process with similar parameters to that used for FSW of 6061 aluminum, the fluid mechanics approach was used in this modeling effort. The Navier-Stokes equations are used to describe fluid mechanics and equate rate of change of momentum due to convection with the addition of applied force due to pressure gradients and rate of change of momentum due to diffusion. (Ref. 12)

$$\rho\frac{DV}{Dt} = F_{pressure} + F_{shear}$$

$$\frac{\partial V}{\partial t} + (\nabla\bullet\nabla)V = -\frac{1}{\rho}\nabla P + \frac{\mu}{\rho}\nabla^2 V$$

Equation 1

where ρ is the material density, V is the velocity vector, P is the pressure, and μ is the viscosity.

The heat generation then is a balance between convection and diffusion or

$$\rho C_p\left(\frac{\partial T}{\partial t} + v_r\frac{\partial T}{\partial r} + v_z\frac{\partial T}{\partial z}\right) = \frac{1}{r}\frac{\partial}{\partial r}\left(kr\frac{\partial T}{\partial r}\right) + \frac{\partial}{\partial z}\left(k\frac{\partial T}{\partial z}\right) + \mu\Phi$$

where

$$\Phi \approx \left(\frac{\partial v_\theta}{\partial z}\right)^2 + \left(\frac{\partial v_\theta}{\partial r}\right)^2$$

Equation 2

where, C_p is heat capacity, T is temperature, μ is viscosity, k is thermal conductivity, and r and z are the independent geometry variables.

Of major importance is the existence of the viscosity term in the heat generation equation, which means the heat generation is self-consistent with the fluid mechanics equations. Thus, if these equations are used as is, without any correction factors, this modeling approach will only work correctly, if and only if, viscous heat dissipation is the source of the heat generation and the equations of fluid mechanics can be used to model the FSW process. The following assumptions have been made regarding the FSW process in this modeling effort:

1) Non-Newtonian flow
2) Viscosity is a function of temperature and shear rate
3) Material velocity equal to tool velocity at tool material interface and decreases linearly to the edge of the material flow zone
4) Maximum temperature is solidus temperature

5) Zero heat transfer into surroundings (tool and samples insulated)

In the first phase, the objective was to determine material properties of the aluminum at elevated temperatures. This information could then be used in the full three-dimensional model. To simplify the process of determining the material properties an axi-symmetric two-dimensional model and experimental system were developed, which we refer to as an infinite sea viscometer system. The experimental system is depicted in Figure 1.

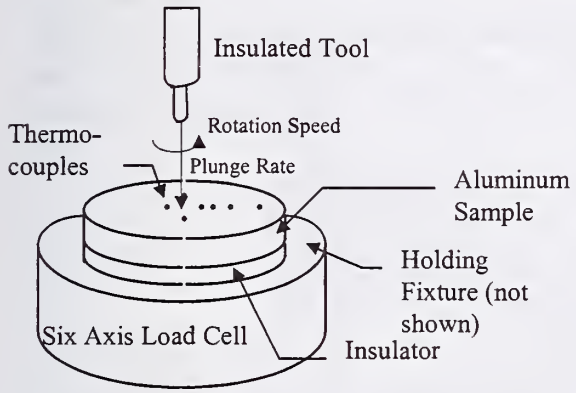

Figure 1: Schematic of Two-Dimensional Axi-Symmetric Experimental System.

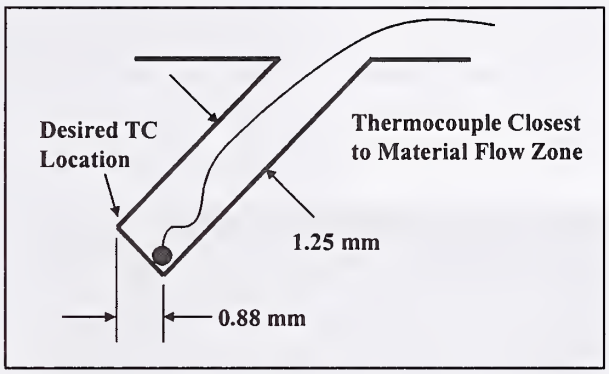

Figure 2: Schematic of Thermocouple Location Closest to Tool.

The system consisted of a 100 mm diameter by 12.7 mm thick 6061-T6 disk located rigidly within a fixture. The fixture was partially fabricated of a ceramic insulator (aluminum silicate), so as to surround the aluminum in order to eliminate the heat transfer into the fixture. The fixture was then mounted to a six-axis load cell, which measured the three force components and three torque components. An array of Type K thermocouples was mounted into the mid-thickness portion of the aluminum disk via 1.25 mm diameter holes drilled to the center of the plate. To determine the temperature as close as possible to the material flow zone, the thermocouple closest to the material flow zone was inserted into a hole that was drilled at a 45° angle from the surface, as shown in Figure 2. The objective was to insure that any effect on the material flow as a result of the hole was negligible. The tool used in the experiments had a smooth profiled 5 mm diameter pin and no shoulder, and was partially comprised of a ceramic insulator. The tool had a ceramic insulator to eliminate heat transfer up into the shank of the tool, in order to provide another simplification to the model.

In the experimental system, force, torque and temperature data were collected using a 16-channel data acquisition system, as the tool was plunged into the center of the aluminum disk at a specified and controlled rate. The data in the initial experiments were collected at a 20 Hz rate. It should be noted that the thermocouple signal conditioning equipment employed a 4 Hz filter. Therefore, useful higher frequency information could only be gleaned from the force and torque data. In the initial experiments, a tool with a 5 mm cylindrical pin (with 3.75 mm radius spherical bottom) was plunged into the aluminum to a depth of 5.56 mm at a rate of 0.25 millimeters per second at 1100 RPM.

The torque data (converted to power) were then entered into the corresponding two-dimensional model. The model then performed an iterative process to determine the viscosity of aluminum as a function of shear rate and temperature. In addition to a viscosity curve, the model outputted the material flow profile and temperature distribution. If a correct viscosity curve were outputted, then the model's temperature and material flow profiles should match the actual temperature data and material flow profile.

Using the viscosity curve that was determined, the model was then used to determine a temperature history of the area surrounding the tool and within the tool. Figure 3 shows the temperature distribution at 17 sec. and Figure 4 shows the experimental data profiles. The temperature profile of the thermocouple closest to the rotating pin is shown in Figure 4, along with the associated torque and thrust force.

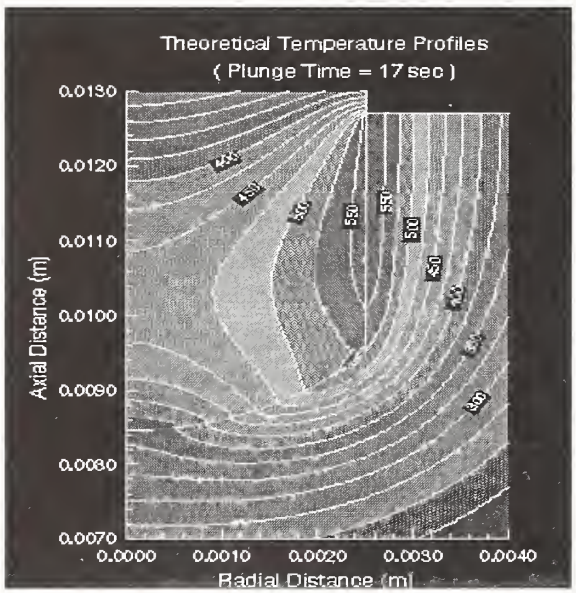

Figure 3: Model Temperature Profile

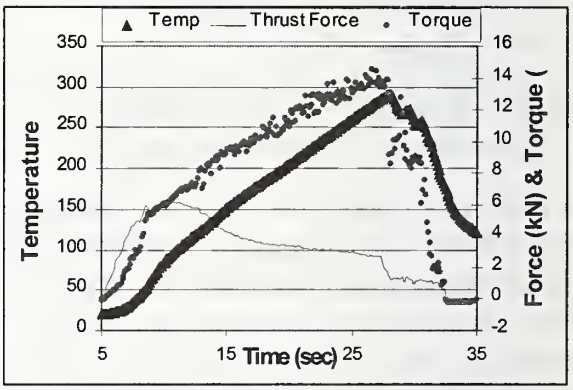

Figure 4: Measured Temperature (TC closest to Tool), Force, & Torque vs. Time

In the initial work to determine material properties, it was found that there were large variations in the outputted viscosity curves based on small changes in the inputted thermocouple location. By observing the above plots it can be seen that the model predicts a very large temperature gradient near the stir weld tool. Thus, the exact location of the thermocouple is very important for the model to predict accurate viscosity curves. Given the fact that the thermocouples closest to the tool were inserted into holes that were 1.25 mm in diameter at a 45° angle to the surface, the precise thermocouple location was unknown, as can be seen in Figure 2. Based on this early finding, further experiments were executed, in which the samples were X-rayed (to determine thermocouple location) prior to being cut for mounting. This did prove to be an effective means of determining the location of the thermocouple. However, the thermocouple tended to favor the lowest point of the hole, which was not the closest point to the tool.

As a result of this, several new methods of thermocouple placement were attempted in which the goal was to obtain a temperature closer to the material flow zone. The experiments executed with the improved method for placing the thermocouple close to the tool were run with the same

parameters as all of the previous experiments. After completion of the experiments, the samples were X-rayed to determine the precise location of the thermocouple nearest the tool. Unfortunately, all attempts showed that material flowed into the hole in which the thermocouple was placed, pushing the thermocouple much further away from the tool than was intended. This is illustrated in Figure 5. As a result, future tests with thermocouples in the samples, did not concentrate on getting a thermocouple near the tool-material interface. In the end, the solution was to place the thermocouple in the tool, 200 microns from the tool's end.

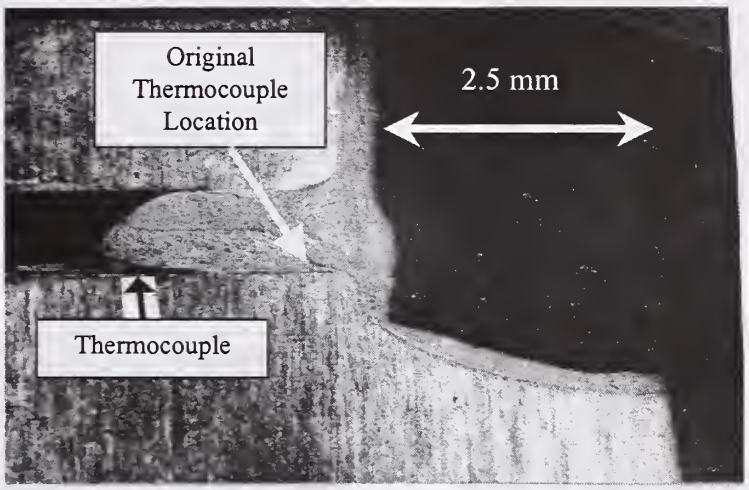

Figure 5: Cross-Section Showing Thermocouple Displacement

At the same time, an observation was made with regard to the model in that a reasonable viscosity curve could not be derived from data within the first few seconds of the plunge of the tool into the aluminum. Also, based on what was believed to be a reasonable viscosity curve, the model did not predict the existence of any material flow in the first few seconds. Furthermore, the model did not predict material flow that completely surrounded the tool until six seconds. To examine these model predictions a series of experimental tests were ran in which the plunge of the tool was stopped at one-second increments. In these experiments, the thermocouple was placed in the tool.

After completing the experiments, the samples were mounted, polished, and etched. A cross-section of the plunge after two seconds is shown in Figure 6 and a cross section of the plunge after six seconds is shown in Figure 7. These pictures indicate that the situation two seconds into the plunge is similar to that produced during sliding wear testing and the plasticized material completely encapsulates the base of the tool by six seconds. These phenomena can also be partly confirmed through visual observation. Particles similar to machining chips were often observed within the first couple seconds of the plunge in these tests and during FSW. Thereafter material can be seen extruding from the bottom of the tool.

Of further interest are the temperature profiles at two and six seconds. Given that the material flow begins after approximately 2 seconds and completely encapsulates the tool at 6 seconds, a temperature of 200° C appears to be a critical temperature where material flow begins. It is seen that the temperature at 2 seconds achieves a maximum of approximately 200° C and at 6 seconds

the temperature all around the tool–material interface is at or above 200° C, as indicated by model predictions. This temperature coincides with a large increase in the effective friction coefficient at 200° C where a rotating aluminum cylinder is forced against a steel counterface during sliding wear testing (Ref. 6). Furthermore, in their experiments Singh and Alpas (Ref. 6) reported material flow characteristics and recrystalized grains in the regions with temperatures exceeding 200° C; these are characteristic features of FSW joints.

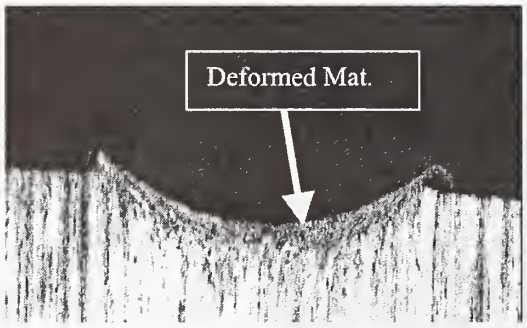

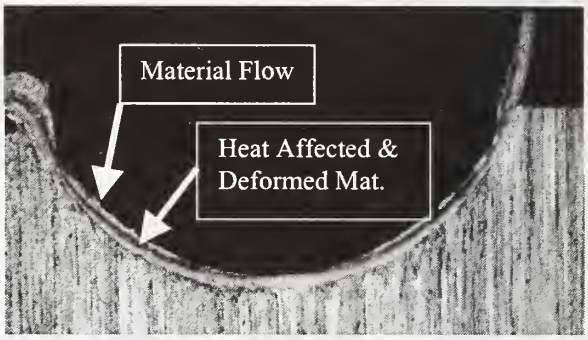

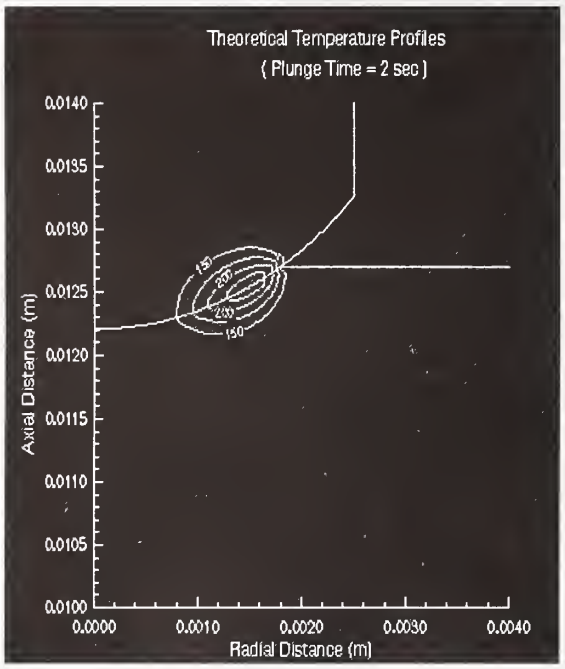

Figure 6: Cross-Section & Temperature after Two seconds

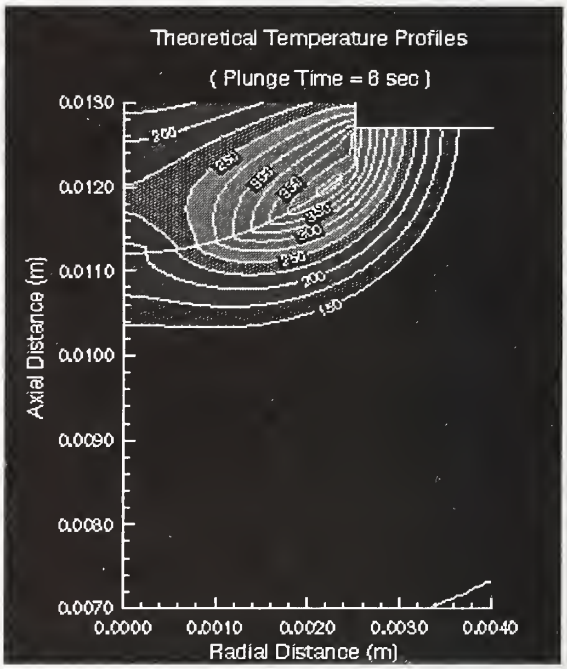

Figure 7: Cross-Section and Temperature after Six Seconds

These observations have important implications for the FSW. For 6061-T6 material these are:

A) Heating is derived from friction and numerous adhesions and seizure events at the beginning of the plunging process.

B) After initial heating, it is believed that the heat generation is through viscous heat dissipation of mechanical energy. This implies that there is no slipping. This statement is essentially correct for the rotation speed and with the tool design used in these experiments. The model

assumes that the material flow rate at the contact point of the tool and the material, is the tool velocity. If this were not the case, then the model would not predict correct results.

For the model to be credible, it should also predict accurate temperature profiles. The theoretical and actual temperature at the center of the tool, 200 microns from the bottom, is plotted in Figure 8. Though it is not displayed, the measured temperature, during the experiment, peaks at 400° C. This is approximately 100° C higher than that measured in the early experiments with the thermocouple placed in the angled hole. From the model output after 20 seconds into the plunge it can be seen that the model predicts a temperature of 410° C while the measured value is 350° C. Over the whole profile the temperature curves are in fairly good agreement, with slopes and slope changes matching well. For a couple of reasons, it would expected that the measured temperature, if there were any deviation, would be lower than the theoretical values. First, the adhesive and the air in the hole in the tool would act to insulate the thermocouple. Another source of error is the assumption of zero heat transfer out of the sample. The insulators significantly decreased conduction into the fixture and tool shank, but could not eliminate it.

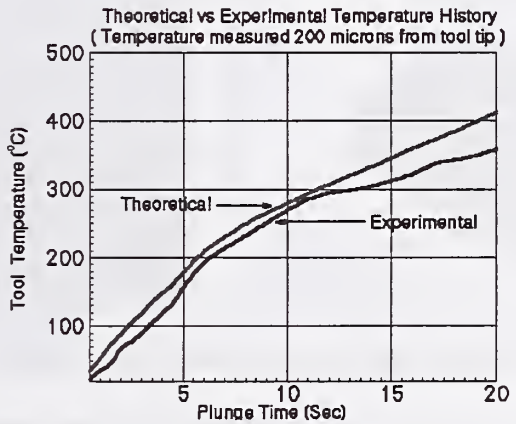

Figure 8: Actual versus Theoretical Temperature Profile (In Tool) at 1100 RPM

With the model predicting behavior that was seen in the time step plunge experiments, confidence in the model's output was achieved for the specific parameters of these experiments. However, the model must also be able to predict the various FSW characteristics using other weld parameter settings. Thus, to further develop the material property parameters, a set of experiments was executed using a range of other rotational speeds (900, 1300, and 1500 RPM). As previously, the model was used to predict viscosity curves, material flow profiles, and temperature distribution with the torque (power), plunge rate, and rotation speed as inputs. From this work, viscosity curves were generated and are shown in Figure 9.

These results can be compared with a theoretical situation where the viscosity relation is well known (Ref. 7, 12). This situation involves a stationary pin surrounded by a fluid, which are both encapsulated by a rotating cylinder. Since the rotating cylinder is also concentric with the pin, this geometry mimics plunging of the pin into the aluminum work-piece, except the rotating features are reversed. The viscosity values in Figure 9 correlate well with this theoretical situation, giving credence to the results that were obtained by using the model.

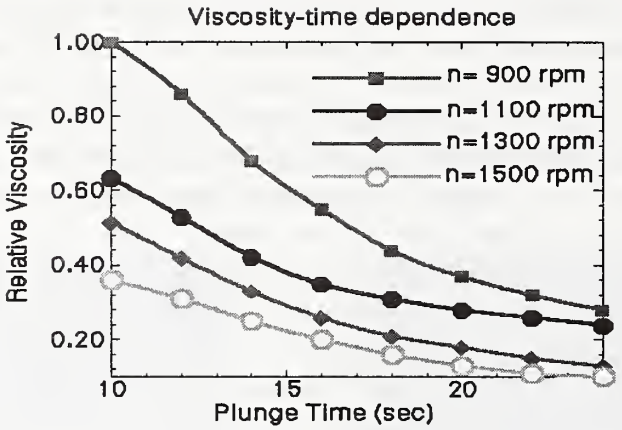

Figure 9: Relative Viscosity at Various Rotation Speeds

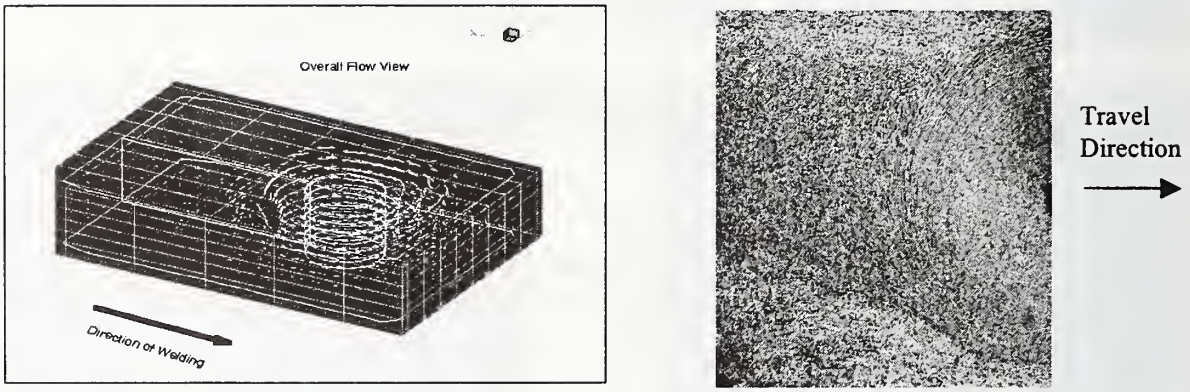

Figure 10: 3-D Model and Corresponding Cross-Section (Plan View < 1 mm off Bottom of Pin)

After determining the viscosity of 6061-T6 as a function of temperature and shear rate, this was used as an input to the three-dimensional model (STIR-3D) of the FSW process. STIR-3D uses tool geometry, alloy, rotation speed, tool position, and travel speed as inputs and outputs the material flow profiles, process loads, and temperature distributions. STIR-3D is currently operating for tools with smooth geometry on the pin, but the goal is to develop a model capable of predicting FSW characteristics for tools having complex geometry. The model will use CAD data as the input and output material flow profiles and temperature distributions in an easy and understandable graphical format. Once the model is able to predict FSW characteristics, the eventual goal is to be able to optimize the tool geometry in order to minimize loads and maximize travel speed.

Initial development of the STIR-3D model involved the simulation of FSW welding using a 5 mm diameter vertical smooth pin (using welding parameters comprising a rotational speed of 1200 RPM and a travel speed of 0.25 m/sec). The program solves for the 3D distributions of velocity and pressure within the weld region as function of viscosity obtained during plunge testing. Figure 10 compares the flow profile produced by STIR-3D and those in a FSW weld.

The behavior of pressure is particularly important during FSW welding. Figure 11 shows the situation that occurs immediately behind the moving tool (at a distance of 200 microns from its periphery). At the edge of the FSW weld, where the rotational speed of the tool and travel speed oppose each other, material encounters increasing resistance as it moves through the rapidly narrowing gap between the rotating pin and wall of the FSW weld. This creates a high-pressure region (P2) between the rotating pin and the wall. In contrast, a low-pressure region (P1) is formed at the edge of the FSW weld where the rotational speed of the tool and travel speed are additive. In this case, material flows through the diverging geometry created by the rotating pin and the wall of the FSW weld. Material transferring from P1 towards P2 is not only slowed down but is also rotated in a counter clockwise direction and this vortex like motion in tends to displace material away from the bottom edge of the weld (see Figure 11). This combination of material displacement away and vortex-like motion explains the formation of a defect at an identical location in an actual FSW weld. Figure 11 shows the remarkable correspondence between the output produced during STIR-3D modeling and the shape and location of a defect formed in an actual FSW weld.

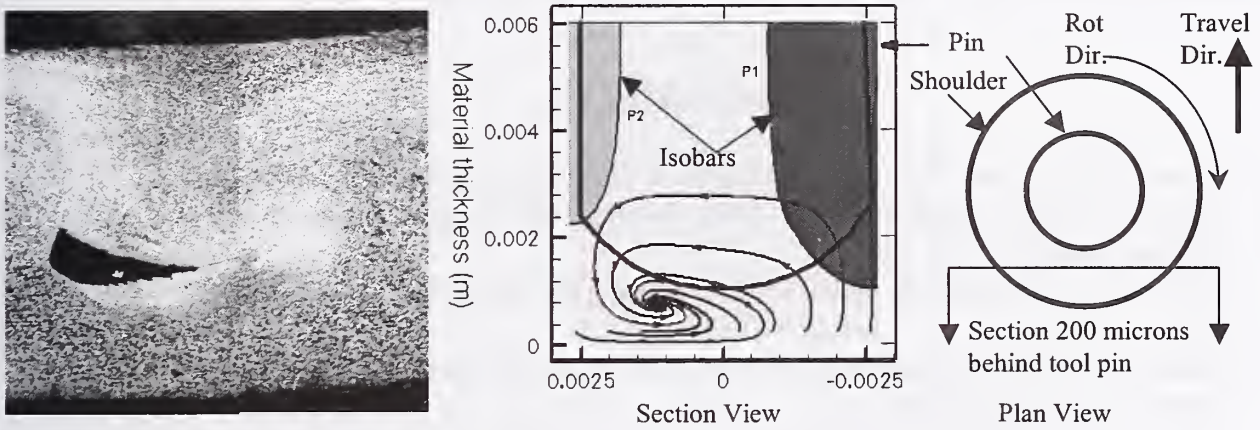

Figure 11: 3-D Model and Corresponding Weld Cross-Section using Smooth Tool

SUMMARY AND CONCLUSIONS

A two-dimensional system (an infinite sea viscometer) has been developed to determine critical material properties for the FSW process. These material properties involve viscosity as a function of shear rate and temperature for a specific aluminum alloy (6061-T6). The material property data was then inputted into a full three-dimensional model (STIR-3D) of the FSW process. This 3D model will yield information about the viability of specific tool designs and lead to a greater understanding of the friction stir welding material flow characteristics. The following conclusions have been made as a result of this modeling effort:

1) During modeling efforts, obtaining accurate measurements of the temperature of the aluminum near the material flow zone is difficult.
2) The principles of fluid mechanics can be applied to the friction stir welding of Al 6061. This modeling effort indicates viscous heat dissipation within the weld as opposed to surface frictional heating is the source of heat generation. Application of the principles of fluid

mechanics to the FSW process will eventually allow for prediction of mixing with the weld, prediction of oxide inclusions, and prediction of weld defects.

3) An infinite sea viscometer system (2D experimental and associated model) predicts critical material properties that can be used for modeling of the FSW process. Given only the power input, rotation speed, plunge rate, and viscosity, the infinite sea viscometer model was able to predict accurately flow profiles and temperature distributions during plunge testing.
4) Plunge testing has shown that the temperature is nearly isothermal within 250 microns of the tool and that the effect of shear rate on viscosity is large.

ACKNOWLEDGEMENTS

The authors would like to acknowledge technical support from Wade Crusan, Tim DeShazer, and Rich Claxton at Tower Automotive and Steve Carian and Terry Allen at A. O. Smith Corp. The authors would also like to acknowledge funding support from NIST (Project #70NAB5H)

REFERENCES

1. Thomas, W.M.; et al. 1991. Friction Stir Butt Welding. U.S. Patent No. 5,460,317.
2. Dawes, C.J.; and Thomas, W.M. 1996. Friction Stir Process Welds Aluminum Alloys, Welding Journal: 75 (3): 41.
3. Nicholas, E.D.; and Kallee, S.W. 1998. Causing a Stir in the Future. Welding & Joining (2): 18-21.
4. Dawes, C. J. 1994. Development of the New Friction Stir Technique for Welding Aluminum – Phase I Report, TWI GSP 5651: (7): 13.
5. Broman, R. E.; Smith, C. B.; Noruk, J. S.; and McDonald, W. M. Challenges of Robotic Welding of Aluminum Structures. Proc. of 38th International Conf. of Metallurgists
6. Singh, J.; and Alpas, A.P. 1996 High Temperature Wear and Deformation Processing Metal Matrix Composites. Metallurgical & Material Transactions: 27A: 1-13.
7. North, T.H.; Bendzsak G. B.; Smith C. B.; Hinrichs J.F.; Noruk, J. S.; and Heideman, R. J. 1999. Submitted to Welding Journal.:
8. Bendzsak, G. B.; North, T. H.; and Li, Z. 1997. Numerical Model for Steady-State Flow in Friction Welding. Acta Metallurgical Material. 45 (4): 1735-1745.
9. Bendzsak, G. B.; and North, T. H. 1997. Numerical Modeling of Fluid Dynamics and Heat Transfer in Friction Welding. Proc. International Seminar of Numerical Analysis of Weldability. ed. H. Czerjack.
10. Bendzsak, G.B.; and North, T. H. 1997. Modeling of Fluid Dynamics and Heat Transfer in Friction Welding. Trans. Japan welding Research. 25 (2): 171-184.
11. Bryant, A.J; Dixon, W; Fielding, A.P; and Macey, G. 1999. Isothermal Extrusion. Light Metal Age: 78 (2): 8-36.
12. Bird, R.R; Stewart, W.E.; and Lightfood, E.N. 1960. Transport Phenomena. 95 New York, NY: John Wiley and Sons.

Tutorials

Developing an Effective Web Page

T.P. Quinn

National Institute of Standards and Technology

Presentation at
http://www.boulder.nist.gov/div853/quinn/webdesign/

The Real Web Designers

- *Creating Killer Web Sites* -- David Siegel www.killersites.com
- *Web Pages That Suck: Learn Good Design by Looking at Bad Design* -- By Vincent Flanders & Michael Willis www.webpagesthatsuck.com
- TLC Systems www.tlc-systems.com

Preparation

- Define your goal
  - Sell something
  - Provide information
  - Form a community

Preparation (cont.)

- Gather content (or at least decide the form)
  - Images
  - Data
  - Text

Organization

- Home page
- Main topic pages
- Subsidiary pages

Home Page

- Purpose: 5 W's
- Kind of Content
- Navigation Scheme

Design Tips: Home Page

- Must be appealing
- Display important information conspicuously
- Keep it small (say 20-50K) (Hold your breath)
- Do not make them scroll

Navigation

- Be consistent
- Make it intuitive
- Try having just one way to get there

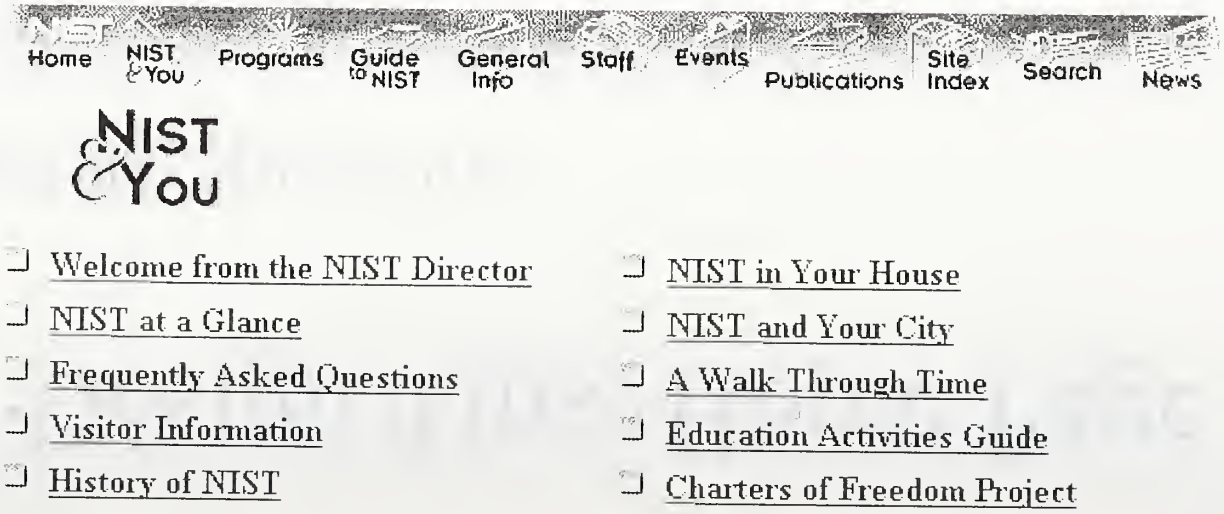

Navigation

- Do not say “click here”
- Be careful not to confuse color text with links
- Do not require mouse position to infer a link

Tips

- Have consistent theme
  - Navigation
  - Color scheme
  - Content organization

Tips

Avoid busy backgrounds

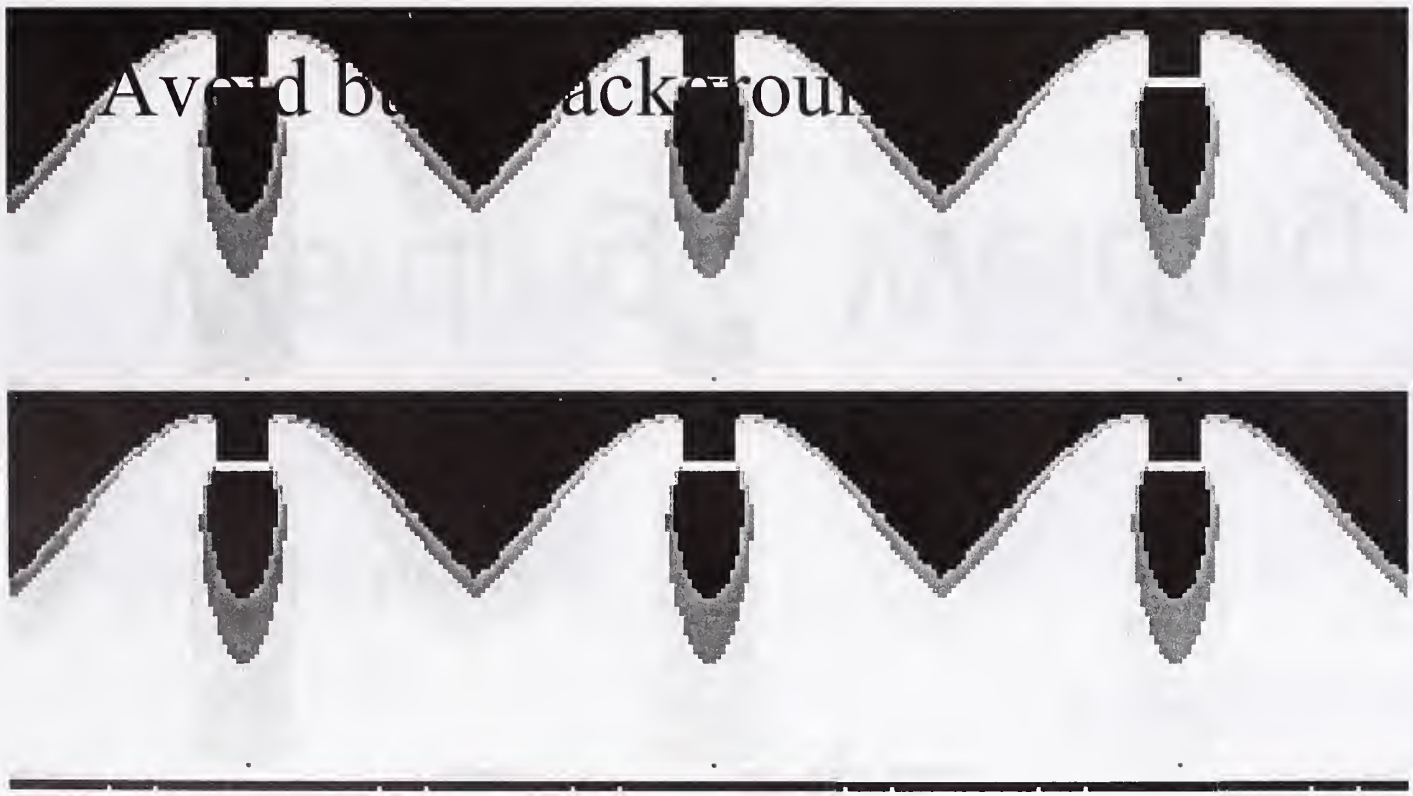

Tips

- Avoid aliasing

Tips

- Use JPEG for photos

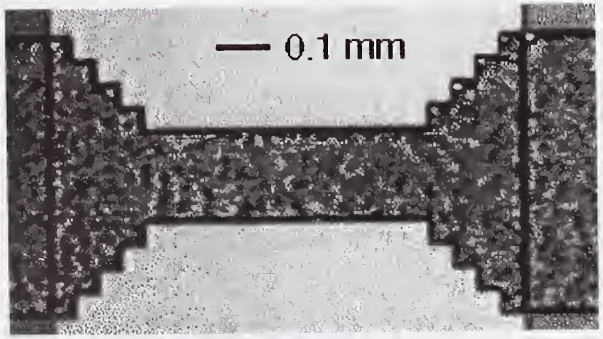

15 KB GIF

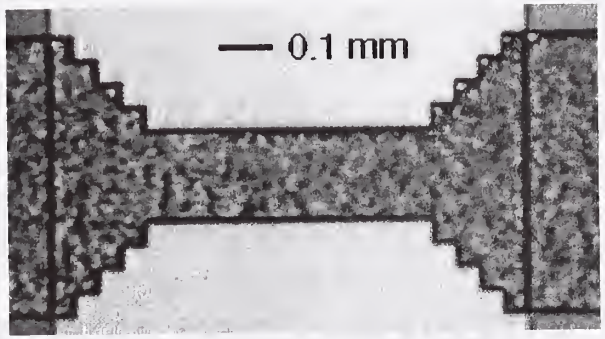

9 KB JPEG with 75% quality parameter

Tips

- Always use height and width tags when inserting an image-- image loads last
- Use alt field for text only browsers

```
<img src="mrd2.gif" alt="MaterialsReliability
Division" align="top" width="409" height="248">
```

Tips

- Use tables

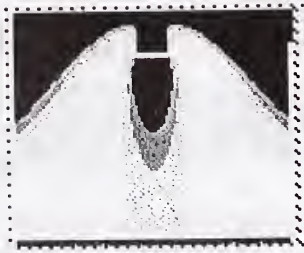

Intelligent Processing of Materials To develop on-line sensors for measuring the materials characteristics and/or processing conditions needed for real-time process control.

Tips

- No plug-ins on home page
- Information should be no more than 2-3 clicks from home page

Testing

- Check out web testing sites (i.e. http://drhtml.imagiware.com)
- Web construction program

RxHTML - Test #11265 - Report Index

Below is a list of pages that were examined by **Doctor HTML**. Each title is hyperlinked to the report itself. The topology analysis of the site is available here

Page	Total Errors	DOC	SPELL	HYP	IMG	Total Size	Total Images	Total HTML	TTL (s)
Microscale Materials Evaluation	0	0							0.0
Materials Reliability Division	18	0	13	0	5	140352	**135082**	5270	78.0
Standard Reference Materials	30	0	29	0	1	18991	3740	15251	10.6
Intelligent Processing of Materials	108	0	107	0	1	47289	8069	39220	26.3

Testing

- Use different browsers and versions
- Turn default settings on
- Turn Java™ off

Testing

- Turn images off
- Use different aspect ratios
- Use different platforms
- Use the print button

Maintenance

- Change can bring people back (i.e. news column)
- Test you external links often
- Contact info on home page
- Follow up
- If possible gather statistics

Finally

- Keep it clean and simple

Networking of Welding Applications

William Rippey, Lance Flitter, Jim Gilsinn

Outline

- What is Networking of Welding Applications?
- Why is networking desireable?
- How do you do it?
- Examples
- Quiz and discussion

Quiz

Why might you want to put your power source on a network?

A. So it can get free email?

B. So it can stay current with the rest of the world?

C. Help its kids with homework?

D. Other

What is Networking of Welding Applications?

- Digital Exchange of Information between welding applications
- Flexible connection
  - physical
  - Logical
- Network hides complexity of communications

What was there before networks?

- Paper, voice
- Point to point electrical links, e.g. analog signals, interlocks, RS-232
- Sneaker net

Why do we need networks?

- Computerization of Welding
- Automation requires more data
- More data requires better/faster communications
- **$$$**

How is a network implemented?

- Medium, connector
- Protocol
- Applications
  - Data Definitions
  - *Nouns, verbs, adjectives*
  - Encoding of data definitions

Medium

- Twisted Pair
- Coax
- Fiber Optics

Connectors

Network Protocols

- Ethernet
- TCP/IP
- DeviceNet
- IPX
- ControlNet
- ARCLink

Variables in network information communication

- Info size
- Frequency of interactions
- Required speed
- Cost
- Number of users

Examples of welding networking

- Intra welding cell
- Intra-factory
- Internet

Applications

- The A9 Welding Information Activity Model
  - Shows applications, called activities
  - Shows information
  - Shows movement of information
  - Does not specify HOW to move information

Activity Model

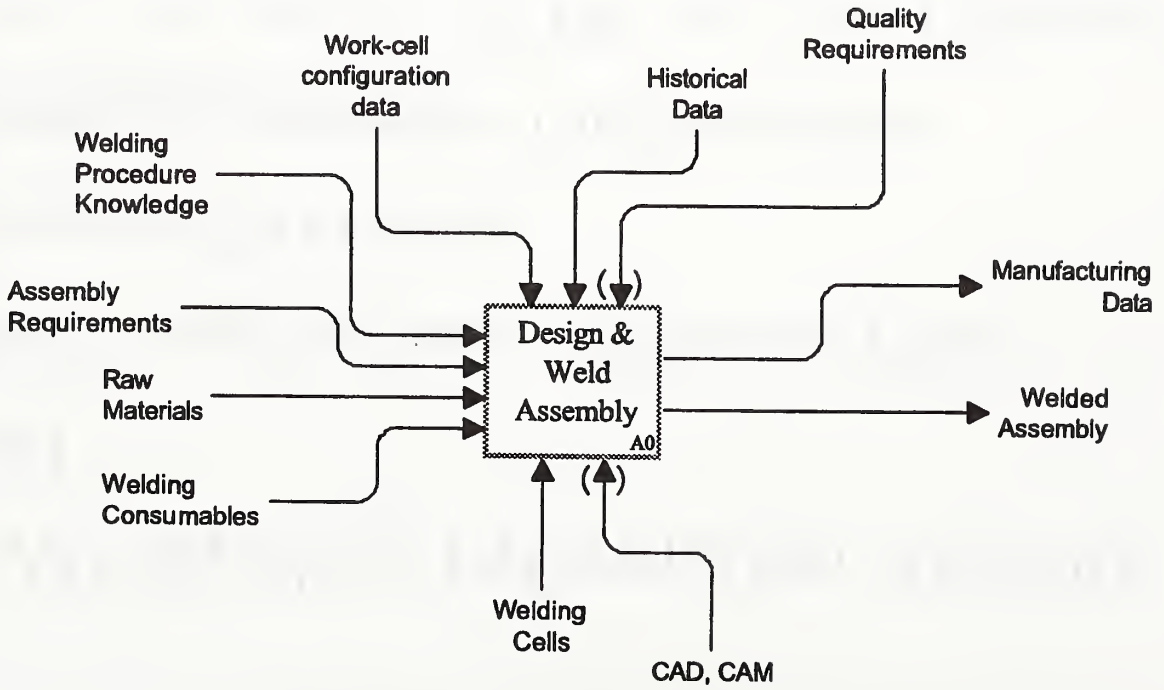

Applications

- Welding Databases
- Planning Systems
- CAD/CAM
- Sensors
- Controllers
- Web Browsers

Applications

- Design
  - Product Design
  - Weldment design
- Planning
  - Process Planning (could include estimating)
  - Programming
- Manufacturing
  - Fabrication
  - Inspection
  - Shipping/Accounting/cost measuring

Networks Future

- Computer Industry is pushing the technology
- Welding Industry needs to define the application of networking technology
- Better, faster, cheaper technology for applications and networks
- Increased use in real-time communications
  - May promote interconnectivity of applications

Quiz

- Why might you want to network your power source?

Appendix A: Participants in Ninth International Conference on Computer Technology in Welding

Appendix A.1: Speakers at the Ninth International Conference on Computer Technology in Welding, September 28-30, 1999, Detroit, Michigan

Mr. Darren M. Barborak
Graduate Research Associate
The Ohio State University
1248 Arthur E. Adams Drive
Columbus, OH 43221

Mr. Zafer Bingul
PhD Candidate
Vanderbilt University
349 Normandy Circle
Nashville, TN 37209

Dr. Annette Brandenburg
Dr.-Ing.
ISF — Welding Institute Aachen
Ponstrasse 49
52062 Aachen 1 Germany

Mr. Andy Brightmore
Manager, Software Development
TWI
Technology Transfer Department
Cambridge CB1 6AL
United Kingdom

Dr. Bill Y.J. Chao
Professor
University of South Carolina
Dept. of Mechanical Engineering
Columbia, SC 29208

Dr. Pawel Cegielski
Assistant Professor
Warsaw University of Technology
Institute of Materials Processing
Welding Department
85 Narbutta Street
02-524 Warsaw, Poland

Dr. Juan R. Donoso
Professor
Universidad Técnica Federica Santa María
Avenida España 1680
Valparaíso, Chile

Dr. John N. Dupont
Assistant Professor
Materials Science & Engineering
Lehigh University
5 East Packer Avenue
Bethlehem, PA 18015

Dr. James R. Dydo
Senior Engineer
EWI
1250 Arthur E. Adams Drive
Columbus, OH 43221

Mr. Erik Engh
General Manager
4X Software AS
Grini Neringspark 1
N-1361 Østerås, Norway

Mr. Lance A. Flitter
Computer Scientist
NSWC
9500 MacArthur Boulevard
Bethesda, MD 20817-5700

Mr. James D. Gilsinn
Electronics Engineer
NIST
Intelligent Systems Division
100 Bureau Drive, Stop 8230
Gaithersburg, MD 20899-8230

Appendix A.1: Speakers at the Ninth International Conference on Computer Technology in Welding, September 28-30, 1999, Detroit, Michigan

Dr. Dariusz Golanski
Assistant Professor
Warsaw University of Technology
Institute of Materials Processing
Welding Department
85 Narbutta Street
02-524 Warsaw, Poland

Dr. Daniel A. Hartman
Los Alamos National Laboratory
PO Box 1663, Mail Stop G770
Los Alamos, NM 87545

Mr. Chris Hsu
Senior Project Engineer
The Lincoln Electric Company
22801 St. Clair Avenue
Cleveland, OH 44117

Mr. Peter W. Hughes
Technical Director
Welding Technology Innovations Pty Ltd.
PO Box 97
Botany, NSW, 2019, Australia

Dr. Jan Paul Huisson
Associate Professor
University of Waterloo
Dept. of Mechanical Engineering
Waterloo, Ontario N2L 3G1 Canada

Dr. Jerald E. Jones
Chief Scientist
NA Technology Company
1317 Washington Avenue
Suite 1
Golden, CO 80401

Dr. You Chul Kim
Associate Professor
JWRI, Osaka University
11-1, Mihogaoka
Ibaraki, Osaka 567-0047, Japan

Mr. Gerald A. Knorovsky
Sr. Member of Technical Staff
Sandia National Lab
1515 Eubank S.E., Mail Stop 0367
Albuquerque, NM 87123

Mr. Poolsak Koseyaporn
Vanderbilt University
Box 1826, Station B.
Nashville, TN 37235

Dr. Radovan Kovacevic
Professor
Mechancial Engineering Dept.
Southern Methodist University
3160 SMU Boulevard
Dallas, TX 75205

Mr. John Lapham
Engineering Manager
Robotic Workspace Technologies, Inc.
17105 San Carlos Boulevard
Suite A-6151
Fort Myers, FL 33931

Mr. Danny O. MacCallum
PTNG
Materials Joining Department
PO Box 5800, Mail Stop 0367
Albuquerque, NM 87185-0367

Appendix A.1: Speakers at the Ninth International Conference on Computer Technology in Welding, September 28-30, 1999, Detroit, Michigan

Mr. Tsuyoshi Maeda
Welding & Joining Research Center
Nippon Steel Corporation
20-1 Shintomi
Futtsu, Chiba, 293-8511 Japan

Dr. Kin-ichi Matsuyama
Visiting Professor
MIT, Mechanical Engineering
77 Massachusetts Avenue
Room 35-231
Cambridge, MA 02139

Dr. Edward A. Metzbower
Branch Head
Naval Research Laboratory
Code 6320
Washington, DC 20375-5320

Dr. Paul E. Murray
Advisory Engineer
Lockheed Martin Idaho Technologies
PO Box 1625
Idaho Falls, ID 83415-2210

Dr. Ole Runar Myhr
Research Scientist
Hydro Raufoss Automotive
PO Box 41
N-2831 Raufoss, Norway

Dr. S.-J. Na
Professor
KAIST
373-1, Kusongdong, Yusonggu
Taejon, 305-701 Korea

Mr. Terumi Nakamura
National Research Center for Metals
1-2-1 Sengen,
Tukuba-shi Ibaraki 305-0047 Japan

Dr. Béla Palotás
Associated Professor
Technical University of Budapest
Bertalan L. U. F.
Budapest, H-1521, Hungary

Dr. Timothy P. Quinn
Mechanical Engineer
NIST - Mail Code 853
Materials Reliability Division
325 Broadway
Boulder, CO 80303

Dr. S. Rajasekara
Assistant Professor
Dept. of Production Engineering
Amrita Institute of Technology & Science
Ettimadai Post, Coimbatore 641 105
Tamil Nadu, India

Mr. William G. Rippey
Electrical Engineer
NIST
Intelligent Systems Division
Manufacturing Engineering Laboratory
100 Bureau Drive, Stop 8230
Gaithersburg, MD 20899-8230

Dr. Thomas A. Siewert
Deputy Chief
NIST - Mail Code 853
Materials Reliability Division
325 Broadway
Boulder, CO 80303

Appendix A.1: Speakers at the Ninth International Conference on Computer Technology in Welding, September 28-30, 1999, Detroit, Michigan

Mr. Christopher B. Smith
Sr. Mechanical Engineer
Tower Automotive
3533 N. 27th Street
Milwaukee, WI 53216

Dr. Wenqi Zhang
Associate Professor
Department of Manufacturing Engineering
Technical University of Denmark
Building 425
2800 Lyngby, Denmark

Prof. Michael Zinigrad
Professor
The College of Judea & Samaria
Ariel, Israel, 44837

Appendix A.2: Attendees of the Ninth International Conference on Computer Technology in Welding, September 28-30, 1999, Detroit, Michigan

Mr. Pat Brousset
Ingenieur Systeme
Framatome Technologies
Plant Component Repair Equipements de Soudage
3315 Old Forest Road/PO Box 10935
Lynchburg, VA 24506-0935

Mr. Dave Cottle
Welding Engineer
DC Fabricators
801 W. Front Street
Florence, NJ 08053

Mr. Eric Halloran
617 Bradley Street
Dubuque, IA 52003

Mr. Dan Hayden
Staff Scientist
GM R&D Center
30500 Mound Road
Warren, MI 48090

Mr. Timothy Heston
Assistant Editor
American Welding Society
550 NW LeJeune Road
Miami, FL 33126

Mr. Carl F. Klein
Manager New Technology
Johnson Controls, Inc.
Automotive Systems Group
49200 Halyard Drive/PO Box 8010
Plymouth, MI 48170

Siri Klokkehaug
Research Scientist
Institute for Energy Technology
Materials and Corrosion Technology Dept.
PO Box 40
N-2007 Kjeller, Norway

Dr. Arnt O. Kluken
Head of Joining Technology Group
Hydro Raufoss Automotive Research Center
PO Box 41
N-2831 Raufoss, Norway

Dr. Kishore N. Lakalapalli
Product Development Engineer
FANUC Robotics North America
3900 W. Hamlin Road
Rochester Hills, MI 48309-3253

Dr. Lin Li
Advanced Welding Engineer
Hydro Raufoss Automotive
365 West 24th Street
Holland, MI 49423

Mr. John F. Negri
APEX Technical School
635 Avenue of the Americas
Manhattan, NY 10011

Mr. Alan R. Nywening
Ingersoll Rand
942 Memorial Parkway
Phillipsburg, NJ 08865

Mr. Juan E. Ochoa
109 South Summit Avenue
Gaithersburg, MD 20877

Appendix A.2: Attendees of the Ninth International Conference on Computer Technology in Welding, September 28-30, 1999, Detroit, Michigan

Mr. Mark A. Onderick
Welding Engineer
John Deere Dubuque Works
18600 John Deere Road
Dubuque, IA 52004

Mr. Sankaran Subramaniam
Technical Specialist
Ford Motor Company
MD 3135, PO Box 2053
Dearborn, MI 48121

Mr. Ilhan Varol
Caterpillar, Inc.
Technical Center
Peoria, IL 61656

Mr. Robert J. Whittman, Jr.
Senior Manufacturing Engineer
DELPHI Automotive Systems
Chassis Systems
Kettering Operations
M/C F.48
PO Box 1042 45401-1042
2000 Forrer Boulevard
Dayton, OH 45420

*U.S. GOVERNMENT PRINTING OFFICE: 2000-460-746-26656

NIST Technical Publications

Periodical

Journal of Research of the National Institute of Standards and Technology—Reports NIST research and development in those disciplines of the physical and engineering sciences in which the Institute is active. These include physics, chemistry, engineering, mathematics, and computer sciences. Papers cover a broad range of subjects, with major emphasis on measurement methodology and the basic technology underlying standardization. Also included from time to time are survey articles on topics closely related to the Institute's technical and scientific programs. Issued six times a year.

Nonperiodicals

Monographs—Major contributions to the technical literature on various subjects related to the Institute's scientific and technical activities.

Handbooks—Recommended codes of engineering and industrial practice (including safety codes) developed in cooperation with interested industries, professional organizations, and regulatory bodies.

Special Publications—Include proceedings of conferences sponsored by NIST, NIST annual reports, and other special publications appropriate to this grouping such as wall charts, pocket cards, and bibliographies.

National Standard Reference Data Series—Provides quantitative data on the physical and chemical properties of materials, compiled from the world's literature and critically evaluated. Developed under a worldwide program coordinated by NIST under the authority of the National Standard Data Act (Public Law 90-396). NOTE: The Journal of Physical and Chemical Reference Data (JPCRD) is published bimonthly for NIST by the American Chemical Society (ACS) and the American Institute of Physics (AIP). Subscriptions, reprints, and supplements are available from ACS, 1155 Sixteenth St., NW, Washington, DC 20056.

Building Science Series—Disseminates technical information developed at the Institute on building materials, components, systems, and whole structures. The series presents research results, test methods, and performance criteria related to the structural and environmental functions and the durability and safety characteristics of building elements and systems.

Technical Notes—Studies or reports which are complete in themselves but restrictive in their treatment of a subject. Analogous to monographs but not so comprehensive in scope or definitive in treatment of the subject area. Often serve as a vehicle for final reports of work performed at NIST under the sponsorship of other government agencies.

Voluntary Product Standards—Developed under procedures published by the Department of Commerce in Part 10, Title 15, of the Code of Federal Regulations. The standards establish nationally recognized requirements for products, and provide all concerned interests with a basis for common understanding of the characteristics of the products. NIST administers this program in support of the efforts of private-sector standardizing organizations.

Order the **following** *NIST publications—FIPS and NISTIRs—from the National Technical Information Service, Springfield, VA 22161.*

Federal Information Processing Standards Publications (FIPS PUB)—Publications in this series collectively constitute the Federal Information Processing Standards Register. The Register serves as the official source of information in the Federal Government regarding standards issued by NIST pursuant to the Federal Property and Administrative Services Act of 1949 as amended, Public Law 89-306 (79 Stat. 1127), and as implemented by Executive Order 11717 (38 FR 12315, dated May 11, 1973) and Part 6 of Title 15 CFR (Code of Federal Regulations).

NIST Interagency or Internal Reports (NISTIR)—The series includes interim or final reports on work performed by NIST for outside sponsors (both government and nongovernment). In general, initial distribution is handled by the sponsor; public distribution is handled by sales through the National Technical Information Service, Springfield, VA 22161, in hard copy, electronic media, or microfiche form. NISTIR's may also report results of NIST projects of transitory or limited interest, including those that will be published subsequently in more comprehensive form.

U.S. Department of Commerce
National Institute of Standards and Technology
325 Broadway
Boulder, Colorado 80303-3328